NUREG/CR-4308
SAND85-1370
R3, R4, R7
Printed July 1986

VANESA: A Mechanistic Model of Radionuclide Release and Aerosol Generation During Core Debris Interactions With Concrete

D. A. Powers, J. E. Brockmann, A. W. Shiver

Prepared by
Sandia National Laboratories
Albuquerque, New Mexico 87185 and Livermore, California 94550
for the United States Department of Energy
under Contract DE-AC04-76DP00789

Prepared for
U. S. NUCLEAR REGULATORY COMMISSION

Available from

Superintendent of Documents
U.S. Government Printing Office
Post Office Box 37082
Washington, D.C. 20013-7982

and

National Technical Information Service
Springfield, VA 22161

NUREG/CR-4308
SAND85-1370
R3, R4, R7

VANESA: A Mechanistic Model of Radionuclide Release and Aerosol Generation During Core Debris Interactions With Concrete

D. A. Powers
J. E. Brockmann
A. W. Shiver

July 1986

Sandia National Laboratories
Albuquerque, New Mexico 87185
Operated by
Sandia Corporation
for the
U.S. Department of Energy

Prepared for
Division of Accident Evaluation
U.S. Nuclear Regulatory Commission
Washington, DC 20555
NRC FIN No. A1019

ABSTRACT

This document describes a model, called VANESA, of the release of radionuclides and generation of aerosol accompanying reactor core melt interactions with structural concrete. The document also serves as a user's manual for an implementation of the VANESA model as a computer code.

The technical bases for the VANESA model are reviewed. This review includes a description of the thermodynamics and kinetics of vaporization from melts sparged by gases evolving from concrete. The thermochemistries of 25 elements of interest in reactor accident analyses are described. Limitations to the rate of vaporization caused by condensed phase mass transport, surface processes, and gas phase mass transport are discussed. Limitations on the extent of vaporization caused by the behavior of bubbles rising in a melt are treated.

Mechanical generation of aerosols as bubbles burst at melt surfaces or as a result of liquid entrainment is considered. A description of these processes based on data for gas-sparged water systems is included in the VANESA model.

Some limiting solutions to the problem of the competitive processes of nucleation of particles from vapor, condensation of vapors on surfaces, and coagulation of particles are examined. From these examinations an approximate model of the aerosol particle size produced during core debris interactions with concrete is devised.

The attenuation of aerosol emission during core debris/concrete interactions by an overlying water pool is discussed. A model of the attenuation is developed. In this model aerosol entrapment is considered to be the result of particle diffusion, inertial impaction, and sedimentation within gas bubbles rising through the water pool. Allowances are made in the model for nonspherical bubbles.

The document concludes with a description of a computer code implementation of the VANESA model. This implementation of the model was used in recent assessments of the behavior of radionuclides during severe reactor accidents. Comparisons of the predictions of radionuclide release during core debris/concrete interactions obtained with the VANESA model and with older models are presented.

CONTENTS

CONTENTS (Continued)

CONTENTS (Continued)

LIST OF FIGURES

LIST OF FIGURES (Continued)

LIST OF FIGURES (Continued)

LIST OF FIGURES (Continued)

LIST OF FIGURES (Continued)

LIST OF FIGURES (Continued)

LIST OF TABLES

LIST OF TABLES (Continued)

LIST OF TABLES (Continued)

LIST OF TABLES (Continued)

I. INTRODUCTION TO THE VANESA MODEL AND ITS USES IN SEVERE REACTOR ACCIDENT ANALYSES

VANESA is a mechanistic model of the release of radionuclides and generation of aerosols during the later stages of a severe reactor accident when reactor core debris interacts with the concrete foundation of the reactor containment. This document describes the technical rationale for the physical and chemical models that make up VANESA. The last chapter of this document describes an implementation of the model as a computer code.

The interactions of high temperature core debris with the concrete foundation of a reactor containment is a most important phase of severe reactor accidents. Since the publication of the Reactor Safety Study in 1975,[1] the loads placed on reactor containments by these interactions and the release of radionuclides from the core debris that occurs during these interactions have been included in severe accident analyses. Early analyses of the interactions were hampered by the lack of experimental data. The analyses were based, therefore, on simple bounding models. These models were intended to be conservative to compensate for unknown or unappreciated features of the interactions.

Substantial improvements have developed in the understanding of severe accident phenomena since publication of the Reactor Safety Study. The many experimental and analytic investigations into core debris interactions with concrete have led to significant revisions of the descriptions of these interactions used in the Reactor Safety Study. Equally dramatic improvements have been made in the ability to predict the response within the reactor containments to accident phenomena.

The VANESA model was formulated to predict radionuclide release and aerosol generation during core debris/concrete interactions in a manner that takes advantage of the many improvements in technology that have occurred since the Reactor Safety Study. A key objective in formulating the model was to obtain predictions that were realistic and avoided deliberately conservative, bounding, assumptions. In this, the VANESA model is a departure from the approach toward radionuclide behavior adopted in past analyses. Realistic estimates of radionuclide release and aerosol generation are essential if the full capabilities of modern tools for predicting phenomena within reactor containments are to be employed in accident analyses. Realistic estimates also permit an understanding of how the peculiarities of reactor plants and accident sequences affect ex-vessel

release and aerosol generation. The efficacy of natural or engineered safety features can be evaluated only if models employed in the analyses portray physical and chemical processes in realistic fashion.

The VANESA model predicts the following features of the radionuclide release and aerosol generation during core debris interactions with concrete:

1. The total mass of aerosol generated and the rate of generation.

2. The concentration of aerosols in the gases evolved during core debris attack on concrete.

3. The composition of the aerosol including the contributions of nonradioactive materials as well as those of radionuclides.

4. The size and size distribution of the aerosols.

5. The material density of the aerosol.

6. The effects coolant pools overlying core debris will have on the production and nature of aerosols.

This body of predictions from the VANESA model is commonly referred to as the "ex-vessel source term." An effort has been made to tailor the predictions of the ex-vessel source term so that they satisfy the input needs of other models used in accident analyses.

The predictions obtained from the VANESA model are in some cases different than the "conventional wisdom" that has been developed from simpler, supposedly bounding models of the ex-vessel source term used in the past. Discussions of the uses that have been made of the VANESA model and the substantive predictions obtained from the model are presented in the next chapter of this document. A thorough discussion of the technology available for the formulation of the VANESA model is attempted in subsequent chapters. This discussion of the technical bases for the model is presented to rationalize the approximations adopted by the model. It also provides an indication of where the model could be improved. The document concludes with a description of a first attempt to implement the model as a computer code.

II. HISTORICAL BACKGROUND AND SUBSTANTIVE PREDICTIONS OF THE VANESA MODEL

Experimental studies of the interactions of reactor core debris with concrete have been sponsored at Sandia National Laboratories for several years by the U.S. Nuclear Regulatory Commission (USNRC). These experiments have shown that models of the ex-vessel core debris interactions with concrete developed for the Reactor Safety Study did not accurately portray the phenomena arising in these interactions that could affect the nature of severe reactor accidents. In response to these experimental findings, the USNRC initiated a program to develop a revised model of ex-vessel core debris behavior. This program has produced the CORCON code[5,6] which describes the thermal and chemical aspects of the attack on concrete by reactor core debris.

The experimental investigations demonstrated that large quantities of aerosols were produced during core debris interactions with concrete.[11] A photograph in Figure 1 shows the production of aerosols during the sustained interaction of about 220 kg of stainless steel at 1700°C with limestone concrete. Aerosol concentrations in the gases evolved as molten steel attacked concrete during this test were about 9 grams per cubic meter of gas at standard pressure and temperature. In tests with so-called "corium" (54 w/o UO_2, 16 w/o ZrO_2, and 30 w/o stainless steel) melts, aerosol concentrations in excess of 100 grams per cubic meter were observed.[12]

Aerosol generation was not considered explicitly in the CORCON development effort although it was obvious from the test results that the aerosol production during core debris/concrete interactions was quite different than that predicted by the models developed for the Reactor Safety Study. Empirical correlation of experimental data led to a model which has recently been termed the Murfin-Powers correlation:[16]

$$[A] = A_o \exp(-E/RT)\ (\alpha V_s + \beta)$$

where [A] = aerosol mass per cubic meter of gas at standard pressure and temperature evolved during core debris attack on concrete (g/m^3),

V_s = superficial velocity of evolved gas passing through the melt at the bulk melt temperature (m/s),

T = absolute melt temperature (K),

R = gas constant,

Figure 1. Photograph Showing Aerosol Productior When About 220 kg of Stainless Steel at 1700°C Interacts With Concrete

$E = 37800$ cal/mole,

$A_o = 10^4$,

$\alpha = 24$, and

$\beta = 3.3$.

This correlation has many attractive features. Aerosol production is, as would be expected, dependent on both temperature and the gas generation rate. The activation energy, E, which characterizes the temperature dependence of aerosol production, has a value that might be expected for vaporization processes involving chemical reactions of melt constituents with evolved gases. Aerosol generation does not go to zero as the superficial velocity of evolved gas goes to zero. The parameter β in the correlation reflects, apparently, a contribution to aerosol release by natural convection of gases over the melt surface. The correlation suffers, however, from all of the failings of an empirical correlation of experimental data. First, parametric values in the correlation (E, $A_o\alpha$, and $A_o\beta$) are determined by fitting the model equation to experimental data. This ties the correlation to the underlying data base and makes application of the model to situations not investigated experimentally most difficult to justify. Second, the correlation does not yield aerosol composition information. Experimental composition data were used directly and without scaling to ascertain the extent of radionuclide release predicted with this correlation. Use of experimentally determined aerosol compositions, again, ties the model intimately to the underlying data base and makes predictions for the diverse circumstances encountered in severe accident analyses quite uncertain. When this uncertain procedure was used, the results suggested that the model developed for the Reactor Safety Study was not a conservative upper bound on ex-vessel radionuclide release.[14]

In 1981, the USNRC initiated a study of the available data concerning the behavior of radionuclides during severe reactor accidents. The intent of this effort was to rationalize fission-product releases observed during the reactor accident at Three Mile Island,[15] to ascertain if the observations had generic applicability to all severe reactor accidents, and to determine if there was a technical basis for altering regulations concerning radionuclide behavior during accidents. The considerations in this review were focused on the behavior of more volatile radionuclides such as Cs, I, and Te during the in-vessel phases of an accident. Radionuclide releases from core debris outside the reactor vessel were not examined in detail. Results of the review were published in a document commonly referred to as NUREG-0772.[16] An important conclusion of the review was that substantial

improvements had occurred in the understanding of radionuclide behavior under accident conditions since the publication of the Reactor Safety Study. The improved understanding made it possible to revise methods for estimating the potential releases of radionuclides during severe reactor accidents.

Shortly after completion of NUREG-0772, an effort was initiated by the NRC to use available models to reassess source terms for radionuclides during severe reactor accidents. Again, the initial focus of this work was on the release and transport of radionuclides within reactor coolant systems. In the fall of 1982, it was recognized that models of ex-vessel release of radionuclides developed for the Reactor Safety Study, too, might deserve improvement. An informal request concerning such improved ex-vessel models was made by the NRC of Sandia National Laboratories.

In response to these requests, the VANESA model was developed. The intent in this development was to produce a mechanistic model for prediction of both radionuclide release and aerosol generation during core debris interactions with concrete. Deliberately conservative assumptions were avoided. Simple correlations of empirical data were not used. An effort was made to devise a model of sufficient depth and sophistication that it would mesh well with future "best-estimate" models of accident phenomena as well as with cruder, risk-assessment, codes available at the time. This treatment of release was adopted recognizing that code validation would be based on small-scale tests. A mechanistic basis is essential to confidently extrapolate from tests to large-scale situations that have not been examined experimentally.

The relationships between the VANESA model of ex-vessel radionuclide and aerosol generation and other models of severe accident phenomena are shown in Figure 2. The VANESA model requires input concerning initial conditions derived from models of core meltdown and radionuclide release within the reactor coolant system. Boundary conditions for the analyses done with the VANESA model are provided by models of core debris interactions with concrete. Results obtained with the VANESA model provide inputs to containment response models and models of engineered safety systems such as steam suppression pools in boiling water reactors.

In the development of the VANESA model, an attempt was made to address ex-vessel release to a level of sophistication consistent with phenomenological treatments in the CORCON[5,6] model of core debris/concrete interactions and the CONTAIN[10] model of containment response.

The earliest applications of the VANESA model were for the NRC-sponsored source term reassessments.[2] In these

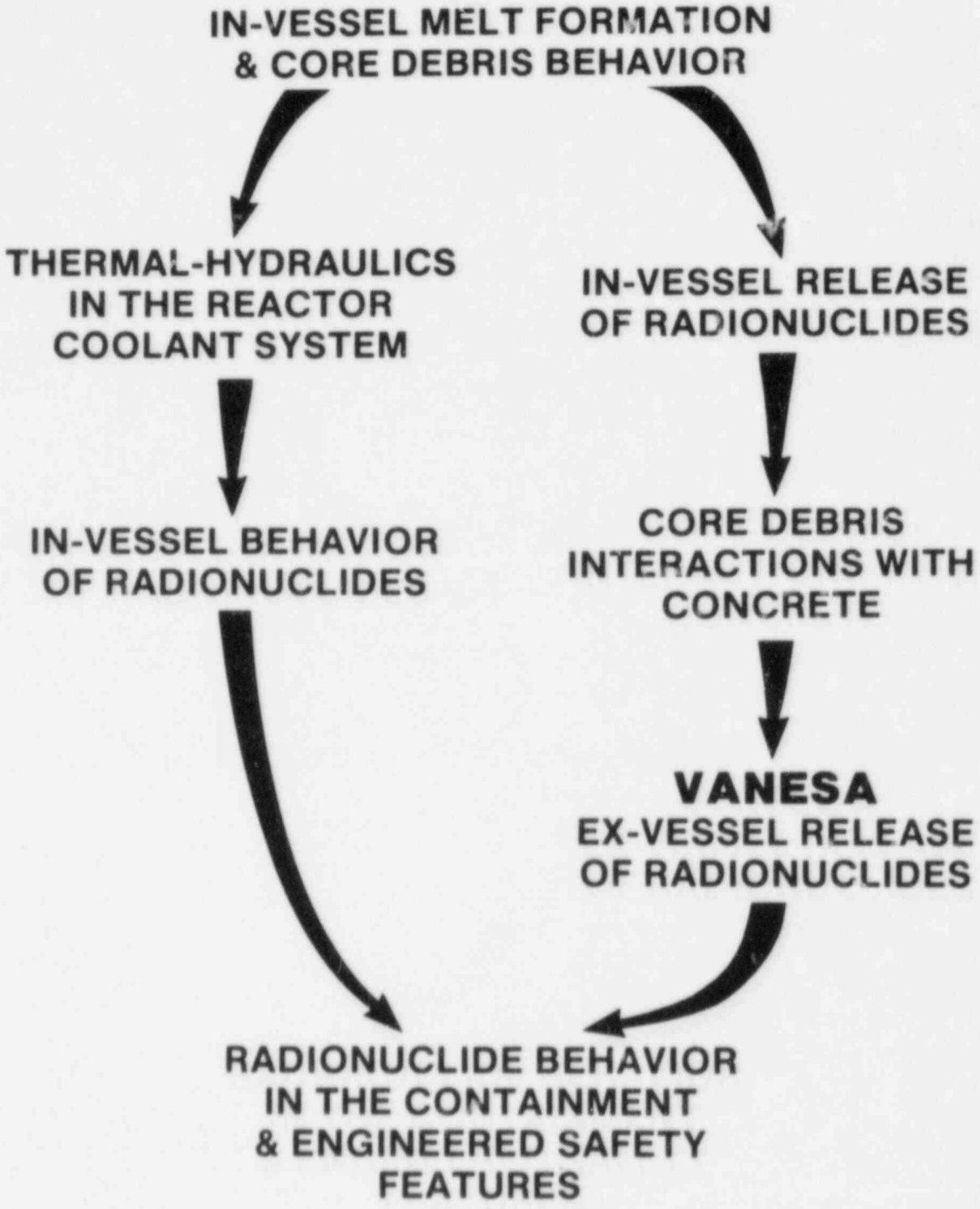

Figure 2. Relationship Between the VANESA Model and Other Phenomena Models Used in the Severe Accident Source Term Evaluation

analyses, initial condition inputs to the model were derived from the risk assessment models of in-vessel processes (MARCH[3]) and in-vessel release (CORSOR[4]). CORCON(mod1)[5] was used to provide boundary condition information concerning core debris/concrete interactions. Results obtained with the VANESA model were used as input to the NAUA-4 model[7] of aerosol behavior within containment and the SPARC model[8] of aerosol trapping by steam suppression pools.

The VANESA model has been used in the analyses of many types of reactors and accidents. For the reassessment effort the model was used in the analysis of about 16 accident sequences hypothesized to occur at the Peach Bottom (Mark I BWR), Grand Gulf (Mark III BWR), Sequoyah (ice condenser containment PWR), Surry (subatmospheric containment PWR), and the Zion (large, dry containment PWR) plants. More recently, the model has been used in analyses of accidents at the Kuo Sheng, Limerick (Mark II BWR), the FitzPatrick (Mark I BWR), and the Brown's Ferry (Mark I BWR) reactors.

These many analyses have shown that the VANESA model frequently produces a substantially different portrait of ex-vessel radionuclide release and aerosol generation than that derived from the model developed for the Reactor Safety Study.[1] The more substantive predictions obtained from the VANESA model are discussed below.

1. Aerosol generation during core debris interactions with concrete is not as intense but lasts far longer than aerosol production during in-vessel phases of an accident

The total rate of aerosol production during a particular, hypothesized reactor accident is shown as a function of time in Figure 3. The aerosol production in-vessel lasts for about 30 minutes. Peak rates of aerosol generation of nearly 1000 g/s are predicted by the combination of the MARCH and the CORSOR models. The peak rates of ex-vessel aerosol production predicted with the VANESA model are about an order of magnitude lower. But, the ex-vessel aerosol production persists for many hours. In fact, aerosol production had not ceased when the calculations were terminated after 10 hours of core debris/concrete interactions.

The timing of ex-vessel aerosol production predicted by the VANESA model is quite different than that arbitrarily assumed in the model used in the Reactor Safety Study. The Reactor Safety Study model was based on an assumption that significant radionuclide release would occur for only two hours after the start of melt/concrete interactions. As shown in Figure 4, the aerosol production is predicted with the Reactor Safety Study model to cease in some accidents just when the VANESA model predicts the production rate to reach a maximum.

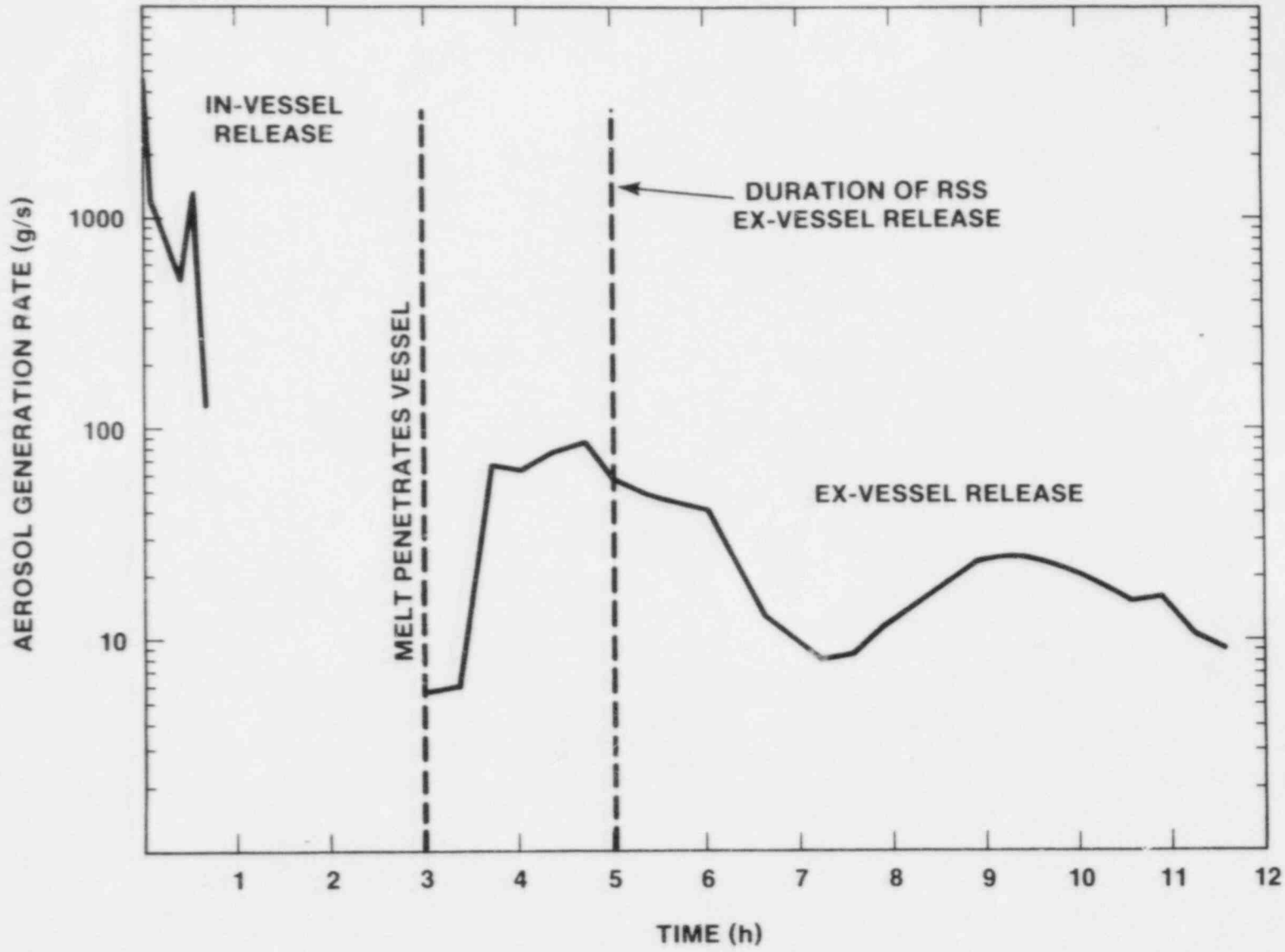

Figure 3. Comparison of the Rate and Duration of Aerosol Generation During the In-Vessel and Ex-Vessel Stages of a Severe Accident

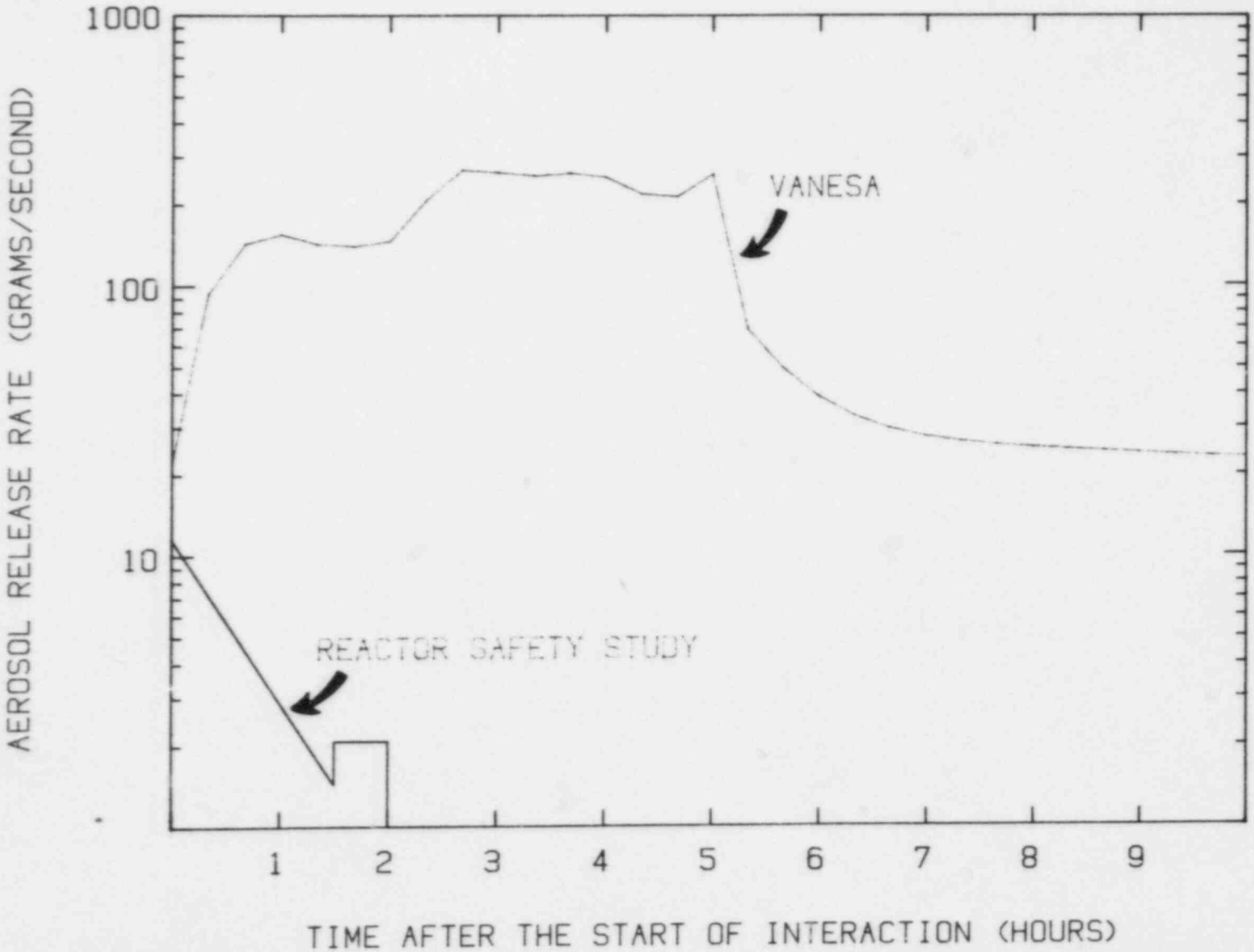

Figure 4. Comparison of the Rates of Aerosol Generation Predicted With the VANESA Model and the Reactor Safety Study Model

2. Aerosols produced during ex-vessel core debris interactions are predicted to consist primarily of nonradioactive materials

The Reactor Safety Study model does not treat aerosol production from sources other than the reactor fuel and radionuclides. The VANESA model includes analyses of vaporization and aerosol formation by constituents of the fuel cladding, control rods, structural steels, concrete as well as aerosol formation by fuel and radionuclides. In most cases the nonradioactive materials are the dominant source of aerosols. The relative contributions of constituents of concrete, steel, and core materials (fuel, clad, etc.) and radionuclide to the aerosol predicted to be produced during a typical reactor accident are shown in Figure 5. Initially, core materials and radionuclides make nearly equal contributions to the aerosol. But, as concrete is ablated, constituents of concrete quickly become major contributors to the aerosol. Of course, the precise values of the contributions of constituents of concrete, steel, and core materials to aerosols produced during melt interactions with concrete vary according to the details of the plant and accident in question. The trend for radionuclides to be very low level contributors and nonradioactive materials to be the dominant contributors is generally predicted. The aerosol mass produced by these nonradioactive sources is of significant importance to the prediction of radionuclide behavior in the containment.[9]

3. The nature of release is quite dependent on plant and accident features

The Reactor Safety Study model was intended to conservatively bound the radionuclide releases that accompany core debris interactions with concrete. The estimates obtained from this model were thought to be of generic applicability to all plants and accidents. Integral release fractions assumed in the Reactor Safety Study model for seven isotopes are shown in Table 1.

The realistic estimates obtained from the VANESA model are sensitive to the features of the plant and accident in question. Estimates of the release for two hypothesized accidents are shown in Table 1. These estimates are shown as ranges rather than point values to reflect the results of sensitivity studies of the VANESA predictions.[9] The results, even recognizing the uncertainty ranges ascribed to the results from sensitivity studies, are quite different. They also differ from the estimates obtained from the Reactor Safety Study model. The sensitivity studies have shown that predictions obtained from the VANESA model are quite dependent on initial conditions specified as input to the model.

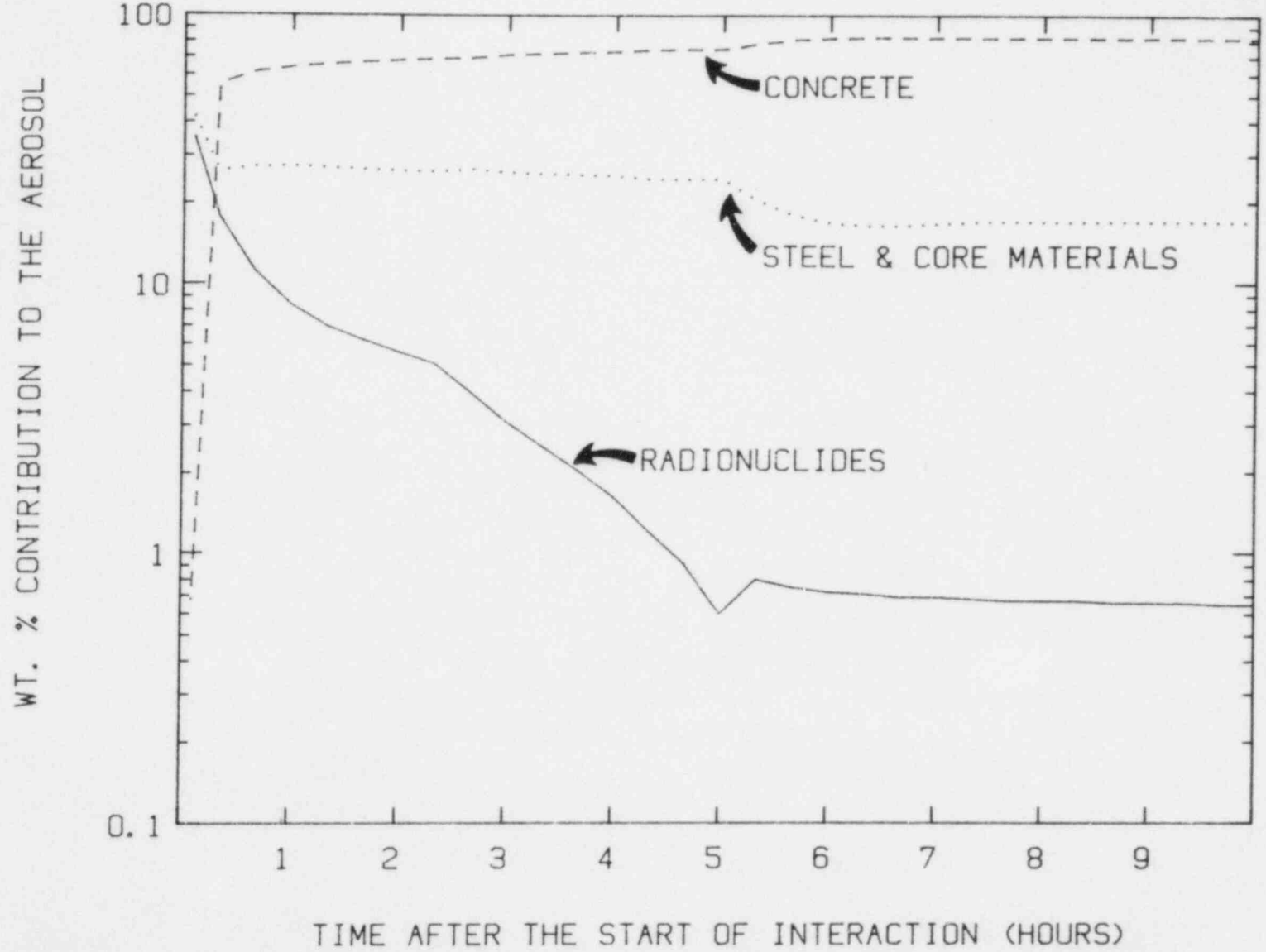

Figure 5. Comparison of the Relative Contributions of Radionuclides and Nonradioactive Materials to the Aerosol Generated During Core Debris Interactions With Concrete

Table 1

Comparison of the Cumulative Radionuclide Releases Predicted With the VANESA Model and the Reactor Safety Study Model

		Ex-Vessel Release Fractions* VANESA Release Predictions for	
	Reactor Safety Study	TMLB' Accident at	AE Accident at
Element	Release Prediction+,[a]	Surry[b]	Peach Bottom[c]
Xe	1.0	1.0	1.0
Cs	1.0	1.0	1.0
I	1.0	1.0	1.0
Te	1.0	0.18-0.62	0.56-0.77
Ba	0.01 (0.002-0.05)	0.0082-0.33	0.32-0.60
Sr	0.01 (0.002-0.05)	0.001-0.66	0.62-0.836
Ru	0.05 (0.01-0.25)	$<5\times10^{-4}$	$<5\times10^{-4}$
La	0.01 (0.002-0.05)	3×10^{-4}-0.29	0.012-0.057
Ce	0.01 (0.002-0.05)	1×10^{-5}-0.21	0.023-0.082

*Fraction of the inventory in the debris at the melt interaction with concrete start.
+Generic prediction--applicable to all reactors.
[a]Uncertainty ranges quoted in Reference 1 are indicated within parentheses.
[b]Siliceous concrete.
[c]Limestone concrete.

These initial conditions are typically obtained from models such as MARCH and CORSOR. The predictions are also somewhat sensitive to the modeling of core debris/ concrete interactions and the nature of concrete assumed to be present in the plant.

4. The extent of radionuclide release is predicted to be different than assumed in the Reactor Safety Study

Examination of results presented in Table 1 shows that predictions of the integral releases of cesium and iodine by the VANESA model and the Reactor Safety Study model are quite similar. The integral release of tellurium is predicted by the VANESA model to be less than the prediction from the Reactor Safety Study model. Some caution needs to be attached to this finding. Tellurium release is predicted usually to be occurring at a significant rate when calculations with the VANESA model are terminated. Had calculations been continued, tellurium release might have approached the value assumed in the Reactor Safety Study. The release rate of tellurium is, however, predicted by the VANESA model to be slower than the rate assumed in the Reactor Safety Study model.

VANESA predictions of the releases of radionuclides such as Ru, Mo, Tc, and Pd are always much less than was assumed in the Reactor Safety Study.

Of more interest perhaps are the predictions obtained with the VANESA model concerning release of the more refractory radionuclides such as Sr, Ba, La, and Ce. In some calculations, integral releases of these refractory elements are predicted to be comparable or even much less than was assumed in the Reactor Safety Study model. In other cases, the refractory radionuclide releases are found to be many times higher than was thought when the Reactor Safety Study model was devised. The VANESA model predictions suggest that there are cases where the Reactor Safety Study model predictions do not conservatively bound releases of the refractory radionuclides.

5. Ex-vessel release can maintain radioactivity suspended in the containment atmosphere

Aerosols evolved ex-vessel accentuate the agglomeration and sedimentation of radioactive particulate injected into the containment atmosphere as a result of the earlier, in-vessel, accident processes. VANESA predictions of the ex-vessel source term lead to particularly efficient sweeping of the atmosphere by these aerosol processes since the VANESA predictions include aerosol mass contributed by nonradioactive sources. But, the radionuclides lost from the atmosphere are replaced by radionuclides released from the core debris ex-vessel. These radionuclides released ex-vessel,

too, agglomerate and settle. However, as long as they are replenished by further ex-vessel releases, there will be suspended radioactivity available for release from the plant should the containment rupture.

The more protracted ex-vessel release predicted with the VANESA model means that a significant inventory of releasable radioactivity is available for long periods as particulate suspended in the containment atmosphere.

The importance of the timing of radionuclide release can be seen by examining the plant releases of Cs, I, and Te shown in Table 2. This table shows the amount of radioactivity that escapes into the environment after natural mitigation processes have operated on material released from the core debris. In all cases, a larger fraction of the tellurium inventory escapes the plant than either cesium or iodine. In some cases, the plant release fraction of tellurium is an order of magnitude larger than the cesium or iodine release fractions. Cesium and iodine escape the reactor fuel early in an accident and are subjected to natural mitigation processes for long periods of time. Tellurium, on the other hand, is released predominantly late in an accident and ex-vessel. The tellurium release occurs slowly so that there is some available to escape the plant even if containment rupture occurs many hours after initiation of the accident.

6. Water pools overlying the debris interacting with concrete can sharply attenuate aerosol emissions into the reactor containment

Water may enter the reactor cavity when core debris is interacting with the concrete. Water can be admitted to the cavity as a deliberate measure to arrest the accident. Or, water may enter the cavity as a natural consequence of the accident. The presence of this water was not considered in developing the Reactor Safety Study model. Water pools overlying the debris are considered in the VANESA model. Such water pools are found to efficiently scrub aerosols from gases evolved during the core debris/concrete interaction. A comparison of the ex-vessel source term for an accident with and without a water pool overlying core debris interacting with concrete is shown in Figure 6. The water pool in this hypothetical accident attenuates aerosol emissions to the containment by about an order of magnitude.

It is clear that the VANESA model is different than previous models of aerosol production and radionuclide release during core debris interactions with concrete. It is clear also that these differences can affect the estimates of radioactive material releases from a plant during an accident. The technical considerations that produced these differences in the modeling of ex-vessel releases are the subjects of the next five chapters of this report.

Table 2

Comparision of Cs, I, and Te Release from Plants During Severe Accidents[2]

Element	Release* From the Plant Predicted for the Indicated Plant and Accident Sequence		
	Surry TMLB'δ	Surry TMLB'ε	Peach Bottom TW
Cs	3.9	0.02	4.5
I	4.6	0.28	4.8
Te	11.0	8.1	19

*Percent of initial core inventory.

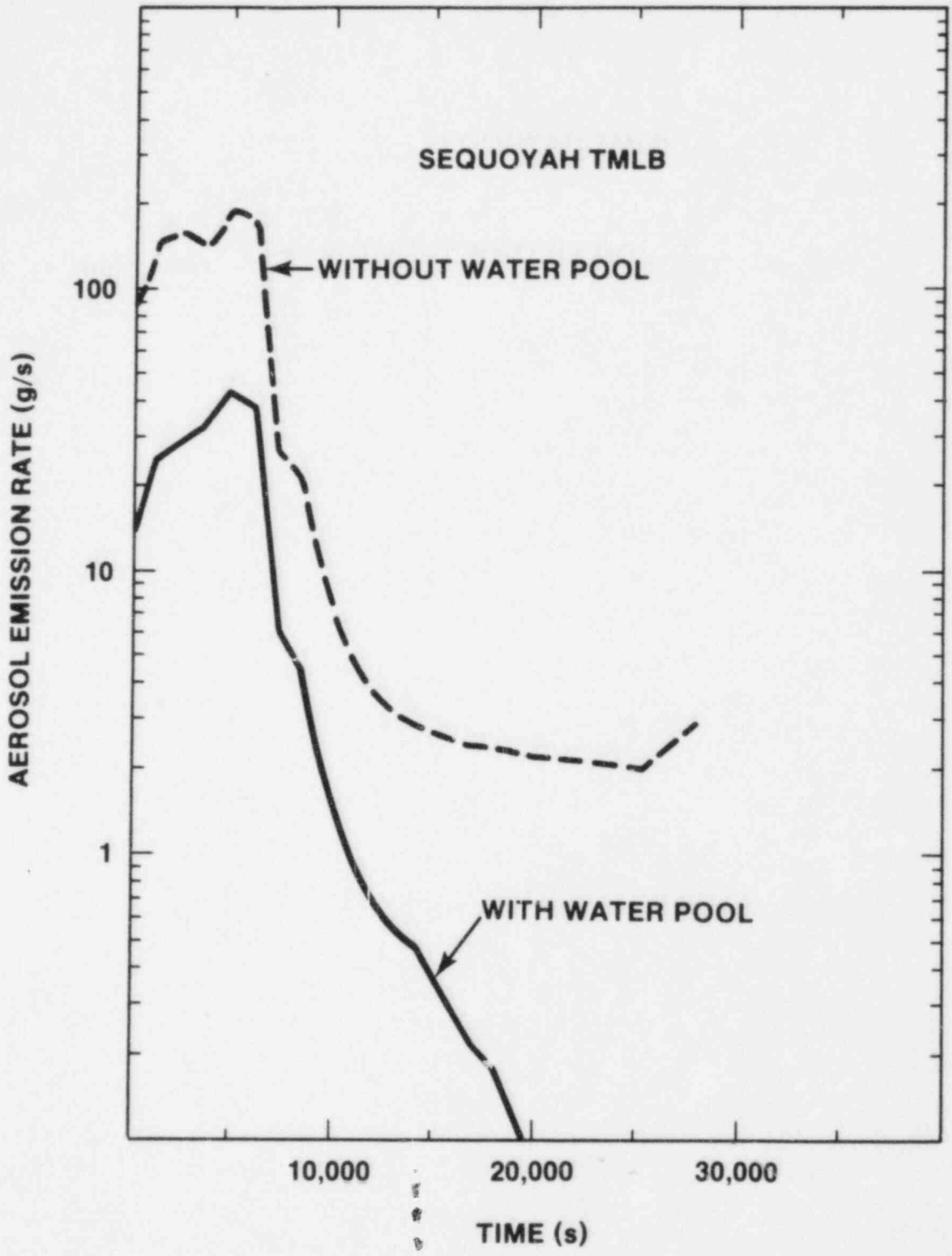

Figure 6. Prediction Obtained from the VANESA Model of the Effect of an Overlying Water Pool on Aerosol Generation During Core Debris/Concrete Interactions

III. THE APPROACH TO EX-VESSEL RELEASE MODELING ADOPTED IN VANESA

A. Overview

The approach adopted for the development of the VANESA model of ex-vessel release involves the following ideas:

1. The model should recognize both the vaporization and the mechanical mechanisms of aerosol formation.

2. The model should consider aerosol generation by both radionuclides and nonradioactive constituents of the molten debris in the reactor cavity.

3. The thermochemistry of vaporization is recognized, but it is also recognized that kinetic factors may limit the realization of the vaporization potential indicated by thermochemical analyses.

4. Aerosol particle characteristics as well as the rate of aerosol production should be predicted by the model.

5. The mitigative effects of an overlying water pool should be recognized in the model.

The Reactor Safety Study model of radionuclide release during core debris interactions with concrete depicts the mechanism of release as exclusively vaporization. Certainly, the high core debris temperatures hypothesized in the Reactor Safety Study would be conducive to extensive vaporization of core debris constituents. A series of thermochemical calculations was done for the Reactor Safety Study to determine the volatility of selected radionuclides as either atomic vapors or gaseous molecular oxides. From these simplified analyses, radionuclide release fractions and release rates were developed.

Experimental studies since the time of the Reactor Safety Study have supported the view that vaporization is a prominent mechanism of release during core debris/concrete interactions. These studies have shown, however, that the chemical environment that exists during core debris/concrete interactions is significantly more vigorous than was supposed in the Reactor Safety Study. Gases, liberated by the thermal attack on concrete, sparge through and react with the melt. The melt itself dissociates into distinct oxide and metallic phases. The chemistry within these condensed phases is further complicated as molten concrete and reinforcing steel are incorporated into the molten core debris. A far richer

vapor phase chemistry than that considered in the Reactor Safety Study is known to develop. In addition to atomic and molecular oxide vapors, vapor phase hydroxides, polymers, hydrides, and mixed metal species such as SnTe and AgTe can form above core debris interacting with concrete.

The improved understanding of chemistry that has evolved since publication of the Reactor Safety Study could be used to redevelop a bounding thermochemical analysis. Were this done, there is little question that higher release fractions would be predicted. Such a bounding approach would not meet one of the important objectives of the NRC source term reassessment which was to develop realistic descriptions of radionuclide behavior under severe accident conditions. Further, it is unlikely that such bounding estimates of release would be at all satisfactory for the interpretation of the many available experimental results.

A substantial portion of the VANESA model is devoted to the analysis of vaporization. This analysis does consider the detailed thermochemistry of vaporization. But, this analysis also considers kinetic factors which might prevent the vaporization process from reaching the equilibrium limit defined by the thermochemistry. This inclusion of kinetic modeling, as well as thermochemical modeling, is an important difference between the VANESA model and previous models of ex-vessel release.

A substantial body of data concerning the kinetics of high temperature vaporization processes has been developed in the steel industry. Of particular interest are kinetic analyses of the "carbon boil" phase of steel manufacture.[19] During the boil, oxygen from a lance is directed at the steel. This causes carbon monoxide bubbles to nucleate under molten steel at the refractory lining of the furnace. These bubbles sparge violently through the melt. The appearance of the melt surface during the "boil" bears a strong resemblance to the melt surface observed in core debris/concrete interactions.[17,18] In both the "boil" of steel and melt/concrete interactions significant aerosol generation is associated with gas sparging.

Studies of aerosol production during carbon boils have suggested two formation mechanisms.[20-22] One mechanism is the familiar vaporization process. The second mechanism is a mechanical produciton of aerosols caused by the bursting of carbon monoxide bubbles at the melt surface. Similar mechanical aerosol production has been hypothesized for some welding processes.[23] Mechanical aerosol production is a phenomenon that is well-known in oceanography[24] and by anyone whose nose has been "tickled" while drinking champagne.

Mechanical aerosol production during core debris interactions with concrete has not been considered in previous reactor accident analyses. Yet, there appear to be two occasions when it is of dominant importance to the ex-vessel source term. The first of these occasions is during the early, transient stages of core debris interactions when gas generation rates are quite high. Superficial gas velocities of over a meter per second have been encountered in experiments.[18] Such high gas generation violently agitates and even levitates the melts. The second of these occasions is late in a reactor accident. Experimental studies and models of core debris/concrete interactions have established that the core debris cools significantly as the interaction progresses. Eventually, temperatures of the core debris are too low to spawn significant aerosol production by vaporization. But, even at such low core debris temperatures gas generation from the concrete is still significant. Mechanical aerosol generation by bubble bursting at the melt surface or by entrainment of melt in the gas flow should then also be significant.

One important aspect of the VANESA model is that it accounts for aerosol production by mechanical processes. Mechanical aerosol production is quite different than aerosol production by vaporization. Mechanically produced aerosols have the bulk composition of the melt from which they are formed rather than being enriched in volatile species as are aerosols formed by vaporization. Within the context of the VANESA model only the uppermost portion of the core debris participates in the mechanical aerosol production process.

Experimental studies have shown that the density differences between the oxidic and the metallic phases of core debris provide a strong driving force for the stratification of core debris into layers.[17,18] Most modern models of core debris/concrete interactions such as CORCON[5,6] and the German model WECHSL[25] consider the melt to be stratified rather than a homogenized mixture of metal and oxide as portrayed in the Reactor Safety Study. The VANESA model, too, assumes the melt is stratified by density into oxide and metallic layers. The oxide layer is assumed to be less dense than the metal layer so that mechanical aerosol generation is then always from the oxide layer.

Radionuclides partition preferentially among the phases of core debris. Some radionuclides such as Te, Ru, and Pd concentrate in the metallic phase. Others, such as Ba, Ce, and La, enrich the oxide phase. In order to properly account for the radionuclide release associated with mechanical aerosol generation, it is necessary that the VANESA model address the partitioning of radionuclides between core debris phases. Phase partitioning also figures in the analyses of thermodynamics and kinetics of vaporization.

The Reactor Safety Study model focused its attentions on the vaporization of radionuclides to form aerosols. Though it was recognized that other constituents of the melt could vaporize, no attempt was made to account for aerosols formed from these nonradioactive vapors.

Experimental studies of core debris/concrete interactions have established that materials which would not be radioactive in an accident not only contribute to the ex-vessel aerosol, they would be the dominant source of aerosol during ex-vessel phases of an accident. Agglomeration and sedimentation of aerosols within reactor containments are among the most important processes that mitigate release of radionuclides from the fuel. These processes proceed at rates proportional to the number concentration of aerosol particles, raised to a power of between 1.3 and 2. Technology applied to date in reactor accident analyses does not indicate any significant sensitivity of aerosol agglomeration and settling rates to the radioactivity of the particles.*[27] Consequently, introduction of significant masses of nonradioactive aerosols to the containment atmosphere would greatly accelerate the settling of all aerosols including those composed of radionuclides. To obtain realistic estimates of the amounts of radioactivity that escape a plant during a severe accident, it is necessary, then, to obtain equally realistic estimates of the generation of both radioactive and nonradioactive aerosols. The VANESA models treat the release of radioactive and nonradioactive materials on an equal footing.

Estimation of the natural mitigation of radionuclide release from a plant that is brought about by aerosol processes in the containment is a key element of modern reactor accident analyses. Several excellent computer codes such as NAUA-4,[7] CONTAIN/MAEROS,[31,32] and QUICK[33] are available for predicting the physics of aerosols in reactor containments under accident conditions.[34] These models all require descriptions of the aerosol sources to the reactor containment. Sensitivity studies[9] have shown that the features of aerosols entering containment that affect most significantly the predictions obtained with the aerosol physics models are:

1. Rate of aerosol generation,
2. Size distribution of the aerosols,
3. Material density of the aerosols, and
4. Aerosol shape factors.

*The accuracy of current aerosol physics models in this regard can be questioned; see References 8, 28-30.

It was recognized in the development of the VANESA model that the characteristics of the particles (density, size, and shape factors) as well as the mass generation rate would have to be described if the model was to be useful for accident analyses.

The Reactor Safety Study considered that core debris expelled from a reactor vessel would interact with concrete in a dry reactor cavity. It is recognized now that ex-vessel core debris behavior may involve combined core debris/concrete/water interactions. Water may enter the reactor cavity as a natural consequence of the accident. In pressurized water reactors, accumulators in the reactor coolant system may dump water into the cavity once core debris has escaped the reactor vessel and the coolant system depressurizes. Or, steam evolved from the reactor during core degradation may condense in the containment and be constrained by the plant geometry to flow into the reactor cavity. Water may also be introduced to the reactor cavity as a deliberate scheme to mitigate severe accident consequences.[35]

Much has been said about the effects water might have on core debris/concrete interactions. It has been proposed in some analyses that water admitted to the reactor cavity would cause core debris to quench and fragment into a coolable debris bed.[36,37] Once core debris is quenched, there is, of course, no significant aerosol generation or radionuclide release to the containment atmosphere.

The experimental evidence available to date[38,39,40] does not support the assertion that water quenches the core debris. Rather, all of the evidence seems to indicate that water admitted to a reactor cavity would form a pool overlying the molten debris. The presence of this water pool does not seem to significantly affect the nature of core debris attack on the concrete. The water pool would be expected, however, to affect aerosol production during core debris interactions. It is well established that aerosol-laden gases are decontaminated as they pass up through a water pool.[7,41,42] This decontamination by a water pool overlying core debris is a significant, natural mitigation process that has to be included in the VANESA model to obtain a realistic estimate of ex-vessel radionuclide release and aerosol generation.

It was recognized in the development of the VANESA model that computer codes such as CORCON[5,6] could provide much of the information needed to estimate ex-vessel release and aerosol generation. It was anticipated, in fact, that any model that was developed would become, eventually, a part of the CORCON computer program. To meet the exacting deadlines imposed by the source term reassessment effort, it was impossible to fully integrate the VANESA model with the CORCON computer program. Consequently, there are some areas

where predictions of VANESA replicate predictions of the CORCON code. At the time the VANESA model was developed, the CORCON code was being revised and, in fact, this code is still being revised. The VANESA model was developed then anticipating changes in CORCON, some of which have yet to be instituted. Because of this, there are areas considered by the VANESA model in manners that are different than those employed in currently available versions of the CORCON code.

B. Physical Depiction of the Core Debris in the VANESA Model

The physical orientation of core debris in the reactor cavity as conceived in the VANESA model is shown in Figure 7. The debris orientation conceived in the Reactor Safety Study and the evolution in the melt configuration modeled in the CORCON code are shown also in this figure. The configuration in the VANESA model is quite simple. A metallic debris is considered to be the most dense phase and forms a layer at the bottom of the molten pool. The oxidic phase, which consists of the urania fuel, zirconium dioxide formed by steam oxidation of zircaloy cladding on the fuel, and ablated concrete, forms a molten layer over the metal layer. A water pool, if present, overlies the oxide melt layer.

The debris configuration in the Reactor Safety Study model is depicted as a "homogeneously heterogenous" mixture of metals and oxides. This is also the debris configuration adopted in the DECOMP model of core debris interactions with concrete developed for the Industry Degraded Core Rulemaking Program.[43] The arguments advanced in attempting to rationalize this configuration follow one of two paths. The first of these paths is a contention that at elevated temperatures metals such as constituents of stainless steel (Cr, Ni, Fe, Mn, and Mo) may be miscible with molten reactor fuel much as are the metals Ta[44] and Zr.[45] A large number of in-pile[46,47,48] and out-of-pile experiments[49] have shown that at temperatures encountered in light water reactor accidents and even at the higher temperatures produced during fast breeder reactor accidents, steel does not dissolve to any significant extent into oxides such as urania or zirconia.

The second pathway for rationalizing the Reactor Safety Study debris configuration is to contend that gases sparging through the melt will entrain and mix the oxide and metallic phases into an approximately homogeneous mixture. (Sparging of the molten core debris by gases evolved from concrete was neglected in the Reactor Safety Study but is now well established by experiments to be an important aspect of debris/concrete interactions.) Certainly, Greene[50] and Greene and Ginsberg[51] have conducted experiments with simulant materials which show that gas sparging can induce

VANESA MODEL:

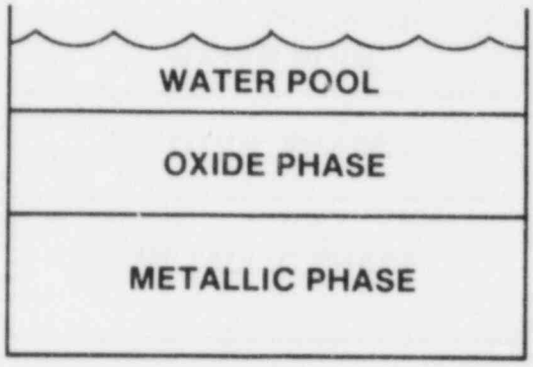

REACTOR SAFETY STUDY MODEL:

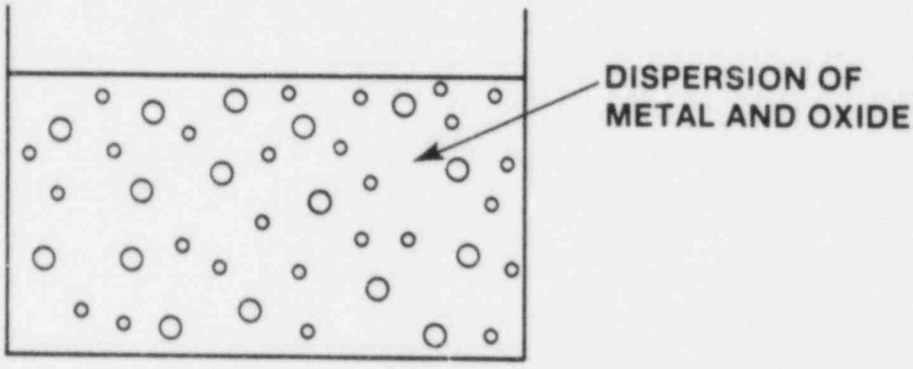

CORCON MODEL:

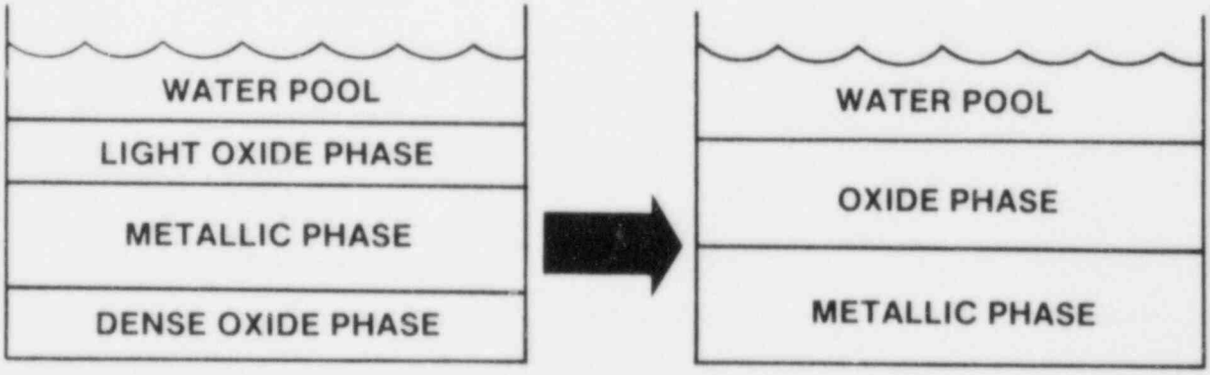

Figure 7. Physical Configuration of Core Debris Depicted in Several Models

intermixing at the interface between immiscible liquids. Lee and Kazimi[52] have argued, however, that these experiments are not directly applicable to the core debris situation and have developed a model which suggests gas sparging would not induce intermixing. Regardless of the outcome of these differences, it is clear intermixing of immiscible fluids at the interface is easier than complete homogenization of a melt.

Air mixing of immiscible phases is a fairly common industrial process done in Pachuca tanks.[53] Such mixing is seldom attempted, however, when the immiscible phases can freely settle as is the case with the oxide and metallic phases of core debris. When free settling is possible impellers are used typically. Calderbank[114] has suggested a correlation for predicting the power, P, that must be expended per unit volume of dispersion, V, to maintain a two-phase suspension well-mixed:

$$\frac{P}{V} = 32(g\Delta\rho)^{4/3}\left(\frac{\mu_c^{1/3}}{\rho_c^{2/3}}\right)$$

where g = gravitational constant,

μ_c = viscosity of the condensed phase,

ρ_c = density of the condensed phase,

$\Delta\rho$ = difference in the density of the continuous condensed phase and the dispersed condensed phase, and

(P/V) = power dissipated per unit volume of mixture.

The power dissipated to the liquid by rising bubbles is given by

$$(P/V) = (\rho_c - \rho_g)gV_s$$

where V_s = superficial gas velocity,

ρ_g = density of gas, and

ρ_c = average density of condensed phase.

Equating these expressions for power density yields an estimate of the superficial gas velocity necessary to homogenize the two-phase, condensed mixture. A plot of the gas superficial velocity necessary to keep a two-phase condensed mixture homogenized against the difference in density of the condensed phases is shown in Figure 8. Superficial gas velocities of about 40 cm/s would be required for a density difference of 2 g/cm^3 and about 140 cm/s would be needed for a density difference of 4 g/cm^3. Superficial gas velocities through melts attacking concrete are typically less than 150 cm/s and usually are less than 20 cm/s. Note that this analysis applies only to maintaining the mixture. Actually getting two liquids homogenized may be more difficult.

Based on this type of analysis it is clearly possible that a homogenized mixture of oxide and metallic melt could be formed because of gas sparging if the densities of the two mixtures were very nearly equal. The densities of the oxide and metal phases of core debris can become similar for brief periods of time during core debris attack on concrete. As the attack progresses, the condensed products of concrete decomposition are incorporated into the oxide phase reducing the density of this phase. The reaction of gases produced by decomposing concrete oxidizes the lower density constituents of the metallic phase (Cr and Zr), thus causing the density of the metal to increase. Depending on the relative densities of the metal and oxide at the start of core debris/concrete interactions (see below), the two phases can reach equal densities. Such a situation would have, of course, only a transient existence. Further concrete attack and incorporation of concrete decomposition products into the oxide melt would create greater disparity in the densities of the metallic and oxide phases. This would make it more difficult to maintain a suspension.

It must be emphasized that the above analysis only demonstrates the possibility that for transient periods of time the metallic and oxidic core debris phases could be mixed. This configuration has never been observed in melt/concrete interaction experiments.

The debris configuration modeling in the CORCON code is very much more complicated than that in either the VANESA model or the Reactor Safety Study model. The CORCON model follows the evolution in the phase densities described briefly above. Classical tabulated densities for phase constituents are used in the analysis. (See Section IV-A-11.) These densities are assumed to be additive and are used to compute the densities of the oxide and metal phases. Based on such analyses, it is usually true that at the start of core debris attack on concrete, the oxide phase composed principally of urania and zirconia is the densest material

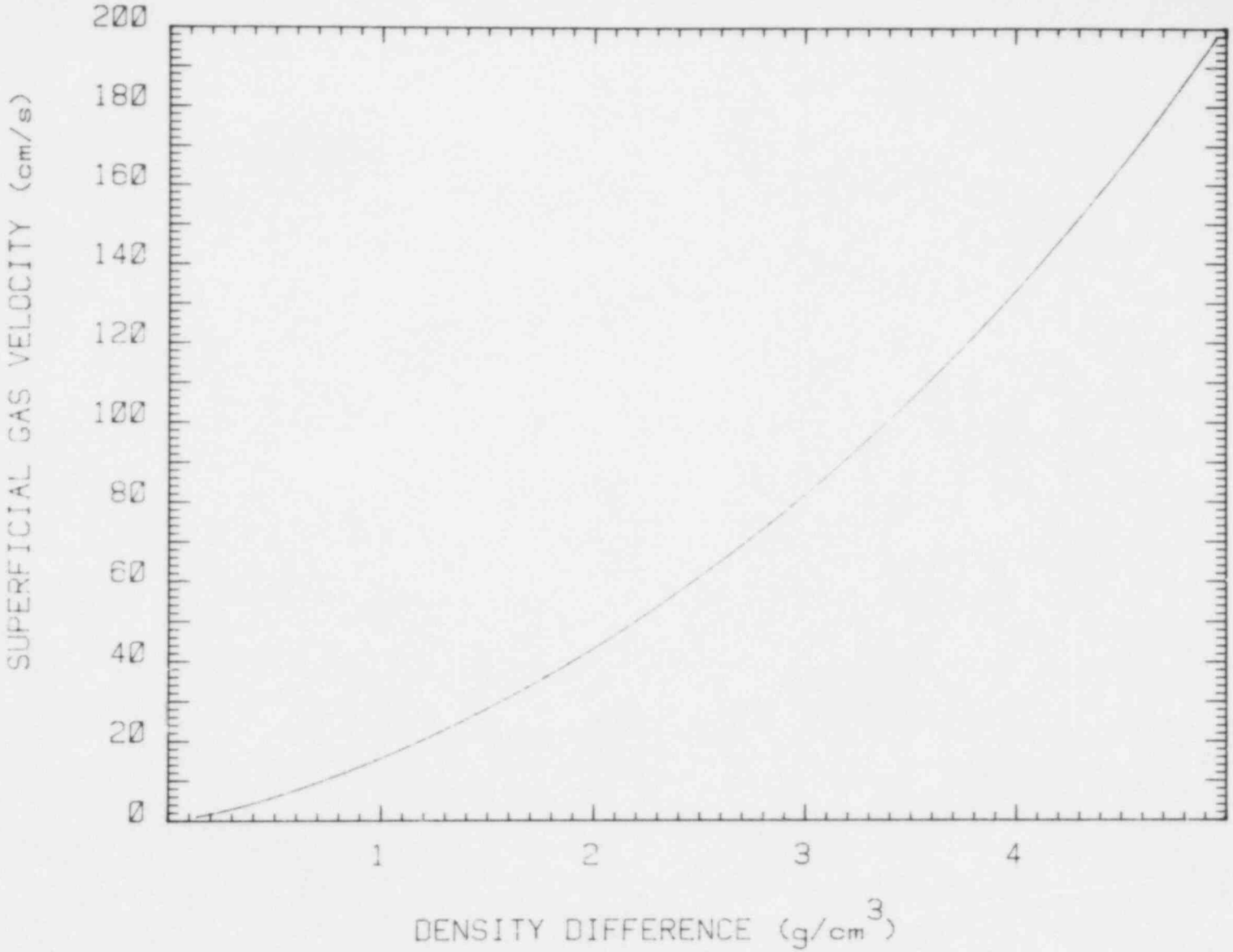

Figure 8. Superficial Gas Velocity Necessary to Maintain a Mixture of Two Condensed Phases Well Mixed as a Function of the Difference in the Densities of the Condensed Phases

in the system. This oxide phase is then assumed to form a coherent layer at the bottom of the molten pool. The steel forms a layer above this dense oxide. Concrete ablated by the metallic layer is assumed to float and to form a light oxide layer over the metal and below any water pool that is present. Concrete ablated by the dense oxide layer is immediately incorporated into the dense oxide layer and reduces the bulk density of this layer. The density of the metallic layer also evolves as zirconium and chromium are oxidized to ZrO_2 and Cr_2O_3 which float to the light oxide layer. Reinforcing steel melted during the attack on concrete is also incorporated into the metallic layer, thereby increasing the density of the layer.

At some point the dense oxide layer incorporates sufficient concrete and the metallic layer becomes dense enough that the oxide layer will float on the metal. When this is predicted to happen, the debris configuration is altered in the CORCON model to be the same as that depicted in the VANESA model. That is, a single oxide melt layer overlies a dense metallic layer. No attempt is made in the CORCON model to describe the transient period in which the urania-rich oxide and the metallic phase have such similar densities that they could be easily homogenized.

Unfortunately, repeated experiments in which clad fuel and steel have been melted together have consistently shown the metallic layer to be the more dense.[49,54] A variety of explanations for this result, which seems so anomalous in light of the apparently well-established densities of the mixture constituents, have been offered. These explanations have invoked scale effects associated with small laboratory crucibles and even highly imaginative liquid-state phase changes. The result has been so consistently observed that the investigators at the Kernforschungszentrum Karlsruhe have constrained their WECHSL model[26] to always have the metallic phase as the lowest layer in the molten pool regardless of the relative densities of the oxide and metal phases. The sole exception to the experimental observations of this debris configuration is a result obtained by Powers and Arellano[55] when they exposed concrete to the action of "corium" melts generated metallothermically. These investigators found that after the melt had solidified, the metallic phase was sandwiched between a dense and a light oxide phase much as depicted in the CORCON model for early stages of ex-vessel debris interactions.

Recently, Powers[56] has provided an explanation for the relative densities of melt phases. The additive use of density data for pure constituents of the melt is criticized in this explanation. The crux of the explanation is that zirconium metal so reduces the oxygen potential that uranium dioxide becomes hypostoichiometric. In doing so, a uranium

metal potential is established. The stainless steel provides a sink for the uranium. Sufficient uranium can be incorporated into the steel to make the metal phase more dense. The sandwich configuration of the metal phase observed in the tests done by Powers and Arellano arose because all of the zirconium metal was oxidized in these tests. Consequently, uranium metal was not incorporated into the metal phase.

Thus, it would be expected that the configuration of the oxide and metal phases of core debris at the start of melt attack on concrete would depend on the extent of zirconium oxidation during in-vessel phases of an accident. In the more usual situations in which in-vessel zirconium oxidation is incomplete, the metallic phase would be the more dense and would remain the more dense phase throughout the core debris/concrete interactions. That is, the debris configuration depicted in the VANESA model would be established though there might be a transient period during which evolved gases would homogenize the phases of the core debris. Further details concerning Powers' arguments on phase relations in core debris are presented below in connection with the thermodynamics of vaporization processes.

From the preceding discussions it is apparent that the details of core debris configuration are not yet well resolved. Various models have adopted various approaches. Eventually, however, the core debris will assume the configuration used in the VANESA model. Fortunately, uncertainties in the debris configuration do not create large uncertainties in the release predictions. As will be shown below, debris configuration has its greatest effects on the mechanical generation of aerosols.*

C. Steps in the Analysis Done by the VANESA Model

A brief outline of the steps of the analysis done in the VANESA model is presented here. These steps are shown schematically in Figure 9.

It is presumed that input data of the following types are available for the model:

1. Initial mass and composition of the core debris including the inventories of radionuclides present in the core debris when it emerges from the reactor vessel.

*Debris configuration can affect predictions of debris temperature, concrete ablation, and the like. Variations in these quantities will affect, of course, the release predictions but they do not mandate changes in the release model.

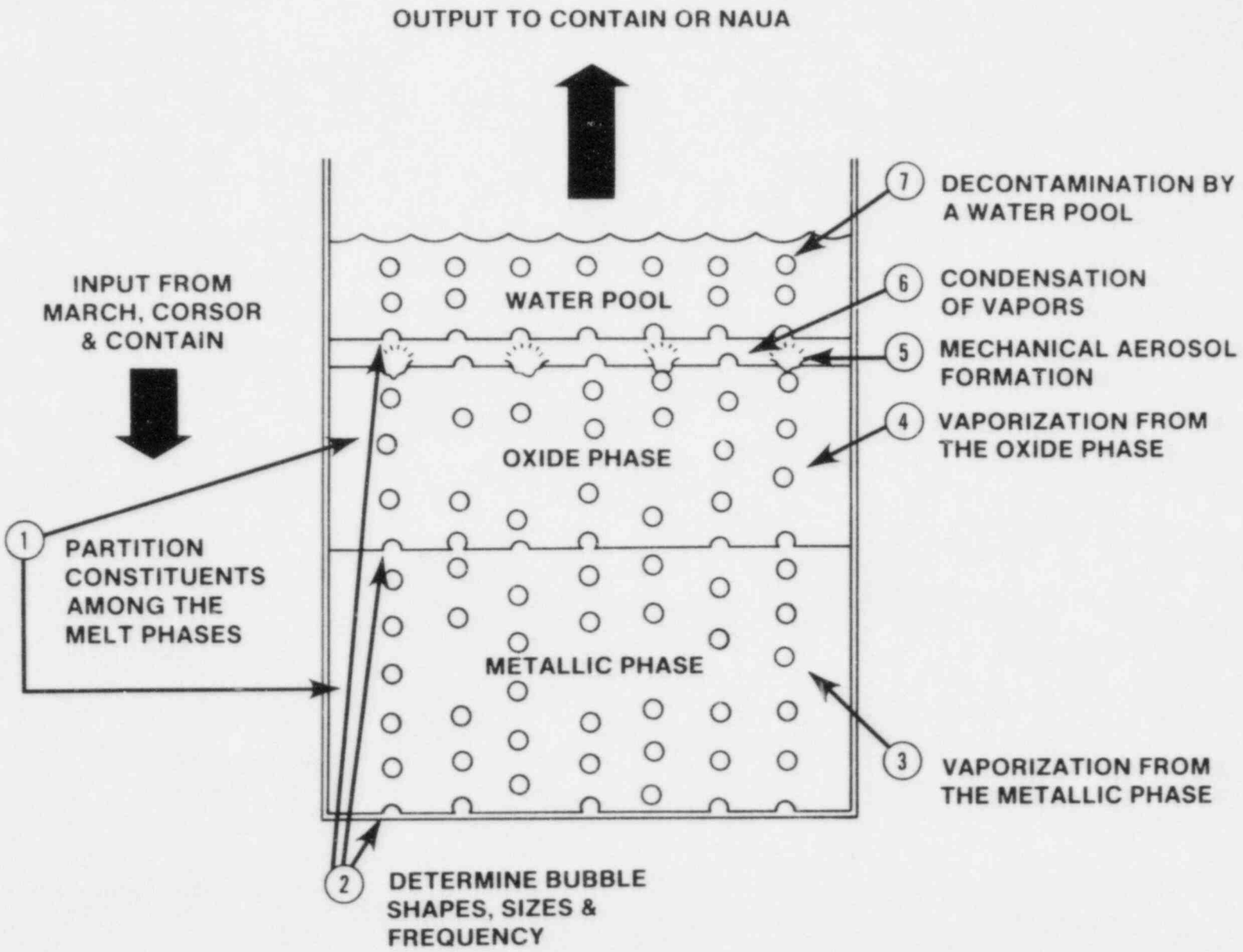

Figure 9. Schematic Diagram of the Steps in the VANESA Analysis

2. Composition of the concrete including the composition of the reinforcing steel used in the concrete.

3. The maximum radius of the molten pool as a function of time.

4. The rate at which condensed products of concrete decomposition are incorporated into the core debris pool as a function of time.

5. Core debris temperatures as a function of time.

6. The rates at which CO_2 and H_2O are evolved from the concrete and pass through the molten pool as functions of time.

As currently implemented as a computer code, the VANESA model is particularly suited to receive necessary inputs from the CORCON code.[5,6] Calculations have been made using input concerning the core debris/concrete interactions derived from the DECOMP code,[43] the INTER subroutine[57] of the MARCH code, and experimental data.[58]

Once the necessary inputs are assembled, the first step in the analysis is to apportion materials between the oxide and the metallic phases of the core debris. Apportioning these materials is a thermodynamic stability process and is discussed below in connection with the thermochemistry of vaporization.

The next step in the analysis is establishing the free surface available for vaporization. Free surfaces are at the perimeters of the melt pool and the surface area provided by gas bubbles sparging through the melt. For typical core debris configurations encountered in reactor accident analyses the surface area provided by gas bubbles far exceeds the geometric surface area of the melt. For instance, a 100-ton molten pool in a 3-meter radius cylindrical cavity might provide a geometric surface area of about 65 square meters. If this core debris were at 2000 K and attacked limestone concrete to produce about 30 moles of gas per second, the gas bubbles sparging through the melt would provide about 2700 square meters of surface area. Consequently, establishing the available free surface for vaporization is a matter of gas bubble dynamics and is discussed below in connection with the kinetics of vaporization.

Analysis of vaporization involves both thermodynamic and kinetic considerations. These considerations must be taken separately for the oxide and metallic phases. The thermodynamic analyses in the VANESA model establish the driving force for and the maximum extent of vaporization of core debris constituents. The kinetic analyses determine the

approach to the maximum extent of vaporization of core debris. Discussion of the thermodynamics and kinetics of vaporization constitute much of the next section of this report.

Once gas bubbles reach the surface two things happen. Bubbles burst at the surface throwing off some amount of surface melt as aerosol-sized droplets. Vapors contained in the bubble are released to the atmosphere above the melt. Analysis of the amount of material converted to aerosols by the mechanical action of the bursting bubbles is the next step in the VANESA model. Once the nature of this mechanically generated aerosol is known, the condensation of vapors either by homogeneous nucleation or by deposition on surfaces such as aerosol surfaces can be evaluated. Such evaluations provide a description of the particle size distribution of the aerosol evolved during core debris interactions with concrete.

Finally, the decontamination of aerosol-laden gases as they pass through any water pool overlying the core debris must be evaluated. The decontamination process is largely of a physical rather than chemical nature. It affects both the amount of aerosol evolved and the particle size distribution of the aerosol. Decontamination will also affect the composition of the bulk aerosol if the composition of individual aerosol particles is allowed to depend on the particle size as is suggested by experiments.

Decont mination of the aerosol-laden gases is the last step in the VANESA analyses. Output from this last step of the model would be provided to a containment behavior model such as NAUA-4 or CONTAIN in an accident analysis effort.

Further descriptions of the steps in the VANESA model are presented in the next few chapters of this document.

IV. VAPORIZATION

Vaporization is the most important of the mechanisms leading to release of radionuclides and generation of aerosols during core debris interactions with concrete. Vaporization is the cause of the largest amount of release especially early in the interactions when core debris temperatures are highest. But, perhaps of more importance, vaporization is the reason aerosols and vapors can be enriched in debris constituents relative to the condensed phase core debris. In particular, the aerosols and vapors can be enriched in radionuclides.

The quantitative evaluation of a vaporization process, in any context, involves two steps. The first of these steps is the determination of the driving force that leads to the condensed-to-vapor phase transformations of core debris constituents. This first step is a thermodynamic analysis. When completed, it defines both the driving force and the maximum extent of vaporization of the debris constituents. Were a bounding result adequate, examination of the vaporization process could be stopped upon completion of the first step. There can be, however, barriers that prevent or retard achieving the maximum vaporization defined by the thermodynamic analysis. To produce more accurate estimates of the vaporization processes, it is necessary to continue the examination to a second step which is a determination of the kinetics of vaporization.

This chapter is devoted to the discussion of the thermodynamics and the kinetics of vaporization processes. An attempt is made to describe the technology available for the quantitative prediction of these processes. These descriptions of the available technology are used to provide a rationalization for the approximations concerning vaporization made in the current implementation of the VANESA model. Vaporization is, of course, acutely dependent on the peculiar chemical and physical properties of the constituents of core debris. Consequently, it is in this chapter that most of the core debris chemistry and the chemistry of core debis interactions with concrete are discussed.

A. The Thermodynamics of Vaporization

Condensed phase core debris, instantaneously extracted from the reactor vessel and deposited into the reactor cavity, would not be a chemically equilibrated system regardless of the time this core debris spent in the reactor vessel, the temperature of the core debris or the extent of mixing of the debris. Core debris has a vapor pressure. Until this equilibrium vapor pressure is established about the

core debris, there will be a net phase change of debris constituents to the vapor phase. The disequilibrium of the core debris is continued and accentuated as gases evolved from the concrete sparge through or around the debris.

At any instant in time, a control volume in the debris can be defined such that this control volume is isothermal and isobaric. The free-energy of the control volume is given by:

$$G(\text{System}) = \sum_{i=1}^{N(c)} n(i)G(i) + \sum_{j=1}^{N(g)} n(j)G(j)$$

where $N(c)$ = number of constituents of the condensed phase,

$N(g)$ = number of constituents of the gas phase,

$n(i)$ = Number of moles of the i^{th} constituent of the condensed phase for $i = 1$ to $N(c)$,

$n(j)$ = Number of moles of the j^{th} constituent of the gas phase for $j = 1$ to $N(g)$,

$G(\text{system})$ = free-energy of the control volume,

$G(i) = \Delta G_f(i) + RT\ell n\,[\gamma(i)\,x(i)]$,

$G(j) = \Delta G_f(j) + RT\ell n\,[\phi(j)\,P(j)]$,

$\Delta G_f(k)$ = free-energy of formation of the constituent k,

R = gas constant,

$X(i)$ = mole fraction of the i^{th} constituent in the condensed phase,

$\gamma(i)$ = activity coefficient of the i^{th} constituent in the condensed phase,

$P(j)$ = partial pressure of the j^{th} constituent in the gas phase,

$\phi(j)$ = fugacity coefficient of the j^{th} constituent in the gas phase, and

T = absolute temperature.

The control volume will be at equilibrium when G(system) is a minimum with respect to variations in n(i) for i = 1 to N(c) and n(j) for j = 1 to N(g), subject to the constraints of mass balance and that all n(i) and n(j) be nonnegative.

The differential of the control volume free-energy is:

$$dG(system) = \sum_{i=1}^{N(c)} G(i)dn(i) + \sum_{j=1}^{N(g)} G(j)dn(j)$$

$$+ \sum_{i=1}^{N(c)} n(i)dG(i) + \sum_{j=1}^{N(g)} n(j)dG(j) \quad .$$

The sum of the third and fourth terms on the right-hand side of this equation are identically zero for the isothermal, isobaric system (Gibbs-Duhem Theorem). Then, equilibrium is achieved when

$$dG(system) = 0 = \sum_{i=1}^{N(c)} G(i)dn(i) + \sum_{j=1}^{N(g)} G(j)dn(j) \quad ,$$

subject still to the mass balance and nonnegativity constraints.

The first approximation made in the current implementation of the VANESA model is that equilibrium can be found separately for the system consisting of the gas phase and the metallic, condensed, core debris phase and the system consisting of the gas phase and the oxidic, condensed, core debris phase. The second approximation is that the equilibrium found for a control volume at the mean phase temperature and pressure is applicable for all regions of the condensed phase in question.

Temperature gradients within the core debris phases should be small and easily neglected as long as the condensed phases are liquid and well stirred by the sparging gases. When the core debris solidifies significant temperature gradients would be expected to exist and these gradients could not be neglected. Solidification would lead, of course, to many other difficulties in the analysis of vaporization. Consequently, the current implementation of the VANESA model is restricted to the analysis of vaporization from liquid core debris.

Neglect of the pressure differentials across a phase of the core debris ought not lead to significant errors in

typical accident analyses. The pressure differentials are the result of the hydrostatic head of the core debris. The pressure differential across 100 tons of core debris spread over 30 m^2 will amount to only about 1/3 atmosphere. The ambient pressure of the debris during a severe accident will be typically 1-10 atmospheres. Neglect of the hydrostatic head will lead then to errors of only 3-30 percent in the pressure within the debris.

Vapor formation processes can be complex. Consider the formation of vapor from a condensed phase species MO_x. The most familiar vaporization process is just unary vaporization described by the stoichiometry:

$$[MO_x] \rightleftharpoons MO_x(g)$$

where the brackets have been used to indicate that the enclosed species is a constituent of the condensed phase.* Evaporation of water and the distillation of alcohol are familiar examples of unary vaporization processes. The delightful feature of such vaporization processes is that the vapor pressure established by the process over a pure condensed species is a function of temperature alone. Even when there are complications such as vapor phase polymerization:

$$n[MO_x] \rightleftharpoons (MO_x)_n(g)$$

the vapor pressure is just a function of temperature. Consequently, data can be obtained and tabulated for the vapor pressure.

Unfortunately, not all vaporization reactions are as simple as the unary process. The atmosphere surrounding a condensed phase need not be inert toward the condensed phase and can induce vaporization. For instance, reaction stoichiometries such as:

$$[MO_x] + H_2O \rightarrow MO_{x+1}(g) + H_2$$

$$[MO_x] + xH_2 \rightarrow M(g) + xH_2O$$

*Parenthetical indications following chemical species used here and elsewhere in the report are defined as follows: g = gas; ℓ = liquid; s = solid; c = condensed material either solid or liquid.

can be envisaged. When the atmosphere is not inert toward the condensed phase, then the vapor pressure is a function of the atmosphere composition as well as the temperature. The indefinite variability of atmosphere compositions makes it impractical to tabulate data for such vaporization processes.

A general reaction stoichiometry for vaporization into a steam/hydrogen atmosphere can be written as

$$MO_x + (w-x)\ H_2O \rightarrow MO_wH_y + (w-x-y/2)H_2 \quad .$$

Clearly, by selecting $y = 0$ and $w = x$, this stoichiometry represents a unary vaporization process. Other choices for y and w yield stoichiometries that reflect vapor species in the M-O-H system. For instance, by setting $y = w \neq o$, vapor phase hydroxides are described. Or, by setting $w = o$, vapor phase hydrides are described if $y \neq o$. The stoichiometry of the general reaction prescribes that the mass balance constraint must be

$$dn(MO_x) = (w-x)\ dn(H_2O) = -dn(MO_wH_y)$$

$$= -(w-y/2-x)\ dn(H_2) \quad .$$

Then, the equilibrium pressure for the single vapor species MO_wH_y is given by:

$$-\Delta G(Rxn)/RT = \ln\left\{\frac{P[MO_wH_y]\ \phi[MO_wH_y]\ \ P(H_2)\ \phi(H_2)^{(w-x-y/2)}}{X[MO_x]\ \gamma[MO_x]\ \ P(H_2O)\ \phi(H_2O)^{(w-x)}}\right\}$$

where

$$\Delta G(Rxn) = \Delta G_f(MO_wH_y) - \Delta G_f(MO_x) + (w-x-y/2)\ \Delta G_f(H_2)$$

$$- (w-x)\ \Delta G_f(H_2O) \quad .$$

Expressions of this type must be written, of course, for each vapor species involved in a vaporization process. The extent of vaporization of the condensed phase species MO_x is then determined by the partial pressures of all the vapor species composed of the element M.

The above equilibrium expression shows the thermochemical features of the system that must be known to characterize the vaporization process:

1. Free-Energies of Formation of Species Involved

Free-energies of formation are available for many of the species thought now to be important to questions of vaporization during core debris interactions with concrete. There is, and always will be, a question of completeness. That is, are there species important to vaporization that have not been characterized in terms of their free-energies of formation?

2. Fugacity and Activity Coefficients

Data for the fugacity coefficients of vapor species and the activity coefficients of condensed phase species are not readily available for sytems as complex as core melts. These features of a system must be obtained from a model.

3. Condensed Phase Concentrations

Were a core melt a homogeneous material, the initial concentrations of the condensed phase constituents are established, of course, by the initial conditions of the problem. The evolution of these concentrations with time is the product of vaporization analysis. But, core melts are not homogeneous. It is necessary to know, then, how constituents partition among the condensed phases of the core debris. Were models of the in-vessel phases of the accident sufficiently sophisticated, the partitioning of melt constituents would be included with melt composition as part of the initial conditions for the vaporization analysis. Since these in-vessel models are not yet developed sufficiently to do this, the vaporization analysis must include a description of the partitioning of constituents among the melt phases.

4. Vapor Pressures

Vapor pressures of the gas phase species are the major product of the thermodynamic analysis of the vaporization. An important input to this determination of vapor pressures is the speciation of the vapor phase.

The general vaporization equation can also be used to ascertain how well the thermodynamic features of the system must be known to limit the uncertainty in the vapor pressure to a prescribed value. If synergistic uncertainties are ignored, then the relative uncertainty in $P(MO_wH_y)$ is given by:

$$\left(\frac{\delta[P(MO_wH_y)]}{P(MO_wH_y)}\right)^2 = \left[\left(\frac{\delta G}{G}\right)^2 + \left(\frac{\delta T}{T}\right)^2\right]\left(\frac{G}{RT}\right)^2 +$$

$$+ (w-x)^2 \left(\frac{\delta[P(H_2)/P(H_2O)]}{P(H_2)/P(H_2O)}\right)^2 + \frac{y^2}{4}\left(\frac{\delta[P(H_2)]}{P(H_2)}\right)^2$$

$$+ \left(\frac{\delta[\gamma(MO_x)]}{\gamma(MO_x)}\right)^2 + \left(\frac{\delta[X(MO_x)]}{X(MO_x)}\right)^2 + \left(\frac{\delta[\phi(MO_wH_y)]}{\phi(MO_wH_y)}\right)^2$$

where $G \equiv \Delta G(Rxn)$ and

$\delta[k]$ = uncertainty in quantity k.

The uncertainty in the standard state free-energy change associated with the vaporization reaction can be important if the vaporization reaction is nearly spontaneous ($\Delta G = 0$). But, in general, this will not be the case. The uncertainty in the vapor pressure caused by uncertainty in the free-energy data will be bounded, usually. An estimate of this uncertainty might be $\delta[G/R] = 0.01G/R$. The uncertainty in the vapor pressure caused by uncertainty in concentrations, activity coefficients, and fugacity coefficients is also bounded. Pessimistic estimates of the uncertainties in the parameters might be

$$\delta[\phi(MO_wH_y)] \cong \phi(MO_wH_y)$$

$$\delta[X(MO_x)] \cong X(MO_x)$$

$$\delta[\gamma(MO_x)] \cong \gamma(MO_x) \quad .$$

The uncertainty in temperature might be about $\pm$ 100 K. Then for temperatures on the order of 2000 K,

$$\left(\frac{\delta T}{T}\right)^2 \sim 2.5 \times 10^{-3} \quad .$$

The uncertainty in the hydrogen pressure cannot exceed the actual system pressure. An estimate of $\delta[P(H_2)]$ might be $4P(H_2)$. Then,

$$\left(\frac{\delta[P(MO_wH_y)]}{P(MO_wH_y)}\right)^2 < 3 + 2.6 \times 10^{-3}\,(G/RT)^2 + 4y^2$$

$$+ (w-x)^2\left(\frac{\delta[P(H_2)/P(H_2O)]}{P(H_2)/P(H_2O)}\right)^2 .$$

The value of y will seldom exceed 4 and the value of w - x will seldom exceed 3, so

$$\left(\frac{\delta[P(MO_wH_y)]}{P(MO_wH_y)}\right)^2 < 67 + 2.6 \times 10^{-3}(G/RT)^2$$

$$+ 9\left(\frac{\delta[P(H_2)/P(H_2O)]}{P(H_2)/P(H_2O)}\right)^2 .$$

Uncertainties caused by temperature may become important if $(G/RT)^2$ is very large. But in this case the vapor pressure would be small and uncertainties in the vapor pressure would be inconsequential. Uncertainties in the hdyrogen-to-steam ratio (which means uncertainties in the oxygen potential of the system) can amount to factors of 10. This means that the uncertainties in the partial pressures of vapor species with oxidation states different than the parent, condensed phase species will be dominated by uncertainties in the oxygen potential. Vapor species produced by either oxidation or reduction of condensed phase species are very important during core debris concrete interactions. Consequently, a lot of attention must be paid to the oxygen potential of debris interacting with the concrete.

The technology available for obtaining information needed to produce thermodynamic descriptions of the vaporization processes during core debris/concrete interactions is the subject of the next few subsections of this chapter.

1. Partitioning Core Debris Constituents Between the Condensed Phases

The equilibrium partial pressure of a vapor over core debris will be a function of the mole fraction of some condensed phase constituent:

$$P(MO_w(OH)_y) = X[MO_x]\ f(P, T, \text{compositions of gas and condensed phases}) .$$

At the start of a reactor accident, the various constituents of interest are located in phases such as the fuel, alloys, or concrete. The locations of these materials at the start of an accident may not be the most thermodynamically favored when the several condensed phases are considered to form a thermochemical system. Consider, for instance, the refractory metal ruthenium. Many studies of spent reactor fuel[59,60] have shown that ruthenium, along with other metals, forms metallic inclusions within the fuel. Formation of these alloy inclusions within the fuel minimizes the free-energy of ruthenium relative to the distribution of ruthenium as a species such as RuO_2 dissolved in the urania lattice. It would seem obvious that further alloying of ruthenium with other metals such as cladding or structural steel would further reduce the free energy of the system. This does not occur during normal reactor operations simply because of the barriers that bar migration of ruthenium to these other metals. During core degradation and melting, these kinetic barriers are lost or are substantially reduced. Once the core material slumps into the lower plenum, the oxidic fuel phase comes into intimate contact with a metallic phase. There is then opportunity for ruthenium to alloy with the bulk metal phase. The opportunities for such alloying are extended when molten core materials are expelled from the reactor vessel into the reactor cavity.

Alloy formation by ruthenium affects its propensity for vaporization via the concentration term X(Ru) in the vapor pressure equation. (There are also effects arising from the activity coefficients but these are typically less important). Thus, different vapor pressures would be calculated if ruthenium were assumed to be evenly distributed throughout the core debris rather than concentrated in the metallic phase.

If kinetic barriers to partitioning of core debris are low, then the extent of partitioning can be estimated by assuming the condensed phases are equilibrated. The partitioning process for an element can be formally described by the stoichiometry:

$$[M]_{metal} + \text{oxidant} \rightarrow [MO_x]_{oxide} \quad .$$

Partitioning requires an oxidant. This oxidant can come from any of a variety of sources. For an equilibrium analysis, the source of the oxidant is not important. Only the oxygen potential of the system needs to be known. The oxygen potential, $P(O_2)$, is conveniently expressed in terms of the hydrogen to steam partial pressure ratio:

$$\left(P(O_2)\right)^{1/2} = \frac{P(H_2O)}{P(H_2)} \exp[\Delta G_f(H_2O)/RT] \quad .$$

Then, the formal stoichiometry of the partitioning process is:

$$[M]_{metal} + xH_2O \rightarrow [MO_x]_{oxide} + xH_2 \quad .$$

The equilibrium disposition of the element between the condensed phases is then given by:

$$-[\Delta G_f(MO_x) + x\Delta G_f(H_2) - \Delta G_f(M) - x\Delta G_f(H_2O)]/RT =$$

$$= \ln\left(\frac{Y[MO_x]\ \gamma[MO_x]}{X[M]\ \gamma[M]}\right) + \ln\left(\frac{P^x[H_2]\ \phi^x[H_2]}{P^x[H_2O]\ \phi^x[H_2O]}\right)$$

where $y[MO_x]$ = mole fraction of MO_x in the oxide phase,

$\gamma[MO_x]$ = activity coefficient of MO_x in the oxide phase,

$X[M]$ = mole fraction of M in the metal phase, and

$\gamma[M]$ = activity coefficient of M in the metal phase.

Solution of this equation is subject to the condition that

$$Y[MO_x]\ M(oxide) + X[M]\ M(metal) = M(M, total)$$

where M(oxide) = moles of condensed oxide phase,

M(metal) = moles of condensed metal phase, and

M(M, total) = total number of moles of element M in the system.

The generality of this abstract example is not reduced if M and MO_x are selected so that their activity coefficients in the metallic and oxide phases at equilibrium,

respectively, are equal to one.* Also, for most reactor accident situations involving temperatures in excess of 1500 K, it is acceptable to set $\phi[H_2] = \phi[H_2O] = 1$ (see Section IV A-3, below). The equilibrium partitioning is then given by:

$$-[\Delta G_f(MO_x) + x\Delta G_f(H_2) - \Delta G_f(M) - x\Delta G_f(H_2O)]/RT =$$

$$= \ln\left\{Y[MO_x]/X[M]\right\} + x \ln\left\{P[H_2]/P[H_2O]\right\} \quad .$$

The partitioning of an element is expressed by the concentration ratio $Y[MO_x]/X[M]$. The equilibrium expression shows that this ratio can never be zero or infinite. (The partial molar free energy of a condensed phase constituent will go to minus infinity if the concentration of a constituent of a phase goes to zero while the concentration in the other phase remains finite). The actual value assumed by the concentration ratio is a function of both temperature and the oxygen potential of the core debris. In general, temperature and oxygen potential will vary significantly over the course of core debris interactions with concrete. As a result, the partitioning of debris constituents between the metallic and oxidic phases of core debris would be expected to vary as the interactions progress. Fortunately, the variations in partitioning are not significant for many constituents of core debris.

Consider as an example, the partitioning of barium between the metallic and oxide phases. For this example, the activity coefficients of barium in the metallic phase and barium oxide in the oxide phase are taken to be one. The total barium inventory in the core debris is taken to be 500 gram moles. The core debris is assumed to consist of 6×10^5 gram moles of oxide and 8×10^5 gram moles of metal. Results of the partitioning calculations for temperatures of 1900, 2200, and 2500 K are shown as functions of the hydrogen-to-steam partial pressure ratio in Figure 10. These conditions span those encountered in typical core debris/concrete interactions.

The partitioning of barium is shown by these results to vary with temperature and the oxygen potential of the debris. But, for all the conditions considered in these

*This selection is rather easily done for the abstract example. For applications to partitioning of real species, it simply shifts the problem from one of determining activity coefficients to one of determining the values of $\Delta G_f(k)$. The difficulties posed by activity coefficients are discussed further, below.

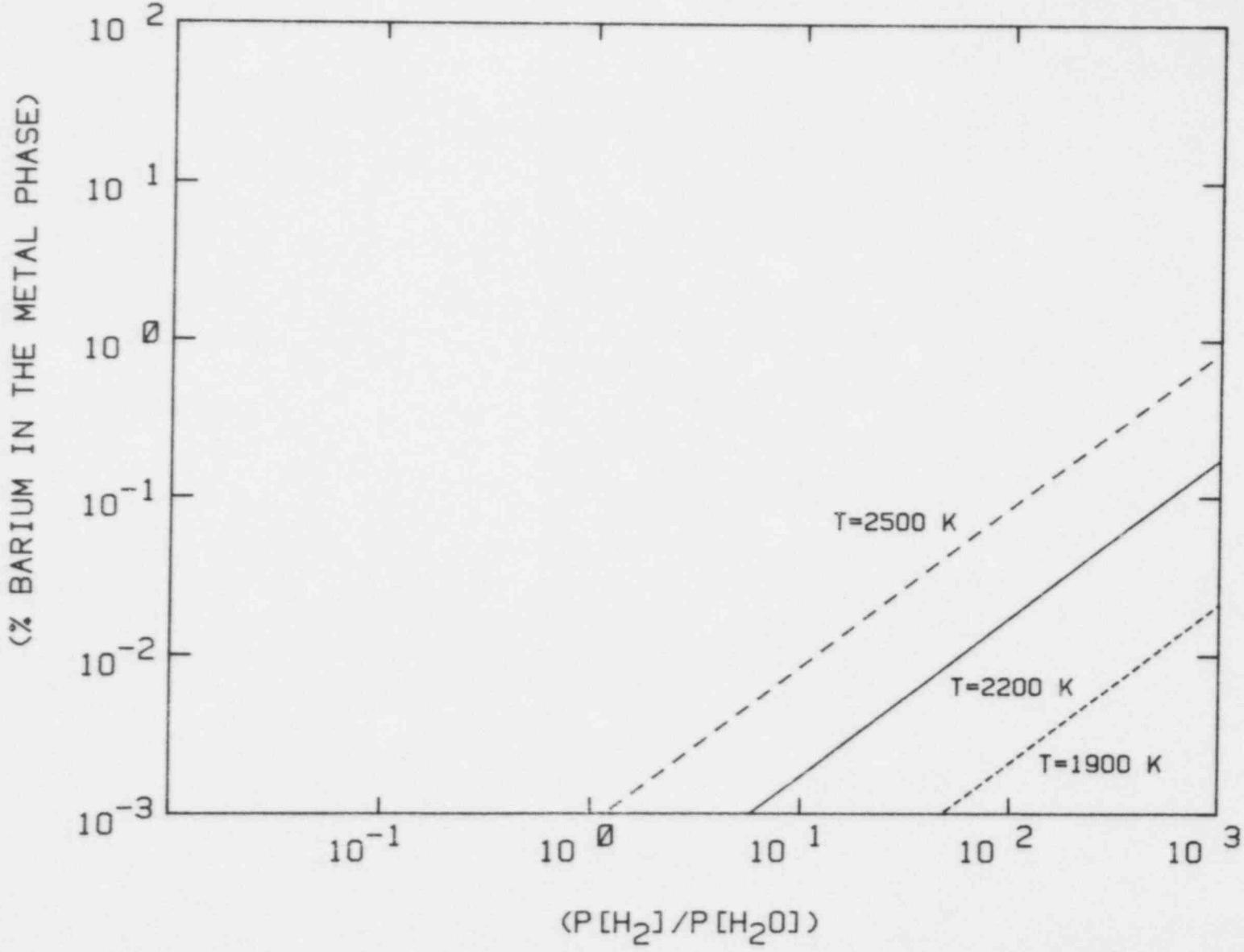

Figure 10. Calculated Partitioning of Barium Between the Oxide and Metallic Phases of Core Debris

calculations, barium is found predominantly in the oxide phase. Even at the highest temperature and lowest oxygen potential (highest hydrogen-to-steam partial pressure ratio) only about 1 percent of the barium is in the metal phase. For less severe conditions, the concentration of barium in the metal phase becomes very small indeed.

The results obtained here for the partitioning of barium are similar to results obtained for many other constituents of core debris. That is, partitioning of most core debris constituents is predominantly into one condensed phase or the other (metallic or oxidic). Though the extent of partitioning varies with conditions, the variation does not change significantly the amount of the constituent found in the preferred phase.

The partitioning behavior calculated for barium and most other constituents of the core debris is not universal. The partitioning of molybdenum between the oxide and metal phase is shown in Figure 11. Here, the variations in the partitioning of molybdenum with oxygen potential are significant. For all the temperatures considered, the partitioning of molybdenum is calculated to vary from predominantly into the oxide phase to predominantly into the metal phase as the hydrogen-to-steam ratio varies from one to ten. Hydrogen-to-steam ratios in this sensitive range are encountered in core debris/concrete interactions once zirconium and chromium in the debris have been oxidized to ZrO_2 and Cr_2O_3, respectively.

The results of the partitioning calculations described above have been obtained assuming condensed phase activity coefficients are equal to one. There are reasons to believe, however, that this assumption concerning activity coefficients may not be adequate for the purposes of partitioning calculations. Examination of the equilibrium expression for partitioning shows that nonunity activity coefficients could alter significantly the predicted partitioning. The alterations are not likely to change qualitatively conclusions derived from the calculations in which partitioning is predominantly into one phase or the other for conditions typical of core debris/concrete interactions. Nonunity activity coefficients might have much more significant effects on partitioning of elements such as molybdenum that is predicted to vary over the range of conditions that could be expected.

There are some useful data on radionuclide partitioning among the phases of core debris. Fischer et al.[62] melted mixtures of iron and urania doped with nonradioactive isotopes of important radionuclides. The melting was done with an arc-furnace in an argon atmosphere of unspecified oxygen potential. Results from these experiments are shown in Table 3. Somewhat similar results have been obtained by

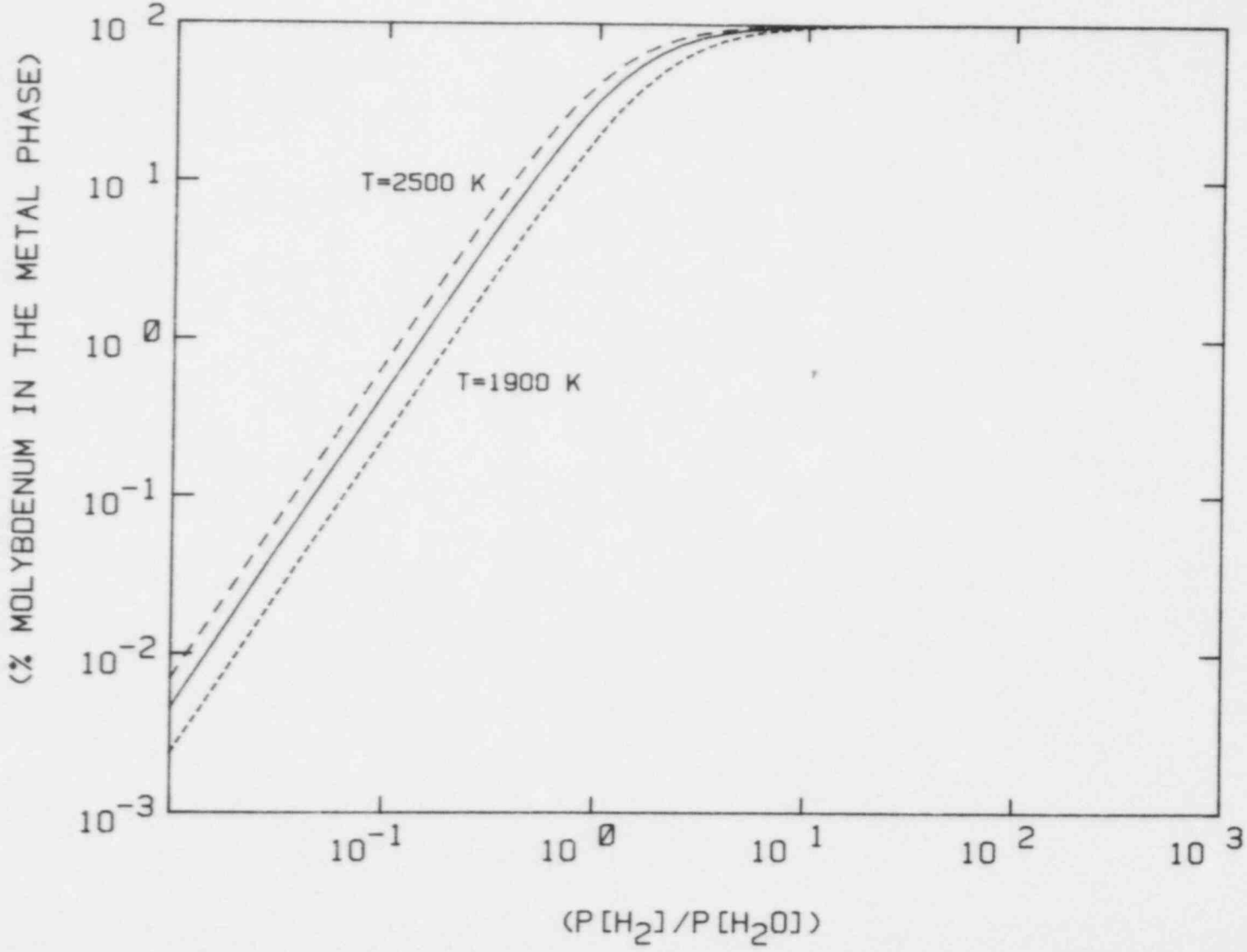

Figure 11. Calculated Partitioning of Molybdenum Between the Oxide and Metallic Phases of Core Debris. The solid line in the figure is for a temperature of 2200 K. The temperature assumed for calculating the dashed lines were 1900 and 2500 K as indicated.

Table 3

Experimental Partitioning of Radionuclides Between Iron and Urania[62]

Element	Wt % in Urania	Wt % in Iron
Zr	0.86	< 0.04
Zr	1.45	< 0.04
Zr	1.02	0.07
Y	1.50	0.10
Y	1.50	0.04
La	0.35	$< 3 \times 10^{-4}$
La	0.35	1×10^{-3} to 1×10^{-5}
Ce	0.68	0.02
Pr	1.94	0.16
Pr	0.55	0.02
Sr	0.86	$< 5 \times 10^{-3}$
Sr	1.02	$< 5 \times 10^{-3}$
Ba	0.41	$< 9 \times 10^{-3}$
Ba	0.51	$< 7 \times 10^{-3}$
Ru	< 0.01	1.29
Ru	< 0.01	1.14
Ru	< 0.01	1.60
Ru	< 0.01	0.21
Ru	< 0.01	0.45
Ru	< 0.01	0.61
Mo	0.08	1.20
Mo	0.06	1.02
Mo	0.07	0.97
Mo	0.12	0.84
Nb	0.32	0.56
Nb	0.36	0.74
Nb	0.68	0.54
Nb	0.30	0.88
Nb	0.90	0.01
Nb	0.60	0.18

Parker et al.[49] in simulated core meltdown experiments using flowing steam/hydrogen atmospheres. In a qualitative sense, the experimental data show that most species partition predominantly into one phase or the other. There are exceptions to this typical behavior. Partitioning of niobium is noteworthy in this context.

Direct application of the experimental data on partitioning is not easily done. In none of the experiments have oxygen potentials been controlled or even measured. The experiments have all been susceptible to kinetic effects. The experiments have not spanned the range of conditions expected to arise in the course of core debris/concrete interactions.

Total lack of attention to the chemistry of core debris during in-vessel phases of severe accident adds to the difficulty of establishing the partitioning of core debris constituents during ex-vessel phases of an accident.

For the current implementation of the VANESA model, a simplified treatment of partitioning has been adopted. Results of the experiments and simplified thermochemical analyses such as those described above for barium and molybdenum are used to define the partitioning of low-concentration species. These species are considered to be exclusively in either the oxide phase or the metal phase as shown in Table 4. This partitioning is taken to be invariant. The bulk constituents of the core debris, UO_2, Zr, Cr, Ni, and Fe, are not partitioned on this basis. The debris description obtained from the in-vessel models are taken at face value for these species. Uranium is assumed always to be exclusively in the oxide phase. As gases from the concrete oxidize Zr, Cr, Fe, and Ni, the products of oxidation, ZrO_2, Cr_2O_3, FeO and NiO, are assumed to pass into the oxide phase of the debris.

Apportioning radionuclides and other low concentration constituents exclusively into one phase or another provides substantial simplification of the VANESA model. The assumption assures that vaporization of a constituent need only be considered from one phase. At first this might seem undesirable. The considerations above concerning the thermochemistry of constituent partitioning hinge on equating the activities of species across a phase boundary. If two condensed phases are in equilibrium with each other then the composition of the vapor phase over each condensed phase will be the same at equilibrium. Thus, the thermochemical driving force for vaporization of constituents will be the same for both condensed phases. For most low concentration constituents of core debris, however, one phase will be quite dilute. Any vaporization from the dilute phase will

Table 4

Partitioning of Species Assumed in the Current Version of the VANESA Model

Species in the Metalic Phase	Species in the Oxide Phase
Elements Invariantly Partitioned	
Ag	Al_2O_3
Mn	BaO
Mo	CaO
Ru	CeO_2
Sb	CsOH
Sn	CsI
Te	K_2O
	La_2O_3
	Na_2O
	NbO
	SiO_2
	SrO
	UO_2
Partioned as Interaction Progresses	
Cr	Cr_2O_3
Fe	FeO
Ni	NiO
Zr	ZrO_2

result in a sharp reduction in the activity of the volatile constituent in the dilute phase. Further significant vaporization from the dilute phase will not occur until additional constituents are provided from the condensed phase which is more concentrated in the volatile material.

Once the core debris has assumed the configuration adopted for the VANESA model, constituents of one condensed phase can be transferred to another condensed phase only by mass transport across the relatively small surface area between the two phases. This type of mass transport between two immiscible phases is routinely encountered in steel manufacturing and can be quite slow.[63,64]

A simple model for the mass transport of a constituent across the oxide/metal phase boundary can be constructed. Assume that agitation of the melt phases by sparging gas keeps each melt phase uniformly concentrated except in a boundary layer adjacent to the interface. Assume, as before, that the transformation of an element from the metallic phase to the oxide phase involves the chemical process

$$M + xH_2O \rightarrow MO_x + xH_2 \quad .$$

At the interface, the concentrations of the elements are assumed in equilibrium. That is, only mass transport away from the interface or to the interface need be considered and any chemical kinetics are rapid. Then, as before,

$$\frac{Y(MO_x;\ \text{interface})}{X(M;\ \text{interface})} = \left(\frac{P_{H_2O}}{P_{H_2}}\right)^x \exp\left[-\Delta G(\text{Rxn})/RT\right] \quad .$$

The mass transport equations to and from the interface for dilute solutions are approximately

$$\frac{1}{A}\frac{dN(M)}{dt} = K(m)\ \rho^{\text{metal}}_{\text{molar}}\ [X(M;\ \text{bulk}) - X(M;\ \text{interface})]$$

$$\frac{1}{A}\frac{dN(MO_x)}{dt} = K(o)\ \rho^{\text{oxide}}_{\text{molar}}\ [Y(MO_x;\ \text{interface}) - Y(MO_x;\ \text{bulk})]$$

where $\frac{dN(M)}{dt}$ = rate per unit geometric surface area that M is supplied from the metal phase to the interface,

$\frac{dN(MO_x)}{dt}$ = rate per unit geometric surface area that MO_x is removed into the bulk oxide from the interface,

K(m) = mass transport coefficient in the metal phase,

K(o) = mass transport coefficient in the oxide phase,

X(M; bulk) = mole fraction M in the bulk metal phase,

X(m; interface) = mole fraction M at the interface,

$Y(MO_x;$ interface) = mole fraction MO_x at the interface,

$Y(MO_x;$ bulk) = mole fraction MO_x in the bulk oxide phase,

ρ^{metal}_{molar} = molar density of the metal phase,

ρ^{oxide}_{molar} = molar density of the oxide phase, and

A = surface area for mass transfer.

Assume that the bulk oxide phase is completely depleted of MO_x so $Y(MO_x;$ bulk) = 0. Also assume that the transfer processes are in quasi-steady state, so:

$$\frac{dN(M)}{dt} = \frac{dN(MO_x)}{dt} = \frac{dN}{dt} \quad .$$

Then,

$$\frac{1}{A}\frac{dN}{dt}\left[\frac{1}{K(m)\rho^{metal}_{molar}} + \frac{1}{K(o)\rho^{oxide}_{molar}\left(\frac{P_{H_2O}}{P_{H_2}}\right)^x \exp\left[-\frac{\Delta G(Rxn)}{RT}\right]}\right]$$

$$= X[M;\ bulk] \quad .$$

The mass transport coefficients, K(m) and K(o), can be found from the Higbie surface renewal model,[65] to be

$$K(m) = 2\left[\frac{D(M)}{\pi t_c}\right]^{1/2}$$

$$K(o) = 2\left[\frac{D(MO_x)}{\pi t_c}\right]^{1/2}$$

where $D(M)$ = diffusion coefficient for M in the metal phase,

$D(MO_x)$ = diffusion coefficient for MO_x in the oxide phase, and

t_c = characteristic time.

The characteristic time for the system can be taken as the reciprocal of the frequency bubbles pass through a unit surface area of the interface

$$t_c = \frac{1}{f} = \left(\frac{V_s}{\frac{4}{3}\pi r_b^3}\right)^{-1} \cong \frac{4}{V_s}$$

where V_s = surficial gas velocity (cm/s) and

r_b = radius of a bubble (cm).

The diffusion coefficients can be taken from the Wilke correlation:[66]

$$D = 7.4 \times 10^{-8} \frac{(M_B)^{1/2} T}{100\mu} \left(\rho_{molar}\right)^{0.6}$$

where M_B = molecular weight of the transporting species,

ρ_{molar} = molar density of the phase, and

μ = viscosity of the phase (Poises).

If the metallic phase is assumed to have a viscosity of 5 cp[63] and the oxide phase is taken to be urania somewhat enriched in silica from the concrete so its viscosity is about 1 poise,[67] then the diffusion coefficients for M and MO_x are about

$$D(M) = 9 \times 10^{-5}$$

and

$$D(MO_x) = 2 \times 10^{-6} \quad .$$

Then the mass transport coefficients for superficial gas velocities of 20 cm/s are

$$K(m) = 0.024 \text{ cm/s}$$

$$K(o) = 0.0036 \text{ cm/s}$$

which are typical of values found by experiments in steel processing.[63,64,66] Then for transfer of molybdenum at 2200 K and $P_{H_2}/P_{H_2O} = 20$, the mass transport equation becomes

$$\frac{1}{A}\frac{dN}{dt}\left[\frac{1}{0.0019} + \frac{1}{1 \times 10^{-7}}\right] = X(M; \text{ bulk})$$

or

$$\frac{dN}{dt} \cong 1 \times 10^{-7} \, X[M; \text{ bulk}]A \quad .$$

For a melt with a geometric surface area of 3×10^5 cm^2, the rate at which molybdenum could partition into the oxide phase is obtained from this model to be about 2×10^{-5} moles/s. This rate of transfer would not seriously alter the composition of the metal phase. Even if all of the transferred material vaporized from the oxide phase, it would not seriously contribute to the release of molybdenum from the melt. An increase in the superficial gas velocity to 200 cm/s would not alter the conclusion. A change in the chemical conditions that leads to more significant partitioning of molybdenum into the oxide phase could alter the conclusion, of course.

Gas phase transport of constituents from one condensed phase to another can be a more efficient process than condensed phase mass transport, if the gas is saturated. Saturating the dilute condensed phase by this process can be rapid. But once the dilute phase is saturated it will not affect the amount of material carried away by a saturated gas. Again, neglect of release from the dilute phase is not a major source of error.

2. Activities and Activity Coefficients

At several points in the discussions of the thermochemistry of vaporization from mixtures, activity coefficients for constituents of the mixture have been mentioned. In this subsection, these activity coefficients are discussed and the technology available for estimating activity coefficients is reviewed.

Consider the free-energy of one mole of a mixture composed of constituents A and B. If this mixture was of a mechanical nature, such as sand and steel balls, so that by some mechanical means it could be separated into batches of its pure constituents, then the free-energy of the mixture would simply be the weighted sum of the free-energies of the constituents:

$$G(\text{mechanical mixture}) = X_A G(A) + X_B G(B)$$

where X_i = mole fraction of the i^{th} mixture constituent and

$G(i)$ = free-energy of the pure i^{th} constituent.

If, however, mixing occurs at the molecular level, the constituents lose part of their individual chemical identities. No longer is a molecule of one constituent, for instance the A constituent, surrounded only by other A molecules. There is some finite probability that a given A molecule will contain in its coordination shell a B molecule. Likewise, the B molecules are no longer in the same coordination environment they experienced as a pure material. By mixing A and B at the molecular level, new sites any individual atom can occupy have been created. That is, it is no longer essential that B molecules reside adjacent to other B molecules *et cetera*. This means that, at a very minimum, molecular mixing has created the opportunity for much greater disordering of the mixture than was possible when the constituents retained their own chemical identities. This opportunity for greater disorder is reflected by greater entropy in the mixture than in the sum of the pure constituents. If the A and B molecules exhibit no preferences for locations in the mixture lattice sites and the interactions between A and B molecules have the same energies as interactions between two A molecules or two B molecules, then the free-energy of the molecular mixture is:

$$G(\text{molecular mixture}) = X_A G(A) + X_B G(B) + RT[X_A \ell n(X_A) + X_B \ell n(X_B)] \quad .$$

The additional term in this expression relative to that in the expression for the free-energy of a mechanical mixture reflects the increased entropy created by molecular mixing:

$$\Delta S(mix) = -R[X_A \ell n(X_A) + X_B \ell n(X_B)] \quad .$$

The expression for the free-energy of the mixture can be differentiated with respect to the amount (not mole fraction) of a constituent in the mixture to get the partial molar free energy of the constituent:

$$\frac{\partial(n_A+n_B)\ G(mixture)}{\partial n_A} = G(A) + RT\ \ell n(X_A) = G(A) + RT\ \ell n(a_A)$$

$$\frac{\partial(n_A+n_B)\ G(mixture)}{\partial n_B} = G(B) + RT\ \ell n(X_B) = G(B) + RT\ \ell n(a_B)$$

where n_i = moles of the i^{th} constituent in the mixture and

a_i = activity of the i^{th} constituent.

From these differentiations, it is immediately apparent that this mixture model, defined by hypothesizing random occupation of available sites by A or B molecules, is the ideal solution model. Activities of the mixture constituents are equal to the mole fractions of the constituents. The ideal model is a popular model for mixtures simply because it can be used with only data for the individual constituents in the pure state. Data for the mixture itself are not needed.

The derivation of this ideal model was done by imposing a severe, and not entirely believable, constraint of random, isoenergetic occupation of available sites. It would seem far more likely that a molecule, say a B molecule, would exhibit some preference for being adjacent to an A or a B molecule. Further, the energy of interaction between A and B molecules would be, in general, different than the interactions between two A molecules and between two B molecules. A formal description of the free-energy of such a more general mixture model can be written as:

$$G(mixture) = X_A G(A) + X_B G(B) + RT[X_A \ell n(X_A) + X_B \ell n(X_B)]$$

$$+ f(X_A, X_B, T) \quad .$$

The new term, $f(X_A,X_B,T)$, is then added to account for the nonideal aspects of the molecular mixing. (The additional term is called the "excess free energy.") Again, the partial molar free-energies of the constituents of this general mixture can be found:

$$\frac{\partial(n_A+n_B)\ G(\text{mixture})}{\partial n_A} = G(A) + RT\ \ell n(X_A) + f(X_A,X_B,T)$$

$$+ (X_B)\ \partial f/\partial X_A$$

$$\frac{\partial(n_A+n_B)\ G(\text{mixture})}{\partial n_B} = G(B) + RT\ \ell n(X_B) + f(X_A,X_B,T)$$

$$- (1-X_B)\ \partial f/\partial X_A$$

or

$$\frac{\partial(n_A+n_B)\ G(\text{mixture})}{\partial n_A} = G(A) + RT\ \ell n(\gamma_A X_A)$$

$$= G(A) + RT\ \ell n(a_A)$$

$$\frac{\partial(n_A+n_B)\ G(\text{mixture})}{\partial n_B} = G(B) + RT\ \ell n(\gamma_B X_B)$$

$$= G(B) + RT\ \ell n(a_B)$$

where $f \equiv f(X_A,X_B,T)$ and a_A and a_B are the activities of A and B, respectively. The activity coefficients of A and B are γ_A and γ_B, respectively.

This nonideal mixture model involves parameters not characteristic of the pure constituents--activity coefficients. The price of introducing greater realism into the mixture model is the requirement for additional information about the specific mixture as well as information on the pure constituents of the mixture. This can be a very high price indeed. As suggested by the functional form of $f(X_A,X_B,T)$, this additional information must be obtained as a function of temperature and a function of composition. It presents a rather serious problem simply because sufficient measurements of $f(X_A,X_B,T)$ may not have been made.

A substantial portion of the research into mixtures has been devoted to the formulation of models for the function $f(X_A, X_B, T)$. The next level of approximation after that used for the ideal solution model is to assume random occupation of sites in a mixture occurs, but that the energy of interactions between A and B molecules is not the same as between just A molecules or just B molecules. This is the "regular solution" model.[165] For this model

$$f(X_A, X_B, T) = LX_AX_B$$

$$RT \ln\gamma_A = L(X_B)^2$$

$$RT \ln\gamma_B = L(X_A)^2$$

where L is a parameter found typically by fitting the model to experimental data. By making more complicated assumptions concerning site occupation and the energetics of interactions, more complicated models can be created. Some of these models are shown in Table 5. Unfortunately, the diversity of chemical behavior exceeds the diversity of thermochemical approximations, so that completely empirical correlations have appeared. A frequently used empirical correlation is that developed by Redlich and Kister:[167]

$$f(X_A, X_B, T) = (X_AX_B)\left[\sum_{j=1}^{N} L_j(T)\,(X_A - X_B)^N\right] .$$

The data requirements for binary mixtures are demanding. For mixtures more complex than those involving just two constituents, the data requirements can become formidable indeed.

Parametric values for the various nonideal models listed in Table 5 can be temperature-dependent. Thus, the activity coefficient of a condensed phase species will depend, in general, on the composition and the temperature of the phase.

Activity coefficients are also dependent on the pressure experienced by the condensed phase:

$$\ln[\gamma(i,P)] = \ln[\gamma(i,P_{ref})] + \int_{P_{ref}}^{P} \frac{\bar{V}(i)}{RT}\, dP$$

where $\gamma(i,P)$ = activity coefficient of the i^{th} condensed phase constituent at pressure P,

Table 5

Some Models of Condensed Phase Mixtures

Model	Excess Free Energy	Activity Coefficients
Ideal Solution	$G^{XS} = 0$	$\gamma_A = \gamma_B = 1$
Regular Solution	$G^{XS} = LX_A(1-X_A)$	$RT\ell n\gamma_A = L(1-X_A)^2$ $RT\ell n\gamma_B = LX_A^2$
Margules	$G^{XS} = RTX_A(1-X_A)[A(1-X_A) + BX_A]$	$RT\ell n(\gamma_A) = RT(1-X_A)^2[A + 2(B-A)X_A]$ $RT\ell n(\gamma_B) = RTX_A^2[B + 2(A-B)(1-X_A)]$
Van Laar	$G^{XS} = RT\left[\frac{1}{AX_A} - \frac{1}{B(1-X_A)}\right]^{-1}$	$RT\ell n(\gamma_A) = A\left[\frac{B(1-X_A)}{AX_A + B(1-X_A)}\right]^2$ $RT\ell n(\gamma_B) = B\left[\frac{AX_A}{AX_A + B(1-X_A)}\right]^2$
Nonrandom Two Liquid	$G^{XS} = X_A(1-X_A)\left[\frac{\tau_{21}G_{21}}{X_A + G_{21}(1-X_A)} + \frac{\tau_{12}G_{12}}{G_{12}X_A + 1 - X_A}\right]RT$ $G_{12} = \exp(-\alpha\tau_{12})$ $G_{21} = \exp(-\alpha\tau_{21})$	$\ell n(\gamma_A) = (1-X_A)^2\left\{\tau_{21}\left(\frac{G_{21}}{X_A + (1-X_A)G_{21}}\right)^2 + \frac{\tau_{12}G_{12}}{(1-X_A+X_AG_{12})^2}\right\}$ $\ell n(\gamma_B) = X_A^2\left\{\tau_{12}\left(\frac{G_{12}}{1-X_A+X_AG_{21}}\right)^2 + \frac{\tau_{21}G_{21}}{(X_A + (1-X_A)G_{21})^2}\right\}$

P_{ref} = reference pressure which is usually one atmosphere, and

$\bar{V}(i)$ = partial molar volume of the i^{th} constituent of the condensed phase.

Partial molar volumes of condensed phase constituents are almost never known. For systems that are not too strongly nonideal at conditions well removed from their critical points, the partial molar volumes of the constituents may be approximated by their molar volumes when pure.

Then,

$$\ell n[\gamma(i,P)] \approx \ell n[\gamma(i,P_{ref})] + \frac{V(i)(P-P_{ref})}{RT} \quad .$$

For typical constituents of core debris, the molar volumes are on the order of 20-30 cm^3/mole. For a pressure of 10 atmospheres and a temperature of 1800 K, the second term (the so-called Poynting correction factor) on the right-hand side of the above equation will have values, typically, of only 0.0012 to 0.0018. Pressures encountered in core debris/concrete interactions, then, cause negligible changes in the activity coefficients of condensed phase species.

The mixtures that are of interest in the study of ex-vessel core debris interactions are very complex. Many constituents must be considered. Studies of these mixtures have never been conducted in sufficient detail to make it possible to rigorously pursue some of the higher level approximations of the free energy of mixtures. Data are available for the pure constituents. In some cases there are data[168] for binary mixtures involving the metallic constituents. But very little information will be found for ternary and higher order combinations. These facts mean that thermochemical models, including those in the VANESA model, will have to rely heavily on ideal solution models. Since the beautiful Rachel cannot be wed, it is wise to examine the virtues of the ugly Leah.[169]

Consider again the ideal and the regular solution models for binary mixtures:

$$G(ideal) = X_A G(A) + X_B G(B) + RT[X_A \ell n(X_A)$$

$$+ X_B \ell n(X_B)]$$

$$G(\text{regular}) = X_A G(A) + X_B G(B) + RT[X_A \ln(X_A) + X_B \ln(X_B)] + L X_A X_B \quad .$$

It is immediately obvious that the entropy of mixing contribution to the free energy of the mixture, $RT[X_A \ln(X_A) + X_B \ln(X_B)]$, is a linear function of temperature. As temperatures increase this entropic contribution will become more important and will, eventually, dominate the mixture free energy. At sufficiently elevated temperatures the correction to the thermochemistry produced by the regular solution term, LX_AX_B, will not be important in comparison to the entropic term. The same will be true for the higher level approximations discussed above and shown in Table 5. At sufficiently high temperatures, all mixtures approach ideal behavior. This is true because thermal excitations of molecules will eventually overwhelm any preference molecules exhibit for sites in the mixture lattice and the energetics of bonding will become small in comparison to the thermal energy.

The VANESA model concerns itself with high temperature vaporization. Vaporization occurs because bonding that keeps a molecule in the condensed state becomes weak in comparison to the thermal energy a molecule can acquire through fluctuations. It would appear then that the VANESA model is concerned with situations in which the entropic contributions to the mixture free energy are important, if not dominant. For this reason, the ideal solution model might be a better-than-expected first approximation.

The ideal solution model was developed above for binary mixtures. What was said for mixtures of two materials can also be said for mixtures containing more constituents. Thus, the free energy of an ideal mixture of N components is

$$G(\text{mixture}) = \sum_{i=1}^{N} X_i G(i) + RT \sum_{j=1}^{N} X_j \ln(X_j) \quad .$$

But note what happens as constituents are added to the mixture. The mole fraction of each constituent becomes smaller and as a result the absolute magnitude of the entropic term becomes larger. This is a most important observation. Consider a mixture of equal parts of A and B. The entropic contribution to the free-energy of the mixture is -0.693 RT. Now, suppose the mixture consists of equal parts A and B and a 1/10 part C. The entropic contribution to the free energy of the mixture is now -0.949 RT--an increase by almost

50 percent. For the very complex mixtures involved in the interaction of core debris with concrete, the entropic contributions to the free-energy of mixing can be huge and may overwhelm in importance any contribution by terms added to the mixture free energy to reflect nonideality. The minimum model to adequately portray this important feature of the mixture is the ideal solution model.

Though the ideal solution model may be suitable for the overall description of mixtures in the VANESA model, the behavior of specific constituents, particularly radionuclides, may be of sufficient interest to require a more detailed treatment. This might at first appear to be a difficulty. The derivations above show that as soon as nonideal characteristics for one constituent are introduced, they must be recognized for all constituents. This is true in a rigorous sense. But it is possible to adopt approximate treatments that are not rigorously correct and still not cause gross violations of thermodynamics that lead to unrealistic behavior. Consider the activity coefficients for mixtures consisting of a large amount of A, which could be urania, and a small amount of B, which could be a radionuclide. The activity coefficients of these constituents are:

$$\ln(\gamma_A) = L\, X_B^2/RT$$

$$\ln(\gamma_B) = L\, X_A^2/RT \quad .$$

Clearly, as the mole fraction of B becomes small, the activity coefficient of A approaches one at a second order rate. The activity coefficient of B, on the other hand, is practically invariant as the mole fraction of B becomes small. Thus,

$$\ln(\gamma_A) \approx 0$$

$$\ln(\gamma_B) \approx L/RT \quad .$$

It is then possible to introduce simplified corrections to the ideal solution model for individual constituents, especially if these constituents are present at low concentrations.

Though an approximate method to correct for nonidealities is available, there is still the problem of determining the correction to be made. One source of information is phase diagrams of binary pairs of melt constituents. The

ideal mixture assumption implies one of two types of phase diagrams:

1. No solid solubility but complete liquid phase miscibility.

2. Complete miscibility in both the solid and liquid phases.

The first of these diagrams will involve a eutectic interaction between the constituents. If the constituents are designated A and B, this eutectic is located at a temperature $T(\epsilon)$ and a composition $X(\epsilon)$ found by the simultaneous solution of:

$$0 = \frac{\Delta H_m(A)}{R}\left[\frac{1}{T(\epsilon)} - \frac{1}{T_m(A)}\right] + \ell n(X(\epsilon))$$

$$0 = \frac{\Delta H_m(B)}{R}\left[\frac{1}{T(\epsilon)} - \frac{1}{T_m(A)}\right] + \ell n(1-X(\epsilon))$$

where the differences in the heat capacities of the liquid and solid have been neglected and $\Delta H_m(i)$ = heat of fusion of the i^{th} constituent, $T_m(i)$ = melting point of the i^{th} constituent.

By comparing the predicted location of the eutectic with that experimentally observed, an indication of the need to model nonideality is obtained.

The second of these ideal phase diagrams will produce a classic, lenticular, two-phase region whose boundaries are found by the simultaneous solution of

$$0 = \frac{\Delta H_m(A)}{R}\left[\frac{1}{T} - \frac{1}{T_m(A)}\right] + \ell n\left[\frac{X(A)}{Y(A)}\right]$$

$$0 = \frac{\Delta H_m(B)}{R}\left[\frac{1}{T} - \frac{1}{T_m(B)}\right] + \ell n\left[\frac{(1-X(A))}{(1-Y(A))}\right]$$

where $X(A)$ = mole fraction of A in the liquid phase and

$Y(A)$ = mole fraction of A in the solid phase.

Again, comparison of the predictions of the ideal solution model to the actual phase diagram will indicate the

need for a more sophisticated treatment of the condensed phase. A thorough study of the various binary interactions that arise in molten core debris has not been attempted. Some analyses have been done which will illustrate the procedure:

1. UO_2-Al_2O_3 System: A calculated phase diagram for this system is shown in Figure 12. The predicted eutectic occurs at T = 2192 and $X(UO_2)$ = 0.291. These results compare well with the experimental determination[170] that the eutectic is at T = 2173 K and $X(UO_2)$ = 0.26. This suggests that ideal solution interactions are appropriate for the UO_2-Al_2O_3 system.

2. UO_2-SiO_2 System: A calculated phase diagram for the the UO_2-SiO_2 system is shown in Figure 13. A eutectic interaction is predicted to occur at T = 1713 K and $X(UO_2)$ = 0.091. The experimental data for the UO_2-SiO_2 system are not firmly established. Lange et al.[171] observed a eutectic interaction at 10-15 mole percent UO_2 but at a temperature of 1923 K. Lungu[172] observed liquid phase immiscibility in this regime and thought any invariant point on the diagram would occur at very low uranium dioxide concentrations. A schematic representation of the Lungu diagram is shown in Figure 13. Obviously, the interactions between SiO_2 and UO_2 are not ideal. If the Lungu diagram is correct then there is a strongly positive excess free-energy of mixing in the system. This implies, of course, activity coefficients that are greater than one. Correction for the nonideality to conform with the Lungu diagram is not easily done. Since the two-phase miscibility gap in the liquid phase is not symmetrically disposed around a mole fraction of 0.5, a regular solution model would not describe the system adequately.

A regular solution model can be used to make the system conform to the diagram proposed by Lange et al. When this is done, the activity coefficients for urania and silica are found to be about

$$\ell n(\gamma(UO_2)) = \frac{750}{T}\left[1 - X(UO_2)\right]^2$$

$$\ell n(\gamma(SiO_2)) = \frac{750}{T}\left[X(UO_2)\right]^2 \quad .$$

Thus, the phase diagram obtained by Lange et al. implies that activity coefficients are greater than one though not as great as values suggested by the Lungu diagram.

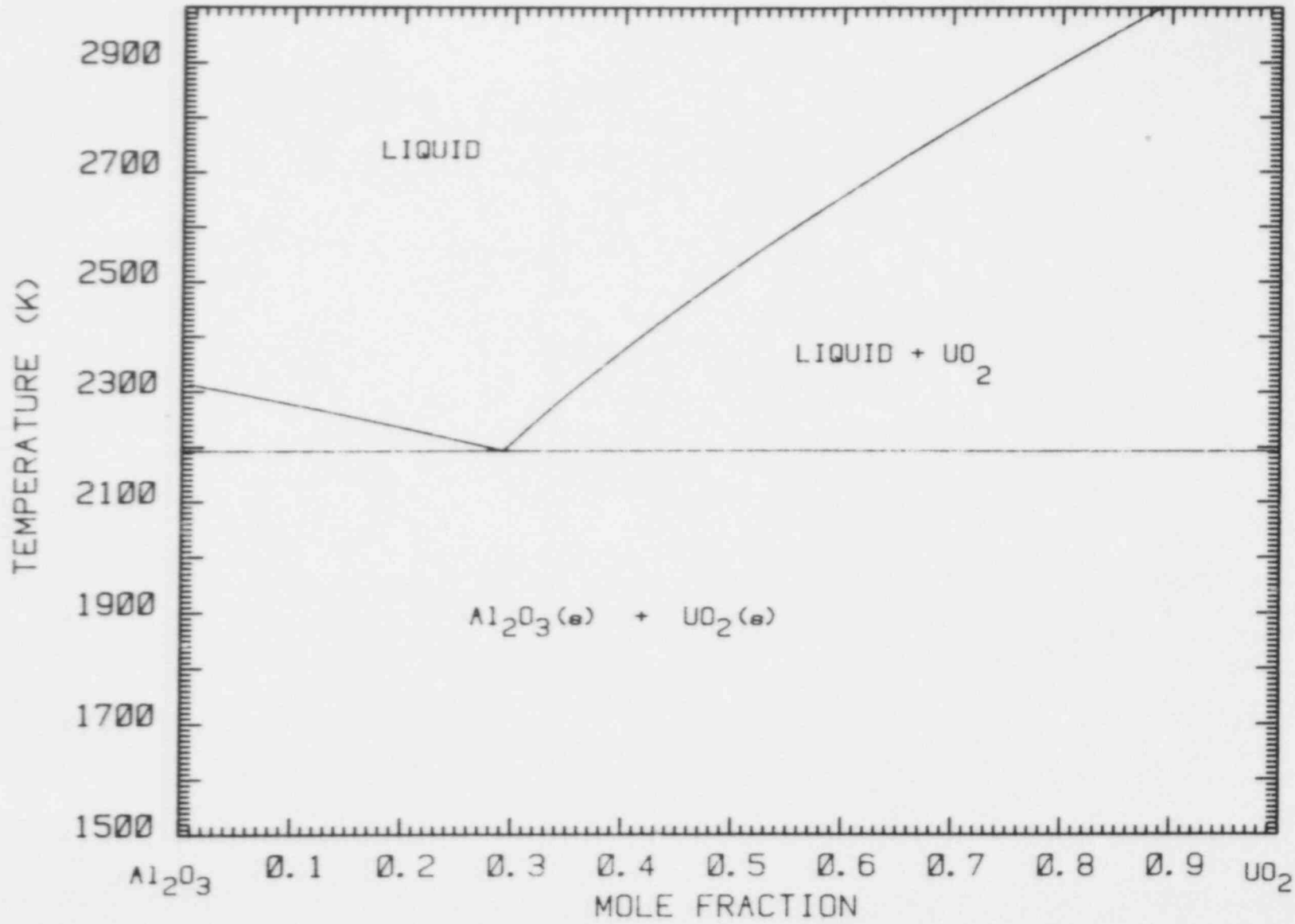

Figure 12. Calculated Phase Diagram for the UO_2-Al_2O_3 System

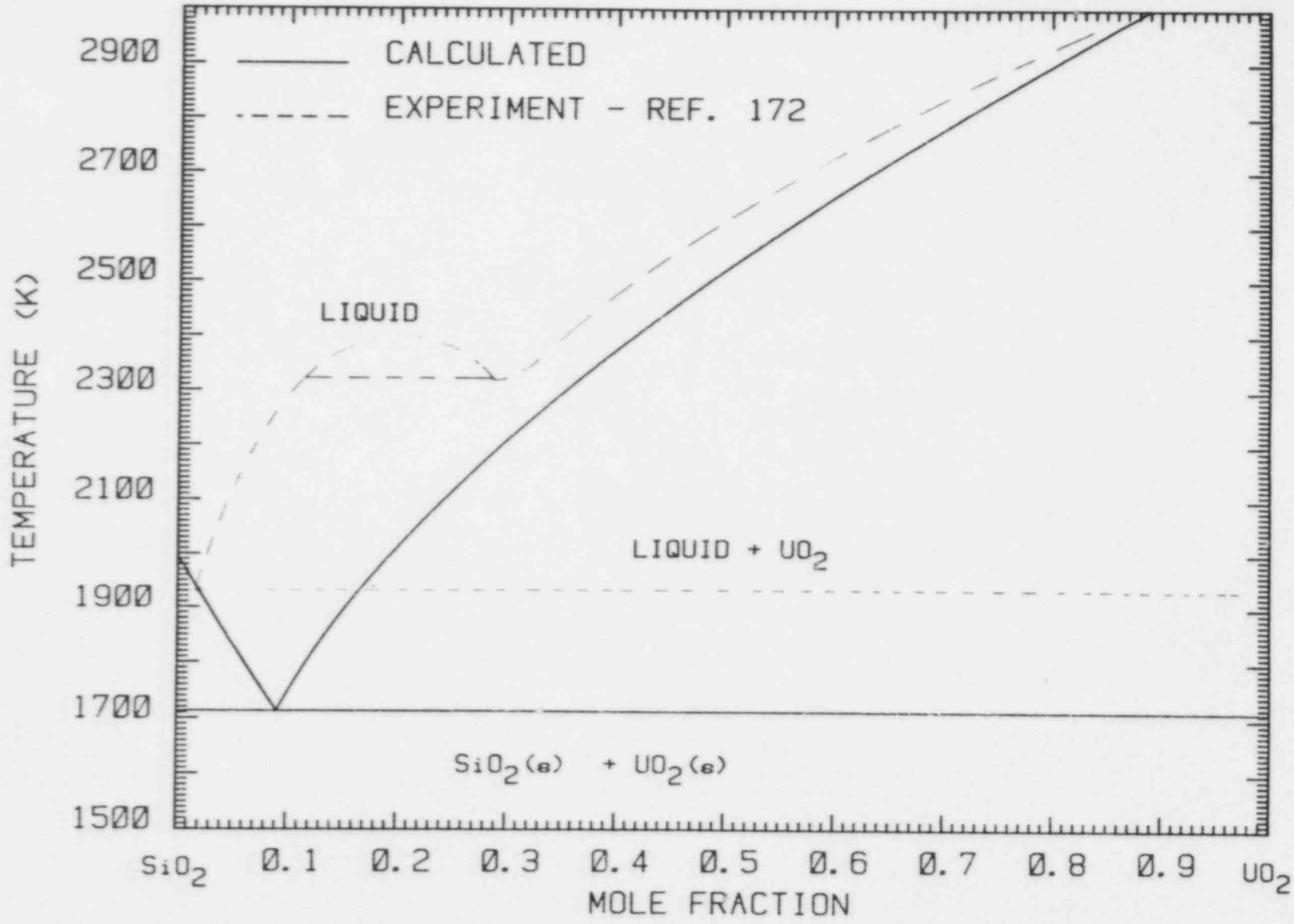

Figure 13. Calculated (Solid Lines) and Observed (Dashed Lines) Phase Diagrams for the UO_2-SiO_2 System

3. UO_2-ZrO_2: The phase diagram for the UO_2/ZrO_2 system at very high temperatures indicates that ZrO_2 and UO_2 are mutually soluble in both the liquid and the solid states.[173] The two-phase region has a minimum rather than a classic lenticular shape. Powers[61] has examined this system using a regular solution model for both the liquid and the solid phases. A comparison of his calculated diagram and data from Reference 85 is shown in Figure 14. Parameterization of the regular solution model yields

$$\ln(\gamma(UO_2)) = \frac{3500}{T}\left[1 - X(UO_2)\right]^2$$

$$\ln(\gamma(ZrO_2) = \frac{3500}{T}\left[X(UO_2)\right]^2 \quad .$$

That is, deviations from ideality are positive.

4. Na_2O-SiO_2 System: Sodium enters into the core melt with ablated concrete. Selection of Na_2O as a constituent for the melt is a convenience for presentation of the results. But it is likely that the material is better considered to be sodium silicate. Considering molten sodium silicate to be an ideal mixture of Na_2O and SiO_2 leads to prediction of a eutectic of T = 1124 K and $X(SiO_2)$ = 0.639. This, of course, is at striking odds with the observed phase diagram for the system.[175] The observed phase diagram includes several compounds and eutectic interactions between these compounds. Attempts to model the behavior of sodium oxide in silica lead to rather complex models.[176]

Some vaporization studies of sodium silicate have been conducted.[177] Data for the activity of Na_2O in a 50 mole percent mixture with silica for temperatures between 1100 and 1400 K can be fit well to an expression of the form:

$$RT \ln(\gamma(Na_2O)) = -29{,}000 \quad .$$

If the system is assumed regular, then

$$\ln(\gamma(Na_2O)) = \frac{-58{,}380}{T}\left(1 - X(Na_2O)\right)^2 \quad .$$

Extrapolation of this regular solution expression to 2500 K indicates the activity of Na_2O entering the melt as a 50 mole percent mixture with silica is only 0.003!

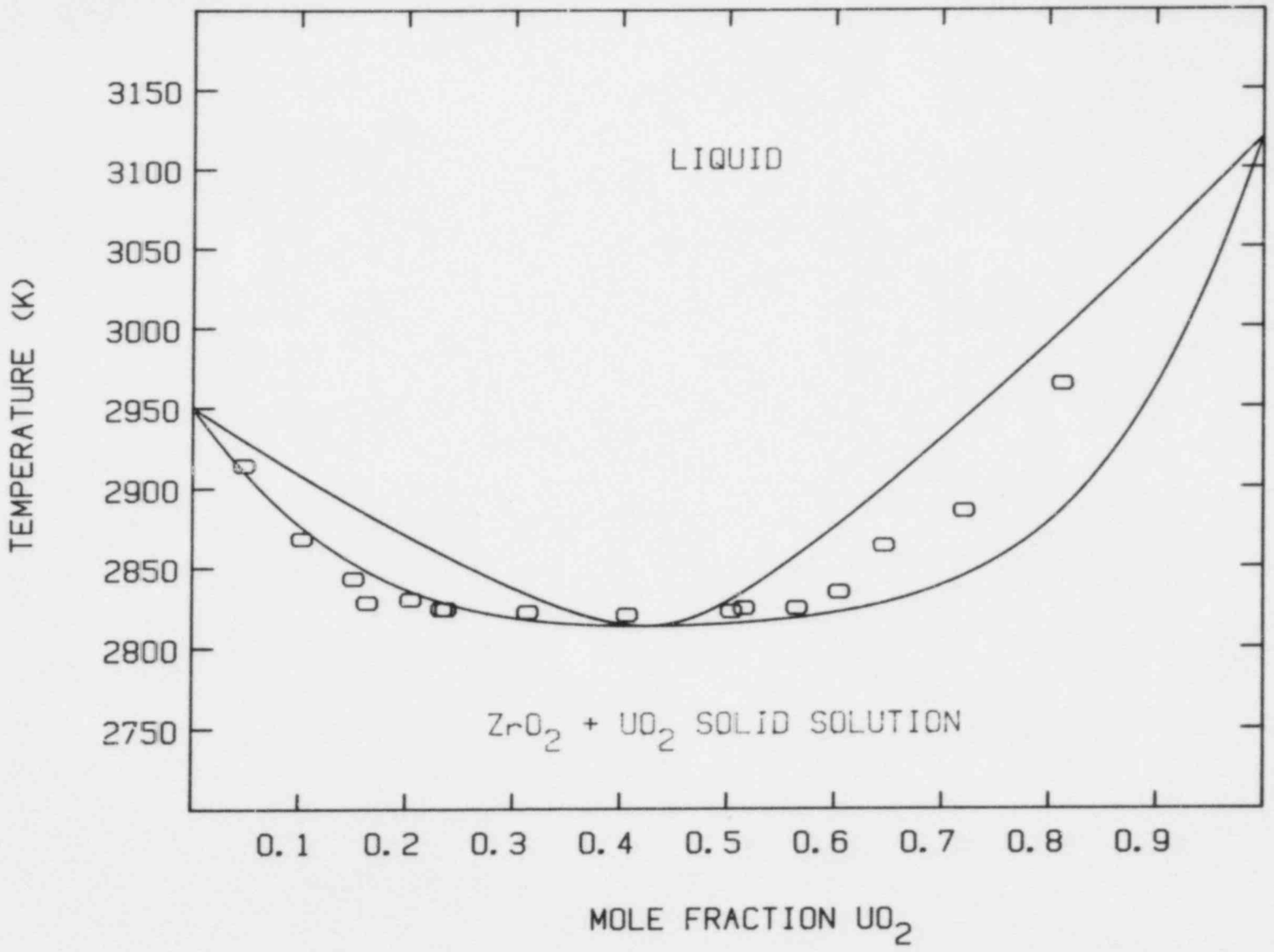

Figure 14. Calculated Phase Diagram (Solid Lines) and Observed Solidus Data (Points) for the UO_2-ZrO_2 System

A similar situation arises also for potassium oxide.[178] The activity of K_2O is very much less than would be suspected from the concentration.[349]

The quantitative model for the Na_2O-SiO_2 system developed above applies only to the activity of sodium oxide as it enters the core melt during ablation of the concrete. Once dissolved in the larger melt, the activity coefficient is affected. Assume that the oxide phase of a core melt can be simplified to be a ternary mixture of UO_2, Na_2O, and SiO_2. Assume further that the UO_2-Na_2O and the UO_2-SiO_2 systems are ideal. Then, the activity coefficient of Na_2O in the mixture will be given by

$$RT \ln[\gamma(Na_2O)] = X^2(SiO_2)\alpha + X(SiO_2)\, X(UO_2)\alpha$$

where $\alpha = -116{,}760$ cal/mole is obtained from the analysis of the Na_2O-SiO_2 system. Clearly, when concrete ablation has just begun $X(SiO_2)$ will be much less than one and Na_2O will behave in an essentially ideal manner. As the ablation progresses, and the silica concentration of the melt increases, Na_2O will become less and less ideal. For a typical analysis with the VANESA model, the activity coefficient of Na_2O estimated in this way falls to 6×10^{-4} when concrete constitutes about 50 mole percent of the core melt.

The behavior of silica incorporated into the core melt is a complex issue that as yet has not been ellucidated by the analyses possible during the limited time available for development of the VANESA model. The analyses above are sufficient to show that Na_2O and K_2O ought not be considered ideal melt constituents.

The presence of silica in the melt may affect the volatility of radionuclides. In particular, ablated concrete that is incorporated into the melt may alter the speciation of barium and strontium in such a way that they are less easily vaporized. Approximation of the melt as a regular ternary system consisting of UO_2 - SiO_2 - BaO (or SrO) and using the barium silicates (Ba_2SiO_4 or $BaSiO_3$) as the basis for parameterizing the regular solution will lead to the conclusion that the melt need contain only about 5 mole percent silica to reduce the activity of barium oxide and consequently the barium volatility by a factor of ten. Such low silica concentrations would be obtained quickly during melt interactions with concrete.

It must be remembered, however, that silica enters the melt in a far from pure state. Typical concretes contain a variety of materials more basic than silica. Iron oxide, sodium oxide, and potassium oxide will compete with barium

or strontium for reaction with silica.[85] But, the most abundant competitors for reaction with silica in typical concretes are magnesium and calcium. Approximation of the melt as a ternary system is then not adequate. The effects of competition for silica must be included.

To obtain a sense of the effects silica might have on the volatility of barium, a simple model is considered here. It is assumed melted concrete can be represented as a mixture of CaO and SiO_2. The oxide phase of the core melt is considered to consist of ablated concrete, barium oxide, and other "inert" oxides. The constituents of the melt are considered to speciate into BaO, CaO, SiO_2, Ba_2SiO_4, $BaSiO_3$, $CaSiO_3$, and Ca_2SiO_4 as well as the "inert" oxides (UO_2, ZrO_2, etc.). The speciation can be expressed by the reactions

$$BaO(\ell) + SiO_2(\ell) \rightleftharpoons BaSiO_3(\ell)$$

$$BaO(\ell) + BaSiO_3(\ell) \rightleftharpoons Ba_2SiO_4(\ell)$$

$$CaO(\ell) + SiO_2(\ell) \rightleftharpoons CaSiO_3(\ell)$$

$$CaO(\ell) + CaSiO_3(\ell) \rightleftharpoons Ca_2SiO_4(\ell) \quad .$$

This speciation is, of course, very simplistic. It is well established that upon melting, silicates exhibit a broad range of polymerization.[87,343-345] Anions such as

$$SiO_4^{4-}$$

$$Si_2O_7^{6-}$$

$$Si_3O_9^{6-}$$

$$Si_3O_{10}^{8-}$$

etc.

have been identified in liquefied silicates.[87]

It is further assumed, despite the simplistic speciation, that the melt is ideal. That is, the activity of barium oxide in the melt is equal to its mole fraction:

$$a(BaO) = X(BaO) = m(BaO)/\sum_i m(i)$$

where $m(i)$ = moles of the i^{th} species,

$$\sum_i m(i) = m(BaO) + m(CaO) + m(SiO_2) + m(BaSiO_3) + m(Ba_2SiO_4) + m(CaSiO_3) + m(Ca_2SiO_4) + m(I), \text{ and}$$

$m(I)$ = moles of "inert" oxides in the melt.

The activity of BaO determined in this way can be compared to the activity of barium oxide neglecting speciation within the melt:

$$\alpha'(BaO) = X'(BaO) = \frac{M(BaO)}{M(BaO) + M(CaO) + M(SiO_2) + M(I)}$$

where $M(i)$ = moles of the i^{th} constituent in the melt where i = BaO, CaO, SiO_2, and inert oxides (I).

The discrepancy between the two estimates of the activity can be expressed in terms of an activity coefficient:

$$X'(BaO)\gamma = X(BaO) \quad .$$

The activity coefficient expresses then the magnitude of the error attendant to the current implementation of the VANESA model which neglects silicate formation.

To pursue the model, free-energy data for the various species are needed. Data for $BaO(\ell)$, $CaO(\ell)$, and $SiO_2(\ell)$ were taken from the JANAF Tables (279 a,c). Thermodynamic data for the silicates in the liquid state were estimated from data for the crystalline silicates[98,290] as follows:

a. The enthalpy of fusion of Ca_2SiO_4 was taken to be the sum of the enthalpies of fusion of $CaSiO_3$ [290] and CaO.[279] The melting point was taken to be 2403 K.[290]

The heat capacity of liquid Ca_2SiO_4 was taken to be 49 cal/mole-K.[290]

b. The enthalpy of fusion of $CaSiO_3$ was taken to be 19800 cal/mole. The melting point was taken to be 1817K, and the heat capacity was taken to be 35 cal/mole-K.[290]

c. The entropies of fusion and the heat capacities of liquid $BaSiO_3$ and Ba_2SiO_4 were taken to be the same as those of the respective calcium silicates. The melting points of $BaSiO_3$ and Ba_2SiO_4 were taken to be 1878 and 2033K, respectively.[98]

This simple model was applied to the binary system CaO - SiO_2. Calculated and experimentally determined activity coefficients for CaO in this system at 1873K are compared below:

Bulk Mole Fraction CaO	Activity coefficient of CaO	
	From expt[155]	Calculated
0.8	0.79	0.845
0.7	0.46	0.474
0.6	0.015	0.105

This comparison is quite pleasing since it is unlikely that the experimental activity coefficients are more accurate than $\pm$0.1.

The model was then applied to a hypothetical core melt consisting of 300,000 moles of inert oxide, 400 moles of barium, and a constant 30,000 kg of concrete represented as a mixture of CaO and SiO_2 with varying ratios of calcium and silicon (C/S ratio). Results obtained for assumed temperatures of 2500 and 2000K are shown below:

	At 2000K for			At 2500K for		
	C/S = 1	C/S = 3	C/S = 7	C/S = 1	C/S = 3	C/S = 7
X(BaO)	4.4×10^{-7}	1.6×10^{-4}	3.7×10^{-4}	1.6×10^{-6}	3.1×10^{-4}	4.9×10^{-4}
γ(BaO)	9×10^{-4}	0.33	0.76	0.003	0.646	1.03
X($BaSiO_3$)	7×10^{-4}	4.1×10^{-4}	1.2×10^{-4}	7×10^{-4}	3.4×10^{-4}	6.5×10^{-4}
X(Ba_2SiO_4)	2.6×10^{-7}	5.6×10^{-5}	3.8×10^{-5}	1.8×10^{-7}	1.8×10^{-5}	5.4×10^{-6}
X(CaO)	0.0045	0.261	0.480	0.0008	0.251	0.478
γ(CaO)	0.0143	0.547	0.858	0.025	0.525	0.855

	At 2000K for			At 2500K for		
	C/S = 1	C/S = 3	C/S = 7	C/S = 1	C/S = 3	C/S = 7
$X(CaSiO_3)$	0.385	0.035	0.008	0.008	0.021	0.090
$X(Ca_2SiO_4)$	0.0362	0.190	0.085	0.087	0.207	0.005
$X(SiO_2)$	0.04	$6x10^{-5}$	$8x10^{-6}$	0.095	$2x10^{-4}$	$2.8x10^{-5}$
$\gamma(SiO_2)$	0.126	$4x10^{-4}$	$1x10^{-4}$	0.30	0.0014	$3.5x10^{-4}$

The results show that the effects of incorporating concrete into the melt on the volatility of barium depend strongly on the ratio of calcium to silicon in the concrete. At ratios near 1, the activity of barium oxide, and consequently the volatility of barium is sharply reduced. As the ratio increases, the activity coefficient of barium oxide rises sharply. The activity coefficient (but not the activity) will actually exceed one because of the varying molecularity of the melt for sufficiently high calcium to silicon ratios. The activity coefficient of calcium behaves in a similar way.

For real concretes, the sensitivity of the barium and calcium activity coefficient is to the ratio of all reactants to silica and not just to the calcium-to-silicon ratio. Thus, to model silicate formation in core melts, account of magnesium, iron, alkali metal oxides, and the like must be taken.

For all cases considered above, the activity coefficient of silicon dioxide is substantially depressed. This activity coefficient does not approach 1 until the calcium to silicon ratio in the ablated concrete falls below 1. Because of the low SiO_2 activity, silica is assumed in the VANESA model to be always in the oxide phase even when calculations assuming ideal solution behavior indicate SiO_2 should reduce to silicon metal. The cases examined here do illustrate that speciation of the melt can affect the volatility of bulk, nonradioactive constituents of the melt as well as affecting radionuclide release.

The results presented above are intended to be illustrative and ought not be interpreted too definitively. They show how melt chemistry can affect volatility. Careful examination of the results will also show that it is difficult to analyze the chemistry of core melts. Data for complex oxides are difficult to obtain. For instance, estimated data for $BaSiO_3$ used in the above example may overemphasize the stability of this species. Even when such data are available, solution phase interactions among various species are difficult to anticipate. Though a model of silicate chemistry superior to that described here can be formulated,[343-345]

there will always be a need to experimentally verify the adequacies of any model of liquid phase chemistry during melt/concrete interactions. Fortunately, as discussed above, the entropic effects of mixture formation tend to mute the importance of detailed analyses of melt speciation.

All of the preceding examples deal with the oxide phase constituents of a core melt. A superior data base is available for estimating activity coefficients in the metal phase at least for temperatures routinely encountered in steel making (<1900 K). A typical model for activity coefficients in the metallic phase was originally proposed by Wagner:[179]

$$\ln \gamma(i) = \ln \gamma^{\infty}(i) + \sum_{j=2}^{N(m)} \epsilon_i^{(j)} X(j) + \sum_{j=2}^{N(m)} \rho_i^{(j)} X(j)^2 + \sum_{j=2}^{N(m)-1} \sum_{k>j}^{N(m)} \rho_i^{(j,k)} X(j)X(k)$$

where N(m) = number of metal phase constituents and the parameters are $\epsilon_i^{(j)}$, $\rho_i^{(j)}$, $\rho_i^{(j,k)}$, and $\gamma^{\infty}(i)$. The parameter $\gamma^{\infty}(i)$ is, of course, just the activity coefficient for the i^{th} constituent when infinitely dilute in the major alloy phase which is designated the number one constituent of the alloy in this model. Tabulated values are available for the parameters appropriate for constituents in an iron-based alloy at 1873 K.[88] Some of these parameters are listed in Table 6.

Based on these parameters, the activity coefficients in a pure 18-8 stainless steel melt at 1873 K are

$$\gamma(Fe) = 0.99943$$

$$\gamma(Cr) = 1.00$$

$$\gamma(Ni) = 0.670 \quad .$$

Clearly, these alloy constituents can be considered to be essentially ideal.

The metallic phase of a core melt may contain zirconium at concentrations much higher than those encountered in deoxidizing steel with zirconium. The limited parametric data shown in Table 6 may be extrapolated to higher concentrations and temperatures to yield

Table 6

Parameters for Calculating the Activity Coefficients of Constituents of the Metallic Phase of Molten Core Debris With the Wagner Model

Constituent	$\gamma^{\infty}(i)$	$\epsilon_i^{(i)}$
Chromium (ℓ)	1.0	0
Nickel	0.66	0.2
Zirconium (ℓ)	0.037	
Uranium (ℓ)	0.027	9.4
Niobium (ℓ)	1	-0.7
Silver (ℓ)	200	-19
Tin (ℓ)	2.8	-0.3
Carbon (graphite)	0.7	6.9
Manganese (ℓ)	1.3	0
Molybdenum (ℓ)	1.0	

$\epsilon_C^{(Ag)} = 11.5$

$\epsilon_C^{(Cr)} = -5.1$

$\epsilon_C^{(Ni)} = 2.9$

$\epsilon_C^{(Sn)} = 19$

$\rho_C^{(c)} = 11.6$

$p_C^{(Cr)} = -0.4$

$\epsilon_{Cr}^{(Ag)} = -2$

$\epsilon_{Cr}^{(c)} = -5.1$

$\epsilon_{Cr}^{(Sn)} = 3.3$

$\epsilon_{Ni}^{(c)} = 2.9$

$\epsilon_{Ag}^{(c)} = 11.5$

$\epsilon_{Ag}^{(Cr)} = -2$

$\epsilon_{Sn}^{(c)} = 19$

$$\ell n(\gamma(Zr)) = \frac{-12270}{RT} [1 - X(Zr)]^2 \quad .$$

At 2200 K and 10 atom percent Zr, the activity coefficient of Zr in iron is then estimated to be 0.1. As termperatures rise Zr in steel becomes more ideal in its behavior.

The alloying behavior of silver, tin, and carbon distinctly differ from ideal. Silver, especially, has a rather large activity coefficient when dissolved in iron. The complexities of carbon dissolved in metallic melts will be discussed further in this document in connection with the reactions of gases with the core melt.

A thorough review of the activity coefficient data for all the constituents of the melts formed in core debris interactions with concrete was not possible in the brief time available for the development of the VANESA model. The approximations adopted in the development were as follows:

1. Nearly all constituents of the metallic and the oxidic phase of the core melt were assumed to be ideal.

2. Na_2O and K_2O were taken to be nonideal and to have activity coefficients of 10^{-8} that were independent of temperature and composition.[356]

3. The difficulties of carbon activity are treated essentially by neglect as is discussed further, below.

3. Fugacity Coefficients for Gas Phase Species

As in the case of mixing condensed-phase species on a molecular level, mixing of gases creates disorder in a system. The activities of gases in a mixture are affected then by an entropic contribution to the free-energy of the mixture. As long as each gas phase molecule is free to occupy without preference any point in the mixture volume--that is, occlusion of some of the volume by the other molecules is negligible--the entropic term means that the partial molar free energy of a mixture constituent is simply a function of its partial pressure:

$$\frac{\partial \left[\sum_{j=1}^{N(g)} n_j \right] G(\text{mixture})}{\partial n_i} = G(i) + RT \, \ell n[P(i)]$$

where $P(i)$ = partial of the i^{th} constituent and

G(i) = free energy of the i^{th} constituent when pure and in its reference state.

This is, of course, just the ideal gas law.

Gas phase species do, of course, have finite volumes and, consequently, they do exclude from each other a certain amount of the volume occupied by a mixture or even a pure gas. Thus, even for pure gases nonideality can affect thermodynamic properties. These nonideal effects are accentuated when there is a tendency for gas phase molecules to either preferentially associate or repel. As long as the finite volume effects and the effects of preferential association are not too strong, they can be accounted for conveniently by introducing a partial fugacity coefficient:

$$\frac{\partial \left[\sum_{j=1}^{N(g)} n_j\right] G(\text{mixture})}{\partial n_i} = G(i) + RT \ln(\phi(i)\, P(i))$$

where $\phi(i)$ is the partial fugacity coefficient.

Preparing models or correlations that yield values for the partial fugacity coefficients has been a prolific field. Nearly all of these developments have proceeded from the formulation of an equation of state for the pure gas:

$$PV/RT = 1 + Z$$

where Z = 0 for an ideal gas. Some of these models, the expression for the fugacity coefficients of the pure gas, and the partial fugacities of gas mixture constituents are shown in Table 7. Obviously, models of the nonideal gas phase can get quite complicated. Models that are currently popular, such as the so-called Lee-Kister model,[166] are substantially more complicated than those shown in the table.

Parameters and data are available to evaluate these models for the permanent gases of interest here--CO_2, CO, H_2, and H_2O. Fugacity coefficients for the pure gases computed with the Redlich-Kwong equation of state for a pressure of 10 atmospheres and ignoring thermal dissociation of the gases are shown in Figure 15. A plot of partial fugacity coefficients for a mixture of 45 percent H_2, 5 percent H_2O, 5 percent CO_2, and 45 percent CO prepared ignoring dissociation or reactions in the gas phase is shown in Figure 16. It is apparent from the plotted results that the noncondensible gases produced during core debris/concrete interactions

Table 7

Some Models of the Nonideal Vapor State

Equation of State	$\ln(\phi)$	$\ln(\phi(i))$
Van der Waals		
$\frac{PV}{RT} = \frac{V}{V-b} - \frac{a}{RTV}$	$\frac{PV}{RT} - 1 - \frac{a}{RTV} - \ln\left[\frac{PV}{RT}\left(1-\frac{b}{V}\right)\right]$	$\frac{b(i)}{V-b} - \ln\left[\frac{PV}{RT}\left(1-\frac{b}{V}\right)\right] - \frac{[4aa(i)]^{1/2}}{RTV}$ where $a = \left[\sum_{i}^{N(g)} y(i)(a(i))^{1/2}\right]^2$ $b = \sum_{i}^{N(g)} y(i)b(i)$ $y(i)$ = mole fraction of i^{th} species in the gas
Redlich-Kwong		
$\frac{PV}{RT} = \frac{V}{V-b} - \frac{aV}{RT^{3/2}(V+b)V}$	$\frac{PV}{RT} - 1 - \ln\left[\frac{PV}{RT}\left(1-\frac{b}{V}\right)\right] - \frac{a}{bRT^{3/2}}\ln\left[1+\frac{b}{V}\right]$	$\frac{b(i)}{b}\left(\frac{PV}{RT}-1\right) - \ln\left[\frac{PV}{RT}\left(1-\frac{b}{V}\right)\right] + \frac{1}{bRT^{3/2}}\left[\frac{ab(i)}{b} - (4aa(i))^{1/2}\right]\ln\left(1+\frac{b}{V}\right)$
Truncated Virial		
$\frac{PV}{RT} = 1 + \frac{BP}{RT}$	$\frac{BP}{RT} - \frac{B^2}{2}\left(\frac{P}{RT}\right)^2 + \frac{2B^3}{3}\left(\frac{P}{RT}\right)^3$	$\frac{P}{RT}\left\{B_{ii} + \frac{1}{2}\sum_{j}^{N(g)}\sum_{k}^{N(g)} y(j)y(k)\zeta\right\}$ $\zeta = 4B_{ji} - 2B_{jj} - 2B_{ii} - 2B_{jk} + B_{jj} + B_{kk}$

Table 7

Some Models of the Nonideal Vapor State (Continued)

Equation of State	$\ln(\phi)$	$\ln(\phi(i))$
Soave		
$\frac{PV}{RT} = \frac{V}{V-b} - \frac{c}{RT(V+b)}$	$\frac{PV}{RT} - 1 - \ln\left[\frac{PV}{RT}\left(1-\frac{b}{V}\right)\right]$ $- \frac{c}{bRT}\ln\left(1+\frac{b}{V}\right)$	$\frac{b(i)}{b}\left(\frac{PV}{RT}\right) - 1 - \ln\left[\frac{PV}{RT}\left(1-\frac{b}{V}\right)\right]$ $+ \frac{c}{bRT}\left[\frac{b(i)}{b} - \frac{2}{c}\sum_{j}^{N(g)} y(j)\right] c(i,j) \ln 1+\frac{b}{V}$ where $c = \sum_{i}^{N(g)}\sum_{j}^{N(g)} y(i)y(j)c(i,j)$ $c(i,j) = [c(i,i)c(j,j)]^{1/2}$ $b = \sum_{i}^{N(g)} y(i)b(i)$
Peng Robinson		
$\frac{PV}{RT} = \frac{V}{V-b} - \frac{cV}{RT(V^2+2bV-b^2)}$	$\frac{PV}{RT} - 1 - \ln\left[\frac{PV}{RT} - \frac{bP}{RT}\right]$ $- \frac{c}{2\sqrt{2}bRT}\ln\left[\frac{V+2.414Pb/RT}{V-0.414Pb/RT}\right]$	$\frac{b(i)}{b}\left(\frac{PV}{RT}-1\right) - \ln\frac{PV}{RT} - \left(\frac{bP}{RT}\right)$ $+ \frac{c}{4.828bRT}\left[\frac{b(i)}{b} - \frac{2}{c}\sum_{j}^{N(g)} y(i)c(i,j)\right]\ln\left[\frac{V+2.414Pb/RT}{V-0.414Pb/RT}\right]$

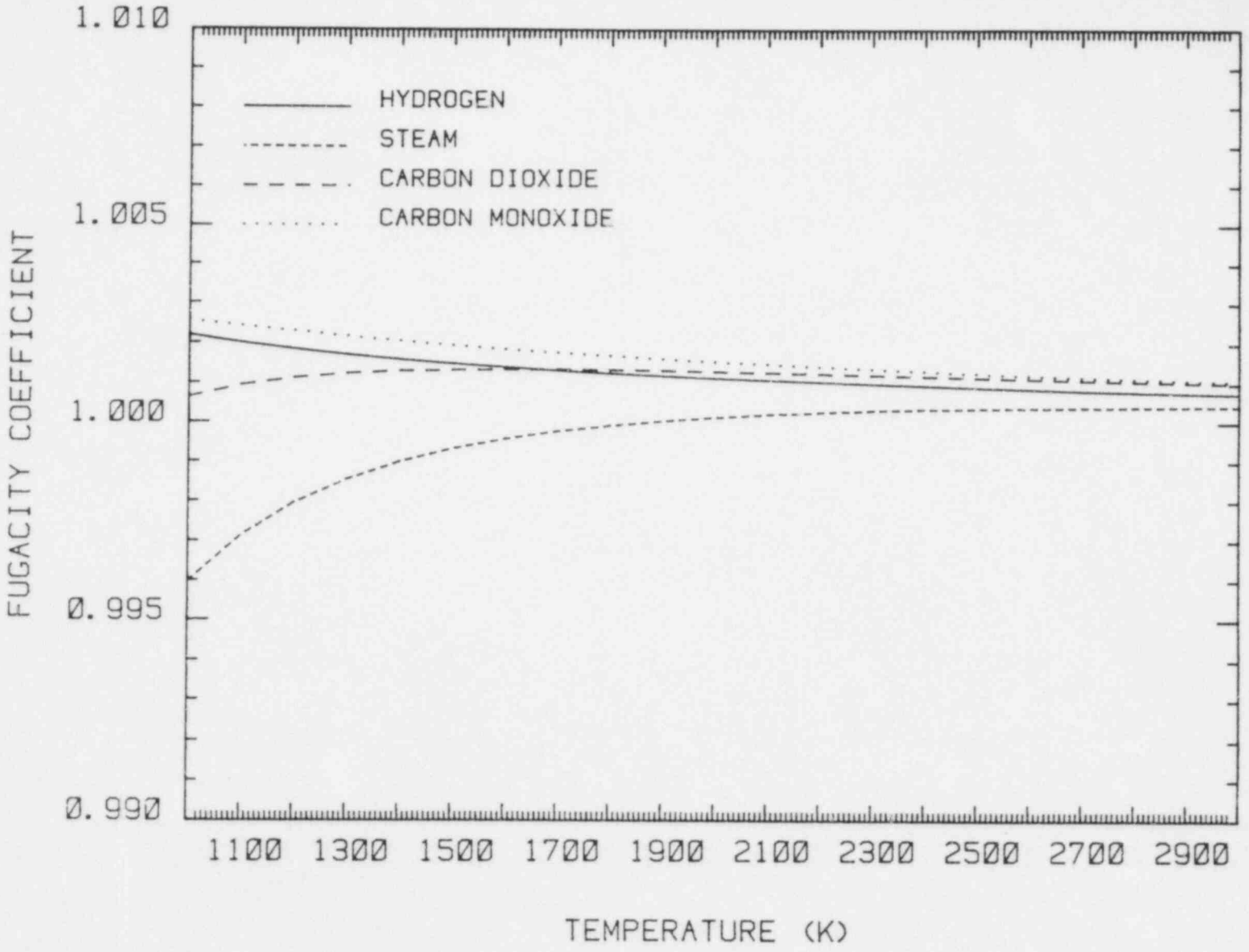

Figure 15. Fugacity Coefficient for Pure H_2, CO, CO_2, and H_2O Calculated With the Redlich-Kwong Equations of State Ignoring Dissociation of the Gases

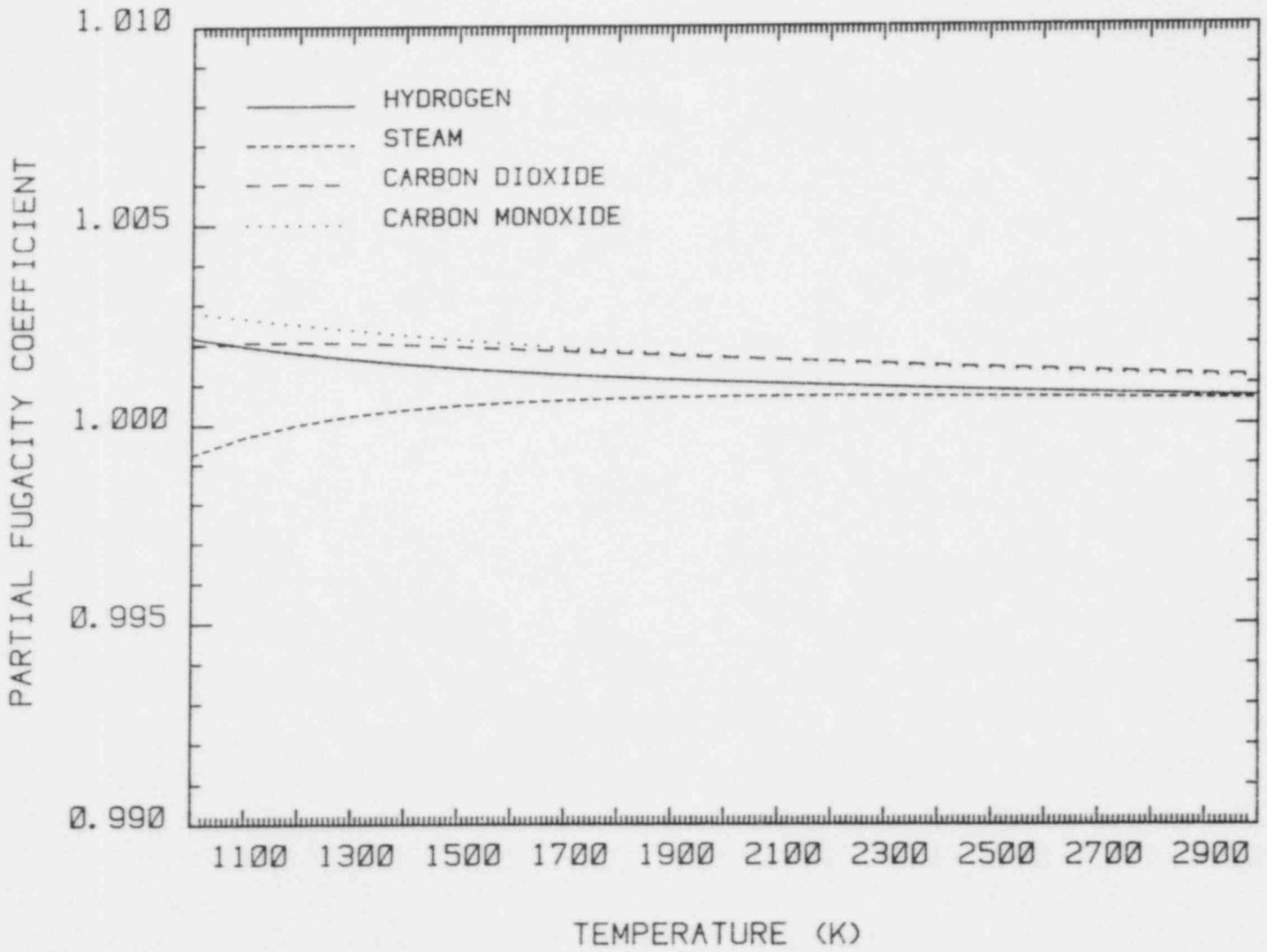

Figure 16. Partial Fugacity Coefficients for Gases in a Mixture of 45 Percent H_2, 5 Percent H_2O, 5 Percent CO_2, and 45 Percent CO. The coefficients were calculated from a Redlich-Kwong equation of state ignoring dissociation or reactions of the gases.

behave sufficiently closely to ideal that a model of nonideality need not be developed.

The absence of extensive data for the exotic, condensible vapors encountered in the study of vaporization during core debris/concrete interactions is a handicap. The magnitudes of the effects of nonideality in the gas phase can be demonstrated, however, with a very simple model. Consider the vapor molecules to be hard spheres. That is, each molecule contains an inpenetrable core of diameter 2a and nonideality of the gas is caused by the volume excluded by the impenetrable cores of the gas molecules. The equation of state is given approximately by:

$$\frac{PV}{RT} = 1 + \frac{BP}{RT} - 0.375\ B^2(P/RT)^2$$

where $B = \frac{2}{3}\pi N_A a^3$ and

N_A = Avogadro's number.

(A more complete equation of state is given in Reference 165.) The fugacity coefficient for the vapor is

$$\ell n\ \phi = \frac{BP}{RT} - 0.1875\left(\frac{BP}{RT}\right)^2 + 0.04167B^3\left(\frac{P}{RT}\right)^3 \quad .$$

Then, for T = 1500 K, P = 10 atmospheres, and a = 10^{-8} cm, the activity coefficient is:

$$\phi = 1.0001 \quad .$$

Increasing the inpenetrable radius to 5 x 10^{-8} cm yields

$$\phi = 1.013 \quad .$$

The effects of volume exclusion on the fugacity of vapors at the low pressures of interest here are, obviously, not especially important.

A similarly simple model can be formulated to evaluate the dispersive attraction among vapor species by including an attractive potential in the model for the molecular interactions. Perhaps the simplest such model would be a so-called square-well potential:

$$u = \begin{cases} \infty & \text{for } r < a \\ -\epsilon & \text{for } ga > r > a \\ o & \text{for } ga < r \end{cases}$$

where u = interaction potential between molecules,

a = inpenetrable radius of a molecule,

$-\epsilon$ = depth of the potential well, and

g = parameter that defines the width of the well.

The equation of state then is approximately

$$\frac{PV}{RT} = 1 + BP/RT$$

where $$B = \frac{2\pi N_A}{3} a^3 \left[1 + (g^3-1)\left(1-\exp\left[\frac{\epsilon N_A}{RT}\right]\right)\right] \quad .$$

Having defined the model, the implementation is not at all obvious. The problem is that a general method for estimating the potential well parameters ϵ and g does not spring immediately to mind. Some sense of the magnitude of effect created by dispersive interactions can be obtained by parametric variations. For $g = 1.5$, $\epsilon N_A/R = 1000$ K, $a = 1 \times 10^{-8}$ cm, $T = 1500$ K, and $P = 10$ atmospheres, the virial coefficient $B = 1.578$ and

$$\phi = 0.99987 \quad .$$

Increasing the depth of the well by a factor of two produces $\phi = 0.9994$ and expanding the width of the well so that $g = 4$ yields $\phi = 0.9901$. It seems likely then that dispersive attractions between vapor molecules will not be important in the analyses of vaporization that are done here

There is one situation in which association can create important nonidealities in gas phase behavior. This situation arises when a gas phase species, which otherwise is ideal in its behavior, dimerizes, but this dimer formation is not recognized in the speciation of the gas. Consider the dimerization reaction

$$2A \rightleftharpoons A_2 \quad .$$

The equilibrium constant is given by

$$K(eq) = P(A_2)/P(A)^2 \quad .$$

If this equilibrium were not recognized, then the system would have an apparent equation of state given by

$$\frac{PV}{RT} = 1 + \frac{BP}{RT}$$

where $B = -RT\ K(eq)$ for small values of P. The apparent fugacity coefficient for A would be

$$\ln \phi = -P\ K(eq) + 1/2\ P^2K^2(eq) \quad .$$

The importance of this activity coefficient is dependent on both the species partial pressure and the equilibrium constant for dimerization. Thus, it would be expected to have its greatest effects on those materials most easily vaporized and consequently of most interest in the analyses.

An analogous difficulty will arise if vapor species from different sources associate in the vapor phase.

The approach toward fugacity coefficients adopted in the current implementation of the VANESA model is to assume all gases and vapors are ideal. A great deal of attention is then paid to the speciation of the gas phase to avoid difficulties such as that described in connection with dimerization.

4. Reaction of Gases With the Metallic Core Melt

The gases evolved from the concrete during interaction with a core melt are primarily CO_2 and H_2O. There is some evidence that sulfur-containing gases and halide-containing gases are also evolved. These gases are neglected here (but see Section IIIA-5). Carbon dioxide and steam at high temperatures are very reactive. They will react with the core melt. Evidence from tests of melt/concrete interactions suggest that the reactions do go to completion.[18,270] That is, an equilibrium composition is obtained. This equilibrium is obtained, apparently, after gases have passed through only a very thin layer of melt.

The reaction of gases with the melt is important to the determination of the vapor pressure of melt constituents as noted in the introduction to Chapter III of this document.

The extent of reaction is a manifestation of the oxygen potential of the melt which determines the relative importance of vapor phase oxides and metals. The extent of reaction also determines the driving force available for the formation of vapor phase hydroxides and hydrides.

For the VANESA model, it is assumed that the metallic phase of a core melt is the more dense phase. It is easiest then to describe the changes in gas composition experienced by gases evolved from concrete in terms of their reactions with the metal phase. For the purposes of the VANESA model, this metal phase is presumed to consist of zirconium, iron, chromium, nickel, and "inert" material that does not participate in reactions with the gases.

CO_2 and H_2O entering the melt create a disequilibrium system. The mechanisms or pathways that lead to equilibrium are, of course, unknown. Conceptually, the types of reactions that take place have the overall stoichiometries:

$$M + b\ H_2O \rightarrow MO_b + b\ H_2$$

$$M + b\ CO_2 \rightarrow MO_b + b\ CO \quad .$$

At the same time, the thermal environment of the gases can cause dissociation of the gases. Again the mechanisms of dissociation are unknown and unimportant for the definition of the equilibrium states. The overall stoichiometries of the reactions are:

$$H_2O \rightarrow H_2 + 1/2\ O_2$$

$$O_2 \rightarrow 2O$$

$$H_2 \rightarrow 2H$$

$$H_2O \rightarrow OH + 1/2\ H_2$$

$$2H_2O \rightarrow HO_2 + 3/2\ H_2 \quad .$$

Inter-reactions of gas phase species can also be imagined which would produce gas phase species such as CH_n(n = 1, 2, 3, 4), C_2O, CHO, CH_2O, C_3O_2, C_2H, C_n(n = 1, 2, 3, 4, 5) and higher hydrocarbons. Such species are neglected here in the belief that their contributions to the gas mixture will be small. This belief is supported by results of analyses done with the CORCON model.[5,6]

The actual equilibrium can be found, of course, by minimizing the free energy of the system. The theoretical

accuracy of such minimization procedures is not easily achieved for low concentration species and consequently the procedure may not be especially useful for this problem. Free-energy minimization methods were devised, in fact, to provide a means for solving a variety of equilibrium problems whose natures could not be anticipated. Here, a different situation is encountered. Essentially the same equilibrium problem must be solved repeatedly. Consequently, a so-called equilibrium constant method[271] is employed. It must be emphasized that this method is entirely equivalent to free-energy minimization.[272] It has, however, superior numerical characteristics for the problem at hand.

There are several ways to develop an equilibrium constant method. The authors have chosen to simply assert the necessary equations rather than presenting an intuitive development. The underlying concept is that during an arbitrary time step, $M(CO_2)$ moles of carbon dioxide and $M(H_2O)$ moles of steam evolve from the concrete, enter, and react with the melt. The melt, at the start of the time step consists of $M°(Zr)$ moles of zirconium, $M°(Cr)$ moles of chromium, $M°(Fe)$ moles of iron, $M°(Ni)$ moles of nickel, and $M°(inert)$ moles of inert materials. The reactions of the gases produce H_2, CO, H, OH, O_2, O, HO_2, and M(oxide) moles of condensed products. The composition of the condensed, oxide product is $Y(ZrO_2)$ mole fraction ZrO_2, $Y(CrO_{1.5})$ mole fraction of $(Cr_2O_3)_{1/2}$, Y(FeO) moles of Wüstite, and Y(NiO) moles of Bunsenite. The condensed phase reactant mixture is presumed to be fully molten. Casual inspection of phase diagrams for metal alloys will show that the mixture is very likely to be molten even at temperatures well below the normal melting points of chromium (2148 K) and zirconium (2125 K). The Cr-Fe system has a minimum in its liquidus at 1780 K and a mole fraction of 0.22 Cr.[183] The Zr-Fe system has eutectics at 1207 K and 1603 K with mole fractions of 0.76 and 0.105 Zr, respectively.[183] There is, however, a compound phase ($ZrFe_2$) that melts congruently at 1878 K.

The products of reaction, too, are assumed to be fully molten because of the colligative properties of mixtures. The FeO-ZrO_2 system has a eutectic at about 1603 K.[184] A eutectic occurs in the Fe_3O_4-ZrO_2 system at 1796 K.[185] The FeO-Cr_2O_3 system has a peritectic reaction at about 1690 K.[186] A eutectic reaction occurs between NiO and a nickel ferrate at about 1800 K. The nickel ferrate itself melts at about 1923 K.[187] Even if the colligative interactions among products of oxidation are insufficient to lead to liquefaction, interactions of the reaction products with ablated concrete would lead to liquid formation.

Then, the equilibrium expressions for the basis gas reactions are:

1. $$-[\Delta G_f[ZrO_2;\ \ell] + 2\Delta G_f(H_2;\ g) - \Delta G_f(Zr;\ \ell) - 2\Delta G_f(H_2O;\ g)] = 2RT\ \ell n\left[\frac{P(H_2)}{P(H_2O)}\right] + RT\ \ell n\left[\frac{Y(ZrO_2)}{X(Zr)}\right] .$$

2. $$-[\Delta G_f(CrO_{1.5};\ \ell) + 3/2\ \Delta G_f(H_2;\ g) - \Delta G_f(Cr;\ \ell) - \tfrac{3}{2}\Delta G_f(H_2O;\ g)] = \tfrac{3}{2}RT\ \ell n\left[\frac{P(H_2)}{P(H_2O)}\right] + RT\ \ell n\left[\frac{Y(CrO_{1.5})}{X(Cr)}\right] .$$

3. $$-[\Delta G_f(FeO;\ \ell) + \Delta G_f(H_2;\ g) - \Delta G_f(Fe;\ \ell) - \Delta G_f(H_2O;\ g)] = RT\ \ell n\left[\frac{P(H_2)}{P(H_2O)}\right] + RT\ \ell n\left[\frac{Y(FeO)}{X(Fe)}\right] .$$

4. $$-[\Delta G_f(NiO;\ \ell) + \Delta G_f(H_2;\ g) - \Delta G_f(Ni;\ \ell) - \Delta G_f(H_2O;\ g)] = RT\ \ell n\left[\frac{P(H_2)}{P(H_2O)}\right] + RT\ \ell n\left[\frac{Y(NiO)}{X(Ni)}\right] .$$

5. $$-[\Delta G_f(CO;\ g) + \Delta G_f(H_2O;\ g) - \Delta G_f(CO_2;\ g) - \Delta G_f(H_2;\ g)] = RT\ \ell n\left[\frac{P(H_2O)}{P(H_2)}\right] + RT\ \ell n\left[\frac{P(CO)}{P(CO_2)}\right] .$$

6. $$-[2\Delta G_f(H;\ g) - \Delta G_f(H_2;\ g)] = 2RT\ \ell n\ [P(H)] - RT\ \ell n[P(H_2)] .$$

7. $$-[1/2\ \Delta G_f(H_2;\ g) + \Delta G_f(OH;\ g) - \Delta G_f(H_2O;\ g)] = RT\ \ell n\left[\frac{P(H_2)^{1/2}\ P(OH)}{P(H_2O)}\right] .$$

8. $$-[1/2\ \Delta G_f(O_2;\ g) + \Delta G_f(H_2;\ g) - \Delta G_f(H_2O;\ g)] = RT\ \ell n\left[\frac{P(H_2)\ \ P(O_2)^{1/2}}{P(H_2O)}\right] .$$

9. $-[\Delta G_f(O;\ g) + \Delta G_f(H_2;\ g) - \Delta G_f(H_2O;\ g)]$

$$= RT\ \ell n \left[\frac{P(H_2)\ P(O)}{P(H_2O)}\right] .$$

10. $-[\Delta G_f(HO_2;\ g) + 3/2\ \Delta G_f(H_2;\ g) - 2\Delta G_f(H_2O;\ g)]$

$$= RT\ \ell n \left[\frac{P(H_2)^{3/2}\ P(HO_2)}{P(H_2O)^2}\right] .$$

These equations must be solved subject to the mass balance constraints:

1. Mass balance on zirconium:

$$M°(Zr) = X(Zr)M + Y(ZrO_2)\ M(oxide)$$

2. Mass balance on chromium:

$$M°(Cr) = X(Cr)M + Y(CrO_{1.5})\ M(oxide) .$$

3. Mass balance on iron:

$$M°(Fe) = X(Fe)M + Y(FeO)\ M(oxide) .$$

4. Mass balance on nickel:

$$M°(Ni) = X(Ni)M + Y(NiO)\ M(oxide) .$$

5. Mass balance on inerts:

$$M°(inert) = X(inert)M .$$

6. Mass balance on hydrogen:

$$2M(H_2O) = 2m(H_2) + 2m(H_2O) + m(H) + m(OH) + m(HO_2) .$$

7. Mass balance on carbon:

$$M(CO_2) = m(CO) + m(CO_2) \quad .$$

8. Mass balance on oxygen:

$$M(H_2O) + 2M(CO_2) = m(OH) + m(H_2O) + m(O) + 2m(O_2) + 2m(HO_2) + m(CO) + 2m(CO_2) + M(\text{oxide}) [1 + 0.5Y\ (CrO_{1.5}) + Y(ZrO_2)] \quad .$$

9. Pressure balance

$$P_{total} = P(H_2) + P(H_2O) + P(OH) + P(H) + P(O_2) + P(O) + P(HO_2) + P(CO) + P(CO_2)$$

where $\Delta G_f(X; Y)$ = free-energy of formation of the species X in the state Y,

$P(X)$ = partial pressure of the species X,

M = $m(Zr) + m(Fe) + m(Cr) + m(Ni) + m(\text{inert})$,

$X(Y)$ = mole fraction of species Y in the metal phase,

$m(X)$ = moles of species X present at equilibrium, and

P_{total} = total pressure.

The relationship between moles of gaseous species present at equilibrium and the partial pressure of the species is, of course, obtained from the ideal gas law.

The problem consists then of a set of nonlinear algebraic equations. At first, a concern might be that the equations are subject to multiple solutions. It can be demonstrated, however, that the equations, as constituted here, have a solution and that this solution is unique.[273] The existence and uniqueness properties may disappear if nonideality in either the gas or condensed phases are considered. In fact, relaxation of several approximations made

in the development of the model can affect the ease of obtaining a solution.

The equations as constituted are susceptible to solution by any of a number of numerical methods. In the current implementation of the VANESA model they are solved by a simple repeated substitution procedure as follows:

1. Initial estimates of $P(H_2)/P(H_2O)$, M(oxide), and M(gas), the moles of gas present at equilibrium, are formed.

2. The equilibria involving the condensed phase species, and the mass balance for the condensed phase species are used to find a revised value of M(oxide), and values of $Y(ZrO_2)$, $Y(CrO_{1.5})$, Y(FeO), and Y(NiO) recognizing that

$$1 = Y(ZrO_2) + Y(CrO_{1.5}) + Y(FeO) + Y(NiO) \quad .$$

3. The oxygen balance is used to find an updated value for the hydrogen-to-steam partial pressure ratio.

4. The shift reaction (Equation (5), above) is used to find a revised value for the carbon monoxide-to-carbon dioxide partial pressure ratio.

5. Equilibrium partial pressures for H, OH, O, and O_2 are found.

6. The carbon balance is used to find P(CO). Then, the carbon monoxide-to-carbon dioxide partial pressure ratio is used to find $P(CO_2)$.

7. The pressure balance is used to find $P(H_2)$. Then, the hydrogen-to-steam partial pressure ratio is used to find $P(H_2O)$.

8. The sum of the hydrogen balance equation and the carbon balance equation is used to find M(gas).

9. Convergence is checked on the solution of the mass balance equations, the pressure balance equation and variations in the hydrogen-to-steam ratio. Convergence is declared when deviations amount to less than one part per million.

The free-energy data used for the calculations are shown in Table 8. Note carefully the reference state for the species. Because of colligative effects, condensed phase species are not necessarily in the most stable state they

Table 8

Free Energy of Formation Data Used to Solve for Fixed Gas Composition

Temperature (K)	Free-Energy of Formation (cal/mole)							
	Cr(ℓ)	Cr_2O_3(ℓ)	Fe(ℓ)	FeO(ℓ)	Ni(ℓ)	NiO(ℓ)	Zr(ℓ)	ZrO_2(ℓ)
500	4732	-216209	2074	-53252	2801	-36718	4381	-224373
600	4430	-210966	1896	-52065	2549	-35142	4007	-220410
700	4130	-205789	1719	-50899	2318	-33587	3645	-216481
800	3828	-200670	1542	-49745	2094	-32045	3295	-212581
900	3526	-195595	1369	-48588	1872	-30518	2958	-208706
1000	3225	-190553	1207	-47418	1651	-29004	2635	-204853
1100	2924	-185538	1076	-46210	1430	-27505	2325	-201024
1200	2623	-180541	960	-44993	1210	-26013	2080	-197166
1300	2321	-175556	842	-43788	991	-24535	1867	-193292
1400	2020	-170575	704	-42612	766	-23065	1653	-189436
1500	1718	-165591	547	-41462	536	-21604	1437	-185618
1600	1420	-160600	376	-40333	303	-20147	1215	-181885
1700	1129	-155594	196	-39218	66	-18700	989	-178159
1800	845	-150574	17	-38104	0	-17092	759	-174436
1900	573	-145546	0	-36819	0	-15206	527	-170719
2000	313	-140522	0	-35524	0	-13293	293	-167009
2100	70	-135488	0	-34231	0	-11308	58	-163304
2200	0	-130133	0	-32945	0	-9260	0	-159454
2300	0	-124661	0	-31667	0	-7148	0	-155554
2400	0	-119208	0	-30392	0	-4975	0	-151664
2500	0	-113780	0	-29118	0	-2743	0	-147794
2600	0	-108366	0	-27849	0	-459	0	-143932
2700	0	-102973	0	-26586	0	+1882	0	-140085
2800	0	-97595	0	-25321	0	4275	0	-136247
2900	0	-92233	0	-24060	0	6717	0	-132418
3000	-1238	-84413	0	-22802	0	9207	0	-128603

Table 8 (Continued)

Free Energy of Formation Data Used to Solve for Fixed Gas Composition

Temperature (K)	Free-Energy of Formation (cal/mole)								
	CO	CO_2	H	H_2	HO	HO_2	H_2O	O	O_2
500	-37144	-94399	46124	0	7426	10222	-52361	52480	0
600	-39311	-94458	44854	0	7049	11351	-51156	50991	0
700	-41468	-94510	43560	0	6677	12501	-49915	49481	0
800	-43612	-94556	42245	0	6309	13663	-48646	47955	0
900	-45744	-94596	40913	0	5967	14838	-47352	46418	0
1000	-47859	-94628	39564	0	5590	16021	-46040	44870	0
1100	-49962	-94658	38203	0	5238	17209	-44712	43314	0
1200	-52049	-94681	36829	0	4889	18401	-43371	41751	0
1300	-54126	-94701	35444	0	4544	19597	-42022	40181	0
1400	-56189	-94716	34051	0	4202	20795	-40663	38607	0
1500	-58241	-94728	32649	0	3863	21996	-39297	37027	0
1600	-60284	-94739	31239	0	3526	23197	-37927	35444	0
1700	-62315	-94746	29823	0	3191	24401	-36549	33857	0
1800	-64337	-94750	28401	0	2858	25605	-35170	32267	0
1900	-66349	-94752	26974	0	2527	26812	-33786	30673	0
2000	-68353	-94752	25542	0	2198	28017	-32401	29078	0
2100	-70346	-94746	24106	0	1870	29226	-31012	27480	0
2200	-72335	-94744	22665	0	1544	30435	-29621	25879	0
2300	-74311	-94735	21221	0	1219	31645	-28229	24277	0
2400	-76282	-94724	19774	0	896	32859	-26832	22673	0
2500	-78247	-94714	18324	0	574	34069	-25439	21068	0
2600	-80202	-94698	16871	0	254	35286	-24040	19461	0
2700	-82153	-94683	15415	0	-65	36502	-22641	17854	0
2800	-84093	-94662	13957	0	-383	37719	-21242	16245	0
2900	-86028	-94639	12497	0	-699	38941	-19838	14635	0
3000	-87957	-94615	11035	0	-1014	40162	-18438	13023	0

would adopt if pure under the ambient pressure and temperature conditions.

To illustrate the nature of gas reactions with the metallic phase of the core debris an example calculation is presented here. For this example, the metallic phase is assumed to consist initially of:

1. 200 molar parts Zr,
2. 740 molar parts Fe,
3. 180 molar parts Cr,
4. 80 molar parts Ni,

and to be at a constant temperature of 2200 K. The pressure is taken to be 2 atmospheres. One mole of H_2O and one mole of CO_2 are assumed to enter this melt per time step.

Plots of the mole fractions of ZrO_2, $CrO_{1.5}$, FeO, and NiO in the condensed products of gas reaction as a function of the extent to which the metal phase has been oxidized are shown in Figure 17. While zirconium metal is present in the core debris, ZrO_2 is calculated to constitute more than 99.9 percent of the condensed product of reaction. Once the zirconium metal content of the melt has been depleted significantly, $CrO_{1.5}$ and FeO are the predominant constituents of the condensed product. The relative amounts of $CrO_{1.5}$ and FeO in the product vary significantly. Initially the product is about 80 mole percent $CrO_{1.5}$. But, as oxidation progresses the $CrO_{1.5}$ contribution falls and FeO becomes the predominant product. Nickel oxide does not become a significant oxidation product until nearly all the iron and chromium in the metallic melt have been oxidized.

The equilibrium hydrogen-to-steam partial pressure ratio is shown in Figure 18 plotted as a function of time. While metallic zirconium is present, this ratio is quite high ($>10^4$). When the metallic zirconium has been oxidized, the ratio falls sharply to 10. As the chromium in the metal mixture is oxidized, the hydrogen-to-steam ratio approaches a value of about two. Once oxidation of the iron is complete, the ratio again falls sharply to about 10^{-2}.

Melt/concrete interaction models have long had to consider the reactions of gases evolved from the concrete with the core debris. Most[5,6,26,43,57] use models somewhat less sophisticated than that described here. For instance, the CORCON code[5,6] uses a model based on assuming the metallic melt to be a mechanical mixture of metals. Many models (DECOMP[43], INTER[57]) use a so-called hierarchical scheme in which first the zirconium is oxidized, then the chromium is oxidized, and then the iron is oxidized. The results

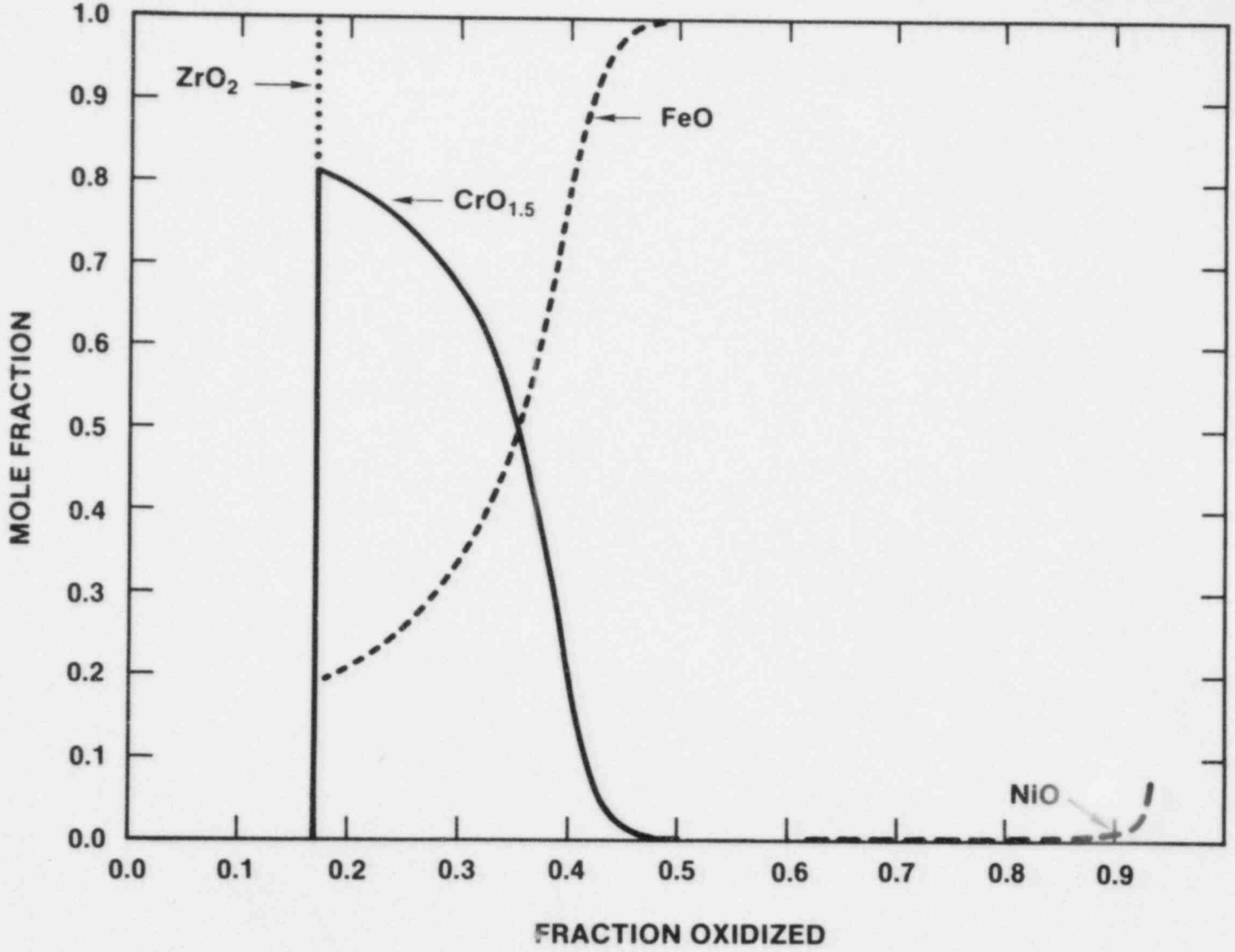

Figure 17. Composition of the Condensed Product of Melt Oxidation as a Function of the Extent of Oxidation. Initial melt composition, temperature, etc., for this example calculation are discussed in the text.

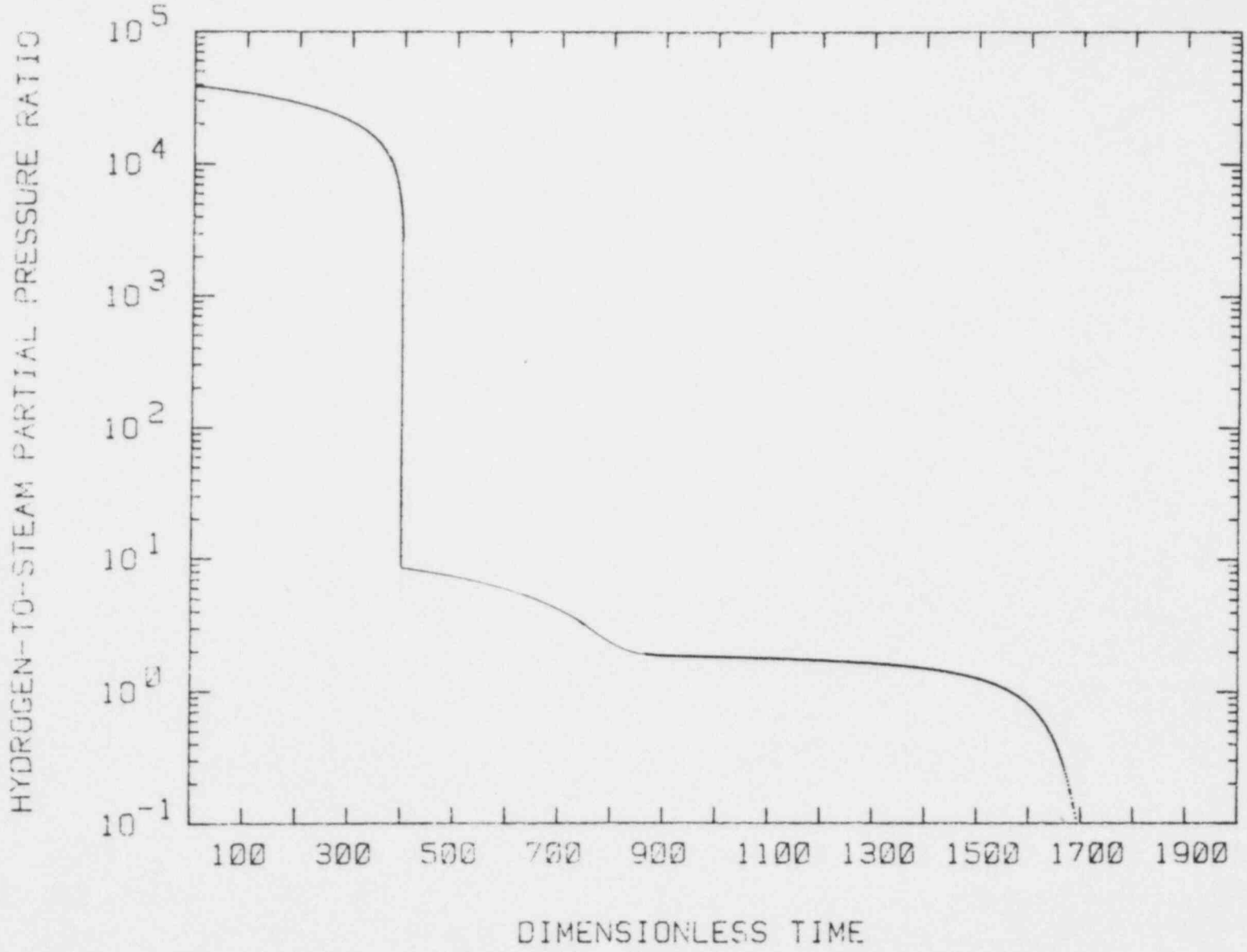

Figure 18. Hydrogen-to-Steam Partial Pressure Ratio as a Function of Time. Conditions for this calculation are discussed in the text.

obtained with the superior, ideal solution model show that the mechanical mixture model of CORCON and the hierarchical models do not make significant errors for the oxidation of zirconium. The mechanical mixture model may overpredict the hydrogen-to-steam partial pressure ratio.

Once zirconium has been oxidized from the melt, the more approximate models become less satisfactory. These approximate models allow chromium to be oxidized completely before iron is oxidized. Two errors arise in this procedure. First, the hydrogen-to-steam partial pressure ratio is overpredicted. The ratio will be that for the $Cr/CrO_{1.5}$ equilibrium and then will fall sharply to the value appropriate for the FeO/Fe equilibrium. In reality, the ratio will be lower always and will evolve toward the low value for FeO/Fe rather than dropping sharply. Second, the chemical heat generation is incorrectly predicted. Chromium oxidation by H_2O and CO_2 is quite exothermic while iron oxidation by these gases is nearly neutral thermally. The mixed iron and chromium oxidation predicted with the ideal solution model gives a more protracted but lower level chemical heat generation than either the mechanical mixture model or hierarchical model.

5. The "Coking" Reaction

Chemical conditions within the core debris can be quite reducing as is shown by results in the preceding section. Conditions are particularly reducing when zirconium metal is present in the metallic phases of the core melt. When conditions are very reducing, another reaction of the gases from the concrete can be important. Evolved carbon dioxide can be reduced not just to carbon monoxide, but, all the way to carbon:

$$\frac{Y}{2} CO_2 + [M] \rightarrow \frac{Y}{2}[C] + MO_y \quad .$$

Condensed-phase carbon, the product of this so-called "coking" reaction, will dissolve in the metallic phase of the core debris

The "coking" reaction is well known in the ferrous metallurgy fields. Reversing the coking reaction is, in fact, the reason for the carbon "boil" phase of steel manufacture. The consequences of coking during core debris interactions with concrete can be multifold. Clearly, this reaction reduces the quantity of gas emerging from the melt. Gases that would be derived from evolved CO_2 are no longer present since carbon is absorbed into the melt. Absorption of the carbon also increases the molarity of the melt phase and thus

dilutes constituents of the metallic melt. The chemical reactions that make carbon available for absorption consume metallic constituents of the melt quite efficiently. Rather than reacting just one oxygen from evolved CO_2 to form CO, both oxygen atoms react with the metal to form metal oxides and carbon. The reactions of evolved CO_2 with the metals are more exothermic when reduction to carbon rather than just reduction to CO occurs. Consider the standard state reactions with metallic zirconium (at 2000 K):

$$2CO_2 + Zr(\ell) \rightarrow ZrO_2(\ell)$$

$$+ 2CO \quad \Delta H[\text{cal/mole } ZrO_2] = -113,399$$

$$CO_2 + Zr(\ell) \rightarrow ZrO_2(\ell)$$

$$+ \Delta H[\text{cal/mole } ZrO_2] = -151,443 \quad .$$

Heat imparted to the melt at 2000 K during formation of ZrO_2 is much greater when CO_2 is reduced to carbon than when CO_2 is reduced to CO. On the other hand, oxidation of carbon by CO_2 is endothermic, consuming 38,044 cal per mole of carbon oxidized. This means that the timing of chemical heat generation during core debris interactions with concrete is altered by coking. Early in the interaction process, the heat generation is greater than it would be if coking did not occur. But, later in time, the chemical heat generation is less.

As the reactions that lead to coking progress, the most reducing constituents of the melt are consumed. As the very reducing constituents of the melt are converted to oxides, a point is reached at which the dissolved carbon becomes the most reducing constituent of the melt. When this occurs, the net effect of melt reaction with gases evolved from the concrete is carbon oxidation:

$$H_2O + [C] \rightarrow CO + H_2$$

$$CO_2 + [C] \rightarrow 2CO \quad .$$

Note the features of these reactions. Each molecule of H_2O or CO_2 that enters the melt and participates in the reaction results in two molecules of gas emerging from the melt. Further, the reactions are endothermic. That is, heat is removed from the melt by these reactions.

Quantitative analyses of the thermochemistry of coke formation in the core melt and the subsequent decarbonization of the melt are easily done by modifying the equilibrium analyses described in the previous section of this document. The modifications necessary are:

1. Introduce an equilibrium basis equation for carbon in the melt. The most obvious equation is derived from the equilibrium:

   $$[C] + H_2O \rightleftharpoons H_2 + CO \quad .$$

   If carbon is treated an an ideal melt constituent, then

   $$P(CO) = \frac{X(C)\ P(H_2O)}{P(H_2)} \exp\left[-(G_f(CO) + G_f(H_2) - G_f(H_2O))/RT\right] \quad .$$

2. Include dissolved carbon in the mass balance for carbon.

3. Adjust the definitions of mole fractions of melt constituents to reflect the presence of carbon.

To illustrate the effects of coking, an example calculation similar to that described in the previous section is performed here. Again, this example involves a melt initial-composed of zirconium (200 parts), chromium (180 parts), iron (740 parts), and nickel (80 parts). The melt temperature is taken to be 2200 K. The gas generation rates are 1 mole/time step of H_2O and 1 mole/time step CO_2. The gas reactions take place at 2 atmospheres pressure.

The extent of carbon deposition into the melt is shown as a function time in Figure 19. Coking of the melt proceeds rapidly up to a maximum of nearly 10 mole percent. The magnitude of coking and the location of the maximum depend, of course, on the CO_2 content of gas entering the melt and the initial zirconium content of the melt. At the maximum, the zirconium content of the melt is reduced to nearly zero and carbon becomes the most reducing constituent of the melt. The evolved gases then react with the dissolved carbon. The carbon content of the melt falls to less than

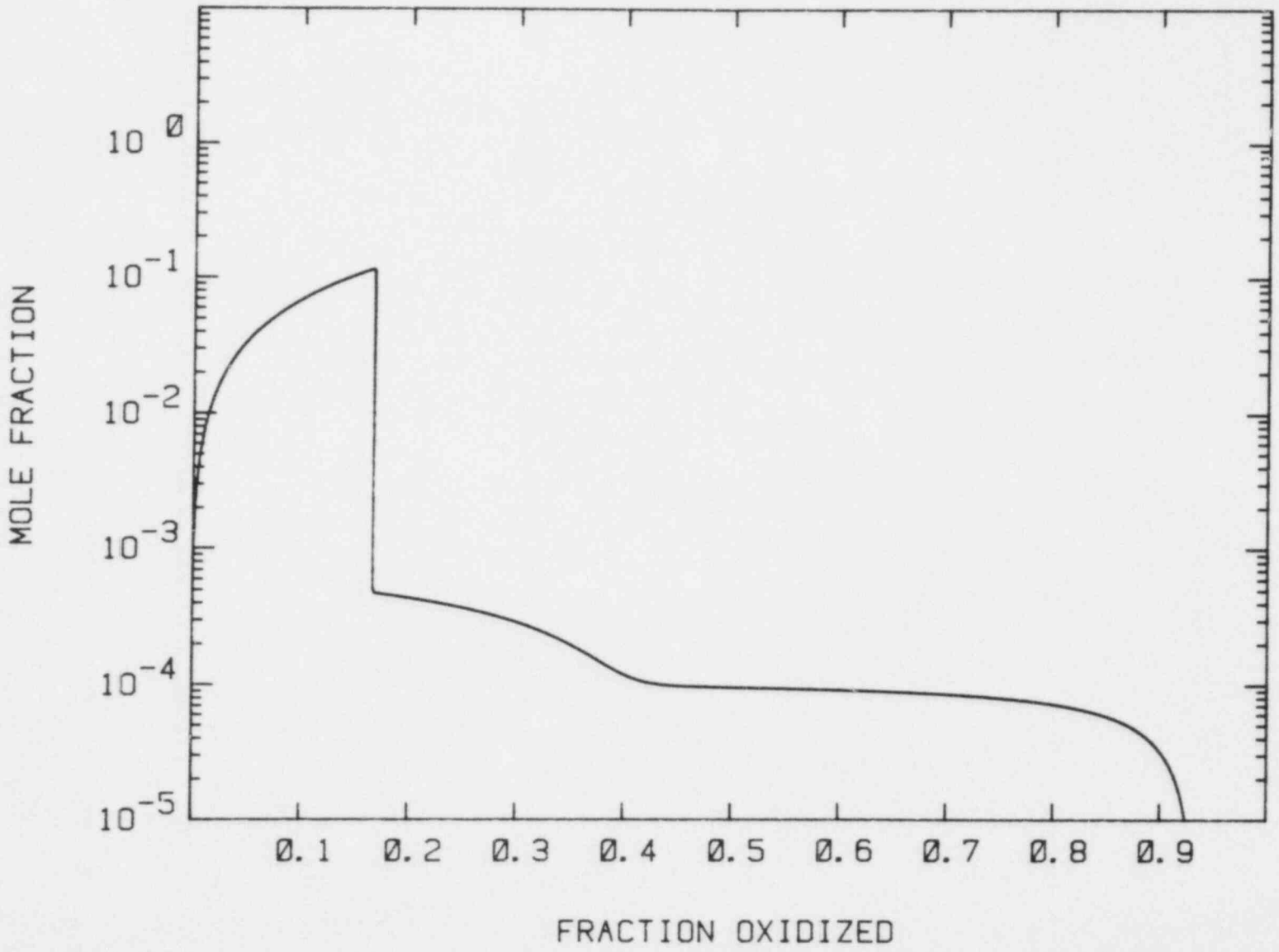

Figure 19. Mole Fraction Carbon in the Melt as a Function of the Extent of Metal Oxidation

1 mole percent with little oxidation of other metallic constituents of the melt. Further reactions of evolved gases proceed in competition with melt oxidation. The carbon content of the melt falls again once chromium in the melt is depleted. Completion of the oxidation of iron is accompanied by nearly complete removal of any residual carbon in the melt which then consists of nearly pure nickel.

The ratio of gases emerging from a melt to the gas generated by concrete pyrolysis is shown as a function of time in Figure 20. Initially this ratio is about 0.5 since nearly all of the CO_2 evolved from the concrete and entering the melt is reduced completely to carbon. This low ratio persists until nearly all of the zirconium in the melt has been oxidized. Then the ratio rises to about two as gases entering the melt react with the carbon to form CO. A high ratio persists until the carbon content has been depleted substantially. The ratio then falls to nearly one. The ratio does not become, however, exactly one. There is some continued CO production within the melt caused by slow decarbonization. Also, thermal dissociation of gases--particularly the dissociation of H_2 to atomic hydrogen--raises the molarity of the evolved gas. Only a few of the possible gas phase reaction processes that will occur are considered here and in the current implementation of the VANESA model. Some neglected gas phase species are created by transformations having stoichiometries such as:

$$CO + 3/2\ H_2 \rightarrow CH_4 + H_2O$$

$$CO + 2H_2 \rightarrow CH_2 + H_2O$$

$$CO + 5/2\ H_2 \rightarrow CH_3 + H_2O$$

$$CO + 3H_2 \rightarrow CH_4 + H_2O$$

$$2CO + H_2 \rightarrow C_2O + H_2O$$

$$CO + H_2 \rightarrow C(g) + H_2O$$

$$2CO + 2H_2 \rightarrow C_2(g) + 2H_2O \quad .$$

These neglected transformations would reduce the molarity of the gas, but quantitative analyses of these reactions show that the effects are quite small for conditions typically encountered in core-melt interactions with concrete.

The effects of coking and decarbonization on the hydrogen-to-steam partial pressure ratio of the equilibrated gas are shown in Figure 21. While metallic zirconium is

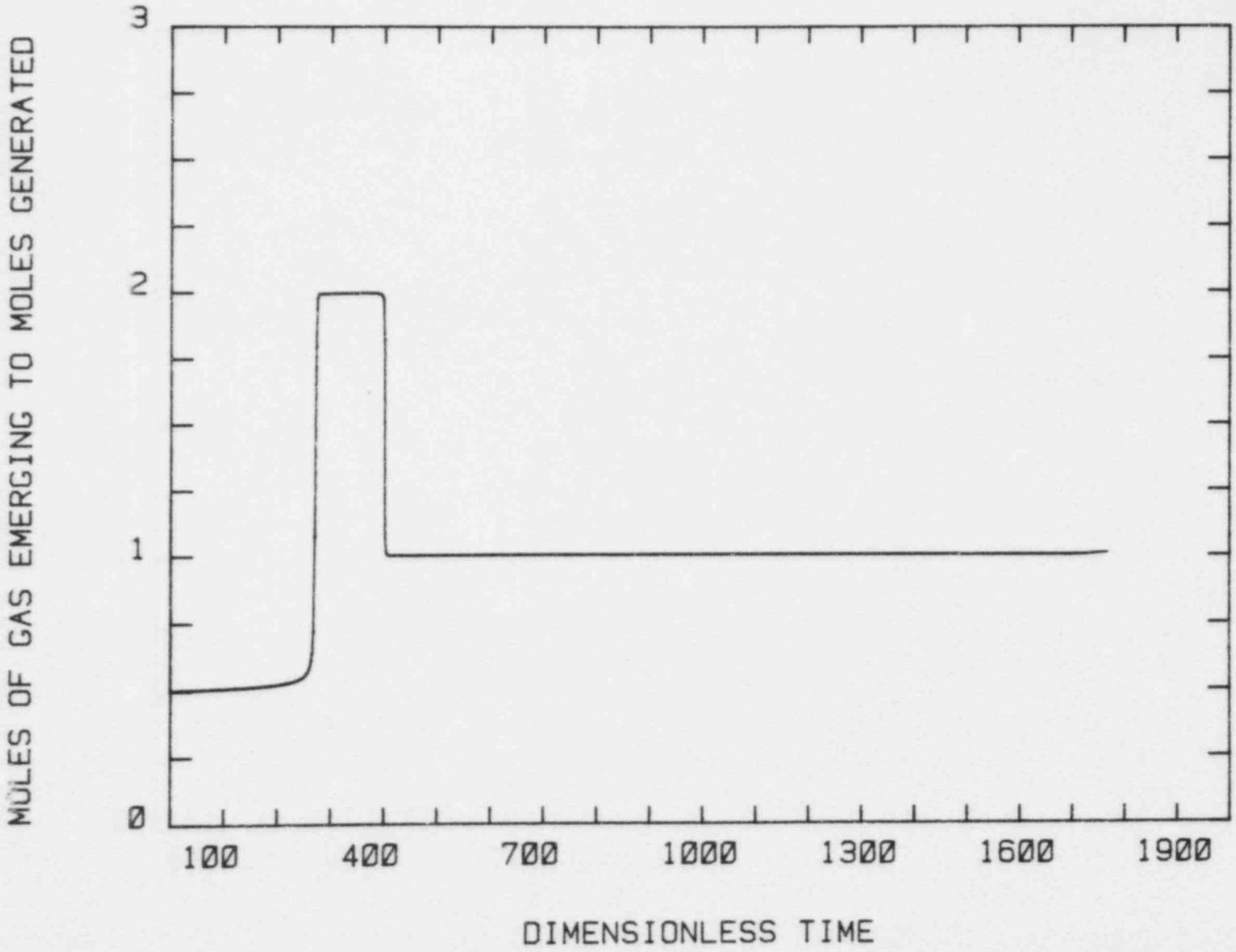

Figure 20. Ratio of the Moles of Gas Emerging From the Melt to the Moles of H_2O and CO_2 Generated by the Concrete

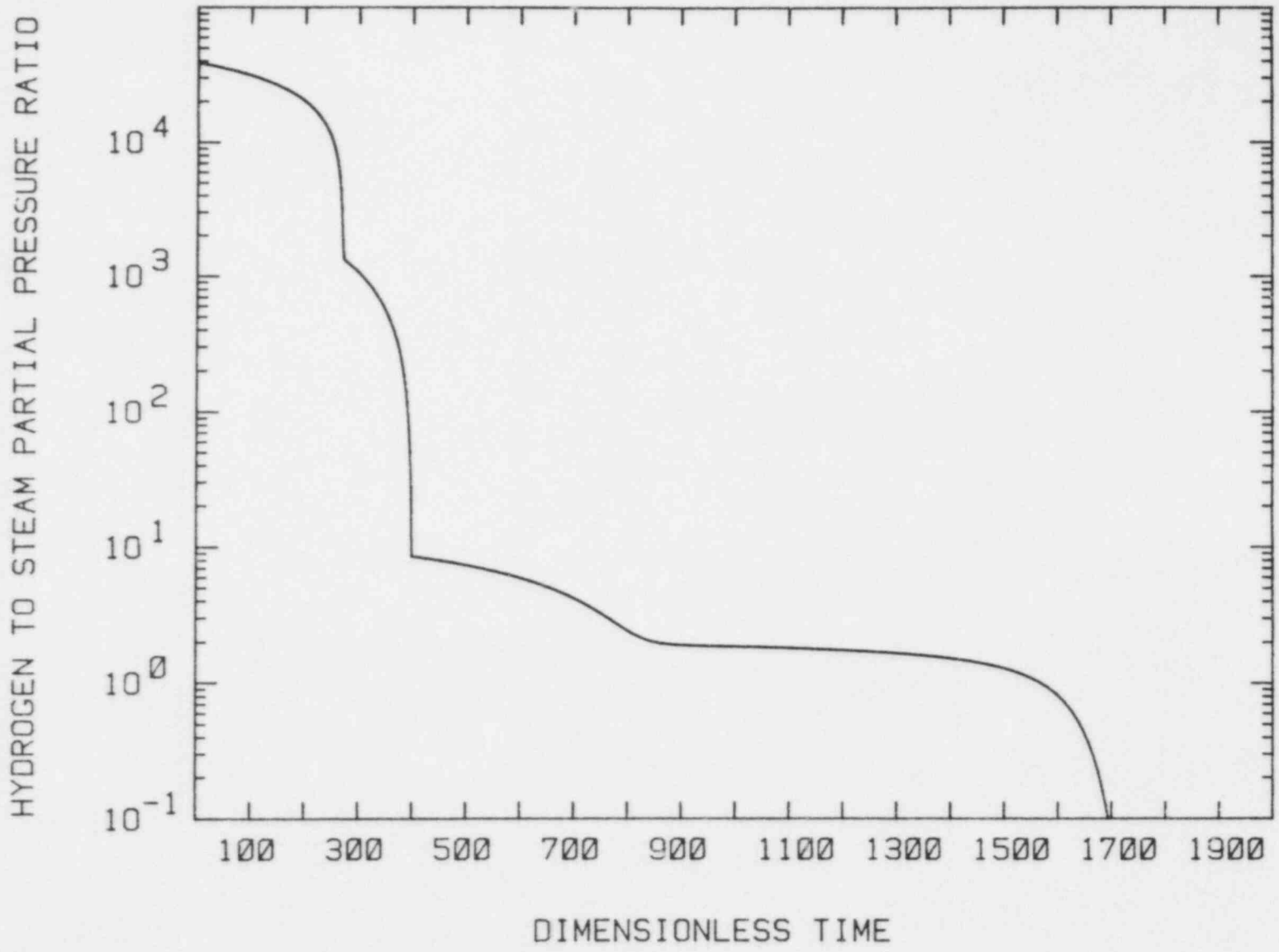

Figure 21. Hydrogen-to-Steam Partial Pressure Ratio When Coking and Decarbonization Are Considered

present in the melt, this ratio is about 10^4. Once the zirconium is largely oxidized and carbon is the most reducing constituent of the melt, the ratio falls to about 10^3. Depletion of carbon causes the hydrogen-to-steam partial pressure ratio to fall to about 10. As simultaneous oxidation of Cr and Fe proceeds, the ratio evolves slowly to a value of about two. Once all the iron and chromium have been oxidized and only nickel is present in the melt, the partial pressure ratio falls sharply to about 0.01.

The variations of the hydrogen-to-steam partial pressure ratio have the greatest effects on the vaporization reactions of the type:

$$[MO_x] + xH_2 \rightarrow M(g) + xH_2O \quad .$$

Such reactions will be driven to the right when zirconium is present in the melt. The driving force for such reactions is reduced somewhat when the metallic zirconium has been depleted and carbon is being oxidized. This reduction in the driving force is not as significant, however, as the reduction that occurs when the carbon is depleted.

Not only is the hydrogen-to-steam partial pressure ratio important to vaporization, but, so too are the absolute pressures of the gas phase constituents. Coking and decarbonization affect these absolute pressures. The partial pressures of H_2O, CO_2, CO, and H_2 are shown as functions of time in Figure 22. Initially, the gas that has equilibrated with the melt is nearly pure hydrogen. When coking is complete and decarbonization begins, the hydrogen pressure in the gas is reduced by nearly a factor of four. The hydrogen pressure rises once extensive decarbonization of the melt is complete. These variations in the absolute hydrogen pressure will affect vaporization reactions with the stoichiometry:

$$[MO] + 1/2\ H_2 \rightarrow MOH(g) \quad .$$

The effects are not especially great, however, if the hydrogen pressure varies by a factor of only four. In fact, for the reaction depicted here, a factor of four variation in the pressure of hydrogen would induce only a factor of two variation in the vapor pressure of MOH(g).

The variations in the H_2O pressure are much larger and these variations will influence the vaporization reactions of the type:

$$[MO] + H_2O \rightarrow M(OH)_2(g) \quad .$$

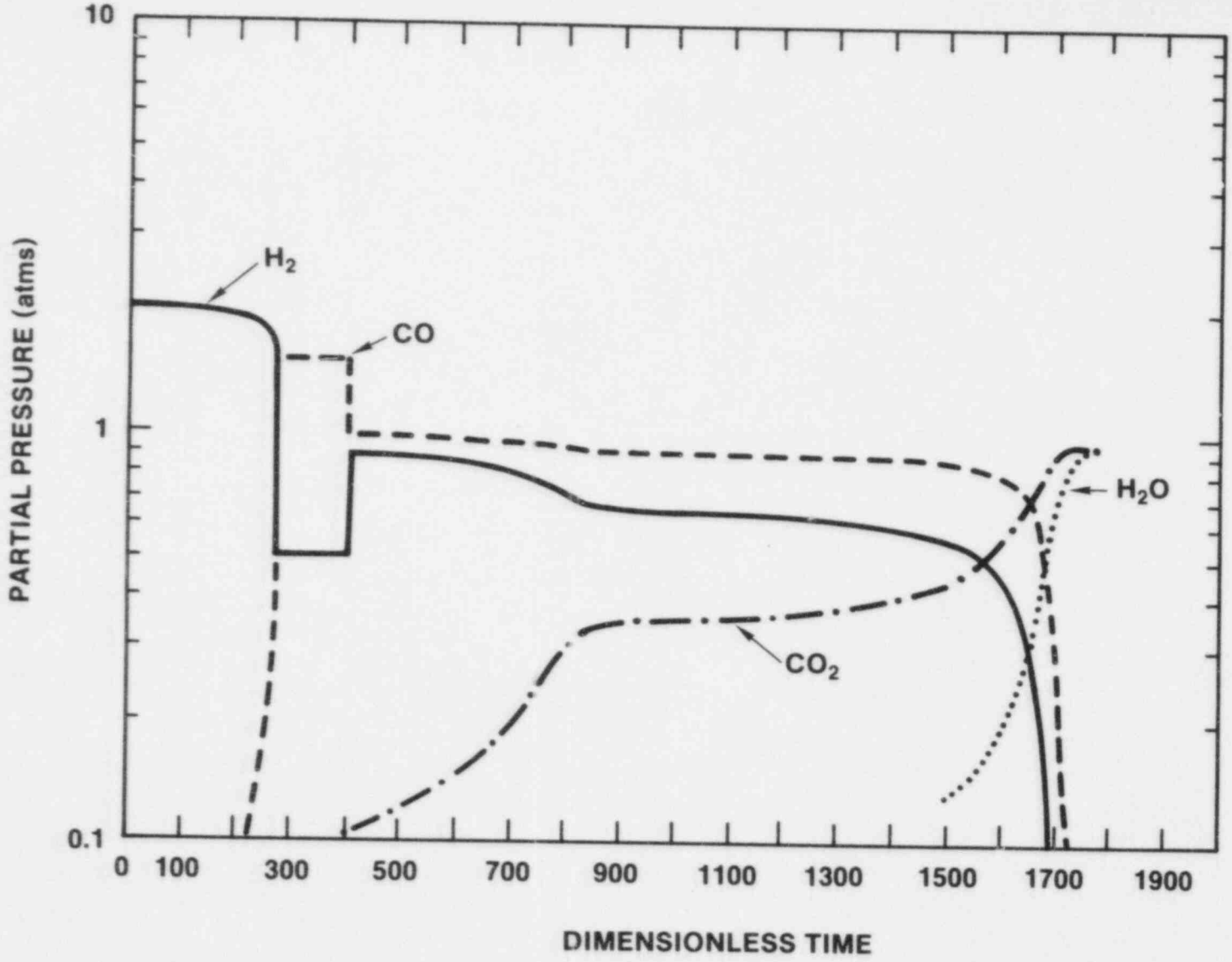

Figure 22. Partial Pressures of CO_2, H_2O, CO, and H_2 When Coking and Decarbonization Are Considered

The most significant variations in the partial pressure of H_2O are the result of variations in the oxygen potential of the melt. The variations in the partial pressure of $M(OH)_2(g)$ parallel the variations in the steam partial pressure. Thus, vaporization as $M(OH)_2$ should be orders of magnitude more important following decarbonization than during Zr oxidation.

The discussions of coking and carbonization thus far have been based on the assumption that carbon dissolved in the metallic phase of a core melt is an ideal melt constituent. This, of course, is definitely not true. The nonideality of carbon in iron-based alloys has been the cause of many of the frustrations and accomplishments of steel alloy development. Because of the importance of carbon in steel making, there are data on the activity of carbon at relatively low temperatures in liquid, iron-based alloys. A model of the nonideality of carbon-containing, iron-based alloys is shown in Table 9. A detailed discussion of this model is to be found elsewhere.[274]

The effects of nonidealities expressed by this model on the coking and decarbonization process are shown in Figure 23. Comparison of these results to those obtained assuming ideal carbon behavior shows that nonidealities make no qualitative change in the processes important to vaporization.

The discussions of coking and decarbonization processes in core melts have been based on theoretical analysis. The coking process has never been observed in experiments designed to simulate core melt/concrete interactions. Failure to observe the process is probably a result of the fact that melts having compositions susceptible to coking have never been used in melt/concrete interaction experiments to date. But, it must also be recognized that the coking reactions are often susceptible to kinetic inhibitions. Such kinetic barriers may prevent the deposition of carbon in the melt. Further, small errors in the actual oxygen potentials estimated for the melt/concrete interactions could mean that the driving force for coking is incorrectly estimated.

The current implementation of the VANESA model does not consider explicitly the coking and decarbonization reactions because (1) there is not a prototypic data base concerning coking, (2) the kinetic effects which may inhibit coking are unknown, and (3) the coking reaction is so sensitive to oxygen potential. The most important features of the reactions--the effects on debris temperature and the volume of gas sparging the melt--will be reflected in the output obtained from the VANESA model if these features are reflected by the input to the model obtained from models of

Table 9

A Model for a Nonideal Metallic Phase

Carbon Activity Coefficient

$$\ln[\gamma(C)] = -0.3567 - 5.1\,X(Cr) + 2.9\,X(Ni) + (7808/T + 2.871)X(C) + (15{,}624/T + 5.323)(X(C))^2 - 0.4(X(Cr))^2$$

Chromium Activity Coefficient

$$\ln[\gamma(Cr)] = -5.1\,X(Cr)$$

Iron Activity Coefficient

$$\ln[\gamma(Fe)] = -0.1(X(Ni))^2 + (3904/T + 1.436)[X(c)]^2 + 5.1\,X(Cr)X(C) - 2.9\,X(Ni)X(C)$$

Nickel Activity Coefficient

$$\ln[\gamma(Ni)] = -0.4155 + 0.2\,X(Ni) + 2.9\,X(C)$$

Zirconium Activity Coefficient

$$\ln[\gamma(Zr)] = -(6175/T)(1-X(Zr))^2$$

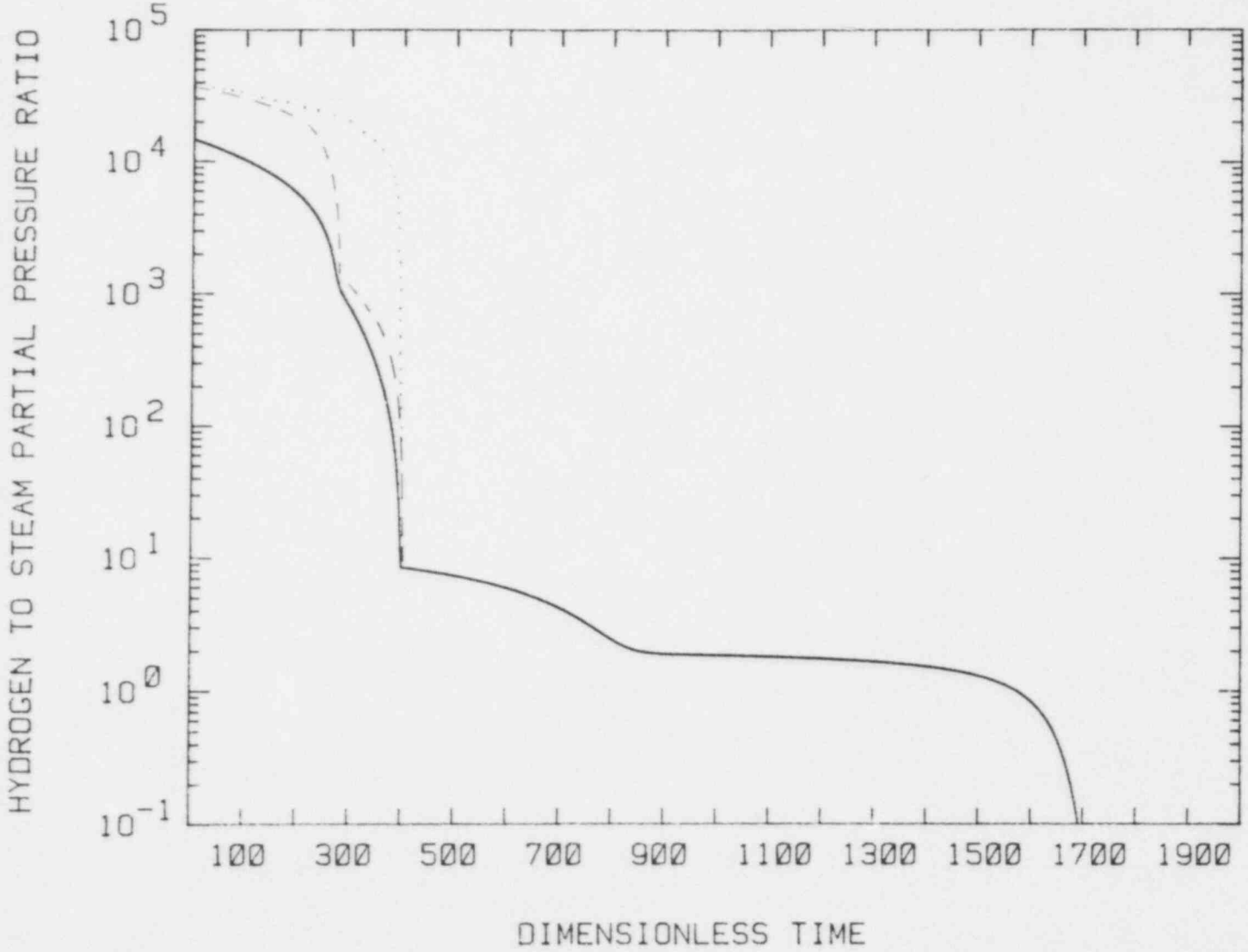

Figure 23. Comparisons Showing the Effects of Nonideality on the Predicted Nature of Coking and Decarbonization. Solid line is obtained when nonideality is considered. The dashed line is the result of considering the melt to be an ideal solution. The doted line is the result of neglecting carbon formation in an ideal solution model.

the core debris interactions with concrete. The CORCON model does include coking, and consequently analyses with VANESA based on input derived from CORCON do reflect the effects of coking to a limited extent. Zirconium inventories predicted by CORCON and VANESA may not match and this can affect release predictions.

6. Boron Chemistry

Boiling Water Reactors (BWRs) use boron carbide (B_4C) as a control blade material. There can be more than 900 kg of boron carbide in the core of a modern BWR. Little attention has been given, however, to the behavior of boron carbide in a severe reactor accident. It was not considered in the recent NRC source term reassessment despite evidence that the behavior of boron carbide could strongly influence the chemical form and transport of radionuclides in the reactor coolant system.[275]

It is well established that boron carbide will react with high temperature steam:[276]

$$B_4C + 6H_2O \rightarrow 2B_2O_3(\ell) + 6H_2 + C$$

$$C + H_2O \rightarrow CO + H_2 \quad .$$

The condensed products of the reactions are quite volatile under the conditions expected to exist during core degradation:

$$B_2O_3(\ell) \rightarrow B_2O_3(g)$$

$$B_2O_3(\ell) + H_2O \rightarrow 2HBO_2(g)$$

It is unclear at this point how much exposure of boron carbide to steam will occur during a reactor accident. It could be that steam will be completely consumed by reaction with the zircaloy fuel cladding and structures within the core before it can contact the boron carbide. Even if boron carbide is exposed to steam and reacts, it is unlikely that the reactions would completely convert the material to the oxide and vapors. It is certainly possible that significant amounts of boron carbide could be present in the core melt that emerges from the reactor vessel and begins to attack the concrete.

The possibility that boron carbide will be present during core debris interactions with concrete has not been

considered analytically or experimentally in the past. The current implementation of the VANESA model does not include boron chemistry largely because models that provide initial conditions for the VANESA model, such as the MARCH code, do not specify a boron inventory for the melt. It is of interest to examine what effects inclusion of boron in the melt inventory might have.

The product of steam corrosion of boron carbide, B_2O_3, would be incorporated into the oxide phase of a core melt. Its effects on the properties of the oxide melt would be similar to the effects of silica. The high volatility of B_2O_3 would mean that it could be an important source of nonradioactive vapors evolved from the core debris.

The behavior of unreacted B_4C in a core melt is less certain. One possibility is that B_4C would dissolve in the metallic melt:

$$B_4C \rightleftharpoons 4[B] + [C] \quad .$$

The dissolution would, of course, enrich the melt in carbon. The effects of dissolved carbon on the melt behavior have been discussed at length in the previous section of this chapter. The effects of boron on melt behavior are of interest here.

Boron dissolved in the melt would be susceptible to oxidation by gases evolved from the concrete. Boron would oxidize in preference to iron and chromium.

The oxidation of dissolved boron to form condensed products could be incorporated into the VANESA model with little difficulty. Boron, however, can also react to form very volatile products. Some reaction stoichiometries are:

$$[B] + 1/2\ H_2 \rightleftharpoons BH(g)$$

$$[B] + H_2 \rightleftharpoons BH_2(g)$$

$$[B] + H_2O \rightleftharpoons BO(g) + H_2$$

$$2[B] + 2H_2O \rightleftharpoons B_2O_2(g) + 2H_2$$

$$[B] + 2H_2O \rightleftharpoons HBO_2(g) + 3/2\ H_2 \quad .$$

Other vaporization reactions are suggested by the list of thermodynamic data for species in the B-O-H system shown in Table 10.

This brief examination of the chemistry of boron in core melts suggests that boron could influence the hydrogen-to-steam partial pressure ratio of gases sparging through the melt.

Vaporization of boron compounds could contribute significantly to the aerosol generation. It may be necessary to recognize the vaporization processes in establishing the chemistry of gases from the concrete sparging through boron rich melts.

7. Reaction of Gases with The Oxidic Core Melt

To this point, the discussions of gas reactions have focused on the reactions with metallic phases. The oxygen potential as well as the absolute gas pressures will affect also the vaporization from the oxide phases of a core melt. Also, it is possible that the oxide phase may be more dense than the metallic phase--contrary to the assumption made in the current implementation of the VANESA model. In this case, gases entering the melt from the concrete will not have been altered by reaction with the metal phase when they encounter the oxide melt. It is necessary, then, to examine the reactions of H_2O and CO_2 with the oxide phase.

At first blush, it might be presumed that the oxide phase is essentially inert toward the oxidizing gases entering the melt. This would be most incorrect. Uranium dioxide exhibits a broad range of stoichiometry.[277] The precise stoichiometry adopted by the urania will depend on the chemical environment--particularly, the oxygen potential and the temperature. A formal stoichiometry for the urania response to the oxygen potential can be written as:

$$UO_{2+y} + (x-y)H_2O \rightleftharpoons UO_{2+x} + (x-y)H_2 \quad .$$

Then,

$$\frac{-\partial \Delta G_f(UO_{2+y})}{\partial y} + \Delta G_f(H_2O) = \ln\left[\frac{P(H_2)}{P(H_2O)}\right] \quad .$$

Blackburn[278] has formulated a simple model for the variation in the stoichiometry of urania with temperature and oxygen potential. The model hypothesizes that urania consists of

Table 10

Thermodynamic Data for the B-O-H System

	Free Energy of Formation (cal/mole)								
T(K)	B(ℓ)	B_2O_3(ℓ)	B	BH	BH_2	BH_3	BO	BO_2	BHO
500	4195	-270481	115083	93767	42874	27432	-11359	-70276	23471
600	3982	-264739	111484	91375	41936	28057	-13612	-70750	24099
700	3769	-259100	107885	89004	41029	28761	-15842	-71225	24700
800	3556	-253593	104290	86651	40145	29523	-18051	-71702	25283
900	3343	-248192	100703	84318	39281	30333	-20236	-72176	25848
1000	3130	-242877	97125	82004	38431	31179	-22399	-72646	26400
1100	2917	-237637	93556	79704	37593	32052	-24544	-73115	26940
1200	2704	-232449	89999	77422	36768	32950	-26668	-73578	27469
1300	2491	-227310	86451	75152	35951	33863	-28774	-74037	27991
1400	2278	-222205	82915	72899	35144	34796	-30862	-74490	28501
1500	2065	-217137	79389	70657	34341	35741	-32935	-74939	29006
1600	1852	-212091	75875	68430	33549	36696	-34989	-75379	29501
1700	1639	-207070	72373	66216	32766	37666	-37028	-75813	29986
1800	1423	-202071	68882	64015	31988	38643	-39051	-76240	30466
1900	1206	-197088	65403	61826	31219	39633	-41058	-76660	30935
2000	989	-192120	61935	59652	30457	40631	-43051	-77073	31398
2100	771	-187165	58476	57487	29704	41637	-45028	-77476	31851
2200	551	-182225	55029	55336	28956	42652	-46992	-77873	32299
2300	329	-177297	51591	53195	28216	43676	-48944	-78264	32738
2400	111	-172373	48166	51068	27486	44709	-50879	-78643	33166
2500	0	-167247	44857	49056	26864	45850	-52696	-78910	33483
2600	0	-161903	41668	47168	26367	47117	-54388	-79057	33677
2700	0	-156565	38491	45291	25876	48391	-56067	-79195	33866
2800	0	-151238	35319	43420	25387	49666	-57737	-79328	34048
2900	0	-145909	32160	41565	24911	50958	-59391	-79450	34219
3000	0	-140593	29003	39710	24435	52243	-61039	-79569	34390

Table 10 (Continued)

Thermodynamic Data for the B-O-H System

T(K)	Free Energy of Formation (cal/mole)								
	HBO_2	H_2BO_2	H_3BO_3	B_2	$H_4B_2O_4$	B_2O	B_2O_2	$B_2O_3(g)$	$H_3B_3O_3$
500	-129459	-102046	-211166	172237	-266679	9483	-112119	-194874	-263204
600	-128401	-99500	-205650	167684	-258337	6844	-112752	-193995	-257329
700	-127297	-96921	-200055	163159	-249949	4249	-113371	-193097	-251385
800	-126159	-94326	-194411	158666	-241546	+1696	-113974	-192182	-245403
900	-124989	-91716	-188726	154204	-233134	-817	-114559	-191248	-239395
1000	-123795	-89100	-183011	149777	-224724	-3290	-115126	-190296	-233374
1100	-122583	-86483	-177279	145379	-216327	-5730	-115680	-189333	-227353
1200	-121351	-83863	-171526	141016	-207939	-8135	-116214	-188352	-221326
1300	-120106	-81245	-165765	136680	-199570	-10508	-116736	-187360	-215305
1400	-118847	-78626	-159993	-132379	-191213	-12848	-117240	-186352	-209281
1500	-117575	-76010	-154212	128102	-182873	-15161	-117731	-185332	-203266
1600	-116292	-73396	-148427	123860	-174547	-17439	-118201	-184294	-197249
1700	-114996	-70779	-142631	119644	-166231	-19691	-118658	-183244	-191231
1800	-113691	-68166	-136834	115455	-157932	-21913	-119099	-182181	-185218
1900	-112376	-65550	-131026	111295	-149643	-24108	-119524	-181101	-179198
2000	-111051	-62937	-125217	107163	-141365	-26274	-119932	-180008	-173180
2100	-109713	-60320	-119400	103057	-133094	-28415	-120323	-178896	-167156
2200	-108370	-57704	-113580	98975	-124836	-30529	-120701	-177775	-161134
2300	-107017	-55088	-107756	94918	-116586	-32622	-121065	-176640	-155109
2400	-105652	-52464	-101921	90885	-108337	-34686	-121411	-175485	-149073
2500	-104176	-49742	-95982	87092	-99890	-36511	-121528	-174105	-142719
2600	-102576	-46896	-89917	83541	-91216	-38092	-121408	-172489	-136018
2700	-100968	-44052	-83850	80015	-82549	-39648	-121269	-170854	-129316
2800	-99354	-41210	-77781	76506	-73896	-41190	-121125	-169215	-122615
2900	-97726	-38356	-71696	73021	-65229	-42700	-120958	-167553	-115893
3000	-96099	-35510	-65619	69548	-56588	-44201	-120789	-165889	-109188

Table 10 (Continued)

Thermodynamic Data for the B-O-H System

T(K)	Free Energy of Formation (cal/mole)		
	$H_3B_3O_6$	B_2H_6	B_5H_9
500	-485268	30795	59459
600	-473601	35498	68744
700	-461951	40316	78228
800	-450388	45203	87825
900	-438757	50133	97493
1000	-427212	55087	107200
1100	-415712	60048	116915
1200	-404245	65015	126642
1300	-392814	69973	136353
1400	-381413	74931	146064
1500	-370046	79877	155759
1600	-358700	84815	165443
1700	-347377	89750	175126
1800	-336081	94671	184790
1900	-324798	99590	194454
2000	-313537	104504	204114
2100	-302285	109410	213769
2200	-291053	114309	223416
2300	-279833	119204	233059
2400	-268615	124101	242712
2500	-257096	129198	252887
2600	-245243	134527	263629
2700	-233397	139849	274372
2800	-221568	145158	285096
2900	-209727	150483	295856
3000	-197917	155787	306571

U^{2+}, U^{4+} and U^{6+} and O^{2-} ions. The abundances of these ions in the urania are found by simultaneous solution of the equations:

$$\frac{n_{U^{6+}}}{n_{U^{4+}}} = \frac{1}{n_{O^{2-}}} \frac{P_{H_2O}}{P_{H_2}} \exp\left(\Delta G_f(H_2O)/RT\right) \exp\left(\frac{16500}{RT} - 5.1\right)$$

$$\frac{n_{U^{4+}}}{n_{U^{2+}}} = \frac{1}{n_{O^{2-}}} \frac{P_{H_2O}}{P_{H_2}} \exp\left[\frac{78300}{T} - 13.6\right] \exp\left(\Delta G_f(H_2O)/RT\right) .$$

Subject to the constraints

$$n_{U^{2+}} + n_{U^{4+}} + n_{U^{6+}} = 1$$

and

$$n_{O^{2-}} = 3n_{U^{6+}} + 2n_{U^{4+}} + n_{U^{2+}} = 2 + x$$

and where $\Delta G_f(H_2O)$ is the free-energy of formation of water vapor. Some values of 2+x calculated with this model for various temperatures and hydrogen-to-steam partial pressure ratios are listed below:

	P_{H_2}/P_{H_2O}					
Temp (K)	1	10	100	1000	10000	50000
2500	2.013	2.001	1.999	1.993	1.938	1.770
2200	2.006	2.0006	2.000	1.999	1.995	1.976
2000	2.003	2.0003	2.000	2.000	1.999	1.997

It is apparent then that urania will respond stoichiometrically to the entire range of oxygen potentials expected to develop during the course of core debris interactions with concrete. When conditions are quite reducing the urania becomes decidedly hypostoichiometric (x<0).

Urania that emerges from the reactor vessel will have been subjected to quite reducing conditions. It will have been exposed after all to a zirconium-rich metallic phase for some protracted period of time. Exposure would have begun at the time fuel rods within the reactor core began to melt. The fuel that emerges from the reactor core would not be perfectly stoichiometric urania, $UO_{2.00}$. Rather it would be hypostoichiometric urania, UO_{2-x}. Clearly, gases evolved from the concrete will react with this hypostoichiometric urania just as they react with the metallic melt.

The variable stoichiometry of urania has some interesting effects on the chemistry of the metallic melt. Application of the Gibbs-Duhem theorem to the U-O system[278] shows that a finite uranium metal activity develops in hypostoichiometric urania (UO_{2-x}):

$$\ln[a(U)] = -\ln\left[\frac{(1-x)}{(1-x_s)}\right] + 2\ln\left[\frac{x}{x_s}\right] + x - x_s$$

where $x_s = \exp[-12{,}913/T + 3.767]$ and is the location of lower phase boundary between urania and uranium metal.

The system consisting of the metal phase and the hypostoichiometric urania will not be in equilibrium until the activity of uranium metal in the oxide equals the activity of uranium in the metal phase. Thus, metallic uranium will be present in the metal phase of a core melt emerging from a reactor vessel. This metallic uranium content of the metal phase can be significant. Enough uranium can be present to cause the metallic phase to be more dense than the oxide phase of a core melt.

Calculation of the equilibrium oxygen potential of the oxide melt during core debris interactions with concrete is not an easy task. The Blackburn model is not applicable since the urania is neither pure nor solid. Contamination of the urania with ZrO_2 and other oxides causes difficulties since these species, too, can be nonstoichiometric.

The current implementation of the VANESA model treats the difficulty of gas reactions with the oxide phase based on the assumption that oxygen transport between the metallic and the oxidic phases is rapid. Then, the oxygen potential of the oxide phase is equal to the oxygen potential of the metallic phase. It is then necessary to calculate only the oxygen potential of the metallic phase. The stoichiometry of the oxide phase is assumed to adjust instantaneously to variations in the oxygen potential of the metal phase.

Assumption of oxygen equilibrium across the oxide/metal interface may seem at first inconsistent with the assumption of disequilibrium for low concentration melt constituents discussed in connection with partitioning (Section III-A-1). The slow transport of melt constituents found by simple models was caused in large measure by the low concentrations in one phase or the other. The low concentrations inhibited mass transport away from the interface which was assumed at equilibrium. No such rate limitations arise to inhibit mass transport necessary to maintain oxygen potential equivalency in the oxide and metal phases. (As will be discussed in the next chapter, it is possible for the metal phase and oxide phase to be well-mixed as a result of gas stirring of the melt. This will assure that there is an equilibration of oxygen potentials in the two phases.)

The assumption that the oxygen potentials in the oxide and the metal phases are equal greatly simplifies the analyses done with the VANESA model. It does not matter for the thermodynamic calculations whether the oxide melt is more or less dense than the metallic melt. The assumption that the melt is stratified rather than well-mixed is no longer consequential. Altering these geometric assumptions will not alter the estimates of the thermodynamic features of the system if the alterations do not affect predictions of melt temperature, gas generation, and the like obtained from models of the core debris interactions with concrete.

8. Speciation

Speciation is an important element of the analysis of vaporization processes. The definition of chemical species must be made for both the condensed phase and the vapor phase. Speciation of the condensed phase is perhaps a difficult concept since the high temperature liquids treated by the VANESA model are seldom molecular in nature. Consequently, molecular species or stoichiometric species do not really exist in the liquid phase. What is present in the liquid is unknown, typically, and in any case probably changes continually. The speciation of the liquid phase is then just a convenience for the purposes of calculation. Any differences between the actual states of interaction in the liquid and the interactions suggested by the choice of species are, in theory, corrected in the calculations by the activity coefficients. When detailed estimates of species activities are not available, as they are not for core melts, the choices for the condensed phase species ought to reflect as closely as possible what species are present in the liquid.

Speciation of the vapor phase is a more transparent process. Vapors are molecular in nature. Data are tabulated for most of the vapor molecules of interest in the analyses considered here. It is, however, absolutely essential to

recognize that the stoichiometry of vapor species need not bear any resemblance to the stoichiometry of the melt species. Failure to understand this point has been the cause of considerable confusion. An example might serve to illustrate the difficulties. At sufficiently low oxygen potentials (high hydrogen-to-steam partial pressure ratios) the vapor over $La_2O_3(\ell)$ would consist of atomic lanthanum:

$$La_2O_3(\ell) + 3H_2 \rightleftharpoons 2La(g) + 3H_2O \quad .$$

This does not mean that the $La_2O_3(\ell)$ has been partially reduced to $La(\ell)$. To be sure, a condensed phase lanthanum activity can be computed for the liquid, but this activity coefficient will be typically much less than one. All too often the equilibrium oxygen potential necessary to have pure $La(\ell)$ (activity = 1) in equilibrium with pure $La_2O_3(\ell)$ has been used to ascertain if there will be any La(g) in the vapor. Though the $La(\ell)/La_2O_3(\ell)$ equilibrium and the $La_2O_3(\ell)/La(g)$ equilibrium are related, the relationship is not so close that simple inspections of the first of these equilibria leads readily to conclusions concerning the second.

The vapor speciation for an element M chosen for the current implementation of the VANESA model is, in general, based on the known vapor species in the M-O-H system. A comprehensive survey of the literature was not attempted in the brief time allowed for the development of the current version of the model. Consequently only the better known of the vapor species in the various M-O-H system have been included. The speciation is probably weakest in the area of vapor phase hydrides.

There are two exceptions to the restriction of the speciation to the M-O-H system. Speciation of cesium and iodine was selected from the Cs-I-O-H system. This was done so that CsI(g) could appear as a vapor species. Also, the speciation of tellurium includes SnTe(g) and SbTe(g). This was done because these particular vapor species appear stable. Recent results of in-pile studies on core degradation seem to confirm the importance of SnTe(g).[340]

Further discussions of the selection of species for the elements considered in the current implementation of the VANESA model are presented below:

a. Aluminum: Aluminum comes into core melts as a result of concrete ablation. Typical concretes contain a few percent of aluminum oxide. The actual chemical form of aluminum oxide in the dehydrated concrete is probably calcium aluminate. The condensed form of aluminum considered in the

VANESA model is $Al_2O_3(\ell)$. Vapor forms bearing aluminum recognized in the model are Al(g), AlO(g), AlOH(g), $Al_2O(g)$, $AlO_2(g)$, $Al_2O_2(g)$, HAlO(g), $Al(OH)_2(g)$, and AlO(OH)(g). Notice that a vapor species having the stoichiometry of the condensed phase species is not included. Thermodynamic data for the aluminum-bearing species are collected in Table 11. Most of these data are from the JANAF Table.[279] Data for $Al(OH)_2(g)$ are from Reference 287.

b. Antimony: Antimony is produced by fissioning in the fuel and can also be an impurity in the fuel cladding. It is assumed in the VANESA model that antimony partitions preferentially into the metallic phase of the core debris. The condensed form of antimony is taken to be $Sb(\ell)$. The vapor forms of antimony are considered to be Sb(g), SbO(g), SbH(g), $SbH_3(g)$, Sb(OH)(g), $Sb(OH)_2(g)$, $Sb_2(g)$, $Sb_4(g)$, and SbTe(g). Thermodynamic data for the antimony-bearing species are collected in Table 12.

Thermodynamic functions for $SbH_3(g)$ were calculated using the rigid rotor-harmonic oscillator approximation and vibrational and structural data from Reference 323. The entropy at 298.15 K found in these calculations is 55.573 e.u. whereas Gunn et al.[324] found 55.65 $\pm$ 2.00. Free-energies of formation were calculated using ΔH_f(298 K) = +34600 $\pm$ 2500[324] and reference state data for Sb from Reference 293 and for H_2 from Reference 279a.

Thermodynamic functions for SbH(g) were calculated from spectroscopic data collected in Reference 314. Data for the antimony hydroxides are from Reference 287. Data for the telluride are discussed in connection with tellurium speciation.

Thermodynamic functions and the enthalpy of formation at 298.15 K for SbO(g) were taken from Reference 289. Data for the condensed phase, Sb(g), $Sb_2(g)$, and $Sb_4(g)$ were taken from Reference 290.

The tabulated data were extrapolated to higher temperatures as follows:

a. Data for $Sb(\ell)$ were extrapolated above 1800 K by assuming the heat capacity to be constant at 7.5 cal/mole-K,

b. Data for Sb(g) were extrapolated above 2000 K by assuming the heat capacity to be constant at 5.231 cal/mole-K,

c. Data for $Sb_2(g)$ were extrapolated above 2000 K by assuming the heat capacity to be constant at 8.936 cal/mole-K,

Table 11

Thermodynamic Data for Aluminum Species

T(K)	Free-Energies of Formation (cal/mole)						
	$Al_2O_3(\ell)$ (279d)	$A\ell(g)$ (279a)	$A\ell O(g)$ (279d)	$A\ell OH(g)$* (279a)	$Al_2O(g)$ (279d)	$A\ell O_2(g)$ (279d)	$Al_2O_2(g)$ (279d)
500	-349382	61787	6063	5932	-42734	-46269	-105581
600	-342514	58602	4097	5695	-44902	-46509	-105759
700	-335676	55447	2169	5501	-47012	-46737	-105887
800	-328871	52321	+276	5340	-49070	-46953	-105971
900	-322087	49224	-1582	5208	-51071	-47153	-106005
1000	-315951	46342	-3220	5285	-52646	-47151	-105619
1100	-307658	43576	-4740	5464	-53992	-47044	-105011
1200	-300385	40835	-6235	5656	-55295	-46923	-104363
1300	-293134	38116	-7708	5856	-56556	-46789	-103678
1400	-285905	35416	-9161	6066	-57779	-46643	-102961
1500	-278701	32735	-10600	6285	-58971	-46486	-102215
1600	-271517	30072	-12023	6509	-60129	-46317	-101438
1700	-264398	27425	-13435	6741	-61256	-46138	-100634
1800	-257380	24794	-14835	6978	-62353	-45948	-99802
1900	-250463	22177	-16228	7224	-63426	-45750	-98948
2000	-243639	19573	-17614	7473	-64475	-45544	-98073
2100	-236898	16982	-18993	7728	-65498	-45327	-97173
2200	-230241	14404	-20366	7990	-66497	-45101	-96253
2300	-223656	11841	-21731	8257	-66469	-44865	-95306
2400	-217148	9285	-23093	8530	-68423	-44620	-94342
2500	-210719	6739	-24454	8807	-69362	-44373	-93366
2600	-204347	4209	-25807	9090	-70274	-44111	-92362
2700	-198046	1684	-27159	9377	-71171	-43845	-91345
2800	-190142	0	-27675	11323	-70386	-42738	-88646
2900	-178953	0	-26515	14198	-66238	-39951	-82586
3000	-167835	0	-25358	17070	-62086	-37165	-76522

*Aluminum monoxyhydride (HAℓO).

Table 11 (Continued)

Thermodynamic Data for Aluminum Species

T(K)	Free-Energies of Formation (cal/mole)			
	AlOH(g)+	$Al(OH)_2(g)$	AlO(OH)(g)	AlH(g)
	(279a)	(287)	(279a)	(279a)
500	-45135	-141916	-104485	50882
600	-45333		-103219	48780
700	-45464		-101908	46720
800	-45541		-100564	44699
900	-45570		-99187	42713
1000	-45372	-128687	-97595	40944
1100	-45050		-95890	39285
1200	-44698		-94164	37646
1300	-44320		-92420	36024
1400	-43919		-90660	34419
1500	-43499	-113463	-88886	32829
1600	-43061		-87100	31252
1700	-42605		-85300	29688
1800	-42134		-83489	28135
1900	-41650		-81669	26595
2000	-41154	-97926	-79840	25065
2100	-40644		-78000	23545
2200	-40122		-76152	22036
2300	-39587		-74293	20535
2400	-39043		-72424	19044
2500	-38493	-82226	-70555	17561
2600	-37928		-68670	16086
2700	-37356		-66781	14619
2800	-35944		-64052	14814
2900	-32849		-59641	15938
3000	-29755	-60564	-55233	17063

+Aluminum monoxyhydride.

Table 12

Thermodynamic Data for Antimony Species*

T(K)	Free-Energies of Formation (cal/mole)								
	Sb(ℓ)	Sb(g)	Sb_2(g)	Sb_4(g)	SbO(g)	SbOH(g)	$Sb(OH)_2$(g)	SbH(g)	SbH_3(g)
	(290)	(290)	(290)	(290)	(289)	(287)	(287)	(314)	
500		46679	35890	29582	2555	-7239	-74428	23646	35997
600		43534	32197	25890	+512			19753	36533
700		40420	28573	22304	-1504			15961	37136
800		37324	25014	18819	-3496			12690	37774
900		34260	21519	15438	-5464			9654	38450
1000	0	31722	19099	14184	-6904	-9774	-63488	7193	39647
1100	0	29239	16782	13116	-8303			4836	40897
1200	0	26770	14520	12139	-9683			2545	42140
1300	0	24325	12307	11245	-11047			+320	43414
1400	0	21905	10141	10431	-12393			-1853	44687
1500	0	19503	8020	9690	-13726	-9290	-49821	-3953	45984
1600	0	17106	5938	9017	-15045			-6026	47269
1700	0	14723	3896	8408	-16350			-8037	48573
1800	0	12364	1888	7858	-17643			-10014	49873
1900	0	9887	-87	7363	-18925			-10419	51176
2000	0	6921	-2029	6946	-20195	-7861	-35523	-10274	52498
2100	0	3961	-3940	6607	-21453			-10132	53803
2200	0	1005	-5821	6340	-22699			-9959	55125
2300	0	0	-7677	6138	-23935			-9768	56454
2400	405	0	-8696	7625	-24756			-8535	58814
2500	2497	0	-6314	15923	-23880	-1741	-16802	-6027	62440
2600	4560	0	-3969	24161	-23022			-3512	66062
2700	6593	0	-1659	32342	-22186			-996	69675
2800	8599	0	+620	40469	-21367			+1530	73291
2900	10581	0	2865	48543	-20566			+4061	76899
3000	12531	0	5080	+56565	-19782	+4402	+1723	+6596	80503

*See also SbTe(g) listed with tellurium species

d. Data for $Sb_4(g)$ were extrapolated above 2000 K by assuming the heat capacity to be constant at 14.852 cal/mole-K,

c. Barium: Barium is an important radionuclide. A typical barium inventory in a large reactor core melt is 65 kg. Within reactor fuel, barium may be present as a substitutional impurity in the urania lattice or as barium zirconate. The condensed phase form of barium assumed in the VANESA model is BaO(ℓ). The vapor phase species involving barium are Ba(g), BaO(g), BaH(g), $Ba(OH)_2(g)$, and BaOH(g). Thermodynamic data for the barium species are shown in Table 13. With the exception of data for BaH(g) all data are from the JANAF tables.[279] Enthalpy of formation and the free-energy functions for BaH(g) were taken from References 291 and 292, respectively.

d. Calcium: Calcium enters the melt as a constituent of ablated concrete. The chemistry of calcium is assumed in the model to be completely analogous to that assumed for barium. That is, the condensed form is taken to be CaO and the vapors containing calcium are taken to be Ca(g), CaO(g), CaH(g), CaOH(g), and $Ca(OH)_2(g)$. The assumed condensed form of calcium may be overly simplistic. For many concretes calcium is present as a calcium silicate. The behavior of calcium in the core debris may involve the complexities described in connection with sodium and potassium oxides in the melt. Thermodynamic data for the calcium-bearing species are shown in Table 14.

e. Carbon: Carbon is taken in the current version of the VANESA model to be a constituent of the vapor--either as CO or CO_2. The behavior of carbon is discussed in far greater detail above.

f. Cerium: Cerium is an important radionuclide. A typical cerium inventory in a core melt is about 200 kg. In the current implementation of the VANESA model the condensed form of cerium is taken to be CeO_2. Cerium dioxide will become hypostoichiometric under reducing conditions at elevated temperatures.[260,261] At sufficiently low oxygen partial pressures the stoichiometry in the solid state is Ce_2O_3. In liquid mixtures, the variable stoichiometry ought not greatly affect vaporization and the tendency for cerium to adopt a trivalent state is ignored here. Thermodynamic data for solid CeO_2 have been tabulated several times.[262-267,290] Unfortunately, the various tabulations of the properties of $CeO_2(s)$ are not in good agreement. The tabulations by Pankratz[264] which are in fair agreement with the properties recommended by Robie et al.[263] and by Vahed and Kay[267] were accepted for this work. These tabulations were extrapolated by fitting heat capacity data[268] to:

Table 13

Thermodynamic Data for Barium Species

T(K)	Free-Energies of Formation (cal/mole)					
	BaO(ℓ)	Ba(g)	BaO(g)	BaOH(g)	$Ba(OH)_2$(g)	BaH(g)
	(279c)	(279b)	(279c)	(279d)	(279d)	(291,292)
500	-109362	30074	-37843	-56643	-139687	42367
600	-107716	27716	-39287	-56948	-137521	40452
700	-106053	25441	-40646	-57171	-135292	38636
800	-104377	23237	-41930	-57326	-133014	36887
900	-102693	21094	-43150	-57422	-130691	35199
1000	-101011	18999	-44319	-57473	-128336	33540
1100	-99133	17144	-45246	-57286	-125759	32159
1200	-97252	15334	-46124	-57056	-123149	30802
1300	-95371	13565	-46959	-56789	-120513	29485
1400	-93493	11829	-47756	-56489	-117857	28201
1500	-91619	10124	-48519	-56160	-115180	26947
1600	-89751	8446	-49251	-55806	-112489	25720
1700	-87893	6791	-49953	-55427	-109779	24520
1800	-86049	5156	-50628	-55026	-107058	23344
1900	-84218	3540	-51276	-54603	-104322	22192
2000	-82400	1938	-51901	-54161	-101576	21061
2100	-80589	350	-52500	-53698	-98813	19952
2200	-77562	0	-51848	-51989	-94812	20093
2300	-74200	0	-50831	-49918	-90455	20597
2400	-70851	0	-49798	-47835	-86090	21113
2500	-67513	0	-48749	-45740	-81721	21649
2600	-64181	0	-47679	-43627	-77334	22199
2700	-60854	0	-46589	-41497	-72937	22773
2800	-57531	0	-45480	-39350	-68527	23363
2900	-54206	0	-44347	-37181	-64095	23979
3000	-50882	0	-43194	-34995	-59651	24614

Table 14

Thermodynamic Data for Calcium Species

T(K)	Free-Energies of Formation (cal/mole)						
	CaO(ℓ)	Ca(g)	CaO(g)	CaOH(g)	$Ca(OH)_2$(g)	Ca_2(g)	CaH(g)
	(279c)	(279a)	(279d)	(279d)	(279d)	(279d)	(291,292)
500	-123482	29400	+1584	-49318	-134915	62167	43513
600	-121594	26783	-105	-49815	-132635	58281	41394
700	-119734	24192	-1765	-50285	-130344	54479	39309
800	-117871	21653	-3370	-50704	-128019	50813	37280
900	-116005	19161	-4923	-51076	-125660	47272	35300
1000	-114136	16712	-6432	-51407	-123274	43844	33362
1100	-112261	14306	-7895	-51697	-120860	40528	31468
1200	-110225	12097	-9159	-51793	-118262	37629	29768
1300	-108180	9928	-10382	-51851	-115638	34834	28109
1400	-106148	7776	-11587	-51894	-113010	32095	26466
1500	-104129	5641	-12777	-51923	-110377	29407	24838
1600	-102123	3520	-13953	-51941	-107744	26768	23222
1700	-100129	1413	-15119	-51946	-105104	24175	21622
1800	-97466	0	-15597	-51261	-101784	22986	20713
1900	-93414	0	-14669	-49165	-97060	24639	21218
2000	-89386	0	-13750	-47072	-92348	26307	21721
2100	-85379	0	-12840	-44979	-87642	27990	22225
2200	-81396	0	-11943	-42889	-82946	29689	22729
2300	-77438	0	-11060	-40800	-78258	31401	23233
2400	-73502	0	-10191	-38711	-73574	33126	23735
2500	-69589	0	-9338	-36626	-68903	34866	24239
2600	-65696	0	-8501	-34539	-64232	36618	24745
2700	-61823	0	-7681	-32453	-59569	38384	25250
2800	-57967	0	-6877	-30367	-54911	41962	25758
2900	-54127	0	-6088	-28278	-50251	43771	26269
3000	-50304	0	-5317	-26192	-45601	45597	26781

$$C_p[CeO_2(s)] = 16.761 + 2.216\ T/1000 - 239200/T^2 \ \frac{cal}{mole\text{-}K}$$

and using the polynomial expression to evaluate:

$$G_T[CeO_2(s)] = H_{298} + \int_{298.15}^{T} C_p dT - T\left[S^o_{298} + \int_{298.15}^{T} \frac{C_p}{T} dT\right] .$$

No allowances for solid-state phase changes in $CeO_2(s)$ were made in the extrapolation. The extrapolated heat capacity may significantly underestimate the high temperature heat capacity of CeO_2 since the fitting equation does not allow for extensive population of low lying, excited, electronic states. As a result the free-energies of formation in Table 14 may provide a lower bound on the stability of $CeO_2(s)$ at elevated temperatures.

The authors are not aware of attempts to tabulate the thermochemical properties of CeO_2 in the liquid state. These properties were estimated here using

$$G_T[CeO_2(\ell)] = G_T[CeO_2(s)] + \Delta H_m(1 - T/T_m)$$

where T_m is the melting point of stoichiometric CeO_2 and ΔH_m is the enthalpy of fusion. This approximate expression is derived assuming that the solid and liquid state heat capacities are the same. This, undoubtedly, is not true. But, there is sufficient uncertainty in the thermochemical properties of $CeO_2(s)$ to make it difficult to justify more accurate treatments of the liquid state properties.

Samsonov[181] cites 2873 K and 19000 cal/mole as the temperature and enthalpy of fusion of CeO_2, respectively. Mordovin et al.[269] measured 2670 K as the melting point of CeO_2. Rouanet[302] found the melting point of $CeO_{1.85}$ to be 2718 K. For this work, the measurement of the melting point by Mordovin et al. was accepted. The heat of fusion was estimated as recommended by Vier[303] to be 18738 cal/mole. Thermochemical properties for $CeO_2(\ell)$ obtained in this way are shown in Table 14.

Vapor forms of cerium are taken to be Ce(g), CeO(g), $CeO_2(g)$, CeOH(g), and $Ce(OH)_2(g)$. Properties of the vapors species other than $CeO_2(g)$ were taken from existing tabulations as indicated in Table 15. The free-energy functions

Table 15

Thermodynamic Data for Cerium Species

T(K)	Free-Energies of Formation (cal/mole)							
	$CeO_2(\ell)$	$CeO_2(s)$	Ce(g)	CeO(g)	CeOH(g)	$Ce(OH)_2(g)$	$CeO_2(g)$	$Ce_2O_2(g)$
			(293)	(289)	(287)	(287)		
500	-219720	-234949	86447	-41016	-20359	-117811	-121804	-153216
600	-215477	-230004	83578	-42693			-121896	-152903
700	-211274	-225100	80715	-44326			-121954	-152519
800	-207100	-220224	77859	-45907			-121975	-152055
900	-202953	-215375	75002	-47448			-121964	-151528
1000	-198818	-210538	72154	-48938	-20990	-105853	-121908	-150915
1100	-194589	-205607	69416	-50276			-121708	-150015
1200	-190295	-200612	66760	-51493			-121394	-148890
1300	-186011	-195626	64109	-52668			-121042	-147695
1400	-181742	-190655	61455	-53810			-120661	-146446
1500	-177496	-185707	58792	-54928	-20780	-93110	-120260	-145163
1600	-173248	-180757	56144	-56000			-119817	-143799
1700	-169020	-175827	53491	-57047			-119352	-142397
1800	-164817	-170922	50830	-58076			-118873	-140971
1900	-160623	-166026	48173	-59076			-118365	-139495
2000	-156445	-161147	45517	-60051	-19908	-79860	-117836	-137980
2100	-152286	-156286	42859	-61006			-117289	-136435
2200	-148148	-151446	40197	-61946			-116727	-134867
2300	-144026	-146623	37537	-62865			-116147	-133264
2400	-139887	-141781	34914	-63729			-115514	-131563
2500	-135800	-136993	32254	-64613	-18542	-66264	-114899	-129906
2600	-131701	-132192	29628	-65448			-114239	-128160
2700	-127651	-127441	26972	-66300			-113594	-126453
2800	-123591	-122678	24348	-67106			-112907	-124663
2900	-119574	-117960	21700	-67923			-112230	-122901
3000	-115546	-113230	19084	-68696	-16801	-52411	-111510	-121057

of $CeO_2(g)$ were calculated using conventional techniques[279a] and the geometric data[304]

$$r(Ce\text{-}O) = 2.03\ A°$$

$$\theta(O\text{-}Ce\text{-}O) = 110°$$

The vibrational contributions to the thermodynamic functions were calculated using the vibrational frequencies:[336]

$$\omega_1 = 720\ cm^{-1}$$

$$\omega_2 = 257\ cm^{-1}$$

$$\omega_3 = 688\ cm^{-1}$$

The electronic ground state was assumed to be doubly degenerate. The enthalpy of formation was estimated based on $D_o(CeO_2) = 350000$ cal/mole.[304] Free energies of formation were calculated using data for Ce(ref) from Reference 293 and data for O_2(ref) from Reference 279a. The free-energies of formation of $CeO_2(g)$ obtained in this way are 10-11 kcal/mole more negative than those recommended by Ackermann and Rauh.[305] Uncertainty in the atomization energy ($\pm$15 kcal/mole) is sufficiently large to encompass the Ackermann and Rauh recommendations. The free energies were increased by 11,000 cal/mole to be consistent with the Ackermann and Rauh data.

The free-energy functions for Ce(g) were calculated using the 86 energy levels listed by Martin.[334] These functions should be superior to those listed by Hultgren et al.[293] which are based on calculations done with only about 15 energy levels.[335]

Thermodynamic properties of $Ce_2O_2(g)$ are based on the vibrational and atomization data cited by Kordis and Gingerich.[336]

Wagman et al.[291] note the existence of a dimer, $Ce_2(g)$, and cite $\Delta H_f(298) = 83891$ cal/mole. No attempt was made to include this species.

g. Cesium and Iodine: Cesium and iodine are important radionuclides. They are quite volatile and little of the cesium or iodine inventory of a reactor core would be expected to remain with the core melt until melt interactions with concrete begin. Occasionally, a few kilograms of cesium and iodine are predicted to be in the core melt. The

chemical form of iodine is taken in the VANESA model to be CsI(ℓ). Cesium not involved as CsI is assumed present as Cs_2O(ℓ). Note that the complexities that arise with sodium and potassium silicates do not arise for cesium until some significant amount of concrete ablation has occurred. The vapor forms of cesium and iodine are considered to be Cs(g), CsOH(g), CsO(g), $(CsOH)_2$(g), Cs_2O(g), Cs_2(g), CsI(g), I(g), HI(g), and I_2(g). Garisto[294] has recommended that $(CsI)_2$(g) and CsO_2(g) should be added to this list.

For typical calculations, cesium and iodine species are quickly vaporized from the core melt. Williams[9] has noted that there could be a source of iodine in the core melt. This source is the radioactive decay of ^{132}Te to ^{132}I. This decay process would provide a continuing inventory of iodine for vaporization. Since no cesium would be present, CsI(g) would not contribute to the vaporization of this iodine. But, many other species are present that could form stable iodide vapor species. Examples are Na_2O, K_2O, and FeO, which may react to NaI, KI and FeI_2. If the decay mechanism suggested by Williams is added to the VANESA model, it may be of use to add, also, other condensed and vapor species bearing iodine.

Cs_2O(ℓ) is chosen in the model as the chemical form of cesium not incorporated as cesium iodide. Cs_2O(s) is a known compound, but this compound melts to form a Cs(O) liquid rather than molecular Cs_2O.[135] Thus, Cs_2O(ℓ), like most of the liquid phase species discussed here is hypothetical. The free-energy of Cs_2O(ℓ) is given by

$$G_T[Cs_2O;\ \ell] = -82996 + 88.478T - \frac{1.8T^2}{1000} - 19.3T\ \ell n(T) \quad .$$

This correlation gives results in good agreement with a correlation recently published by Lamoreaux and Hildenbrand.[136] Free-energies of formation were calculated using data for elements in their reference states from Reference 279a.

Thermodynamic data for the cesium and iodine species are collected in Table 16.

h. Chromium: Chromium enters the core melt as a constituent of structural steel from the reactor internals. Two condensed forms of chromium are considered in the model--Cr(ℓ) and Cr_2O_3(ℓ). The vapor species that contain chromium are Cr(g), CrO(g), CrO_2(g), CrO_3(g), and H_2CrO_4(g). Thermodynamic data for these species are shown in Table 17.

Table 16

Thermodynamic Data for Cesium and Iodine Species

T(K)	Free-Energies of Formation (cal/mole)						
	$Cs_2O(\ell)$	Cs(g)	CsOH(g)	CsO(g)	$Cs_2(OH)_2(g)$	$Cs_2O(g)$	$Cs_2(g)$
		(279a)	(279b)	(279a)	(279b)	(279a)	(279a)
500	-64851	8002	-61735	7365	-145896	-26436	12818
600	-62316	6167	-61466	6053	-141608	-26865	10795
700	-59820	4372	-61163	4779	-137223	-27212	8864
800	-57375	2611	-60831	3536	-132766	-27491	7009
900	-54967	882	-60471	2326	-128247	-27703	5224
1000	-50959	0	-59268	1962	-122041	-26219	5138
1100	-45189	0	-57187	2482	-114079	-22968	6822
1200	-39676	0	-55109	3001	-106129	-19714	8507
1300	-34155	0	-53035	3522	-98193	-16458	10195
1400	-28709	0	-50965	4042	-90272	-13201	11883
1500	-23332	0	-48896	4565	-82360	-9938	13575
1600	-18028	0	-46833	5088	-74466	-6673	15266
1700	-12786	0	-44771	5612	-66581	-3405	16958
1800	-7614	0	-42712	6137	-58712	-134	18649
1900	-2499	0	-40655	6665	-50852	+3142	20342
2000	+2549	0	-38601	7193	-43006	6420	22033
2100	7545	0	-36548	7723	-35169	9703	23723
2200	12477	0	-34497	8254	-27344	12989	25413
2300	17360	0	-32446	8788	-19525	16282	27104
2400	22183	0	-30395	9325	-11713	19580	28793
2500	26957	0	-28348	9863	-3915	22883	30482
2600	31678	0	-26295	10405	+3886	26195	32712
2700	36356	0	-24244	10951	11679	29514	33864
2800	40982	0	-22192	11500	19468	32841	35555
2900	45560	0	-20134	12054	27261	36179	37250
3000	50095	0	-18077	12613	35048	39526	38947

Table 16 (Continued)

Thermodynamic Data for Cesium and Iodine Species

T(K)	Free-Energies of Formation (cal/mole)							
	CsI(ℓ)	CsI(g)	I(g)	HI(g)	I_2(g)	$(CsI)_2$	CsO_2(g)	CsH(g)
	(294)	(294)	(279c)	(279a)	(279a)	(294)	(294)	(294)
500	-77453	-51694	12004	-2413	0	-123998	-29654	20624
600	-75691	-52772	10768	-2620	0	-123364	-29178	19432
700	-74006	-53803	9524	-2813	0	-122664	-28668	18280
800	-72387	-54794	8274	-2997	0	-121908	-28127	17161
900	-71703	-56629	7018	-3176	0	-122861	-28439	15190
1000	-68488	-55852	5757	-3351	0	-118605	-26144	15824
1100	-65343	-55070	4491	-3525	0	-114358	-23851	16454
1200	-62260	-54286	3221	-3696	0	-110118	-21559	17081
1300	-59235	-53499	1948	-3867	0	-105884	-19268	17705
1400	-56262	-52709	+672	-4038	0	-101655	-16978	18325
1500	-53338	-51916	-608	-4210	0	-97431	-14687	18943
1600	-50460	-51122	-1890	-4381	0	-93210	-12397	19558
1700	-47624	-50325	-3175	-4552	0	-88992	-10106	20171
1800	-44827	-49526	-4463	-4725	0	-84777	-7814	20781
1900	-42067	-48725	-5753	-4897	0	-80563	-5521	21389
2000	-39343	-47921	-7047	-5070	0	-76351	-3226	21996
2100	-36650	-47116	-8342	-5242	0	-72138	-930	22601
2200	-33989	-46308	-9640	-5416	0	-67925	1369	23205
2300	-31356	-45496	-10940	-5589	0	-63711	3669	23809
2400	-28751	-44685	-12242	-5761	0	-59494	5973	24412
2500	-26171	-43869	-13548	-5936	0	-55274	8280	25015
2600	-23616	-43050	-14855	-6109	0	-51051	10591	25618
2700	-21083	-42227	-16164	-6283	0	-46822	12905	26223
2800	-18571	-41401	-17475	-6456	0	-42587	15225	26828
2900	-16078	-40570	-18788	-6628	0	-38345	17549	27436
3000	-13604	-39735	-20105	-6803	0	-34095	19879	28046

Table 17

Thermodynamic Data for Chromium Species

T(K)	Free-Energies of Formation (cal/mole)						
	Cr(ℓ)	Cr_2O_3(ℓ)	Cr(g)	CrO(g)	CrO_2(g)	CrO_3(g)	$CrO_2(OH)_2$
	(279c)	(279c)	(279c)	(279c)	(279c)	(279c)	(295)
500	4732	-216209	77056	31590	-22718	-62105	-155000
600	4430	-210966	73523	28997	-23562	-60450	
700	4130	-205789	70018	26440	-24373	-58780	
800	3828	-200670	66540	23913	-25157	-57102	
900	3526	-195595	63087	21418	-25912	-55412	
1000	3225	-190553	59659	18952	-26641	-53710	-127900
1100	2924	-185538	56260	16517	-27343	-51997	
1200	2623	-180541	52886	14113	-28016	-50267	
1300	2321	-175556	49541	11740	-28661	-48521	
1400	2020	-170575	46226	9400	-29276	-46756	
1500	1718	-165591	42940	7094	-29858	-44969	-104100
1600	1420	-160600	39686	4823	-30407	-43158	
1700	1129	-155594	36463	2588	-30921	-41320	
1800	845	-150574	33272	390	-31401	-39457	
1900	573	-145546	30114	-1770	-31843	-37563	
2000	313	-140522	26988	-3891	-32249	-35642	-79500
2100	+70	-135488	23896	-5972	-32613	-33684	
2200	0	-130133	20994	-7857	-32783	-31539	
2300	0	-124661	18176	-9649	-32861	-29308	
2400	0	-119208	15372	-11419	-32916	-27059	
2500	0	-113780	12579	-13171	-32955	-24800	-54700
2600	0	-108366	9798	-14901	-32971	-22522	
2700	0	-102973	7027	-16613	-32969	-20232	
2800	0	-97595	4265	-18307	-32948	-17926	
2900	0	-92233	1511	-19982	-32908	-15606	
3000	+1238	-84413	0	-20404	-31614	-12037	

Table 17 (Continued)

Thermodynamic Data for Chromium Species

T(K)	Free-Energies of Formation (cal/mole)	
	CrOH(g)	$Cr(OH)_2$
	(287)	(287)
500	17143	-60710
600		
700		
800		
900		
1000	11307	-48579
1100		
1200		
1300		
1400		
1500	6556	-35584
1600		
1700		
1800		
1900		
2000	2778	-21906
2100		
2200		
2300		
2400		
2500	540	-6944
2600		
2700		
2800		
2900		
3000	583	+10087

i. Hydrogen: The hydrogen-bearing species recognized by the model are H(g), H_2(g), OH(g), H_2O(g), and the vapor phase hydroxides and hydrides of the various condensed species. Thermodynamic data for species other than the hydrides and hydroxides have been discussed above.

j. Iron: Iron enters the melt as structural steel from the reactor, reinforcing bar from the concrete, or as a constituent of concrete. Two condensed forms are considered--Fe(ℓ) and FeO(ℓ). Ferrous oxide is assumed to be completely stoichiometric. When pure, ferrous oxide (FeO) is not stoichiometric. But, when part of a mixture, it is usefully treated as stoichiometric.

Vaporization is assumed in the model to come only from FeO. The vapors bearing iron are taken to be Fe(g), FeO(g), FeOH(g), and $Fe(OH)_2$(g). Thermodynamic data for the iron species are shown in Table 18. Murad[318] has published spectroscopic data which might be used to derive superior thermochemical properties for FeOH(g).

k. Potassium: Potassium becomes part of the core melt as a result of concrete ablation. The potassium content of concretes is small typically, and it is tempting to neglect it. But, potassium is quite volatile and contributes to the vapors evolved during core melt/concrete interactions to an extent far beyond its contribution to the condensed phase. Formally, the condensed potassium species is declared in the VANESA model to be K_2O(ℓ). But, it is recognized that potassium will be highly associated with other constituents of the concrete. Consequently, the activity of K_2O(ℓ) is taken to be 10^{-8} (see Reference 356). That is, what is actually present in the melt is not K_2O but some other material. K_2O is selected as the chemical form simply as a convenience. Thermodynamic data for K_2O(ℓ) were calculated from correlations found in references 296 and 297. Vapor phase species containing potassium are K(g), KOH(g), KO(g), $(KOH)_2$(g), KH(g), and K_2(g). Thermodynamic data for the potassium species are presented in Table 19.

l. Lanthanum: Lanthanum is an important radionuclide. A typical inventory of lanthanum in a core melt is about 98 kg. The VANESA model assumes this lanthanum is present as La_2O_3(ℓ). Thermodynamic data for La_2O_3 solid have been tabulated by several authors[262,263,264,290] and these tabulations are in good agreement. Here, the tabulations by Pankratz[264] have been adopted. The data for the solid were extrapolated to temperatures above 2000 K as was described in connection with extrapolating data for CeO_2(s) (see section f, above). For this extrapolation, heat capacity data for temperatures less than 2100 K were fit to:

Table 18

Thermodynamic Data for Iron Species

T(K)	Free-Energies of Formation (cal/mole)					
	Fe(ℓ)	FeO*(ℓ)	Fe(g)	FeO(g)	FeOH(g)	$Fe(OH)_2$(g)
	(279e)	(279a)	(279e)	(279a)		(279a)
500	2074	-53252	81021	46739	22502	-69312
600	1896	-52065	77396	44202		-67306
700	1719	-50899	73804	41715		-65285
800	1542	-49745	70248	39280		-63251
900	1369	-48588	66736	36904		-61190
1000	1207	-47418	63279	34593	16845	-59100
1100	1076	-46210	59898	32369		-56957
1200	960	-44993	56578	30209		-54780
1300	842	-43788	53303	28099		-52584
1400	704	-42612	50052	26020		-50388
1500	547	-41462	46823	23965	12990	-48191
1600	376	-40333	43617	21939		-45995
1700	196	-39218	40438	19944		-43787
1800	17	-38104	37293	17991		-41564
1900	0	-36819	34341	16250		-39145
2000	0	-35524	31435	14558	10450	-36701
2100	0	-34231	28556	12898		-34239
2200	0	-32945	25703	11264		-31769
2300	0	-31667	22874	9658		-29288
2400	0	-30392	20068	8079		-26793
2500	0	-29118	17284	6528	9335	-24289
2600	0	-27849	14519	4999		-21770
2700	0	-26586	11775	3492		-19239
2800	0	-25321	9048	2011		-16699
2900	0	-24060	6339	553		-14141
3000	0	-22802	3647	884	8882	-11576

*Assumed stoichiometric.

Table 19

Thermodynamic Data for Potassium Species

T(K)	Free-Energies of Formation (cal/mole)						
	$K_2O(\ell)$	K(g)	KOH(g)	KO(g)	$K_2(OH)_2(g)$	KH(g)	$K_2(g)$
	(296,297)	(279a)	(279b)	(279a)	(279b)	(279a)	(279a)
500	-66316	10305	-55634	8953	-139088	21738	16876
600	-63582	8340	-55409	7569	-134994	20470	14688
700	-60902	6412	-55151	6219	-130808	19241	12586
800	-58273	4514	-54868	4898	-126557	18041	10554
900	-55694	2644	-54559	3605	-122250	16868	8585
1000	-53160	798	-54230	2335	-117903	15715	6670
1100	-48618	0	-52858	2112	-111471	15607	6854
1200	-42564	0	-50689	2689	-103450	16295	8642
1300	-36587	0	-48526	3265	-95446	16979	10430
1400	-30685	0	-46364	3843	-87451	17663	12224
1500	-24855	0	-44205	4421	-79470	18343	14019
1600	-19095	0	-42050	4999	-71504	19021	15817
1700	-13403	0	-39898	5577	-63552	19697	17612
1800	-7775	0	-37749	6156	-55612	20372	19412
1900	-2209	0	-35602	6736	-47685	21045	21211
2000	+3292	0	-33457	7317	-39768	21718	23013
2100	8737	0	-31314	7899	-31863	22389	24814
2200	14123	0	-29173	8481	-23970	23060	26616
2300	19451	0	-27035	9063	-16089	23729	28416
2400	24726	0	-24896	9647	-8213	24399	30218
2500	29945	0	-22762	10231	-354	25066	32020
2600	35110	0	-20623	10820	+7510	25738	33828
2700	40219	0	-18489	11405	15354	26406	35628
2800	45283	0	-16355	11994	23195	27075	37432
2900	50293	0	-14216	12587	31038	27748	39242
3000	55255	0	-12083	13179	38865	28417	41047

$$Cp[La_2O_3(s)] = 28.617 + 3.4\ T/1000 - 322800/T^2 \quad .$$

Polymorphism of solid La_2O_3 [320] was neglected in the extrapolation. The tendency for La_2O_3 to become nonstoichiometric under high temperature, reducing conditions was also neglected.

There appear to be no tabulations of thermodynamic data for La_2O_3 in the liquid state. Thermochemical properties of liquid La_2O_3 were estimated from

$$G_T[La_2O_3(\ell)] = G_T[La_2O_3(s)] + \Delta H_m(1-T/T_m)$$

where T_m and ΔH_m are the temperature and enthalpy of fusion of La_2O_3, respectively.

Samsonov[181] recommends $T_m = 2490 \pm 30$ K and $\Delta H_m = 36000$ cal/mole. Coutoures et al.[306] measure $T_m = 2593$ K in air. Vier[303] recommends $T_m = 2590$ K. Sibieude and Foex[307] consider $T_m = 2583$ K to be sufficiently accurate for pyrometer calibration. Here, the melting point of La_2O_3 is taken to be 2590 K and the enthalpy of fusion was estimated using procecedures recommended by Vier[303] to be 30501 cal/mole. Free-energies of formation of the liquid are listed in Table 20.

Vapor phase lanthanum species are considered to be La(g), LaO(g), LaOH(g), $La(OH)_2$(g), La_2O(g), and La_2O_2(g), and LaTe(g). Data for all but the telluride are listed in Table 20. Data for the telluride are listed in Table 30. The free-energies of formation found for LaO(g) from data in reference 289 are about 5 kcal/mole more negative than values recommended by Ackermann and Rauh.[308] Uncertainties in the data are, however, at least as large as 5 kcal/mole. Thermodynamic data for La(g) were calculated using conventional statistical mechanics technique[279a] and the 120 energy levels below the dissociation limit listed in reference 329. Thermodynamic functions for La_2O(g) and La_2O_2(g) were calculated using vibrational data from reference 336.

In addition to the vapor species listed in Table 20, Wagman et al.[291] note the species La_2(g)($\Delta H_f(298) = 146{,}988$ cal/mole), La_2O($\Delta H_f(298.15) = -3203$ cal/mole), and $(LaO)_2$(g) ($\Delta H_f(298) = -146{,}606$ cal/mole). These species were not considered in earlier versions of the VANESA code, but have been added recently.

m. Manganese: Manganese can enter the core melt from a variety of sources. The most important sources are the

Table 20

Thermodynamic Data for Lanthanum Species*

T(K)	Free-Energies of Formation (cal/mole)							
	La_2O_3(s)	La_2O_3(ℓ)	La(g)	LaO(g)	LaOH(g) (287)	$La(OH)_2$(g) (287)	La_2O(g)	La_2O_2(g)
500	-393759	-369146	87550	-38451	-19193	-141968	-13475	-138768
600	-386955	-363520	84502	-40225			-15744	-139021
700	380216	-357958	81473	-41955			-17931	-139207
800	-373549	-352470	78456	-43656			-20057	-139351
900	-366931	-347029	75454	-45322			-22116	-139444
1000	-360372	-341648	72460	-46965	-22111	-131364	-24128	-139504
1100	-353828	-336281	69492	-48565			-26057	-139495
1200	-347217	-330848	66588	-50089			-27828	-139341
1300	-340332	-325141	63848	-51432			-29239	-138839
1400	-333501	-319487	61107	-52765			-30623	-138320
1500	-326653	-313817	58399	-54052	-23733	-119392	-31914	-137718
1600	-319890	-308231	55670	-55349			-33216	-137136
1700	-313099	-302618	52978	-56599			-34418	-136464
1800	-306353	-297050	50285	-57839			-35596	-135776
1900	-299660	-291534	47585	-59077			-36763	-135084
2000	-292958	-286010	44908	-60284	-24567	-106744	-37856	-134325
2100	-286333	-280563	42214	-61499			-38962	-133586
2200	-279661	-275068	39559	-62668			-39963	-132747
2300	-273131	-269716	36853	-63879			-41044	-131995
2400	-266517	-264279	34205	-65023			-41984	-131108
2500	-259960	-258900	31545	-66176	-25034	-93858	-42926	-130227
2600	-253414	-253540	28893	-67310			-43829	-129314
2700	-246956	-248252	26221	-68458			-44752	-128423
2800	-240466	-242939	23579	-69572			-45593	-127457
2900	-234059	-237709	20910	-70703			-46466	-126527
3000	-227627	-232456	18270	-71800	-25166	-80745	-47263	-125524

*See also LaTe(g) tabulated with the tellurium species

steels used for the reactor vessel and its internal structures. Manganese is a low concentration constituent of these alloys and it is tempting to neglect it. But, manganese is quite volatile and contributes to vapors evolved from core debris to an extent far in excess of its contribution to the condensed phase melt. Manganese is assumed in the VANESA model to partition completely into the metal phase. It is likely to be incorrect when zirconium metal in the core melt has been oxidized to ZrO_2.

Thermodynamic data for Mn(ℓ) were taken from Reference 293. Thermodynamic data for MnO(ℓ) were found by extrapolating data from Reference 319 for temperatures between 3000 and 2058 K to lower temperatures assuming the liquid had a constant heat capacity of 14.5 cal/mole-K.

The vapor phase forms of manganese considered in the model are Mn(g), MnO(g) (a recent addition), MnOH(g), MnH(g), and $Mn(OH)_2$ (g). Data for MnH(g) were calculated from spectroscopic data found in References 313 and 314. Data for Mn(g) were calculated using the 268 energy levels listed in Reference 337. Thermodynamic data for the manganese species are shown in Table 21.

n. Molybdenum: Molybdenum is an important radionuclide and is a low-concentration constituent of structural steel used in a reactor. As noted above in the discussion of phase partitioning of melt constituents, molybdenum is assumed to partition into the metal phase as Mo(ℓ). This partitioning is probably reversed once chromium and zirconium are oxidized from the melt. Then molybdenum would begin to concentrate in the oxide phase, probably as MoO_2(ℓ), at a mass-transport controlled rate.

The vapor phase chemistry of molybdenum is rich and readily accessible for experiments. Data for the vapor species Mo(g), MoO(g), MoO_2(g), MoO_3(g), and $MoO_2(OH)_2$(g) were obtained from the JANAF Tables.[279] Thermochemical properties for $(MoO_3)_2$ and $(MoO_3)_3$ were obtained for the temperature range of 1500-1800 K using partial pressure measurements by Ikeda et al.[309] and the expression:

$$G_T[(MoO_3)_n] = nG_T[MoO_3;G] - RT\ \ell n\left[\frac{P_{(MoO_3)_n}}{P^n_{MoO_3}}\right] .$$

The partial pressure measurements by Ikeda et al. seem in good agreement with those by Burns et al.[310] Values of

Table 21

Thermodynamic Data for Manganese Species

T(K)	Free-Energies of Formation (cal/mole)						
	Mn(ℓ)	MnO(ℓ)	Mn(g)	MnO(g)	MnOH(g)	$Mn(OH)_2$(g)	MnH(g)
	(290)	(319)	(293)	(290,289)	(287)	(287)	
500		-73861	50870	13071	-2972	-94668	49836
600		-72590		10769			47234
700		-71370		8517			44827
800		-70188	41180	6314			42202
900		-69033		4157			39757
1000		-67893	34950	2055	-7650	-83208	37364
1100		-66719	31950	41			35066
1200		-65557	28964	-1931			32794
1300		-64405	26035	-3867			30564
1400		-62246	23152	-5749			28388
1500		-62032	20360	-7539	-10598	-70233	26295
1600	0	-60617	17780	-9124			24419
1700	0	-59157	15272	-10638			22601
1800	0	-57691	12782	-12114			20821
1900	0	-56220	10320	-13553			19049
2000	0	-54745	7900	-14957	-11077	-55078	17337
2100	0	-53263		-16331			15663
2200	0	-51776	3152	-17670			13998
2300	0	-50284		-18980			12358
2400	1499	-47066	0	-18767			12239
2500	3784	-43324	0	-17735	-6703	-35327	12939
2600	6046	-39599	0	-16702			13640
2700	8285	-35892	0	-15665			14340
2800	10502	-32201	0	-14629			15042
2900	12696	-28525	0	-13588			15740
3000	14870	-24865	0	-12549	+5257	-8199	16443

$G_T[(MoO_3)_n]$ were fit to equations that are linear in temperature:

$$G_T[(MoO_3)_2] = -162.690\ T - 216259\ \frac{cal}{mole}$$

$$G_T[(MoO_3)_3] = -219.021\ T - 379727\ \frac{cal}{mole}$$

and these linear equations were used to extrapolate the data to higher and lower temperatures.

Ikeda et al.[309] report two sets of measurements of the partial pressures of $(MoO_3)_3$, $(MoO_3)_4$, and $(MoO_3)_5$ at 800-900 K. These data were used to find thermodynamic properties of $(MoO_3)_4$ and $(MoO_3)_5$ using the expressions:

$$G_T[(MoO_3)_4] = \frac{4}{3}\ G[(MoO_3)_3] - RT\ \ell n\left[\frac{P_{(MoO_3)_4}}{P^{4/3}_{(MoO_3)_3}}\right]$$

and

$$G_T[(MoO_3)_5] = \frac{5}{3}\ G[(MoO_3)_3] - RT\ \ell n\left[\frac{P_{(MoO_3)_5}}{P^{5/3}_{(MoO_3)_3}}\right] .$$

The data by Ikeda et al. seem superior to similar data published in Reference 311. The results of the calculations with the two data sets by Ikeda et al. were averaged and fit to:

$$G_T[(MoO_3)_4] = -325506 + 51.75\ T\ \frac{cal}{mole}$$

$$G_T[(MoO_3)_5] = -416951 + 74.55\ T\ \frac{cal}{mole}$$

These linear expressions were used to extrapolate the data to higher and lower temperatures. Free-energies of formation were found using data for the elements in their reference states from the JANAF Tables.[279]

Thermodynamic data for the molybdenum species are shown in Table 22.

o. Nickel: Nickel enters the core melt as a constituent of structural steels. It is recognized in the condensed phase as Ni(ℓ) and NiO(ℓ). Vaporization is presumed to occur only from the metal phase. The amount of nickel that is oxidized to NiO(ℓ) is small in typical calculations. Data for NiO(ℓ) are estimated from data to 1800 K for NiO(s).[263]

Vapor phase forms of nickel are Ni(g), NiO(g), NiOH(g), NiH(g), and Ni(OH)(g). Thermochemical properties of NiH(g) were calculated from spectroscopic data from Reference 314. Nickel chloride vapors and nickel carbonyl are known and perhaps should be added to the speciation used in VANESA.

Thermodynamic data for the nickel species are shown in Table 23.

p. Niobium: Niobium is produced during the fissioning of uranium. Another important source of niobium is the neutron activation of zircaloy cladding on the fuel. Niobium can also enter the melt from 316L stainless steel where it is used as a carbon getter to improve the machinability of the steel. The inventory of niobium in a core melt is often small (typically <10 kg). Consequently, for many of the calculations done for the NRC source term reassessment the niobium inventory was not specified. Niobium was included in the VANESA model because it has been used as a fission-product simulant in some melt/concrete interactions tests.

Niobium is assumed to be present in the melt as NbO(ℓ). There are other stable, condensed forms of niobium--NbO_2(ℓ), Nb_2O_5(ℓ), and Nb(ℓ). The hydrogen-to-steam partial pressure ratios at the phase boundaries between these forms of niobium are given below.

	P_{H_2}/P_{H_2O} at		
Phases	1500 K	2000 K	2500K
Nb_2O_5(ℓ)/NbO_2(ℓ)	270	15	3
NbO_2(ℓ)/NbO(ℓ)	670	87	28
NbO(ℓ)/Nb(ℓ)	5510	660	200

Table 22

Thermodynamic Data for Molybdenum Species

T(K)	Free-Energies of Formation (cal/mole)											
	Mo(ℓ)	Mo(g)	MoO(g)	MoO_2(g)	MoO_3(g)	H_2MoO_4(g)	MoOH(g)	$Mo(OH)_2$(g)	$(MoO_3)_2$	$(MoO_3)_3$	$(MoO_3)_4$	$(MoO_3)_5$
	(279e)	(279e)	(279a)	(279a)	(279a)	(279a)	(287)	(287)				
500	8197	139239	79839	-8279	-79416	-177825	64040	-35199	-215378	-365899	-135179	-174111
600	7850	135640	77400	-9218	-78014	-172726			-213513	-360600	-93736	-121321
700	7502	132063	74993	-10130	-76610	-167660			-211046	-354398	-51089	-67026
800	7155	128508	72614	-11020	-75205	-162633			-208060	-347418	-7404	-11434
900	6808	124972	70262	-11887	-73796	-157636			-204606	-339735	+37217	+45329
1000	6459	121455	67931	-12737	-72386	-152675	57708	-24926	-200746	-331444	82650	103107
1100	6112	117956	65624	-13569	-70975	-147746			-196463	-322518	128929	161942
1200	5765	114475	63336	-14385	-69560	-142845			-191850	-313067	175868	221602
1300	5417	111011	61068	-15183	-68142	-137972			-186906	-303179	223469	282089
1400	5069	107564	58819	-15966	-66718	-133123			-181655	-292801	271684	343344
1500	4722	104135	56593	-16730	-65287	-128292	52204	-14033	-176110	-281983	320487	405334
1600	4375	100723	54384	-17477	-63849	-123483			-170290	-270752	369840	468012
1700	4027	97328	52195	-18207	-62402	-118687			-164214	-259136	419705	531329
1800	3680	93951	50027	-18919	-60946	-113907			-157889	-247147	470068	595269
1900	3331	90590	47880	-19612	-59479	-109136			-151322	-234795	520915	659814
2000	2984	87248	45749	-20289	-58003	-104378	47282	-2842	-144523	-222095	572226	724939
2100	2637	83925	43644	-20943	-56512	-99623			-137508	-209071	623969	790604
2200	2289	80620	41559	-21578	-55007	-94874			-130271	-195714	676156	856824
2300	1944	77334	39494	-22194	-53489	-90129			-122835	-182059	728741	923542
2400	1601	74066	37455	-22783	-51949	-85377			-115192	-168093	781740	990777
2500	1263	70818	35435	-23359	-50402	-80640	42917	+8652	-107343	-153819	835151	1058527
2600	931	67590	33443	-23904	-48827	-75884			-99309	-139266	888932	1126739
2700	607	64382	31473	-24429	-47237	-71130			-91075	-124414	943113	1195452
2800	291	61195	29531	-24925	-45622	-66365			-82653	-109279	997670	1264634
2900	0	58042	27641	-25373	-43961	-61564			-74004	-93804	1052681	1334384
3000	0	55191	25982	-25587	-42072	-56552	39437	+20820	-64756	-77431	1108890	1405632

Table 23

Thermodynamic Data for Nickel Species

T(K)	Free-Energies of Formation (cal/mole)						
	Ni(ℓ)	NiO(ℓ)	Ni(g)	NiO(g)	NiOH(g)	$Ni(OH)_2$(g)	NiH(g)
	(279e)		(279e)				
500	2801	-36718	84662	53561	28953	-52276	69844
600	2549	-35142	81097	51362			67365
700	2318	-33587	77567	49220			65087
800	2094	-32045	74060	47121			62594
900	1872	-30518	70572	45058			60273
1000	1651	-29004	67101	43026	24830	-41970	57983
1100	1430	-27505	63647	41026			55726
1200	1210	-26013	60212	39055			53471
1300	991	-24535	56796	37113			51298
1400	766	-23065	53396	35199			49123
1500	536	-21604	50017	33312	21475	-30849	46976
1600	303	-20147	46658	31455			44855
1700	66	-18700	43317	29625			42759
1800	0	-17092	40170	27991			40859
1900	0	-15206	37108	26452			39050
2000	0	-13293	34066	24935	19368	-18600	37262
2100	0	-11308	31043	23446			35500
2200	0	-9260	28038	21975			33755
2300	0	-7148	25050	20532			32029
2400	0	-4975	22079	19107			30330
2500	0	-2743	19124	17702	18434	-5310	28646
2600	0	-459	16184	16315			26978
2700	0	+1882	13259	14951			25327
2800	0	4275	10349	13603			23694
2900	0	6717	7453	12272			22075
3000	0	9207	4570	10959	17983	+8350	20472

Clearly, at very high hydrogen to steam partial pressure ratios, such as those arising when Zr and C are present in the melt, $Nb_2O_5(\ell)$ will be reduced certainly to $NbO_2(\ell)$ and perhaps to $Nb(\ell)$. Once Zr and C have been oxidized, the oxygen potentials of the melt are sufficiently high that Nb_2O_5 could be the stable chemical form.

Thermodynamic data for the niobium species are listed in Table 24.

q. Ruthenium: Ruthenium is an important radionuclide. A typical inventory of ruthenium in a core melt is about 170 kg. Ruthenium is presumed to be present in the melt as $Ru(\ell)$ and to partition exclusively into the metal phase. Its activity coefficient in the metal phase is assumed to be one. Kaufman and Bernstein[330] have attempted to model phase relationships in the Fe-Ru system and have found good agreement between model predictions and data when the ruthenium activity coefficient is taken to be:

$$RT\ \ell n(\gamma[Ru]) = -1800[1-X(Ru)]^2 \quad .$$

The vapor species containing ruthenium recognized by the VANESA model are $Ru(g)$, $RuO(g)$, $RuO_2(g)$, $RuO_3(g)$, and $RuO_4(g)$. Thermodynamic data for the ruthenium species are listed in Table 25.

Thermodynamic data for $Ru(\ell)$ were found by extrapolating to lower temperatures data listed in Reference 293. For this extrapolation, liquid ruthenium was assumed to have a constant heat capacity of 10 calories per mole-degree.

Thermodynamic properties for Ru(g) were found by statistical mechanic calculations using the 328 energy levels below the dissociation limit listed in Reference 330.

Thermodynamic functions for RuO(g) were calculated from spectroscopic data.[314] Molecular distortion in the excited electronic states was neglected. Reasonable agreement with the thermodynamic functions published by Pedley and Marshall[289] is achieved by assuming both the ground state and the first excited electronic state are five-fold degenerate.

Norman et al.[325] report that the entropy change associated with the reaction

$$Ru(s) + O_2 \rightarrow RuO_2(g)$$

Table 24

Thermodynamic Data for Niobium Species

T(K)	Free-Energies of Formation (cal/mole)						
	$Nb_2O_5(\ell)$	$Nb(\ell)$	$Nb(g)$	$NbO(g)$	$NbO_2(g)$	$Nb(OH)(g)$	$Nb(OH)_2(g)$
	(279c)	(279c)	(279c)	(279c)	(279c)		
500	-388339	5806	157249	35677	-51331	61903	-75488
600	-378738	5545	153611	33407	-51945		
700	-369256	5285	149967	31170	-52533		
800	-359881	5025	146321	28961	-53101		
900	-350597	4765	142676	26776	-53649		
1000	-341395	4505	139035	24615	-54177	58328	-65610
1100	-332275	4245	135398	22476	-54691		
1200	-323221	3984	131767	20357	-55187		
1300	-314293	3724	128144	18257	-55667		
1400	-305541	3464	124528	16177	-56132		
1500	-296946	3203	120920	14115	-56581	55561	-55130
1600	-288497	2944	117322	12072	-57014		
1700	-280181	2683	113731	10046	-57432		
1800	-271991	2423	110150	8037	-57835		
1900	-263914	2161	106578	6045	-58223		
2000	-255947	1900	103016	4072	-58595	53323	-44405
2100	-248073	1637	99465	2116	-59949		
2200	-240295	1376	95923	+178	-59288		
2300	-232600	1116	92392	-1742	-59610		
2400	-224978	860	88872	-3643	-59912		
2500	-217437	607	85363	-5526	-60199	51531	-33490
2600	-209952	360	81866	-7389	-60463		
2700	-202528	118	78381	-9232	-60710		
2800	-194926	0	75025	-10939	-60820		
2900	-187151	0	71792	-12514	-60798		
3000	-179441	0	68564	-14077	-60763	50752	-21771

Table 25

Thermodynamic Data for Ruthenium Species

T(K)	Free-Energies of Formation (cal/mole)							
	Ru(ℓ)	Ru(g)	RuO(g)	RuO_2(g)	RuO_3(g)	RuO_4(g)	RuOH(g) (287)	$Ru(OH)_2$(g) (287)
500	2453	136863	75787	30889	-12530	-26097	71144	5384
600	2624	133114	73220	30957	-11272	-22523		
700	2725	129361	70674	31028	-10021	-18975		
800	2780	125618	68159	31113	-8765	-15441		
900	2776	121863	65653	31192	-7523	-11938		
1000	2752	118128	63188	31296	-6262	-8431	64116	14438
1100	2678	114378	60724	31389	-5019	-4956		
1200	2594	110651	58302	31512	-3752	-1470		
1300	2464	106908	55878	31621	-2503	+1986		
1400	2334	103192	53496	31761	-1226	5459		
1500	2187	99465	51115	31894	+39	8910		
1600	2003	95764	48774	32059	1334	12382	57908	24106
1700	1805	92052	46433	32215	2616	15832		
1800	1614	88369	44130	32400	3924	19299		
1900	1397	84680	41834	32588	5233	22760		
2000	1190	81018	39575	32804	6568	26240	52315	34104
2100	961	77352	37321	33020	7900	29709		
2200	743	73713	35105	33269	9265	33206		
2300	507	70071	32896	33518	10627	36693		
2400	283	66456	30723	33800	12020	40207		
2500	52	62847	28568	34095	13427	43729	47329	44454
2600	0	59429	26611	34583	15025	47437		
2700	0	56060	24715	35129	16679	51196		
2800	0	52732	22868	35719	18376	54993		
2900	0	49387	21014	36298	20062	58775		
3000	0	46079	19207	36923	21793	62599	43597	55847

is ΔS_{rxn} = -1.5 e.u. at 1500 K. This implies the entropy of $RuO_2(g)$ at 1500 K is about 77.22 e.u. These authors also report the heat of reaction is 29700 $\pm$ 1000 calories per mole at 1500 K.

To calculate the thermodynamic functions for $RuO_2(g)$, the Ru-O bond length was taken to be 1.71 A° which is about the average of the Ru-O bond lengths in RuO(g) and $RuO_4(g)$. The molecule was assumed to be linear. A similar assumption has been made by Brewer and Rosenblatt[331] and can be criticized based on theoretical calculations by Walsh.[332]

To calculate vibrational contributions to the thermodynamic functions, a normal coordinate analysis of $RuO_2(g)$ was undertaken using a Urey-Bradley force field. The force field was parameterized using values found by Müller et al.[332] for $RuO_4(g)$. The entropy of $RuO_2(g)$ implied by the work of Norman et al. was well matched when the molecular vibrations were taken to be 900 cm^{-1} for both the symmetric and asymmetric stretches and 430 cm^{-1} for the doubly degenerate bending motion. Substantial alterations of the Urey-Bradley force field constants were necessary to match the measured entropy if $RuO_2(g)$ was assumed to be bent. Based on the results of the calculations and the heat of reaction reported by Norman et al., the heat of formation of $RuO_2(g)$ at 298.15 K was found to be 30800 $\pm$ 2000 cal/mole.

Thermodynamic functions for $RuO_3(g)$ are based on rigid rotor/harmonic oscillator calculations. The Ru-O bond length was taken to be 1.71 A°. Vibrational analysis was done assuming a Urey-Bradley force field and using the G, matrices developed by Wilson et al.[333] The G and F matrices are:

A_1 vibrations

$$G[1,1] = \mu_O + \mu_{Ru}(1+2\cos(\alpha))$$

$$G[1,2] = G[2,1] = -\left(\frac{2}{R}\right)\frac{(1+2\cos(\alpha))}{\sin(\alpha)}(1-\cos(\alpha))\mu_{Ru}$$

$$G[2,2] = \left(\frac{2}{R^2}\right)\frac{(1+2\cos(\alpha))}{(1+\cos(\alpha))}(\mu_O + 2\mu_{Ru}(1-\cos(\alpha))$$

$$F[1,1] = K + 4F\sin^2(\alpha/2)$$

$$F[1,2] = F[2,1] = 1.8R\ F\sin(\alpha/2)\cos(\alpha/2)$$

$$F[2,2] = R^2[H + F\{\cos^2(\alpha/2) + 0.1\sin^2(\alpha/2)\}]$$

E vibrations

$$G[1,1] = \mu_O + \mu_{Ru}(1-\cos(\alpha))$$

$$G[1,2] = G[2,1] = \left(\frac{1}{R}\right) \frac{(1-\cos(\alpha))^2}{\sin(\alpha)} \mu_{Ru}$$

$$G[2,2] = \frac{1}{[R^2(1+\cos(\alpha))]} [(2+\cos(\alpha))\mu_O + (1-\cos(\alpha))\mu_{Ru}]$$

$$F[1,1] = K + [\sin^2(\alpha/2) - 0.3\cos^2(\alpha/2)]F$$

$$F[1,2] = F[2,1] = -1.9R\ F \sin(\alpha/2)\cos(\alpha/2)$$

$$F[2,2] = R^2[H + F\{\cos^2(\alpha/2) + 0.1 \sin^2(\alpha/2)\}]$$

where $\mu_O = 0.0625012$,

$\mu_{Ru} = 0.00989413$,

R = Ru-O bond length,

and H, F, K are parameters of the Urey-Bradley force field. From Reference 322 the parameters are:

K = 6.23 mdyne/A°

F = 0.27 mdyne/A°

H = 0.24 mdyne/A°.

In this way, an entropy at 298.15 K of 68.1 ± 0.4 e.u. was calculated for variations of α between 89 and 95°, of K from 6.23 to 6.13 dynes/A°, and of R from 1.71 to 1.706 A°. These values of the entropy at 298.15 K agree well with those reported in References 326 and 327. They are about 2 e.u. higher than that in Reference 290 and somewhat higher than the estimate obtained by Bell and Tagami[328] of 63.7 ± 4.0 e.u. The discrepancy between the calculation here and the actual experimental results obtained by Bell and Tagami is, however, less than 1 e.u. at 1400 K.

Thermodynamic functions for $RuO_4(g)$ were calculated using the vibrational data published by McDowell et al.[321]:

frequency (cm^{-1})	degeneracy
885	1
326	2
935	3
342	3

and $I_aI_bI_c = 8756.787 \times 10^{-117}\ g^3cm^6$. The resulting functions agree well with those reported by Muller et al.[322] but are somewhat at odds with those found in Reference 290.

r. Silicon: Silicon enters the core melt primarily from ablated concrete. Many reactor cores do contain a borosilicate glass as a burnable poison, and silicon is a common impurity in steels. These sources of silicon pale in comparison to the source provided by ablating concrete. Some types of concrete are made using silica-rich aggregate. It has been common in the nuclear safety field to refer to such concrete made with siliceous aggregate as "basaltic" concrete. In fact, few concretes used for structural applications employ basalt aggregate, and basalt is one of the siliceous rocks least enriched in silica.

The silicon in many rocks is not present as SiO_2. Rather, it is present as silicates such as calcium or iron silicates or potassium aluminum silicates. Even when actual SiO_2 is present in the concrete, the melting of the concrete will lead to silicate formation. Only when granitic or granodiorite aggregates are used will SiO_2 be incorporated into the core melt.

The VANESA model assumes silicon to be present in the melt as $SiO_2(\ell)$. An activity coefficient of one is assigned to the SiO_2 though evidence from the UO_2-SiO_2 phase diagrams suggests the activity should be greater than one. If the silicon is present as silicates, the activity coefficient should be less than one. Vapor species considered in the model are Si(g), SiO(g), SiO_2(g), SiOH(g), and $Si(OH)_2$(g). A tri-hydroxide and a tetra-hydroxide are known and should, perhaps, be added to the list. Of more interest is the possibility that silicon halide species, and in particular SiF_4(g), could form and be important to the vaporization of silicon. The source of the halides is, of course, the complex aggregates used to make concrete.

Thermodynamic data for the silicon species are presented in Table 26.

s. Silver: The primary source of silver in a core melt is from the silver-indium-cadmium control rods used in pressurized water reactors (PWRs). Some debate has occurred over

Table 26

Thermodynamic Data for Silicon Species

T(K)	Free-Energies of Formation (cal/mole)								
	$SiO_2(\ell)$	Si(g)	SiO(g)	SiO_2(g)	SiOH(g)	$Si(OH)_2$(g)	SiH(g)	Si_2(g)	Si_3(g)
	(279a)	(279a)	(279a)	(279a)	(287)	(287)	(279e)	(279a)	(279a)
500	-194690	89882	-34694	-73534	5328	-101788	76502	118148	126846
600	-190490	86326	-36761	-73593			73875	113671	121919
700	-186311	82783	-38801	-73640			71281	109230	117044
800	-182159	79251	-40817	-73679			68710	104814	112212
900	-178028	75734	-42809	-73708			66165	100428	107432
1000	-173921	72229	-44782	-73730	678	-88534	63637	96061	102690
1100	-169837	68737	-46736	-73746			61128	91716	97990
1200	-165772	65257	-48672	-73755			58635	87392	93331
1300	-161728	61790	-50590	-73758			56157	83087	88711
1400	-157699	58335	-52491	-73753			53694	78806	84131
1500	-153687	54892	-54374	-73741	-3247	-74732	51246	74545	79591
1600	-149691	51459	-56244	-73722			48809	70306	75084
1700	-145611	48145	-57992	-73589			46493	66298	70931
1800	-140952	45445	-59118	-72844			44794	63523	68631
1900	-136321	42753	-60237	-72096			43104	60761	66351
2000	-131719	40067	-61341	-71340	-4474	-58509	41424	58017	64100
2100	-127139	37388	-62435	-70582			39752	55284	61869
2200	-122586	34715	-63522	-69819			38087	52563	59658
2300	-118052	32045	-64598	-69053			36431	49857	57468
2400	-113539	29384	-65661	-68279			34784	47165	55299
2500	-109047	26726	-66721	-67506	-4088	-40925	33140	44482	53143
2600	-104572	24073	-67768	-66725			31506	41813	51009
2700	-100118	21422	-68807	-65942			29877	39151	48886
2800	-95679	18779	-69839	-65150			28256	36507	46786
2900	-91254	16139	-70861	-64358			26642	33870	44694
3000	-86849	13499	-71878	-63562	-3469	-23317	25030	31238	42613

the extent to which silver from these control rods will be vaporized during the course of core degradation and consequently be unavailable for the melt/concrete interactions. For most of the calculations done in the NRC source term reassessment, it was assumed that there would be extensive formation of aerosols from silver during core degradation. More recent analyses suggest that there would be little silver loss in-vessel.

The VANESA model assumes silver to be present as Ag(ℓ) and that it dissolves exclusively in the metallic phase of the core melt. This dissolution of silver is questionable. The solubility of silver in iron is quite limited even when both metals are liquid. It is also assumed in the model that the activity coefficient of silver is one. The activity coefficient of silver in iron at 1873 K is in reality much larger than one as was discussed above.

Vapor species involving silver recognized in the model are Ag(g), AgO(g), AgH(g), AgOH(g), and $Ag(OH)_2(g)$. $Ag_2(g)$ and $Ag_3(g)$ are known species that may contribute to Ag vaporization.[180] Thermodynamic properties of AgH(g) were calculated from spectroscopic data from Reference 314. Vapor-phase silver halides can be formed and may be important to the vaporization of silver.

Thermodynamic data for the silver species are listed in Table 27.

t. Sodium: Sodium is treated in a fashion completely similar to the treatment of potassium. The thermodynamic data for sodium species are listed in Table 28.

u. Strontium: Strontium is an important radionuclide. A typical strontium inventory in a core melt will be about 60 kg. The chemistry of strontium is very similar to that of barium. The two elements are treated very much the same way in the VANESA model. Thermodynamic data for the strontium species are shown in Table 29.

v. Tellurium: Tellurium is a very important fission product. Typically there will be about 25 kg of tellurium in a core melt. Tellurium is, by itself, quite volatile and it might seem surprising that the tellurium inventory has not been vaporized completely prior to the onset of core debris interactions with concrete. Empirical evidence from radionuclide release experiments has been used to suggest that tellurium binds to unoxidized zirconium.[341] The evidence for this binding is not overwhelming and recent studies suggest tellurium may be vaporized as SnTe.[299] In any event, typical accident calculations suggest that much of the tellurium inventory of the core is still present when interactions with the concrete begin.[2]

Table 27

Thermodynamic Data for Silver Species

T(K)	Free-Energies of Formation (cal/mole)							
	Ag(ℓ)	Ag(g)	AgO(g)	Ag_2(g)	Ag_3(g)	AgOH(g)	$Ag(OH)_2$	AgH(g)
			(289,293)			(287)	(287)	
500	1480	52406	57273	77376	119165	5216	-3498	52204
600	1285	49369	54945	73488	114657			50046
700	1090	46355	52641	69666	110224			48059
800	735	43205	50360	65580	105379			45841
900	699	40397	48101	62190	101562			43784
1000	500	37454	45866	58539	97337	3658	+7705	41752
1100	290	34530	43653	54935	93172			39745
1200	74	31626	41462	51379	89069			37761
1300	0	28891	39440	48167	85470			35945
1400	0	26253	37518	45155	82164			34226
1500	0	23637	35617	42192	78922	3241	+20226	32531
1600	0	21040	33739	39273	75741			30856
1700	0	18463	31879	36396	72619			29199
1800	0	15904	30039	33560	69550			27563
1900	0	13361	28218	30763	66537			25940
2000	0	10834	26414	27999	63569	3748	+33597	24336
2100	0	8322	24625	25268	60648			22746
2200	0	5825	22852	22569	57773			21170
2300	0	3343	21094	19904	54947			19607
2400	0	873	19349	17263	52157			18063
2500	1584	0	19190	17823	54167	6046	+48647	
2600	4030	0	19916	20131	58800			
2700	6464	0	20644	22442	63438			
2800	8884	0	21369	24748	68070			
2900	11297	0	22099	27063	72719			
3000	13697	0	22827	29374	77362	19321	+74574	

Table 28

Thermodynamic Data for Sodium Species

T(K)	Free-Energies of Formation (cal/mole)						
	$Na_2O(\ell)$	Na(g)	NaOH(g)	NaO(g)	$Na_2(OH)_2(g)$	NaH(g)	$Na_2(g)$
	(279a)	(279a)	(279b)	(279a)	(279b)	(279a)	(279a)
500	-75476	13890	-48001	11373	-128607	21550	18409
600	-72837	11757	-47910	9884	-124654	20199	16041
700	-70316	9660	-47788	8429	-120609	18890	13757
800	-67893	7593	-47641	7004	-116497	17612	11545
900	-65560	5550	-47471	5603	-112335	16359	9390
1000	-63306	3529	-47284	4224	-108137	15125	7285
1100	-61126	1526	-47082	2864	-103913	13907	5222
1200	-58089	0	-46406	1981	-98744	13165	4119
1300	-52090	0	-44207	2626	-90535	13947	6073
1400	-46176	0	-42012	3270	-82341	14726	8030
1500	-40337	0	-39819	3916	-74157	15504	9990
1600	-34569	0	-37629	4563	-65989	16279	11955
1700	-28867	0	-35441	5212	-57830	17055	13922
1800	-23229	0	-33258	5860	-49689	17827	15889
1900	-17649	0	-31075	6510	-41557	18599	17860
2000	-12127	0	-28897	7158	-33442	19368	19829
2100	-6658	0	-26721	7809	-25337	20136	21799
2200	-1236	0	-24546	8461	-17242	20904	23774
2300	+4135	0	-22374	9112	-9160	21671	25746
2400	9466	0	-20200	9768	-1081	22439	27724
2500	14746	0	-18034	10419	+6974	23201	29695
2600	19993	0	-15863	11076	15034	23968	31673
2700	25194	0	-13697	11731	23076	24731	33646
2800	30357	0	-11533	12387	31110	25494	35621
2900	35491	0	-9364	13047	39147	26261	37602
3000	40584	0	-7201	13705	47165	27022	39577

Table 29

Thermodynamic Data for Strontium Species

T(K)	Free-Energies of Formation (cal/mole)					
	SrO(ℓ)	Sr(g)	SrO(g)	SrOH(g)	$Sr(OH)_2$(g)	SrH(g)
	(279c)	(279b)	(279c)	(279d)	(279d)	(291,292)
500	-114858	25883	-12061	-52137	-132392	40898
600	-113160	23315	-13723	-52629	-130321	38796
700	-111477	20792	-15337	-53077	-128225	36744
800	-109804	18315	-16904	-53482	-126103	34742
900	-108117	15901	-18404	-53825	-123933	32803
1000	-106424	13538	-19851	-54119	-121729	30914
1100	-104624	11326	-21145	-54265	-119389	29174
1200	-102755	9223	-22329	-54305	-116955	27543
1300	-100895	7148	-23482	-54320	-114508	25938
1400	-99045	5100	-24609	-54311	-112047	24359
1500	-97205	3076	-25711	-54279	-109573	22803
1600	-95375	1075	-26791	-54229	-107091	21268
1700	-92650	0	-26947	-53253	-103690	20660
1800	-88881	0	-26033	-51206	-99229	21125
1900	-85143	0	-25125	-49161	-94776	21588
2000	-81433	0	-24225	-47119	-90335	22052
2100	-77753	0	-23333	-45078	-85902	22516
2200	-74104	0	-22453	-43039	-81478	22979
2300	-70483	0	-21584	-41002	-77061	23442
2400	-66888	0	-20728	-38964	-72648	23907
2500	-63321	0	-19887	-36930	-68249	24369
2600	-59776	0	-19060	-34892	-63847	24838
2700	-56254	0	-18249	-32857	-59454	25305
2800	-52753	0	-17453	-30820	-55065	25775
2900	-49272	0	-16673	-28781	-50674	26246
3000	-45809	0	-15908	-26742	-46291	26722

The VANESA model assumes tellurium to be present as Te(ℓ) and that it partitions into the metal phase. The vapor species in the Te-O-H system recognized by the VANESA model are Te(g), Te_2(g), TeO(g), TeO_2(g), Te_2O_2(g), $TeO(OH)_2$(g), and H_2Te(g). Thermodynamic data for all of these vapor species except $TeO(OH)_2$(g) were obtained from conventional sources as indicated in Table 30. Data for $TeO(OH)_2$(g) were derived from equilibrium constants for the reaction

$$TeO_2(s) + H_2O(g) \rightarrow TeO(OH)_2(g)$$

reported by Malinauskus et al.[312] Experimentally determined equilibrium constants, K_p, were fit to the expression

$$\ell n\ K_p = A + B/T$$

to determine A = 7.58924 and B = -15307.4. Then the Gibbs free-energy for $TeO(OH)_2$(g) was found at 800, 900, and 1000 K from

$$G_T[TeO(OH)_2;g] = G_T(TeO_2;s) + G_T(H_2O) - RT\ \ell n\ K_p$$

where $G_T(TeO_2;g)$ and $G_T(H_2O)$ were taken from Reference 290. These results were then fit to

$$G_T[TeO(OH)_2;g] = -89209 - 106.045\ T\ cal/mole$$

and this expression was used to extrapolate the Gibbs energy to higher and lower temperatures. Free-energy of formation data were derived using reference state data for Te from Reference 293 and data for O_2 and H_2 from Reference 279a. Results of these calculations at 1000 K agree to within about 3 kcal/mole with results obtained with data for $TeO(OH)_2$ from Reference 2.

Mixed metal tellurides can also form in the gas phase over core debris. The species considered here are LaTe(g), AgTe(g), SbTe(g), and SnTe(g). Thermodynamic data for LaTe(g) were taken from Reference 288. These data were extrapolated to temperatures above 2000 K by assuming the free-energy function $(-[G_T(LaTe(g)) - H_{298}]/T)$ to be a linear function in the reciprocal of temperature. Thermodynamic

Table 30

Thermodynamic Data for Tellurium Species

T(K)	Free-Energies of Formation (cal/mole)						
	Te(ℓ)	Te(g)	TeO(g)	TeOH(g)	$Te(OH)_2$(g)	Te_2(g)	$TeO(OH)_2$
	(293)	(288)	(288)	(287)	(287)	(288)	(298)
500	1288	34766	7340	-14586	-64772	19462	-82590
600	709	31694	5365			15918	-80042
700	+131	28669	3444			12482	-77049
800	0	26139	2023			10045	-73231
900	0	23792	+790			7979	-68915
1000	0	21488	-393	-17083	-51642	6005	-64288
1100	0	19223	-1531			4112	-59380
1200	0	16993	-2630			2289	-54191
1300	0	14794	-3691			+531	-48773
1400	0	12624	-4718			-1169	-43123
1500	0	10480	-5713	-14881	-34053	-2816	-37263
1600	0	8360	-6678			-4413	-31201
1700	0	6263	-7615			-5964	-24954
1800	0	4185	-8526			-7472	-18529
1900	0	2128	-9411			-8938	-10403
2000	0	88	-10273	-10024	-14106	-10365	-1618
2100	1936	0	-9176			-7884	+7299
2200	3943	0	-7986			-5222	16348
2300	5936	0	-6790			-2554	25518
2400	7915	0	-5587			+122	34810
2500	9880	0	-4379	-8023	-6945	+2805	44220
2600	11834	0	-3165			5497	53736
2700	13775	0	-1945			8199	63361
2800	15706	0	-719			10912	73087
2900	17626	0	+514			13638	82912
3000	19536	0	1752	-307	+25051	16378	92840

Table 30 (Continued)

Thermodynamic Data for Tellurium Species

T(K)	Free-Energies of Formation (cal/mole)						
	$(TeO)_2$(g)	TeO_2(g)	H_2Te(g)	AgTe(g)	LaTe(g)	SnTe(g)	SbTe(g)
	(288)	(288)	(288)				
500	-28615	-79587	18223	50375	42200	14006	23646
600	-28995	-79923	17332	46175	38554	10721	19753
700	-29304	-80213	16521	42067	35014	7543	15961
800	-28642	-80008	16228	38481	32000	4906	12690
900	-27629	-79620	16136	35124	29218	2490	9654
1000	-26541	-79189	16102	31837	26520	+143	7193
1100	-25385	-78718	16116	28617	23892	-2169	4836
1200	-24166	-78213	16173	25482	21412	-4346	2545
1300	-22890	-77674	16268	22539	19136	-6532	+320
1400	-21562	-77106	16396	19736	16918	-8614	-1853
1500	-20185	-76511	16553	16992	14772	-10693	-3953
1600	-18762	-75890	16736	14300	12662	-12683	-6026
1700	-17296	-75245	16942	11656	10629	-14653	-8037
1800	-15792	-74577	17169	9062	8638	-16585	-10014
1900	-14250	-73889	17413	8040	8193	-16926	-10419
2000	-12674	-73180	17675	7560	8334	-16696	-10274
2100	-7194	-70517	19886	7099	8635	-16563	-10132
2200	-1540	-67764	22182	6658	8981	-16389	-9959
2300	4112	-65009	24474	6235	9333	-16192	-9768
2400	9763	-62251	26762	5833	9799	-15954	-8535
2500	15412	-59491	29045		10350	-15715	-6027
2600	21059	-56728	31324		10869	-15493	-3512
2700	26704	-53963	33596		11460	-15208	-996
2800	32346	-51195	35863		12128	-14942	+1530
2900	37984	-48424	38123		12814	-14069	4061
3000	43620	-45651	40376		13576	-11325	6596

data for AgTe(g), SbTe(g), and SnTe(g) were calculated using conventional statistical mechanical methods[279] and spectroscopic data from References 313 and 314. Results obtained for SnTe(g) were in close agreement with results cited by Mills.[288] Results obtained for AgTe(g) and SbTe(g) indicated greater stability for these species than suggested by the data tabulated by Mills.[288] Results obtained for SbTe(g) are in good agreement with those published recently by Sullivan et al.[315]

Sullivan et al.[315] also report a dimer $(SbTe)_2$ which is not considered here.

Thermodynamic data for the tellurium species are listed in Table 30.

w. Tin: Tin is produced as a product of fissioning, but the most important source of tin is the zircaloy clad on the reactor fuel. The VANESA model presumes tin to be present as Sn(ℓ) and that it partitions into the metal phase where it has an activity coefficient of one. Evidence discussed above can be marshalled to suggest the tin dissolved in steel will have a higher activity coefficient. On the other hand, tin in zircaloy has an activity coefficient much less than one.[299] The vapor species recognized for tin are Sn(g), SnO(g), SnOH(g), $Sn(OH)_2$(g), and SnTe(g). There are several hydrides of tin that could be added to this list.

Thermodynamic data for the tin species are shown in Table 31.

x. Uranium: Uranium is taken to be present in the core melt as urania. No explicit adjustment is made to account for the variation in the stoichiometry of urania and its effects on vaporization aside from the effects on the oxygen potential. Vapor species containing uranium considered in the model are U(g), UO(g), UO_2(g), UO_3(g), and $UO_2(OH)_2$(g). Thermodynamic data for the uranium species are listed in Table 32.

Thermodynamic data for $UO_2(OH)_2$(g) were estimated from Gibbs energy data reported in Reference 316 for the reaction:

$$UO_3(g) + H_2O(g) \rightarrow UO_2(OH_2)(g) \quad .$$

These data were used to determine $G_T[UO_2(OH)_2;g]$ at 1300, 1400, 1500, and 1600 K. Results were correlated by

Table 31

Thermodynamic Data for Tin Species*

T(K)	Free-Energies of Formation (cal/mole)						
	Sn(ℓ)	Sn(g)	SnO(g)	SnOH(g)	$Sn(OH)_2$(g)	SnH	SnH_4(g)
500	-	58077	-4712	-2777	-82631	48353	49316
600	0	55670	-6113			46547	52021
700	0	53286	-7457			44798	54416
800	0	50897	-8770			43078	57611
900	0	48499	-10057			41380	60440
1000	0	46089	-11320	-4110	-68368	39697	63263
1100	0	43669	-12564			38027	66894
1200	0	41237	-13789			36365	69944
1300	0	38758	-14994			34714	72968
1400	0	36351	-16185			33070	75944
1500	0	33898	-17359	-4631	-53700	31433	78876
1600	0	31440	-18519			29802	81727
1700	0	28979	-19666			28177	84515
1800	0	26516	-20798			26559	87225
1900	0	24051	-21919			24946	89848
2000	0	21585	-23026	-4680	-38911	23340	93069
2100	0	19118	-24122			21741	94825
2200	0	16652	-25206			20147	97166
2300	0	14187	-26280			18558	99402
2400	0	11724	-27342			16975	101528
2500	0	9259	-28394	-4346	-24026	15396	103538
2600	0	6795	-29436			13824	105439
2700	0	4334	-30467			12257	107216
2800	0	1877	-31488			10697	108880
2900	-	0	-31910			9730	111001
3000	-	0	-30467	-1360	-6714	10625	114849

*See also SnTe(g) tabulated with the tellurium species.

Table 31 (Continued)

Thermodynamic Data for Tin Species

T(K)	Free-Energies of Formation (cal/mole)			
	$Sn_2(g)$	$(SnO)_2(g)$	$(SnO)_3(g)$	$(SnO)_4(g)$
500	78264	-48133	-97006	-146551
600	75324	-50057	-97649	-146356
700	72501	-51587	-97700	-145372
800	69746	-52810	-97292	-143775
900	67051	-53764	-96478	-141639
1000	64408	-54476	-95304	-139020
1100	61811	-54971	-93803	-135967
1200	59255	-55270	-92007	-132521
1300	56741	-55382	-89932	-128702
1400	54262	-55327	-87606	-124548
1500	51815	-55113	-85042	-120077
1600	49400	-54751	-82254	-115308
1700	47013	-54249	-79259	-110262
1800	44654	-53616	-76065	-104951
1900	42321	-52857	-72683	-99391
2000	40013	-51979	-69122	-93590
2100	37728	-50986	-65390	-87561
2200	35466	-49882	-61491	-81311
2300	33223	-48678	-57440	-74858
2400	31002	-47371	-53237	-68202
2500	28799	-45970	-48891	-61355
2600	26614	-44474	-44404	-54320
2700	24449	-42889	-39783	-47106
2800	22301	-41216	-35030	-39717
2900	21348	-38280	-28382	-29801
3000	24125	-31548	-16041	-12294

Table 32

Thermodynamic Data for Uranium Species

	Free-Energies of Formation (cal/mole)							
	$UO_2(\ell)$	U(g)	UO(g)	$UO_2(g)$	$UO_3(g)$	UOH(g)	$U(OH)_2(g)$	$UO_2(OH)_2(g)$
	(301)	(301)	(300)	(300)	(300)	(287)	(287)	
500	-205545	+110256	-5700	-112800	-185400	14180	-75952	-258680
600	-202402	106969	-7700	-113100	-184200			-256864
700	-199285	103741	-9600	-113400	-182900			-254528
800	-196194	100581	-11500	-113700	-181600			-251745
900	-193128	97494	-13400	-113900	-180300			-248541
1000	-190089	94482	-15200	-114100	-179000	9132	-67982	-244909
1100	-187076	91549	-16800	-114200	-177500			-240850
1200	-184089	88694	-18400	-114200	-175900			-236440
1300	-181127	85919	-19900	-114200	-174300			-231749
1400	-178192	83225	-21400	-114200	-172700			-226804
1500	-175283	77433	-22800	-114000	-171000	6207	-57896	-221455
1600	-172400	74668	-24100	-113800	-169200			-215959
1700	-169542	71932	-25400	-113600	-167400			-210190
1800	-166711	69219	-26600	-113400	-165500			-204157
1900	-163906	66527	-27800	-113100	-163700			-197859
2000	-161126	63851	-29000	-112800	-161800	4808	-46423	-191311
2100	-158373	61189	-30200	-112500	-159900			-184762
2200	-155646	58539	-31300	-112200	-158000			-177988
2300	-152944	55900	-32400	-111900	-156100			-171006
2400	-150269	53269	-33500	-111500	-154100			-163812
2500	-147619	50644	-34600	-111200	-152200	4197	-34301	-156408
2600	-144996	48025	-35600	-110800	-150200			-149006
2700	-142399	45411	-36600	-110400	-148200			-141418
2800	-139827	42800	-37600	-109900	-146200			-133655
2900	-137282	40191	-38600	-109500	-144200			-125715
3000	-134762	37584	-39600	-109100	-142100	4182	-21700	-117599

$$G_T[UO_2(OH)_2;g] = -260621 - 140.536\ T \quad .$$

This correlation was used to extrapolate the Gibbs energy data to higher and lower temperatures.

y. Zirconium: Zirconium is an important radionuclide. Typically more than 200 kg of zirconium produced by fissioning will be present in a core melt. But, this is a trivial amount of zirconium in comparison to the amount that is contributed to the core melt by the cladding on the reactor fuel.

The VANESA model treats two condensed forms of zirconium--Zr(ℓ) and ZrO_2(ℓ). The metallic zirconium is assumed to be present in the metallic phase and to have an activity coefficient of one. Evidence presented above suggests that the activity coefficient of Zr dissolved in steel will be somewhat less than one. The analyses described above concerning gas reactions with the oxide phase raise questions about whether metallic zirconium will actually be present. It may have all reacted to reduce the urania so that uranium metal will be present in the metallic phase of the core melt.

ZrO_2 is presumed to be in the oxide phase and to have an activity coefficient of one. Evidence from the UO_2-ZrO_2 phase diagram suggests that the activity coefficient of ZrO_2 in UO_2 may be somewhat greater than one. Vapor phase species containing Zr considered in the model are Zr(g), ZrO(g), ZrO_2(g), ZrOH(g), and $Zr(OH)_2$(g). There are several zirconium hydrides that could be added to this list. Vaporization of zirconium is assumed for the purposes of the VANESA model to occur only in the oxide phase.

Thermodynamic data for the zirconium species are to be found in Table 33. Ackermann, Rauh, and Alexander[317] have recently published data for ZrO_2(g) that indicate this molecule may be more stable than is suggested by data in Table 33.

At several points in the discussion above it has been noted that the vapor species recognized by the VANESA model do not constitute an exhaustive set. Some of the most notable omissions are:

1. Halide vapor species formed by reaction HF and HCℓ vaporized from concrete,

2. Sulphides formed by reaction with sulfur from gypsum used in concrete to retard setting of the cement,

Table 33

Thermodynamic Data for Zirconium Species

T(K)	Free-Energies of Formation (cal/mole)						
	$ZrO_2(\ell)$	Zr(g)	ZrO(g)	$ZrO_2(g)$	Zr(OH)(g)	$Zr(OH)_2(g)$	ZrH(g)
	(279a)	(279a)	(279a)	(279a)	(287)	(287)	(279a)
500	-224373	131284	3873	-71830	24626	-89999	110186
600	-220410	127875	1968	-72418			107676
700	-216481	124472	+108	-72972			105213
800	-212581	121083	-1717	-73495			102789
900	-208706	117709	-3508	-73988			100399
1000	-204853	114353	-5276	-74454	19981	-80559	98038
1100	-201024	111016	-7026	-74898			95704
1200	-197166	107750	-8714	-75267			93443
1300	-193292	104521	-10359	-75580			91240
1400	-189436	101297	-11999	-75871			89059
1500	-185618	98077	-13634	-76140	16656	-70070	86898
1600	-181885	94862	-15268	-76388			84757
1700	-178159	91652	-16904	-76621			82634
1800	-174436	88444	-18538	-76832			80529
1900	-170719	85241	-20172	-77025			78441
2000	-167009	82042	-21809	-77204	-6017	-79236	76368
2100	-163304	78846	-23441	-77362			74313
2200	-159454	75831	-24906	-77338			72440
2300	-155554	72878	-26303	-77232			70647
2400	-151664	69928	-27696	-77107			68871
2500	-147794	66981	-29086	-76971	-12634	-47343	67108
2600	-143932	64037	-30469	-76813			65360
2700	-140085	61094	-31849	-76644			63626
2800	-136247	58153	-33225	-76457			61904
2900	-132418	55213	-34590	-76253			60199
3000	-128603	52275	-35952	-76040	-11959	-34991	58502

3. Hydrides, and

4. Mixed metal species.

It is not just a matter of speculation that these omitted species may be important for the vaporization from core melts interacting with concrete. Some species identified in aerosol samples collected during melt/concrete interaction experiments are shown in Table 34. The presence of halides such KCl and sulphides such as $KSbS_2$, is notable and suggestive of a richer vapor-phase chemistry than has been considered in the VANESA model.

Another class of vapor species that has not been considered is metal carbonyls. Many metal carbonyls are unstable at elevated temperatures and would not contribute significantly to vaporization during melt/concrete interactions. Some such as $Ni(CO)_4$ are surprisingly stable. Though evidence of their importance is not available, carbonyls do merit some further attention.

Because so many potentially important vapor species are not considered in the VANESA calculations, the results of the calculations at least with respect to speciation must be considered lower bounds on the true vaporization.

9. Storage of the Thermodynamic Data

Tabulated thermodynamic data are inconvenient to store in computer models. Such data are stored in the current implementation of the VANESA model in terms of parameters derived by fitting an equation linear in temperature to the data over a limited temperature range:

$$\Delta G_f(j,i) = B[j,i,1] + B[j,i,2]T$$

where $\Delta G_f(j,i)$ = free energy of formation of the i^{th} species involving the j^{th} element.

Values for the parameters, B[j,i,1] and B[j,i,2] are shown in Table 35. Such simple correlations of thermodynamic data have been recommended for high temperature studies.[342] Though crude, the correlations will reproduce tabulated data to within about ± 2 kcal/mole if suitable corrections are made when there is a phase change in the reference state for the element. Earlier versions of VANESA used somewhat different parametric values based on older data than those in Table 35.

A superior method for storaging thermodynamic data is to fit the free-energy functions of the species to a polynomial:

Table 34

Chemical Species Identified in Aerosol Samples
Taken During Melt/Concrete Interaction Tests

Metals:

- Te
- Sn
- Sb
- Cr

Oxides:

- Fe_3O_4
- $ZnFe_2O_4$
- Cr_2O_3
- SiO_2
- $ZnMnO_3$
- $Na_2Cr_2O_7$

Halides:

- CsI
- NaCl
- KCl
- $MnCl_2$
- $CsFeF_4$

Sulphides:

- Cr_4S_7
- $KSbS_4$

Table 35

Parametric Values for Linear Fits to the Free-Energies of Formation

Species	H_2O	H_2	H	OH	O	O_2	CO_2	CO
α	-60202	0	54626	8590	61221	0	-94433.8	-27236.5
β	13.9079	0	-14.5252	-3.20424	-16.0633	0	-0.12502	-20.444

Species	Fe(ℓ)	FeO(ℓ)	Fe(g)	FeO(g)	FeOH	$Fe(OH)_2$
α	0	-60690.4	89117.3	47788.6	18235	-85585.3
β	0 [note a]	12.6211	-28.617	-16.4727	-3.655	24.5329

Species	Cr(ℓ)	Cr_2O_3(ℓ)	Cr(g)	CrO(g)	CrO_2(g)	CrO_3(g)	H_2CrO_4(g)
α	0	-245364	86235.6	34923.3	-27748.9	-77459	-178233
β	0 [note b]	52.633	-29.4334	-19.1964	-2.04107	21.098	49.400

Species	Ni(ℓ)	NiO(ℓ)	Ni(g)	NiOH	$Ni(OH)_2$
α	0	-57218.9	93479	24449.5	-70501
β	0 [note c]	21.9373	-29.7314	-2.282	26.1774

Species	Mo(ℓ)	Mo(g)	MoO(g)	MoO_2	MoO_3	$MoO_2(OH)_2$	$(MoO_3)_2$	$(MoO_3)_3$
α	9846.5	153160	87315	-7736.1	-88268	-204525	-291258	-492225
β	-3.42752 [note n]	-32.9923	-20.718	-6.21571	15.173	50.1436	74.1897	136.299

Species	Ru(ℓ)	Ru(g)	RuO(g)	RuO_2(g)	RuO_3(g)	RuO_4(g)
α	0	152015	82641.7	29700	-21938.7	-44873.7
β	0 [note o]	-35.7451	-21.4272	1.5	14.3307	35.6096

Species	Sn(ℓ)	Sn(g)	SnO(g)	SnOH(g)	$Sn(OH)_2$	SnTe(g)
α	0	71062.5	-117.8	-6016	-100967	-22591.4
β	0	-24.5446	-11.1795	0.668	31.1686	2.791

Species	Sb(ℓ)	Sb(g)	SbOH	$Sb(OH)_2$	Sb_2	Sb_4	SbTe
α	0	59377.1	-24861	-103115	39341	16068.1	-17272
β	0 [note e]	-26.3207 [note f]	9.4392	34.6706	-20.1311	-4.4583 [note g]	5.0891

Species	Te(ℓ)	Te(g)[d]	TeO(g)	TeO_2(g)	Te_2O_2	$TeO(OH)_2$	Te_2	H_2Te
α	-39042.3	42665.5	-34710.8	-128552	-125753	-193043	-64526.6	-27903.2
β	19.5494 [note n]	-21.3755 [note i]	12.1422	27.6285	56.4627	95.0807	27.9473	22.7711

Table 35 (Continued)

Parametric Values for Linear Fits to the Free-Energies of Formation

Species	Ag(ℓ)	Ag(g)	AgOH	$Ag(OH)_2$
α	-58023.8	61805.9	-29228	-50170
β	23.8095 [note p]	-25.3814 [note q]	15.573	40.977

Species	Mn(ℓ)	MnO(ℓ)	Mn(g)	MnOH	$Mn(OH)_2$
α	0	-102286	61865.7	-45009	-134843
β	0 [note l]	24.4256	-27.3856 [note m]	16.334	41.1706

Species	CaO(ℓ)	Ca(g)	CaO(g)	CaOH	$Ca(OH)_2$
α	-164320	0	-30888.8	-83408	-181654
β	37.838	0 [note k]	8.58022	18.7607	45.0673

Species	Al_2O_3(ℓ)	Al(g)	AlO	AlOH	Al_2O	AlO_2	Al_2O_2	$Al(OH)_2$	AlO(OH)
α	-374635	71220.5	9998.8	-52434	-48675	-50151	-116076	-160346	-116422
β	65.3834	-25.7858	-13.7847	5.69176	-7.41536	2.81036	9.07451	31.2370	18.331

Species	Na_2O(ℓ)	Na(g)	NaOH(g)	NaO	$Na_2(OH)_2$	NaH	Na_2
α	-120262	0	-72401	-5877.2	-195334	4004.9	-19614.7
β	53.8745	0	21.7455	6.52036	80.9114	7.67821	19.7252

Species	K_2O(ℓ)	K(g)	KOH	KO	$K_2(OH)_2$	KH	K_2
α	-102623	0	-78776.8	-4337.3	-197654	8293.1	-13012.8
β	52.29324	0	22.7109	5.82946	78.91	6.70982	18.0146

Species	SiO_2(ℓ)	Si(g)	SiO	SiO_2(g)	SiOH	$Si(OH)_2$
α	-222060	94350.9	-38839.9	-85810	-2254.3	-125669
β	45.1743	-27.0477	-11.1438	7.32411	-0.841	33.807

Species	UO_2(ℓ)	U(g)	UO	UO_2(g)	UO_3(g)	$UO_2(OH)_2$
α	-215349	118744	-5200	-118267	-199267	-328948
β	27.0138	-26.779	-11.8	2.8	18.8	69.4686

Species	ZrO_2(ℓ)	Zr(g)	ZrO(g)	ZrO_2(g)	ZrOH	$Zr(OH)_2$	Zr(ℓ)
α	-243016	143385	8292	-76752	6756	-103585	4918
β	38.0834	-30.5455	-14.9321	-0.045	-0.9120	+20.887	-2.314 [note d]

Table 35 (Continued)

Parametric Values for Linear Fits to the Free-Energies of Formation

Species	$Cs_2O(\ell)$	Cs(g)	CsOH(g)	CsO(g)	$Cs_2(OH)_2$	Cs_2O	Cs_2
α	-95686	0	-79662	-3476	-191531	-59396	-11781
ß	48.9015	0	20.5264	5.34	74.0936	32.9214	16.9059

Species	BaO(ℓ)	Ba(g)	BaO(g)	BaOH	$Ba(OH)_2$
α	-135168	34466	-75720	-80521	-173806
ß	27.133	-16.27 [note j]	10.8107	14.0164	36.9321

Species	SrO(ℓ)	Sr(g)	SrO(g)	SrOH	$Sr(OH)_2$
α	-152988	0	-40250	-86505	-177450
ß	35.8252	0	8.11732	19.8232	43.6659

Species	$La_2O_3(\ell)$	La(g)	LaO(g)	LaOH	$La(OH)_2$
α	-392621	98072	-37522	-21843	-157733
ß	53.4425	-26.6068	-11.4459	-1.301	25.534

Species	$CeO_2(\ell)$	Ce(g)	CeO(g)	CeOH(g)	$Ce(OH)_2$
α	-239160	96333	-41572	-24994	-133973
ß	41.2974	-25.0814	-9.15712	2.6606	27.1386

Species	$Nb_2O_5(\ell)$	Nb(g)	NbO(g)	NbOH	$Nb(OH)_2$	$NbO_2(g)$
α	-412132	173642	42613	60090	-88645	-52064
ß	77.8143	-35.2791	-19.2143	-3.2438	22.1984	-3.2126

Species	CsI(ℓ)	CsI(g)	I(g)	HI(g)	$I_2(g)$
α	-92450	-64134	18934	-1612	0
ß	26.4353	8.11524	-12.9994	-1.72965	0

*$\Delta G_f(T) = \alpha + \beta T(K)$

a) Applies for T > 1805 K. For T < 1805 K, α = 2054, ß = -1.P63.
b) Applies for T > 2148 K. For T < 2148 K, α = 5319, ß = -2.484.
c) Applies for T > 1726 K. For T < 1726, α = 4094, ß = -2.372.
d) Applies for T < 2125 K. For T > 2125, α = 0, ß = 0.
e) Applies for T < 2378 K. For T > 2378, α = -48384, ß = 20.348.
f) Applies for T < 2378 K. For T > 2378, α = 0, ß = 0.
g) Applies for T < 2378 K. For T > 2378, α = -187188, ß = 81.281.
h) Applies for T > 1997 K. For T < 1997 K, α = 0, ß = 0.

Table 35 (Continued)

Parametric Values for Linear Fits to the
Free-Energies of Formation

Notes (Continued)

i) Applies for T < 1997 K. For T > 1997 K, α = 0, β = 0.
j) Applies for T < 2118 K. For T > 2118 K, α = 0, β = 0.
k) Applies for T > 1767 K. For T < 1767 K, α = 37350, β = -21.14.
l) Applies for T < 2330 K. For T > 2330 K, α = -51924, β = 22.2832.
(m) Applies for T < 2330 K. For T > 2330 K, α = 0, β = 0.
(n) Applies for T < 2873 K. For T > 2873 K, α = 0, β = 0.
(o) Applies for T > 2541. For T < 2541, α = 5434.2, β = -2.1388.
(p) Applies for T > 2437. For T < 2437, α = 0, β = 0.
(q) Applies for T < 2437. For T > 2437, α = 0, β = 0.

$$fef = -\frac{[G(i,j,T) - H(i,j,298)]}{T}$$

$$= a[i,j,1] + a[i,j,2]x + a[i,j,3]x^2 + a[i,j,4]x^3 + a[i,j,5]\ell n(x) + a[i,j,6]/x + a[i,j,7]x\,\ell n(x)$$

where $x = T/10{,}000$, $G(i,j,T)$ is the free energy of the i^{th} species involving the j^{th} element at temperature T, and $H(i,j,298)$ is the enthalpy of the species at 298.15 K. An effort is underway to switch the current implementation of the VANESA model to this data storage method. Parametric values are shown in Table 36. These parametric values were obtained by nonlinear least-squares fitting of tabulated values of the free-energy function.[350] Free-energy functions taken from the JANAF tables or calculated as part of this work were fit at 298.15 K and at 100 K increments between 300 and 3500 K. Free-energy functions from some other sources were fit only in the temperature range of 298.15 to 3000 K. In some cases free-energy function values were not available. In these cases, the fit was to values of $-G(i,j,T)/T$ and $\Delta H_f(298)$ was taken to be a parameter equal to zero. Estimated thermodynamic properties of monohydroxides prepared by Jackson[287] were not employed in this work. Rather, the free-energy functions were recalculated using structural and vibrational information deduced by Jackson. Jackson's estimated properties of the dihydroxides were used, but the fitting process was constrained so that $a[i,j,3] = a[i,j,4] = a[i,j,7] = 0$.

The fit to the polynomial expression is simply a way of reproducing for computational purposes the tabulated values of the free-energy function and the free-energy of melt and vapor species. The polynomial ought not be used to extrapolation beyond the applicable temperature range of 298.15 to 3500 K in most cases or 298.15 to 3000 K in some cases. Nor should the polynomial be differentiated to derive other thermodynamic properties such as heat capacity, entropy, or enthalpy increments.

It should be noted that the correlations for cesium and iodide species shown in Table 36 were developed from a recent assessment of the applicable data base.[355]

10. Material Compositions

The material compositions that must be considered in the analysis of aerosol production during core debris interactions with concrete are:

Table 36

Parametric Values for Fits to the Free-Energy Functions

Species	x[a]	Parameters[b] a(1)	a(2)	a(3)	a(4)	a(5)	a(6)	a(7)	$\Delta H_f(298)$
H_2	1.7×10^{-7}	52.4592	8.99920	-11.5069	-0.535448	7.88464	0.218586	10.9317	0
H	6×10^{-8}	40.6169	2.97997	-6.87160	4.04623	5.14533	0.150063	2.54691	52103
HO	6.3×10^{-7}	71.5378	32.4806	-64.0862	27.2162	9.44937	0.236795	31.6799	9318
HO_2	9×10^{-8}	60.0565	6.65713	21.4050	-5.20988	4.39921	0.199272	-27.4861	5000
H_2O	1×10^{-6}	71.7494	50.6925	-80.5005	34.4291	9.38704	0.247921	32.7046	-57798
O	8×10^{-8}	54.1746	6.02702	-15.2663	7.59333	5.83413	0.161465	7.58793	59554
O_2	1×10^{-6}	56.8750	-3.60972	24.0527	-6.87305	4.48401	0.175303	-19.9288	0
CO	2.6×10^{-7}	65.9644	29.5348	-51.5543	29.0582	7.06968	0.201526	14.4314	-26420
CO_2	1.0×10^{-7}	48.2563	-7.95997	60.1207	-18.1687	2.58053	0.192449	-53.5637	-94054
Fe(l)	1.49×10^{-4}	-26.7094	12.4934	11.7840	64.4449	-7.47004	-0.0264174	-87.4710	3138
FeO(l)	2.38×10^{-5}	115.401	304.487	-647.011	344.391	27.7545	0.519625	246.503	-59642
Fe(g)	1.8×10^{-7}	61.6476	-16.3970	28.7130	-19.6689	7.07047	0.199693	-0.648036	99500
FeO(g)	1.1×10^{-7}	63.8722	-22.7199	61.1325	-25.1464	4.41229	0.191706	-34.5155	60000
FeOH(g)	4.5×10^{-7}	69.0027	-24.0422	79.6153	-38.8707	6.27434	0.270178	-44.3103	31900(c)
$FeOH_2$(g)	1×10^{-6}	77.3755	-20.4630	103.018	-39.4526	9.21232	0.441334	-79.0554	-79000

Table 36

Parametric Values for Fits to the Free-Energy Functions

Species	x	Parameters(b) a(1)	a(2)	a(3)	a(4)	a(5)	a(6)	a(7)	$\Delta H_f(298)$
Cr(l)	5.8×10^{-6}	54.9312	149.757	-305.347	154.621	13.2615	0.252637	117.993	6239
Cr_2O_3(l)	5×10^{-5}	-22.2339	-438.570	1072.80	-639.742	-1.96021	0.486279	-393.344	-243398
Cr(g)	1.4×10^{-7}	47.1007	-35.9076	83.2688	-44.9622	3.34238	0.132257	-27.0831	95000
CrO(g)	7×10^{-8}	63.6252	-20.2933	56.5166	-24.1462	4.49084	0.191943	-32.7168	45000
CrO_2(g)	1.5×10^{-7}	62.7879	-43.3870	121.571	-51.2797	3.65963	0.238627	-72.3154	-18000
CrO_3(g)	8.8×10^{-7}	44.5336	-93.2615	251.626	-109.533	0.731595	0.273470	-143.367	-70000
$CrO_2(OH)_2$	16	183.650	0	0	0	0	15.5075	0	0(d,e)
CrOH(g)	2×10^{-8}	70.4646	5.18048	20.0508	-6.55124	5.58878	0.223247	-22.7895	24318
$Cr(OH)_2$(g)	4.73×10^{-3}	100.352	24.3613	0	0	14.5745	0.476921	0	-71364
Ni(l)	5.88×10^{-6}	54.0141	123.076	-249.879	121.101	13.0012	0.260486	101.346	4178
NiO(l)	4.1×10^{-6}	47.6231	48.0682	-79.1438	30.5808	12.7622	0.352047	30.1776	-56821
Ni(g)	7×10^{-8}	48.0656	-21.7172	48.5237	-19.3530	3.26913	0.140570	-26.9932	102800
NiO(g)	1.1×10^{-7}	62.4585	-20.5891	56.0348	-24.4042	4.73436	0.196807	-31.7319	71000
NiOH(g)	4.9×10^{-7}	64.4304	-28.2417	90.6833	-43.8240	5.49610	0.257445	-50.4026	34118
$Ni(OH)_2$(g)	4.5×10^{-3}	107.665	22.4899	0	0	15.2968	0.498923	0	-60964
NiH(g)	1.3×10^{-7}	64.8843	23.2095	-35.8713	23.6792	6.25005	0.192832	5.21247	83057

Table 36

Parametric Values for Fits to the Free-Energy Functions (Continued)

Species	x	Parameters[b] a(1)	a(2)	a(3)	a(4)	a(5)	a(6)	a(7)	ΔH_f(298)
Mo(l)	1.47×10^{-6}	12.8152	-51.9742	140.669	-96.3579	2.98673	0.146456	-43.0007	9935
Mo(g)	7×10^{-8}	56.6341	6.11244	-17.1965	19.2879	5.11599	0.149150	3.55208	157500
MoO(g)	1.2×10^{-7}	63.6927	-16.8853	48.7557	-19.2101	4.53104	0.190378	-30.2766	92500
MoO_2(g)	1.8×10^{-7}	65.4134	-42.4941	118.263	-47.4707	3.81369	0.241773	-71.3540	-3100
MoO_3(g)	5.6×10^{-7}	58.2084	-78.9974	213.618	-93.3311	3.58789	0.320529	-121.609	-86200
H_2MoO_4(g)	8.7×10^{-7}	80.9218	-82.3227	266.167	-112.115	8.71985	0.576757	-167.625	-203400
$MoOH_2$(g)	1×10^{-8}	73.8563	7.63798	13.8696	-3.73939	5.96229	0.228966	-19.5147	71618
$Mo(OH)_2$(g)	4.63×10^{-3}	105.040	24.3950	0	0	14.5328	0.475106	0	-44064
$(MoO_3)_2$	2×10^{-9}	162.166	-2.19131	5.17599	-3.29856	-0.125821	21.6245	-1.82241	0(d,e)
$(MoO_3)_3$	9×10^{-8}	220.809	7.57443	-17.7664	11.1873	0.425689	37.9773	6.27459	0(d,e)
$(MoO_3)_4$	2×10^{-8}	-51.4933	0.866101	-2.04223	1.19061	0.0639808	32.5515	0.804603	0(d,e)
$(MoO_3)_5$	3×10^{-8}	-73.6865	3.57213	-8.43694	5.35736	0.207593	41.6975	2.98550	0(d,e)
Ru(l)	2.1×10^{-7}	26.7076	-2.89800	6.71462	-3.44956	9.74981	0.294822	-2.93769	568
Ru(g)	1.9×10^{-7}	38.1289	-33.4318	82.3193	-25.2697	0.339676	0.0966265	-50.5756	155700(d)

Table 36

Parametric Values for Fits to the Free-Energy Functions (Continued)

Species	x	Parameters (b) a(1)	a(2)	a(3)	a(4)	a(5)	a(6)	a(7)	ΔH_f(298)
RuO(g)	1.1×10^{-7}	65.3954	-19.2298	52.5813	-22.6198	4.78456	0.196663	-30.4929	89000
RuO_2(g)	1.3×10^{-7}	44.7614	-80.0797	208.992	-101.544	1.65021	0.230582	-107.958	30797(d)
RuO_3(g)	1.9×10^{-7}	55.2444	-102.308	267.884	-129.777	2.67438	0.313907	-139.047	-18690(d)
RuO_4(g)	4.3×10^{-7}	42.4961	-149.139	390.449	-189.166	0.779315	0.364465	-202.613	-44000(d)
RuOH(g)	1×10^{-8}	75.0334	7.55034	14.0396	-3.86000	5.96701	0.229096	-19.5487	80018
$Ru(OH)_2$(g)	4.59×10^{-3}	107.281	24.3473	0	0	14.5455	0.475421	0	-1664(d)
Sn(l)	8.56×10^{-3}	-239.256	-1034.30	2365.31	-1338.93	-57.9346	-0.531044	-908.829	1369
Sn(g)	3.39×10^{-6}	15.7636	-31.2352	87.6997	-8.99949	-4.47612	0.0260421	-83.4031	72000
SnO(g)	1.1×10^{-7}	62.7612	-20.9508	56.6704	-24.7530	4.75654	0.197606	-31.8953	4500
SnOH(g)	8×10^{-8}	72.9545	-3.71228	35.4914	-15.8655	6.26104	0.244465	-26.3363	1318
$Sn(OH)_2$(g)	3.5×10^{-3}	110.195	20.0400	0	0	16.4694	0.530989	0	-94364
SnH(g)	1×10^{-7}	64.2425	12.8472	-12.4775	12.1629	5.44286	0.185016	-5.65615	63210
SnH_4(g)	2×10^{-2}	1843.37	5359.24	-12392.5	6640.44	453.487	6.35271	5310.05	38910(d)
Sn_2(g)	1×10^{-8}	82.0783	-6.44996	16.3669	-7.62477	7.97006	0.251767	-8.44740	97376
$(SnO)_2$(g)	9×10^{-8}	108.191	4.69070	-8.76265	9.98694	-1.06027	-3.00821	-4.52354	-59990(d)
$(SnO)_3$(g)	2.0×10^{-7}	137.997	1.67244	-0.367075	7.91755	-2.06753	-4.51745	-12.1945	-125956(d)
$(SnO)_4$(g)	2.1×10^{-7}	172.992	-0.120652	5.01862	6.93315	-2.86690	-6.29064	-18.0873	-193117(d)

Table 36

Parametric Values for Fits to the Free-Energy Functions (Continued)

Species	x	Parameters (b) a(1)	a(2)	a(3)	a(4)	a(5)	a(6)	a(7)	$\Delta H_f(298)$
Sb(l)	6×10^{-8}	33.1323	-2.41886	5.60375	-3.13208	7.32655	0.221415	-2.23833	4190
Sb(g)	1.8×10^{-7}	52.5490	-18.7234	45.4676	-32.0268	4.29700	0.142468	-12.8262	63230(d)
$Sb_2(g)$	3.4×10^{-5}	100.069	79.1379	-184.468	118.511	12.8112	0.303824	62.5994	55260(d)
$Sb_4(g)$	5.0×10^{-5}	209.695	358.141	-827.487	487.668	37.6601	0.772697	282.834	49360(d)
SbO(g)	2.8×10^{-7}	65.3068	10.8518	-7.24283	16.2672	4.82644	0.191156	-17.2061	19000
SbOH(g)	5×10^{-8}	71.0300	-0.224686	29.1858	-12.1116	6.06200	0.237523	-24.7105	-2991
$Sb(OH)_2(g)$	4.01×10^{-3}	110.854	22.2349	0	0	15.4911	0.501927	0	-83673
$SbH_3(g)$	2.2×10^{-7}	47.9143	32.3029	-3.86007	31.9040	1.42458	0.186461	-52.0198	34600(d)
Te(l)	1.5×10^{-7}	37.8787	-2.59293	5.98417	-3.48195	8.83957	0.266625	-2.25428	3445(d)
Te(g)	4.2×10^{-5}	8.87581	-195.162	438.304	-207.601	-6.29150	0.0257892	-164.534	46910(d)
TeO(g)	3.7×10^{-7}	75.6283	-25.4980	53.6979	-30.1010	8.52075	0.277680	-18.7436	16500
TeOH(g)	2.7×10^{-7}	76.1464	-13.0384	51.9499	-26.0131	6.92472	0.265590	-29.9950	-8663
$Te(OH)_2(g)$	3.69×10^{-3}	111.075	21.3812	0	0	15.8517	0.511794	0	-74345(d)
$Te_2(g)$	2.0×10^{-6}	99.9413	120.705	-250.705	145.622	12.1566	0.281981	77.9751	40240
$TeO(OH)_2$	2.3×10^{-7}	106.197	0.663988	-1.53576	0.94306	0.0355040	8.92114	0.545038	0(d,e)
$(TeO)_2(g)$	5.6×10^{-4}	-222.230	-1477.42	3420.49	-1932.75	-64.0618	-0.339317	-1220.56	-26000(d)

Table 36

Parametric Values for Fits to the Free-Energy Functions (Continued)

Parameters (b)

Species	x	a(1)	a(2)	a(3)	a(4)	a(5)	a(6)	a(7)	$\Delta H_f(298)$
$TeO_2(g)$	2.3×10^{-4}	-137.668	-959.533	2229.32	-1246.94	-43.8074	-0.251683	-807.592	-14200(d)
$H_2Te(g)$	1.3×10^{-4}	-27.9007	-391.158	913.310	-446.480	-16.3242	-0.0135465	-349.197	23800(d)
Ag-Te(g)	1×10^{-8}	86.9663	-3.93403	10.4179	-5.21079	8.42435	0.259304	-4.95003	72386
LaTe(g)	3.3×10^{-4}	286.560	925.587	-2164.07	1328.89	55.8524	0.755185	732.120	61600(d)
SnTe(g)	1×10^{-8}	82.5107	-4.76677	12.7754	-5.48619	8.16781	0.255165	-6.76879	33220
SbTe(g)	1×10^{-8}	82.9246	-7.29218	18.3692	-9.01534	7.96931	0.252197	-8.96180	44129
Ag(l)	1.12×10^{-5}	41.3038	109.137	-228.334	138.092	8.95869	0.195529	69.6458	2457
Ag(g)	1.0×10^{-7}	54.0367	0.968621	-2.27304	1.40579	5.02399	0.148747	0.808334	67900
AgO(g)	2×10^{-8}	74.9204	-9.98302	26.8716	-11.1487	7.26635	0.240944	-14.1501	75000
$Ag_2(g)$	2.2×10^{-9}	82.2973	-1.76200	6.64896	-3.04850	8.53773	0.261183	-3.47901	97679
$Ag_3(g)$	4.5×10^{-8}	116.124	9.07643	-18.9140	6.8503	14.9912	0.442341	5.37953	142655
AgOH(g)	5.0×10^{-7}	61.8690	-28.1273	90.1117	-43.7040	5.60290	0.259568	-4[illegible].8727	7218
$Ag(OH)_2(g)$	4.57×10^{-3}	106.688	24.3368	0	0	14.5531	0.475610	0	-13464
AgH(g)	1.1×10^{-7}	61.4137	14.4688	-15.6580	13.0504	5.57391	0.186220	-3.87650	63612
Mn(l)	3×10^{-8}	33.0745	-1.70854	3.92016	-2.13436	10.8778	0.326590	-1.59156	1391
MnO(l)	1.5×10^{-7}	54.6189	4.16032	-9.76299	5.71909	14.7928	0.435997	3.79360	-81196(d)
Mn(g)	8×10^{-8}	54.6930	4.26097	-10.6465	8.57890	5.13145	0.149609	2.97260	67700

Table 36

Parametric Values for Fits to the Free-Energy Functions (Continued)

Species	x	Parameters (b) a(1)	a(2)	a(3)	a(4)	a(5)	a(6)	a(7)	$\Delta H_f(298)$
MnO(g)	1.3×10^{-7}	63.6890	-21.4379	57.8293	-25.3145	4.66894	0.195932	-32.5173	31000
MnOH(g)	$2.\times10^{-8}$	71.0589	5.46033	19.3156	-6.11542	5.62519	0.223856	-22.4765	4018
$Mn(OH)_2(g)$	4.73×10^{-3}	104.411	24.4419	0	0	14.5408	0.476137	0	-103664
MnH(g)	5×10^{-8}	60.5066	4.81430	5.64921	3.44778	4.87767	0.180615	-13.9712	63564
$Al_2O_3(l)$	9×10^{-4}	-114.709	-817.565	2056.46	-1344.56	-22.1296	0.229510	-672.239	-383710
Al(g)	3.3×10^{-7}	53.9982	3.61327	-8.95985	3.58840	5.56246	0.157424	5.10406	78000
AlO(g)	1.08×10^{-6}	61.9375	-26.8409	86.6782	-61.3980	5.34942	0.203400	-27.9351	16400
AlOH*(g)	7.6×10^{-8}	29.4419	-46.3782	151.000	-56.5538	-2.33103	0.127361	-103.234	8000
$Al_2O(g)$	1.3×10^{-7}	74.0262	-32.1706	87.9237	-38.0039	7.98519	0.327953	-50.7978	-31200
$AlO_2(g)$	6.5×10^{-7}	62.2584	-46.4235	124.008	-52.9842	5.56330	0.290491	-70.8897	-44900
$Al_2O_2(g)$	5.6×10^{-7}	64.9976	-77.8086	203.432	-91.3902	5.90743	0.366996	-111.038	-104000
AlOH(g)	9×10^{-8}	42.4441	-14.2953	80.1092	-30.6129	0.460085	0.142345	-61.6279	-43000
$Al(OH)_2(g)$	5.65×10^{-3}	99.3718	25.0653	0	0	14.3993	0.475490	0	-152664
AlO(OH)(g)	3.7×10^{-7}	53.8290	-41.1768	141.998	-59.8394	2.95187	0.263771	-91.3414	-110000
AlH(g)	1.5×10^{-7}	56.4504	11.7580	-9.75223	10.5794	5.35903	0.184454	-6.87924	62000
$Na_2O(l)$	1.0×10^{-7}	84.0755	-1.95312	4.34279	-1.96154	24.8420	0.743392	-1.94517	-89112
Na(g)	7×10^{-8}	49.2478	0.903043	-2.42850	2.48196	4.97513	0.147996	0.440758	25755

*Aluminum monoxyhydride

Table 36

Parametric Values for Fits to the Free-Energy Functions (Continued)

Species	x	Parameters (b) a(1)	a(2)	a(3)	a(4)	a(5)	a(6)	a(7)	$\Delta H_f(298)$
NaOH(g)	2.5×10^{-7}	78.4141	-3.42958	24.3820	-14.6712	10.3845	0.338181	-13.1227	-47300
NaO(g)	1.2×10^{-7}	69.8972	-12.0222	32.8293	-15.3953	6.99223	0.237397	-16.8907	20000
$Na_2(OH)_2(g)$	3.5×10^{-7}	74.1495	-29.3757	146.072	-59.2380	7.28736	0.434825	-105.550	-145200
NaH(g)	1.0×10^{-7}	50.8363	-12.9615	44.5156	-17.3389	4.16590	0.180648	-29.4685	29700
$Na_2(g)$	9×10^{-8}	76.3201	-0.226766	5.40396	-2.83600	8.66869	0.264243	-2.52112	32870
$K_2O(l)$	8×10^{-10}	77.3784	17.7642	0.558292	-0.334618	19.2835	0.591222	-0.213502	-79442
K(g)	9×10^{-8}	51.3703	4.11834	-10.7685	10.0865	5.09888	0.149174	2.66496	21310
KOH(g)	2.8×10^{-7}	80.7651	-2.50210	22.2528	-13.8024	10.5063	0.340068	-12.0243	-55600
KO(g)	9×10^{-8}	74.7784	-6.80746	20.2236	-9.69016	7.73306	0.248947	-10.3533	17000
$K_2(OH)_2(g)$	2.0×10^{-7}	85.4866	-16.8364	114.810	-44.0035	8.99828	0.460657	-90.1200	-156500
KH(g)	8×10^{-8}	53.1865	-18.6118	55.3315	-23.5730	4.29966	0.187742	-32.7551	29400
$K_2(g)$	8×10^{-8}	81.3567	0.757003	4.05905	-2.15654	8.78070	0.266636	-1.76115	30374
CaO(l)	9×10^{-7}	7.37238	-91.3367	232.704	-123.561	2.33847	0.227551	-101.444	-133206
Ca(g)	9×10^{-8}	51.2456	10.3319	-26.0652	21.6073	5.37351	0.151933	7.24890	-42850
CaO(g)	8.4×10^{-7}	32.8481	-160.179	380.703	-211.038	-1.43737	0.139387	-137.084	10500
CaOH(g)	4.2×10^{-7}	71.0367	-14.8965	55.1193	-26.3928	7.87554	0.296789	-31.7173	-46340
$Ca(OH)_2(g)$	1.59×10^{-6}	88.5388	-33.8560	119.083	-61.0843	12.0418	0.481751	-64.3843	-145980

Table 36

Parametric Values for Fits to the Free-Energy Functions (Continued)

Species	x	Parameters (b) a(1)	a(2)	a(3)	a(4)	a(5)	a(6)	a(7)	$\Delta H_f(298)$
$Ca_2(g)$	$9x10^{-8}$	102.805	28.0207	-78.9020	32.9209	13.7070	0.323413	47.5506	82660
CaH(g)	$3.2x10^{-7}$	54.4278	-7.50234	31.7223	-7.84527	4.17089	0.176620	-25.8671	54708
$SiO_2(l)$	$3.18x10^{-5}$	-25.9438	-174.345	466.220	-274.913	-4.53144	0.172800	-195.502	-215740
Si(g)	$6x10^{-8}$	55.2901	-0.502102	0.902520	-3.65042	5.73746	0.161459	3.97287	107700
SiO(g)	$6x10^{-8}$	56.3991	-12.4373	41.9451	-16.1112	4.11636	0.177280	-28.5533	-24000
$SiO_2(g)$	$1.1x10^{-7}$	50.6256	-41.2040	123.120	-50.4828	3.03633	0.232284	-77.0454	-73000
SiOH(g)	$1x10^{-8}$	64.7102	4.28492	23.4018	-7.67066	5.12663	0.214433	-25.3356	12218
$Si(OH)_2(g)$	$6.16x10^{-3}$	94.8480	26.2297	0	0	13.9033	0.462748	0	-112464
SiH(g)	$2.8x10^{-7}$	67.4878	33.7742	-61.0398	34.7966	7.47895	0.209146	17.9395	90000
$SiH_4(g)$	$7.1x10^{-7}$	22.9692	29.9016	41.6064	11.9835	-3.06951	0.139283	-91.0320	8200
$Si_2(g)$	$1.29x10^{-6}$	51.5288	-19.2336	59.5033	-8.99393	2.10592	0.167617	-54.0617	141000
$Si_3(g)$	$1.4x10^{-7}$	80.9581	-36.2189	90.9269	-39.3214	9.37613	0.358474	-47.3268	152000
$UO_2(l)$	$2.2x10^{-4}$	-152.821	43.1505	53.1917	284.998	-47.6594	21.3678	-360.950	0(d,e)
U(g)	$1.08x10^{-6}$	71.9546	3.22295	9.09601	-28.6141	8.27829	0.205665	20.5484	125000
UO(g)	$1.0x10^{-7}$	69.9035	-20.3699	54.6321	-23.6815	4.82848	0.198343	-31.0666	6000
$UO_2(g)$	$6.6x10^{-6}$	75.9650	-35.6410	98.6217	-38.5309	8.50254	0.363935	-60.4592	-111500
$UO_3(g)$	$9x10^{-6}$	77.1029	-40.2534	134.652	-55.9500	6.67864	0.365459	-87.5735	-191200

Table 36

Parametric Values for Fits to the Free-Energy Functions (Continued)

Species	x	Parameters (b) a(1)	a(2)	a(3)	a(4)	a(5)	a(6)	a(7)	$\Delta H_f(298)$
UOH(g)	3.6×10^{-7}	82.4412	-13.4225	50.3815	-26.3681	8.62776	0.310078	-27.2334	20318
$U(OH)_2(g)$	3.24×10^{-3}	119.782	20.2735	0	0	16.3009	0.52346	0	-82364
$UO_2(OH)_2(g)$	8×10^{-8}	142.207	6.17843	-14.5065	8.70108	0.408899	26.0671	5.47793	0 (d,e)
$ZrO_2(l)$	1.8×10^{-4}	102.665	278.439	-589.462	345.978	25.8024	0.555671	196.776	-244550
Zr(l)	5.24×10^{-6}	43.0384	53.0062	-99.9312	36.2116	9.52972	0.219050	48.8161	6351
Zr(g)	1.8×10^{-6}	65.9328	-11.6544	26.9932	-29.1579	8.30943	0.226252	6.61296	148300
ZrO(g)	3.86×10^{-6}	115.856	195.681	-392.463	186.234	17.5113	0.327486	157.398	14000
$ZrO_2(g)$	2.1×10^{-7}	68.7070	-43.4639	116.839	-51.1663	5.13948	0.268792	-66.1376	-68400
ZrOH(g)	4×10^{-8}	72.7354	1.10695	26.8053	-10.6823	5.97798	0.234743	-24.1293	27818
$Zr(OH)_2(g)$	4.16×10^{-3}	111.005	22.7667	0	0	15.2597	0.495663	0	-100864
ZrH(g)	1.2×10^{-7}	59.5027	-2.28505	20.9051	-4.68328	4.54106	0.179290	-20.2708	123400
$Cs_2O(l)$	1.2×10^{-7}	89.1136	17.4762	1.14042	-0.494175	19.2595	8.29920	-0.521822	0 (d,e)
Cs(g)	5×10^{-7}	55.2417	6.55067	-18.1618	19.4856	5.14749	0.149563	3.95293	18320
CsOH(g)	2.09×10^{-6}	90.7817	11.9227	-12.2683	4.27126	11.9591	0.360430	3.24478	-62000
CsO(g)	1.2×10^{-7}	80.7553	-3.16482	10.4747	-4.43004	8.20453	0.255807	-5.91461	15000
$Cs_2(OH)_2(g)$	2.1×10^{-7}	96.5937	-11.7521	101.644	-38.1523	9.89020	0.474727	-82.8928	-164400
$Cs_2O(g)$	1.1×10^{-7}	104.020	-11.2969	28.9991	-13.1597	12.0330	0.385473	-15.5524	-22000

Table 36

Parametric Values for Fits to the Free-Energy Functions (Continued)

Parameters (b)

Species	x	a(1)	a(2)	a(3)	a(4)	a(5)	a(6)	a(7)	$\Delta H_f(298)$
$Cs_2(g)$	1.4×10^{-7}	89.1610	-0.0897744	5.61591	1.57390	8.69867	0.266413	-3.09525	25400
CsI(l)	8×10^{-8}	75.2082	0.375753	-0.867230	0.499939	17.3228	0.516051	0.321957	-79592
CsI(g)	1×10^{-6}	87.5492	-0.217848	3.06455	-1.50460	8.77548	0.265011	-1.50804	-39004
I(g)	6×10^{-8}	54.1911	-6.63604	15.4075	-8.35029	4.61835	0.144341	-5.31883	25517
HI(g)	1.9×10^{-7}	69.4679	32.6933	-58.1720	31.5970	7.40906	0.205671	18.2666	6300
IO(g)	2.4×10^{-7}	68.8660	14.3691	-16.2626	18.8136	5.72625	0.206762	-10.9152	42628
$I_2(g)$	9×10^{-8}	83.0887	-1.94509	6.71410	-2.99443	8.50236	0.260342	-3.61888	14924
$(CsI)_2(g)$	1×10^{-6}	150.799	-2.48774	6.26606	-2.92743	19.4992	0.586797	-3.23356	-118676
$CsO_2(g)$	1.10^{-6}	83.950	-23.9502	68.5863	-28.4498	7.8139	0.308602	-41.7360	-22843
CsH(g)	1×10^{-6}	58.2842	-17.8761	52.4918	-21.6654	4.60728	0.194155	-31.2780	27962
BaO(l)	9.3×10^{-6}	39.3171	-33.6912	114.437	-85.5852	8.50280	0.315413	-37.7596	-117502
Ba(g)	2.48×10^{-6}	29.3097	-101.752	228.233	-106.005	-0.690541	0.0873429	-84.3210	42800
BaO(g)	1.7×10^{-7}	69.8650	-1.19230	5.77212	12.2821	6.39311	0.221384	-13.8092	-29600
BaOH(g)	3.7×10^{-7}	79.5042	-8.81893	37.8912	-16.0445	9.06906	0.316625	-22.7179	-54120
$Ba(OH)_2(g)$	1.46×10^{-6}	105.600	-18.7384	79.5194	-43.4925	14.7903	0.526093	-42.6046	-149750
BaH(g)	4×10^{-8}	55.4561	-22.9893	64.5276	-21.1396	3.51077	0.172926	-38.4000	53059
SrO(l)	1.34×10^{-6}	18.0402	-79.7882	214.156	-124.495	4.02918	0.254137	-86.9276	-123636
Sr(g)	7×10^{-8}	54.0657	13.7115	-34.9189	29.7712	5.48307	0.152880	9.43624	39200

Table 36

Parametric Values for Fits to the Free-Energy Functions (Continued)

Parameters (b)

Species	x	a(1)	a(2)	a(3)	a(4)	a(5)	a(6)	a(7)	$\Delta H_f(298)$
SrO(g)	8.38×10^{-5}	37.5805	-144.119	337.589	-174.373	-0.904345	0.145090	-127.326	-3200
SrOH(g)	4.8×10^{-7}	77.2505	-9.31504	40.2751	-18.9822	8.85681	0.312721	-23.9293	-49120
$Sr(OH)_2(g)$	1.54×10^{-6}	100.190	-23.5991	91.9449	-48.9544	13.9680	0.513070	-49.3748	-142400
SrH(g)	1×10^{-8}	56.8871	-9.97990	36.3308	-9.57170	4.18688	0.179283	-27.6294	52103
$La_2O_3(l)$	3.7×10^{-7}	68.1142	-78.4977	237.173	-122.520	16.7144	0.692610	-111.795	-398199(d)
La(g)	9×10^{-8}	66.8137	29.1110	-55.3691	23.6762	7.64847	0.194009	25.7704	103000(d)
LaO(g)	3.3×10^{-7}	67.9946	-17.8110	56.9905	-34.1712	5.63136	0.209245	-23.9778	-29000
LaOH(g)	4.3×10^{-7}	74.6822	-20.0646	67.9072	-34.2453	7.39733	0.29008	-36.8680	-12682
$La(OH)_2(g)$	3.85×10^{-3}	113.841	22.0150	0	0	15.5607	0.503273	0	-148364
$La_2O(g)$	9×10^{-8}	89.8219	-31.7152	84.4489	-37.2793	7.75091	0.313347	-47.2644	-983
$La_2O_2(g)$	5×10^{-7}	77.6150	-76.3411	203.093	-89.5495	5.07757	0.349182	-113.696	-136470
$CeO_2(l)$	4.3×10^{-7}	28.6712	-64.3687	186.692	-97.1016	7.60645	0.375180	-87.1574	-241462(d)
Ce(g)	1.6×10^{-6}	50.1089	65.7121	-115.172	81.7907	2.59836	0.111546	7.40403	101000
CeO(g)	3×10^{-8}	66.9638	-19.3996	53.1120	-22.9510	4.79202	0.196877	-30.5892	-32000
CeOH(g)	3.1×10^{-7}	83.4429	-9.44044	39.9905	-21.7671	9.34667	0.321666	-21.5147	-14682
$Ce(OH)_2(g)$	2.82×10^{-3}	120.087	19.0783	0	0	16.7890	0.536485	0	-124364
$CeO_2(g)$	2.0×10^{-7}	74.2754	-42.9464	112.420	-50.3277	6.14530	0.289277	-61.5935	-120883

Table 36

Parametric Values for Fits to the Free-Energy Functions (Continued)

Species	x	Parameters[b] a(1)	a(2)	a(3)	a(4)	a(5)	a(6)	a(7)	$\Delta H_f(298)$
$Ce_2O_2(g)$	5.2×10^{-7}	76.9729	-77.1758	205.971	-90.6391	4.72843	0.342614	-115.707	-153653
$NbO_2(g)$	2.6×10^{-7}	64.4885	-43.7615	121.204	-51.5121	3.98076	0.245786	-71.3163	-47800
Nb(g)	9×10^{-8}	65.3601	-16.0440	22.4500	-10.9175	8.02050	0.228398	-0.973984	175200
NbO(g)	1.0×10^{-7}	63.3709	-17.0485	49.3130	-18.6794	4.37165	0.187288	-31.1114	47500
NbOH(g)	1×10^{-8}	70.0761	7.21713	14.8616	-4.30824	5.93032	0.22855	-19.9070	66718
$Nb(OH)_2(g)$	4.6×10^{-3}	107.678	24.4035	0	0	14.5282	0.474994	0	-83964
$NbO_2(l)$	2.06×10^{-5}	114.017	461.821	-997.702	657.465	26.2264	0.509684	283.557	-169902
Nb(l)	8×10^{-5}	26.0792	-1.04656	18.4887	-22.7424	5.93399	0.179397	-0.774587	7107
NbO(l)	7.76×10^{-6}	18.6966	-116.245	323.192	-248.226	3.89661	0.242232	-94.9570	-80484
$Nb_2O_5(l)$	1.12×10^{-3}	433.779	1226.78	-2544.86	1231.31	107.658	1.84416	1057.98	-437589

(a) $x = [fef(tabulated) - fef(calculated)]^2/(N - 7)$ where N is the number of tabulated points used to parameterize the correlation. Typically 34 data points were used. The square root of x gives a crude estimate of the magnitude of the average discrepancy between the values for the free-energy function calculated with the correlation and the tabulated values.

(b) $G(T) = \Delta H_f(298) - T[a(1) + a(2)x + 2(3)x^2 + a(4)x^3 + a(5)\ln(x) + a(6)/x + a(7) \times \ln(x)]$ where $x = T/10000$.

(c) Using structual and vibrational data from reference 318.

(d) Applicable only in range 298.15 to 3000 K.

(e) Parameter only; this is not the enthalpy of formation of the species.

1. Composition of the melt that emerges from the reactor vessel.

2. Composition of the condensed products of concrete decomposition and melting.

3. Composition of reinforcing steel from the concrete that is incorporated into the melt.

The composition of the core debris that initiates attack on the concrete is obtained from a model of the in-vessel phases of core meltdown such as MARCH.[3] Since models of the particular aspects of severe reactor accidents that determine the composition of the core debris are undergoing some evolution, it is a bit difficult to anticipate just what predictions of the core debris composition will be. The current implementation of the VANESA model was constructed to handle core material having the compositions hypothesized for the NRC's source term reassessment. An example of the core debris composition anticipated by the VANESA model is shown in Table 37. The composition is specified from the MARCH and CORSOR largely in terms of elemental composition. The physical and chemical states of the core debris are not specified, with two exceptions. Uranium is specified to be present as UO_2 though it is dubious that the analyses done in the MARCH and CORSOR codes are adequate to determine the urania to be exactly stoichiometric. A certain fraction of the zirconium is estimated to have reacted and to be present as ZrO_2. On occasions, input specifications note the presence of FeO. Ferrous oxide would be unstable if any metallic zirconium is present in the melt.

From the input specifications and the partitioning calculations discussed above, the initial core debris composition shown in Table 37 is produced for the VANESA model. Note that UO_2 is specified as the stoichiometric compound even though the analyses presented above indicate it may not be.

Not all of the elements of interest in the analysis of core meltdown accidents are treated explicitly in the current implementation of the VANESA model. For the NRC source term reassessment, releases of some elements were treated by analogies to the releases of other elements. The analogies were based on the chemistries of the elements and were similar in principle to the analogies made in the Reactor Safety Study.[1]

Chemistry by analogy is at best a qualitative procedure and depends very much on the chemical situation. For instance, the treatment of the physical chemistries of Kr and Xe as similar during reactor accidents is widely

Table 37

Typical Initial Melt Compositions Obtained From the MARCH and CORSOR Models

Pressurized Water Reactor		Boiling Water Reactor*	
Constituent	Amount (Kg)	Constituent	Amount (Kg)
Cs	0.7	Cs	0.30
I	0.1	I	0.02
Te	16.4	Te	27.99
Ba	49.1	Ba	86.70
Sn	152	Sn	557
Ru	103	Ru	171
UO_2	79,630	UO_2	159,908
Zr	6,690	Zr	41,070
ZrO_2	13,210	ZrO_2	32,990
Fe	34,140	Fe	70,160
FeO	5,000	FeO	625
Mo	140	Mo	209.1
Sr	43.7	Sr	58.4
Ag	1,460	Ag	0
In	433	In	0
Sb	0.31	Sb	0
Rb	0.1	Rb	0.03
Y	22.9	Y	36.17
Te	36.7	Te	58.4
Rh	20.7	Rh	33.0
Pd	52	Pd	82.7
La	62.3	La	98.2
Ce	131	Ce	207.8
Pr	50.7	Pr	80.34
Nd	171	Ne	270.8
Sm	34	Sm	53.76
Pu	469	Pu	742.4
Cr	5411	Cr	11,100
Mn	157	Mn	1,208
Ni	3,006	Ni	6,164

Recently the MARCH Code has been modified to report also the inventory of B_4C which is about 900 kg.

accepted. This analogy between Kr and Xe would be wholly inappropriate, however, in discussions of filtered venting of reactor containments using activated-charcoal gettering. Xenon is easily trapped on charcoal and krypton is not. Chemical analogies are best done after the detailed chemistry for the situation of interest has been carefully examined. Needless to say, it is preferable to treat each element individually. Sometimes the available time and resources are not sufficient to do this.

The analogies drawn for the source term assessments were as follows:

1. Indium was assumed to vaporize as does silver.

2. Cadmium was assumed to vaporize as does Cs_2O.

3. Ru, Pd, Pt, and Tc were assumed to vaporize in identical fashions.

4. Ce, Pu, and Np were assumed to vaporize in analogous manners.

5. La, Y, Pr, Nd, Pm, Sm, Eu, and Gd were assumed identical in their vaporization behavior.

Conventional ideal solution analyses of silver and indium vaporization under accident conditions support the first of these analogies. More accurate considerations of the vaporization of silver-indium alloys[180] suggest that this analogy may overestimate the rate of indium vaporization. The discussion in Section III A-2 suggests, however, that the treatment of activity coefficients adopted in the VANESA model may underestimate the rate of silver vaporization. The analogy drawn to account for cadmium vaporization may appear mysterious. It is, however, no more mysterious than how cadmium could possibly be a major constituent of a core melt which had reached temperatures in excess of 2000 K! Careful analyses of cadmium vaporization[180] have shown quantitative cadmium vaporization is to be expected during the early stages of a core melt down accident when the reactor control rods rupture. The analogy was drawn simply as a means of assuring reasonably rapid cadmium vaporization. There is no justification for modifying the VANESA model to explicitly treat cadmium vaporization since upgraded models of the in-vessel accident processes will show cadmium is not a significant constituent of any melt that emerges from the reactor vessel.

In the Reactor Safety Study, the elements Mo, Ru, Pd, Pt, and Tc were assumed to vaporize in similar manners. The VANESA model provides explicit and distinct treatment of the

vaporization of the early transition element molybdenum and the platinoid ruthenium. However, time constraints mandated that treatments for Pt, Pd, and Tc vaporization be done by analogy. There is little to fault the analogy between Ru vaporization and the vaporization of Pd and Pt. Inclusion of Tc in this analogy has been criticized by the authors of the VANESA model.[9] An analogy with either Mo or Mn vaporization might be more justifiable--at least to the extent chemistry by analogy can ever be justified.

The analogy drawn for the vaporization of the trivalent rare-earths seems unexceptional. Data available on the vaporization rates for the pure oxides are shown in Table 38.[181] From these results, it is apparent that the analogy can involve errors of a factor of 10 in either direction. Release of yttrium, for instance, is overpredicted. On the other hand, release of europium is underpredicted.

The analogy drawn between plutonium release and cerium release is useful. More is said on the technical basis for the analogy in Appendix A to this document.

Concrete ablated by the molten core material is assumed in the VANESA model to be composed of:

1. CaO.
2. Al_2O_3.
3. K_2O.
4. Na_2O.
5. SiO_2.
6. FeO.
7. Reinforcing steel.

The reinforcing steel is assumed to be iron in the metallic state and to be incorporated into the metal phase of the core melt. It is assumed 0.149 grams of steel is added to the core melt for each gram of molten oxidic material produced from the concrete by ablation. Some actual steel compositions are shown in Table 39. Clearly, reinforcing steel is predominantly iron, but it does contain some manganese. One result of the model analyses of aerosol production during core debris/concrete interactions is that manganese is an important contributor to the release. Consequently, inclusion of manganese from the reinforcing steel might improve the model.

Table 38

Comparison of the Vaporization Rates of Pure Rare Earth Oxides

Species	Relative Vaporization Rate of Pure Species	
	2000 K	2500 K
La_2O_3	1.0	1.0
Nd_2O_3	1.6	0.7
Sm_2O_3	0.2	0.5
Eu_2O_3	20	32
Gd_2O_3	0.02	0.1
Dy_2O_3	0.05	1.0
Y_2O_3	0.01	0.02

Table 39

Chemical Compositions of Concrete Reinforcing Steel From Several Reactors[182]

Element	Percent by weight in steel from WPPSS #1	Bellefonte	Susquehanna	Waterford
Cr	0.11	0.16	0.16	0.09
Mn	1.30	0.90	0.77	0.94
Fe	98.0	98.0	98.0	98.5
Co	0.012	0.0085	0.012	-
Ni	0.126	0.113	0.120	0.059
Mo	0.019	0.026	0.026	0.016
Cu	0.276	0.320	0.253	0.355

The actual composition of concretes used in the construction of nuclear reactors is often difficult to determine. The chemical composition of the concrete is not required as part of the plant documentation. Chemical compositions are not routinely determined in the conduct of standard concrete construction practice.

Powers and Arellano[17] have surveyed available data on concrete found in existing nuclear power plants. From this survey, they defined and characterized three concretes that approximately span the range of materials found in the plants they examined. Their survey was directed toward the study of the ablation of concrete by core debris and not the vaporization that accompanies core debris/concrete interactions. Nevertheless, the concretes they characterized provide a useful indication of the types of concrete that might arise in analyses of accidents. The compositions for these three concretes are shown in Table 40. These concretes are the default concretes incorporated into the CORCON code.[5,6] They are also the basis for concrete compositions utilized in the INTER subroutine[3,57] of the MARCH model. The INTER subroutine is a very simple model of core debris/concrete interactions that utilizes very simple concrete compositions. In particular, the model does not consider the Na_2O and K_2O contributors to the concrete composition. Since Na_2O and K_2O are the most volatile constituents of concrete and have been observed to make major contributions to the aerosol produced during melt/concrete interactions, they really should not be omitted from the analyses done with the VANESA model.

The conversion of the concrete compositions listed in Table 40 to the compositions of molten material utilized by the VANESA model yields the results shown in Table 41. To formulate these compositions, the H_2O, CO_2, and SO_2 are assumed to vaporize during the pyrolysis of concrete that precedes melting. MgO is combined on a molar basis with CaO. TiO_2 is combined with Al_2O_3 and MnO is combined with FeO which is derived from the reported Fe_2O_3 content of the concrete.

11. Some Discussion of the Physical Properties of Core Melts

The melt produced by the degradation of reactor fuel is quite complicated. Descriptions of this melt derived from models such as MARCH and used as input to the VANESA model, little reflect the chemical complexity. Indeed, the necessary investigations of reactor core melts have only recently been undertaken.[49,80] Discoveries that alter radically current perceptions concerning the chemical nature of the molten material that streams from the reactor vessel in an accident may well occur as these investigations develop.

Table 40

Compositions of Some Concretes[17]

Constituent	Weight Percent in Basaltic Concrete	Limestone/ Common Sand Concrete	Limestone Concrete
Fe_2O_3	6.25	1.44	1.2
MnO	-	0.03	0.01
TiO_2	1.05	0.18	0.12
K_2O	5.38	1.22	0.68
Na_2O	1.8	0.82	0.08
CaO	8.8	31.2	45.4
MgO	6.2	0.48	5.67
SiO_2	54.73	35.7	3.6
Al_2O_3	8.3	3.6	1.6
CO_2	1.5	22.0	35.7
H_2O	5.0	4.8	4.1
SO_2	0.2	0.2	0.02

Table 41

Approximate Compositions of the
Condensed Products of Concrete Decomposition

Constituent	Weight Percent in Basaltic Concrete	Weight Percent in Limestone/ Common Sand Concrete	Weight Percent in Limestone Concrete
CaO	16.40	42.99	87.52
Al_2O_3	9.80	4.87	2.95
Na_2O	1.97	0.11	0.14
K_2O	5.88	1.65	1.17
SiO_2	59.84	48.43	6.17
FeO	6.11	1.95	2.05

The crude descriptions that are now available portray the reactor core melt as a metallic phase and an oxide phase. The metallic phase consists of steel with added amounts of control rod materials, zircaloy cladding, and the like. The oxide phase consists primarily of the urania fuel and the products of steam oxidation of zirconium and steel. The oxide phase is further complicated as ex-vessel interactions of the melt with concrete progress. During these interactions, the condensed products of concrete decomposition, which are themselves quite complicated mixtures, are incorporated into the melt.

Especially for the kinetic analyses described below, it is necessary to have at least a semiquantitative sense of the physical properties of reactor core melts. The density, viscosity, and surface tension of each melt phase arise in the kinetic analyses. Most of these properties of melts encountered in the analyses of ex-vessel core debris interactions have not been measured. Fortunately, procedures exist for estimating such properties of the melts. Data for simplified melts and procedures for extrapolating these data to more realistic and consequently more complex melts are described briefly below. The objectives of these discussions are to provide the needed "order-of-magnitude" sense of the properties and to rationalize the approximate values for the properties used in the current implementation of the VANESA model.

a. Melt Densities

The volume of a mixture of two or more melt constituents will not be, in general, the sum of the volumes of the pure constituents. The volume change of mixing, however, tends to be small in most cases. Consequently, additivity of constituent volumes is a useful approximation. The Hull equation for mixture densities:[82]

$$\frac{1}{\rho_{mix}} = \sum_i \frac{x(i)}{\rho(i)}$$

where $\rho(i)$ = molar density of the i^{th} mixture constituent,

$x(i)$ = mole fraction of the i^{th} constituent in the mixture, and

ρ_{mix} = mixture molar density

is a useful implementation of the idea of volume additivity. Kim[83] has found this procedure of use for predicting the densities of liquefied stainless steels to be:

Type 304 stainless steel (18-20 w/o Cr, 8-11 w/o Ni, bal. Fe)

$$\rho(\text{liquid} = 7.5512 - 0.11167(T/1000) - 0.15063(T/1000)^2 \text{ g/cm}^3.$$

Type 316 stainless steel (16-18 w/o Cr, 10-14 w/o Ni, 1.75-2.5 w/o Mo, bal. Fe)

$$\rho(\text{liquid}) = 7.4327 + 0.039338(T/1000) - 0.18007(T/1000)^2 \text{ g/cm}^3 \quad .$$

Some approximate formulae for the densities of constituents of the metallic phase of core melts are shown in Table 42.

Notice that because of the colligative properties of mixtures, the mixture can remain fully liquid at temperatures below the normal melting points of some or all of the constituents. It is necessary then to extrapolate data for the pure constituents to obtain mixture densities at low temperatures. The extrapolation for metals is usually not especially severe. The extrapolations for oxides can be much more dramatic.

Density data for molten UO_2 have been reviewed by Fink et al.[84] These authors recommend the relationship

$$\rho(UO_2;\ \text{liquid}) = \frac{8.699}{[1 + 9.3\text{x}10^{-5}(T-3120)]} \text{ g/cm}^3 \quad .$$

This relationship was developed from data that indicate the volume change upon fusion of uranium dioxide is 10.5 percent.

Data on the density of liquid ZrO_2 were not found. Thermal expansion data suggest the density of solid ZrO_2 above the monoclinic to tetragonal phase change is given by:[74]

$$\rho(\text{g/cm}^3) = 5.89/(1+\alpha)^3$$

where $$\alpha = -0.00314 + 0.01304(T/1000) - 0.009092(T/1000)^2 + 0.004084(T/1000)^3 \quad .$$

Table 42

Liquid Densities of Some Metals[79]

Chromium

$\rho(g/cm^3) = 6.924 - 0.30(T/1000)$

Indium

$\rho(g/cm^3) = 7.315 - 0.6798(T/1000)$

Iron

$\rho(g/cm^3) = 8.612 - 0.883(T/1000)$

Manganese

$\rho(g/cm^3) = 6.790 - 0.7(T/1000)$

Molybdenum

$\rho(g/cm^3) = 9.34$

Nickel

$\rho(g/cm^3) = 9.908 - 1.16(T/1000)$

Silver

$\rho(g/cm^3) = 10.465 - 0.907(T/1000)$

Tin

$\rho(g/cm^3) = 7.309 - 0.6127(T/1000)$

Uranium

$\rho(g/cm^3) = 19.350 - 1.031(T/1000)$

Zirconium

$\rho(g/cm^3) = 5.8$

Data for this correlation are available only to about 1800 K. Linear extrapolation of the data from 1700 K to the ZrO_2 melting point (2950 K) indicates that the density of the solid at the melting point is 5.30 g/cm^3. If the change in volume of fusion is approximately 10 percent, then the liquid density is 4.86 g/cm^3. A temperature-dependent expression for the density of liquid ZrO_2 is:

$$\rho(g/cm^3) = \frac{4.86}{[1 + 5.8 \times 10^{-5}(T-2950)]} .$$

Bottinga and Weill[86] have examined data for a large number of molten, siliceous mixtures similar to the molten products of concrete decomposition. They formulated a model of melt densities based on partial molar volumes:

$$\rho = \frac{\sum_i x_i w_i}{\sum_i x_i v_i}$$

where x_i = mole fraction of the i^{th} constituent of the melt,

w_i = molecular weight of the i^{th} constituent, and

v_i = partial molar volume of the i^{th} constituent in in the melt.

Expressions for the partial molar volumes of several species used in the Bottinga-Weill correlation are shown in Table 43. Powers and Frazier[67] have found the correlation predicts densities of complex melts of geological interest to within $\pm$1 percent.

The current implementation of the VANESA model uses estimated, temperature-independent densities of the melt constituents and assumes the volumes are additive in accordance with the Hull equation. The estimated densities of pure liquid species are shown in Table 44. The densities of oxides were estimated to be 88 percent of the room temperature densities of the corresponding solids.

b. Surface Tensions

Surface tension is a thermodynamic property. Values for the surface tensions of pure materials of interest here are shown in Table 45. Two consistent patterns are observed from

Table 43

Partial Molar Volumes for Use in
the Bottinga-Weill Correlation of Density

Constituent	Partial Molar Volume (cm^3/mole)
SiO_2	16.15 + 0.0054(T/1000)
FeO	12.89 + 0.144(T/1000)
MnO	8.67 + 0.144(T/1000)
CaO	10.12 + 0.108(T/1000)
Na_2O	17.65 + 0.144(T/1000)
K_2O	28.01 + 0.181(T/1000)
Al_2O_3	22.89 + 0.016(T/1000)

Table 44

Estimated Liquid Phase Densities of the Melt Constituents

Constituent	Estimated Density (g/cm^3)
Fe	6.917
FeO	5.016
Cr	6.33
Cr_2O_3	4.58
Ni	7.83
NiO	5.87
Mo	8.98
Ru	10.74
Sn	6.42
Sb	5.82
Te	5.49
Ag	9.24
Mn	6.54
MnO	4.80
CaO	2.90
Al_2O_3	3.49
Na_2O	1.998
K_2O	2.042
SiO_2	2.332
UO_2	9.65
ZrO_2	4.93
Cs_2O	3.74
BaO	5.034
SrO	4.136
La_2O_3	5.73
CeO_2	6.276
NbO	6.518
CsI	3.969

Table 45

Surface Tensions of Some Liquid Metals[79] and Pure Oxides

Chromium
σ(dyne/cm) = 2387 - 0.32 T

Indium
σ(dyne/cm) = 595 - 0.09 T

Iron
σ(dyne/cm) = 2758 - 0.49 T

Manganese
σ(dyne/cm) = 1393 - 0.2 T

Molybdenum
σ(dyne/cm) = 3114 - 0.3 T

Nickel
σ(dyne/cm) = 2434 - 0.38 T

Silver
σ(dyne/cm) = 1100 - 0.16 T

Tin
σ(dyne/cm) = 579 - 0.07 T

Uranium
σ(dyne/cm) = 1749 - 0.14 T

Zirconium
σ(dyne/cm) = 1905 - 0.2 T

Uranium Dioxide
σ(dyne/cm) = 450 at 3120 K[84]

Ferrous Oxide
σ(dyne/cm) = 585 at 1693 K[156]

Silicon Dioxide
σ(dyne/cm) = 307 at 1800 K[157]

these data. The first is that metals typically have higher surface tensions than do oxides. Metallic surface tensions usually fall in the range of 1200-1800 dyne/cm whereas surface tensions of oxides are 200-600 dyne/cm. The second pattern is that surface tension is not strongly temperature-dependent. The surface tension of a pure material should approach zero as temperatures rise toward the critical point of the material. For most of the materials of interest here, their critical temperatures are much higher than even the high temperatures encountered in core debris interactions with concrete. Consequently, strong variations in the surface tension with temperatures are not expected and are not observed.

Surface tensions are not easily measured with great accuracy. Contaminants, which are present at very low concentrations, can preferentially inhabit the surface of the material and radically alter its surface properties. Consider the effects of oxygen dissolved in iron. At an oxygen concentration of 0.001 w/o, the surface tension of iron is 1700 dyne/cm. Increasing the oxygen concentration to 0.10 w/o, reduces the surface tension of iron to 1000 dyne/cm.[153]

The method of deforming the surface to obtain an indication of the surface tension, too, seems to affect the result obtained. Boni and Derge[150] found that surface tensions obtained for sodium silicate by four methods differed by a factor of three although the precision of each method was quite high.

As for most properties, surface tension data are not abundant for mixtures in general and are especially scant for mixtures of interest here. The radical alterations of surface tension caused by some low-level contaminants mentioned above makes this lack of data disturbing. Fortunately, most mixture constituents do not cause radical changes in the surface properties. If a mixture can be taken to be an ideal solution, then the surface tension of the mixture can be derived from:[88]

$$\exp[-\beta\sigma(mix)/T] = \sum_i X(i) \exp(-\beta\sigma(i)/T)$$

where $\sigma(mix)$ = surface tension of the mixture,

$\sigma(i)$ = surface tension of the pure i^{th} constituent of the mixture, and

$X(i)$ = mole fraction of the i^{th} constituent in the mixture.

The parameter ß is the area occupied by a molecule of a mixture constituent on the surface of the mixture divided by the gas constant. The assumption of ideality implies that each constituent of the mixture has the same size so the parameter may be estimated from:

$$ß = 1.105\ (V(mix))^{2/3}$$

where V(mix) is the molar volume (cm^3) of the mixture. This type of model seems adequate for estimating the surface tension of molten stainless steel and iron/chromium alloys.[154] Zirconium, manganese, molybdenum, platinum, palladium, vanadium, as well as chromium and nickel do not seem surface active when dissolved in iron.[63] Consequently, the surface tensions of alloys of these metals can be estimated using the ideal solution model. Interestingly, carbon, which interacts with iron in a highly nonideal manner, does not appear to cause radical changes in the surface tension of iron.[154] Some data for iron-carbon alloys are shown below:

Iron/Carbon Alloy	Surface tension at 1873 K (dyne/cm)
0.03 w/o C	1627 ± 20
0.45	1660
1.23	1660
1.84	1643
2.66	1647

Apparently, the effects of carbon addition on the surface tension of iron are not much greater than the uncertainty in the surface tension measurements.

Some solutes, which behave in strongly nonideal ways, do cause radical changes in the surface tension of iron. Unfortunately, the consequences of nonideality on surface tension even when this nonideality is well-described by regular solution models have not been well-explored.[89] Consequently, the quantitative description of the effects of surface active agents on surface tension are depicted usually with a more empirical formula:

$$\frac{\partial\sigma(mix)}{\partial x(i)} = -\ 0.226\ T\upsilon^{\infty}(i)$$

where $\upsilon^{\infty}(Te) = 27 \times 10^{3}$,

$\upsilon^{\infty}(Sn) = 700$,

$\upsilon^{\infty}(Sb) = 2400$,

$\upsilon^{\infty}(Cr) = 2.8$,

$\upsilon^{\infty}(Ni) = 0.1$, and

$\upsilon^{\infty}(C) = 0.7$.

Note that this model only applies to infinitely dilute solutions. It is apparent though that tellurium is a melt constituent that is very surface active. Tellurium will reduce the surface tension of iron by 600 dyne/cm when present at a concentration of only 0.04 a/o.[19]

In the field of oxide and glass melts, empirical models of surface tension have evolved. The most popular of these are the factor formulas:[150-152]

$$\sigma(mix) = \sum_{i} F_i X(i) \quad .$$

Some values for F_i are shown in Table 46. Surface tensions at 1800 and 2400 K calculated for molten concrete composiions listed in Table 41 are:

Concrete Type	Surface Tension (dyne/cm) at 1800 K	2400 K
Basaltic	370	333
Limestone/ Common Sand	392	327
Limestone	554	432

For the current implementation of the VANESA model, the surface tensions of the metallic and the oxidic phases of core debris were taken to be 1200 and 400 dyne/cm, respectively.

Table 46

Factors for Estimating Surface Tensions of Complex Melts

Constituent	F(i)	Note
K_2O	357 - 0.12 T	(a)
Na_2O	481 - 0.11 T	(a)
BaO	366	(a)
CaO	976 - 0.22 T	(a)
MnO	854 - 0.12 T	(a)
FeO	861 - 0.17 T	(a)
Al_2O_3	807 - 0.10 T	(a)
ZrO_2	470	(a)
ZrO_2	825.5 - 0.13 T	(b)
SiO_2	286	(a,c)
SiO_2	200	(a,d)
UO_2	855.6 - 0.13 T	(b)

Notes:

(a) Fit of data from Reference 150 to a function linear in temperature

(b) Suggested temperature dependence from Reference 155.

(c) For melts containing 83-50 mole percent SiO_2.

(d) For melts containing 50-33 mole percent SiO_2.

c. Viscosity

Some expressions for the viscosity of pure metals are shown in Table 47. Fink et al.[149] recommend that the viscosity of UO_2 be obtained from the expression:

$$\mu(\text{poise}) = 0.00988 \exp [4620/T] \quad .$$

Data obtained at temperatures below the melting point of UO_2 and therefore data for nonstoichiometric urania suggest viscosities a factor of 10 higher than would be indicated by this equation for stoichiometric urania.[158,159] An alternate correlation for the viscosity of urania is then

$$\mu(\text{poise}) = 4.7 \times 10^{-9} \exp[55,682/T] \quad .$$

Inspection of the viscosity correlations for metals and UO_2 shows that the viscosities are low--a few centipoises. The viscosities of molten concrete and siliceous melts, in general, are much higher. Powers and Arellano[160] estimated viscosities of molten concrete produced in their tests of molten steel/concrete interactions to be 10-150 poises.

The problem of combining viscosity data for pure species to obtain viscosity estimates for mixtures has been much discussed.[161] The CORCON model uses the Kendell Monroe equation[162] for low silica content melts:

$$\mu(\text{mix}) = \sum_{i=1}^{N} \mu(i)^{1/3} X(i)^3$$

where $\mu(\text{mix})$ = viscosity of the mixture,

$\mu(i)$ = viscosity of the pure i^{th} constituent of the mixture, and

$X(i)$ = mole fraction of the i^{th} constituent.

The pure species viscosities used with the Kendell Monroe equation are

$$\mu(UO_2) = \mu(ZrO_2) = 0.00098 \exp[4620/T]$$

$$\mu(Cr_2O_3) = \mu(Al_2O_3) = 3 \times 10^{-5} \exp[17,560/T]$$

Table 47

Viscosities of Some Liquid Metals[79]

Indium

$\mu(\text{poise}) = 0.00302 \exp [800/T]$

Iron

$\mu(\text{poise}) = 0.003699 \exp [4980/T]$

Nickel

$\mu(\text{poise}) = 0.001663 \exp [6038/T]$

Silver

$\mu(\text{poise}) = 0.004532 \exp [2670/T]$

Tin

$\mu(\text{poise}) = 0.0185$ at $T = 505$ K

Uranium

$\mu(\text{poise}) = 0.004848 \exp [3656/T]$

Zirconium

$\mu(\text{poise}) = 0.08$ at $T = 2123$ K

$$\mu(CaO) = 3 \times 10^{-4} \exp[10{,}700/T]$$

$$\mu(FeO) = 1 \times 10^{-4} \exp[14{,}070/T] \quad .$$

Bottinga and Weill[163] have devised a correlation for the viscosities of silica-rich melts that is:

$$\ln\mu = \sum_i D_i(T, X(SiO_2))X(i)$$

where the $D_i(T, X(SiO_2))$ coefficients are dependent on both temperature and the mole fraction of SiO_2. The Bottinga-Weill correlation is used in CORCON mod 1, but has been replaced by a simpler correlation developed by Shaw[164] in CORCON mod 2.

The high viscosities of molten concrete mean that as core debris interactions with concrete progress, the oxide phase will undergo radical changes in viscosity. Explicit modeling of the melt viscosities is not attempted in the current implementation of the VANESA model. Rather, the model has been devised assuming the melt phase to have a viscosity of 5 centipoises and the oxide phase to have a viscosity of 10 poises.

12. Heat Effects Associated with Vaporization

Vaporization is a very endothermic process. Enthalpies of vaporization of the more volatile consituents of the core debris may be as low as 20000 cal/mole. The enthalpy of vaporization of more refractory oxides can be as high as 150,000 cal/mole. The enthalpies of vaporization of structural metals are about 85,000 cal/mole.

The current implementation of the VANESA model does not consider the possibility that heat may pose a rate limitation to vapor production. Clearly, such a limitation is conceptually possible in light of the very endothermic nature of vaporization processes. It is useful then to consider the relative magnitudes of heat effects on the core debris to ascertain if a limitation due to heating ought to be included in the core debris.

From the discussions above, it is evident that concrete can be the dominant contributor to the aerosol evolved during core debris interactions with concrete. If the vaporization of CaO is taken to be representative of the aerosol, then the enthalpic cost of vaporization can be estimated to be

$$\Delta H_v = 2460\ \delta \quad \text{calories/s}$$

where δ = aerosol generation rate in grams per second.

Decay heat rates in the core debris amount to 7.2×10^6 to 4.8×10^6 cal/s. Then, the enthalpic cost of vaporization can be expressed in terms of the available decay heat as:

$$\Delta H_v < 5.1 \times 10^{-4}\delta \quad \text{fraction of decay heat} \quad .$$

Thus, at an aerosol production rate of 100 g/s, vaporization consumes only about 5 percent of the decay heat. Vaporization is not, then, a major source of heat loss from the core debris.

Melt/concrete interactions are predicted[6] to rapidly assume a steady state character. That is, heat losses from the core debris match the generation of heat by radioactive decay and by chemical reaction. A steady state temperature of the core debris is achieved. Most calculations of this steady-state temperature are based on analyses that neglect the heat loss due to vaporization.[6,26,43] It is of use to ascertain the magnitude of perturbation in steady state temperature that is likely to be caused by vaporization.

The heat capacity of a large core melt will be about 2×10^7 cal/K. The rate of temperature change caused by vaporization from a core melt which is calculated to have a steady temperature when vaporization is neglected is:

$$\frac{dT}{dt} = \frac{-2460\delta}{C_p(\text{melt})} = -1.2 \times 10^{-4}\delta \quad .$$

Thus, at an aerosol production rate of 100 g/s, the core debris temperature will fall at the rate of 0.012 K/s. In view of the many phenomenological uncertainties that affect predicted melt temperatures during core debris interactions with concrete,[9] the effect of vaporization on the core debris temperature appears negligible.

Vaporization and aerosol production in general removes radionuclides from the core debris. Since the decay of the radionuclides is the source of significant heat for the

core debris (chemical reaction is the other major source), vaporization ought to be recognized in models of core debris interactions with concrete. The effect will be important only if significant fractional releases of radionuclides are predicted. The VANESA model will predict, in general, large fractions of the tellurium are released from the core debris. In some situations large fractions of other radionuclides are predicted to escape the debris. When such large releases are predicted, it should be recognized this will affect core debris behavior, especially late in the course of interactions with concrete. These effects are not recognized in most models of core debris/concrete interactions.

B. Kinetics of Vaporization

The thermochemistry of vaporization defines one limit to the rate at which materials are released from core debris interacting with concrete. The vapor concentrations in the gases sparging through the molten core debris will not exceed the limit defined by the chemical thermodynamics of the system. An upper bound estimate of the rate of material release from core debris by vaporization can be found by assuming that the sparging gases are saturated as they pass through the melt. Then by specifying the rate of gas production from the interaction of core debris with concrete, an upper bound on the rate of vapor production is determined.

The limit to vaporization defined by thermodynamics is never violated. There are, however, other limitations that can prevent vapor concentrations in the sparging gases from reaching saturation. These other limitations are the kinetic features of the vaporization process that are of interest here.

Vaporization processes involve the transfer of a volatile constituent to the vapor phase. Spontaneous nucleation of vapor in a condensed phase is a very difficult process. Equilibrium vapor pressures must, at the very minimum, be equal to the ambient pressure (atmospheric pressure plus any hydrostatic head). In fact, pressures must actually exceed this equilibrium pressure to overcome the surface tension energy penalty and pressure-volume work of forming free surfaces:[218]

$$\Delta G = 4\pi r^2 \sigma + \frac{4}{3}\pi r^3 (P_{amb} - p)$$

where r = radius of a vapor bubble,

σ = liquid surface tension,

P_{amb} = ambient pressure,

p = pressure within the bubble, and

ΔG = excess free-energy required for homogeneous nucleation.

Consequently, spontaneous nucleation of vapor by volatiles in the condensed phase is a relatively unimportant process in steady-state situations.

A more facile way for condensed-to-vapor transitions to proceed is at a pre-existing free surface. The first limitation encountered in this type of vaporization process is, of course, the availability of free surfaces. This limitation is more a matter of geometry than any intrinsic feature of the condensed phase or its volatile constituents. Once free surfaces are available, several additional actions must occur for vaporization to progress:

1. The volatile constituent of the condensed phase must migrate to the free surface,

2. Once the constituent reaches the free surface, it must transform into a vapor, and

3. Vapors at a surface must be conducted away from the surface lest the gas phase become locally saturated and net vaporization ceases.

In a sense, pre-existing free surfaces catalyze the vaporization process. That is, with free surfaces available, the energy intensive, spontaneous, nucleation route to vapor formation can be avoided at the expense of progressing through several lower energy steps.

Each of the above steps is a kinetic process that requires time. Because the steps are serially related any one of them can become rate-limiting. These steps are the rate processes considered in the VANESA model.

The above list of processes does not exhaust the possible rate limitations to vaporization. Condensed-to-vapor phase changes are endothermic. Consequently, the availability of heat could be rate-limiting. (The availability of heat will become rate-limiting in vaporization processes driven by sufficient disequilibrium to cause spontaneous nucleation of vapor.) Also, the condensed-to-vapor phase change can be prompted by chemical reaction. The intrinsic chemical kinetics of the reaction could be rate-limiting. Or, if reactants other than the volatile of interest are

involved in the chemical reaction, transport of these reactants to the free surface could be rate-limiting. No considerations of these other possible rate limitations are incorporated into the VANESA model. The rationale for their neglect will be mentioned in the discussions below.

Conventional, formal, rate expressions for the processes considered in the VANESA model are:

1. Transport of the i^{th} volatile constituent of the condensed phase to a free surface:

$$\frac{1}{A}\frac{dN(i,m)}{dt} = K(i,m)\rho_{molar}[x(i,bulk) - x(i,surface)]$$

where $\frac{dN(i,m)}{dt}$ = molar rate at which the i^{th} volatile constituent of the condensed phase is conducted to the free surface,

A = free surface area,

$K(i,m)$ = rate constant for the condensed phase mass transport of the i^{th} constituent of the condensed phase,

ρ_{molar} = molar density of the condensed phase,

$x(i,bulk)$ = mole fraction of the i^{th} constituent in the bulk condensed phase, and

$x(i,surface)$ = mole fraction of the i^{th} constituent in the condensed phase at the interface with the free surface.

2. Conversion of the i^{th} constituent of the condensed phase into the j^{th} constituent of the vapor phase:

$$\frac{1}{A}\frac{dN(i,j,s)}{dt} = K_v(i,j)[P_{eq}(j,surface) - P(j,surface)]$$

where $\frac{dN(i,j,s)}{dt}$ = molar rate at which the i^{th} condensed phase species is converted to the j^{th} vapor phase species at the surface,

$K_v(i,j)$ = vaporization rate constant,

$P_{eq}(j,surface)$ = equilibrium partial pressure of the j^{th} constituent of the vapor phase over a condensed phase of composition x(i,surface), and

$P(j,surface)$ = actual partial pressure of the j^{th} constituent of the vapor phase at the free surface.

3. Gas phase mass transport of the j^{th} constituent away from the vicinity of the surface:

$$\frac{1}{A}\frac{dN(j,g)}{dt} = \frac{K_g(j)}{RT}\,[P(j,surface) - P(j,bulk)]$$

where $\frac{dN(j,g)}{dt}$ = molar rate of transport of the j^{th} vapor species away from the surface,

$K_g(j)$ = gas phase mass transport coefficient of the j^{th} vapor species, and

$P(j,bulk)$ = partial pressure of the j^{th} vapor species in the bulk gas phase.

Solution of these rate equations for a completely general case is a formidable chore. There are two well-recognized simplifications that facilitate solution.[188] One of these is to assume vaporization at the surface produces an invariant partial pressure of volatile species so that

$$\frac{dN(i,j,s)}{dt} = 0 \quad .$$

The other method of solution is to assume vaporization is in a quasi-steady state. The steady-state assumption is made in the VANESA model for reasons that will be discussed in connection with the determination of $K_v(i,j)$.

Before the steady-state assumption can be profitably employed, the condensed phase mass transport equation must be modified. As formulated, this equation describes the transport of the i^{th} condensed constituent to the surface. The remaining rate expressions describe movements of the j^{th} vapor species. From the discussions of vapor phase speciation it is apparent that a general constituent of the condensed phase can be removed from the surface as any one

of a number of vapor species. If the steady-state assumption were invoked based on the flux of the condensed species to the interface, then

$$\frac{dN(i,m)}{dt} = \sum_j \frac{dN(i,j,s)}{dt} \quad .$$

This would pose some difficulty in evaluation though this difficulty is not insurmountable. To avoid this problem, the steady-state assumption is invoked for the vapor species. The condensed phase transport is then evaluated for that portion of the flux of the i^{th} constituent that becomes the j^{th} vapor species. That is, the i^{th} constituent migrates to the surface. Any i^{th} constituent at the surface instantly transforms into surface species having the stoichiometries of the vapor species. The proportion of these surface species having the stoichiometry of the j^{th} vapor species is exactly the same as the proportion of the j^{th} vapor at equilibrium over a condensed phase with the composition $x(i,surface)$. Note that this is a construct to simplify the mathematics and has nothing to do with actual molecular behavior.

From the discussions of thermochemistry of vaporization, it is apparent that:

$$\frac{P_{eq}(j,surface)}{\gamma(i,surface)x(i,surface)} = \frac{P_{eq}(j,bulk)}{\gamma(i,bulk)x(i,bulk)} \quad .$$

Then

$$\frac{1}{A}\frac{dN(i,j,m)}{dt} = K(i,m)\rho_{molar}x(i,bulk)\left\{1 - \left[\frac{\gamma(i,bulk)P_{eq}(j,surface)}{\gamma(i,surface)P_{eq}(j,bulk)}\right]\right\}$$

where $\frac{dN(i,j,m)}{dt}$ = rate at which the i^{th} condensed constituent is transported to the surface to become the j^{th} vapor species.

If the activity coefficient of the i^{th} constituent of the condensed phase is 1,

$$\frac{1}{A}\frac{dN(i,j,m)}{dt} = \frac{K(i,m)\rho_{molar}x(i,bulk)}{P_{eq}(i,bulk)} \left[P_{eq}(i,bulk) - P_{eq}(i,surface)\right] .$$

From the quasi-steady state assumption:

$$\frac{1}{A}\frac{dN(i,j,m)}{dt} = \frac{1}{A}\frac{dN(i,j,s)}{dt} = \frac{1}{A}\frac{dN(j,g)}{dt} = \frac{1}{A}\frac{dN(j)}{dt} .$$

Then,

$$\frac{1}{A}\frac{dN(j)}{dt} = \frac{P_{eq}(j,bulk) - P(j,bulk)}{\left\{\frac{P_{eq}(j,bulk)}{K(i,m)\rho_{molar}x(i,bulk)} + \frac{1}{K_v(i,j)} + \frac{RT}{K_g(j)}\right\}}$$

or

$$\frac{1}{A}\frac{dN(j)}{dt} = K(j,eff)[P_{eq}(j,bulk) - P(j,bulk)]$$

where $\frac{dN(j)}{dt}$ = molar rate the j^{th} vapor species is injected into the gas phase and

$K(j,eff)$ = effective rate constant for the formation of the j^{th} vapor species.

This is the rate expression used in VANESA.

Before discussing the parameterization and use of the rate expression, it is useful to examine some of its features. First, note that by using this description, vaporization is described as a reversible process because of the thermodynamic driving force term, $P_{eq}(j,bulk) - P(j,bulk)$. Should the vapor phase become supersaturated in the vapor species j, vaporization would actually become deposition. The system is attempting to achieve equilibrium and will do so given sufficient time. In the absence of sudden changes

in the conditions leading to vaporization (sudden changes in the system temperature or pressure), vapor pressures predicted with this rate expression will not exceed the equilibrium vapor pressure.

This explicit inclusion of the equilibrium limit to the vaporization is most important. Thermodynamic equilibrium is a very strong limit to the vaporization from core debris. To the author's knowledge, no other, commonly used, model of release during severe accidents has this feature. Without it, very unusual, very unrealistic results can be obtained.

If the volume of the gas phase is V(gas), the rate expression can be rewritten as:

$$\frac{1}{A}\frac{dN(j)}{dt} = \frac{RT\ K(j,eff)}{V(gas)}\left\{\frac{P_{eq}(j,bulk)\ V(gas)}{RT} - N(j)\right\} .$$

Then, if K(j,eff) is independent of N(j) and the extent of vaporization is sufficiently small that the effect of vaporization on V(gas) can be neglected, the rate expression is first order. (It would not be first order, in general, if the intrinsic chemical kinetics of vapor formation were included as a rate-limiting process.) The approach to equilibrium by the first-order process is shown in nondimensional form* in Figure 24. The rate is most rapid initially and slows continuously as equilibrium is approached.

The actual rate of vaporization depends first on the available free surface area per unit volume of gas. Second, it depends on the value of K(j,eff) which is the result of three processes. Because three processes determine the value of K(j,eff), no one process will be rate controlling over the whole range of possible vaporization conditions. Also, the rate of reaction will not have, in general, an Arrhenius temperature dependence over a large range of temperatures. As temperatures increase, so too will the rate of vaporization increase. But, at some point there will be a change in the process that has the dominant influence on the rate. Since each of the processes reflected in K(j,eff) has a different dependence on temperature, the temperature dependence of K(j,eff) will be more complex than the simple Arrhenius dependence.

---

*If time and N(j) are the only variable quantities the rate expression has an analytic solution:

$$N(j) = \frac{P_{eq}(j,bulk)\ V(gas)}{RT}\left[1 - \exp\left(-\frac{A}{V(gas)}\ RT\ K(j,eff)t\right)\right] .$$

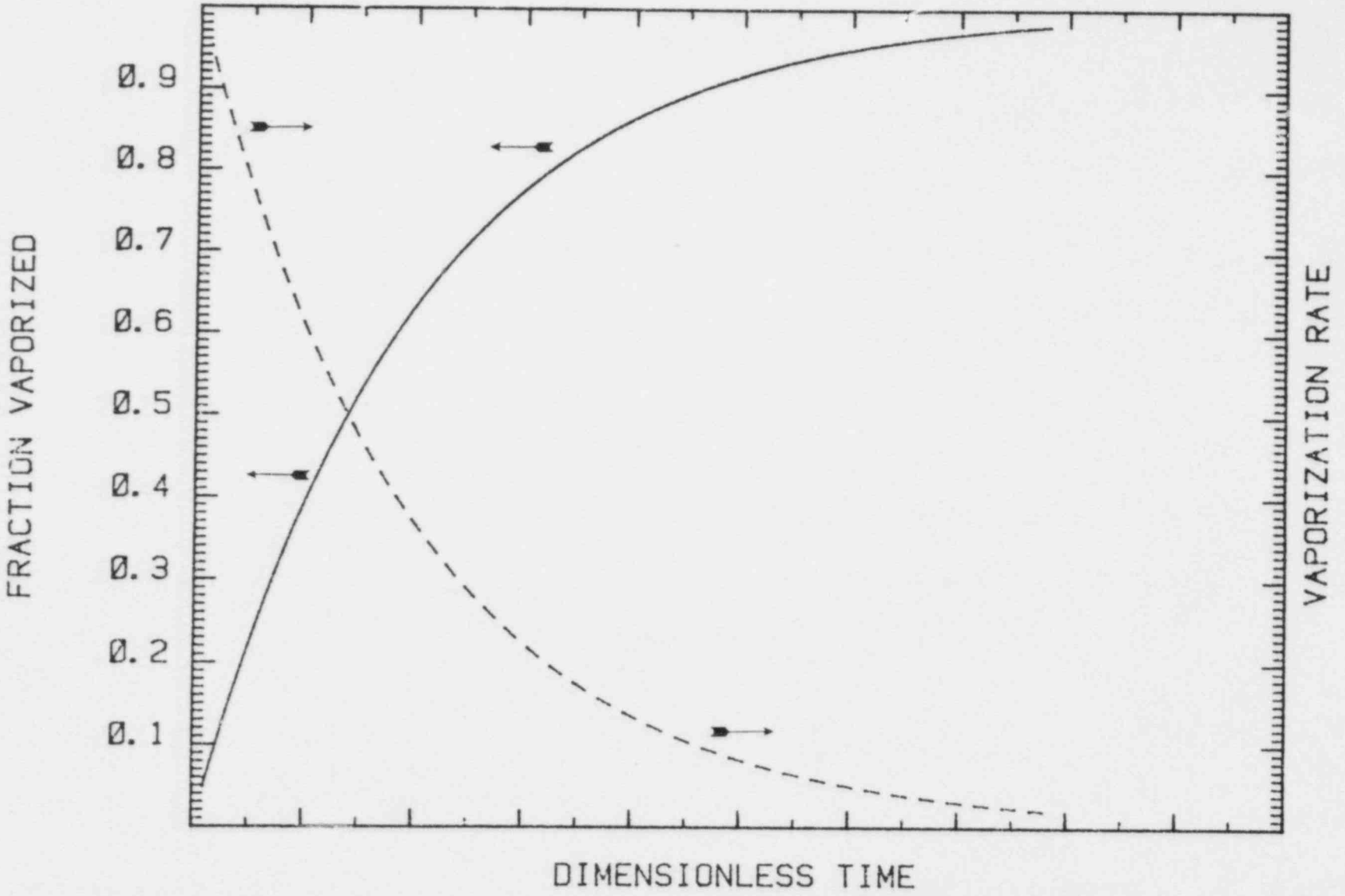

Figure 24. Approach to Equilibrium by First-Order Kinetics

It is readily apparent from the rate expression what needs to be known to characterize the kinetics of vaporization. The equilibrium vapor pressures, $P_{eq}(j,bulk)$, has been discussed at length in the previous section in connection with thermodynamics of vaporization. The remaining quantities to be determined are the surface area available for vaporization, the condensed phase mass transport coefficient, $K(i,m)$, the rate constant for surface vaporization, $K_v(i,j)$, and the rate of gas phase mass transport, $K_g(j)$. These parameters are discussed in the subsections below.

1. The Behavior of Gas Bubbles in Core Melts

The sparging of molten core debris by gases liberated from the concrete is a key element of aerosol production during core debris/concrete interactions. Clearly, any model of vaporization kinetics must address the nature of gas sparging of the core melt. Experimental evidence shows that after an initial transient when molten material first contacts the concrete, gases sparge the melt as bubbles. The behavior of gas bubbles rising through the core melt must be considered in a vaporization kinetics model in order to establish:

1. The surface area available for vaporization that is created by the sparging gases,

2. The time available for vaporization through the surface,

3. The efficiency of mass transport of a volatile constituent of the condensed phase to the surface, and

4. The efficiency of mass transport of vapors away from the surface.

A substantial technology exists to establish these features of the system. The technology of bubble behavior has been developed in terms of many dimensionless parameters. Several of these parameters are described in Table 48. The physical properties used in the definition of the dimensionless numbers are also shown in the table. Approximate values of these properties for both the metallic and oxidic phases of the core debris are shown as are the ranges for the dimensionless numbers derived from these property values. Because the oxide and the metal phases are physically so different, rather broad ranges for the dimensionless numbers need to be considered.

Table 48

Dimensionless Numbers and Physical Properties That Arise in the Analysis of Bubble Behavior

Quantity	Definition	Meaning	Potential Range
Dimensionless Numbers			
Eotvos Number	$E_o = g(\rho_\ell - \rho_g)d^2/\sigma_\ell$	$\frac{\text{Gravitational force}}{\text{Surface tension force}}$	0.02 to 1300
Morton Number	$M = g\mu_\ell^4(\rho_\ell - \rho_g)/\rho_\ell^2\sigma_\ell^3$	$\frac{\text{Gravitational force x viscous force}}{\text{Surface tension force}}$	3×10^{-13} to 25×10^3
Peclet Number	$Pe = dU/D_\ell$	$\frac{\text{Mass transfer by bulk motion}}{\text{Mass transfer by diffusion}}$	2×10^4 to 1×10^7
Rayleigh Number	$Ra = d^3(\rho_\ell - \rho_g)g/\mu_\ell D_\ell$	$\frac{\text{Convective mass transfer}}{\text{Mass transfer by diffusion}}$	163 to 2×10^{12}
Reynolds Number	$Re = U\rho_\ell d/\mu_\ell$	$\frac{\text{Inertial force}}{\text{Viscous force}}$	0.03 to 25×10^3
Schmidt Number	$Sc = \mu_\ell/\rho_\ell D_\ell$	$\frac{\text{Momentum diffusion}}{\text{Molecular diffusion}}$	50 to 6×10^6
Sherwood Number	$Sh = K^m d/D_\ell$	$\frac{\text{Total mass transport}}{\text{Mass transport by diffusion}}$	-
Takada Number	$Ta = Re M^{0.23}$	Used for empirical correlation of ellipsoidal bubble shapes	4×10^{-5} to 2.6×10^5
Weber Number	$We = U^2 d\rho_\ell/\sigma_\ell$	$\frac{\text{Inertial force}}{\text{Surface tension force}}$	0.13 to 160
	E	$\frac{\text{Maximum bubble width}}{\text{Maximum bubble height}}$	-

Table 48 (Continued)

Dimensionless Numbers and Physical Properties That Arise in the Analysis of Bubble Behavior

Quantity	Definition	Meaning	Potential Range
Properties			
	d	Diameter of a spherical bubble with the same volume	0.1 to 5 cm
	D_ℓ	Diffusion coefficient in the liquid phase	1×10^{-4} to 1×10^{-5} cm^2/s
	g	Gravitational constant	980 cm/s^2
	ρ_ℓ	Density of the liquid	2.5 to 10 mg/cm^3
	ρ_g	Density of the gas	1×10^{-5} to 1×10^{-3} g/cm^3
	σ_ℓ	Surface tension of the liquid	200 to 1200 dynes/cm
	μ_ℓ	Viscosity of the liquid	0.05 to 150 poises
	U	Rise velocity of the bubble	~25 cm/s
	Km	Mass transport coefficient	

a. Bubble Shape

Gas bubbles rising through a liquid can assume a number of geometries. The geometry of a bubble would be expected to affect significantly the behavior of the bubble during its transit through the liquid. Grace and coworkers[90,91] have found that they can correlate the shapes assumed by gas bubbles in terms of the Reynolds, Eotvos, and Morton dimensionless numbers. Note that correlation in terms of these dimensionless numbers indicates that the shape of a bubble is determined by the physical properties of the liquid and not those of the gas. The graphical correlation developed by Grace and coworkers is shown in Figure 25.

Obviously, as greater precision is required, a rather large number of shape categories could be defined. For the purposes here, it should be sufficient to consider only three categories:

1. "Spherical" bubbles,

2. "Ellipsoidal" bubbles, and

3. "Spherical cap" bubbles.

The labels attached to these categories ought not be interpreted too literally. Gas bubble shapes do not, in general, have the symmetry that might be attributed to the simple geometries recalled by these labels. In particular, symmetry fore and aft is nearly never present. Also, the dividing lines between shape categories are not sharp. It is convenient to characterize the bubble shape in terms of a parameter E defined by:

$$E = \frac{\text{maximum width of the bubble in the horizontal plane}}{\text{maximum height of the bubble in the vertical plane}} .$$

Then, arbitrary boundaries for the shape categories can be defined as

1. Spherical: $0.9 < E < 1.1$,

2. Ellipsoidal: $1.1 < E < 3.5$, and

3. Spherical cap: $E >= 3.5$.

These categories have been widely adopted.[92,93,94]

The spherical bubble, so familiar from experiences with carbonated beverages, is relatively unusual. It is encountered only for small Reynolds numbers (Re < 1000)--that is,

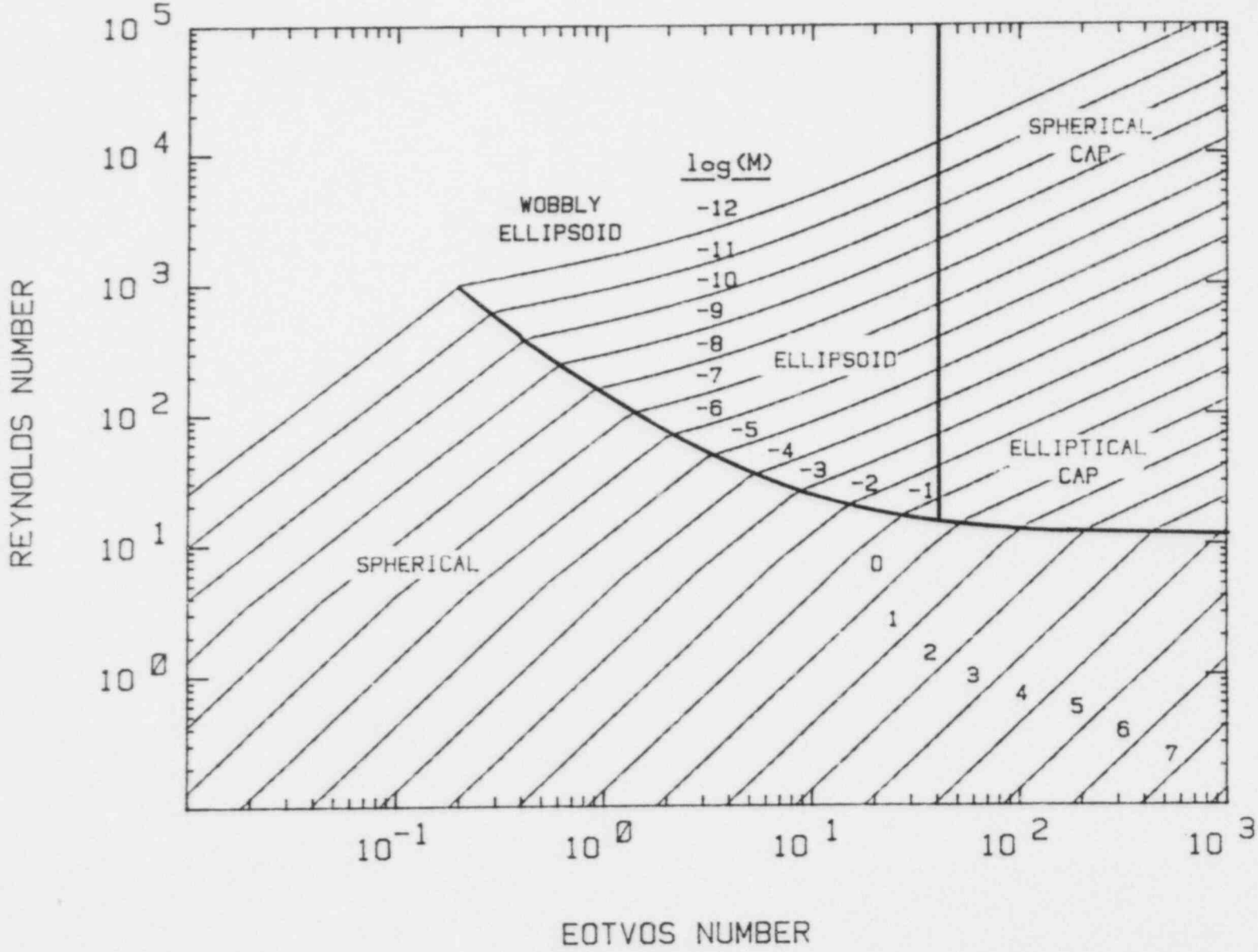

Figure 25. Graphical Correlation of Bubble Shapes

conditions where the bubble is small or moving at low velocities. Within the spherical bubble category, two types of behavior are encountered. Very small bubbles appear to behave as rigid spherical bodies. The gases within these small bubbles are not coupled hydrodynamically to the motion of the liquid phase and apparently do not circulate. On the other hand, gases within larger spherical bubbles have been observed to circulate.[92,95,96] The boundary between internal gas circulation behavior and stagnant internal gas behavior is not well defined. Bond and Newton[97] have suggested that internal circulation of the gas phase begins as Eo exceeds 4. This suggestion has not been endorsed universally.[92] Others have suggested internal circulation is a characteristic of the regime for Re > 400.[65]

Internal circulation of gas is predicted by classic analyses of the motion of fluid spheres through a liquid.[92,99] The ample evidence that such circulation does not occur in small bubbles has prompted many attempts to refine the hydrodynamic analyses of bubble motion.[100] A most convincing case has been made, however, that failure to observe internal gas motion is the result of accumulation of surface active agents at the bubble/liquid interface.[101,102] Accumulation of surface active agents at the interface would be expected on the basis of thermodynamic arguments.[103] Because of the high surface-to-volume ratio of small bubbles, surface active contaminants, even at very low concentrations with respect to the bulk liquid, can affect apparently the motion of the gas in the bubble. Investigations with very pure water[104] and mercury[102] have suggested that circulation of gases will develop in small bubbles if the liquid is free of surface active agents.

Investigations of bubble behavior in high temperature systems have not been so thorough as those of aqueous systems. As a result, questions of internal gas circulation and the effects of surface active agents in high temperature melts are not well resolved. Powers et al.[189] showed that gases do circulate within small spherical bubbles rising in glass melts free of obvious surface active agents. Oxidic melts encountered in reactor accidents will be more complex and may contain surface active agents. Cooper and Kitchner[190] showed P_2O_5 to be surface active in molten FeO and to some extent in calcium silicate. P_2O_5 may be present in core melts since phosphorous is a common impurity in steel. Swisher and McCabe[191] showed the Cr_2O_3 will stabilize foams in some silicate melts as a result of its surface active properties. Cr_2O_3 will be present in core melts when stainless steel is oxidized by gases from the concrete. The previous discussions of surface tension show that tellurium is surface active in metallic melts. Tellurium is, of course, an important radionuclide expected to be present in core debris during ex-vessel phases of a severe accident. There

is evidence from studies of nitrogen dissolution in molten steel that sulfur, too, is surface active.[105] Sulfur would be injected into core debris as a result of concrete ablation. It is not known if these surface active materials expected to be present in core debris will exert an effect sufficient to inhibit circulation of gases within spherical bubbles rising through the debris.

As the Reynolds number of a bubble rising in a liquid exceeds about 1000, the bubble distorts considerably from spherical. A correlation of the eccentricity of the distorted, ellipsoidal, bubbles is:[92]

$$\left(\frac{1}{E}\right) = 1 \quad \text{for } Ta = ReM^{0.23} \leq 1$$

$$\left(\frac{1}{E}\right) = [0.81+0.206 \tanh\{2(0.8 \log_{10} Ta)\}]^3$$

$$\text{for } 1 \leq Ta \leq 39.8$$

$$\left(\frac{1}{E}\right) = 0.24 \text{ for } Ta \geq 39.8 \quad .$$

Plots of the eccentricity, E, against the bubble Reynolds number for various Morton numbers are shown in Figure 26. To prepare this figure, the Morton number was defined to be approximately:

$$M = g\mu_\ell^4/\rho_\ell\sigma_\ell^3 \quad .$$

The density and the viscosity of metallic melt phases in core debris will be about 7 g/cm^3 and 0.05 poises, respectively. Surface tensions will be between 1200 and 600 dynes/cm. Consequently, Morton numbers for the metallic phase will be between 5×10^{-13} and 4×10^{-12}. The oxidic melt phase in core debris will have a density similar to the metal phase, but typically a higher viscosity (~1-10 poise) and a lower surface tension (~400 dyne/cm). The Morton number for the oxide phase will be then between 3×10^{-9} and 200.

It is apparent that as the melt surface tension falls, bubbles distort more easily. Bubbles in oxide melts can be distorted from spherical even at rather low Reynolds numbers. The ellipsoidal regime is rather narrow for such bubbles. In fact, the bubble distortion at these lower

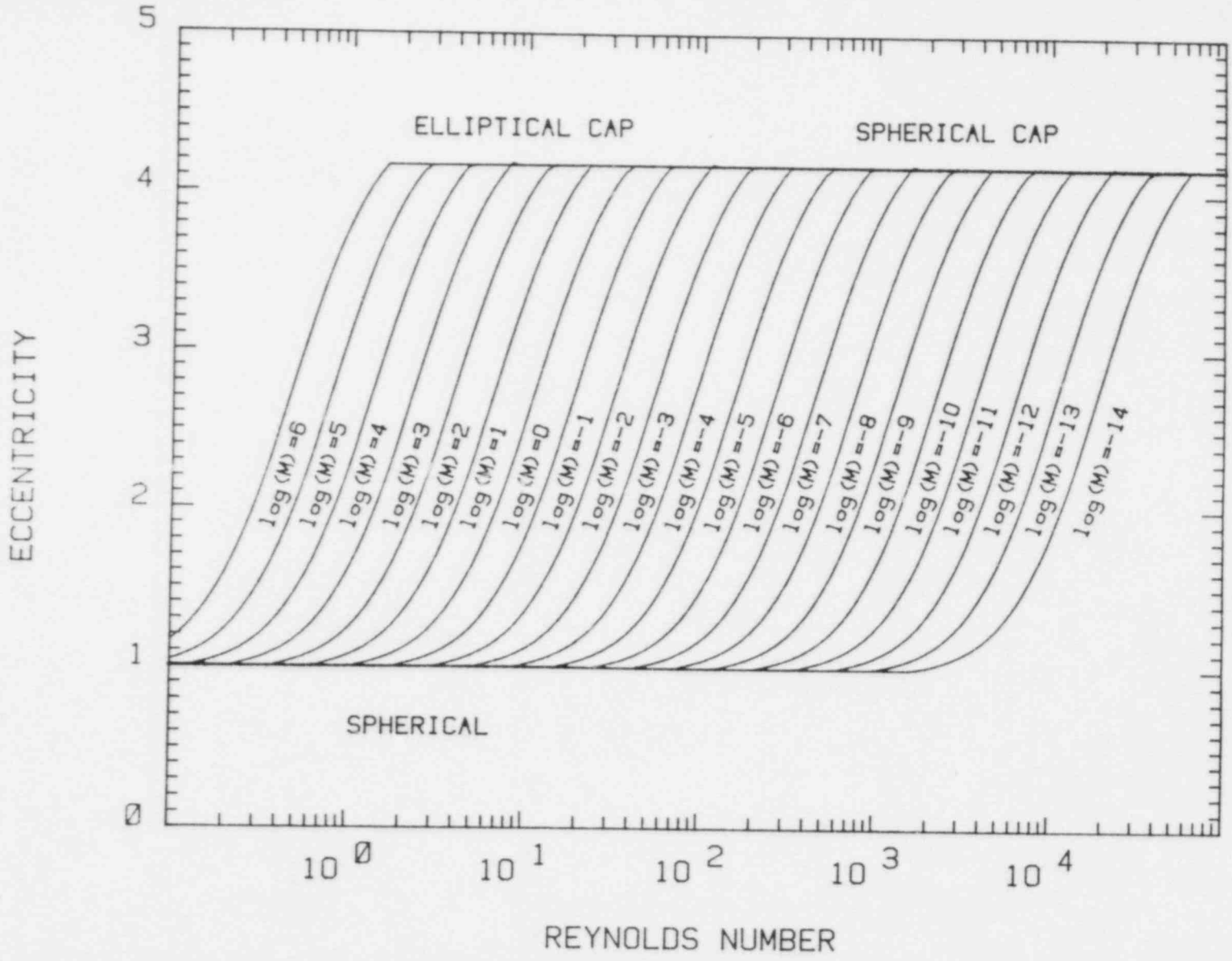

Figure 26. Bubble Eccentricities as Functions of the Reynolds Number and the Morton Number. Morton numbers for the metallic melt will be between 5×10^{-13} and 4×10^{-12}. Morton numbers for the oxidic melt will be between 3×10^{-9} and 200.

Reynolds numbers will be to a shape often termed "elliptical cap" rather than to the more ideal spherical cap shape. Bubbles in the metallic melt resist distortion since the surface tension forces are so much greater than the viscous forces. The ellipsoidal regime is rather more extensive for bubbles in the metallic melt.

Ellipsoidal bubbles need not be stable in their rise through a liquid. "Wobbling" of ellipsoidal bubbles is undoubtedly caused by shedding of vortices in the wake of the bubble. The natural vibrational frequency of a bubble can be estimated to be:[81]

$$f_N = \left[\frac{48\sigma_c}{2\pi^2 d_e^{\,3} \rho_c} \right]^{1/2}$$

where f_N = natural vibrational frequency. The frequency of vortex shedding can be estimated to be:[234]

$$f_w = \frac{0.30\ U_T}{d_e \langle E \rangle^{1/3}}$$

where f_w = frequency of vortex shedding and

$\langle E \rangle$ = time averaged value of E for the bubble.

Then if it is assumed the bubble oscillates like a harmonic oscillator driven by an impulse from the vortex shedding:

$$\frac{1}{E(t)} - \frac{1}{\langle E \rangle} \propto \left(\frac{f_w + f_n}{f_w - f_n} \right) \sin [\pi(f_w - f_n)t] \cos [\pi(f_w + f_n)\, t]$$

where E(t) is the instantaneous eccentricity of the bubble. Because the vibration amplitude is frequency modulated, the bubble motion can appear quite chaotic.

With further increases in the Reynolds number, bubbles adopt the spherical cap configuration. Spherical cap bubbles are conveniently characterized by a wake angle defined as shown in Figure 27. For Eotvos numbers in excess of 40, wake angles are correlated by the expression:[92]

$$\theta = 50 + 190 \exp[-0.62\ Re^{0.4}] \qquad Re > 1.2$$

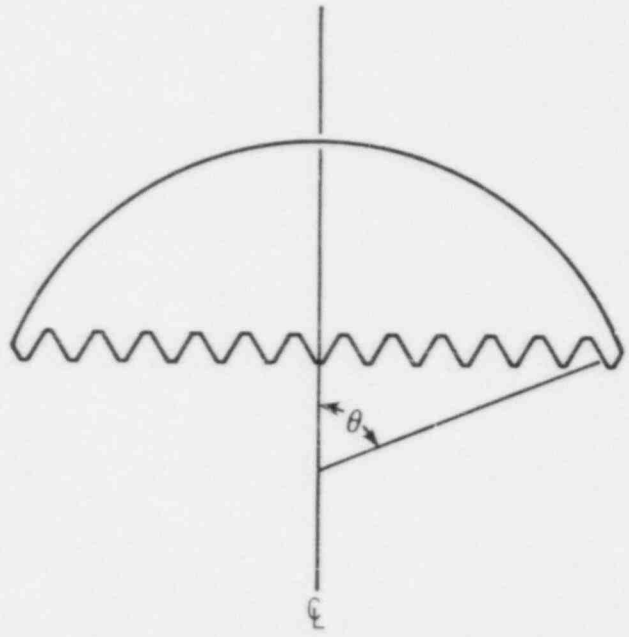

Figure 27. Definition of Wake Angle for a Spherical Cap Bubble

where θ is in degrees. Thus, for spherical cap bubbles of interest here $\theta \cong 50°$. The limiting value of θ corresponds to $E = 4.29$.

Very frequently correlations for bubble properties are given in terms of the diameter of the sphere with the same volume as the bubble. For ellipsoidal bubbles, this equivalent sphere diameter, d_e, is given by

$$d_e = 2a\left(\frac{1}{E}\right)^{1/3}$$

where 2a is the maximum dimension of the bubble in the horizontal plane. The bubble surface area is:

$$A = 2\pi a^2 + \frac{\pi a^2}{E\,E^2-1^{1/2}} \ln\left[\frac{E + \left(E^2-1\right)^{1/2}}{E - E^2-1^{1/2}}\right] .$$

For spherical cap bubbles, the equivalent sphere diameter is:

$$d_e = \frac{2^{1/3}a}{\sin\theta}\left[2 - 3\cos\theta + \cos^3\theta\right]^{1/3}$$

where, again, 2a is the maximum bubble dimension in the horizontal plane. For $\theta = 50°$,

$$d_e \cong 0.572(2a) .$$

The surface area of the spherical cap bubble

$$A(\theta) = \frac{2\pi a^2(1-\cos\theta)}{\sin^2\theta} + \pi a^2$$

and

$$A(50) = 3.825a^2 + \pi a^2 .$$

Note that the curved and the flat surface areas have been distinguished in these formulae. The two types of surfaces

in a spherical cap bubble affect transport properties differently.

Spherical cap bubbles themselves can be deformed. The deformation can be viewed as the development of "skirts" on the bubble or as the bubble base developing curvature. This deformation develops when the Reynolds number is greater than nine:[92]

$$\frac{We}{Re} > 2.32 + \frac{11}{(Re-9)^{0.7}}$$

where We = Weber number = $U_T^2 d_e \rho_\ell / \sigma_\ell$.

b. Trajectories and Rise Velocities

The rise velocity of a bubble will determine how long a bubble resides in a liquid and consequently how much time is available for it to absorb vapors given off by the fluid. The rise of single bubbles need not be, however, along linear paths. Some data[92,106] on the paths taken by bubbles in water are listed in Table 49. Very small and very large bubbles rise to the surface along straight line paths. The larger bubbles may be affected by secondary motions so they appear to "rock" as they rise. Intermediate-sized bubbles can follow rather complicated pathways. These paths can be a "zig-zag" motion along a plane--sensibly an exaggeration of the rocking motion of large bubbles. This zig-zag motion can evolve into a helical pattern. Or, a helical pattern of motion can be established immediately. The complexities of motion for intermediate-sized bubbles are not easily described by analytical models.[107-109] The complex motions must surely affect mass transport to and within the gas bubbles. There may be, however, little need to consider in detail the complexities of bubble motion. Both the rise velocities and the mass transport coefficients can be correlated in an overall sense without explicitly recognizing the details of motion. Further, the complex motions of single bubbles do not necessarily arise when the bubbles become part of a swarm such as when gases sparge a melt of core debris.

The overall rise velocity of a spherical bubble depends on whether gases within a bubble circulate. When these gases do not circulate, the bubble behaves like a rigid sphere and its rise velocity is given by "Stokes Law":

$$U_T = gd^2 \rho_\ell / 18 \mu_\ell$$

Table 49

Trajectories of Single Bubbles

d_e (cm)	Re	E	Path
<0.13	<565	<1.25	linear
0.13 - 0.2	565 - 880	2 - 1.25	helical
0.2 - 0.36	880 - 1350	2 - 2.78	plane zig-zag then helical
0.36 - 0.42	1350 - 1510	2.78 - 3.57	plane zig-zag
0.42 - 1.7	1510 - 4700	3.57 - 4.35	linear-rocking

where U_T is the terminal velocity of the bubble. When the gases do circulate, the rise velocity obtained from classic hydrodynamic analyses[92,99] is:

$$U_T = gd^2\rho_\ell/12\mu_\ell \quad .$$

That is, the circulation of gases leads to an increase in the bubble rise velocity by as much as 50 percent. Experimental data show good agreement with one or the other of these expressions for the terminal velocity depending on whether or not the liquid phase is free of surface active contaminants that could retard internal circulation of gases.

Two correlations for the rise velocity of ellipsoidal bubbles are also available. When internal circulation of gas is possible, data for the terminal velocity of ellipsoidal bubbles can be correlated by[92,110,111]

$$U_T = \left(\frac{2.14\ \sigma_\ell}{\rho_\ell d_e} + 0.505\ gd_e\right)^{1/2} \quad .$$

Grace[91] has developed a fairly complex correlation for rise velocities in liquids which are contaminated with surface active agents:

$$U_T = \frac{\mu_\ell}{\rho d_e} M^{-0.149}(J-0.857)$$

where $J = 0.94H^{0.757}$ for $2 \leq H \leq 59.3$,

$J = 3.42H^{0.441}$ for $H > 59.3$,

$H = 0.6895EoM^{-0.149}(\mu_\ell)^{-0.14}$,

$M < 10^{-3}$,

$Eo < 40$, and

$Re > 0.1$.

The discontinuity in the definition of the dimensionless group J occurs at about the point ellipsoidal bubbles transform into the so-called "wobbly ellipsoid" bubbles. That is, the correlation recognizes that secondary motions affect rise velocities.

For spherical cap bubbles the conventional correlation for rise velocities is given by the Davies-Taylor formula[112]

$$U_T = 0.721 \sqrt{g d_e} \cong \frac{2}{3}\sqrt{ga}$$

where 2a is the maximum horizontal dimension of the bubble. For greater precision, the terminal velocity can be given as a function of wake angle

$$U_T = \frac{2}{3}\sqrt{ga}\left(\frac{1-\cos(\theta)}{\sin^2\theta}\right)^{1/2} .$$

For ellipsoidal bubbles that approach the shape of spherical caps:[113]

$$U_T = f(E)\ \sqrt{(ga/E)}$$

where $$f(E) = \frac{E^3}{(E^2-1)^{3/2}}\left\{\sin^{-1}\left[\frac{\sqrt{E^2-1}}{E}\right] - \frac{\sqrt{E^2-1}}{E^2}\right\} .$$

The terminal velocities of bubbles in the oxide and metal phases of the core debris are shown in Figure 28 as functions of d_e. To prepare this figure the metal phase was assumed to have a density of 7 g/cm^3, a viscosity of 0.05 poises, and surface tension between 1000 and 1200 dynes/cm. The oxide phase was assumed to have a density of 7 g/cm^3, a surface tension of 400 dynes/cm and a viscosity between 1 and 100 poises. The terminal rise velocities were calculated from the equation

$$\frac{Eo^{1.5}}{M^{1/2}} = Re^2\ C_D$$

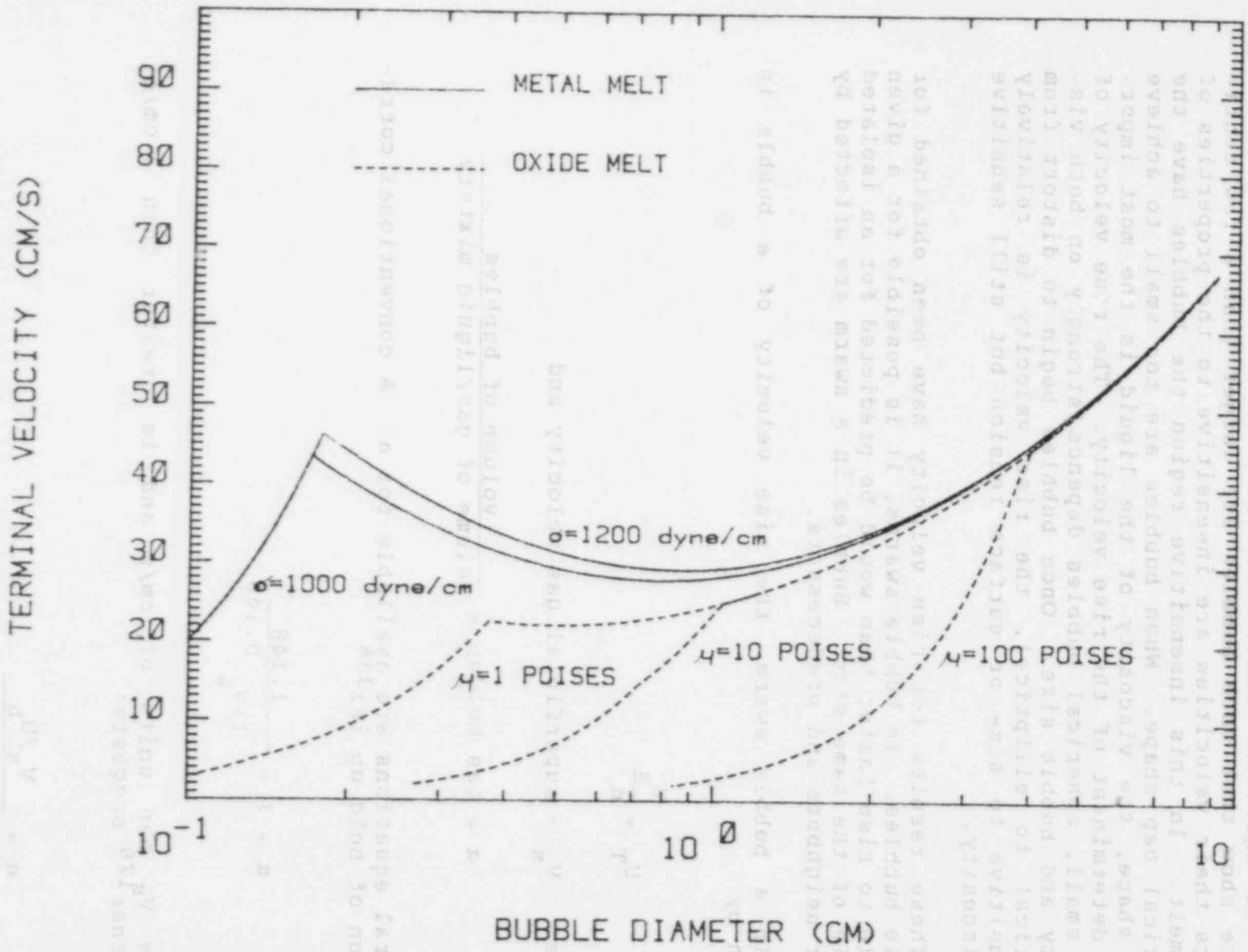

Figure 28. Terminal Velocities of Bubbles of Various Sizes in the Oxide and Metal Phases of Core Debris

where C_D, the drag coefficient, was found as the maximum from the equations listed in Table 50. Velocities in the figure show that once bubbles are larger than a few centimeters their velocities are insensitive to the properties of the melt. In this insensitive region the bubbles have the spherical cap shape. When bubbles are too small to achieve this shape, the viscosity of the liquid is the most important determinant of the rise velocity. The rise velocity of very small, spherical bubbles depends strongly on both viscosity and bubble size. Once bubbles begin to distort from spherical to elliptical, the rise velocity is relatively insensitive to size or surface tension but still sensitive to viscosity.

These results for rise velocity have been obtained for single bubbles. In bubble swarms, it is possible for a given bubble to rise faster than would be predicted for an isolated bubble of the same size. Bubbles in a swarm are affected by their neighbors and predecessors.

In a bubble swarm, the rise velocity of a bubble is given by

$$U_T = \frac{V_s}{\alpha}$$

where V_s = superficial gas velocity and

$$\alpha = \text{gas holdup} = \frac{\text{volume of bubbles}}{\text{volume of gas/liquid mixture}} .$$

Several equations are available for α. A conventional correlation of hold up is:[338]

$$\alpha = 1 - \frac{1.148}{1+V_s^{0.146}}$$

where V_s has units of cm/s and is greater than 3 cm/s. Blottner[128] suggests:

$$\alpha = \frac{V_s/U_b}{1 + V_s/U_b}$$

Table 50

Definitions of Drag Coefficients Used
To Prepare Figure 17

Spherical Bubble With No Internal Gas Circulation:

$$C_D = 576\ M^{1/2}/Eo^{1.5}$$

Spherical Bubble With Internal Gas Circulation:

$$C_D = 83.8\ M^{0.3033}/Eo^{0.959}$$

Elliptical Bubble in a Fluid With No Surface Active Agents:

$$C_D = Eo/(2.14 + 0.505Eo) \qquad Eo > 0.2$$

Spherical Cap Bubble:

$$C_D = 8/3$$

where U_b is the rise velocity of a single bubble. Yoshida and Akita[129] provide a correlation of data that can be fit to the equation:

$$\ell n(\alpha) = -3.4723 + 0.9537\ \ell n(V_s) - 0.05541\ (\ell n(V_s))^2$$

where V_s has units of cm/s.

Calderbank[114] cites an equation:

$$\ell n\left[\frac{1}{1-\alpha}\right] = 0.185F + 0.15$$

where $F = V_s \sqrt{\rho_g}$

ρ_g = density of the gas (g/cm^3)

V_s = superficial gas velocity (cm/s).

G. A. Hughmark[192] offers a correlation in graphic form of holdup in terms of the variable

$$\beta = V_s \left[(1/\rho_\ell)(72/\sigma_\ell)\right]^{1/3} .$$

Hughmark's correlation is quite interesting since it is derived from data taken in columns up to 106 cm in diameter. The curve given by Hughmark can be reproduced by the equation:

$$\ell n(\alpha) = -3.5349 + 0.93587\ \ell n(\beta) - 0.06553[\ell n(\beta)]^2 .$$

Hughmark's correlation is attractive because it includes terms containing properties of the liquid phase. Other correlations for gas holdup have been devised to reflect the properties of the liquid. Kataoka[202] has derived from experimental data the correlation:

$$\alpha = 0.67\left[\frac{V_s}{\left(\frac{\sigma_\ell g(\rho_\ell - \rho_g)}{\rho_g^2}\right)^{1/4}}\right]^{2/3}\left(\frac{\mu_g \rho_\ell}{\mu_\ell \rho_g}\right)^{-2/9}$$

$$\left(\frac{D_H}{\sqrt{\frac{\sigma_\rho}{g(\rho_\ell-\rho_g)}}}\right)^{-1/6}\left(\frac{\rho_g}{\rho_\ell}\right)^{-1/3}$$

where D_H is the hydraulic diameter of the vessel containing the liquid phase. Wilson[185] has offered a similar correlation:

$$\alpha = 0.68\left[\frac{V_s}{\left(\frac{\sigma_\ell g(\rho_\ell-\rho_g)}{\rho_g^2}\right)^{1/4}}\right]^{0.62}\left(\frac{D_H}{\sqrt{\frac{\sigma_\ell}{g(\rho_\ell-\rho_g)}}}\right)^{-0.1}\left(\frac{\rho_g}{\rho_\ell-\rho_g}\right)^{-0.14}.$$

Sterman[186] has presented the correlation:

$$\alpha = 1.07\left[\frac{V_s}{\left(\frac{\sigma_\ell g(\rho_\ell-\rho_g)}{\rho_g^2}\right)^{1/4}}\right]^{0.8}\left(\frac{D_H}{\sqrt{\frac{\sigma_\ell}{g(\rho_\ell-\rho_g)}}}\right)^{-0.25}\left(\frac{\rho_g}{(\rho_\ell-\rho_g)}\right)^{-0.23}.$$

These various correlations have been developed from data for aqueous systems. They are compared for aqueous systems in Figure 29. The correlations agree well for superficial gas velocities of less than 15 cm/s. The predicted holdups diverge for higher superficial gas velocities. With the exception of Blottner's correlation the correlations are empirical and do not reflect the change in flow pattern that occurs at a holdup of about 0.4. At high superficial gas velocities, flow is termed "churn-turbulent" and will not produce such high gas holdups as are predicted by extrapolating the empirical correlations.

The current implementation of the VANESA model uses terminal velocities for isolated bubbles and does not consider the swarm effects on holdup.

c. Initial Bubble Size and Bubble Growth During Rise

Gas is formed during the attack on concrete by high temperature melts at locations in the concrete below the interface with the melt. These gases migrate up through the still-solid products of concrete decomposition. The gases can then enter the melt as bubbles. This mechanism of bubble

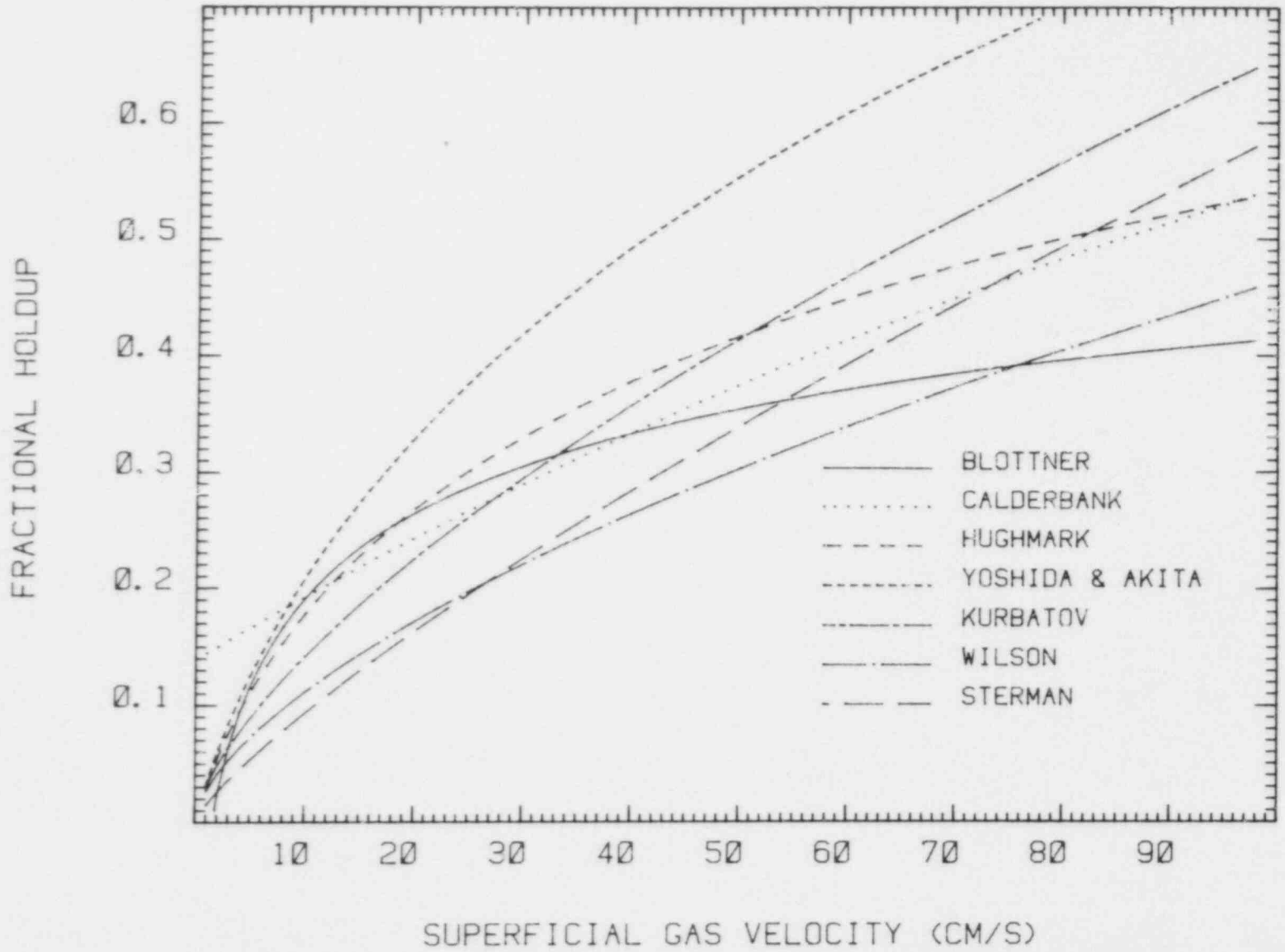

Figure 29. Comparison of Correlations of Holdup With Superficial Gas Velocity in Aqueous Systems. The Calderbank correlation was computed assuming the sparge gas was CO_2 at 298 K.

formation is very much like bubble formation at the base of a liquid column caused by forcing gas through a porous plate. It is also quite similar to the formation of bubbles during the "carbon boil" phase of steel manufacture. It is unlike the formation of bubbles at an orifice below the liquid. An immediate problem with this mechanism of bubble formation is determining the size of the gas bubble that eventually breaks free of the interface and rises through the liquid.

Fritz[137] has used a force balance to determine that this initial bubble size will be

$$d_e = 0.0105\left[\theta\ \sigma/g(\rho_\ell-\rho_g)\right]^{1/2}$$

where θ = the contact angle in degrees between the melt and concrete,

ρ_ℓ = density of the melt (g/cm^3),

ρ_g = density of the gas (g/cm^3), and

σ_ℓ = surface tension (dyne/cm).

For metallic melts of the type of interest here $\rho_\ell \approx 7$ g/cm^3, $\theta \approx 120°$, and σ_ℓ might be between 1200 and 800 (dyne/cm). The Fritz equation would yield, then, estimates of the initial bubble size of 0.53-0.43 cm.

Studies of porous plate bubblers have shown that two flow regimes may develop. In the first regime, usually depicted as developing for superficial gas velocities of less than 7 cm/s, individual bubbles are formed at various locations over the surface of the plate. In this regime, the Fritz formula is applicable. At higher superficial gas velocities, a continuous gas film forms over the surface of the porous plate. The Fritz equation is not applicable in this regime.

The gas film that forms at high superficial gas velocities has assumed a significant role in the analysis of core debris/concrete interactions. In at least two of the major models of these interactions[6,26] it has been assumed that such a gas film develops at the interface between core debris and concrete. This film is assumed, further, to be the dominant source of resistance to heat transfer from core debris to concrete. The film has never been directly observed during core debris interactions with concrete[18] and there is some doubt that such a film would be the dominant resistance to heat transfer.

Several analyses of gas film formation have been undertaken.[138,194] A product of these analyses is a prediction of the diameter of bubbles formed from the film:

$$d_e = 2C\ \sigma/g(\rho_\ell - \rho_g)^{1/2} \quad .$$

The various analyses differ only in the choice of the parameter, C, which is given values of 2.2 to 2.72. Again, for metallic melts, bubble diameters are estimated with this film equation to be 2.3-1.5 cm which are 6-3 times as large as is predicted by the Fritz equation. Because the existence of a gas film during melt/concrete interactions is in doubt, this range of initial bubble diameters obtained with the Fritz equation and the gas film equations creates significant uncertainty in the initial bubble diameter to be used for analysis of vaporization.

The Davidson and Schüler equations[195,196] for the volume of a bubble are:

Low Viscosity Liquids:

$$V_{(bubble)} = \frac{\pi d_e^3}{6} = \frac{V_s^{1.2}}{g^{0.6}} \quad .$$

High Viscosity Liquids:

$$V_{(bubble)} = \frac{\pi d_e^3}{6} = \left(\frac{V_s \mu_\ell}{\rho_\ell g}\right)^{3/4} \quad .$$

These equations were derived for orifices, but properties of the orifice and the surface tension of the liquid cancel out of the correlations for the limiting viscosity cases. The low viscosity correlation would be expected to apply for bubbles formed in steel melts. For superficial gas velocities of 120 to 10 cm/s, the Davidson and Schüler equation may be used to predict spherical equivalent bubble diameters of 2.1 to 0.9 cm.

Predictions of the various models for the diameters of bubbles are shown in Figure 30. It is apparent from this figure that the Fritz formula and the gas film model represent some sort of limiting equations for the low viscosity formula by Davidson and Schüler.

Regardless of the initial value of the bubble diameter, the bubble will grow as it rises through the core debris pool. Growth will occur for three reasons:

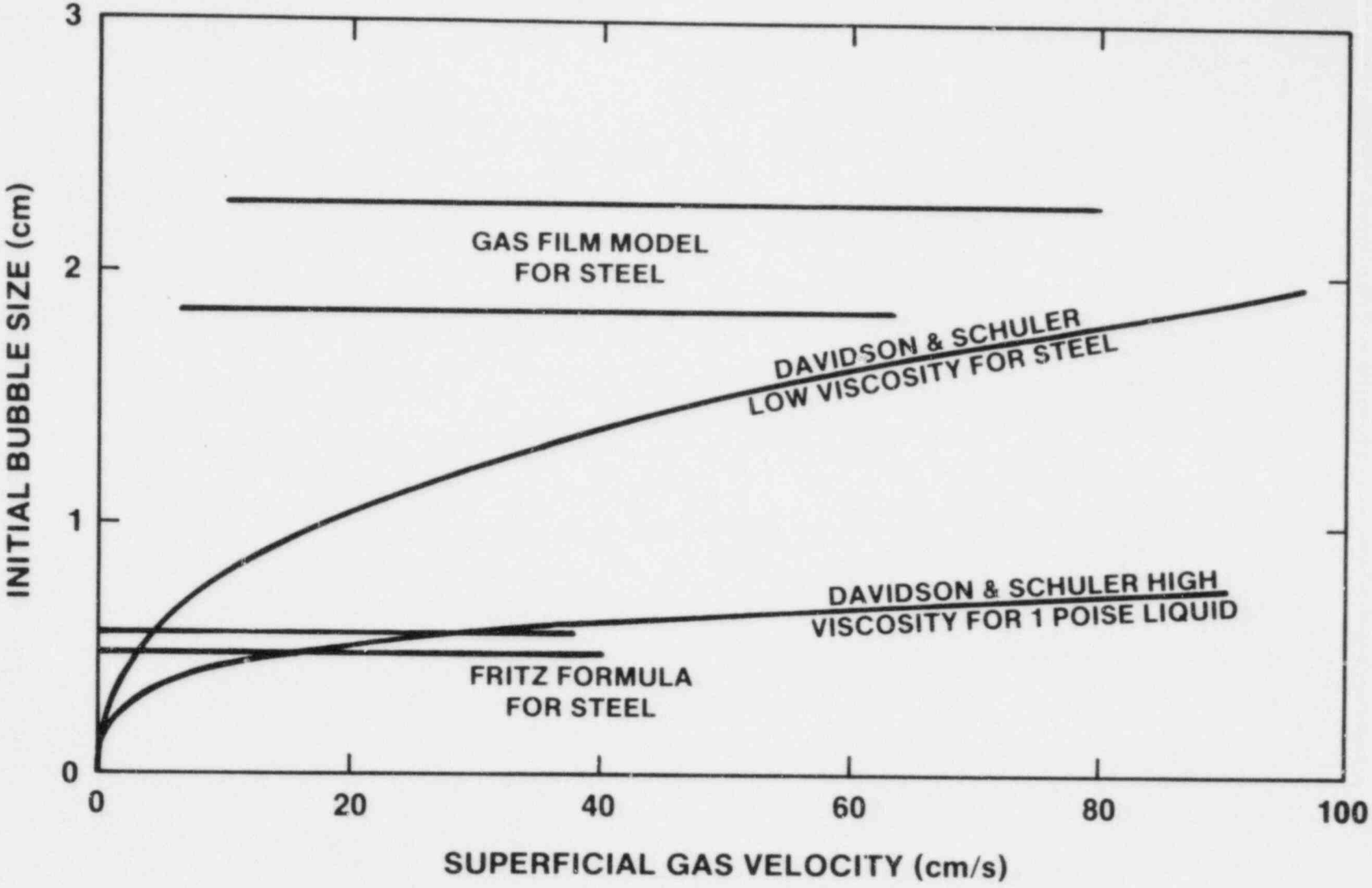

Figure 30. Comparison of Predictions From Various Models for the Initial Bubble Size

1. Dissociation of gases in the bubble will increase the molar density within the bubble which will be relieved by bubble growth,

2. Vaporization of melt constituents into the bubble will also increase molar densities, and

3. As the bubble rises the hydrostatic head decreases, which will permit the bubble to grow.

Only the third of these reasons for bubble growth is especially significant. Were typical melt constituents to vaporize sufficiently to double the volume of a bubble, or increase the bubble diameter by 25 percent, aerosol concentrations in the evolved gas would be about 4000 g/m^3! This is, of course, a much greater aerosol concentration than could ever be expected. On the other hand, the volume of a bubble could double due to loss of hydrostatic head as the bubble rose through a core debris pool.

To analyze the growth of a bubble as it rises, consider a spherical bubble at a location X = 0 at t = 0 at the base of a pool of height H. Assume the initial radius of the bubble is R(0). Let the ambient atmospheric pressure be P (atms). Then, the continuity equation for liquid flow around the bubble is:

$$r^2 U_r = R(t) \frac{\partial R(t)}{\partial t} \quad \text{for} \quad R(t) \leq r \leq \infty$$

where U_r is the radial velocity in the liquid caused by bubble expansion. The equation of motion is

$$\frac{\partial U_r}{\partial t} + U_r \frac{\partial U_r}{\partial r} = -\frac{1}{\rho_\ell} \frac{\partial P(r)}{\partial r} - 4\mu \frac{\partial^2 U_r}{\partial r^2} \quad .$$

Assume that the viscous term is negligible. Then solution of the continuity equation and the equation of motion yields:

$$\frac{1}{r^2}\left[R^2(t) \frac{\partial^2 R(t)}{\partial t^2} + 2R(t)\left(\frac{\partial R(t)}{\partial t}\right)^2\right] - \frac{2R^4(t)}{r^5}\left(\frac{\partial R}{\partial t}\right)^2 = -\frac{1}{\rho_\ell} \frac{dP(r)}{d(r)} \quad .$$

Integration of this equation between the limits

$r = \infty$ where $P = P(\infty, x)$ and

$r = R(t)$ where $P = P(R, x)$

where x is the distance above the bottom of the pool yields:

$$R(t)\frac{\partial^2 R(t)}{\partial t^2} + \frac{3}{2}\left(\frac{\partial R(t)}{\partial t}\right)^2 = \frac{P(R,x) - P(\infty,x)}{\rho_\ell} \quad .$$

(Note that pressures used here are in rational units.) Since the vapor in the bubble is assumed to be an ideal gas:

$$R(t)\frac{\partial^2 R(t)}{\partial t^2} + \frac{3}{2}\left(\frac{\partial R(t)}{\partial t}\right)^2 = \left[\frac{1}{\rho_\ell}\frac{P(0,\infty)R^3(0)}{R^3(t)} - P(\infty,x)\right] \quad .$$

$P(\infty,x)$ is the pressure at a distance far from the bubble and is:

$$P_a + g\rho_\ell(H-x) = P(\infty,x)$$

$$\frac{\partial^2 R(t)}{\partial t^2} + \frac{3}{2R(t)}\left(\frac{\partial R(t)}{\partial t}\right)^2 = \frac{1}{\rho_\ell R(t)}\left[\frac{R^3(0)}{R^3(t)}\right.$$

$$\left.[P_a + g\rho_\ell H] - P_a - g\rho_\ell(H-x)\right] \quad .$$

This differential equation shows that the pressure within the gas bubble is higher than the pressure imposed on the fluid by an amount that depends on the rate of bubble expansion. Plots of the relative correction to bubble volume as a result of the pressure difference are shown in Figure 31. Obviously, this correction is significant only for very low ambient pressures.[139]

Since the pressure differential can be neglected at ambient atmospheric pressures of interest here, the terms of the left-hand side of the equation of motion may be neglected. The growth of a bubble as it rises through the fluid is then given by

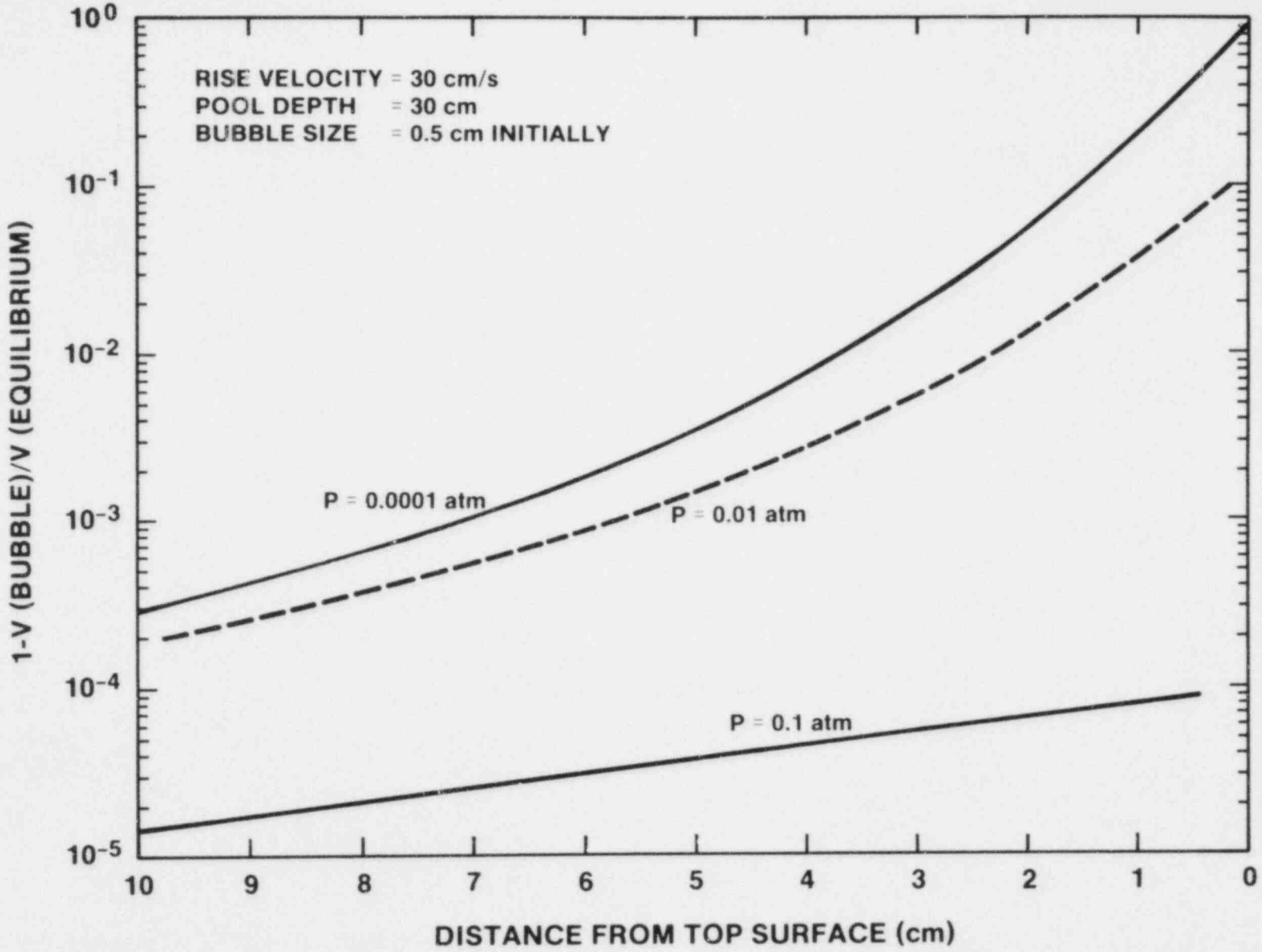

Figure 31. Correction to the Bubble Volume Necessary Because of the Finite Growth Rate

$$\frac{R^3(0)}{R^3(t)}\left[P_a + g\rho_\ell H\right] = P_a + g\rho_\ell (H-x)$$

where $dx/dt = U_T$.

Gas bubbles rising through a liquid cannot grow to be arbitrarily large. Eventually, Rayleigh-Taylor instability will cause a growing bubble to be unstable and to shatter. Sketches drawn from photographs of an unstable bubble shattering are shown in Figure 32. As can be seen in these photographs, the shattering process is initiated by a disturbance in the gas/liquid interface at the top of the bubble. The disturbance grows until it is similar in size to the bubble dimension.

A frequently cited criterion for bubble instability is that deduced by Levich.[102] This criterion is based on the dynamic pressure created by circulation of gases within the bubble. Once this dynamic pressure exceeds the surface tension forces, the bubble is unstable. Levich suggests the maximum bubble size will be:

$$d_{(bubble)} = 1.8\ \frac{\sigma_\ell}{U_T^2\left(\rho_g \rho_\ell^2\right)^{1/3}} \quad .$$

For core melt/concrete interactions, the Levich criterion suggests that bubbles on the order of 3 to 4 cm in diameter would be unstable.

A more "pleasing," but algebraically "messy" analysis of the instability of bubbles proceeds from examination of the growth of disturbances at an interface.[199,200] Surface tension will resist the growth of short wavelength disturbances. An estimate of the critical wavelength for a disturbance to overcome the effects of surface tension is:

$$\lambda_c = 2\pi\sqrt{\rho_\ell g/\sigma_\ell} \quad .$$

Very large disturbances are, in fact, just complete deformations or translations of the entire bubble. Such disturbances are better considered to be "secondary" motions of the bubble since they do not result in the bubble shattering. A somewhat arbitrary upper limit to the wavelength of

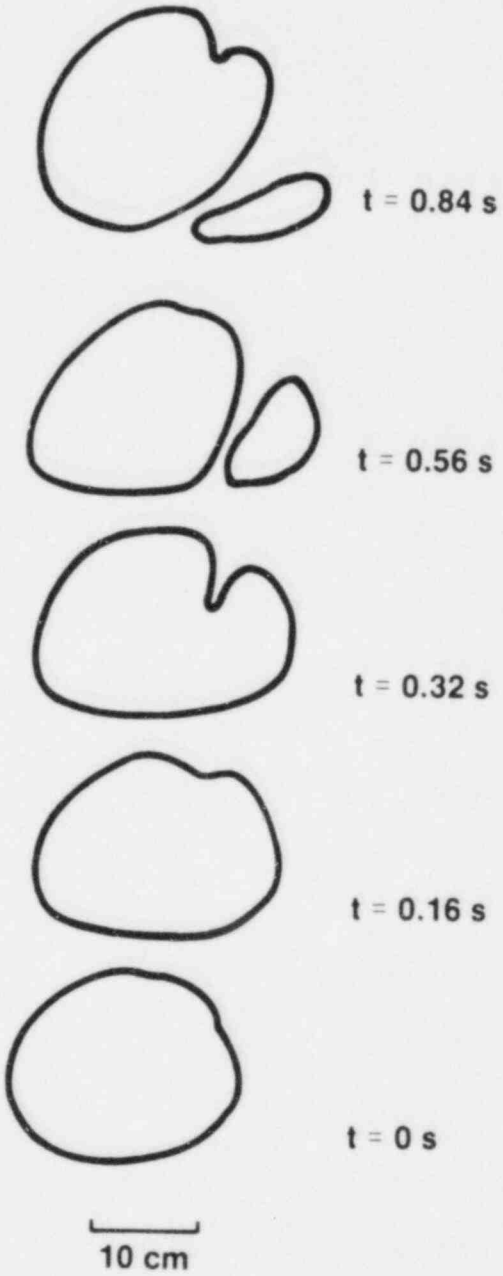

Figure 32. Disintegration of a Gas Bubble[197]

interfacial disturbances of interest to questions of bubble shattering is

$$\lambda_u = \frac{\pi d_{(bubble)}}{2} \quad .$$

Disturbances with wavelengths between λ_c and λ_u will grow. At the same time, such disturbances are swept across the interface as the bubble rises. The time available for the disturbance to grow is given approximately by

$$t(a) = \frac{2d_{(bubble)}}{U} \ln \left\{ \cot \left(\lambda / 4d_{(bubble)} \right) \right\}$$

where $t(a)$ = time available for disturbance growth,

U = rise velocity of the bubble which is a function of the bubble size and the liquid phase properties, and

$d_{(bubble)}$ = diameter of the sphere with the same volume as the bubble.

Disturbances grow with time as does $\exp(\alpha t)$ where α is a parameter characteristic of the system and the disturbance wavelength. The analysis of interfacial motions to determine α is algebraically complex. Fortunately, for gas/liquid systems, the viscosity and the density of the gas are negligible in comparison to the physical properties of the liquid. For this special case, the parameter α can be determined from:

$$\left[\left(\frac{2\pi}{\lambda} \right)^2 + \frac{\alpha \rho_\ell}{\mu_\ell} \right]^2 \left(\frac{\lambda}{2\pi} \right)^4 + \frac{\lambda^2}{2\pi^2} \left[\left(\frac{2\pi}{\lambda} \right)^2 + \frac{\alpha \rho_\ell}{\mu_\ell} \right]$$

$$- \left[\left(\frac{2\lambda}{\rho} \right) \frac{2\pi}{\lambda}^2 + \frac{\alpha \rho_\ell}{\mu_\ell} \right]^{1/2} + \frac{\lambda \rho_\ell}{2\pi \mu_\ell^2} \left(\sigma - \frac{g \rho_\ell \lambda^2}{(2\pi)^2} \right) = 0 \quad .$$

Plots of $t(a)\alpha$ against the disturbance wavelength for various sized bubbles rising through a steel melt are shown in

Figure 33. Surface tension forces resist interfacial motion for small wavelength motions and keep t(a)α small. Similarly, t(a)α is small for long wavelength disturbances because viscous forces damp interfacial motions. Between these extremes t(a)α as a function of the disturbance wavelength passes through a maximum. If the product α(maximum)t(a) is large enough the bubble will shatter. Empirical evidence suggests that for gas bubbles rising in a liquid the product must exceed about 3.8 for a bubble to be unstable.

Figures 34 and 35 show the unstable regime for gas bubbles rising in metallic and oxidic core debris phases, respectively. In these figures, the unstable regimes are shaded. The limits of the shaded regions were found by determining when α(maximum)t(a) just equaled 3.8. Bubbles rising in the metallic phase become unstable when their diameters exceed about 7 cm. Bubbles are unstable in the oxide phase when their diameters exceed about 6 cm. These unstable dimensions exceed those derived with the Levich criterion by about a factor of two. In part, larger bubbles are predicted because the kinetics of disturbance growth is recognized in this development.

If bubbles of gas at the melt/concrete interface are 2-3 cm in diameter, then for most situations these bubbles will not grow sufficiently during their rise through the core debris to become unstable. This, however, is true only for single, isolated bubbles. There is evidence that in bubble swarms, factors not considered in the above analysis conspire to keep bubbles small.

2. Mass Transport in the Condensed Phase to a Bubble

The development of the vaporization kinetics equation above included the rate of mass transport to a bubble in terms of a mass transport coefficient. This type of empirical description implies that a Sherwood number relationship for bubbles rising in a liquid is to be developed. There are, however, several factors to be considered in developing such relationships. It is apparent from the preceding discussions that bubble shape and the flow regime will affect mass transport. In addition, it is likely that bubbles flowing through a melt in a swarm will behave differently with respect to mass transport than single, isolated bubbles. It is also true that bubbles entering a liquid experience a transient period of mass transfer which may differ from the mass transfer that occurs when bubbles are well-established in a liquid. It might be expected that mass transfer rates would be higher immediately following a step change in the ambient conditions of a bubble than well

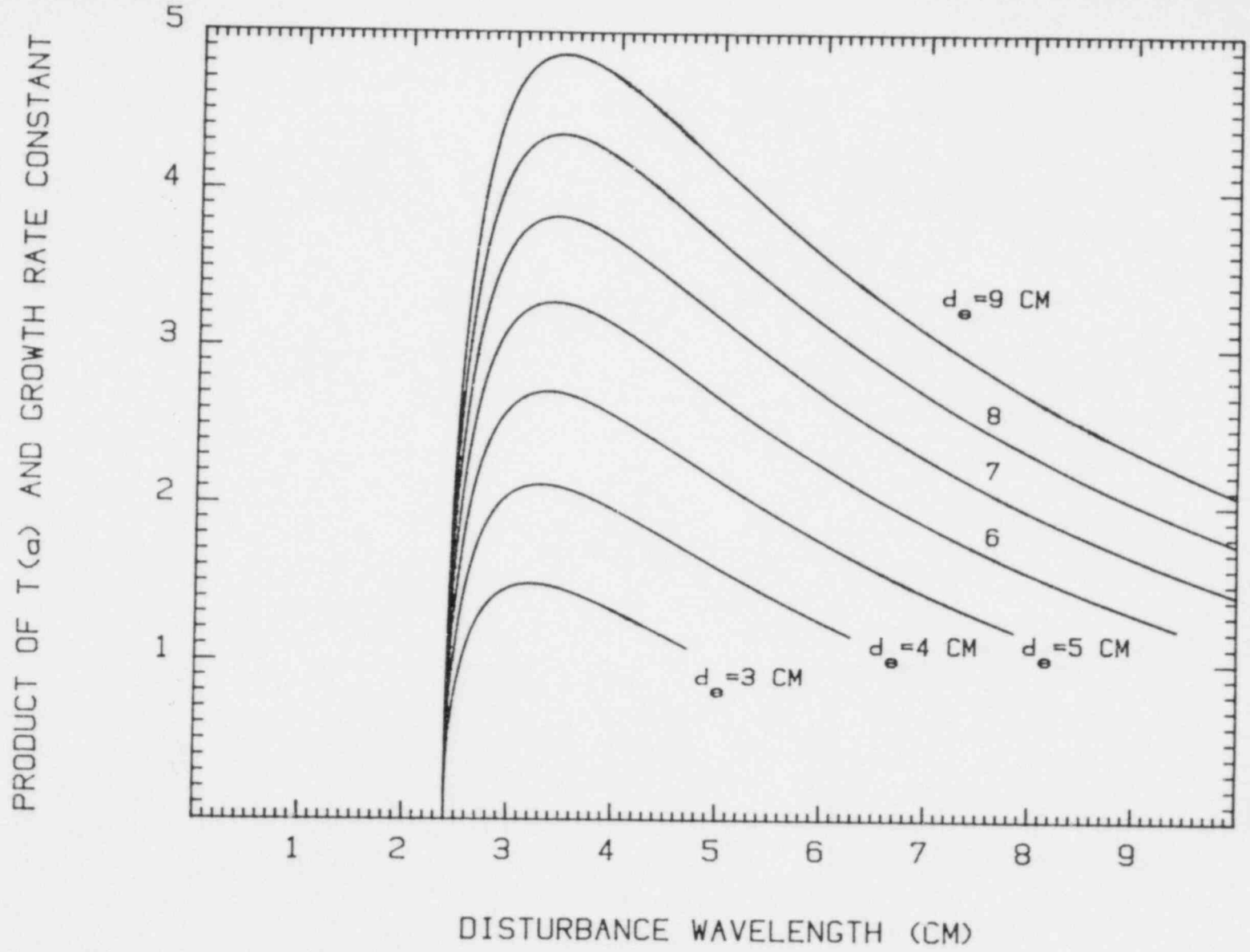

Figure 33. Variation in the Product of the Time Available for Growth, t(a), and the Disturbance Growth Rate Constant, α, With Wavelength for Bubbles of Various Sizes

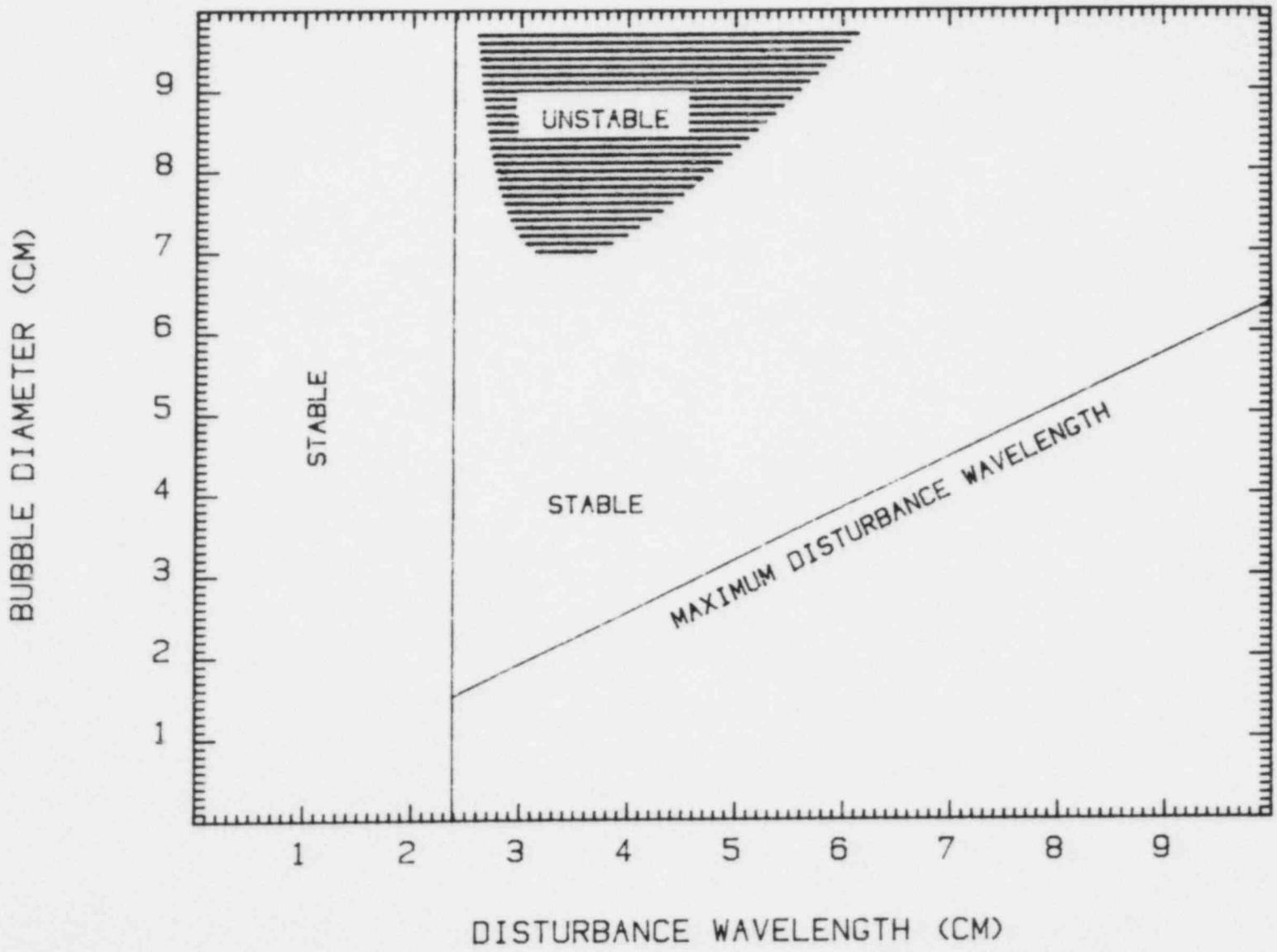

Figure 34. Stability Regime for Gas Bubbles in a Metallic Melt

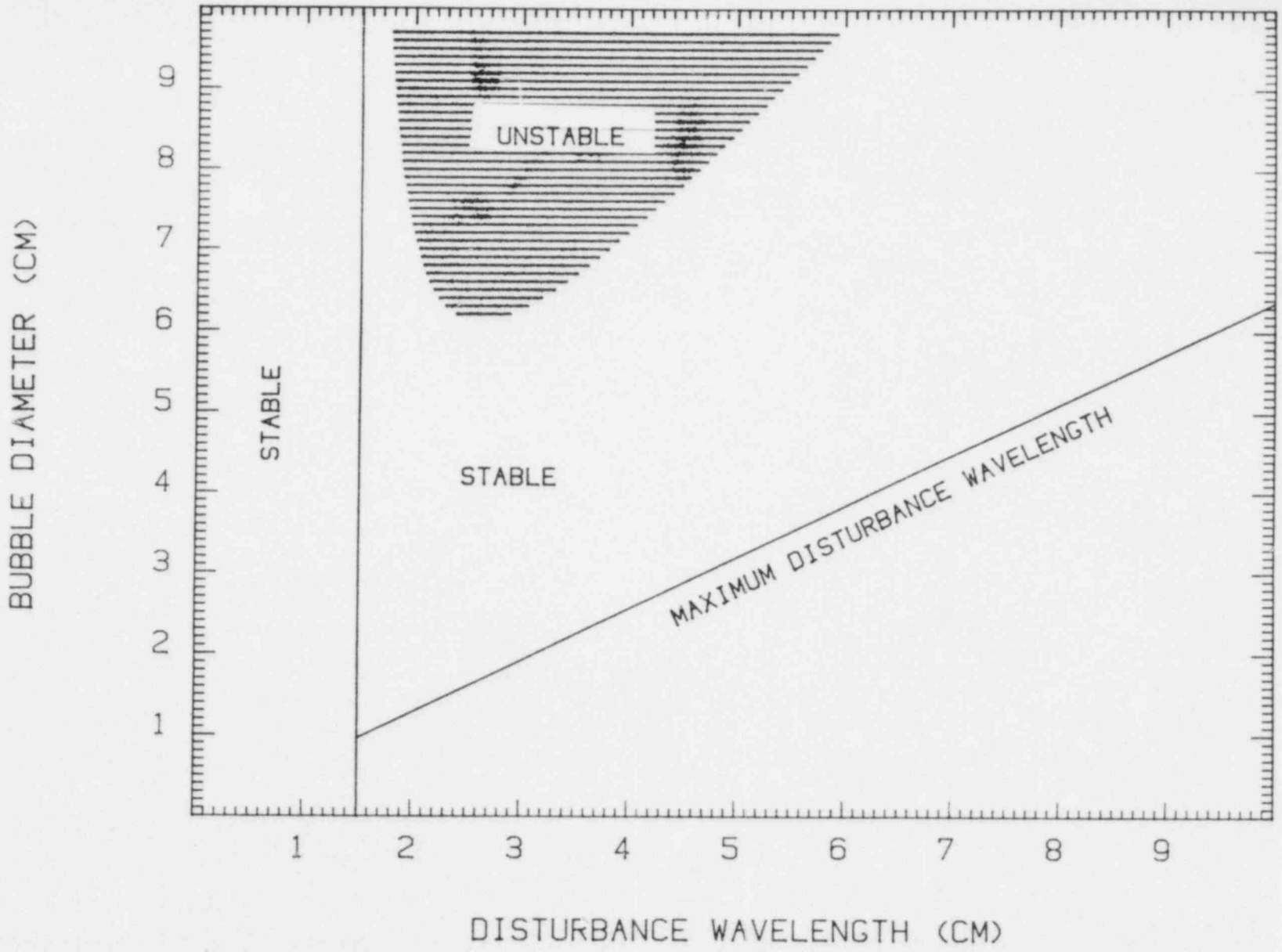

Figure 35. Stability Regime for Gas Bubbles in an Oxidic Melt

after this change has occurred. As a result the Sherwood number may be a function of time until this transient has been damped.

In this subsection, mass transport to single bubbles of various shapes will be discussed. This will be followed by a discussion of the effects of sudden changes in the ambient environment on mass transport to single bubbles. Finally, the effects of bubble swarms on mass transfer will be described.

a. Single Bubble Correlations

Gas bubbles of interest here are axisymmetric bodies. Consider the geometry and coordinate system of such an axisymmetric body shown in Figure 36. The continuity equation for this body is given by

$$\frac{\partial UR}{\partial X} + \frac{\partial VR}{\partial Y} = 0$$

where $U = u/U_T$,

$V = v/U_T$,

$X = x/R_e$,

$Y = y/R_e$,

$R = r/R_e$, and

$R_e = 0.5d_e$.

Then using the thin boundary layer approximation

$$U \frac{\partial C}{\partial X} + V \frac{\partial C}{\partial y} = \frac{2}{Pe} \frac{\partial^2 C}{\partial Y^2}$$

where C is the dimensionless concentration of the volatile constituent of interest and is defined by C(X,Y)/C(bulk), where C(bulk) is the concentration at a point far away from the bubble. If Sc >> 1, which it is for the conditions of interest here, then the dimensionless tangential fluid velocity around the body can be expressed as a Taylor expansion referenced to the velocity at the gas-liquid interface (Y = 0):

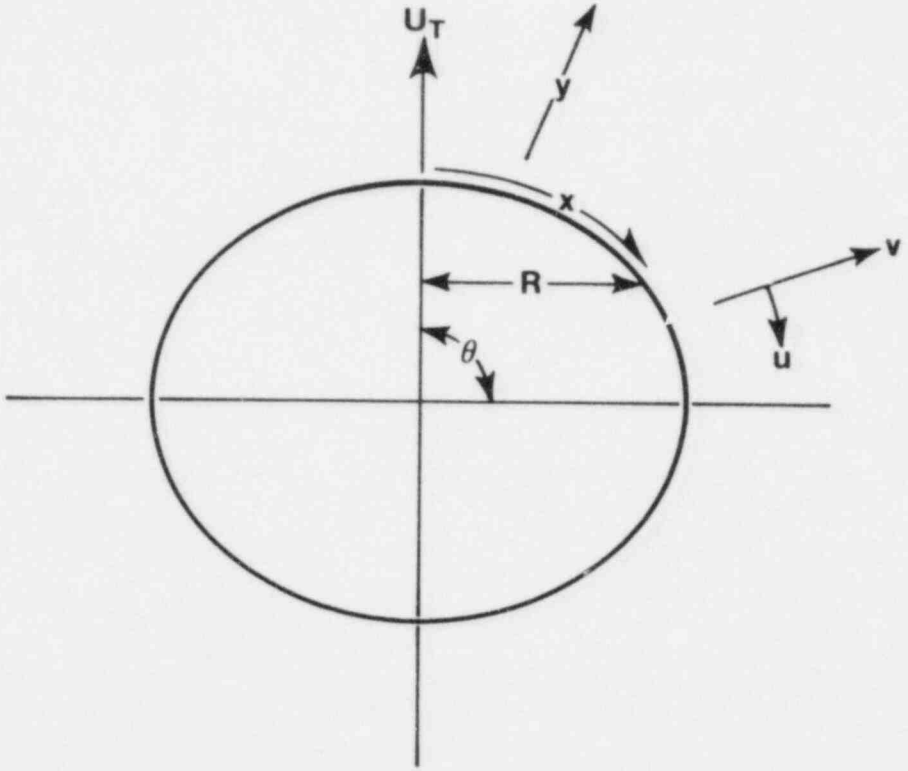

Figure 36. Coordinate System for Analysis of Mass Transport to an Axisymmetric Body of Revolution

$$U(Y) = U(0) + \left.\frac{\partial U}{\partial Y}\right|_{Y=0} Y = U(0) + U'(0)Y \quad .$$

The thin boundary layer equation is then

$$(U(0)+U'(0)Y)\frac{\partial C}{\partial X} - \frac{1}{R}\frac{\partial}{\partial X}\left\{\left(U(0)Y + \frac{U'(0)Y^2}{2}\right)R\right\}\frac{\partial C}{\partial Y}$$

$$= \frac{2}{Pe}\frac{\partial^2 C}{\partial Y^2} \quad .$$

This equation can be solved in the two limiting situations:[201]

a. The interface between the gas and the liquid is rigid so that $U(0) = 0$.

Then the differential equation becomes:

$$U'(0)Y\frac{\partial C}{\partial X} - \frac{1}{R}\frac{\partial}{\partial X}\left(\frac{U'(0)Y^2R}{2}\right)\frac{\partial C}{\partial Y} = \frac{2}{Pe}\frac{\partial^2 C}{\partial Y^2} \quad .$$

This equation transforms to:

$$\eta\frac{\partial C}{\partial \phi} = \frac{\partial^2 C}{\partial \eta^2}$$

where $\eta = Y(U'(0)R)^{1/2}$ and

$$d\phi = \frac{2(U'(0)R)^{3/2}}{Pe\ U'(0)}\ dx.$$

The solution of this differential equation is

$$C = 1 - \frac{\int_0^{\zeta} \exp[-z^3]\ dz}{\Gamma(4/3)}$$

where $\zeta = \eta/(9\phi)^{1/3}$ and

$\Gamma(4/3)$ = gamma function of 4/3 $\cong$ 0.893.

Then

$$Sh = 0.641\left(\frac{\pi d_e^2}{A}\right)\left[\int_0^X (U'(0)R)^{1/2} R\, dx\right]^{2/3} Pe^{1/3}$$

where A is the actual surface area of the axisymmetric body and d_e is the diameter of the sphere with the same volume as the axisymmetric body.

b. The interface between the gas and the liquid is mobile and moves rapidly relative to the translation velocity of the bubble.

Then,

$$U(0) >> 1/2\ U'(0)Y$$

and the differential equation becomes:

$$U(0)\frac{\partial C}{\partial X} - \frac{1}{R}\frac{\partial}{\partial X}(U(0)YR)\frac{\partial C}{\partial Y} = \frac{2}{Pe}\frac{\partial^2 C}{\partial Y^2} .$$

This differential equation can be transformed to:

$$\frac{\partial^2 C}{\partial \zeta^2} + \partial\zeta\frac{\partial C}{\partial \zeta} = 0$$

where $\zeta = \eta/2\sqrt{\phi}$.

$\eta = YU(0)R$, and

$$d\phi = \frac{2(U(0)R)^2}{PeU(0)}\, dx.$$

The solution to the differential equation is

$$C = 1 - \frac{2}{\pi} \int_0^{\zeta} \exp(-z^2)\, dz \quad .$$

Then,

$$Sh = \left(\frac{2}{\pi}\right)^{1/2} \left(\frac{\pi d_e^2}{A}\right) \left[\int_0^X U(0) R^2\, dx\right]^{1/2} Pe^{1/2} \quad .$$

Solution of the integral for the case of rigid spheres yields:

$$Sh = 0.99\ Pe^{1/3} \qquad \text{for } Re < 1$$

$$Sh = 0.62\ Re^{1/2} Sc^{1/2} \qquad \text{for } Re > 1 \quad .$$

The coefficient for the correlation at high Reynolds number is obtained[114] by neglecting flow separation at the sphere's surface. In fact, separation will occur at higher Reynolds numbers. If separation is assumed to occur at an angle of 108° to the direction of flow,* then the coefficient in the correlation is reduced to 0.56. In view of the general uncertainty in bubble behavior and values of Re and Sc in the correlation, the uncertainty in questions of flow separation are not significant.

Clift et al.[92] suggest that available numerical analyses of mass transfer to a rigid sphere can be correlated by the expression

$$\frac{(Sh-1)}{Sc^{1/3}} = \left(1 + \frac{1}{ReSc}\right)^{1/3} Re^{0.41}$$

---

*Some correlations for the angle of flow separation are:[92]

$$\theta = 180 - 42.5[\ln(Re/20)]^{0.483} \qquad 20 < Re < 400$$

$$\theta = 78 + 275\ Re^{-0.37} \qquad 400 < Re < 3 \times 10^5$$

for $1 \leq Re \leq 400$ and $0.25 \leq Sc \leq 100$.

Solution of the above integral for fluid spheres yields

$$Sh = 0.65\ Pe^{1/2} \qquad \text{for } Re < 1$$

$$Sh = 1.13\left(1 - \frac{2.96}{Re^{1/2}}\right)^{1/2} Pe^{1/2} \qquad 100 \leq Re \leq 400 \ .$$

Others[115,116] have obtained

$$Sh = 1.128\left(1 - \frac{2.89}{Re^{1/2}}\right)^{1/2} Pe^{1/2}$$

using boundary layer theory. Asymptotic solutions by other numerical methods for $Sc \to \infty$ are:[117]

$$Sh = 1.128\left[1 - \frac{0.6667}{\left\{1 + \left(0.1415\ Re^{2/3}\right)\right\}^{3/4}}\right]^{1/2} Pe^{1/2} \ .$$

A solution for the mass transfer to ellipsoidal bubbles that do not oscillate is given by:[115]

$$Sh = 1.128\ Pe^{1/2}\ g(E)/f(E)$$

where $$g(E) = \left[\frac{8(E^2-1)^{3/2}}{3E^{10/3}\left\{\sin^{-1}\left[(E^2-1)^{1/2}/E\right] - \frac{(E^2-1)^{1/2}}{E^2}\right\}}\right]^{1/2} ,$$

and

$$f(E) = 1 + \frac{1}{2E(E^2-1)^{1/2}}\ \ell n\left[\frac{E + (E^2-1)^{1/2}}{E - (E^2-1)^{1/2}}\right]$$

where the Sherwood and the Peclet numbers are defined using d_e rather than 2a as the characteristic dimension.

Some attempts have been made to define the mass transport coefficients for ellipsoidal particles that do oscillate.[92] Unfortunately, solution of the resulting equations requires information such as the frequency of oscillation and the ratio of the maximum to the minimum surface area during an oscillation cycle. Such detailed information would be most difficult to determine for gas bubbles sparging through a core melt. A simple estimate of the mass transport to an oscillating bubble is:[92]

$$Sh = \frac{2.41}{\sqrt{\pi}} \sqrt{\frac{d_e f}{D}}$$

where $f = (f_N + f_w)/2$,

f_N = natural vibration frequency, and

f_w = frequency of vortex shedding.

For spherical cap bubbles, mass transfer to the curved and the flat surfaces must be considered. Mass transfer to the curved surface is, however, much more efficient. The conventional mass transport correlation:[114]

$$Sh = 1.28\ Pe^{1/2}$$

where both the Sh and the Pe numbers are based on d_e is, in fact, an equation just for mass transfer to the curved surface. Szekeley[65] suggests that mass transport will be about 20 percent greater if the flat surface is considered even though the area of the flat surface is almost equal to the area of the curved surface.

Combining the above mass transfer correlation with the Davies-Taylor formula for the rise velocity of spherical cap bubbles, yields

$$K_m = 1.08 g^{1/4} D^{1/2} d_e^{-1/4} \quad .$$

This equation may be compared to an equation developed by Baird:[118]

$$K_m = \frac{0.975 g^{1/4} D^{1/2}}{d_e^{1/4}}$$

which accounts for mass transfer to the flat surface of the spherical cap bubble. The VANESA model uses the Baird formula.

b. Effects of Sudden Changes in Composition

At two points in the sparging process bubbles injected into molten core debris experience sudden changes in the ambient composition:

1. When bubbles are first formed in the melt, and

2. When bubbles cross the metallic/oxide phase boundary.

Following these sudden changes in the ambient composition, transient effects should make mass transport coefficients for the bubble time-dependent. Detailed analyses of this effect have only been reported for spheres. These results should give an indication of the effects for other bubble shapes.

For rigid bubbles, following a step change in ambient conditions, the asymptotic solution for $Pe \to \infty$ and $Re < 1$ is[121]

$$Sh = Pe^{1/3}\left[0.956 + \left(\frac{2}{\pi\tau}\, Pe^{-1/3}\right)^5\right]^{1/5}$$

where $\tau = 4Dt/d^2$. A similar equation for spheres with internal gas circulation is[119,120]

$$Sh = Pe^{1/2}\left[0.117 + \left(\frac{2}{\pi\tau Pe}\right)^5\right]^{1/5} .$$

For the case of bubbles with internal gas circulation, the Sherwood number has evolved to within 10 percent of the steady-state value after a time, t, given by:[92]

$$t = \frac{0.9d}{U_T} .$$

That is, the bubble needs to rise only about one diameter to be in a condition of nearly steady-state mass transfer.

For spheres with internal gas circulation and Re > 70, the time-dependent Sherwood number is given by:

$$Sh = Pe^{1/2}\left[1.829 + \left(\frac{2}{\pi\tau Pe}\right)^5\right]^{1/5} .$$

Again, it is apparent that transient effects caused by the sudden changes are dissipated after the bubble has moved a few diameters.

c. Effects of Bubble Swarms

The preceding discussions of mass transfer to bubbles have considered single, isolated bubbles. Intuition might suggest that swarms of bubbles would behave differently. Calderbank and Moo-Young[122] have examined experimental data for bubble swarms produced in sieve and sintered plate columns. They found two correlations that represented these data well:

1. For $d_e < 0.25$ cm

$$Sh = 0.31Ra^{1/3} \qquad \text{or } K_m Sc^{2/3} = 0.31\left(\frac{\mu_\ell g}{\rho_\ell}\right)^{1/3} .$$

2. For $d_e > 0.25$ cm

$$Sh = 0.42Sc^{1/2}Gr^{1/3} \qquad \text{or } K_m Sc^{1/2} = 0.42\left(\frac{\mu_\ell g}{\rho_\ell}\right)^{1/3} .$$

A comparison of the Baird formula for mass transfer to spherical cap bubbles, the Calderbank and Moo-Young correlation for bubbles larger than 0.25 cm in swarms, and data for CO_2 dissolution from bubble[122] is shown in Figure 37. The Baird formula and the Calderbank and Moo-Young correlation bracket these data. Using the Baird formula, then, may lead to an underestimate of the condensed phase mass transport to the bubbles.

LeClair and Hamielec have derived theoretical equations for the mass transfer to swarms of bubbles.[284] Their correlations are:

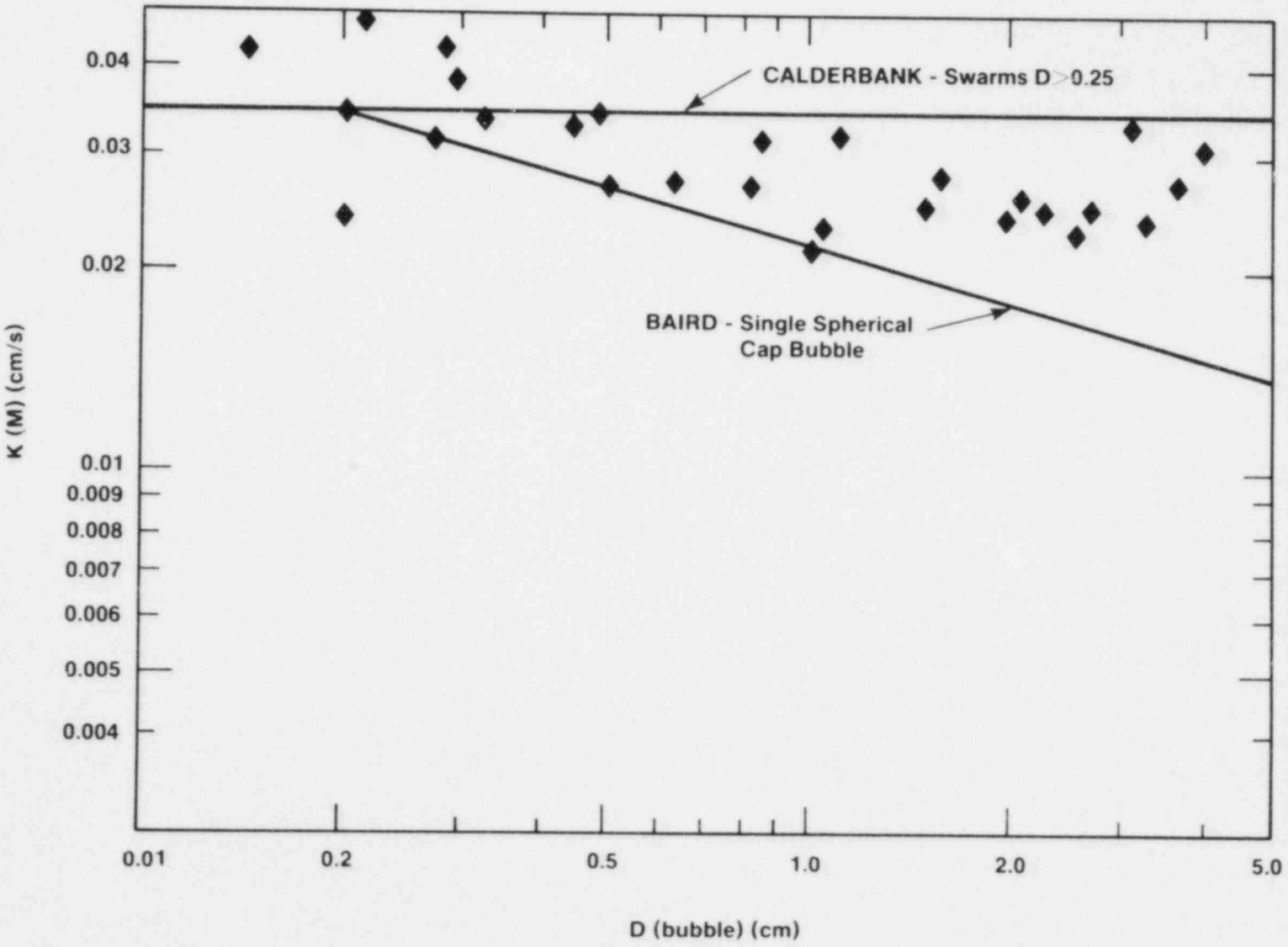

Figure 37. Comparison of Data for Mass Transport From Bubble Swarms With Predictions From the Calderbank and Moo-Young Correlation and With Predictions From the Baird Model

$$Sh = \begin{cases} \dfrac{1.13\ Pe^{1/2}}{\sqrt{\alpha}} & \text{for } Re > 1000 \\ \dfrac{2.213\ Pe^{1/2}}{\sqrt{(\alpha)}\ Re^{0.108}} & \text{for } 10 < Re < 1000 \\ \dfrac{(0.65 + 0.06\ Re^{1/2})\ Pe^{1/2}}{\left[\dfrac{5 - 6(1-\alpha)^{1/3} + (1-\alpha)^2}{5\alpha}\right]^{1/2}} & \text{for } Re < 10 \end{cases}$$

where α is the gas holdup.

Calderbank[114] claims that the mass transport coefficients for large bubbles decrease with pool height and bubble residence time. In pools of sufficient depth, the mass transport coefficients approach values that would be obtained from the correlation for small bubbles. The data available to Calderbank were, however, largely for aqueous systems in which contamination by surface active agents might have occurred. His observation concerning the effects of pool height and residence time, which have been noted by others,[123,124] may reflect the accumulation of surface active agents at the bubble surface and the concomitant retardation of internal gas circulation.

Calderbank[114] also suggested that the mass transport coefficients may be affected by the gas flow rate. As gas flows become high, hindered motions of the bubbles causes mass transport rates to fall to values predicted with the small bubble correlations. He characterized gas flow rates in terms of Crozier's F-factor which is a dimensional quantity defined by

$$F = V_s\sqrt{\rho_g}$$

where V_s = superficial gas velocity in ft/sec and

ρ_g = density of the gas in lb/ft^3.

Calderbank found that mass transport coefficients for large bubbles approached values found from his small bubble correlation when $F > 1.5$ or when superficial gas velocities were about 5 ft/sec (152 cm/s). If these observations can be translated from aqueous systems to high temperature melt

systems, then the gas flow effects on mass transfer will be important only during very early stages in the core debris/concrete interaction.

3. Internal Resistance to Mass Transport

The equation for vaporization kinetics described above was developed including a resistance to mass transport within the vapor phase. This resistance was expressed in terms of a mass transport coefficient, K_g. Little work has been done on the resistance to mass transport of vapors within rising bubbles. This is probably because such resistance is exceptionally difficult to measure and not, typically, of great importance.

Based on simple dimensional analysis it would be expected that

$$K_g = a\left(\frac{D_{AB}}{d_e}\right) + b$$

where D_{AB} is the diffusion coefficient of the vapor species in question in the gas within the bubble. The parameters a and b could, of course, vary with details of bubble behavior.

Newman[125] has analyzed the classic diffusion problem for a stagnant sphere which yields:

$$\frac{K_g d_e}{D_{AB}} = \frac{2\pi^2}{3} \frac{\sum_{n=1}^{\infty} \exp[-n^2\pi\tau]}{\sum_{n=1}^{\infty} \frac{1}{n^2} \exp[-n^2\pi\tau]}$$

where $\tau = 4D_{AB}t/d_e^2$ and

t = time.

For long times this result simplifies to

$$K_g = \frac{2\pi^2}{3} \frac{D_{AB}}{d_e} = \frac{6.58D_{AB}}{d_e} \quad .$$

For short times,

$$K_g = 2\sqrt{D_{AB}/\pi t} = 1.13\left(D_{AB}/t\right)^{1/2} \quad .$$

Koenig and Brink[126] have analyzed the mass transport within a a sphere when gases are circulating. For long times,

$$K_g = 17.66\ D_{AB}/d_e \quad .$$

Calderbank[114] recommends for short contact times,

$$K_g = 1.7\left(D_{AB}/t\right)^{1/2} \quad .$$

Comparison of the Koenig-Brink results with those obtained by Newman suggest that the rather mild gas circulation within spherical gas bubbles causes an effective increase in the gas diffusion coefficient of about a factor of 2.25 above the molecular value.

Oscillations within the bubble can produce, presumably, higher effective gas mass transport within a bubble. Hondlos and Baron[253] analyzed this problem theoretically and obtained

$$K_g = 0.00375\ U_T \quad .$$

This surprising result that the gas phase mass transfer is independent at the gas phase diffusion coefficient has not been universally accepted. Cliff, Grace, and Weber[92] suggest:

$$\frac{K_g d_e}{D_{A,M}} = \frac{2.41}{\sqrt{\pi}} \sqrt{\frac{d_e\ f}{D_{A,M}}}$$

where $f = (f_N + f_w)/2$,

f_N = natural vibration frequency of the bubble,

f_w = frequency of vortex shedding, and

$D_{A,M}$ = diffusion coefficient of the gas.

The VANESA model uses the gas phase mass transport coefficient $K_g = 2D_{AB}/d_e$. Based on the above discussions, it is clear that the model does not overestimate gas phase mass transport.

4. Condensed Phase Diffusion Coefficients

To utilize the various mass transport correlations derived above, it is necessary to know the diffusion coefficient for the species of interest. Such liquid phase diffusion coefficients are seldom measured for high temperature systems and certainly have never been measured for melts of the type of interest here.

Theoretical considerations have suggested that a spherical solute of molecular radius r_A in a solvent of viscosity μ_B will have a diffusion coefficient given by[130]

$$D_{AB} = \frac{RT}{6\pi\mu_B r_A} .$$

This simple equation cannot be expected to apply to real situations significantly different than those assumed for its derivation. But, it has established a framework for empirical correlation of diffusion coefficient data:

$$\frac{D_{AB}\mu_B}{T} = f \text{ (solute and solvent sizes)} .$$

Most of the data available for correlation are for relatively low temperature, organic systems. As a result, many of the correlations involve data that are not readily obtained for condensed phase constituents of interest here.[131] Some empirical correlations that appear attractive are:

1. Wilke-Chang Correlation:[132]

$$D_{AB} = 7.4 \times 10^{-10} \frac{\left(\Phi M_B\right)^{1/2} T}{\mu_B \left(V_A\right)^{0.6}}$$

where M_B = molecular weight of the solvent,

μ_B = viscosity of the solvent (poise), and

V_A = molar volume of the solute

and ϕ is a parameter to describe association of the solvent molecules. Here, however, ϕ can be used to adjust the model to accommodate the unfamiliar circumstances of higher temperatures.

2. Scheibel Modification of the Wilke-Chang Correlation:[133]

$$D_{AB} = 8.2 \times 10^{-10}\left[1 + \left(\frac{3V_B}{V_A}\right)^{2/3}\right] T \Big/ \mu_B V_A^{1/3}$$

where V_B = molar volume of the solvent.

3. Reddy Doraiswamy Correlation:[134]

$$D_{AB} = \frac{K M_B^{1/2} T}{\mu_B \left(V_A V_B\right)^{1/3}}$$

where $$K = \begin{cases} 1 \times 10^{-9} \text{ for } \dfrac{V_B}{V_A} \leq 1.5 \\ \\ 8.5 \times 10^{-10} \text{ for } \dfrac{V_B}{V_A} \geq 1.5. \end{cases}$$

It must be emphasized that these correlations were developed from data for systems radically different than those of interest here. A likely consequence of this is that the coefficients for the correlations may be inappropriate. Some data for systems that more closely approximate those of interest here are:[62]

Solvent	Solute	T (K)	$D_{AB}(cm^2/s)$
Fe + 2.5 w/o C	Fe	1673	9×10^{-5}
Fe + 3.5 w/o C	C	1823	6×10^{-5}
40 w/o CaO, 20 w/o Al_2O_3, 40 w/o SiO_2	SiO_2	1703	1×10^{-7}
43 w/o CaO, 22 w/o Al_2O_3, 35 w/o SiO_2	FeO	1773	0.3×10^{-5}
61 w/o FeO, 39 w/o SiO_2	Fe	1548	9.6×10^{-6}

The Scheibel modification of the Wilke-Chang correlation predicts these observed diffusion coefficients to within about a factor of ten.

After obtaining expressions for binary diffusion coefficients, one is immediately confronted with a difficulty. The melts of interest here are far from binary melts. Consequently, what is needed is not a binary diffusion coefficient, but an effective binary diffusion coefficient for a multicomponent mixture. Such effective binary diffusion coefficients, D_{Am}, are readily defined:

$$\frac{1}{\rho_{molar} D_{Am}} = \frac{\sum_{j=1}^{N} \left(1/\rho_{molar} D_{Aj}\right)\left(X_j N_A - X_A N_j\right)}{N_A - X_A \sum_{j=1}^{N} N_j}$$

where D_{Aj} = binary diffusion coefficients for constituent A in pure constituent j,

ρ_{molar} = molar density of the mixture,

N = number of constituents in the mixture,

X_j = mole fraction of constituent j in the mixture, and

N_j = molar flux of constituent j in the mixture.

Obviously, this equation would be quite difficult to solve for the circumstances of core debris interacting with

concrete. Fortunately, the equation simplifies for certain situations:

1. When the mixture consists of a major constituent B and all other constituents are at low concentrations

$$D_{Am} = D_{AB} \quad .$$

2. When all D_{ij} are nearly the same

$$D_{Am} = D_{ij} \quad .$$

3. When all species save A move at similar velocities

$$\frac{1 - X_A}{D_{Am}} = \sum_{j \neq A}^{N} \frac{X_j}{D_{Aj}} \quad .$$

The second of these special situations seems particularly likely to apply approximately to the core melt situation.

5. Gas Phase Diffusion Coefficients

Theoretical and experimental studies of binary gas diffusion coefficients have been extensive indeed.[143] Most theoretical developments produce expressions of the type

$$D_{AB} = \frac{1.858 \times 10^{-3} \; T^{3/2} \; (M_A + M_B)/M_A M_B \; ^{1/2}}{P \sigma_{AB}^2 \Omega_D}$$

where σ_{AB} = characteristic dimension of molecular interactions in the gas phase and

Ω_D = diffusion collision integral.

The nature of the diffusion collision integral, Ω_D, and σ_{AB} depend on the nature of the interatomic forces thought to exist between molecules. When interactions are of the

dispersive type and a Lennard-Jones potential is used to describe these interactions:

$$\Omega_D = \frac{A}{T_R^B} + \frac{C}{\exp(DT_R)} + \frac{E}{\exp(FT_R)} + \frac{G}{\exp(HT_R)}$$

where $T_R = kT/\varepsilon_{AB}$,

k = Boltzmann's constant,

$\varepsilon_{AB} = (\varepsilon_A \varepsilon_B)^{1/2}$,

ε_A, ε_B = parameters characteristic of molecular interactions in pure A or pure B, and

$A = 1.06036$ $B = 0.15610$ $C = 0.1930$

$D = 0.47635$ $E = 1.03587$ $F = 1.52996$

$G = 1.76474$ $H = 3.89411$ $\sigma_{AB} = 1/2(\sigma_A + \sigma_B)$.

The theoretical treatments of the diffusion coefficient are appropriate for nonpolar gases. Treatments of polar gases are usually developed as a perturbation to the treatment of nonpolar gases. The collision integral for polar gases is taken to be:[131]

$$\Omega_D(\text{polar}) = \Omega_D(\text{nonpolar}) + \frac{0.19}{T_R} \delta_{AB}^2$$

where $\delta_{AB} = (\delta_A \delta_B)^{1/2}$,

$\delta_A = 1.94 \times 10^3 \, \mu_A^2 / V_b T_b$,

μ_A = dipole moment of gas species A in Debyes,

$V_b(A)$ = molar volume of pure, condensed A at its normal boiling point, $T_b(A)$, and

$\frac{\varepsilon(A)}{k} = 1.18 \, (1 + 1.3 \, \delta_A^2) T_b(A)$.

The collision cross-section is taken to be the geometric average:

$$\delta_{AB} = (\delta_A \delta_B)^{1/2}$$

where $$\delta_A = \left[\frac{1.585 V_b(A)}{1+1.13\ \delta_A^2}\right]^{1/3}$$

rather than usual arithmetic average of the pure species cross-sections.

These equations have been quite successful for predicting diffusion coefficients at pressures less than 10 atmospheres. But, the equations rely on knowing characteristics of the pure gases that will not be available for many gas phase species that arise during core debris interactions with concrete. Even approximation expressions such as

$$\sigma_A = 1.18\ V_A^{1/3} \qquad \varepsilon/k = 1.15\ T_b$$

do not help since the boiling points of many gas phase species that do not exist as condensed species are not easily defined.

The absence of suitable data needed to use expressions for the binary diffusion coefficients derived from theories of molecular interactions leads to the use of empirical correlations. Many such correlations exist and they have functional forms reminiscent of the theoretical expressions. These correlations have been derived, of course, using data for gases and vapors quite different than those of interest here.

One of the earliest empirical correlations is the Gilliland equation:[144]

$$D_{AB} = \frac{0.0043\ T^{3/2}}{P\left(V_A^{1/3}+V_B^{1/3}\right)^2}\left(\frac{M_A+M_B}{M_A M_B}\right)^{1/2} .$$

The Andrusow correlation[145] has enjoyed some success:[146]

$$D_{AB} = \frac{0.0007895\ T^{1.78}}{P\left(V_A^{1/3}+V_B^{1/3}\right)^2}\ \frac{1+\sqrt{M_A+M_B}}{\sqrt{M_A M_B}} \quad .$$

Recently, Singh and Singh[147] have proposed the equation:

$$D_{AB} = \frac{0.00279\ T^{1.622}\left(\frac{M_A+M_B}{M_A M_B}\right)^{1/2}}{P\left(V_A^{1/3}+V_B^{1/3}\right)^2} \quad .$$

The difficulty with diffusion in multicomponent mixtures encountered with diffusion in liquids is also encountered with diffusion in gases. The gases in bubbles rising through core debris will be predominantly CO and H_2. These gases are, of course, relatively light. A suitable approximation for estimating the diffusion coefficients of vapors in multicomponent mixtures is:

$$\frac{1 - P_A/P_T}{D_{A,m}} = \frac{P_{CO}/P_T}{D_{A,CO}} + \frac{P_{H_2}/P_T}{D_{A,H_2}}$$

where $D_{A,m}$ is the diffusion coefficient of A in the mixture, P_i ($i = H_2$ or CO) is the partial pressure of the i^{th} constituent of the gas, and P_T is the total pressure. Molecular volumes of CO and H_2 are about 30.7 and 14.3 cm^3, respectively.

6. Surface Vaporization

Once a volatile constituent of the condensed phase reaches a free surface, it will contribute to the vapor only after it has undergone a transformation from a condensed species to a vapor species. Two possibilities can be envisaged for this transformation. On the one hand, the volatile constituent of the condensed phase may have the same molecular stoichiometry as the gas phase species in question. The transformation to a vapor species is then merely a matter of overcoming the attractive interactions of the condensed phase species with its neighbors on the surface. On the other hand, the molecular stoichiometry of the surface species may

not be similar to that of the vapor species. Then, the stoichiometry must change at some point in the vaporization process. Exactly how and when the alteration in molecular stoichiometry occurs is not readily determined. One possibility is that the alteration occurs at the surface. Then the altered species undergoes the condensed-to-vapor phase transition.

The alteration of the stoichiometry of a surface species can be the result of a series of chemical reactions. Consider the hypothesized chemical kinetics scheme for the transformation of surface ruthenium to surface RuO:

$$\text{Ru(surface)} \xrightarrow{K_0} \text{Ru*(surface)}$$

$$\text{surface site} + \text{H}_2\text{O(v)} \underset{K_{-1}}{\overset{K_1}{\rightleftarrows}} \text{H}_2\text{O(surface)}$$

$$\text{surface site} + \text{H}_2\text{O(surface)} \xrightarrow{K_2} \text{H(surface)} + \text{OH(surface)}$$

$$\text{Ru*(surface)} + \text{OH(surface)} \xrightarrow{K_3} \text{RuO(surface)} + \text{H(surface)}$$

$$2\text{H(surface)} \underset{K_{-4}}{\overset{K_4}{\rightleftarrows}} \text{H}_2\text{(surface)} + \text{surface site}$$

$$\text{H}_2\text{(surface)} \underset{K_{-5}}{\overset{K_5}{\rightleftarrows}} \text{H}_2\text{(v)} + \text{surface site} \quad .$$

Overall:

$$\text{Ru(surface)} + \text{H}_2\text{O} \rightarrow \text{RuO(surface)} + \text{H}_2 \quad .$$

In this scheme, Ru*(surface) denotes an activated surface ruthenium atom capable of reacting with a surface hydroxyl

group. Rate constants for the elementary steps in the kinetic scheme are denoted by K_j. An overall rate expression for the transformation could be formulated from this scheme. But, quantitative evaluation of the rate would be quite difficult since, in general, there are not data suitable for the evaluation of the rate constants in the kinetic scheme. Depending on the values of the rate constants, this transformation process could be limited by any of a variety of factors. The activation of surface ruthenium, the availability of surface sites for H_2O adsorption, the vapor phase concentration of H_2O, as well as the kinetic rate of ruthenium reaction with hydroxyl could limit the rate of transformation. A further complexity in the evaluation of the kinetic scheme comes about because the concentration of surface sites arises explicitly in the rate expressions. This means that this kinetic scheme is coupled with kinetic schemes for surface transformations of all other chemical species. Quantitative evaluation of the kinetic network is then a very formidable task, indeed.

Were interests in the vaporization of radionuclides from solid surfaces, the evaluation of surface kinetic networks of the type shown for the Ru to RuO transformation would be difficult to avoid. Here, interests are in the vaporization from high temperature liquids. Chemical reaction rates, steam adsorption rates, and hydrogen desorption rates are fast, typically, at the temperatures of interest here. Further, surfaces are continuously renewed in the liquid systems of interest so contamination and "poisoning" of surfaces that often interfere in reactions on solids are not major concerns. The expedient of asserting chemical transformations are too fast to limit the rate of vaporization seems to be reasonable on an intuitive basis. Transport of reactants to the surface to participate in the chemical transformation could still be rate limiting. These transport processes are considered elsewhere in this document.

The VANESA model considers, then, only the kinetic limitations at the gas/liquid interface that arise from desorption of a surface species into the gas:

$$M\ (\text{surface}) \rightarrow M\ (\text{gas})$$

where M designates a molecular entity. A surface species interacts with its neighbors in an attractive sense. This interaction can be as weak as simple dispersive or van der Waals attractions. On the other extreme, actual bonding of the surface species to its neighbors can arise. These attractive interactions are stronger than the mean thermal

energy of the surface species. Consequently, the surface species acquires sufficient energy to overcome these interactions only as a result of fluctuations about the mean energy. Such fluctuations arise only sporadically in time and consequently vaporization of a surface species can proceed only at a finite rate.

An expression for the net rate of surface species vaporization is:

$$\frac{1}{A}\frac{dN(i)}{dt} = \frac{f(\alpha_i)}{(2\pi M(i)R)^{1/2}}\left[\frac{P_s(i,eq)}{\sqrt{T_s}} - \frac{P_v(i)}{\sqrt{T_v}}\right]$$

where $\frac{1}{A}\frac{dN(i)}{dt}$ = molar flux of the i^{th} species from the surface,

α_i = condensation coefficient for the i^{th} species,

$M(i)$ = molecular weight of the i^{th} species,

R = gas constant,

$P_s(i,eq)$ = equilibrium partial pressure of the i^{th} species over a condensed phase at the surface concentration and temperature T_s,

$P_v(i)$ = actual partial pressure of the i^{th} species in the vapor phase, and

T_v = vapor phase temperature.

The condensation coefficient, α_i, is the probability that when a molecule of the i^{th} species strikes a surface, it will stick to that surface. The nature of the function $f(\alpha_i)$ distinguishes various forms of this surface vaporization rate expression.

When $f(\alpha_i) = \alpha_i$ and $T_s = T_v$, the surface vaporization rate expression is the familiar Hertz-Knudsen equation.[69] This form of the vaporization rate equation is derived by assuming that vapor molecules have Maxwell-Boltzmann velocity distributions in the vicinity of the surface:

$$N(V)dV = 4\pi N_A\left(\frac{M(i)}{2\pi RT}\right)^{3/2} \exp\left[\frac{-M(i)V^2}{RT}\right]V^2 dV$$

where $N(V)$ = number of molecules with velocities in the interval of V to V + dV and

N_A = Avogadro's number.

That is, the Hertz-Knudsen vaporization rate is obtained when the velocity distribution of the vapor phase molecules is assumed to be symmetrically disposed about zero.

Quite clearly, for net vaporization to occur, the velocity distribution of vapor phase species near the surface must not be disposed, symmetrically, about zero. The velocity distribution must be biased toward velocities directed away from the surface. Applying a biased velocity distribution yields the rate equation:[70]

$$\frac{1}{A}\frac{dN(i)}{dt} = \left(\frac{2\alpha_i}{2-\alpha_i}\right)\frac{(4-\pi)}{\sqrt{2\pi M(i)R}}\left[\frac{P_s(i,eq)}{\sqrt{(T_s)}} - \frac{P_v(i)}{\sqrt{(T_v)}}\right] .$$

When $T_s = T_v$, the rate of vaporization obtained with this equation with $\alpha_i = 1$ is about 1.78 times that obtained with the Hertz-Knudsen equation.

Derivation of the rate equation with a biased velocity distribution assumes that the vapor species have velocity distributions characteristic of the vapor phase temperature. This, of course, will not be true, in general. The net flux of vapor species away from the surface is the sum of evaporated molecules and molecules that strike the surface but do not adhere to the surface. The reflected molecules will have velocity distributions characteristic, in general, of neither the surface nor the vapor temperatures. Correction for this yields:[69,71]

$$\frac{1}{A}\frac{dN(i)}{dt} = \left[\frac{8\alpha_i(\alpha_i+1)}{5\alpha_i^2-4\alpha_i+8}\right]\frac{\left(P_s(i,eq) - P_v(i)\right)}{\left(2\pi M(i)RT_s\right)^{1/2}}$$

where it has been assumed $T_s = T_v$ and that the thermal accommodation coefficient is 1.

The various expressions for $f(\alpha_i)$ obtained treating vaporization at various levels of sophistication are plotted against α_i in Figure 38. At low values of α_i there is little difference among the expressions of $f(\alpha_i)$. As α_i approaches 1, the variation in the values of $f(\alpha_i)$approaches about 1.[78]

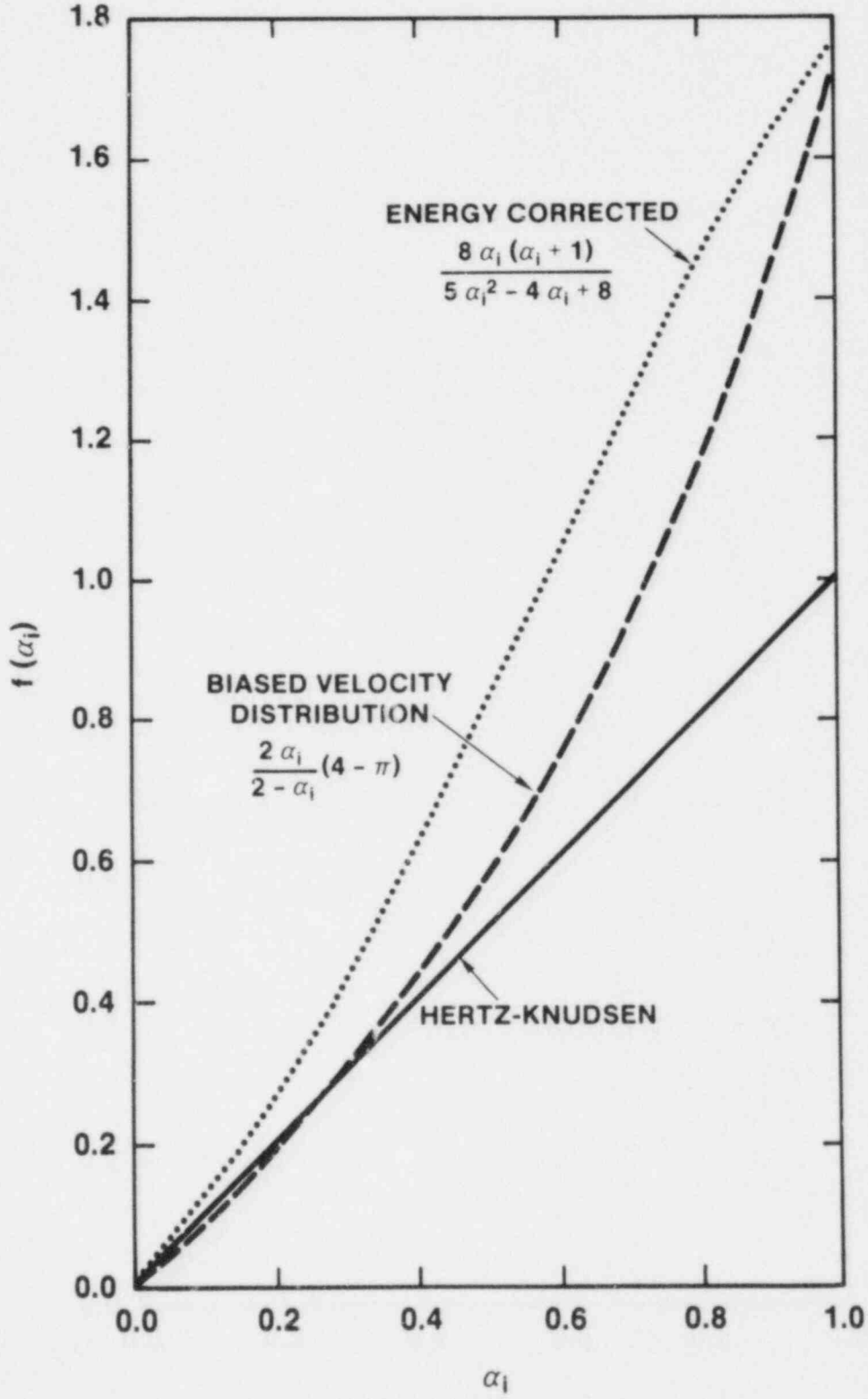

Figure 38. Variation of $f(\alpha_i)$ With α_i in Various Models of the Surface Vaporization Process

The values of α_i that have been reported for conventional liquids exhibit, in many cases, far greater variability than would be obtained using various expressions for $f(\alpha_i)$. There seems to be a fair base of data to support the contention that α_i for pure liquid metals is 1.[72] Certainly many studies of alloy vaporization have been predicated on the assumption that $\alpha_i = 1$ and that the Hertz-Knudsen equation applies.[73,74,75] For more complex liquids, such as water, reported values of α_i span a greater range. Ziemniak[69] cites values of α_i for water that vary between 1 and 10^{-3}.

Theoretical analyses of vaporization of molecular compounds have focused on the restriction of molecular rotation on the surface in comparison to the vapor state.[76] Such analyses have suggested that α_i should be the ratio of the inhibited rotational partition function of the surface species to the rotational partition function of the vapor phase molecule. This would suggest that, in general, α_i for species other than monatomic metals would be less than 1.

Baranaev[77] has taken note of the time-dependence of the surface tension of freshly-formed liquid surfaces. He has argued that surface molecules must adjust their orientation to an energetically more favorable configuration than that they adopt in the bulk liquid. As a result, α_i values for freshly-formed surfaces are likely to be nearer unity than are surfaces which have aged. Such arguments have been used to explain the higher values of α_i obtained with liquid jets than those obtained with stagnant liquid pools.[78] This would seem pertinent to vaporization during core debris/concrete interactions since a bubble rising through the core debris continuously creates fresh surfaces.

For the current implementation of the VANESA model, surface vaporization is taken to occur at a rate described by the Hertz-Knudsen equation with $\alpha_i = 1$ for all species.

V. MECHANICAL GENERATION OF AEROSOLS

The previous chapter described the release of materials from the core debris as a result of vaporization. The sparging of the core debris by gases liberated from the concrete was a key aspect of the vaporization release mechanism. Gas sparging of the molten core debris also gives rise to another release mechanism--mechanical generation of aerosols. Forces on the liquid debris created by sparging gases are sufficient to comminute melt into droplets sufficiently small that they will be borne into the containment atmosphere as an aerosol.

The mechanical aerosol generation process can occur in two ways--bursting of bubbles at a melt surface and melt entrainment. When gas generation rates are low, gases pass through the melt as discrete bubbles. At the surface of the molten core debris the bubbles burst. The breaking of bubbles is known to create some of the highest material accelerations readily obtained on earth--over 10,000 times the earth's gravity for small bubbles.[280] Not surprisingly, these high accelerations lead to melt material being thrown upward in droplets of small dimension. As the rate of gas generation rises, more profound disruption of the melt surface can occur. Gas velocities can be reached that are sufficient to entrain droplets of melt. Much of the entrained melt is in the form of droplets too large to remain suspended in the flowing gas. These larger drops will fall back into the melt pool. Some material entrained by the gas flow will be droplets sufficiently small to remain entrained in the flow and contribute to the aerosol mass evolved from the core debris.

Mechanical production of aerosols when gases sparge liquids is a commonly encountered phenomenon. Generation of small droplets of liquid when carbonated beverages degas is well-known and is an example of the production of droplets by discrete bubbles. Salt deposits found near ocean coasts are also the result of mechanical aerosol production. Waves breaking at shore lines or even at sea, create bubbles that rise to the surface, break, and throw off water droplets. The droplets evaporate (Kelvin curvature effects can lead to droplet evaporation even at high ambient humidity). The residual salt left after evaporation is in the form of fine particles that can be carried long distances by the prevailing breezes. Evidence is accumulating to show that these surface phenomena have a very important effect on the nature of the ocean surface as well as the corrosion of man's creations near the sea.

A less familiar, but perhaps more pertinent example of mechanical aerosol production is the formation of aerosols

during the carbon "boil phase" of steel manufacture. As noted in Chapter IV the "boil" is the occasion of carbon removal from molten steel. Carbon is lost from the melt as CO gas formed when oxygen is dissolved in the melt. The oxygen is provided by a lance that directs a stream of gas at the melt surface. The carbon loss rates can be quite high during the early stages of the boil. The evolved carbon monoxide is accompanied by formidable aerosol concentrations. Some typical data for aerosol concentrations during lancing of melts in 10 ton and 100 ton steel converters are shown in Figure 39. The concentrations of aerosols amount to hundreds of grams per cubic meter. These rates of production of aerosol are encountered for superficial gas velocities of 0-300 cm/s. Such superficial gas velocities are similar to those encountered during early stages of core debris interactions with concrete.

The exact cause of the aerosol production during a "carbon boil" has been the subject of some debate.[281] At one time, it was thought production of aerosol was the result of vaporization processes entirely analogous to those discussed in Chapter IV. It is now established that mechanical aerosol production is dominant early in the decarburization process when the rates of carbon monoxide evolution are high. Vaporization becomes more important later in the process when most of the carbon has been removed and the gas generation rate is slower.

Aerosols produced by mechanical processes will be different from those produced by vaporization. Of particular interest for reactor source term considerations will be differences in the aerosol compositions. Ellis and Glover[20] have examined the effects of the mechanism of aerosol production on the composition of aerosols formed over manganese-iron alloys. Examples of their results are shown in Table 51. Manganese is the more volatile constituent of the alloys examined by Ellis and Glover. When vaporization followed by condensation is the dominant mechanism of aerosol formation, the aerosol is enriched in manganese by about a factor of 20 relative to the bulk melt. Aerosols produced during melt decarburization, when mechanical processes are the dominant formation mechanisms, have compositions little different than the bulk melt phase. Also noteworthy in the results obtained by Ellis and Glover is how much mechanical processes enhanced aerosol production during decarburization. Typically, the rate of aerosol formation was about 20 times higher during decarburization than during simple vaporization.

Data for aerosol production during steel manufacture are quite interesting because the melt masses are similar to those anticipated in core debris/concrete interactions, melt

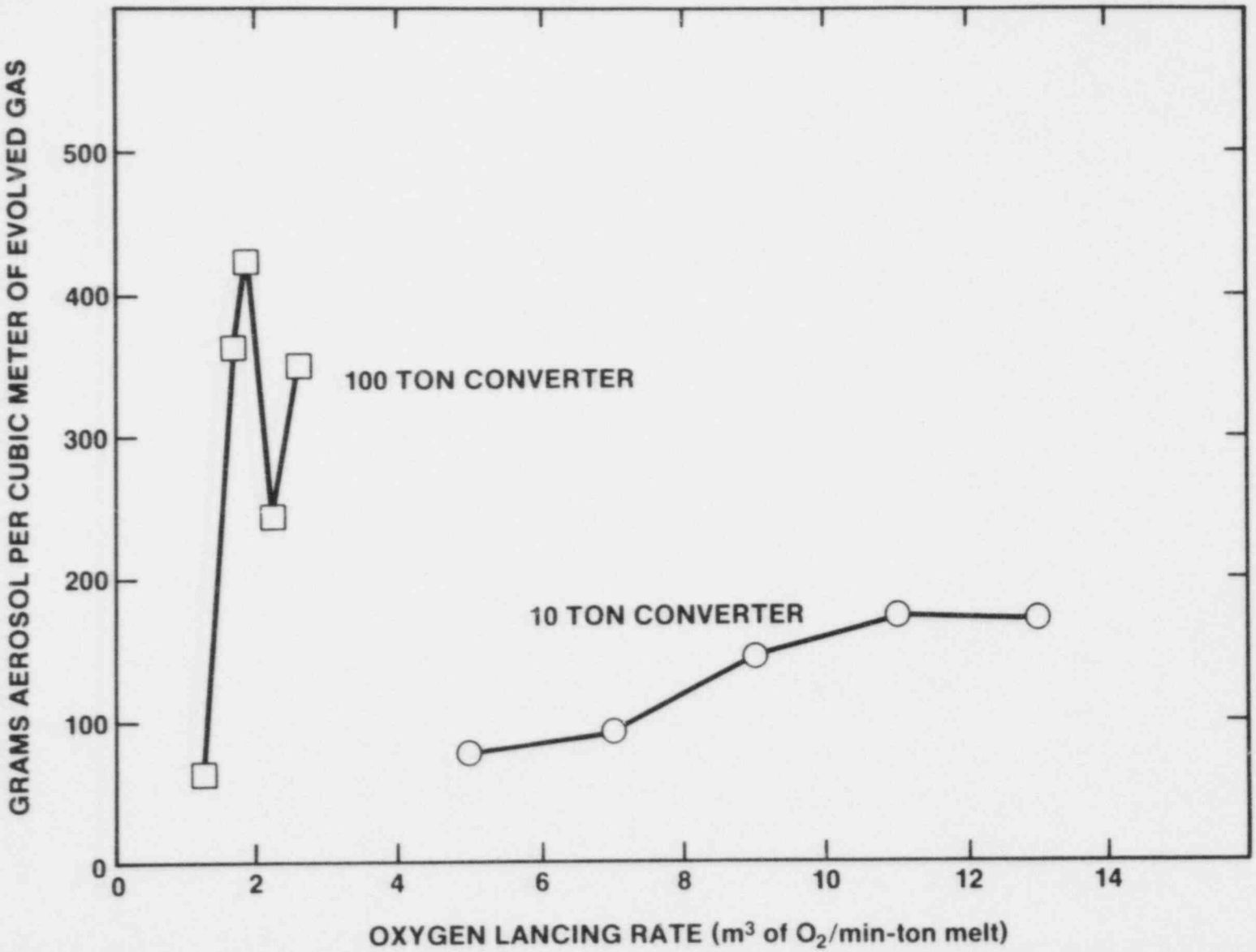

Figure 39. Data on Aerosol Production During the "Carbon Boil" Phase of Steel Manufacture Obtained at Two Commercial Converters

Table 51

Data on Aerosol Composition Obtained by Ellis and Glover

Processes	Wt % Mn in Melt	Wt % Mn in Aerosol	Relative Rate of Aerosol Production
Decarburization*	4.43	4.05	33.4
Decarburization*	4.65	3.72	73.4
Vaporization	4.12	77.8	1.8
Vaporization	4.22	79.3	2.9

*Mechanical processes are the dominant mechanism of aerosol formation though some vaporization does occur.

temperatures are similar, and certainly the melt chemistry is at least analogous. The data and their interpretations suggest strongly that aerosol production during core debris/concrete interactions will involve a mechanical mechanism as well as the obvious vaporization process.

Clearly, aerosols produced by vaporization during core debris/concrete interactions can be enriched in volatile constituents. Of particular interest are situations when the aerosols are enriched in radionuclides. Mechanically produced aerosols, on the other hand, will have compositions similar to those of the bulk condensed phase.* In particular, the mechanically-generated aerosols will reflect the composition of the top-most phase of the core debris. Within the approximations of the current implementation of the VANESA model this is the oxidic melt. Radionuclides in the mechanically generated aerosols will be no more concentrated than in the oxide phase. The radionuclide concentrations in the oxide phase are continuously reduced throughout the core debris/concrete interactions as ablated concrete and oxides produced by gas-metal reactions are incorporated into the phase. Since the fractional loss of core debris by aerosolization will be small, mechanical aerosol generation processes will not produce large fractional releases of the radionuclide inventory of the core debris.

On the other hand, the mechanically generated aerosol is not negligible. The additional mass of suspended particulate injected into the containment atmosphere as a result of mechanical aerosol generation will have an effect on the agglomeration and settling of all particulate including aerosol particles containing high concentrations of radionuclides. Thus, the mechanical aerosol generation during core debris interactions with concrete will have a bearing on the radioactivity available for release from the containment. This effect might be quite important if mechanical aerosol generation occurs to the extent observed in carbon boils.

Even the modest radioactivity releases associated with mechanical aerosol generation may be nonnegligible. Late in the course of core debris interactions with concrete, the temperatures of the core debris will be low. Eventually,

---

*Some enrichment of the mechanically-produced aerosols can occur if the melt contains surface active agents. Enrichment of the surface relative to the bulk has proved important for the interpretation of the compositions of aerosols produced mechanically at sea. This effect is ignored here largely because of uncertainties in the surface properties of core debris constituents. See, however, Section IV A-8.

the temperatures will be so low that they will not spawn significant vaporization of radionuclides from the debris. Even when core debris temperatures are low, they will still be sufficient to cause significant pyrolysis of concrete and thus significant gas generation. The generation of aerosols by mechanical processes is most sensitive to the generation of gas and much less sensitive to melt temperatures. Consequently, late in the course of core debris interactions with concrete, mechanical processes may be the dominant source of aerosols. The radioactivity of these mechanically generated aerosols will provide a continuing, low intensity source to the containment atmosphere and to the plant environment if the containment is breached. Mechanical aerosol formation can define a limit to the extent of source term reduction possible because of delaying containment failure.

Other differences between aerosol produced mechanically and vaporization can arise in connection with size. Aerosol particles formed by vaporization and condensation are typically submicron in size though the individual particles can agglomerate to form larger structures. Aerosol particles produced by mechanical processes are found typically to be larger than 1 micron. The size of the aerosol particle can have an enormous bearing on the subsequent behavior of the particle.

Quite clearly any realistic model of aerosol generation during core debris interactions with concrete must include a description of aerosol production by mechanical processes. The characterization of mechanically-produced aerosols must consist of three elements:

1. Aerosol composition,

2. Aerosol generation rate, and

3. Particle size distribution of the aerosols.

The first of these tasks is fairly simple since the aerosols have the bulk composition of the upper stratum of the core debris. The technology available for predicting the second and third of these characteristics of mechanically generated aerosols and the approach toward the mechanical processes adopted in the current implementation of the VANESA model are reviewed in the next two subsections of this report.

A. Aerosol Generation Rates by Mechanical Processes

The mechanical aerosol generation caused by gas sparging is usefully distinguished according to gas flow regimes. One regime involves discrete gas bubbles rising through the

melt and bursting at the surface. This flow regime is often termed "bubbly flow." The other flow regime of interest involves gas sparging rate sufficiently high that liquid melt is entrained in the flow. This regime is often called "churn turbulent" flow. The extent of aerosol production possible in each of these flow regimes is described in the subsections below.

1. Aerosol Production by Bubble Bursting

Aerosol production during bubbly flow is caused by the accelerations experienced by liquid when the film defining the bubble bursts. This bubble bursting process has been examined several times in studies of aqueous systems. Two types of behavior have been observed. As shown schematically in Figure 40 very small bubbles produce aerosol droplets upon bursting as a result of rarefaction of the surrounding liquid. Rapid flow to fill the void created by a bursting bubble creates a jet of liquid. This jet disintegrates into droplets which are fairly large (on the order of 100 microns) in comparison to the sizes of aerosols of interest in reactor accident analyses.

Bubbles larger than about 2 mm do not yield aerosol particles as a result of liquid jet disintegration. Rather, aerosols produced when large bubbles burst are the result of accelerations experienced by liquid films during the bursting process. There is evidence that when large bubbles burst, they inject small (<1 mm) bubbles into the liquid. The bubbles could then rise, burst, and inject mass into the gas flow by the jet disintegration process. The aerosols produced by the acceleration of liquid films can be small (<10 μm). It is the bursting of these larger bubbles that is of primary interest for accident analyses.

Ginsberg[204,205] has reviewed the literature on the amount of aerosol created by the bursting of relatively large bubbles. He cites two possible models. Toba[211] has attempted to determine the volume of liquid that constitutes the film defining the bubble at a liquid surface. Utilizing Toba's results and assuming that all the film is rendered into aerosols makes the ratio of the volume of aerosols to the volume of the bubble

$$V(\text{aerosol})/V(\text{bubble}) = \delta_c$$

where δ_c is the average film thickness in centimeters. The film thickness varies with time since liquid will drain

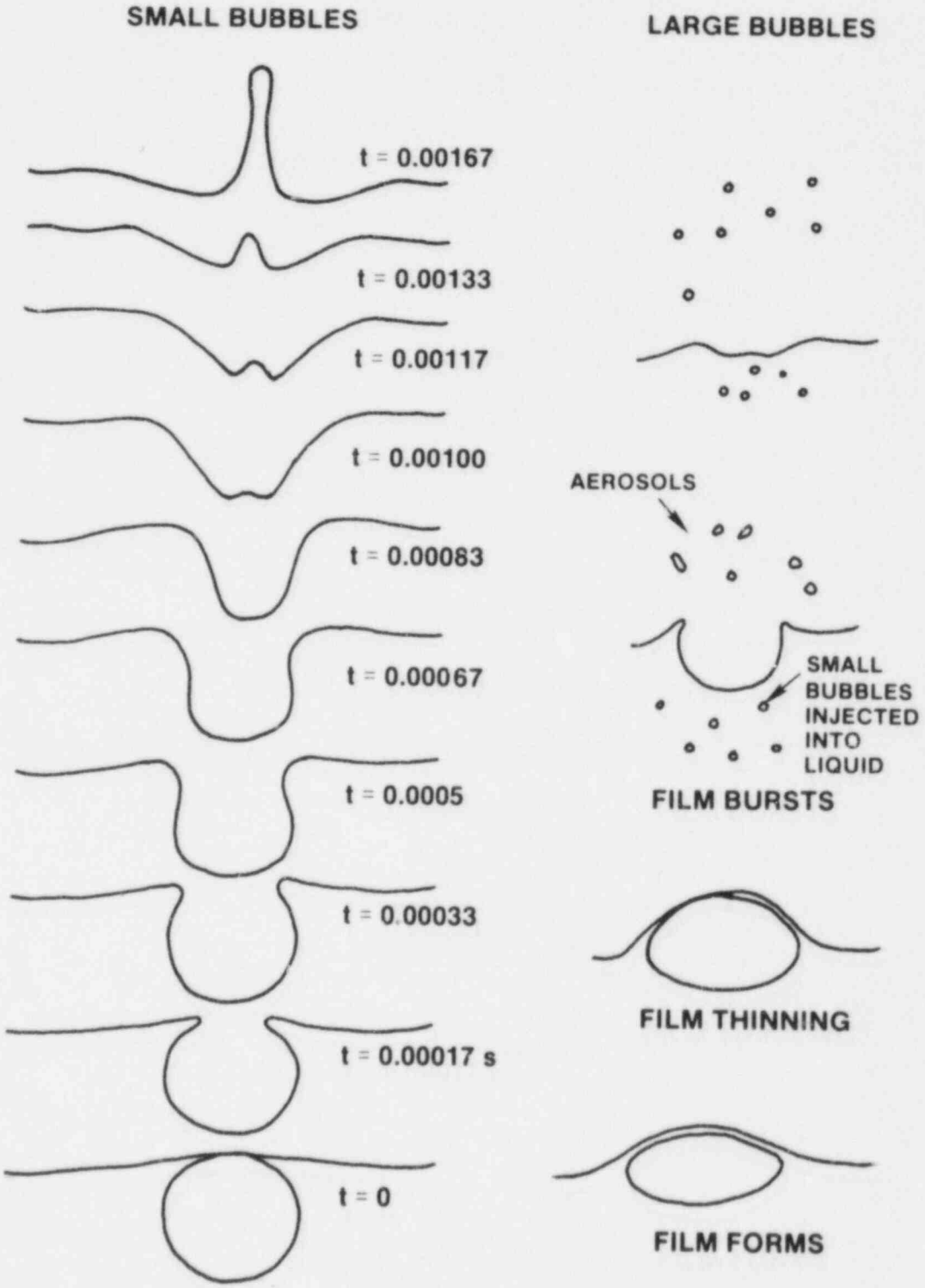

Figure 40. Schematic Diagrams of the Bursting of Small Bubbles[210] and Large Bubbles

out of the film. The time available for this draining depends on the stability of the bubble which in turn depends on the surface tension of the liquid. Ginsberg suggests

$$10^{-5} \leq \delta_c \leq 10^{-3} \text{ cm} \quad .$$

Azbel et al.[212] have considered the aerosolization process from nearly an identical point of view and have arrived at the equation:

$$E = \frac{\rho_\ell \, V(\text{aerosol})}{\rho_g V(\text{bubble})} = \frac{3K_1}{2\pi\rho_g D(\text{bubble})}$$

$$\left\{ \frac{\left[1 - \frac{D(\text{bubble})^2}{2K_2} + \frac{9}{16}\frac{D(\text{bubble})^4}{K_2^2}\right]^{1/2} + \left[\frac{D(\text{bubble})^2}{4K_2} - 1\right]}{1 + \frac{3}{4}\frac{D(\text{bubble})^2}{K_2} - \left[1 - \frac{D(\text{bubble})^2}{2K_2} + \frac{9}{16}\frac{D(\text{bubble})^4}{K_2^2}\right]^{1/2}} \right\}^{1/2}$$

where $K_1 = 1.15\pi\sigma_\ell/c^2$,

$K_2 = 6\,\sigma_\ell/g(\rho_\ell - \rho_g)$,

D(bubble) = bubble diameter,

c = speed of sound in the gas
$\approx 1.08 \times 10^4 \sqrt{T/M}$, and

M = mean molecular weight of the gas.

(Note that typographical errors in Azbel's equation as cited in reference 205 have been corrected in reference 204.)

Predictions obtained from the Azbel et al. model are shown as a function of bubble diameter in Figure 41. The ratio of aerosolized mass to gas mass rises to a maximum for bubble sizes of slightly less than 1 cm. The ratio then varies slowly about 10^{-4} for larger bubbles. For the example problem, a value of $E = 10^{-4}$ corresponds to V(aerosol)/ V(bubble) $\approx 10^{-9}$. Comparison of this value to that predicted using the Toba estimate of the film volume indicates not all the film is aerosolized.

Tomaides and Whitby[113] examined aerosol formation when 0.55 cm bubbles burst at the surface of an aqueous solution

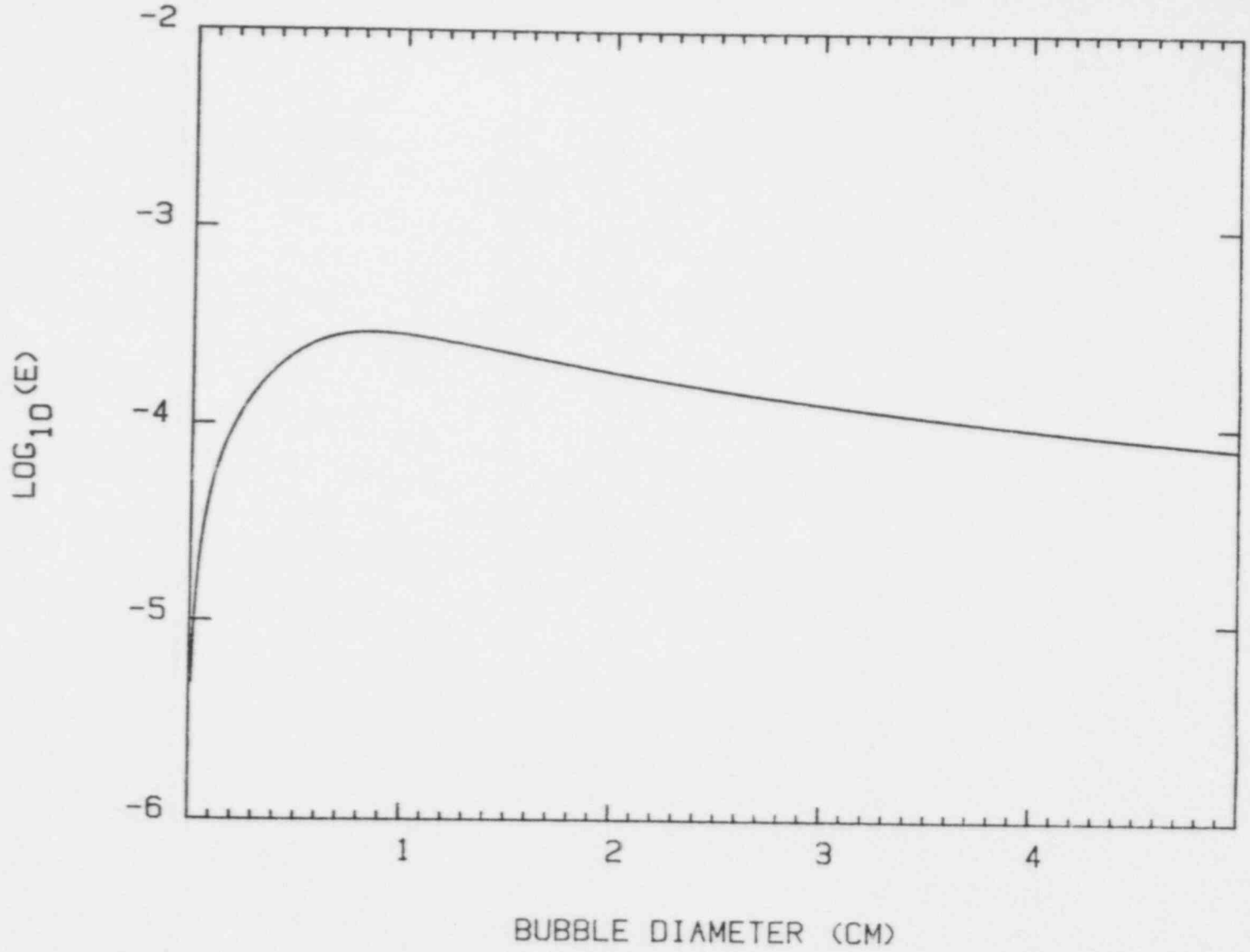

Figure 41. Predictions of the Mechanical Aerosolization by b bble Bursting Obtained With the Azbel et al. Model. Calculations were done assuming ρ_ℓ = g/cm^3, σ_ℓ = 400 dyne/cm, M = 15, T = 2200 K, and pressure = 1 atmosphere.

of 0.1 percent NaCl. They found about 200 droplets were formed per bubble burst. They reported the size distribution of the droplets to be multimodal with a mean size of about 5.1 μm. This mean size implies

$$V(\text{aerosol})/V(\text{bubble}) \sim 2 \times 10^{-7} \quad .$$

This result is somewhat larger than would be predicted with the Azbel et al. model. It is much smaller than would be predicted with the Toba analysis. Again, it appears not all of the liquid film is converted to aerosols during bubble bursting. Tomaides and Whitby argued that the mass of aerosol formed during bubble bursting would not vary with bubble size once a critical bubble size is reached. This conclusion is not too different than the prediction of the Azbel et al. model which shows a mild decline in aerosol production with bubble size.

Garner et al.[214] examined aerosols formed by bubbles 0.6 to 1.2 cm in diameter bursting in a variety of liquids. Their results indicate

$$V(\text{aerosol})/V(\text{bubble}) \approx 2 \times 10^{-5} \quad .$$

This result is much larger than what would be predicted with the Azbel et al. model.

Ginsberg[204] also examined data by Cipriano and Blanchard[215] and concluded with the aid of the Azbel et al. model that these data indicated:

$$V(\text{aerosol})/V(\text{bubble}) = 4 \times 10^{-6}$$

for 1.0 cm bubbles and 10 μm aerosol particles.

Obviously, the data and models available for the amount of aerosol formed when bubbles burst are not yet well reconciled. It appears probable that the model formulated by Azbel et al. may be useful if some multiplicative correction were made. Similarly, a model based on Toba's results could be useful if a correction was made so that not all of the bubble film was aerosolized.

Such a correction factor is implied by Ginsberg in the $F(\zeta)$ multiplier he applies to the Azbel model. The term

$F(\zeta)$ is defined as the droplet mass fraction below the critical size ζ where ζ is the largest particle which may be transported by the gas flow. If the actual distribution of droplets produced by the bubble burst is known, then the factor $F(\zeta)$ is easily calculated.

This factor may also be determined by experimental measurement of V(aerosol)/V(bubble). This method, however, would yield a factor which would include both $F(\zeta)$ and additional adjustments to correct errors in the model. A more detailed discussion of droplet distributions and transport size limitations is included in the section on liquid entrainment by churn turbulent flow.

2. Aerosol Production by Entrainment

As the rate of gas sparging of the melt during interactions with concrete increases, the flow through the melt is expected to pass from the bubbly regime to the churn-turbulent regime. In the churn-turbulent regime gas velocities are sufficiently high to entrain melt in the flow. There are two instances in the course of core debris interactions with concrete when gas flows are expected to be particularly high and liquid entrainment is particularly likely:

a. When melt is first deposited on the concrete,

b. When decarburization of the melt occurs.

Powers and Arellano[17,18] have reported that gas generation rates when melt first contacts concrete are sufficient to levitate even large-scale (200 kg) melts. They observed with x-rays that small melts (~2 kg) upon first contact with concrete were violently disrupted into long filaments. The extensive disruptions of the melt were observed in experiments with relatively dry concrete. Presumably even higher gas generation and more extensive melt disruption would have occurred if the concrete were fully hydrated or had standing water been present as might be expected in a reactor accident.

Decarburization of the melt was discussed extensively in Chapter 4. The decarburization is in essence the same process that occurs during the carbon boil phase of steel manufacture. Gas generation rates are high during decarburization of core melts because gases from the concrete are reacting with carbon in the melt to form carbon monoxide:

$$H_2O + [C] \rightarrow H_2 + CO$$

$$CO_2 + [C] \rightarrow 2CO \quad .$$

These reactions can double the volumetric flow of gas through the melt.

The entrainment of liquid by sparging gases has been ably reviewed by Kataoka and Ishii[202,203] and by Ginsberg.[204,205] Only a summary discussion of this topic is presented here. The discussion will rely on several unfamiliar dimensionless groups. These groups are defined in Table 52.

Kataoka and Ishii claim that gas flows through liquids are in the churn-turbulent regime and can cause noticeable entrainment when:

$$j_g^* \geq 0.325\left(\frac{\rho_g}{\rho_\ell}\right)^{1/2} \quad \text{or} \quad V_s \geq 0.325\left(\frac{g\sigma_\ell}{\rho_\ell}\right)^{1/4} .$$

Thus, for core melt/concrete interactions entrainment is likely when superficial gas velocities exceed 10-15 cm/s. This critical superficial gas velocity is usually exceeded throughout the first 10 hours of core debris/concrete interactions.

Entrainment by the gas flow occurs near the surface of the melt where gas velocities are quite high. Much of the entrained melt is too large in size to remain in the gas flow once the gas velocities drop after emerging from the melt. Then the overly large droplets of entrained material will fall back into the liquid pool. Only the material sufficiently small to have terminal velocities less than the superficial gas velocity can be carried long distances from the pool by the gas flow. As a result of the entrainment and deentrainment, Kataoka and Ishii found that correlations of the amount of material entrained had to be categorized in terms of distance from the liquid surface. They defined three regions:

1. Near Surface Region: All entrained material in the near surface region has a velocity vector pointed away from the liquid surface.

2. Momentum Controlled Region: Over this region entrained droplets too large to remain suspended in the flow fall back toward the pool.

3. Far Field Region: Only droplets of entrained material small enough to remain suspended by the gas flow are present in this region. Loss of this material can still occur as a result of deposition on constraining walls of the system of interest.

Table 52

Dimensionless Groups Used in the Discussion of Aerosol Formation by Entrainment

Group Name	Symbol	Definition
Dimensionless Gas Flux	j_g^*	$V_s \Big/ \left[\frac{\sigma_\ell g(\rho_\ell-\rho_g)}{\rho_g^2}\right]^{1/4}$
Dimensionless Height Above the Pool Surface	h^*	$h \Big/ \left[\frac{\sigma_\ell}{g(\rho_\ell-\rho_g)}\right]^{1/2}$
Dimensionless Gas Viscosity	$N(\mu_g)$	$\mu_g \Big/ \left[\frac{\rho_g \sigma_\ell^{1.5}}{g^{1/2}(\rho_\ell-\rho_g)^{1/2}}\right]^{1/2}$
Dimensionless Liquid Viscosity	$N(\mu_\ell)$	$\mu_\ell \Big/ \left[\frac{\rho_\ell \sigma_\ell^{1.5}}{g^{1/2}(\rho_\ell-\rho_g)^{1/2}}\right]^{1/2}$
Dimensionless Vessel Diameter	D_H^*	$D_H \Big/ \left[\frac{\sigma_\ell}{g(\rho_\ell-\rho_g)}\right]^{1/2}$
Entrainment Parameter	E^*	$\frac{\rho_\ell j_\ell}{\rho_g V_s}$

Where h = height above the pool surface, D_H = hydraulic diameter of the molten pool, j_ℓ = volumetric flux of entrained melt.

Obviously, the amount of material entrained and present in any region depends on the flux of gas through the melt. The boundaries between the regions, too, are dependent on the gas flux through the liquid pool. Kataoka and Ishii could develop single correlations for the amount of entrained material present in the near surface and the far-field regions. They found, however, that correlations for the material present in the momentum-controlled region had to be categorized in terms of the magnitude of the gas flux. They developed correlations for low flux and intermediate flux flow regimes in the momentum-controlled region. They could find no correlation for the amount of material present in this region once flux exceeded a critical level. They suggested that the amount present could be bounded by the correlation for the near surface region. This near surface correlation is distance-independent so that when it is applied to the momentum-controlled region it is very much an upper bound.

The correlations and the boundaries between the regions and regimes for entrainment are shown in Table 53. The correlations shown in the table are not precisely those defined by Kataoka and Ishii. The boundary between the intermediate flux and the high flux regime in the momentum-controlled region has been altered to avoid a discontinuity in the entrainment at this boundary. Also, a limit has been imposed to the high flux entrainment and the entrainment in the near surface region to reflect work reported by Rozen et al.[206,207] in which E* reached a maximum of four and was independent of gas flux.

The far-field correlation found by Kataoka and Ishii includes a term to describe the loss of entrained particulate as a result of deposition on the system walls--$\exp(-0.205\ h/D_H)$. For most reactor accident analyses, release of aerosols from core debris and the subsequent behavior of the aerosols are treated in distinct models. Consequently, the alternate correlation suggested by Kataoka and Ishii which does not include deposition is probably preferable for release models.

Rozen et al.[206] have suggested a correlation for the far field entrainment:

$$E^* = 7.6 \times 10^{-5} \left\{ j_g^*[N(\mu_g)]^{1/6} + 4870 \left(j_g^*\right)^{4.2} \right\} [N(\mu_g)]^{0.7} \left\{ \frac{\rho_\ell - \rho_g}{\rho_g} \right\}^{1/2} \exp[-0.23\ h/D_H] \quad .$$

Table 53

Correlations of Entrainment Found by Kataoka and Ishii

NEAR SURFACE

$$0 \leq h^* < 1038 j_g^*[N(\mu_g)]^{1/2}[D_H^*]^{0.42}[\rho_g/(\rho_\ell-\rho_g)]^{0.23}$$

$$E^* = \frac{0.00484(\rho_\ell-\rho_g)}{\rho_g} \leq 4$$

MOMENTUM CONTROLLED

$$1038 j_g^*[N(\mu_g)]^{1/2} < \frac{h^*(\rho_\ell-\rho_g)^{0.23}}{[D_H^*]^{0.42}\rho_g^{0.23}} \leq 1970[N(\mu_g)]^{0.33}$$

Low Gas Flux:

$$j_g^* \leq 6.39 \times 10^{-4} h^*$$

$$E^* = 2.213[N(\mu_g)]^{1.5}[D_H^*]^{1.25}\left[\frac{(\rho_\ell-\rho_g)}{\rho_g}\right]^{0.31}\frac{j_g^*}{h^*}$$

Intermediate Gas Flux:

$$6.39\times10^{-4} h^* < j_g^* \leq 9.6315\times10^{-4} h^* N(\mu_g)^{-1/2}(D_H^*)^{-0.4167}\left[\frac{\rho_\ell-\rho_g}{\rho_g}\right]^{0.23}$$

$$E^* = 5.417\times10^6 \frac{(j_g^*)^3}{(h^*)^3}[N(\mu_g)^{1.5}(D_H^*)^{1.25}[(\rho_\ell-\rho_g)/\rho_g]^{0.31}$$

High Gas Flux:

$$E^* \approx \frac{0.00484(\rho_\ell-\rho_g)}{\rho_g} \leq 4$$

Table 53 (Continued)

Correlations of Entrainment Found by Kataoka and Ishii

FAR FIELD

$$h^* \geq 1970[N(\mu_g)]^{0.33}[D_H^*]^{0.42}[\rho_g/(\rho_\ell-\rho_g)]^{0.23}$$

Considering Deposition:

$$E^* = 7.13\times10^{-4}(j_g^*)^3[N(\mu_g)]^{1/2}\left\{\frac{(\rho_\ell-\rho_g)}{\rho_g}\right\}\exp[-0.205h/D_H]$$

Without Deposition:

$$E^* = 0.002(j_g^*)^3[N(\mu_g)]^{1/2}\left\{\frac{(\rho_\ell-\rho_g)}{\rho_g}\right\}$$

This correlation differs from that suggested by Kataoka and Ishii primarily in that it predicts more entrainment at the lower gas fluxes.

It should be noted that all of the correlations described here refer to isothermal systems. They do not reflect the effects a temperature gradient above the pool might have. Such a temperature gradient would be expected above melts interacting with concrete.

To utilize the correlations, it is necessary to know the density and viscosity of the gas. Correlations for the viscosities of the pure gases that are the principle constituents of gas sparging the melts in core debris/concrete interactions are:

$$\mu(H_2) = \frac{1.5769\ T^{0.705712}}{(1 - 3.378/T)} \quad \text{micropoises}$$

$$\mu(H_2O) = \frac{0.950\ T^{0.892912}}{(1 + 207.219/T)} \quad \text{micropoises}$$

$$\mu(CO) = \frac{14.151\ T^{0.502012}}{(1 + 117.178/T)} \quad \text{micropoises}$$

$$\mu(CO_2) = \frac{15.957\ T^{0.497212}}{(1 + 246.744/T)} \quad \text{micropoises} \ .$$

Plots of the viscosities predicted with these correlations and data[208] used in the derivation of the correlations are shown in Figure 42. Predictions of the viscosities of mixtures from viscosity data for pure constituents have a long and checkered history. A variety of procedures has been developed to make these predictions. One of the simplest of these procedures is the Herning-Zipperer equation:[209]

$$\mu(\text{mixture}) = \frac{\sum_{i=1}^{N} P(i)\mu(i)M(i)^{1/2}}{\sum_{i=1}^{N} P(i)M(i)^{1/2}}$$

where N = the number of constituents in the mixture,

P(i) = partial pressure of the i^{th} constituent,

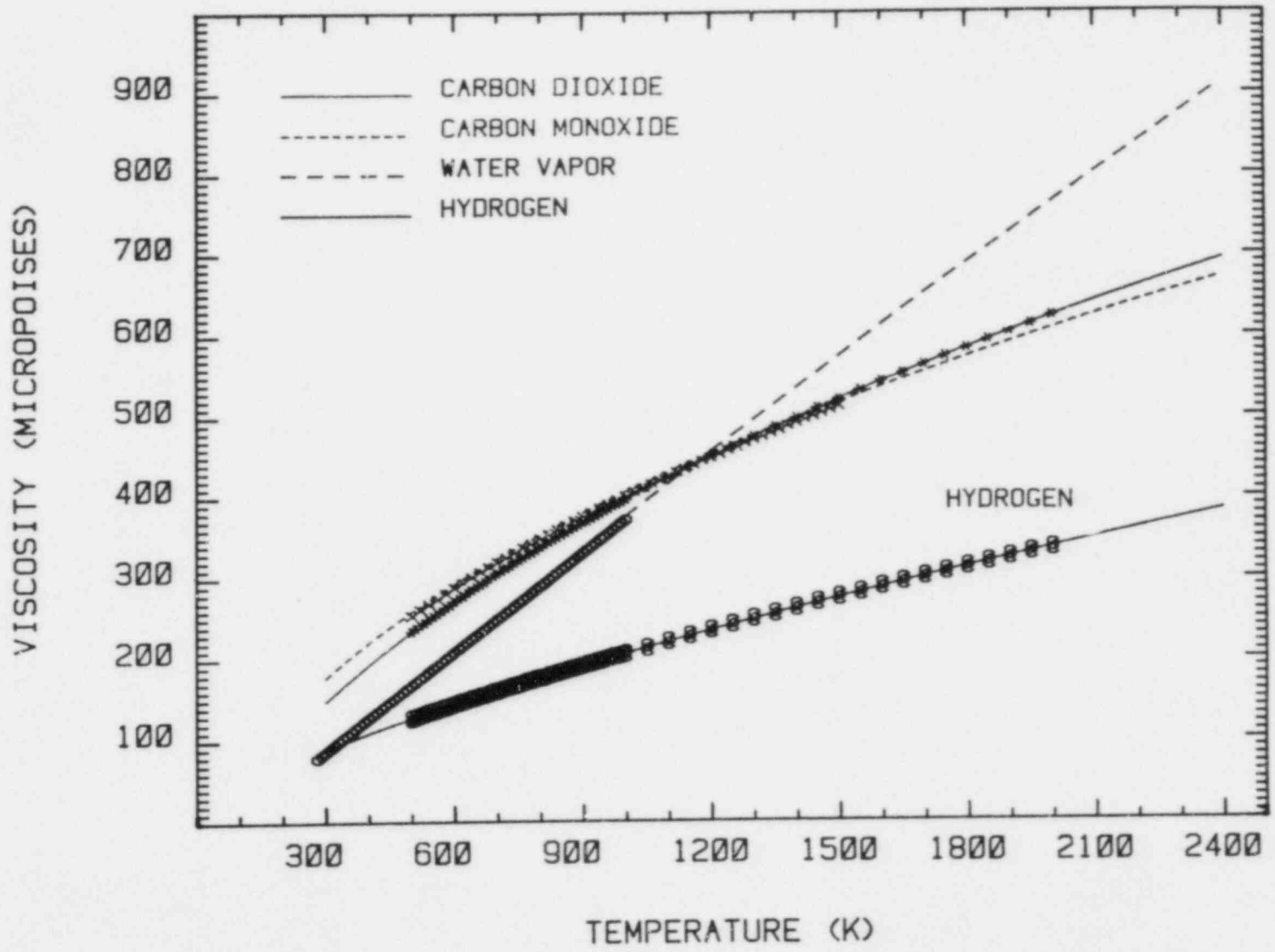

Figure 42. Viscosities of Pure Gases as Functions of Temperature. Data points are indicated by symbols, and the predictions of the correlations are represented by lines.

$\mu(i)$ = viscosity of the i^{th} constituent when pure, and

$M(i)$ = molecular weight of the i^{th} constituent.

The Herning-Zipperer equation is applicable, in truth, only for nonpolar gases. As with most gas property correlations, generalization of the equation to low molecular weight gases where quantum effects are significant has to be suspect.Predictions with the Herning-Zipperer equation may be most erroneous then for mixtures of CO, a polar gas, and H_2, a "quantum gas," at low temperatures. A comparison of the predicted viscosities of CO/H_2 mixtures at 298 K with viscosities of such mixtures recommended in the literature is shown in Figure 43. The discrepancy between predicted and recommended viscosity is greatest in the compositional regime where mixture effects would be expected to be most manifest--approximately equal concentrations of the constituents. The maximum discrepancy is, however, not especially large. It would be expected that the small discrepancy at 298 K would become even smaller at higher temperatures as thermal energies of the gas molecules overwhelmed dipole and quantum effects. If these small errors in the predicted mixture viscosities obtained with the Herning-Zipperer equation are objectionable, many, more sophisticated, approaches are available for making such predictions.[209]

Entrainment predicted with the correlations is shown in Figure 44 as a function of superficial gas velocity for several locations above a melt pool. The calculations of entrainment were made assuming the sparging gas was an equimolar mixture of H_2 and CO at 2000 K. Other quantities used for the calculation were

ρ_ℓ = 7 grams/cm^3

σ_ℓ = 400 dynes/cm

D_H = 400 cm .

At an elevation of 500 cm above the pool, the far-field correlations apply. The Kataoka and Ishii correlation indicates that entrainment rises from truly negligible levels to $E^* \sim 10^{-3}$ as the superficial gas velocity varies between 1 and 300 cm/s. The most rapid variations in the predicted values of E^* are in the superficial gas velocity range typically encountered in core debris/concrete interactions. For typical situations, E^* values of 10^{-3} to 10^{-4} will amount to aerosol concentrations of 0.1 to 1 gram/m^3 (STP)

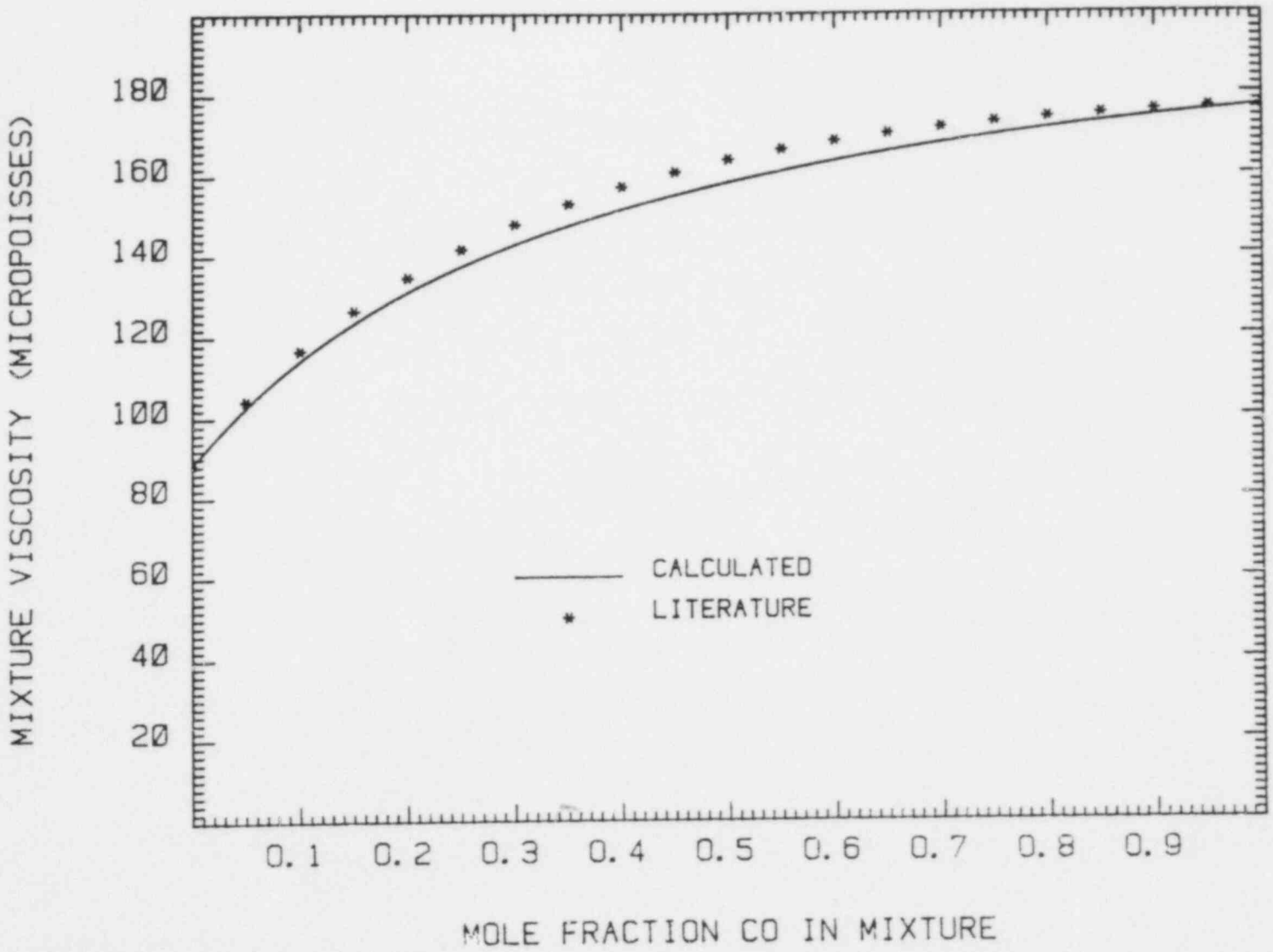

Figure 43. Comparison of the Viscosities of Carbon Monoxide-Hydrogen Mixtures at 298 K Predicted With the Herning-Zipperer Equation to Mixture Viscosities Recommended in the Literature[209]

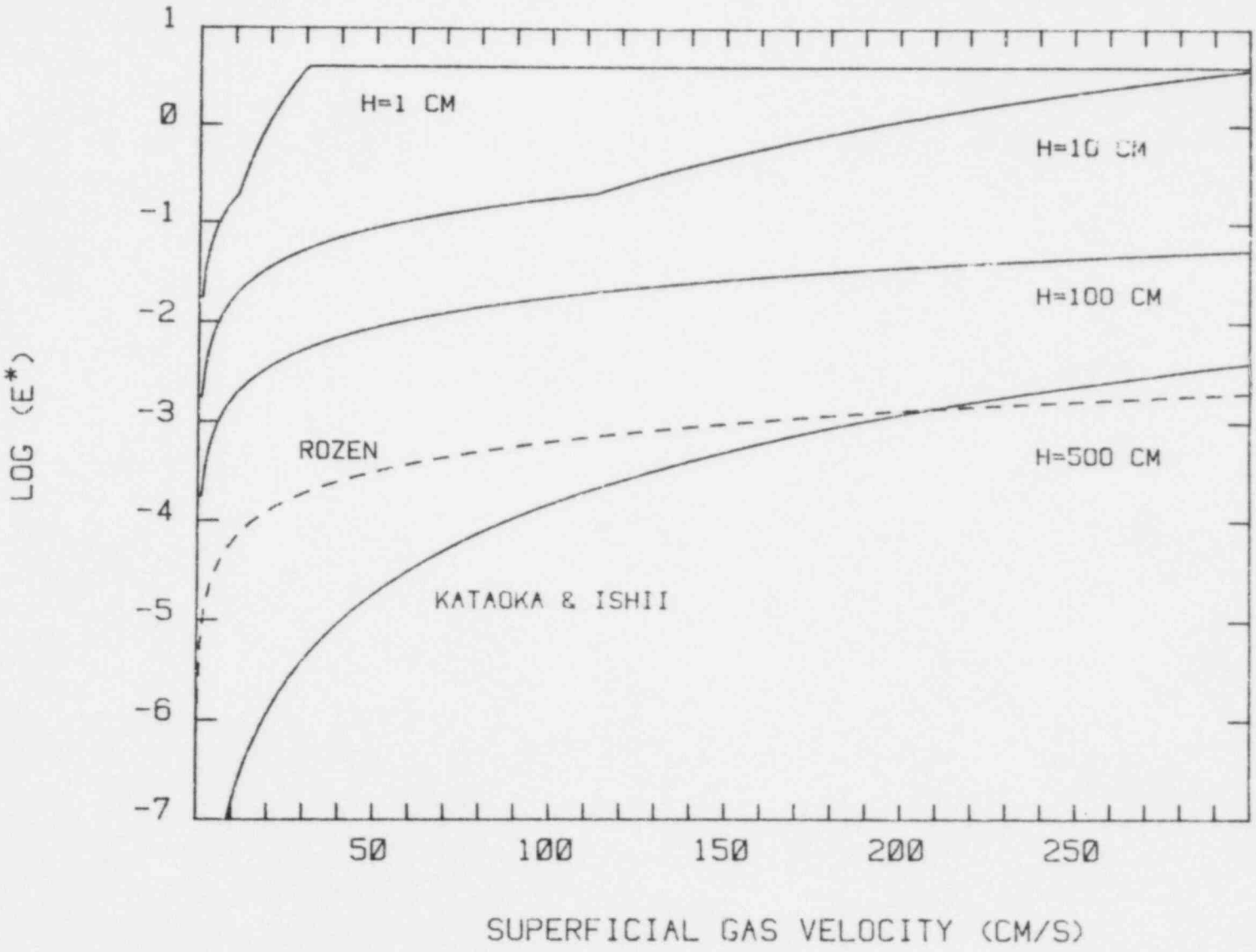

Figure 44. Examples of Predictions of Entrainment. The conditions for the example are described in the text. Curves are marked according to the elevation above the pool surface.

in the gases evolved during core debris/concrete interactions. The Kataoka and Ishii correlation predicts entrainment contributions to the aerosol production reach such levels when gas velocities exceed about 70 cm/s.

The Rozen correlation for the far-field entrainment shows a very steep dependence on gas velocity at low gas velocities. Values of E* are in the 10^{-4} to 10^{-3} range when superficial gas velocities exceed about 20 cm/s. Increasing the superficial gas velocity above about 80 cm/s has a relatively weak effect on the predicted entrainment.

Both the Rozen correlation and the Kataoka and Ishii correlation show that predicted entrainment in the churn-turbulent flow regime does not converge smoothly with the entrainment described above for the bubbly flow regime. Surprisingly, the far-field estimates for entrainment at low gas fluxes are lower than what would be predicted for aerosol generation by bubble bursting. A satisfactory explanation has not been advanced for this discontinuity in mechanical aerosol production. A rationalization that the result is indicative of the effects of bubble coalescence and surface disruption has been offered.[204]

The far-field correlations provide an estimate for the amount of mechanically generated material that could enter the reactor containment as an aerosol. The materials entrained in the near surface and momentum-controlled regions are not negligible. The curves in Figure 44 for locations 100 cm and closer to the liquid surface describe the entrained mass in the momentum-controlled region. The entrainment 10 cm above the pool surface shows the transition between the low flux flow regime to the intermediate flux flow regime that takes place as the superficial gas velocity through the melt increases. The curve for 1 cm above the pool surface shows the transition from the intermediate flux to high flux regime. Clearly, most of the material present in the flow at these lower elevations falls eventually back into the pool. For instance, more than 90 percent of the entrained material at the 100 cm evolution must reenter the pool before the flow reaches the 500 cm elevation. But, before the material falls back into the pool it can affect the condensation of vapors if there is any significant temperature gradient along the flow path. Vapors, if cooled, can condense on the available surfaces rather than nucleating aerosol particles. Vapors that condense on entrained droplets that fall back into the pool will have to be revaporized to contribute to the particulate mass evolved into the reactor containment atmosphere.

The effects of temporarily entrained material on the behavior of vapors may not be great. The fact that so much

high temperature melt gets levitated above the pool assures that temperature gradients above the pool will not be particularly steep. Consequently, temperatures low enough to cause vapor condensation may not be reached until the flow has passed out of the momentum-controlled region.

B. Sizes of Aerosol Particles Produced by Mechanical Processes

1. Aerosols from Bubble Bursting

Very small bubbles, when they burst, produce relatively large droplets. Tomaides and Whitby[213] suggest the number and size of droplets produced by liquid jets formed when small bubbles burst can be found from:

$$N_p^j = 0.095/D(\text{bubble})^{1.9}$$

$$d_p = 0.1546\ D(\text{bubble})^{1.3}$$

where all dimensions are in centimeters, N_p^j is the number of "jet" droplets, and d_p is the mean diameter of these droplets. These correlations suggest that jet droplets are not produced once bubbles are larger than about 0.4 cm.

Small bubbles also produce finer droplets by the film rupture mechanism. Results obtained by Toba,[211] Whitby and Tomaides,[213] and by Day[116] suggest

$$N_p^f = A^{1/2}$$

where N_p^f = number of fine droplets and

A = the area of the film forming the bubble.

Tomaides and Whitby indicate that the fine droplets have a size greater than 5 μm.

Correlations for the size of droplets produced when bubbles larger than about 0.6 cm burst have not been developed. Garner el al.[214] indicate a mass weighted mean size of about 12 μm for aerosol droplets produced by bursting

0.7 cm bubbles. Tomaides and Whitby indicate the mass weighted mean size is about 5 μm. The number frequency data obtained in the two investigations are compared in Figure 45. In light of the differences in the procedures and conditions, the results are in close agreement.

2. Aerosols Produced by Entrainment

Kataoka and Ishii[202,203] have attempted to characterize the size distribution of droplets entrained by gases sparging liquids. They obtained a frequency distribution function for droplets in the so-called "near surface" region

$$\frac{dF(D<\bar{D})}{dD} = f\left(\bar{D}, j_g^*\right) = \begin{cases} 1.5\ \bar{D}^{1/2}/D_{max}^{3/2} & \text{for } D \leq D_{max} \\ 0 & \text{for } D > D_{max} \end{cases}$$

where $F(D<\bar{D})$ = fraction of the mass of entrained droplets with sizes less than $\bar{D}$,

$\bar{D}$ = entrained droplet size, and

$$D_{max} = \frac{7.24}{j_g^*}\left(\frac{\sigma_\ell}{g(\rho_\ell-\rho_g)}\right)^{1/2}.$$

In deriving this distribution function, Kataoka and Ishii relied heavily on the entrainment data for aqueous systems obtained by Garner et al.[214]

The size distribution function applies only to a very narrow region adjacent to the liquid surface where all entrained droplets have nonnegative upward velocity vectors. As the two-phase flow mixture moves upward, gas velocities are insufficient to keep the larger entrained droplets suspended. These larger droplets fall back into the liquid pool being sparged by gas. This loss of large-sized entrained droplets continues throughout the region called the "momentum-controlled" region by Kataoka and Ishii. Beyond this region only droplets with terminal velocities less than or equal to the superficial gas velocity are entrained in the flow.

When larger droplets fall back into the liquid pool, they will sweep smaller droplets out of the flow. The efficiency with which a larger droplet impacts a smaller droplet is a

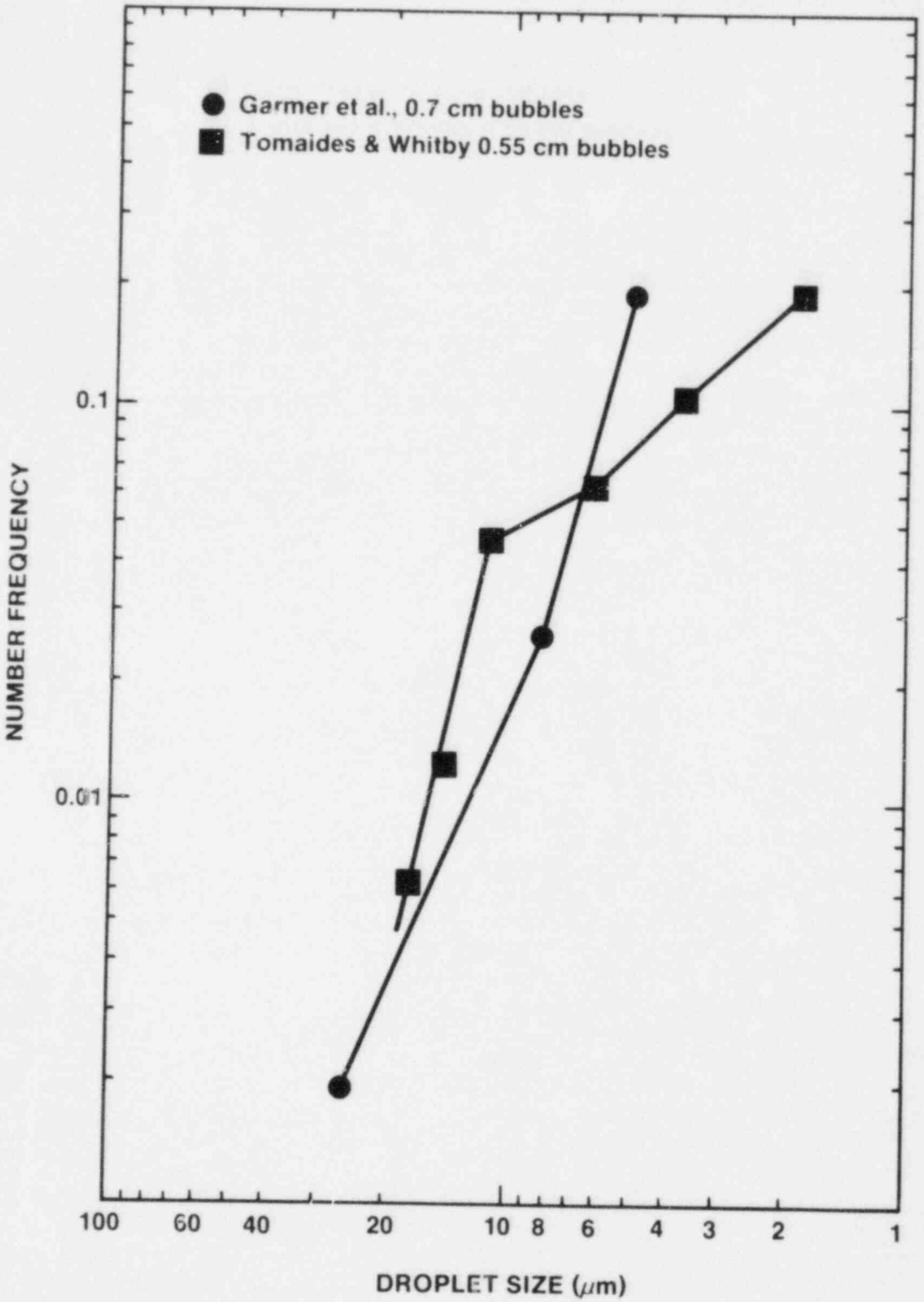

Figure 45. Comparison of Droplet Number Frequency Data for 0.55 cm Bubbles and for 0.7 cm Bubbles. Lines connecting data points are only intended to be visual aids.

complex function of both the diameter of the large droplet and the diameter of the small droplet as well as the velocities involved. This problem is somewhat analogous to the treatment of aerosol sweepout by water spray droplets. For the time scales of interest the mechanisms of sweepout of interest are impaction, interception, and diffusion. For an account of the difficulties of analysis of these processes see reference 174.

If the collection of small droplets by the falling drops is ignored, the Kataoka and Ishii distribution function can be used to find the size distribution of droplets entrained in the flow far away from the liquid pool. (To the extent Kataoka and Ishii use experimental data to define the size distribution, some account is taken of sweep out by falling droplets.) This is done simply by finding the maximum droplet size that will have a terminal velocity equal to the superficial gas velocity. This limiting droplet size is found by solving:[92]

$$Re^2 f(Re) - \frac{4\rho_g(\rho_\ell-\rho_g)g\, d_o^3}{3\mu_g^2} = 0$$

where Re = Reynolds number = $\rho_g V_s d_o/\mu_g$,

$f(Re)$ = drag coefficient =

$$= \begin{cases} 3/16 + 24/Re & \text{for } Re < 0.01 \\ 24/Re\,[1 + 0.1315\, Re^Z] & \text{for } 0.01 \leq Re \leq 20 \end{cases},$$

$Z = 0.82 - 0.05\,(\log_{10}Re)^2$, and

d_o = upper limit droplet size.

(Note an alternate definition of $f(Re)$ is $0.2924\,[1 + 9.06/Re]^2$. This definition, offered by Abraham,[198] does not have a discontinuity at $Re = 0.01$ as does the definition presented above.)

If deposition of droplets on the constraining walls of the system is ignored, then the weight fraction of entrained droplets having sizes less than d_o is given by:

$$F(D<d_o) = \left(\frac{d_o}{D_{max}}\right)^{3/2} .$$

$F(D<d_o)$ will not equal, in general, the ratio E*(far field)/E*(near surface) specified by Kataoka and Ishii--which is a deficiency of their model. But, an approximate distribution function for the sizes of droplets entrained in the flow far from the pool can be defined as:

$$F_{ff}(D<\bar{D}) = \begin{cases} \left(\frac{\bar{D}}{d_o}\right)^{3/2} & \text{for } \bar{D} < d_o \\ 1 & \text{for } \bar{D} > d_o \end{cases}$$

where $F_{ff}(D<\bar{D})$ is the fraction of the entrained mass with droplet sizes less than $\bar{D}$. This cumulative distribution function is plotted against droplet size for several superficial gas velocities in Figure 46. In preparing this figure it was assumed σ_ℓ = 400 dyne/cm, ρ_ℓ = 7 g/cm^3, and that the sparging gas was an equal parts mixture of CO and H_2 at 2200 K. From the figure it is apparent that the limiting size of entrained droplets decreases from about 130 μm when the superficial gas velocity is 100 cm/s to about 40 μm when the gas velocity is 10 cm/s. The mass weighted size distribution is sharply peaked near the limiting size. The entrained droplets for this example are somewhat larger than what is typically considered an aerosol. Their residence time within a reactor containment will be short.[9]

C. Some Experimental Results and the Approach Taken in the VANESA Model Toward Mechanical Aerosol Generation

A fairly sophisticated formalism exists for predicting aerosol generation by entrainment. A cruder data base exists for aerosol generation by bubble bursting. In all cases these models and data have been obtained in studies of aqueous systems or conventional liquids. Naturally, there arises the question of applicability to molten core debris.

There are differences between conventional liquids and molten core debris having to do with physical properties. The molten oxide phase of core debris will have density and surface tension 3 to 8 times the density and surface tension of water. The viscosity of the molten core debris could be more than 10^5 times the viscosity of water. That liquid viscosity has not appeared in the models and correlations of mechanical aerosol generation may reflect the fact that most of the work to date has focused on very low viscosity fluids.

Arellano and Brockmann[339] have undertaken an investigation of mechanical aerosol generation when gases sparge

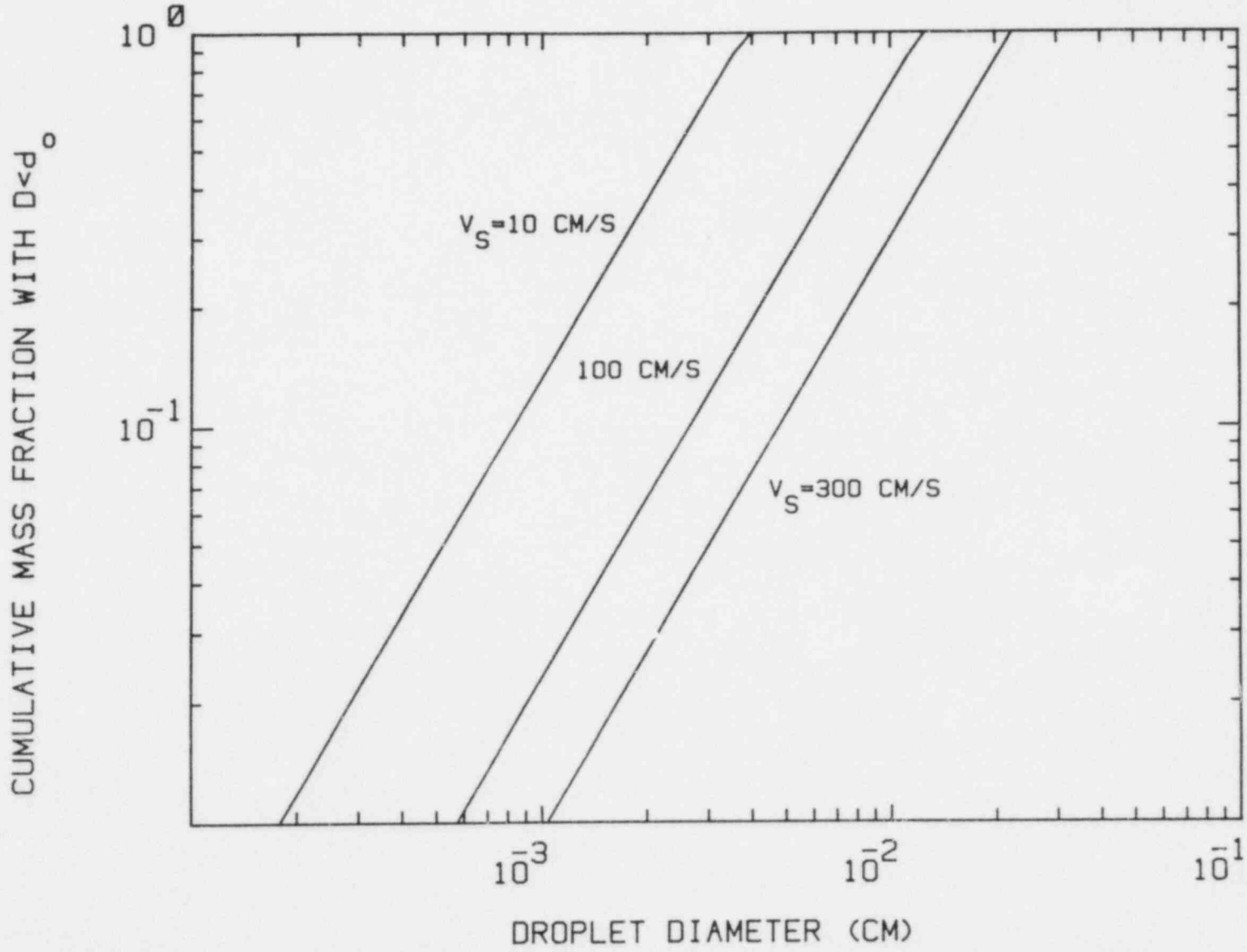

Figure 46. Cumulative Mass Fraction of Entrained Droplets in the "Far-Field" Region as a Function of Droplet Size for Several Superficial Gas Velocities

high temperature liquids. This work has just begun. Early results do indicate some similarities between high temperature fluids and aqueous systems. A photomicrograph of aerosol particles produced by gas bubbles bursting in molten concrete is shown in Figure 47. The particles are approximately spheres. Their sizes seem to be less than about 2 μm which is somewhat smaller than might be expected from data for aqueous systems.

High temperature liquid systems can form solidified surface crusts. Crust formation is particularly likely when a water pool overlies molten core debris interacting with concrete. Whether mechanical aerosol generation will occur when there is a solidified crust over a liquid is not known. The disposition of the crust relative to the underlying liquid may have a bearing on this issue. Crusts floating on the liquid may inhibit mechanical aerosol formation. Crusts separated from the liquid by a gas space may affect the transport but not the generation of aerosols. Blose et al. have undertaken some examinations of these questions in connection with their studies of combined core debris/concrete/coolant interactions.[39,40]

The questions of mechanical aerosol generation were considered highly uncertain during the development of the current implementation of the VANESA model. Consequently, a simple relationship between the number of gas bubbles emerging from the molten core debris and the amount of mechanically generated aerosol is incorporated into the model. Each bubble is hypothesized to produce a number of particles of specified size. For most of the calculations done to date, a bursting bubble was assumed to form 2000 particles each of which was 1 μm in diameter. This is a quite low mechanical aerosol generation rate. It will produce, typically, an aerosol concentration of about 0.2 grams per cubic meter (STP) of evolved gas.

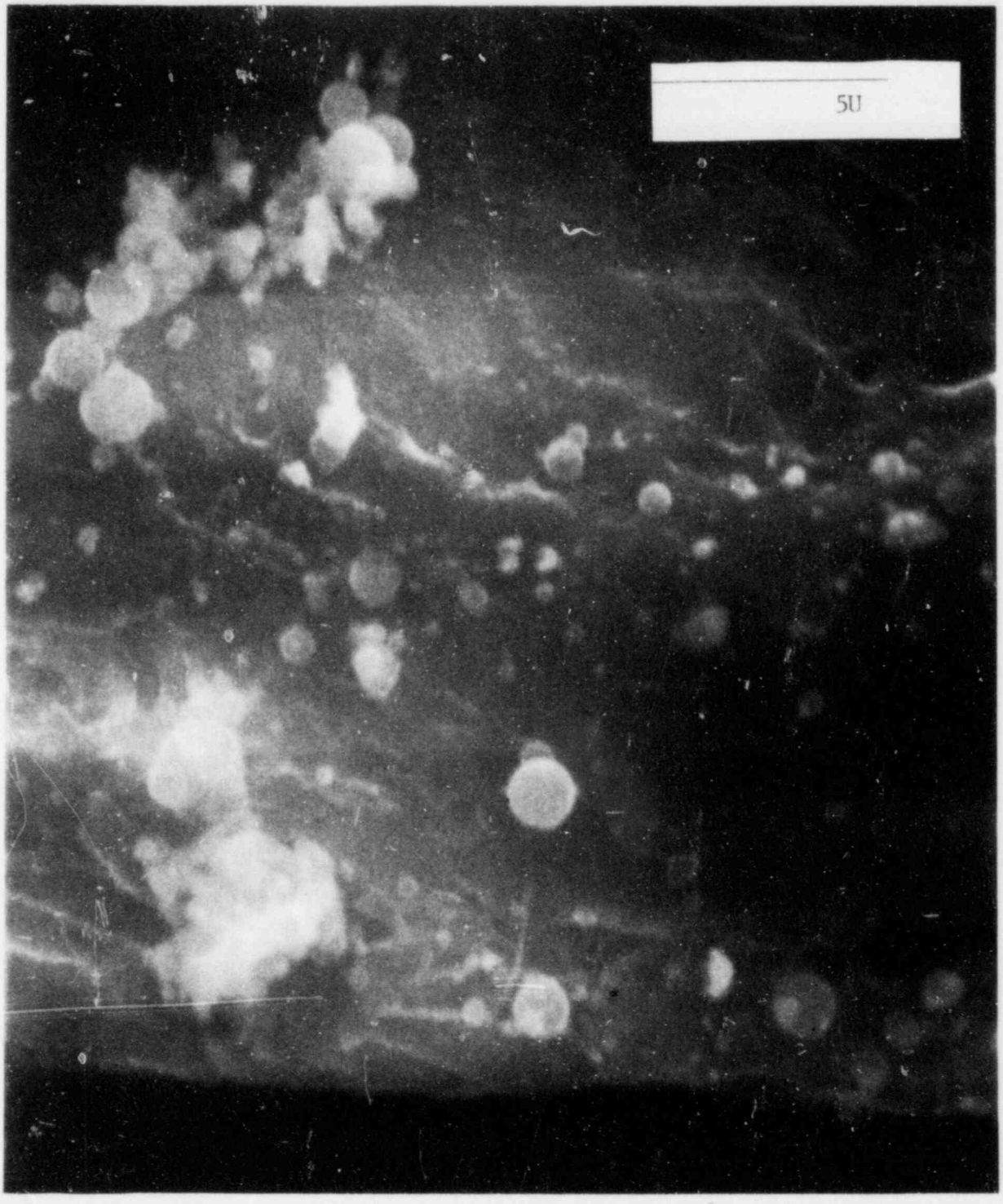

Figure 47. Photomicrograph of Aerosols Produced by Gas Sparging Molten Concrete

VI. VAPOR CONDENSATION AND THE FORMATION OF AEROSOLS

To this point in the discussion of the VANESA model, vapor generation and the mechanical formation of aerosol particulate have been described. As the mixture of gas, vapor, and particulate rises, it will cool. Estimation of the quantitative details of the cooling process is not simple and is not a part of the current implementation of the VANESA model. It can be assured that at some point temperatures in the mixture will become low enough that the vapors will condense. The nature of the condensation process will affect the physical characteristics of the particulate matter injected into the containment atmosphere as a result of core debris interactions with concrete. These physical characteristics have a very significant bearing on the behavior of the particulate in the containment and, as a result, a significant bearing on the radionuclide release possible from a nuclear plant during a severe accident.

The condensation process can involve many processes. Assume, for the moment, that the mixture of gas, vapor, and mechanically generated aerosol has cooled uniformly to the point that the vapors are supersaturated. Then,

1. Vapors could homogeneously nucleate particles,
2. Vapors could heterogeneously nucleate particles,
3. Vapors could condense on the surfaces of the mechanically generated particulate or on the nucleated particles,
4. Particles could coagulate.

These are, of course, competitive processes. Nucleation, whether it is homogeneous or heterogeneous nucleation, creates very fine particles. Condensation leads to growth of particles which may already be quite large. Coagulation of particles reduces the surface area available for condensation and enlarges particles produced by nucleation. The technology available for predicting the rates of these various processes is outlined in the subsections below.

A. Homogeneous Nucleation of Particles

Once a vapor is sufficiently supersaturated, it can spontaneously form condensed phase particles. A substantial body of literature exists to describe the conditions and rates of homogeneous nucleation of condensed phase materials from supersaturated vapor.[217-220] The several models that have been developed to describe the process attempt to predict the rate of formation of a particle of a size that will grow faster than it reevaporates.

Five of the available homogeneous nucleation rate expressions are summarized in Table 54. Of particular interest is the Loethe-Pound rate expression as modified by Feder. This rate expression acknowledges the heat effects of condensation and the presence of a noncondensible carrier gas.

The nucleation rate of tin at 2000 K is shown as a function of the saturation ratio in Figure 48. (Note that it is the base 10 logarithm of the nucleation rate that is plotted in this figure.) Typically, nucleation is assumed to occur when the nucleation rate is 1 nuclei/cm^3-s. When tin is taken to have a surface tension of 439 dyne/cm (see Chapter IV), this rate is reached when the saturation ratio is about 3.1. However, the rate of nucleation accelerates to 10^{10} nuclei/cm^3-s by increasing the saturation ratio to just 4. Nucleation rate is obviously an extraordinarily sensitive function of the vapor supersaturation and consequently it is a sensitive function of temperature! Accurate prediction of homogeneous nucleation rate requires predictions of the actual partial pressures of vapors and equilibrium partial pressures of vapors that have an accuracy far beyond what is likely to be achieved in the analysis of core debris/concrete interactions.

The example calculation shows that nucleation does not occur just when the vapor partial pressure reaches the saturation partial pressure. Some additional cooling is required. For the example calculation, nucleation did not begin until the vapor had cooled to a temperature about 131 K less than the temperature at which the vapor was saturated. Cooling of the vapor is accomplished as the mixture moves along the temperature gradient. The time required for this cooling to take place offers an opportunity for other vapor processes such as heterogeneous nucleation and vapor condensation on surfaces to take place. If efficient, these other processes can relieve the supersaturation of the vapor and prevent homogeneous nucleation conditions from arising.

A simple estimate of the time required to achieve supersaturations necessary to cause homogeneous nucleation can be made as follows. The boundaries of a reactor cavity are concrete. These boundaries are typically 1-2 meters away from the pool surface. They are heated by radiation and convection. A lower bound estimate of the thermal gradient above the melt pool can be constructed by assuming the boundaries are at the concrete solidus and that temperatures fall at a constant rate over the distance from the pool surface to the farthest visible boundary. Then a gradient of about 3 K/cm is usually found. (Powers and Arellano[17] reported gradients above molten steel interacting with concrete of about 15 K/cm.) Then to achieve the 131 K cooling necessary

Table 54

Homogeneous Nucleation Rate Expressions

Becker-Doring Theory[221]

$$J = \frac{5.54 \times 10^{31} S^2 \left(\frac{P(eq)}{T}\right)^2 M^{1/2} \sqrt{(\sigma)}}{\rho_\ell} \exp\left\{\frac{-17.553\sigma^3 M^2}{T[\rho_\ell T \ell n(S)]^2}\right\}$$

$$r^* = \frac{2.405\sigma M}{\rho_\ell T \ell n(S)} \quad A°$$

Loethe-Pound Nonisothermal Theory[222,223]

$$J = \frac{0.088\rho_\ell^2 k^3}{(2\pi m)^{1/2} h^6}\left(\frac{b^2}{b^2 + q^2}\right)\rho_v T^3 \sqrt{\sigma}(r^*)^{12} \exp\left\{\frac{-4\pi(r^*)^2\sigma}{3kT}\right\}$$

$$r^* = \frac{2\sigma m}{\rho_\ell kT \ell n(S)}\left[1 - \frac{3kT}{2\pi\sigma(r^*)^2}\right]$$

$$b^2 = \left(C_v(\text{vapor}) + \frac{k}{2}\right)kT^2 + \frac{\beta_C}{\beta_v}\left(C_v(\text{carrier}) + \frac{k}{2}\right)kT^2$$

$$q = L - \frac{kT}{2}$$

$$\beta_C = \frac{P_C}{(2\pi m_C kT)^{1/2}}$$

$$\beta_v = \frac{P(\text{vapor})}{(2\pi m_v kT)^{1/2}}$$

Reiss-Katz-Cohen Upper Bound Theory[224]

$$J = \frac{1}{\rho_\ell}\sqrt{\frac{2}{\pi m^3}}\,\rho_v^2 \sqrt{\sigma}\left[1 + \frac{9\bar{x}^{4/3} q''}{2\gamma}\right]^{1/2} \exp\left\{g - \bar{x}g' - \frac{\gamma\bar{x}^{2/3}}{3}\right\}$$

Table 54 (Continued)

Homogeneous Nucleation Rate Expressions

$$g = \frac{7.465RT\rho_\ell}{MP(eq)} - \ell n(S) + 1/2\ \ell n\bar{x}$$

$$g' = \frac{1}{2\bar{x}}$$

$$g'' = -\frac{1}{2\bar{x}^2} \qquad \gamma = \left[\frac{36\pi m^2}{\rho_\ell^2}\right]^{1/3} \frac{\sigma}{kT}$$

Reiss-Katz-Cohen Lower Bound Theory[224]

$$J = \frac{1}{\rho_\ell}\sqrt{\frac{2}{\pi m^3}}\ \rho_v^2\sqrt{\sigma}\left[1 + \frac{9\bar{x}^{4/3}g''}{2\gamma}\right]^{1/2} \exp\left\{g - \bar{x}g' - \frac{\gamma\bar{x}^{2/3}}{3}\right\}$$

$$g = 0.97 + \frac{3}{2}\ \ell n(\bar{x})$$

$$g' = \frac{1.5}{\bar{x}}$$

$$g'' = \frac{-1.5}{\bar{x}^2}$$

Reiss Nucleation Theory[225]

$$J = \frac{1}{\rho_\ell}\sqrt{\frac{2}{\pi m^3}}\ \rho_v^2\sqrt{\sigma}\left[1 + \frac{9\bar{x}^{4/3}g''}{2\gamma}\right]^{1/2} \exp\left\{g - \bar{x}g' - \frac{\gamma\bar{x}^{2/3}}{3}\right\}$$

$$g = \frac{2\gamma}{3\bar{x}^{1/3}} - \ell n(S)$$

$$g' = \frac{2\gamma}{9\bar{x}^{4/3}} \qquad g'' = \frac{8\gamma}{27\bar{x}^{7/3}}$$

where J = nuclei formed per unit volume per unit time,

S = saturation ratio = P(vapor)/P(equilibrium),

Table 54 (Continued)

Homogeneous Nucleation Rate Expressions

$P(eq)$ = $P(equilibrium)$ = equilibrium partial pressure of vapor,

M = molecular weight of vapor,

σ = surface tension of condensed vapor,

ρ_ℓ = density of condensed vapor,

r^* = radius of nuclei,

h = Planck's constant,

m = mass of a vapor molecule,

ρ_V = vapor density = $MP(eq)/RT$,

R = gas constant,

k = Boltzmann's constant,

$C_V(vapor)$ = constant volume heat capacity of vapor,

$C_V(carrier)$ = constant volume heat capacity of noncondensing gas,

P_C = partial pressure of noncondensing gas, and

$\bar{x}$ = average number of vapor molecules in the critical nuclei which is found from

$$\ell n(S) = \frac{2\gamma}{3\bar{x}^{1/3}} - g'.$$

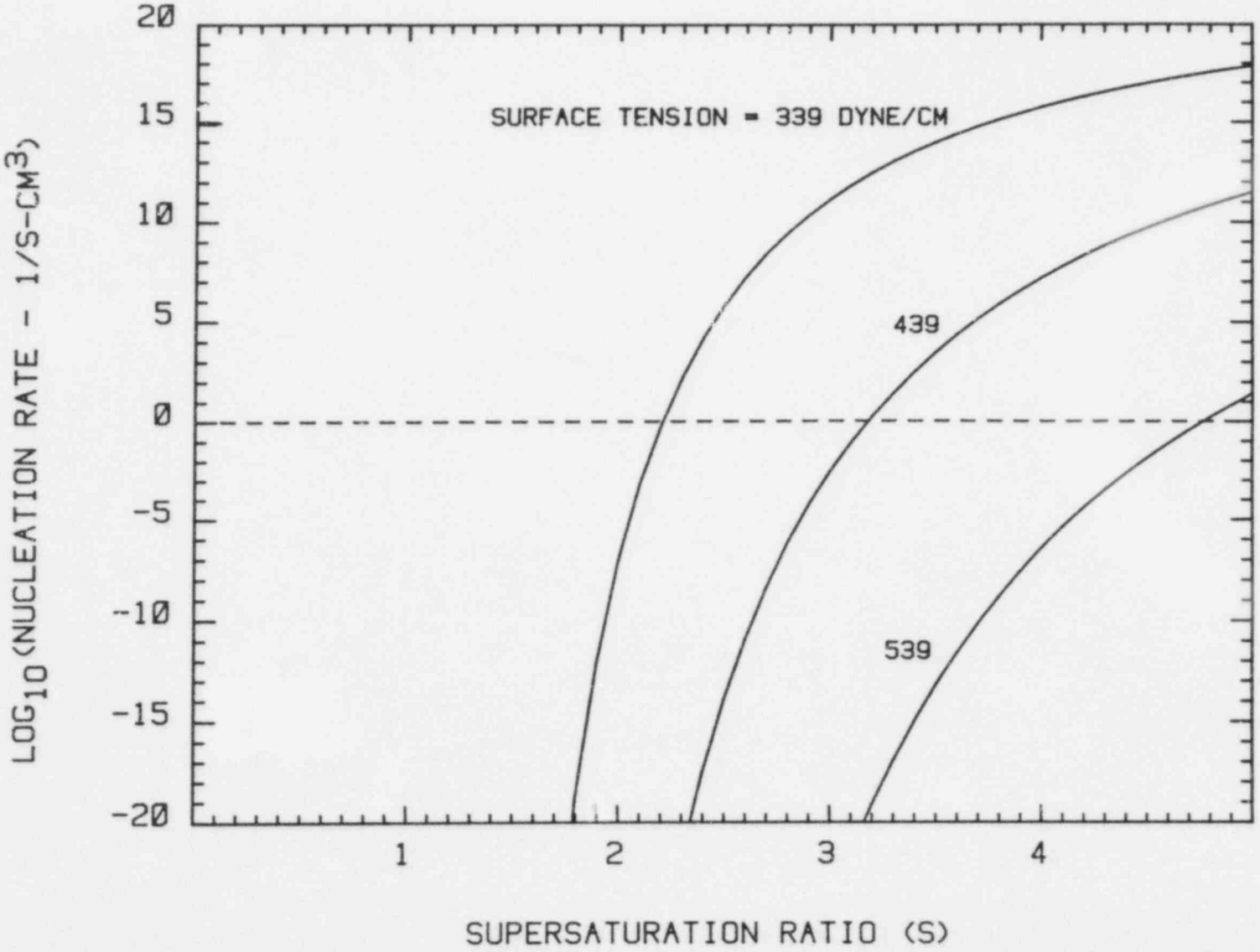

Figure 48. Nucleation Rate of Tin at 2000 K as a Function of the Supersaturation of the Vapor. Curves are marked by the assumed surface tension of liquid tin. Correlations of surface tension presented in Chapter 4 would yield 439 dyne/cm.

to initiate homogeneous nucleation, the vapor must travel about 44 cm. The vapor would have to travel an additional 12.5 cm for the rate to reach 10^{10} nuclei/cm^3-s. At low superficial gas velocities many seconds would be available for competitive processes to relieve the supersaturation of the vapor. But, at superficial gas velocities on the order of 100 cm/s, it would be difficult for the competitive processes to prevent homogeneous nucleation.

The tin nucleation example also illustrates another problem encountered in the estimation of homogeneous nucleation rates. The rates are quite sensitive to the surface tension of the condensed vapor. Varying the surface tension of tin by a factor of about $\pm$25 percent changes the supersaturation necessary to initiate homogeneous nucleation from 2.1 to more than 4.5. The sensitivity of nucleation rates to surface tension is such that a 22 percent variation in surface tension of tin would produce greater variations in the rates than the variation in predictions of five models shown in Table 54.

There are at least two difficulties raised by the influence of surface tension on the predictions of the homogeneous nucleation rate. The first is that it is unclear whether conventional surface tensions should be used in the rate expressions. Conventional surface tensions are properties of macroscopic, flat, surfaces. They are being applied to nuclei of very small dimensions and, consequently, very high curvatures. It is known that curvature has an effect on surface tension[226] and that a value substantially higher than that obtained for bulk liquids should apply to the nuclei. Some arguments have been made that using surface tensions appropriate for bulk liquids compensates for some of the approximations in the nucleation rate models.[220]

A second problem is that nucleation during reactor accidents will not involve just a single vapor. Many species will nucleate simultaneously. The surface tension of a multicomponent liquid will not be the same as that of any of its constituents when pure. In fact, the rate expressions shown in Table 54 are not really applicable to multicomponent condensation. Even for simultaneous condensation of just two vapors, the rate expressions can be vastly more complex.[217]

B. Heterogeneous Nucleation on Ions

Ionized species in the gas phase will polarize adjacent, neutral, vapor species. The induced dipoles in these neutral species will cause the species to form a shell around the ionized constituent of the vapor. The effect is to reduce the free-energy of the vapor by reducing the charge density associated with the gas phase ion. These assemblages of an

ion surrounded by polarized vapor species are embryonic forms of nucleated droplets. Fluctuations in the number of vapor species polarized by the ion can make the structure large enough that it grows spontaneously when vapor concentrations are supersaturated. Note, the ion responsible for formation of the assemblage need not be derived from the condensing vapor.

Ions in the gas phase can then lead to vapor nucleation. Volmer and Weber[226] developed an expression for the rate of vapor nucleation on ions following the same sort of logic employed in developing the Becker-Doring theory of homogeneous nucleation. Two molecular dimensions are needed in this theory. One of these dimensions is the radius of the nuclei that will grow spontaneously in the supersaturated vapor--r_k. The other dimension is the radius of the ion and surrounding cluster of polarized vapor species--r_a. These dimensions are the roots of the equation:

$$-kT\ell n(S) + \frac{2V_m\sigma}{r} - \frac{e^2(1-1/\varepsilon)V_m}{8\pi r^4} = 0$$

where S = P(vapor)/P(equilibrium),

V_m = molecular volume of the vapor
= $(M/N)\ 1/\rho_\ell$,

σ = surface tension of the condensed vapor,

e = charge on an electron = 4.803×10^{-10} statcoulombs,

ε = dielectric constant for the condensed vapor,

r = radius, and

N = Avogadro's number.

The two pertinent roots of this equation are on either side of r_x where

$$r_x = \left[\frac{e^2(1-1/\varepsilon)}{4\pi\sigma}\right]^{1/3} .$$

The critical nucleus radius is greater than r_x and the ionized cluster radius is less than r_x. The roots are

readily found by the Newton-Raphson method for low supersaturations. As supersaturation increases, r_a increases until $r_a = r_x$. At this point the model is no longer valid. (Typically, supersaturations high enough for $r_a = r_x$ promote homogeneous nucleation.) Once the necessary dimensions are found, the nucleation rate can be computed from:

$$J(\text{nuclei/cm}^3\text{-s}) =$$

$$= \frac{4\pi r_k^2 SP(eq)}{(2\pi mkT)^{1/2}} \left(\frac{4\pi r_k^2 \sigma - e^2/r_k}{9\pi kTn_k^2} \right)^{1/2} \exp\left[- \frac{G(r_k)}{kT} \right] N_{ion}$$

where m = mass of a vapor molecule,

n_k = number of molecules in a critical nucleus =

$$= \frac{4/3\pi r_k^3}{V_m} = \frac{4/3\pi r_k^3 N \rho_\ell}{M},$$

$$G(r_k) = \frac{4\pi\sigma}{3}\left(r_k^2 - r_a^2\right) - \frac{2e^2}{3}\left(\frac{1}{r_k} - \frac{1}{r_a}\right),$$

$P(eq)$ = equilibrium partial pressure of the vapor in units of dynes/cm^2, and

N_{ion} = number of ions per unit volume.

The rate of nucleation is seen to be proportional to the concentration of ions in the gas phase. Heterogeneous nucleation on ions can be important in melt/concrete interactions because temperatures are high enough to induce thermal ionization of gas species:

$$M \rightarrow M^+ + e^- \quad .$$

Thermal ionization of alkali metals such as sodium and potassium from the concrete or the radionuclide cesium can be sufficiently extensive to facilitate heterogeneous nucleation. Consider the ionization of sodium vapors. At 1000 K and a sodium partial pressure of 1×10^{-6} atmospheres, the

partial pressure of Na^+ in the gas phase is about 3×10^{-16} atmospheres which corresponds to only 3×10^3 ions/cm^3. When temperatures rise to 2000 K, the partial pressure of Na^+ rises to about 2×10^{-9} atmospheres and the ion concentration is about 1×10^{10} ions/cm^3. Such high ion concentrations will promote nucleation.

During core debris interactions with concrete, there is another source of ions. This additional source is the result of intense gamma irradiation of the gases passing through the core debris. Ions produced by irradiation will, of course, discharge rapidly if their concentrations exceed that dictated by the thermal equilibrium. But, because the irradiation is continuous, a metastable concentration of ions in excess of the thermal equilibrium concentration can develop.

Russell[227] has developed a rate expression for nucleation on ions that follows the logic used to derive the Loethe-Pound model of homogeneous nucleation. The rate expression is:

$$J(\text{nuclei/cm}^3\text{-s}) =$$

$$= \frac{4\pi r_k^2 P(eq) S}{(2\pi m k T)^{1/2}} \left\{ \frac{4\pi r_k^2 \sigma - e^2/r_k\,(1-1/\epsilon) - 18kT}{9\pi k T n_k^2} \right\}^{1/2}$$

$$\times N_{ion} \left(\frac{r_k}{r_a}\right)^{12} \exp\left\{ -\left[\frac{\frac{4\pi}{3}\,\sigma\,(r_k^2 - r_a^2) + \frac{2}{3}\,e^2(1-1/\epsilon)\left(\frac{1}{r_k} - \frac{1}{r_a}\right)}{kT} \right] \right\} .$$

The dimensions r_k and r_a used in this rate expression are found from:

$$\frac{-4\pi r^2}{V_m}\, kT \ell n(S) + 8\pi r\sigma - \left(\frac{e^2}{2r^2}\right)(1-1/\epsilon) - \frac{12kT}{r} = 0 \quad .$$

Results obtained with Russell's model are usually quite similar to those obtained with the Volmer and Weber model.

Nucleation rates for tin at 2000 K are shown as functions of supersaturation for various ion concentrations in Figure 49. Though ions promote nucleation, the effects for high temperature vapors of the type of interest in connection with core debris/concrete interactions is not strong.

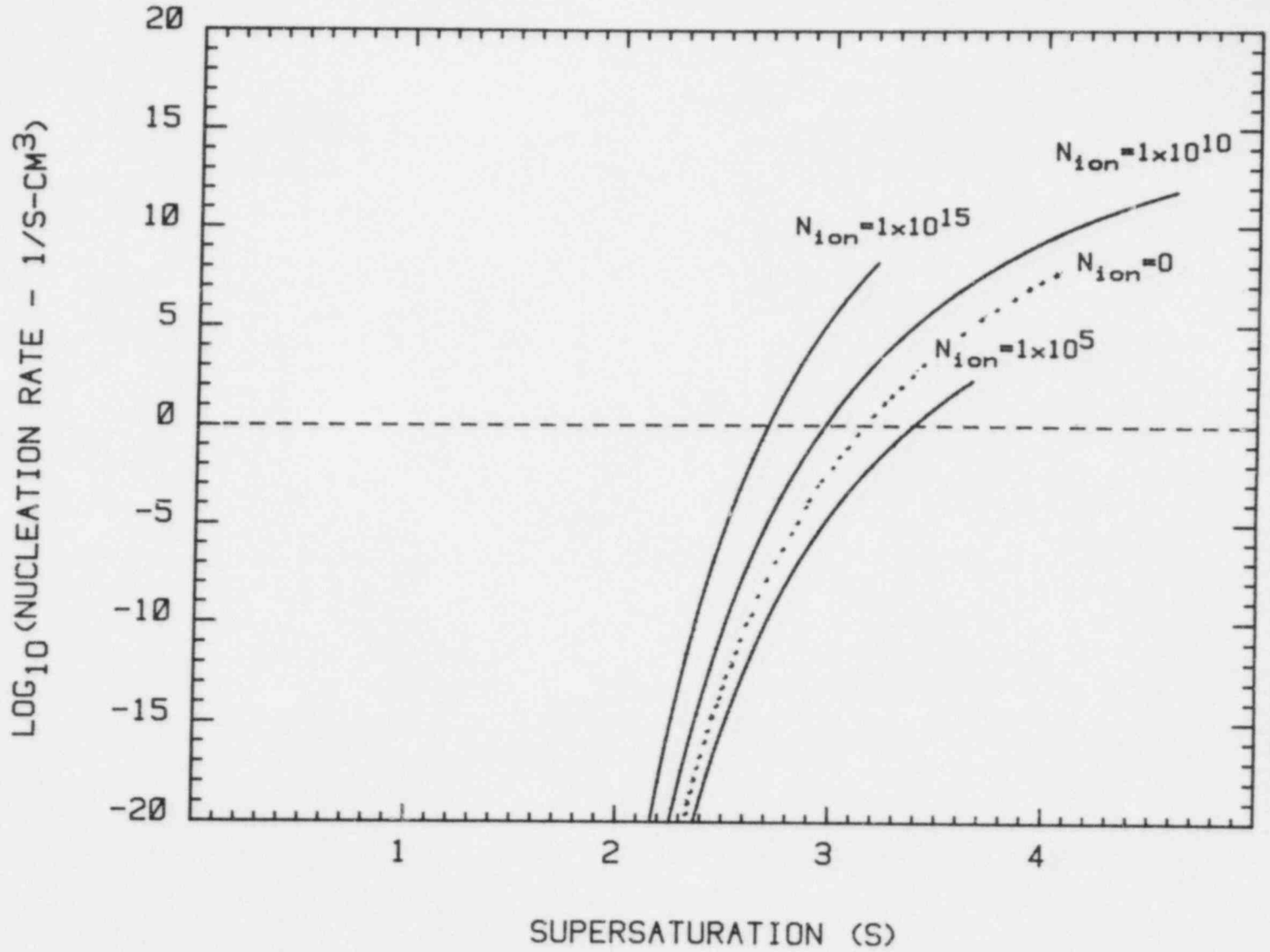

Figure 49. Heterogeneous Nucleation Rates for Tin in Atmospheres With Various Ion Concentrations. The dotted line for $N_{ion} = 0$ was calculated using the Becker-Doring model of homogeneous nucleation.

In fact, some critical ion concentration must be present for the heterogeneous process to surpass in rate homogeneous nucleation. It is difficult to imagine that the effect could be readily distinguished from homogeneous nucleation in accident analyses.

C. Particle Growth

Whether nucleation of particles* from the vapor occurs or not, the flow stream produced by core debris interactions with concrete will consist of gas, vapor, and particles. If nucleation by the homogeneous or heterogeneous mechanisms has occurred, vapor concentrations will still exceed saturation because of the Kelvin effect on the vapor pressure over surfaces of nonzero curvature. If nucleation does not occur, particles of condensed phase will be present in the flow as a result of entrainment from the melt or bursting of gas bubbles at the surface of the melt.

Because condensible vapor is still present in the flow stream, the characterization of the source term from core debris/concrete interactions is not complete at this stage of the analysis. This principle missing component of the characterization is a description of the physical characteristics of the aerosol particles passing out of the reactor cavity into the reactor containment. Numerous studies of the models employed in the analyses of severe accident phenomena in the reactor containment have shown how important are the descriptions of the size distribution of aerosols produced by melt/concrete interactions.

Safety systems such as containment sprays, ice condenser beds, and the steam suppression pools found in boiling water reactors can attenuate significantly the release of radioactivity from a plant during an accident. The attenuation comes about because the systems trap aerosols produced during fuel release processes, including aerosols produced during melt/concrete interactions. The efficiency with which aerosols are captured depends significantly on the aerosol particle size. As an example of this sensitivity in performance to the aerosol particle size consider the decontamination of aerosol-laden gases as they pass through a suppression pool. The decontamination is shown as a function of particle size in Figure 50. Clearly, very coarse

*The terms "droplet" and "particle" are used interchangeably in this section. This is done simply to follow the terminology of the field and does not constitute an indication of the physical state of condensed material in the flow stream. Eventually, of course, any liquids in this flow will freeze.

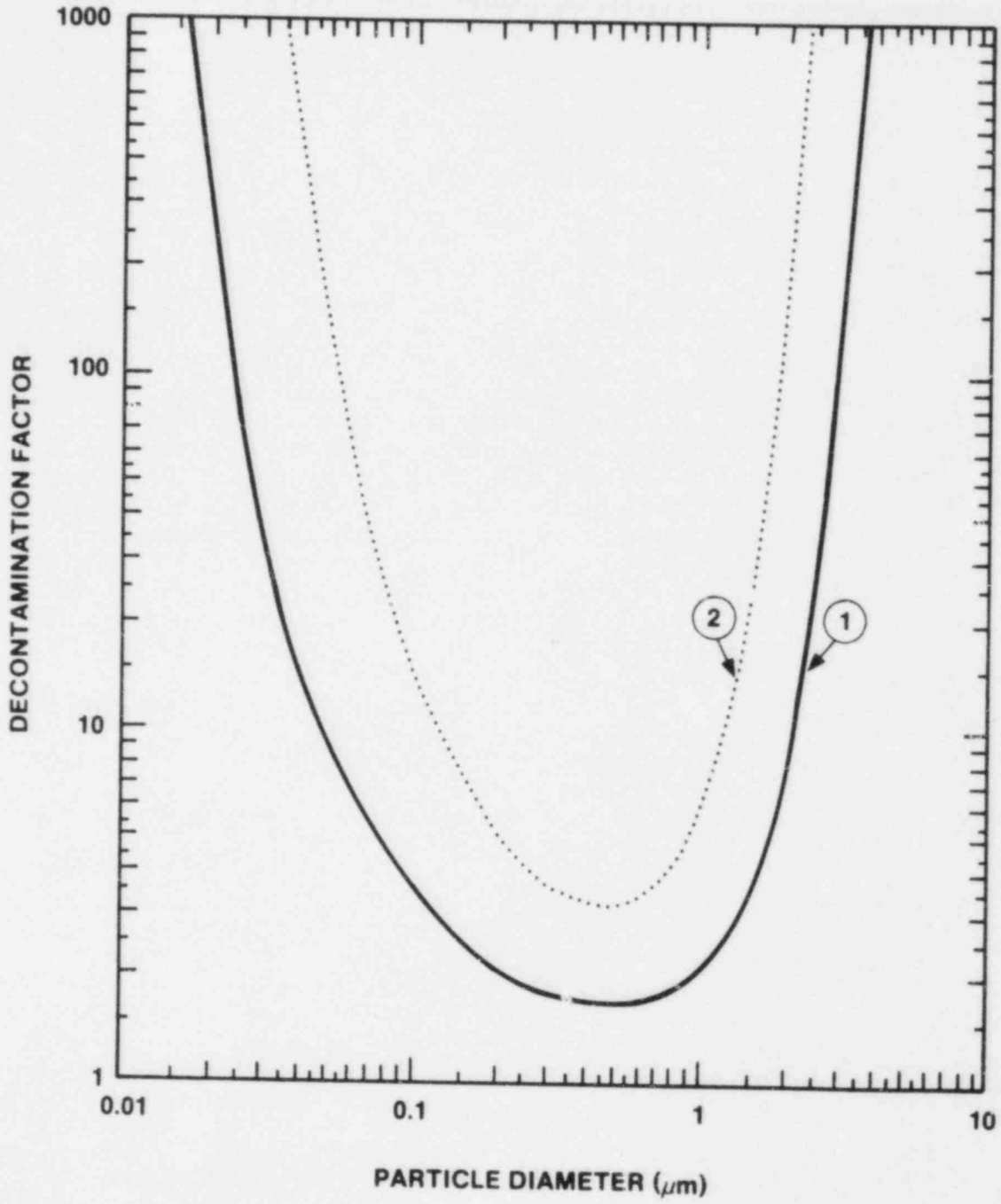

Figure 50. Decontamination Produced by a Steam Suppression Pool as a Function of the Aerosol Particle Size.[174] Solid curve marked "1" is for a pool 3.91 m deep and bubbles 0.75 cm in diameter. Dotted curve marked "2" is for a pool 5.43 m deep and bubbles 0.55 cm in diameter.

and very fine aerosol particles will be efficiently trapped in the suppression pool. Particles of an intermediate size will be little affected during passage through the suppression pool.

Two processes are responsible for the development of the aerosol size distribution:

1. Condensation of vapors on surfaces, and

2. Coagulation of particles formed or entrained in the flow stream.

There has been much debate in the literature on the nature of processes that affect the size distribution of aerosols produced by high-temperature processes. The aerosols produced by electrical arcs and flame combustion of metals have been studied. Granquist and Buhrman[240] have found that arc melting Al, Fe, Co, and Sn yields aerosols having a log-normal size distribution with a geometric standard deviation of 1.5 irrespective of the conditions employed. Fuchs and Sutugin[241] suggest such a result would be obtained in a system in which coagulation little affects the size distribution because of rapid quenching and dilution of vapors. Hermsen and R. Dunlap[242] have argued that nucleation and condensation have the dominant influence on the size distribution of aerosols produced by flame combustion. Ulrich[243] disputes this contention and argues that coagulation by Brownian motion is the most important determinator of the size distribution. Senior and Flagan[244] have found it satisfactory to consider only nucleation and condensation for estimating the size distribution of aerosols formed during combustion of coal particles. Several investigators have called attention to the effects of cooling rate and dilution on the relative importance of coagulation and condensation on aerosol particle size distribution.[245-248]

It is apparent from the survey of available literature on aerosol production from high-temperature systems that no absolute definition of the dominant factors affecting the aerosol size distribution can be made. Though it is apparent that coagulation and condensation are the important processes, the relative contributions of these processes are dependent on the cooling rate of the vapor and the dilution of the vapor and particle mixture. Thus, the particle size distribution of aerosols formed during core debris interactions with concrete will depend on the velocity of gas flow through the reactor cavity, the nature of core debris attack on the concrete, and the natures of both vaporization and entrainment as release mechanisms. An absolute prescription of the size distribution that is generically applicable probably cannot be formulated. It is necessary then to delve further into the details of the coagulation

and condensation processes that influence the size distribution of aerosols injected into the reactor containment as a result of core debris/concrete interactions. These processes are discussed further below.

1. Vapor Condensation

When vapor concentrations exceed saturation, the vapors can condense on surfaces. The surfaces available for vapor condensation are:

1. Structural surfaces in the reactor cavity,
2. Surfaces of material entrained in the flow stream, and
3. Surfaces of nucleated particles.

Condensation of vapors on structural surfaces is neglected here. The surface area presented by structures in reactor cavities is not large in comparison to surface areas of condensed materials suspended in the gas. The flow pathways available to the effluent produced by melt/concrete interactions are broad so that there is a considerable difficulty in transporting vapors to the structure surfaces. Attentions here are focused then on the condensation of vapors on particles entrained or nucleated in the flow stream.

Mass transport of the vapors to the surfaces is an omnipresent limitation to the rate of condensation. Two regimes for vapor mass transport can be distinguished. In the first of these regimes the particles are large in comparison to the mean free path of vapor molecules.* Then the flux of vapor molecules to the surface of the particles is found from:

$$J(\text{moles/cm}^2\text{-S}) = \frac{1}{A}\frac{dn(\text{vapor})}{dt} = \frac{k_g(\text{vapor})}{RT}[P(\text{bulk})-P(\text{eq})]$$

where k_g is a gas phase mass transport coefficient.

*The concept of a "mean free path" for gas phase molecules can be readily understood if the gas molecules are considered to be hard spheres with no mutual attraction. The concept of a mean free path is neither useful nor used when dispersive attractions among gas molecules are recognized. Fortunately, at high temperatures the importance of dispersive forces wanes in the face of the high thermal energies of gas molecules and a mean free path for gas molecules is a useful approximation.

The second regime arises when the particles are very small relative to the mean free path of the vapor molecules. Then, the surface is subjected to molecular bombardment. The flux of vapors to the surface, that remain at the surface, is given by:

$$J(\text{moles/cm}^2\text{-S}) = \frac{\alpha Z[P(\text{bulk}) - P(\text{eq},d_p)]}{(2\pi mkT)^{1/2}N_A}$$

where α = condensation coefficient discussed in connection with surface vaporization in Chapter 4,

Z = factor for converting the units of pressure,

m = mass of a vapor molecule,

N_A = Avogadro's number, and

$P(eq,d_p)$ = the vapor pressure in equilibrium with a surface of a sphere having the diameter of the particle, d_p.

Note that this rate expression recognizes the elevation in the vapor pressure over very small particles. The pressure at such particles is given by:

$$\ell n\left[\frac{P(eq,d_p)}{P(eq)}\right] = \frac{\sigma M}{d_p \rho_\ell N_A kT}$$

where ρ_ℓ is the density of the condensed liquid. It can be seen then that fine particles such as those produced by nucleation are unstable. Small increases in d_p or decreases in P(eq), say as the result of cooling, will drive vapor to condense on the particles.

Davis et al.[249] have suggested a formula for interpolating between the two regimes of vapor mass transport.

Consider now the condensation of vapors on particulate entrained in the flow. As the effluent produced by the core debris/concrete interaction cools, the condensation of vapors on the entrained particles directly competes with nucleation as a mechanism for relieving supersaturation of the vapor. The results of condensation on entrained particulate and nucleation of vapor are not equivalent. Nucleation will produce very fine particles which are easily maintained in

suspension in the flow stream. Within the region termed by Kotaoka and Ishii the "momentum-controlled" region vapors can condense on entrained particles that fall eventually back into the core debris pool. Even in the so-called "far-field" region, condensation of vapors will cause particles that are already large to grow further. Whether growth of these particles will be sufficient to cause them to fall out of suspension is problematical. What is clear is that growth of these entrained particles will affect the subsequent behavior of the particles in the containment atmosphere.

The entrained particles are reasonably approximated as spheres. As long as the particles are not too large, they may be considered rigid. Then, if there is a significant differential velocity between the particles and the bulk flow, the mass transport coefficient, k_g, is found from:

$$Sh = 1 + \left[1 + \frac{1}{ReSc}\right]^{1/3} Re^{0.41} Sc^{1/3} \quad \text{for } 1 \leq Re \leq 400$$

where $Sh = k_g d_p / D_{AB}$.

$Re = \Delta U d_p \rho_g / \mu_g$.

ΔU = differential velocity between the flow and the particle, and

$Sc = \mu_g / \rho_g D_{AB}$.

When the differential velocity between the flow and the particle is negligible, then the mass transport of vapor to the particle surface is the result of molecular diffusion and natural convection. The mass transport coefficient is then found from:[250]

$$Sh = \begin{cases} 2 + 0.569\ (GrSc)^{1/4} & \text{for } GrSc < 10^8 \\ 2 + 0.0254\ (GrSc)^{1/2}\ Sc^{0.244} & \text{for } GrSc > 10^8 \end{cases}$$

where $$Gr = \frac{\rho_g g d_p^3}{\mu_g^2} \left[\frac{\partial \rho_g}{\partial P(vapor)}\right] P(vapor).$$

A lower bound on the mass transport coefficient is found by considering only molecular diffusion and ignoring both natural and forced convection:

$$Sh = 2$$

or

$$k_g = \frac{2D_{AB}}{d_p} \quad .$$

Then, the molar rate of gas condensation on an entrained particle is:

$$\frac{dn}{dt} = \frac{2\pi d_p}{RT} D_{AB} P(eq)(S-1)$$

where S is the saturation ratio, P(vapor)/P(eq). The effect of condensation on entrained particles on the saturation ratio is given by:

$$\left.\frac{dS}{dt}\right|_{COND} = 2\pi d_p N_p D_{AB}(S-1)$$

where N_p is the number of entrained particles per unit volume. The rate at which supersaturation is relieved by condensation can be compared to the rate at which homogeneous nucleation relieves supersaturation (Becker-Doring theory):

$$\left.\frac{dS}{dt}\right|_{NUCL} = \frac{2.65 \times 10^{11} S^2 P(eq) M^{5/2} \sigma^{7/2}}{\rho_\ell^3 T^4 [\ell n(S)]^3} \exp\left[\frac{-17.553\sigma^3 M^2}{\rho_\ell^2 T^3 [\ell n(S)]^2}\right] \quad .$$

The ratio of $dS/dt|_{COND}$ to $dS/dt|_{NUCL}$ for tin vapor at 2000 K is shown in Figure 51 as a function of the saturation ratio and for several sizes of entrained particles. The amount of entrained mass was taken to be 1 gram/m^3 in preparing this figure. It is apparent from the results in the figure that the importance of condensation increases as the particle size decreases and there is more surface area available for condensation. The importance of condensation as a mechanism for relieving supersaturation of the vapor is overwhelmingly dependent on the saturation ratio. Condensation on entrained particles will be the dominant means for relieving supersaturation if the saturation ratio is low. As the supersaturation increases nucleation becomes progressively more important.

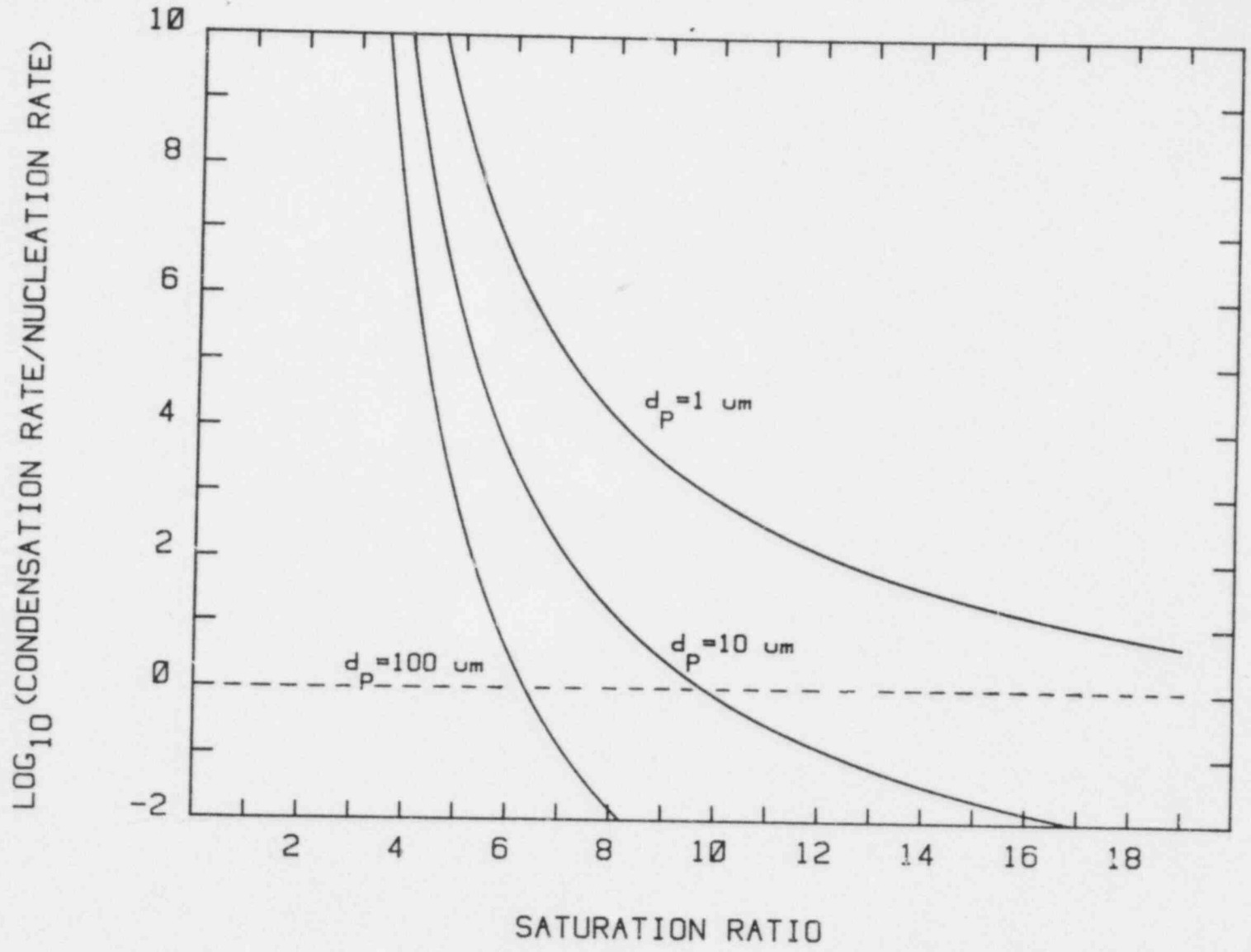

Figure 51. Comparison of the Rates of Condensation and Nucleation of Tin Vapor at 2000 K and Various Levels of Supersaturation. The curves shown in the figure were calculated assuming there was 1 g/m^3 of entrained core debris having the indicated particle size.

The saturation ratio of the vapor depends, of course, on the cooling experienced by the effluent produced from the melt/concrete interaction. When flow rates are slow and the temperature gradient above the melt is small, vapor condensation on entrained particles may be sufficiently rapid to prevent nucleation of particles in the flow stream. When gas production by the melt attack on concrete is high so that flow velocities are high and the effluent stream can rapidly cool, nucleation of particles will be the first important step in relieving supersaturation of the gas. Even though condensation on entrained particles will occur, the extent of condensation under high flow conditions will be too low to prevent the development of saturation ratios necessary to promote extensive nucleation.

Nucleation alone cannot relieve totally the supersaturation of the gas phase. The small particles produced by nucleation exist only if the vapor concentration is elevated relative to the equilibrium vapor pressure over bulk condensed phase. The results obtained in the analyses of condensation on entrained particles suggest, however, that once nucleation begins, continued reduction in the vapor concentration would occur by condensation on the nuclei.

Analysis of the nucleation of particles followed by vapor condensation on the particles is complicated by the behavior of the particles. The particles will coagulate. Coagulation, of course, changes the sizes of the particles and the surface area available for condensation. There is then a coupled problem of condensation and particle coagulation to be solved.

2. Coagulation and Condensation

The equations necessary to describe a system involving simultaneous coagulation and condensation are written relatively easily. Let $n(i)$ be the number of particles per unit volume that are each composed of i condensed vapor molecules. Let $\beta(i,j)$ be the coagulation rate constant between particles containing i and j condensed vapor molecules. Then from continuity considerations:

$$\frac{dn(k)}{dt} = \frac{1}{2}\sum_{j=k_o}^{k-k_o} \beta(j,k-j)n(j)n(k-j) - \sum_{j=k_o}^{\infty} \beta(k,j)n(k)n(j)$$

$$+ \beta(1,k-1)n(1)n(k-1) - [\beta(1,k) + q(k)]n(k)$$

$$+ q(k+1)n(k+1) + r_o(t)\delta(k_o) \qquad \text{for } k \geq k_o$$

where q(k) is the rate at which a vapor molecule escapes a particle containing k condensed vapor molecules. The first two terms on the right-hand side of this equation describe the coagulation process. The next three terms account for the possibility that vapor evaporates from the particles. The final term accounts for the possibility tnat particles may continue to be nucleated at a rate $r_o(t)$ from the vapor. Nucleated particles will contain a critical number of condensed vapor molecules here denoted by k_o.

The size spectrum of particles to be produced by coagulation and condensation can be huge. Consequently, it is convenient to replace the summations by integrals. Let $n(V,t)dV$ be the number of particles per unit volume that have volumes within the interval of V to V + dV. Let $V_o = k_o\Delta V$ where ΔV is the molecular volume assumed by a vapor molecule when it condenses. Then the equation becomes

$$\frac{\partial n(V,t)}{\partial t} = \frac{1}{2}\int_{V_o}^{V-V_o} \beta(V-x,x)n(V-x,t)n(x,t)dx$$

$$- \int_{V_o}^{\infty} \beta(x,V)n(V,t)n(x,t)dx - \frac{\partial}{\partial V}\alpha_o(V)n(V,t)$$

$$+ \frac{\partial^2}{\partial V^2}\alpha_1(V)n(V,t) + r_o(t)\delta(V_o)$$

where $\alpha_o(V) = \Delta V\ \beta(V)n_g - q(V)$,

$$\alpha_1(V) = \frac{(\Delta V)^2}{2}\beta(V)n_g + q(V), \text{ and}$$

n_g = number density of vapor molecules.

The second derivative term involves the diffusion of particles, which is slow relative to vapor diffusion. Consequently, this second derivative term can be neglected.[228] The nucleation of particles is assumed in this discussion to have occurred, so that for the ensuing analysis of the system $r_o(t)$ is set to zero. Finally, the lower limits of integration can be extended to zero rather than V_o because $n(V,t)$ will always be zero for $V < V_o$. The equation is then

$$\frac{\partial n(V,t)}{\partial t} = \frac{1}{2}\int_0^V \beta(V-x,x)n(V-x,t)n(x,t)dx$$

$$- \int_0^\infty \beta(V,x)n(x,t)n(V,t)dv - \frac{\partial}{\partial V}\ \alpha_o(V)n(V,t)$$

subject to the initial condition that

$$n(V,0) = n_o(V)$$

and the boundary condition that

$$n(0,t) = 0 \quad .$$

There is, in addition, the equation for vapor concentration to consider. Here, however, it is convenient to consider the vapor to be at a fixed concentration.

Having written the equation, there then comes the problem of solving it. Casual examination of the equation shows that it would be a numerical nightmare to solve in the general case. Only recently have there been numerical solutions of some limiting forms of the equation.[229-230]

Fortunately, analytic solutions to the equations exist for situations that approximate real conditions.[231] Three such analytic solutions are examined here. The situations to be addressed are:

1. Pure coagulation of particles with no vapor condensation,

2. Pure condensation of vapor with no coagulation of particles, and

3. Simultaneous coagulation of particles and condensate of vapors with simplified rate expressions.

The objective of the consideration of these situations is to gain some understanding of how particle coagulation and vapor condensation affect the particle size distribution. It may then be possible to ascertain how careful a solution to the problem needs to be included in the VANESA model.

The first of the special cases is pure coagulation. Particles can coagulate as a result of being brought into contact by any of a variety of processes.* Brownian motion is the predominant mechanism of particle collisions for the systems of interest here. Turbulent diffusion and laminar shear may augment Brownian motion as causes of particle-particle collisions.

The agglomeration of a monodisperse aerosol as a result of Brownian motion is a problem first solved by Smoluchowski.[232,233] The differential equation considered by Smoluchowski is:

$$\frac{dn(t)}{dt} = \frac{-\beta_o}{2}[n(t)]^2$$

where n(t) is the total number of particles in the system at time t and β_o is a coagulation coefficient which is taken to be independent of the size of the particles. Smoluchowski's solution is

$$n(t) = N_o\left(\frac{2}{2 + \beta_o N_o t}\right) .$$

The number of particles present in the size range of kV_o to $(k+1)V_o$ is

$$N(kV_o) = N_o\left[\frac{2}{2 + \beta_o N_o t}\right]^2 \left[\frac{\beta_o N_o t}{2 + \beta_o N_o t}\right]^{(k-1)}$$

where N_o is the total number of particles present at time zero. Smoluchowski took the coagulation coefficient to be†

---

*It is common in the analysis of particle coagulation to presume that particles adhere 100 percent of the time when they contact. The suitability of this assumption probably rests upon the approximate cancellation of the effects of recoil and dispersive attractions of particles.

†Sometimes the coagulation coefficient is defined to include the factor 1/2 shown in the above definition of the coagulation rate. When this is done, the coagulation coefficient is half the value used here.

$$\beta_o = \frac{8kT}{3\mu_g} \quad .$$

This coagulation coefficient is appropriate when the particle diameters are large in comparison to the mean free path of the gas molecules. At elevated temperature the mean free path of a gas molecule can become large (at 2000 K and a pressure of 1 atmosphere the mean free path is on the order of 0.3 μm). An expression for the coagulation coefficient that accounts for small particle sizes is:

$$\beta_o = \frac{8kT}{3\mu_g}\left\{1 + \frac{2C\bar{\ell}}{d_p}\right\}$$

where $\bar{\ell} = \dfrac{1}{\sqrt{2}\pi d_g^2 n_g}$ = mean free path of the gas,

d_g = diameter of a gas molecule,

n_g = number density of gas molecules, and

C = Cunningham slip correction =

$$= 1 + \frac{2\bar{\ell}}{d_p}\left(1.257 + 0.4\exp\left[\frac{-0.55d_p}{\bar{\ell}}\right]\right) \quad .$$

Fuchs[41] has suggested that the coagulation coefficient should be corrected by multiplication by a factor f given by:

$$f = \begin{cases} \dfrac{1}{1 + \dfrac{2\ell_p}{d_p}} & \text{for } \ell_p < d_p \\ \dfrac{\sqrt{2}d_p}{\pi\ell_p} & \text{for } \ell_p \gg d_p \end{cases}$$

where $\ell_p = \dfrac{1}{\sqrt{2}\pi d_p^2 n(t)}$.

Such modifications of the coagulation coefficient would complicate substantially Smoluchowski's solution.

Smoluchowski's solution for the time variations of n(t) in systems containing 10^{15} to 10^{8} particles/cm^3 coagulating at 2000 K are shown in Figure 52. This figure illustrates a most important point. Particle coagulation will rapidly reduce number densities. Typical values of the coagulation coefficient result in predictions that coagulation slows significantly once number concentrations are between 10^7 and 10^9/cm^3.

Plots of the dimensionless quantity $V_pN(V_p)/V_oN_o$ where V_p is the volume of the aerosol particle and V_o is the volume of the nucleated particle as a function of the particle diameter are shown in Figure 53. In preparing this figure, it was assumed that all particles were spheres. These plots show how agglomeration of the particles changes the volume-weighted* mean particle size. Again, the rapid agglomeration effects for systems with high initial number concentrations are apparent. A system which initially contains 10^{12} particles/cm^3 will agglomerate to have a volume-weighted mean size of about 1×10^{-6} cm in about 10 seconds. It would require about 10,000 seconds for aerosols having an initial concentration of 10^9 particles/cm^3 to agglomerate to such a size.

The Smoluchowski solution provides useful insights into the coagulation behavior of aerosols. It is, however, difficult to ascribe quantitative accuracy to the solution for real systems. It would be expected that coagulation of particles would be more rapid than predicted if the gas phase were flowing or the particles were not spherical.[234,239] The predicted linear variation in the quantity $1/n(t) - 1/N_o$ with time has been observed in many high-temperature systems.[235-237] It is often found, however, that theoretically derived coagulation coefficients do not predict the experimental data well.[238]

Further discussions of pure coagulation of particles as well as simultaneous coagulation of particles and condensation on particles are presented below. For these discussions it is useful to relieve the assumption of an initially monodisperse aerosol used in the Smoluchowski problem. Instead the aerosol is presumed to have initially a number concentration that is continuous over the entir spectrum of aerosol sizes. A gamma distribution is used here:

---

*Volume weighting is chosen here because the resulting distribution has a close relationship to the aerosol size distributions obtained with conventional cascade impactors.

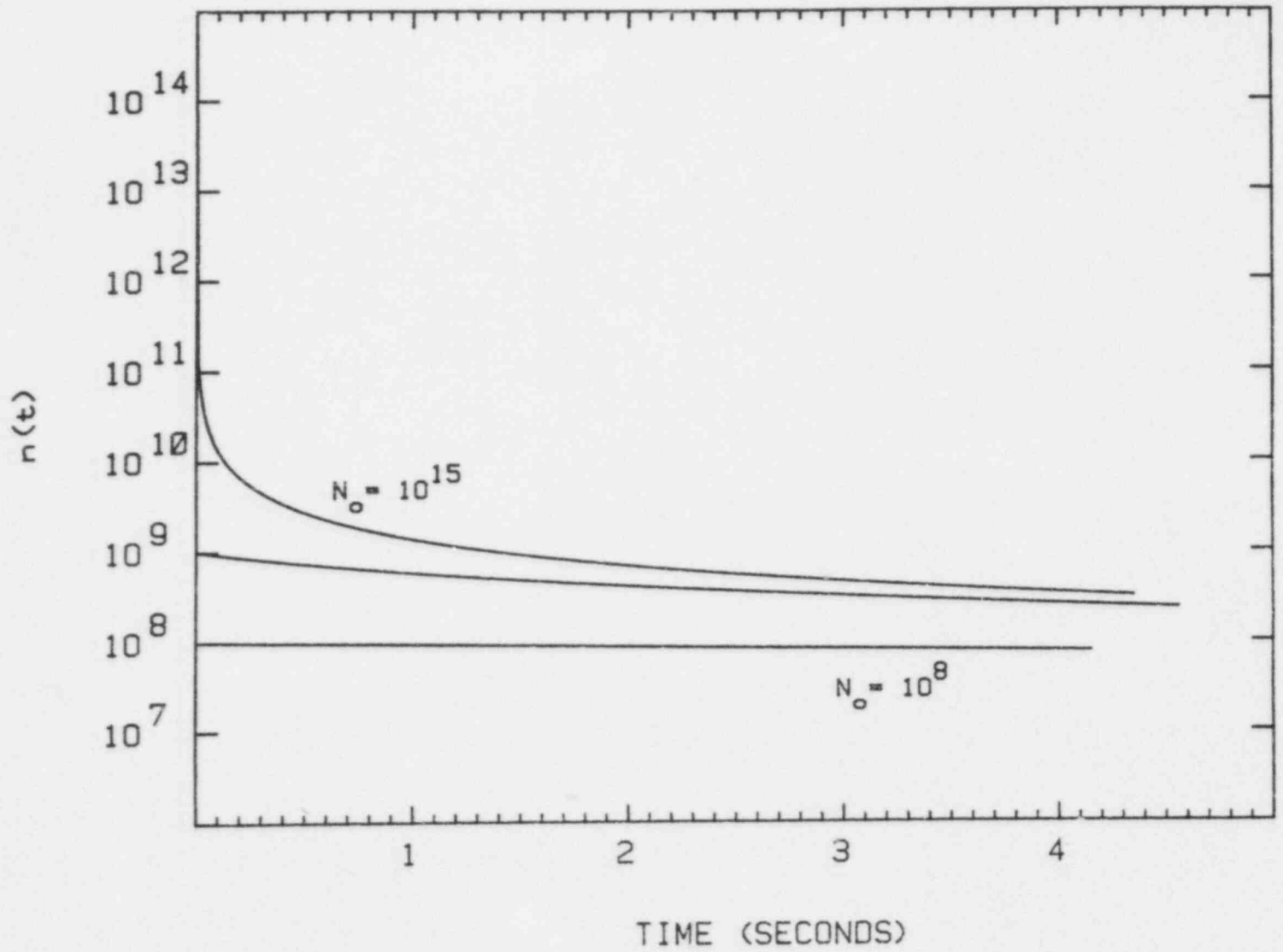

Figure 52. Effects of Pure Coagulation on the Number Concentration of Particles in Systems Containing Initially 10^{15}, 10^{9}, and 10^{8} Particles/cm^3 at 2000 K

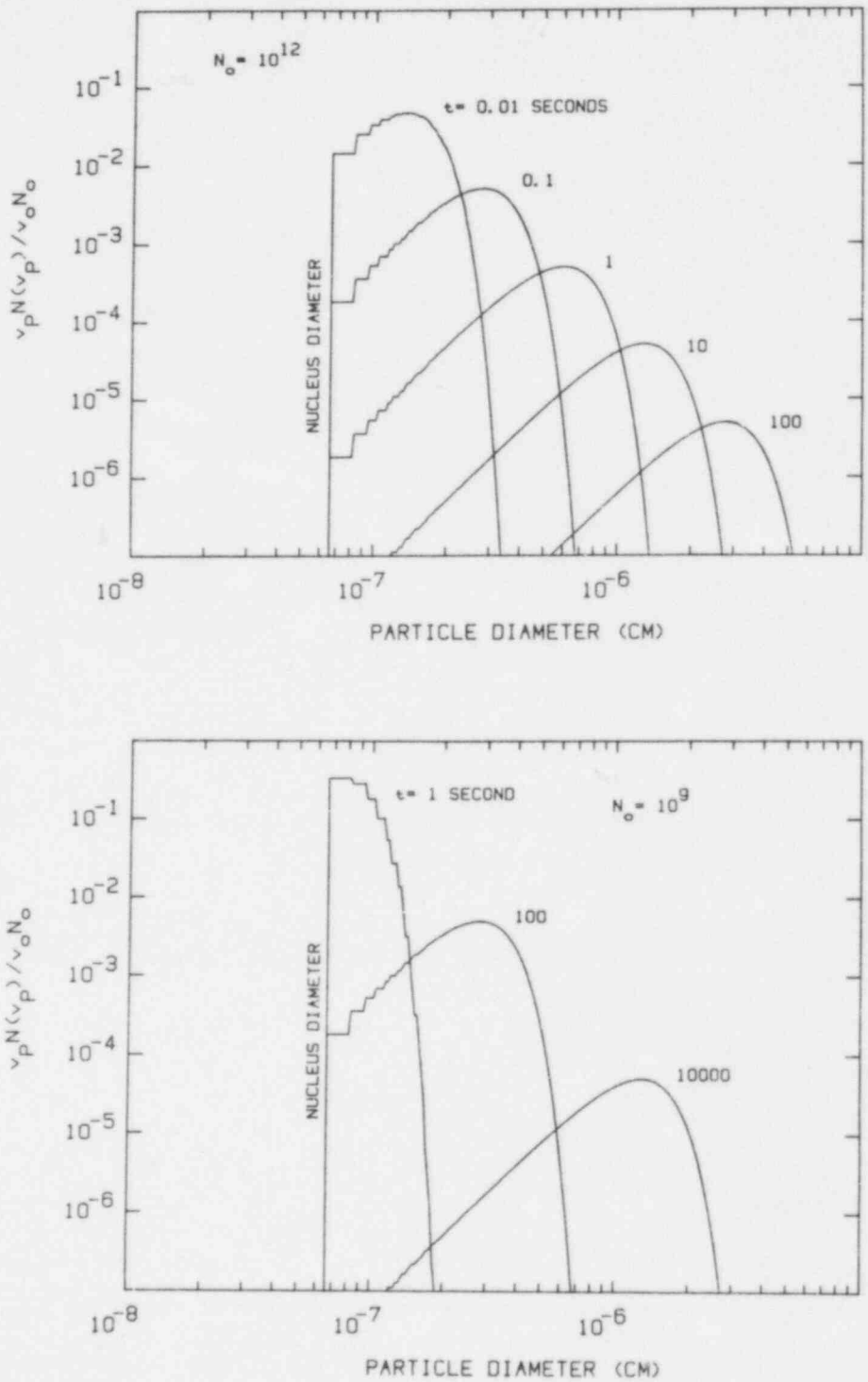

Figure 53. Variations in $V_pN(V_p)/V_oN_o$ as a Function of Particle Diameter, d_p, as a Result of Pure Coagulation in Systems Containing Initially 10^{12} and 10^9 Particles/cm^3

$$n(V,t) = \frac{N_o V}{V_o^2} \exp -\left[\frac{V}{V_o}\right] .$$

A plot of $V_p N(V_p)/N_o$ derived from this distribution is shown in Figure 54. Also shown is the nature of $V_p N(V_p)/N_o$ obtained from the monodisperse distribution.

Solutions for the pure coagulation problem obtained with this initial distribution, and a constant coagulation coefficient, are:

$$n(V,t) = \frac{[n(t)]^2}{V_o N_o}\left[\frac{1}{\left(1 - \frac{n(t)}{N_o}\right)^{1/2}}\right]$$

$$\exp -\left[\frac{V}{V_o}\right]\sinh\left\{\frac{V}{V_o}\left[1 - \frac{n(t)}{N_o}\right]^{1/2}\right\}$$

where $n(t) = N_o \frac{2}{2 + \beta_o N_o t}$.

Qualitative results obtained with this solution are very similar to those obtained with the Smoluchowski solution.

Consider now the special case of pure condensation of vapor. For a mass transport limited circumstance, the rate of particle growth will be proportional to $V_p^{1/3}$. Then,

$$\frac{\partial n(V,t)}{\partial t} = - \frac{\sigma \partial V^{1/3} n(V,t)}{\partial V}$$

where σ is the mass transport rate constant. The solution to the partial differential equation, given that $n(V,0)$ is the gamma function, is

$$n(V,t) = \begin{cases} 0 & \text{for } V^{2/3} - 2/3\sigma t < 0 \\ n(\tilde{V},o)\ \dfrac{(V^{2/3} - 2/3\sigma t)}{V^{1/3}} & \text{for } V^{2/3} - 2/3\sigma t > 0 \end{cases}$$

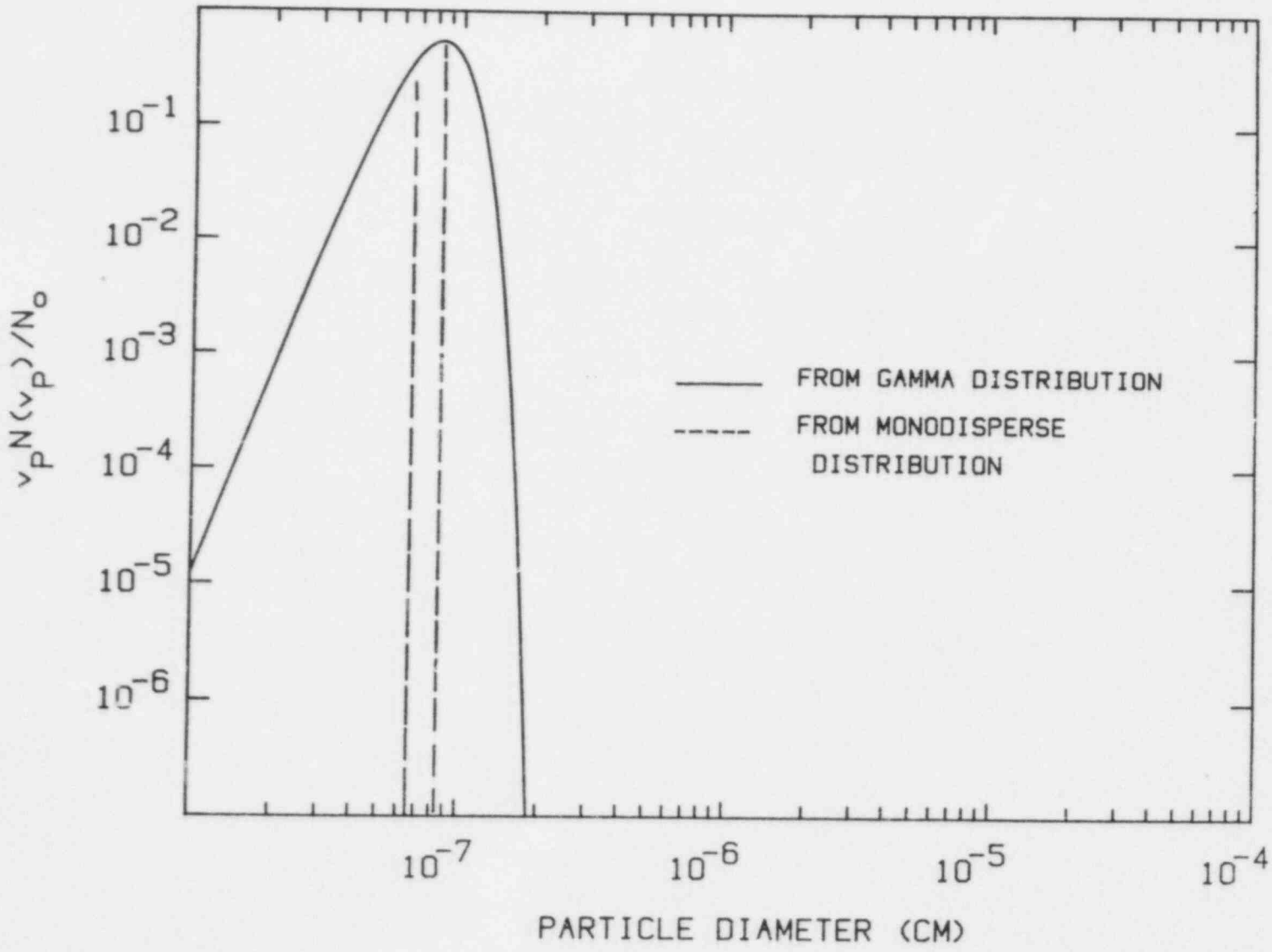

Figure 54. Comparison of the Gamma and the Monodisperse Number Concentration Distribution Functions for Nucleated Particles

where $\tilde{V} = [V^{2/3} - 2/3\sigma t]^{3/2}$.

Plots of $V_p n(V_p,t)/N_o$ against particle diameter for various values of σt are shown in Figure 55. These results show that condensation can sharpen the volume-weighted size distribution of an aerosol at the same time it increases the mean particle size. Note that the number of aerosol particles is not altered by the condensation process, so $n(t) = N_o$ for all t.

Mass transport need not be the rate-controlling step for the condensation of vapors on very fine particles. Hermsen and Dunlap[242] have argued that chemical reaction within the condensed phase may be the rate-controlling step in the formation of Al_2O_3 particles from aluminum vapor. This can be understood as follows. Initial nuclei formed from the vapor are composed of aluminum. Condensation of vapor on these nuclei is inhibited by their high vapor pressure. This vapor pressure is reduced dramatically, however, if the condensed phase is converted to Al_2O_3. The condensed phase can be oxidized readily even by trace concentrations of oxidant.

Chemical reaction-controlled condensation may be of particular interest in connection with core debris/concrete interactions. Condensation of Ba(g), LaO(g), Na(g), and similar vapors may be controlled by chemical transformations of the condensed phase.

If condensation is limited by chemical reaction within the condensed particle, the rate of particle growth will be proportional to the particle volume. Then,

$$\frac{\partial n(V,t)}{\partial t} = -\sigma \frac{\partial V n(V,t)}{\partial V}$$

where σ is the rate constant for particle growth. The solution to this differential equation is:

$$n(V_p,t) = n(\tilde{V},o) \exp[-\sigma t]$$

where $\tilde{V} = V \exp(-\sigma t)$. Plots of $V_p n(V_p,t)/N_o$ against the particle diameter for various values of σt are shown in Figure 56. When particle growth is proportional to the particle volume, the shape of the size distribution is not altered by condensation when plotted on the logarithmic scale. Note that the rate of particle growth becomes very

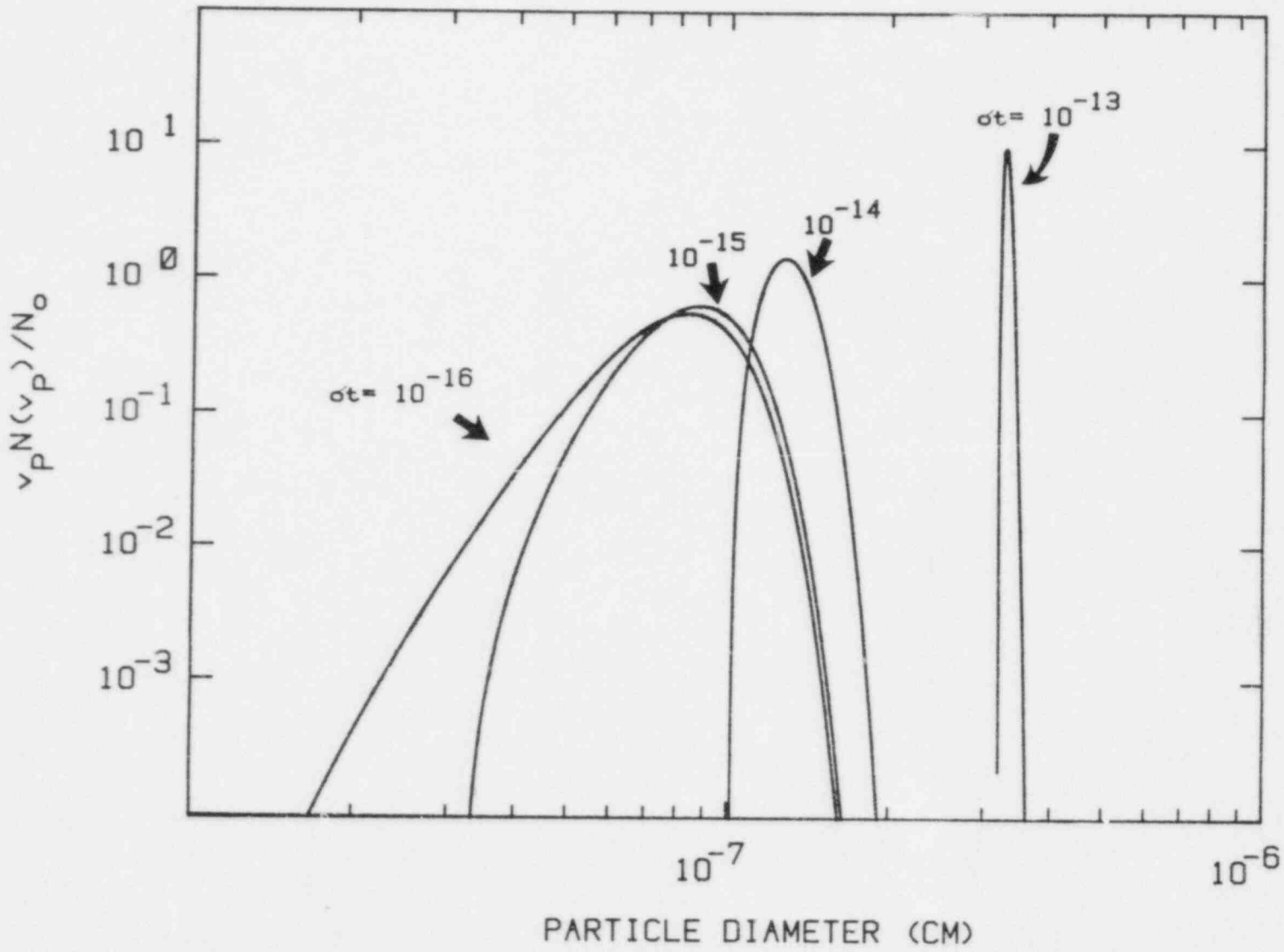

Figure 55. Evolution of the Aerosol Particle Size as a Result of Condensation Limited by Mass Transport of Vapor to the Particle Surface. The several curves were calculated assuming the indicated values of σt where σ is the rate constant for particle growth by condensation.

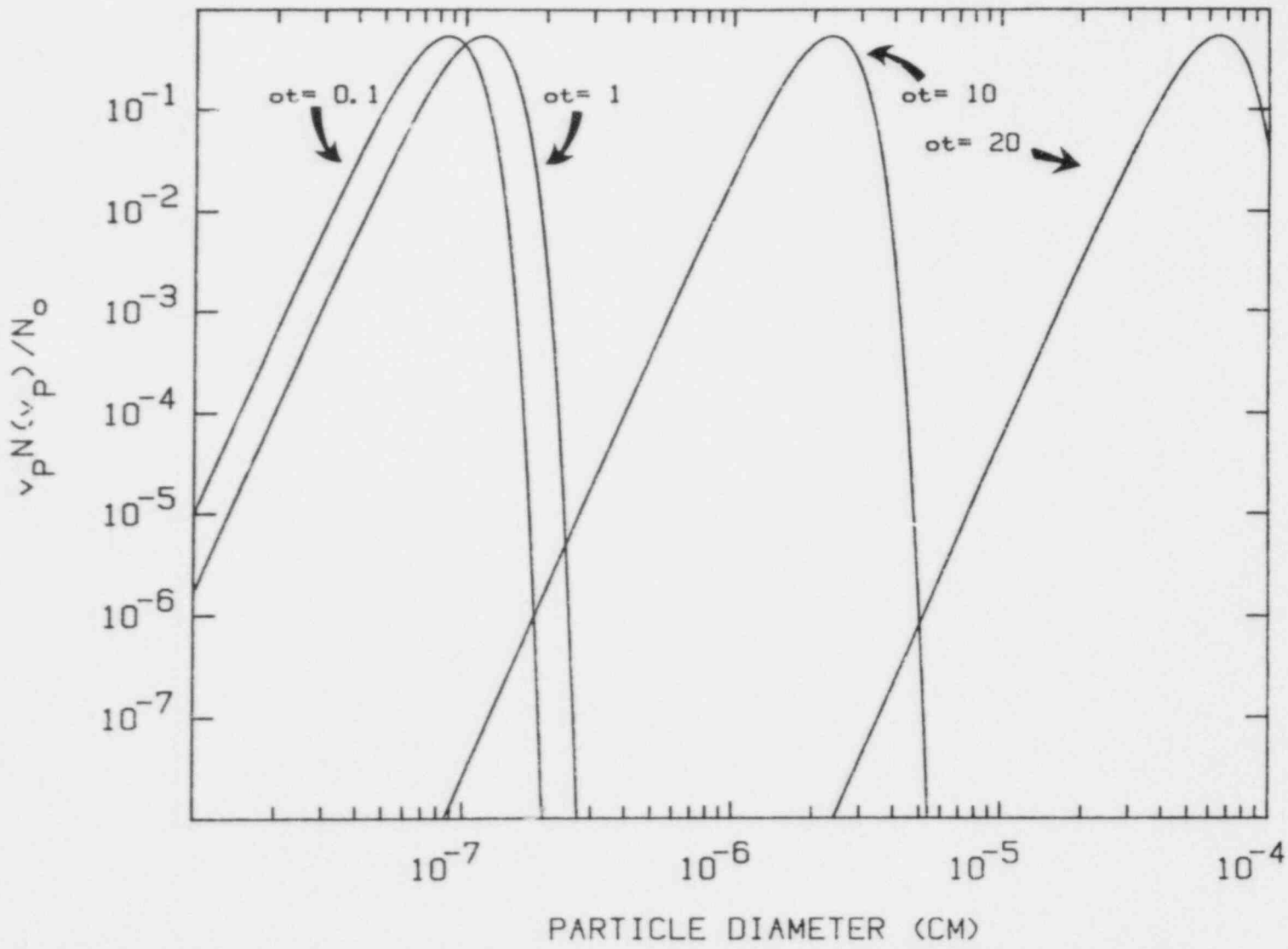

Figure 56. Evolution of the Particle Size Distribution as a Result of Vapor Condensation at a Rate Proportional to Particle Volume. The several curves in the figure were calculated assuming the indicated values of σt where σ is the rate constant for particle growth.

rapid once diameters in excess of about 10^{-6} cm are achieved. Again, the number of particles is not altered by the condensation process.

Condensation of vapor provides a means for the growth of particles once they have nucleated. The extent to which condensation on particles will relieve supersaturation of the vapors depends, of course, on the amount of particle surface area available for condensation. The available surface area is increased by nucleation of particles and by growth of these particles by condensation. The surface area is reduced by coagulation of particles. Thus, to model the vapor-particle mixture evolved during core debris attack on concrete, it is necessary to consider the simultaneous and competitive influences of particle coagulation and vapor condensation.

An analytic solution to the problem of simultaneous coagulation and vapor condensation is possible when particle growth by vapor condensation is proportional to the particle volume and the rate of particle coagulation is independent of particle volume.[231] The particle concentration distribution is then given by:

$$n(V_p,t) = \frac{[n(t)]^2}{1 - n(t)/N_o} \frac{\sinh\left\{\left[\frac{V}{V_o \exp(\sigma t)}\right]\left[1 - \frac{n(t)}{N_o}\right]^{1/2}\right\}}{N_o V_o \exp(\sigma t)}$$

$$\exp -\left[\frac{V}{V_o \exp(\sigma t)}\right]$$

where $n(t) = N_o(2/(2+\beta_o N_o t))$. Note that the number of particles present in the system is determined by coagulation and that the number of particles varies just as predicted by the Smoluchowski solution.

To illustrate the nature of combined coagulation and condensation, the behavior of a mixture of tin vapor and tin nuclei at 2000 K is considered. The coagulation coefficient is calculated from:

$$\beta_o = \frac{8kT}{3\mu_g}$$

where the viscosity of the gas is calculated for a mixture of hydrogen and carbon monoxide. A dimensionless parameter,

λ, can be used to characterize the relative rates of particle growth by condensation and coagulation:

$$\lambda = \frac{\sigma}{\beta_o N_o} \quad .$$

Results of calculations with λ = 0.1, 0.01, and 10^{-6} are shown in Figures 57 to 59. These results demonstrate the pervasive influence of condensation on the size of the particles. The value of λ must fall to a level of 10^{-5} to 10^{-6} before the evolution in the particle size distribution begins to assume the characteristics of a pure coagulation system. For larger values of λ, the particle size is determined largely by condensation. The number of particles is, of course, determined by coagulation.

When condensation is taking place efficiently the evolution in the particle size distribution is rapid. The calculated results show that for λ between 10^{-2} and 10^{-1}, the nuclei diameters increase from about 10^{-7} cm to 10^{-4} cm over a period of less than 1 second. Unless the initial number of particles is very large ($\sim 10^{15}/cm^3$), coagulation cannot produce such rapid growth. It appears, then, that the final size of the particles is very likely to be controlled more by the availability of vapor to condense than by the details of either condensation kinetics or to coagulation kinetics.

Based on the analyses of combined coagulation and condensation a qualitative description can be constructed of the evolution of the particle and vapor mixture evolved during core debris/concrete interactions. This mixture flows upward and cools until a critical supersaturation of the vapor is reached. There is a burst of particle nucleation from the vapor. The number of particles nucleated in the vapor depends on the details of the cooling rate. As the particles form, vapor condensation can begin and the rate of vapor condensation accelerates as more nuclei are formed. Similarly, as more particles are formed the rate of coagulation increases and tends to decelerate vapor condensation. Quite quickly, however, supersaturation of the vapor is reduced to levels too small to spawn nuclei. Continued relief of the vapor supersaturation is the result of vapor condensation. The particle number density in the vapor is then controlled by coagulation.

D. Approach Adopted in the Current Implementation of the VANESA Model

The discussions of the preceding section show that it is possible to construct at least a qualitatively correct model of the behavior of the effluent stream of vapors, particles,

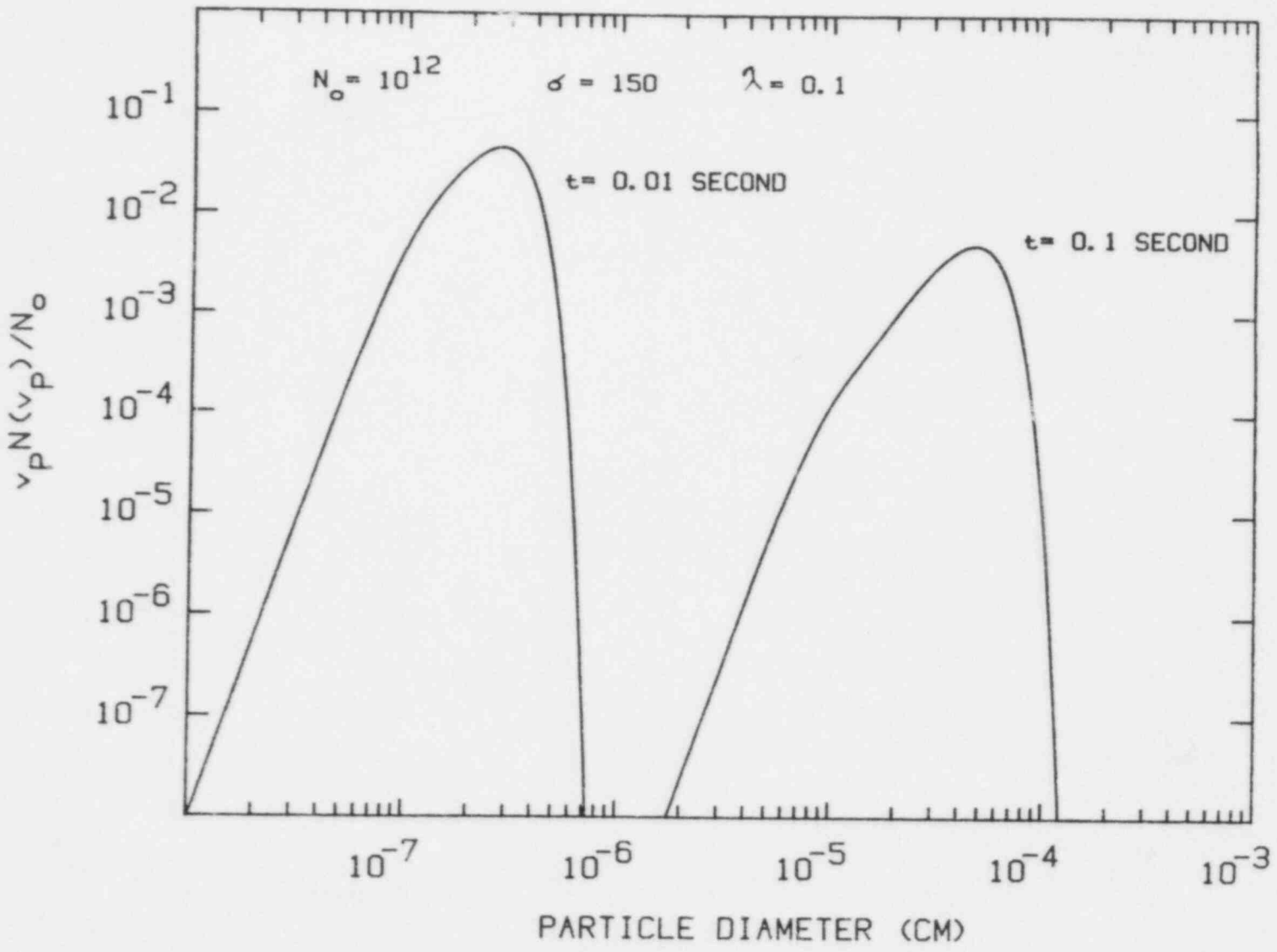

Figure 57. Effects of Combined Coagulation and Condensation on the Evolution of Tin Particles Nucleated at 2000 K When $\lambda = 0.1$

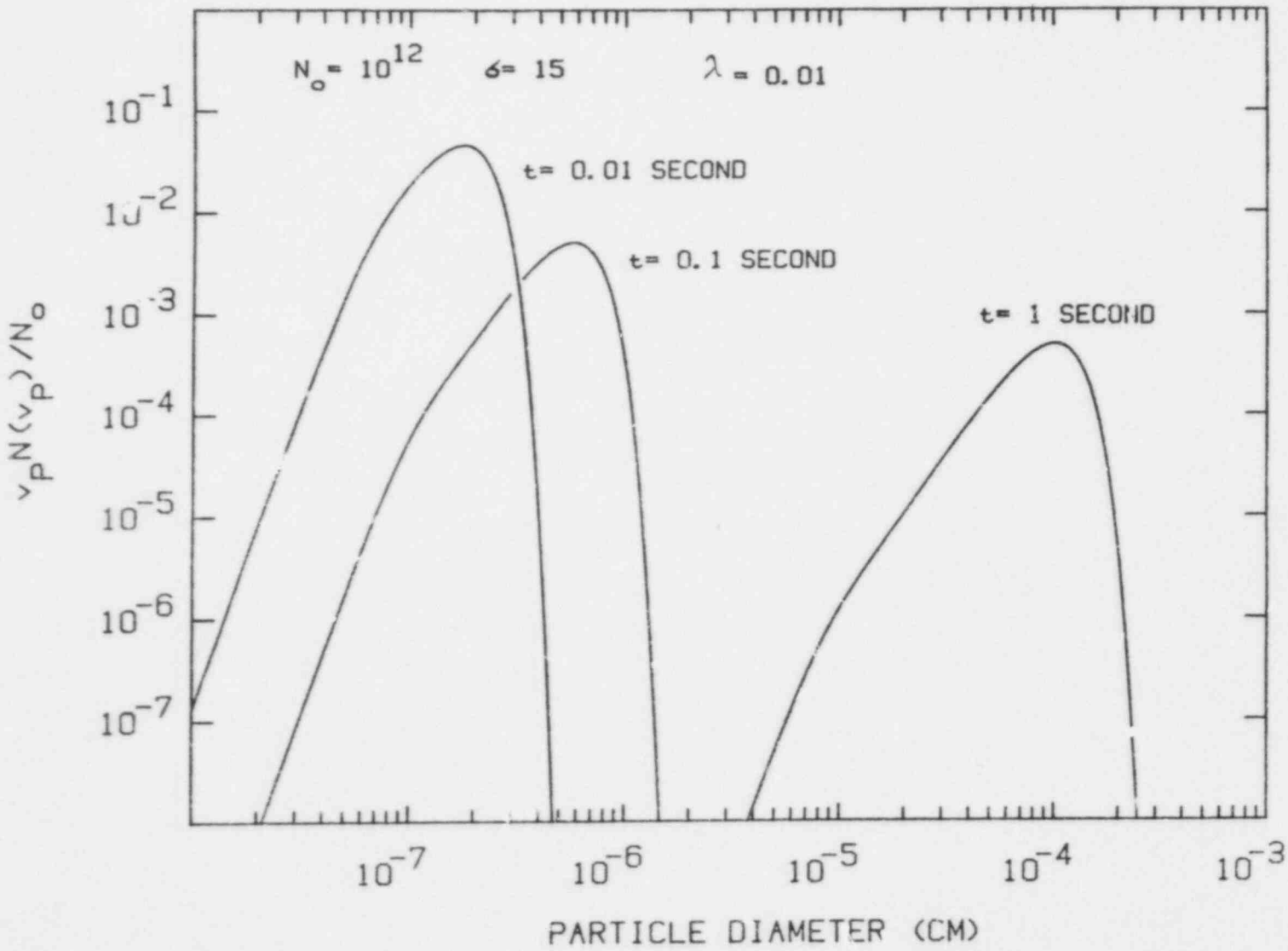

Figure 58. Effects of Combined Coagulation and Condensation on the Evolution of Tin Particles Nucleated at 2000 K When $\lambda = 0.01$

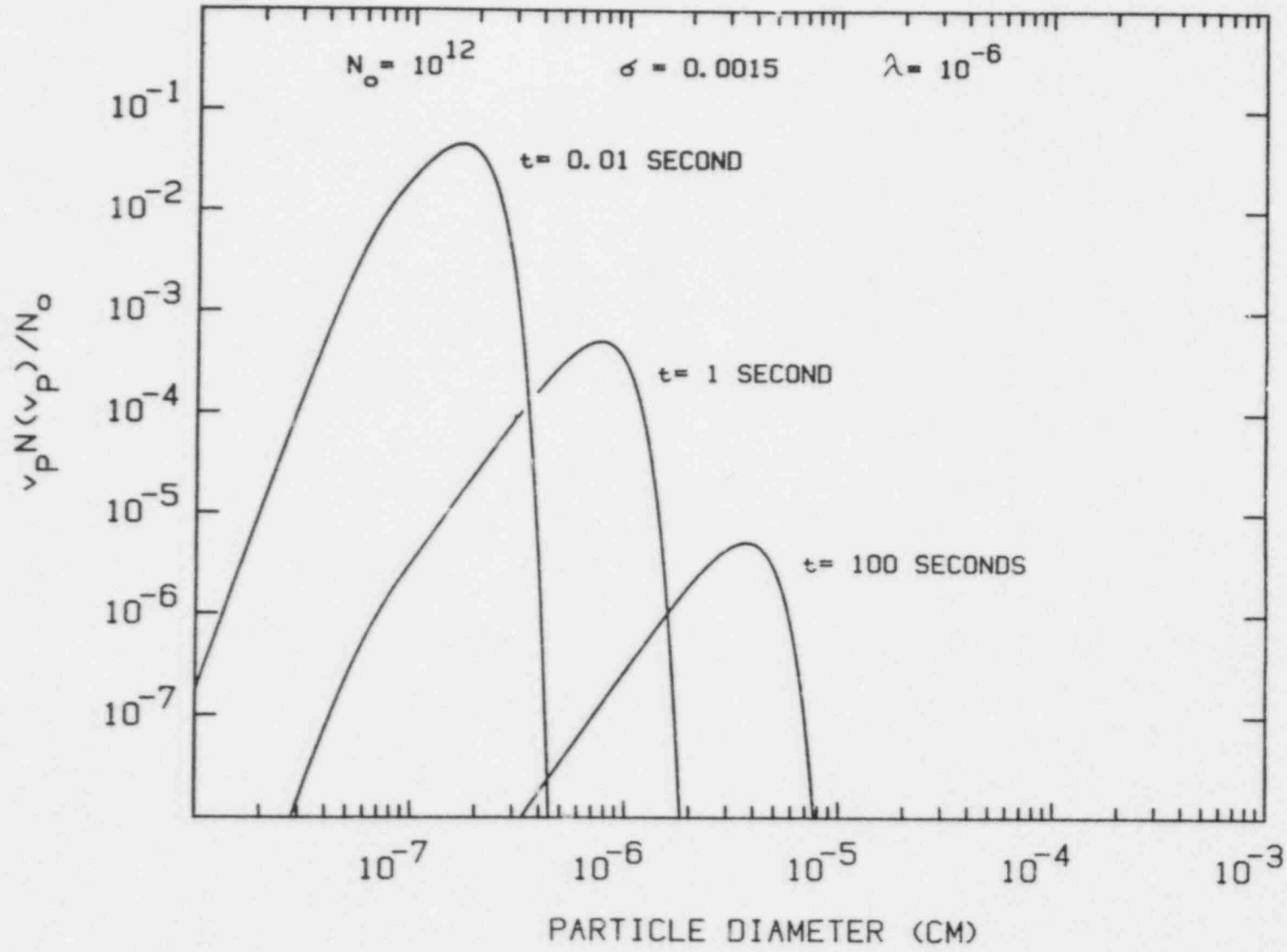

Figure 59. Effects of Combined Coagulation and Condensation on the Evolution of Tin Particles Nucleated at 2000 K When $\lambda = 10^{-6}$

and gases produced during core debris/concrete interactions. To do so, however, would require detailed models of the rate of cooling of the vapor stream evolved from the melt. Current models of core debris/concrete interactions do not provide a sophisticated treatment of the temperature gradient experienced by the flowing mixture. Construction of a model of cooling would not be easily done and could not be done without recognizing the nucleation and condensation of vapor. Latent heat liberated during the phase change of the vapor would provide heat to the flowing gas. Nucleated particles would inhibit the radiation cooling of the particle-vapor mixture.

Further, a mechanistic model of nucleation and condensation would require quite a lot of detailed descriptions of condensation thermodynamics and reaction kinetics. The condensation thermodynamics is, at least conceptually, tractable. But, the complex condensed phase species known from melt/concrete experiments to form in the aerosols suggest that any analysis would be challenging. The kinetic analysis appears even more formidable simply because of the lack of data. Technical debates arise even for simple vapor condensation problems. The multicomponent system encountered in core debris/concrete interactions would assuredly elicit more debate.

These considerations of the difficulties of a mechanistic analysis, as well as the limitations on the time available for model development, led to a more empirical description of the vapor condensation problem in the current implementation of the VANESA model. The logic for the development of this empirical model stems from the analyses described in the previous section. It was presumed that nucleation of the vapors would occur over the core debris pool. The number of particles nucleated from the vapor could not be predicted confidently. But, coagulation would assure that the number concentration of particles would fall rapidly to 10^9 to 10^7 per cm^3. The coagulation of particles would have a relatively small effect on the particle size. Particle size would be dictated instead by the condensation of vapors on he particle aggregates. Since the particles eventually reach rather low temperatures (~400 K), sensibly all of the vapors will condense. Then,

$$d_p = \left[\frac{6A}{\pi\rho n(t)}\right]^{1/3}$$

where A is the mass concentration of the condensing vapors initially. A variety of aerosol samples taken during high temperature melt/concrete interactions have shown that the

mass-weighted mean particle size is on the order of 1.2 μm when the condensing vapor concentrations are 50-150 g/m^3. This experimental result implies n(t) is about 10^8 particles/cm^3. Analyses of the coagulation of particles presented above shows that at concentrations of 10^8 particles/cm^3 further coagulation of the aerosol will be quite slow relative to the flow velocity of gas evolved during melt attack on concrete. Then, from these experimental results,

$$d_p = 0.266\left[\frac{A}{\rho}\right]^{1/3}$$

where d_p is the particle diameter in units of μm, A in units of g/m^3, and ρ is aerosol material density in units of grams/cm^3. (The mixture of units in this equation has been accepted simply to accommodate the common practice for reporting the pertinent quantities.) On those occasions when the actual size distribution of aerosol particles is of use, the distribution is recommended to be log-normal with a geometric standard deviation of 2.3. This recommendation is based on the available experimental data for aerosol produced by high-temperature melt interactions with concrete.

This empirical model has some attractive features.* The size of aerosol particles should depend on both the amount of vapor available for condensation and the density of the condensed vapor. The model will, of course, predict results of many high-temperature melt/concrete interaction tests.

It is important, too, to remember how much is lost by adopting this empirical model. The chemical form of the condensed aerosol is not predicted. In fact, for the current implementation of the VANESA model, vapors are presumed to revert to the chemical form they had in the melt. That is, vapors of Ba(g) or BaOH(g) condense as BaO, etc.

The sensitivity of the aerosol size distribution to details of vapor cooling are lost when the empirical model is used. This may not be a serious deficiency for melt/concrete interactions taking place without a water pool

*It is interesting to note that almost identical logic was used in developing a model for the initial aerosol size in the TRAP-MELT code.[282] For this code, however, a number density of particles was derived based on experimental data for the particle size.

present. Such interactions will be quite similar to tests used for parameterization of the model. The sudden quenching of vapors when a water pool is present, on the other hand, is likely to yield a rather different size distribution. Such a distribution would be expected to be dominated by the effects of nucleation and not vapor condensation. As will be discussed below, the details of the aerosol size distribution has an important bearing on how efficiently aerosols evolved during core debris/concrete interactions are trapped by the water pool.

The empirical model cannot predict a size-dependence of the aerosol composition. Some data on the compositions of various size particles of aerosol produced during a "corium" melt/concrete interaction test are shown in Table 55. These data suggest that the more volatile constituents of a high-temperature melt are concentrated preferentially in the finer portions of the aerosol size distribution. Such behavior can be understood on mechanistic grounds and has been observed for multicomponent aerosols produced by other high-temperature processes.[283] Such size-dependent aerosol compositions may be pertinent to the estimation of radioactivity release from the reactor containment and the consequences posed by the release.

Finally, the empirical formulation poses a barrier to the prediction of aerosol shape factors using models such as that formulated by Brockmann.[9]

Table 55

Aerosol Composition Data for Particles of Various Sizes

	Composition (w/o) in Samples of Particle Size in the Range		
	25-15μm	2-1μm	0.6-0μm
UO_2	1.0	0.5	0.015
CeO_2	0.5	0.5	0.0003
La_2O_3	0.5	0.1	0.0008
Al_2O_3	0.13	0.025	0.013
SiO_2	1.0	1.0	0.21
Cs_2O	0.39	0.5	0.5
Sn	0.29	1.0	1.0
Mo	0.17	0.11	0.50

VII. EFFECTS OF AN OVERLYING WATER POOL

In some reactor accidents, water will be in the reactor cavity while the core melt attacks concrete. The final step in the VANESA treatment is estimating how an overlying water pool affects the aerosol generation and radionuclide release during melt/concrete interactions.

One of the obvious ways that an overlying water pool could affect core debris/concrete interactions is to cool the debris. Any reduction in the core debris temperature would have a significant effect on aerosol production. The VANESA model does not attempt to predict core debris temperatures. Such temperatures are provided as input to the model. The model predictions of aerosol generation will reflect the cooling of the core debris by a water pool only if the core debris temperatures input to the model reflect this cooling.

Cooling provided by an overlying water pool may induce a solidified crust to form on the core debris. Because of the volumetric heating of core debris by radioactive decay, this crust can grow to only a finite thickness--typically one to a few centimeters during the first few hours of an accident. Nevertheless, the crust could affect aerosol production. The crust could inhibit or even eliminate aerosol generation by mechanical processes. This is quite likely if the crust remains in contact with the molten core debris. The crust could also affect aerosol formation from vapors liberated by the core debris. In some experiments crusts have been allowed to form on core debris attacking concrete. These crusts are quite porous and they are easily penetrated by gases produced during melt attack on concrete. It is possible for vapors to pass through the crusts. But, the convoluted, narrow passages through the crust provide large amounts of relatively cool surface onto which vapors could condense and be removed at least temporarily from the mixture emerging from the core debris. Also, the thermal gradient across a crust should be much sharper than the variation in temperature above core debris without a water pool present. The sharp temperature drop within the crust must affect the nucleation and growth of particles from the vapor. The size distribution of aerosol particles emerging from the crust could be quite different than that predicted with the empirical model which is based on data from tests with neither an overlying water pool nor a solidified crust.

No attempt is made in the current implementation of the VANESA model to account for the effects on aerosol emissions caused by a solidified crust.

Finally, a water pool overlying the core debris can trap aerosol particles evolved by the core debris. Attentions in the current implementation of the VANESA model focus on this effect of an overlying water pool. Scrubbing of aerosols from gases rising through the overlying water pool is analogous to the scrubbing of aerosols by a steam suppression pool in a boiling water reactor. Scrubbing of aerosols by suppression pools is a subject that has received much experimental and analytic attention lately.[8,42,251,252] At least three rather sophisticated models have been developed though debate persists on the adequacy of these models.[254]

Water pools overlying core debris will be, typically, shallower than steam suppression pools. The overlying water pools are unlikely to be subcooled, or at least they will not remain subcooled for long periods of time. Injection of aerosol laden gases into overlying water pools will occur at an enormous number of locations all over the core debris surface rather than at a few, fixed locations as in a steam suppression pool. These features of overlying water pools obviate some of the more contentious aspects of the analysis of scrubbing by steam suppression pools. A simpler analysis than that used for steam suppression pools may be adequate for predicting the effects on aerosol emissions caused by a pool of water overlying core debris attacking concrete.

To calculate the aerosol scrubbing by a water pool in the VANESA model, it is presumed that the mixture of gas and vapor evolved from the core debris emerges into the steam film that develops between the water pool and the crust. This mixture and the steam thermally equilibrate. Bubbles form by Taylor instability and rise through the pool. Decontamination occurs by three mechanisms:

1. Sedimentation of aerosol particles within the bubble,

2. Impaction of particles on the bubble walls, and

3. Diffusion of particles to the walls.

No decontamination by diffusiophoretic processes is considered. Gas evolved from concrete will contain little condensable steam. Even if steam from the film between the debris and the water pool is mixed with the evolved gases, the gas in the bubbles will be unsaturated. Consequently, steam diffusion to and condensation on the bubble walls will not be a mechanism to drive aerosol trapping.

Several other mechanisms for trapping aerosols are not treated. Interception of aerosols by the bubble walls as a result of secondary motions of a rising bubble is neglected.

The thermal equilibration that occurs before bubble formation assures that thermophoretic aerosol motions can be neglected. Finally, transient processes associated with bubble formation are presumed not to cause aerosol entrapment by the pool.

The description of aerosol capture by sedimentation, diffusion, and impaction is based on a model formulated by Fuchs.[41] The rate of aerosol removal is given by:

$$\frac{dm(d_p,x)}{dx} = -\left[\alpha(S,d_p) + \alpha(I,d_p) + \alpha(D,d_p)\right] m(d_p,x)$$

where $m(d_p,x)$ = the mass of particulate having particle diameters d_p at an elevation x above the core debris surface,

$\alpha(S,d_p)$ = coefficient describing particle removal by sedimentation,

$\alpha(I,d_p)$ = coefficient describing particle removal by impaction, and

$\alpha(D,d_p)$ = coefficient describing particle removal by diffusion.

The sedimentation coefficient is given by:[41]

$$\alpha(S,d_p) = 1.5J(d_p)/D(bubble)V(rise)$$

where $J(d_p) = g\rho_p d_p^2 C/18\mu_g$,

ρ_p = material density of the aerosol particle,

$$C = 1 + \left(\frac{2\lambda}{d_p}\right)\left(1.257 + 0.4\exp\left[\frac{-0.55d_p}{\lambda}\right]\right),$$

$$\lambda = \frac{1}{\sqrt{2}\,\pi d_g^2 N_A (P/82.06T)},$$

d_g = diameter of gas molecule,

N_A = Avogadro's number,

D(bubble) = bubble diameter,

V(rise) = rise velocity of the bubble, and

d_p = particle size.

Sedimentation is calculated ignoring the possibility that water vapor may condense on particle surfaces. Were water vapor to condense on the particles, it would cause an increase in the appropriate particle diameter to use in the equation for the sedimentation coefficient. Inspection of the definition of the sedimentation coefficient shows that increasing the particle diameter should increase the rate of sedimentation. To some extent the effects of an increased particle diameter would be compensated by a reduction in the overall particle density.

The bubble rise velocity appearing in the definition of the sedimentation coefficient depends on the diameter of the bubble. The correlations discussed above in connection with bubble rise in molten core debris are applicable also to bubble rise in the water pool. Single bubble rise velocity correlations are probably useful until gas holdup reaches about 10 percent. For holdups much above 10 percent, bubble swarm correlations may be better descriptions of the rise velocity.

The coefficient for particle diffusion is given by:[41]

$$\alpha(D,d_p) = 1.8[8\theta/(V(rise)D^3(bubble))]^{1/2}$$

where $\theta = kTC/(3\pi\mu_g d_p)$,

k = Boltzmann's constant and

T = pool temperature.

Diffusion would be retarded, of course, if there were a flux of water vapor coming from the bubble walls. Such a flux would be expected since the gases entering the pool are not steam saturated. The retardation of diffusion by a water vapor flux is neglected here.

The impaction coefficient describes the loss of aerosol particles from the gas because these particles cannot stay in the flow of gases circulating within the bubble. As noted and discussed at some length in connection with bubble behavior in high temperature melts, circulation of gases within a bubble depends very much on the purity of the bubble surfaces. Surface active agents will retard the circulation of gases within bubbles. Particles collected on the bubble walls will interfere in the circulation of the gases also. These interferences become more pronounced as the bubbles get smaller.

The centrifugal force on a particle in the circulating gas adjacent to the walls of a bubble is:

$$F = \frac{V^2(\tan)\tau}{R_c}$$

where $V(\tan)$ = tangential velocity,

R_c = radius of curvature of the bubble wall,

$\tau = \rho_p d_p^2 C/18\mu_g$,

C = Cunningham slip correction,

d_p = particle diameter,

ρ_p = particle density, and

μ_g = viscosity of the gas.

Then, the number of particles deposited on the bubble walls is

$$\frac{dn}{dt} = \int F n dS = \int \frac{V^2(\tan)\tau n}{R_c}\, dS$$

where n = particle concentration and the integration is over the surface of the bubble. The number of particles deposited per unit distance of bubble rise is

$$\frac{dn}{dx} = \frac{1}{V(\text{rise})} \int \frac{V^2(\tan)\tau n}{R_c}\, dS \ .$$

The coefficient of aerosol impaction is the ratio of the particles deposited per unit rise distance to the total number of particles in the bubble:

$$\alpha[I, d_p] = \frac{\int V^2(\tan)\tau n/R_c}{V(\text{bubble}) n V(\text{rise})}\, dS$$

where $V(\text{bubble})$ = volume of the bubble.

For perfectly spherical bubbles rising at creeping flow rates (Re < 1) in pure water, the tangential velocity of gas within the bubble adjacent to the wall is found from the Hadamard-Rybcynski equations[99] to be:

$$V(\tan) = 0.5\ V(\text{rise})\ \sin\theta$$

where θ is the angle from the stagnation point on the top of the bubble. The tangential velocity of gases for bubble rise in the potential flow regime is:

$$V(\tan) = 1.5\ V(\text{rise})\ \sin\theta \quad .$$

Designate $V(\tan) = \beta V(\text{rise})\ \sin\theta$. Then for spheres:

$$\alpha(I,d_p) = \frac{2\tau n\beta^2 V^2(\text{rise})\ \frac{\pi}{2}\ [D(\text{bubble})]^2 \int_o^{\pi} \sin^3\theta d\theta}{D(\text{bubble})\ \frac{\pi}{6}\ [D(\text{bubble})]^3 nV(\text{rise})}$$

$$= \frac{8\beta^2 V(\text{rise})\tau}{[D(\text{bubble})]^2} \quad .$$

Fuchs chose $\beta = 1.5$ for his analyses.[41] Thus,

$$\alpha(I,d_p) = \frac{18V(\text{rise})\tau}{[D(\text{bubble})]^2} \quad .$$

At higher Reynolds numbers bubbles distort into oblate ellipsoids characterized by a semimajor axis, a, and a semiminor axis, b. Moody[251,255] has undertaken an analysis of particle scrubbing from such distorted bubbles. The coefficient for sedimentation is altered to refect the smaller distance between the leading and trailing edges of an ellipsoidal bubble in comparison to a spherical bubble of the same volume. Thus,

$$\alpha(S,d_p) = 1.5\ J(d_p)/b\ V(\text{rise})$$

$$= 3\ J(d_p)\ E^{2/3}/V(\text{rise})d_e$$

where d_e = diameter of the equivalent volume sphere and

$E = a/b$.

The determination of the impaction coefficient in an ellipsoidal bubble is more involved. The analyses are done with confocal ellipsoidal coordinates[256] designated ξ and η where:

x = distance along axis coincident with the semi-minor axis = $C \sin(\xi)\cos(\eta)$ and

w = distance along axis coincident with the semi-major axis = $C \cosh(\xi)\sin(\eta)$.

The radius of curvature at a point on the bubble surface is by definition:

$$R_c = \left| \frac{\left(\frac{\partial x}{\partial \eta}\right)^2 + \left(\frac{\partial w}{\partial \eta}\right)^2}{\frac{\partial x}{\partial \eta}\frac{\partial^2 w}{\partial \eta^2} - \frac{\partial w}{\partial \eta}\frac{\partial^2 x}{\partial \eta^2}} \right| = \frac{d_e}{2} \frac{(E^2-1)^{3/2}}{E^{5/3}} \left[\frac{1}{E^2-1} + \cos^2\eta\right]^{3/2}$$

where $E = a/b$. In the creeping flow regime:[256]

$$V(\tan) = \frac{-V(\text{rise})E\sqrt{E^2-1}\left\{1 - \frac{1}{E^2-1}\tan^{-1}\left(\sqrt{E^2-1}\right)\right\}\sin(\eta)}{\left[\sqrt{E^2-1} - E^2\tan^{-1}\left(\sqrt{E^2-1}\right)\right]\left[\frac{1}{E^2-1} + \cos^2\eta\right]^{1/2}} .$$

The tangential velocity in the potential flow regime is found to be:

$$V(\tan) = \frac{-V(\text{rise})(E^2-1)\sin(\eta)}{\left[\sqrt{E^2-1} - E^2\tan^{-1}\left(\sqrt{E^2-1}\right)\right]\left[\frac{1}{E^2-1} + \cos^2\eta\right]^{1/2}} .$$

Expansion of $\tan^{-1}(x)$ as $x - x^3/3$ for $x^2 << 1$ shows that this formula converges to the formula for tangential velocity on a sphere as E approaches 1. It also shows that the tangential velocities adjacent to the bubble wall are higher for the oblate ellipsoid than for a sphere. At $\eta = \pi/2$ where velocities are highest, the ratios of the

tangential velocities in ellipsoids with various aspect ratios, E, to the tangential velocity in a sphere at $\theta = \pi/2$ are:

E	$\frac{V(\text{tan, ellipsoid})}{V(\text{tan, sphere})}$
1.01	1.004
1.1	1.040
3	1.828
5	2.672

Higher velocities will enhance, of course, particle deposition.

The coefficient for particle impaction from a gas in an ellipsoidal bubble is then*

$$\alpha[I,d_p] = \frac{6V(\text{rise})}{[D(\text{bubble})]^2} \frac{(E^2-1)E^{4/3}\tau}{\left[\sqrt{E^2-1} - E^2\tan^{-1}\left(\sqrt{E^2-1}\right)\right]^2} \int \frac{\sin^3(\eta)}{\left(\frac{1}{E^2-1} + \cos^2\eta\right)^2} d\eta$$

where note has been taken of

$$dS = \frac{\pi}{2} \frac{[D(\text{bubble})]^2}{E^{1/3}} \sqrt{E^2-1} \left[\frac{1}{E^2-1} + \cos^2(\eta)\right]^{1/2} \sin(\eta)d\eta$$

D(bubble) = diameter of the spherical bubble with the equivalent volume

$= 2a/E^{1/3}$.

Then,

*Note typographical errors in Reference 255.

$$\alpha[I,d_p] = \frac{6V(rise)\tau}{[D(bubble)]^2}$$

$$\frac{(E^2-1)E^{4/3}\ E^2 - 1 + (E^2-2)\sqrt{E^2-1}\ \tan^{-1}\left(\sqrt{E^2-1}\right)}{\left[\sqrt{E^2-1} - E^2\tan^{-1}\left(\sqrt{E^2-1}\right)\right]^2}$$

$$= \frac{8V(rise)\tau}{[D(bubble)]^2}\beta^2 = \frac{8V(rise)\tau}{[D(bubble)]^2}\left[\frac{V(rel)}{V(rise)}\right]^2$$

where D(bubble) is the diameter of the spherical bubble with the same volume as the ellipsoidal bubble and β is a constant dependent on the shape of the bubble. The constant β is chosen here to be identified as V(rel)/V(rise) where V(rel) is a fictitious relative velocity. V(rel)/V(rise), of course, has physical significance for perfectly spherical, isolated bubbles rising in pure water. Otherwise, it is best considered an adjustable parameter. Some values of this parameter for bubbles of various aspect ratios are:

E = a/b	β = V(rel)/V(rise)
1.001	1.501
1.01	1.510
1.1	1.600
1.5	1.997
2.0	2.495
2.5	3.000
3.0	3.514
4.0	4.565
4.167	4.743

A value of E = 4.167 corresponds to a spherical cap bubble (see Chapter IV of this document). Once a bubble is sufficiently distorted to adopt the spherical cap shape, the geometrical specifications used to derive the impaction coefficient are no longer valid.

The form of the impaction coefficient for ellipsoidal bubbles provides a method for dealing with both the distortion of bubbles and possible retardation of gas circulation within a bubble. The impaction coefficient is defined as

$$\alpha[I,d_p] = \frac{8V(rise)\tau}{[D(bubble)]^2}\beta^2 = \frac{8V(rise)\tau}{[D(bubble)]^2}\left[\frac{V(rel)}{V(rise)}\right]^2$$

and the ratio V(rel)/V(rise) is treated as a parameter. Values of this parameter less than 1.5 can be used to describe the impaction coefficient for particles in a bubble in which gas circulation is retarded. Values greater than 1.5 can be used to reflect enhanced impaction brought on by distortion of bubbles from spherical to ellipsoidal forms.

The β parameter can also describe deviations from the potential flow regime. This can be important for large bubbles. Measurements[92] have shown β values increasing from 0.56 to 0.81 as Reynolds numbers vary between 2.5 and 42.

The coefficient for particle scrubbing caused by particle diffusion is only modestly affected by bubble distortion. A derivation of the altered description of diffusion is given in reference 255.

The Fuchs model would have an obvious analytic solution were the coefficients not so strongly dependent on the bubble size. The bubble size varies during the rise through the pool in a way adequately described by:

$$\left[\frac{D(\text{bubble},x)}{D(\text{bubble},o)}\right]^3 = \frac{P_{amb} + H\rho(\text{water})/1033.23}{P_{amb} + (H-x)\rho(\text{water})/1033.23}$$

where $D(\text{bubble}, x)$ = bubble diameter at an elevation x above the debris surface,

P_{amb} = ambient pressure in atmospheres,

H = total depth of the water pool in centimeters, and

$\rho(\text{water})$ = water density in g/cm^3.

The bubble cannot grow to an unlimited size, however. The stability analysis described in connection with bubbles in the melt (see Section IV) can also be applied to bubbles in the pool. The results of such an analysis are shown in Figure 60. Apparently, bubbles that grow larger than about 5 cm will not be stable in the water pool.

Disintegration of excessively large bubbles does not take place by shattering, typically. Rather, small volumes of the bubble (10-25 percent) cleave off. (This is sometimes called "calving.") Cleavage of a bubble is sometimes accompanied by the formation of very tiny bubbles (<1 mm) as well as the two larger bubbles.

The behavior of bubbles that have grown too large to be stable is difficult to predict because of the stochastic

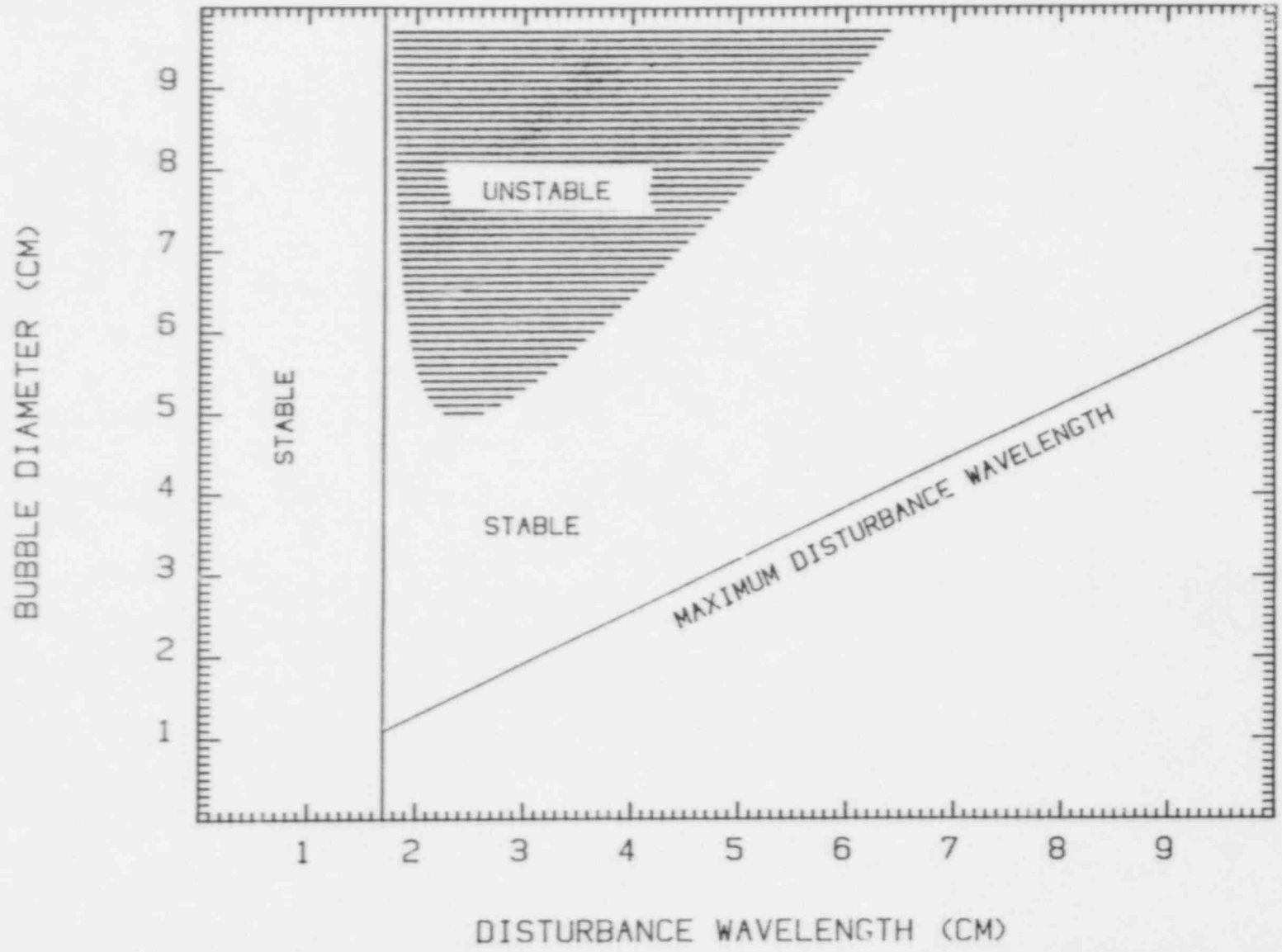

Figure 60. Stability of Gas Bubbles in Water Toward Surface Disturbances of Various Wavelengths

nature of cleavage. No attempt is made in the model to predict the disintegration of overly large bubbles.

Calderbank[114] has noted that in very deep water pools, bubbles may coalesce. No attempt is made to include bubble coalescence in this model of aerosol scrubbing by overlying water pools.

To complete the description of the model, it is necessary to have a model for the initial bubble size. Many of the models discussed in connection with the formation of bubbles in molten core debris are applicable also to the formation of bubbles in the overlying water pool. The Taylor instability models[138,194] for the equivalent sphere diameter are of the form:

$$d(\text{bubble}) = 2C\,[\sigma_{\ell}/g(\rho_{\ell}-\rho_{g})]^{1/2}$$

where C = 2.2 to 2.72 and yield predictions of initial bubble sizes of 1.1 to 1.5 cm for conditions expected to arise in water pools overlying core debris. The Davidson and Schüler model[195, 196] is

$$d(\text{bubble}) = \left(\frac{6V_{s}^{1.2}}{\pi g^{0.6}}\right)^{1/3}$$

and predicts bubble sizes of 1-2 cm for superficial gas velocities likely to develop during core debris interactions with concrete. During a test called TWT-0,[256] Blose observed 2 cm diameter bubbles at the surface of a 50-cm deep water pool overlying a thermitically generated melt. This experimental result suggests that the bubbles initially formed in the water pool were of sizes consistent with either of the above correlations.

The aerosol scrubbing achieved by an overlying water pool is conveniently described in terms of a so-called decontamination factor, DF. The decontamination factor is defined as:

$$DF = \frac{\text{Mass of aerosol entering the water pool}}{\text{Mass of aerosol emerging from the water pool}} .$$

Plots of the decontamination factor calculated for aerosols 0-1.5 μm in size and assuming that various combinations of the aerosol scavenging process are operative are

shown in Figure 61. In preparing this figure, it was assumed that the water pool was 300 cm deep and that the bubbles formed initially in the water pool were 1 cm in diameter. The solid curve in the figure shows the decontamination that could be achieved if all aerosol scrubbing mechanisms were operative. The curve labeled "no diffusion" indicates the scrubbing that would occur if the flux of water vapor from the bubble walls blocked totally the diffusion of particles to the bubble walls. The curve marked "no impaction" indicates the aerosol scrubbing that would occur if gases within the bubble did not circulate sufficiently to cause particle impaction on the bubble walls.

As shown by the dotted line, sedimentation alone is a relatively inefficient mechanism for scrubbing aerosols from bubbles.

Results shown in Figure 61 indicate that very small aerosol particles (<0.1 μm) are entrapped by the water pool because these particles diffuse quickly to the bubble walls. Large aerosol particles (>0.5 μm) diffuse quite slowly. Such large particles are efficiently scrubbed because of the sedimentation and the impaction mechanisms. As a consequence of the varying dependencies of the scrubbing mechanisms on particle size, the overall decontamination is not a monotonic function of aerosol particle size. Rather, there is some particle size for which the combined effects of diffusion, impaction, and sedimentation yield a minimum decontamination factor.

The minimum decontamination factor for an overlying water pool is a strong function of the pool depth. Shown in Figure 62 are plots of the decontamination factor as a function of particle size for pools 100 to 700 cm deep. It is apparent from this figure that a factor of 10 reduction in the aerosol mass having particle sizes in the vicinity of the minimum decontamination can be achieved only by pools that are quite deep.

The effects of circulation of gases within a bubble on the decontamination factor are shown in Figure 63. For this figure the pool depth was assumed to be 100 cm, the initial bubble size was taken as 1 cm and the ratio V(rel)/V(rise) was varied between 0.5 and 5. Values of the ratio that are less than 1.5 are indicative of what happens to the decontamination factor when contamination of the bubble walls inhibits the circulation of gases or rise velocities are insufficiently described by the potential flow approximation. Values of V(rel)/V(rise) greater than 1.5 show the effects of distortion of the bubble from an approximately spherical shape. Obviously, the shape of the bubble and the nature of gas circulation within the bubble have significant effects on the decontamination achieved by an overlying water pool.

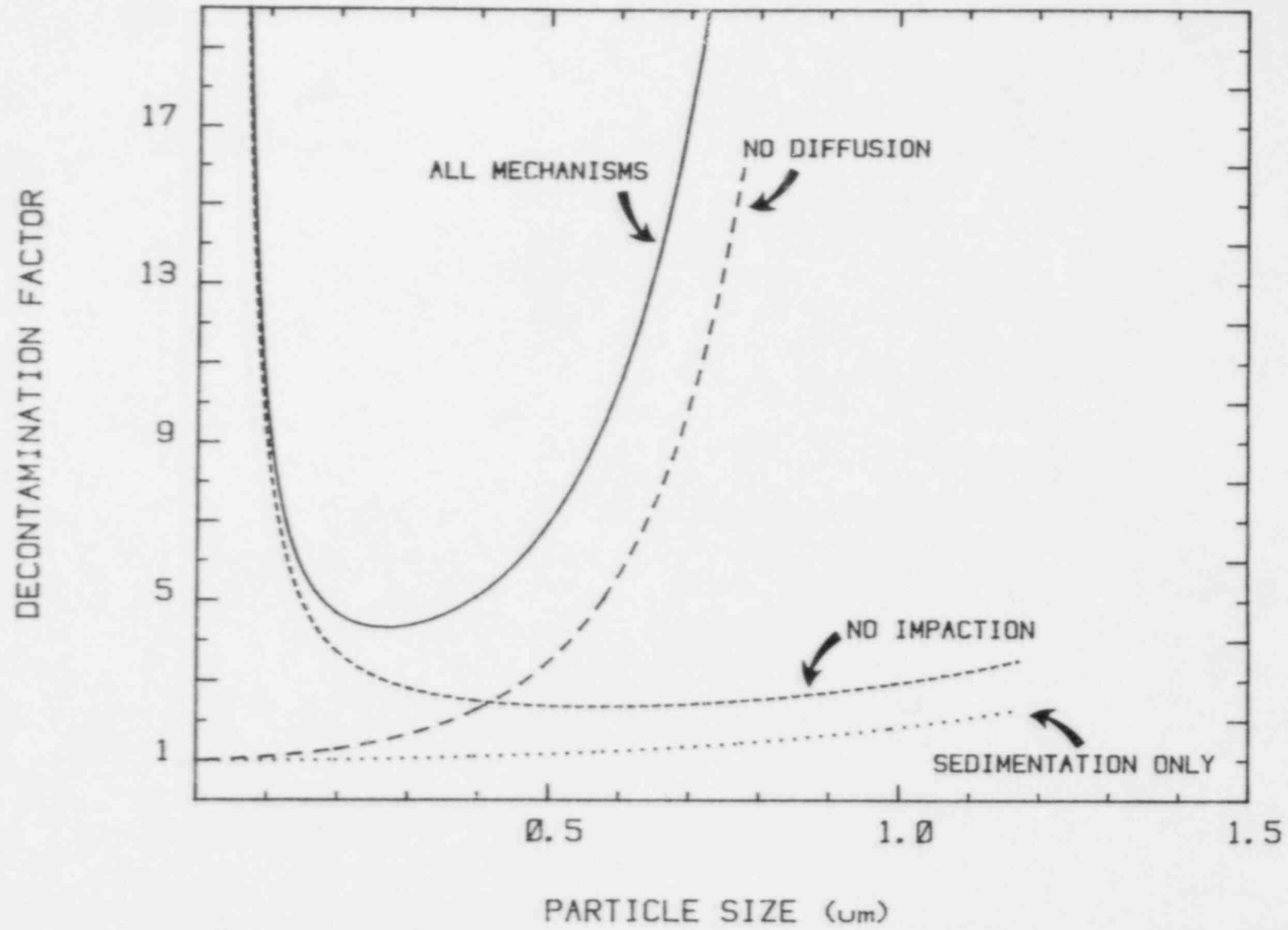

Figure 61. Decontamination Factors Shown as Functions of Particle Size and Computed Assuming Various Combinations of Scrubbing Mechanisms are Operative. Pool depth is 700 cm and the initial bubble size is 1 cm.

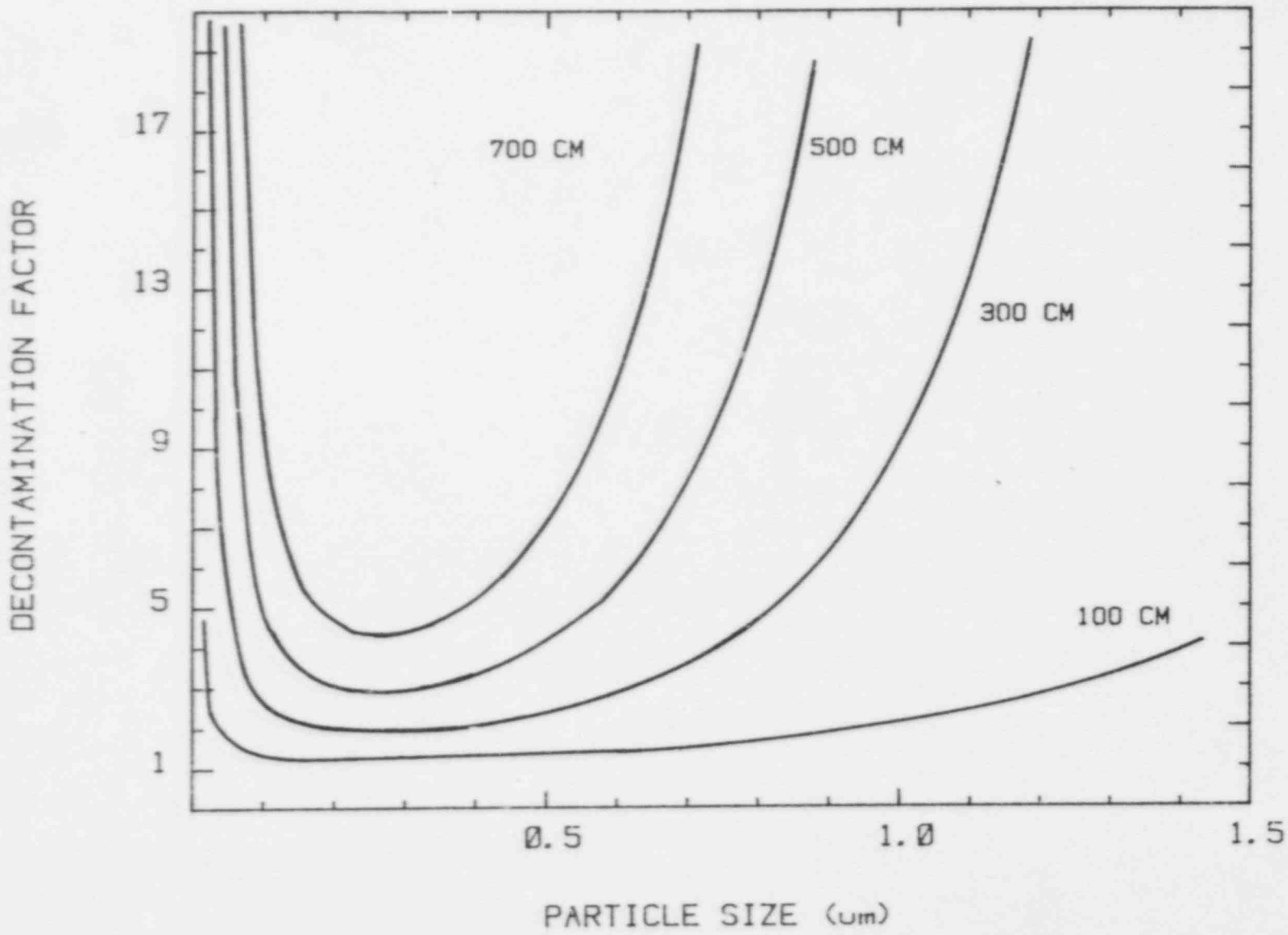

Figure 62. Decontamination Factors for Pools of Various Depths V(rel)/V(rise = 1.5 and bubble diameter is 1 cm

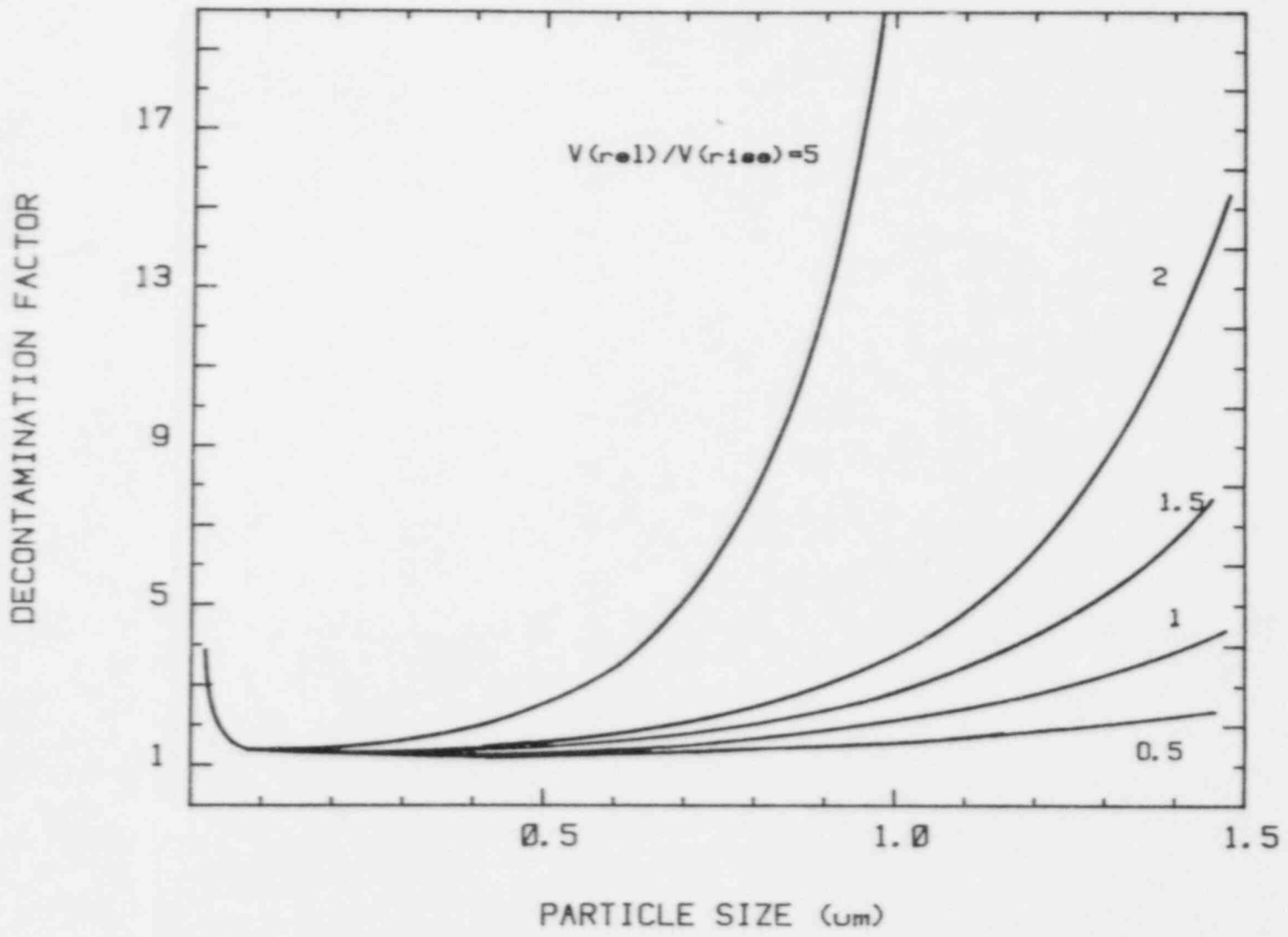

Figure 63. Effects of the V(rel)/V(rise) Ratio on the Decontamination Factors. Values (V(rel)/V(rise) <1.5 are indicative of decontamination of bubbles with inhibited internal gas circulation. Values of V(rel)/V(rise) >1.5 are indicative of decontamination of ellipsoidal bubbles. Pool depth is 200 cm and bubble diameter is 1 cm.

The effects of the initial bubble size on the decontamination factor are shown in Figure 64. The decontamination factors shown in this figure demonstrate that it is of some importance to establish the initial bubble size to within at least a factor of two if accurate predictions of the aerosol decontamination are to be obtained.

The results of calculations with the aerosol scrubbing model show that aerosol scrubbing is dependent strongly on the aerosol particle size. It can be assumed that aerosol particles produced by core debris interactions with concrete will have a distribution of sizes. The decontamination achieved as bubbles of gas laden with these aerosols will not be uniform over the entire size spectrum. The variation in the particle size distribution as gas bubbles rise various distances in a water pool is shown in Figure 65. The scrubbing action of the water pool not only removes mass, it also narrows the size distribution and changes the mean aerosol size. The variations in the mean size are, of course, toward the size for which decontamination is a minimum. Thus, distributions with means that are initially less than the minimum decontamination size are shifted to larger sizes. Initial distributions with large mean sizes are shifted to smaller sizes by the scrubbing actions.

The narrow, but attenuated, aerosol distribution that emerges from the water pool passes into the containment and out of the domain of interest for the VANESA model.

This concludes the description of the VANESA model.

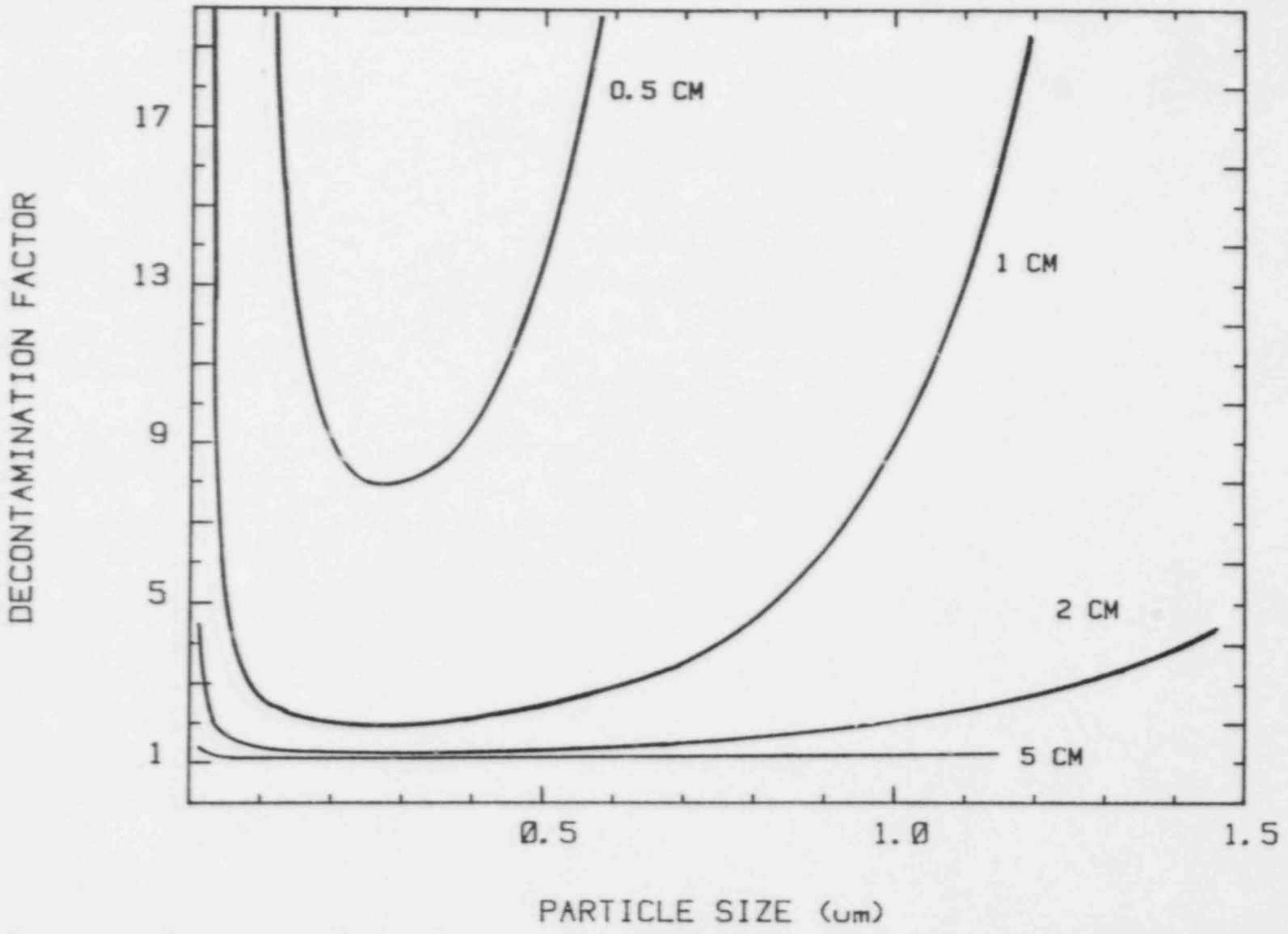

Figure 64. Effects of Bubble Diameter on the Decontamination Factors
Pool depth is 300 cm and V(rel)/V(rise) = 1.5

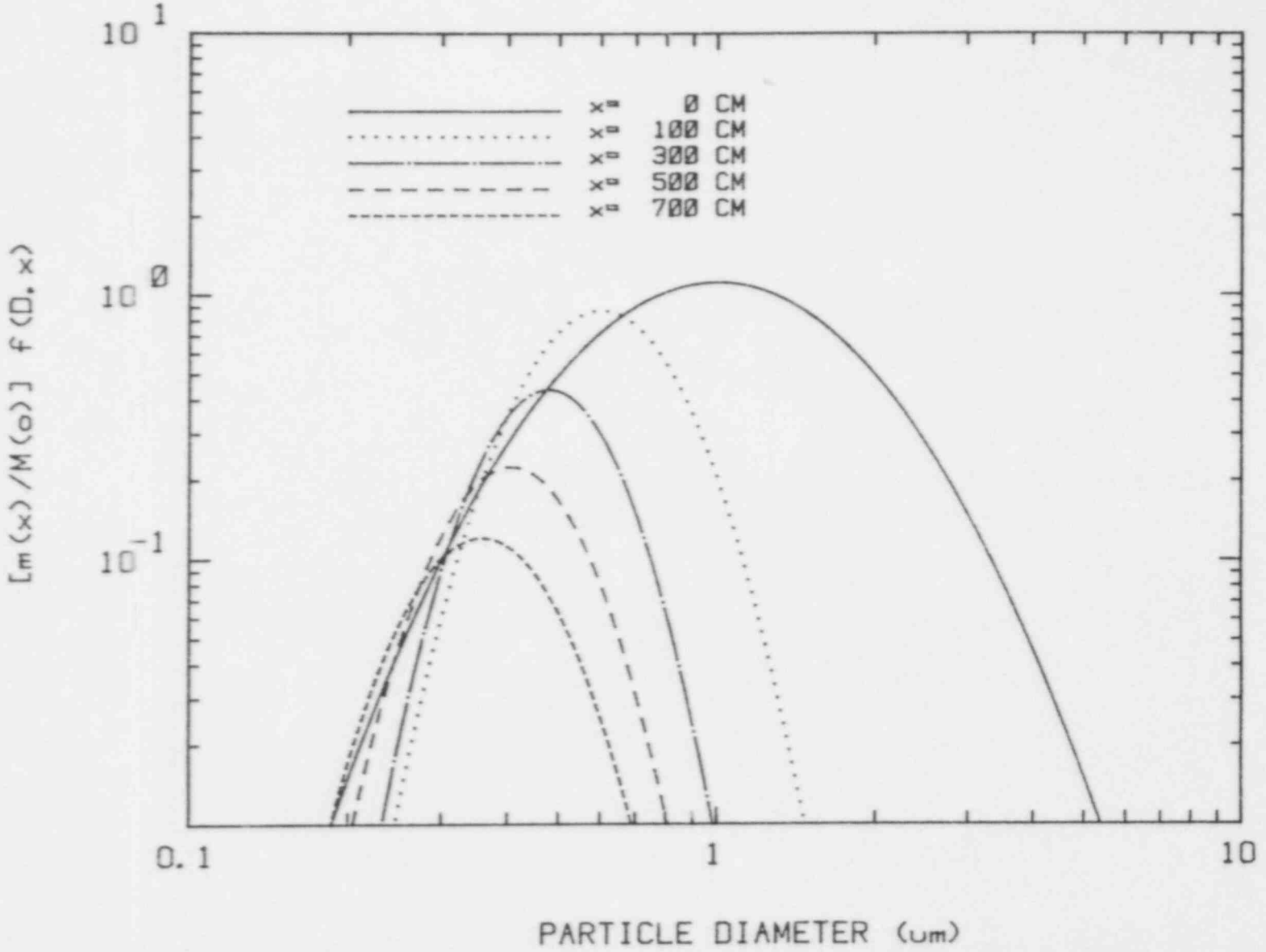

Figure 65. Variations of the Particle Size Distribution as Bubbles Rise in a Pool

VIII. AN IMPLEMENTATION OF THE VANESA MODEL

The VANESA model has been discussed in the previous chapters of this document. The VANESA model is a description of the physical and chemical processes that result in the release of radionuclides and the production of aerosols during core debris interactions with concrete. The model also describes those factors that influence the physical characteristics of the aerosols and the attenuation of aerosol emissions into the reactor containment by a water pool overlying the core debris.

Predictions of the source term of radionuclides and aerosols during core debris interactions with concrete can be obtained from the model by formulating the descriptions into mathematical terms. The lengthy discussions in the previous chapters demonstrate that there is a significant technological basis for the mathematical formulation of the VANESA model. Many of the more important aspects of the model can be treated in great detail. Even when the formulations are done simply, there are so many processes affecting the production of aerosols from core debris, that the model formulations are evaluated efficiently only by using a computer. Also, predictions obtained from simple formulations of the VANESA model still outstrip the experimental data base on radionuclide release and aerosol generation by core debris interacting with concrete.

The evaluation of radionuclide release and aerosol production during core debris/concrete interactions proved to be an important aspect of the recent USNRC-sponsored, severe accident source term reassessment.[2] To service the need of this effort, an implementation of the VANESA model as a computer code was hurriedly assembled. Unlike other computer codes used in the source term reassessment, this implementation of the VANESA model was <u>not</u> the product of a rigorous code development effort. The code was formulated for the convenience of the authors to meet their obligations to the source term reassessment effort. There was never any intention of producing a computer code that could be generally distributed and used for analyses widely different than those arising in the source term reassessment. The computer code devised by the authors evolved as the nature and the scope of the source term reassessment work changed.

Interest has arisen apparently in the computer code devised for the source term reassessment work. It is because of this interest that a description of the code is included in this document. Those who use this computer code are cautioned that the code reflects its informal origins and the very limited time available for its development. No attempt has been made to streamline the calculations done in the code or to observe the niceties of computer programming

characteristic of codes developed in NRC-sponsored research programs. Of more importance, perhaps, is that no attempt has been made to incorporate restrictions in the code to assure it is used only for analysis of problems in an applicable range.

A. An Overview of the Computer Code

A schematic diagram of the major elements of the computer code is shown in Figure 66. The calculational procedures can be divided into three steps. The first of these steps is the receipt and processing of input data. Data are received into the computer code by the DRIVER routine. These data are received in the form usually provided in the course of work for the NRC-sponsored, source term reassessment. The data are manipulated into the form used in the code calculations by calls to the subroutines BCLTOV, CVRMSI, and CVGAS. The data are organized and thermodynamic data for melt constituents are calculated in a call to the subroutine ASSEMB.

Once the necessary data are in hand, control of the calculations passes to the VANESA routine. In the VANESA routine, the release and the physical characteristics of the released materials are calculated. Calls to the subroutines SRG and SRPP provide oxygen potentials, fixed gas compositions, and equilibrium partial pressures of volatile species. Results of the calculations in the VANESA routine are periodically printed by calls to the subroutine OUTPUT. At these times, too, the boundary conditions for the VANESA calculations are updated to reflect changes brought on by the core debris interactions with concrete.

The results of the VANESA calculations are the descriptions of the radionuclide release and aerosol production by core debris/concrete interactions. Any attenuation of the source term by an overlying water pool is found by calculations done with the POOL subroutine. Attenuation of the source term by an overlying water pool is presumed to be a physical process that leaves unaltered the composition of the released material calculated in the VANESA routine. The POOL routine prints out revised physical characteristics of the released materials separately from the printout of the VANESA calculations.

The calculational sequence is terminated by a return from the POOL subroutine to the VANESA routine.

B. Description of the Subroutines

The DRIVER routine is simply an interface to the CORCON code and allows the input data to be received by the computer code. The subroutines do the actual calculations.

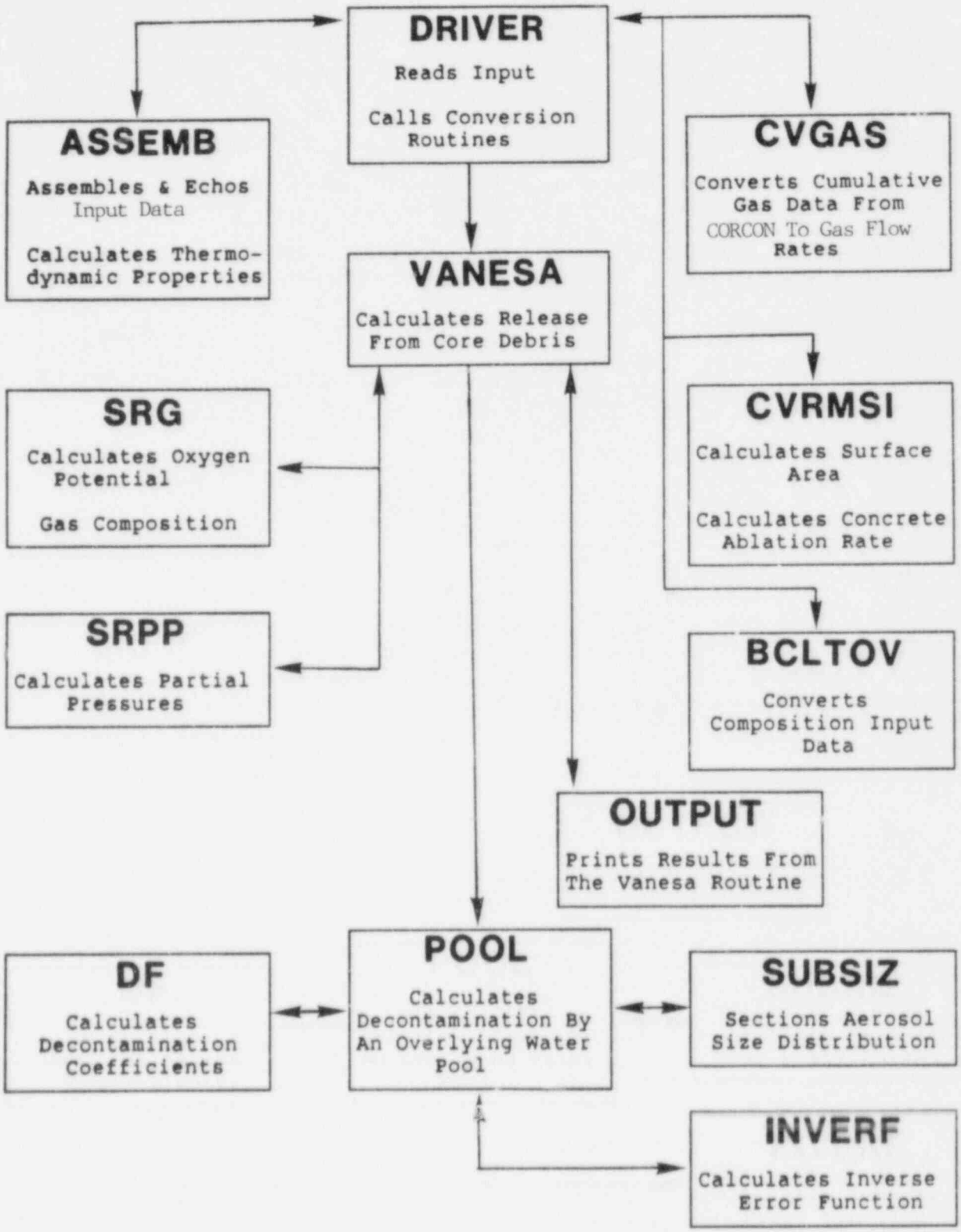

Figure 66. Schematic Diagram of the Elements of the Computer Code

Some of the more salient features of these subroutines are described in the subsections below. The discussions are organized alphabetically in terms of the subroutine name for the convenience of user reference.

1. Subroutine ASSEMB (p1, p2, A1, A2, A3, A4, A5, A6)

Parameters and arrays in the calling sequence for subroutine ASSEMB are:

p1 = problem name

p2 = number of data sets generated by CORCON

A1 = array of times after the start of melt attack on concrete for which there are data sets

A2 = array of molar rates of H_2O production from concrete

A3 = array of molar rates of CO_2 production from concrete. Note that CO_2 which reacts to form carbon in the melt is excluded from entries in the array. Carbonaceous gases produced by decarburization of the melt are included as though they were produced directly from CO_2 evolved from the concrete.

A4 = array of gas production rates in standard cm^3 per second

A5 = array of floor areas exposed to melt (m^2)

A6 = array of rates of concrete addition to the melt (kg/s).

The subroutine summarizes and prints the input data. It computes thermodynamic data for the species considered in the VANESA analyses. It converts entries in the floor area array to units of square centimeters and concrete addition rates to g/s. The input is then written on a disk for use by the VANESA routine.

2. Subroutine BCLTOV

Subroutine BCLTOV converts melt compositions from kilograms mass of the elements to kilograms mass of metals, oxides, and CsI as discussed in the description of the input. It is also in subroutine BCLTOV that the groupings of elements are done. The groups are formed from:

1. Cs and Rb
2. Ru, Tc, Rh, and Pd
3. La, Y, Pr, Nd, and Sm
4. Ce, Pu

Grouping is done by molar addition. For some analyses, it is necessary to include additional elements to the lanthanum and the cerium groups. This is most conveniently done by adjusting the input. Thus, if a new element of mole weight M is to be added to the lanthanum group, the lanthanum inventory, La, is increased by

$$138.91\ W(x)/M$$

where W(x) is the kilograms mass of the additional element in the lanthanum group. For additions to the cerium group, increase the input inventory of cerium by

$$140.12\ W(x)/M \quad .$$

3. Block Data BARRAY

The block data BARRAY contains parameters for the free-energies of formation of the species considered in the analyses as discussed in Chapter IIIA of this document. The correlations are of the form:

$$B[I,J,1] + B[I,J,2]T = \Delta G_f(I,J) \quad .$$

The key to the indexing system is shown in Table 56.

4. Subroutine CVGAS (p1, A1, A2, p2, A3, A4, A5)

Subroutine CVGAS determines the rates at which H_2O and CO_2 liberated from the concrete pass through the melt. The determination is done based on the cumulative masses of CO, CO_2, H_2O, and H_2 predicted by CORCON to have been evolved during core debris interactions with concrete. This procedure circumvents some questions about dealing with the coking reaction without denying it occurs.

The parameters and the arrays in the calling sequence for CVGAS are:

p1 = time step between input data calculated by CORCON

A1 = array of cumulative masses (kg) of gas species ordered as follows:

A1(1,p2) = mass CO
A1(2,p2) = mass CO_2
A1(3,p2) = mass H_2
A1(4,p2) = mass H_2O

Table 56

Index to Array Number Sequences for an Array XM[I,J]

J=	1	2	3	4	5	6	7	8	9	10
I										
1	$H_2O(g)$	$H_2(g)$	H(g)	OH(g)	O(g)	$O_2(g)$	$CO_2(g)$	CO(g)	NU*	NU*
2	Fe(c)	FeO(c)	Fe(g)	FeO(g)	FeOH(g)	$Fe(OH)_2(g)$	NU	NU	NU	NU
3	Cr(c)	$Cr_2O_3(c)$	Cr(g)	CrO(g)	$CrO_2(g)$	$CrO_3(g)$	$H_2CrO_4(g)$	CrOH	$Cr(OH)_2$	NU
4	Ni(c)	NiO(c)	Ni(g)	NU	NiOH	$Ni(OH)_2$	NiH	NU	NU	NU
5	Mo(c)	NU	Mo(g)	MoO(g)	$MoO_2(g)$	$MoO_3(g)$	$H_2MoO_4(g)$	$(MoO_3)_2$	$(MoO_3)_3$	MoOH
6	Ru(c)	NU	Ru(g)	RuO(g)	$RuO_2(g)$	$RuO_3(g)$	$RuO_4(g)$	RuOH	$Ru(OH)_2$	
7	Sn(c)	NU	Sn(g)	SnO(g)	SnOH(g)	$Sn(OH)_2(g)$	SnTe(g)	SnH	SnH_4	Sn_2
8	Sb(c)	NU	Sb(g)	NU	SbOH(g)	$Sb(OH)_2(g)$	$Sb_2(g)$	$Sb_4(g)$	SbTe(g)	SbH_3
9	Te(c)	NU	Te(g)	TeO(g)	$TeO_2(g)$	$Te_2O_2(g)$	TeOH	$TeO(OH)_2(g)$	$Te_2(g)$	$H_2Te(g)$
10	Ag(c)	NU	Ag(g)	AgO(g)	AgOH(g)	$Ag(OH)_2(g)$	AgTe	AgH	Ag_2	Ag_3
11	Mn(c)		Mn(g)	MnO(g)	MnH	MnOH(g)	$Mn(OH)_2(g)$	NU	NU	NU
12	CaO(c)	NU	Ca(g)	CaO(g)	CaOH(g)	$Ca(OH)_2(g)$	CaH	Ca_2	NU	NU
13	$Al_2O_3(c)$	NU	Al(g)	AlO(g)	AlOH(g)	$Al_2O(g)$	$AlO_2(g)$	$Al_2O_2(g)$	$Al(OH)_2(g)$	AlO(OH)(g)
14	$Na_2O(c)$	NU	Na(g)	NaOH(g)	NaO(g)	$Na_2(OH)_2(g)$	NaH(g)	$Na_2(g)$	NU	NU
15	$K_2O(c)$	NU	K(g)	KOH(g)	KO(g)	$K_2(OH)_2(g)$	KH(g)	$K_2(g)$	NU	NU
16	$SiO_2(c)$	NU	Si(g)	SiO(g)	$SiO_2(g)$	SiOH(g)	$Si(OH)_2(g)$	SiH	SiH_4	Si_2
17	$UO_2(c)$	NU	U(g)	UO(g)	$UO_2(g)$	$UO_3(g)$	$H_2UO_4(g)$	UOH	$U(OH)_2$	NU
18	$ZrO_2(c)$	NU	Zr(g)	ZrO(g)	$ZrO_2(g)$	ZrOH(g)	$Zr(OH)_2(g)$	ZrH	NU	NU
19	$Cs_2O(c)$	NU	Cs(g)	CsOH(g)	CsO(g)	$Cs_2(OH)_2(g)$	$Cs_2O(g)$	$Cs_2(g)$	CsH	CsO_2
20	BaO(c)	NU	Ba(g)	BaO(g)	BaOH(g)	$Ba(OH)_2(g)$	BaH	NU	NU	NU
21	SrO(c)	NU	Sr(g)	SrO(g)	SrOH(g)	$Sr(OH)_2(g)$	SrH	NU	NU	NU
22	$La_2O_3(c)$	NU	La(g)	LaO(g)	LaOH(g)	$La(OH)_2(g)$	La_2O	$(LaO)_2$	NU	NU
23	$CeO_2(c)$	NU	Ce(g)	CeO(g)	CeOH(g)	$Ce(OH)_2(g)$	CeO_2	$(CeO)_2$	NU	NU
24	NbO(c)	NU	Nb(g)	NbO(g)	NbOH(g)	$Nb(OH)_2(g)$	$NbO_2(g)$			
25	CsI(c)	NU	CsI(g)	I(g)	HI(g)	$I_2(g)$	IO	NU	NU	NU

A2 = array of cumulative volumes (cubic centimeters at 298.15 K and 1 atmosphere) of gas species organized and structured as is array A1

p2 = number of data sets

A3 = array of molar rates of H_2O production (moles/second)

A4 = array of molar rates of CO_2 production (moles/second)

A5 = array of volumetric gas generation rates at 298.15 K and 1 atmosphere.

Rates are computed by central differences except for the first and last entries in the rate arrays which are calculated by forward and backward differences respectively. (Note: in newer versions of the code forward differences are used to calculate the rates at all time steps.)

5. Subroutine CVRMSI (p1, A1, A2, A3, p2, p3, A4, A5)

Subroutine CVRMSI converts the maximum molten pool radius and the cumulative SiO_2 content of the molten pool calculated by CORCON into the area of the base of a cylinder and the rates at which molten concrete are added to the molten pool. The parameters and arrays in the calling sequence are:

p1 = time step between results produced by CORCON

A1 = array of times in seconds after the start of melt interactions with concrete for which input data have been calculated

A2 = array of maximum pool radii calculated by CORCON (m)

A3 = array of kilograms SiO_2 in the molten pool calculated by CORCON

p2 = number of data sets or array entries

p3 = weight fraction of SiO_2 in the molten concrete

A4 = array of horizontal pool areas calculated by the routine (m^2)

A5 = array of concrete mass addition rates (kg/s).

Calculation of the areas is trivial. Cumulative masses of silica in the core melt are converted to the cumulative mass of molten concrete added to the melt by dividing by the weight fraction of SiO_2 in molten concrete. The concrete addition rate is found by central differences for all of the

data sets, save the first and the last. Forward and backward differences are used to calculate the first and the last concrete addition rates, respectively. (Note: in more recent versions of the code forward differences are used to calculate the concrete addition rates at all time steps.)

6. Subroutine DF (p1, p2, p3, p4, p5, p6, p7, p8)

The DF subroutine calculates $dm(d_i,x)/dx$ for the process of decontamination by an overlying water pool. The parameters in the calling sequence are:

p1 = characteristic aerosol particle size = d_i

p2 = ambient pressure

p3 = water pool depth

p4 = water temperature

p5 = particle material density

p6 = distance of the bubble from the bottom of the water pool = x

p7 = aerosol mass in the size segment

p8 = $dm(d_i,x)/dx$.

The density of the water pool is calculated in the subroutine as though the pool were pure water. The equation is:

$$\rho_\ell(H_2O) = 0.920848 + 0.000917696T - 2.19011 \times 10^{-6} T^2 \quad .$$

The viscosity of the gas phase is calculated as though it were pure water vapor using the equation:

$$\mu_g = \frac{0.9499942\ T^{0.892912}}{(1 + 207.219/T)} \times 10^{-6} \text{ poises} \quad .$$

The mean free path of the gas phase is calculated as though only steam were present:

$$\lambda = 0.0002058\ T/P(\text{atms}) \quad .$$

The bubble rise velocity is calculated from

$$V(\text{rise}) = 25\left(V(x)_{\text{bubble}}\right)^{1/6} \text{ cm/s}$$

where $V(x)_{\text{bubble}}$ is the volume of the bubble at an elevation of tion of x centimeters above the bottom of the water pool. This is a rise velocity appropriate for a spherical cap bubble. The spherical cap shape is expected based on results of tests in which water pools were formed over high temperature melts attacking concrete. This definition of the rise velocity can be replaced readily with any other correlation of bubble rise velocity discussed above in Section III of this document. The equations are labeled with comment cards in the subroutine listing.

Other equations evaluated in subroutine DF are described in Section VII of this report. The subroutine returns a value of

$$\frac{dm(d_i,x)}{dx} = -\left[\alpha[s,d_i] + \alpha[i,d_i] + \alpha[D,d_i]\right]m(d_i,x) \quad .$$

7. Function Erf(x)

This is a function routine to calculate the value of

$$\frac{2}{\sqrt{\pi}} \int_0^x \exp(-y^2)dy = \text{erf}(x) \quad .$$

The function routine is documented in Reference 260.

8. Subroutine INVERF (y,x)

This subroutine solves the equation

$$y = \text{erf}(x) = \frac{2}{\sqrt{\pi}} \int_0^x \exp(-z^2)dz$$

for x given y. A Newton Raphson procedure is used. The zero order approximations for x are 0.5 and -0.5 when y is positive and y is negative, respectively. Then, if $x^{(k)}$ is the k^{th} approximation of x,

$$x^{(k+1)} = x^{(k)} - \frac{[\mathrm{erf}(x^{(k)}) - y]}{\frac{2}{\sqrt{\pi}} \exp[-(x^{(k)})^2]}$$

a solution is declared when

$$\left| x^{(k+1)} - x^{(k)} \right| \leq 10^{-6} \quad .$$

The loose convergence criterion has been chosen so that the routine will operate on short word-length machines.

Subroutine INVERF will produce an error message if $|y| > 1$.

9. Subroutine OUTPUT

Subroutine OUTPUT produces the output from the analyses done in the VANESA routine. The output is produced each time updated information on the boundary conditions concerning the melt/concrete interactions are required. Note that output reflecting the effects of an overlying water pool is produced separately in the POOL subroutine.

10. Subroutine POOL (p1, A1, A2, A3, A4, A5, A6)

The subroutine POOL calculates the decontamination of the aerosol-laden gases emerging from the core debris by an overlying water pool. The calling sequence for the POOL subroutine requires the following information:

p1 = number of data sets to be processed

A1 = array produced by the VANESA subroutine of mean particle sizes for the aerosols

A2 = array produced by the VANESA subroutine of aerosol mass generation rates

A3 = array produced by the VANESA subroutine of aerosol material densities

A4 = array of water pool depths supplied by the user as input to the code

A5 = array of ambient pressures supplied by the user as input to the code

A6 = array of water pool temperatures supplied by the user as input to the code.

The number of data sets is, of course, the number of times printed output is obtained from the VANESA subroutine. If the number of data sets is set to zero, the POOL subroutine prints a message and stops. If a pool depth for a data set is zero, the routine does no calculations of decontamination. It simply advances to the next data set. This makes it permissable for the overlying water pool to completely evaporate and then be reformed in the course of the accident.

The user should exercise some caution in the interpretation of results obtained in the cases involving complete evaporation of the water pool. Radionuclides and other material trapped in the water pool are assumed to be permanently removed from consideration. Thus, should the water pool evaporate completely, trapped radionuclides are not added back into the core melt and are not made available for re-release.

Calculations with the pool subroutine may be omitted altogether. See the discussion of card group 7 in the description of the format of the input--section VIII-E.

The subroutine reads from the input file operational parameters:

1. Number of size segments to be used to describe the aerosol size distribution entering the water pool,

2. The assumed geometric standard deviation for the aerosol size distribution which is assumed to be lognormal in shape,

3. Flags indicating whether the diffusion and impaction mechanisms of aerosol entrapment are operative,

4. The size of the gas bubbles forming at the bottom of the water pool, and

5. The circulation velocity of gases within the bubbles relative to the bubble rise velocity.

If the number of segments used to describe the aerosol size distribution is less than four, an error message is printed and the calculation stops. If more than 50 size segments are specified, a warning statement is printed and 50 size segments are used.

The input data to the POOL subroutine is printed prior to the start of calculations.

The calculational sequence in the POOL subroutine is repeated for each data set with a positive pool depth. The

first step in this sequence is the segmentation of the aerosol size distribution into size ranges containing equal fractions of the mass. The I^{th} size segment is characterized by the limiting sizes D[I] and D[I+1] where D[1] = 0 and D[N+1] = 10^{29} where N is the number of segments specified by the user. The limiting size D[I+1] is found for I + 1 = 2 to N by a call to the subroutine SUBSIZ to solve the equation:

$$\frac{I}{N} = 0.5 \left(1 + \text{erf}\left[\frac{\ell n(D[I+1]/\mu)}{\sqrt{2}\ \ell n(\sigma)}\right]\right)$$

where μ = mean particle size predicted for the data set by the VANESA routine, and

σ = assumed geometric standard deviation for the size distribution.

The characteristic sizes for the size segments, RSIZ[I] for I = 1 to N, are chosen such that half the mass within the segment is composed of particles of smaller diameter. The selection of the characteristic sizes is done by calls to the subroutine SUBSIZ to solve the equation:

$$\frac{I + 0.5}{N} = 0.5 \left(1 + \text{erf}\left[\frac{\ell n(RSIZ[I]/\mu)}{2\ \ell n(\sigma)}\right]\right) .$$

For these calls to SUBSIZ the zero order approximation to RSIZ[I] is taken to be

$$RSIZ[I]^{(0)} = \frac{1}{2} (D[I] + D[I+1]) .$$

A fourth order Runge-Kutta method is then used to solve for each size segment:

$$\frac{dM[I,x]/M_T}{dx} = -(\alpha[S,I] + \alpha[i,I] + \alpha[D,I]) \frac{M[I,x]}{M_T}$$

where M[I,x] = aerosol mass in the I^{th} size segment at a distance x from the bottom of the water pool,

M_T = total aerosol mass generation rate found in calculations with the VANESA routine,

$\alpha[S,I]$ = coefficient for sedimentation of particles of the diameter RSIZ[I],

$\alpha[i,I]$ = coefficient for impaction of particles of the diameter RSIZ[I], and

$\alpha[D,I]$ = coefficient for diffusion of particles of the diameter RSIZ[I].

Function evaluations required by the Runge-Kutta integration are done by the subroutine DF. Step sizes in the integration are controlled to be greater than or equal to 10^{-6} cm and such that the change in M[I,x] over one step is less than the minimum of 0.01 grams and 0.05 $M[I,x]/M_T$. Should $M[I,x]/M_T$ fall below 10^{-6}, M[I,x]/M is set equal to 10^{-6} and integration for the I^{th} size segment is terminated.

Results of the integration are printed as a table showing:

1. The number of the data set,
2. The size classes,
3. The characteristic sizes for the classes,
4. The aerosol mass remaining in the size class after passage through the water pool, and
5. The size class decontamination factor, DF[I], which is

$$\frac{M_T/N}{\text{Mass remaining in the } I^{th} \text{ class}} = DF[I] \quad .$$

An overall decontamination factor,

$$DF = \frac{M_T}{\sum_{i=1}^{N} M[I,H]}$$

where H = pool depth, is printed along with the aerosol mass per second emerging from the water pool.

The results of the integration are fit by linear least squares to a lognormal size distribution. This is done by minimizing with respect to a and b

$$S^2 = \sum_{i=1}^{N-1} [y[i] - bx(i) - a]^2$$

where $y[i] = \text{erf}^{-1}[2z[i] - 1]$,

$$z[i] = \sum_{j=1}^{i} M[j,H]/M_T,$$

$x(i) = \ln(D[i+1])$,

$$b = \frac{1}{\sqrt{2}\ \ln(\sigma')},$$

$$a = \frac{-\ln(\mu')}{\sqrt{2}\ \ln(\sigma')},$$

σ' = revised geometric standard deviation for the size distribution of aerosols emerging from the pool,

μ' = revised mean size for the size distribution of aerosols emerging from the pool, and

$\text{erf}^{-1}(x)$ = inverse of the error function of x.

The solution to this minimization is well known to be:[258]

$$a = \frac{\sum_{i=1}^{N-1} x_i^2 \sum_{i=1}^{N-1} y_i - \sum_{i=1}^{N-1} x_i \sum_{i=1}^{N-1} x_i y_i}{(N-1)\sum_{i=1}^{N-1} x_i^2 - \left(\sum_{i=1}^{N-1} x_i\right)^2}$$

$$b = \frac{(N-1)\sum_{i=1}^{N-1} x_i y_i - \sum_{i=1}^{N-1} x_i \sum_{i=1}^{N-1} y_i}{(N-1)\sum_{i=1}^{N-1} x_i^2 - \left(\sum_{i=1}^{N-1} x_i\right)^2}.$$

The revised values of the parameters for the size distribution of the aerosols are then

$$\mu' = \exp\left[-\frac{a}{b}\right]$$

$$\sigma' = \exp(1/b\ 2) \quad .$$

If the uncertainty in the parametric values a and b derived by the least squares fitting is due entirely to mislocation of the y_i values, then the uncertainties* in a and b are:

$$\delta a = \left[\frac{\chi^2 \sum_{i=1}^{N-1} x_i^2}{(N-1)\sum_{i=1}^{N-1} x_i^2 - \left(\sum_{i=1}^{N-1} x_i\right)^2}\right]^{1/2}$$

$$\delta b = \left[\frac{\chi^2 (N-1)}{(N-1)\sum_{i=1}^{N-1} x_i^2 - \left(\sum_{i=1}^{N-1} x_i\right)^2}\right]^{1/2}$$

where $$\chi^2 = \left(\frac{1}{N-3}\right)\left\{\sum_{i=1}^{N-1} y_i^2 + a^2(N-1) + b^2 \sum_{i=1}^{N-1} x_i^2, \text{ and } -2\left[a\sum_{i=1}^{N-1} y_i + b\sum_{i=1}^{N-1} x_i y_i - ab\sum_{i=1}^{N-1} x_i\right]\right\} .$$

The uncertainty in $\ell n(\mu')$ is then:

$$\delta(\ell n(\mu')) = \left|\ell n(\mu')\right|\left[\left(\frac{\delta a}{a}\right)^2 + \left(\frac{\delta b}{b}\right)^2\right]^{1/2}$$

and the uncertainty in $\ell n(\sigma')$ is:

$$\delta(\ell n(\sigma')) = \left|\ell n(\sigma')\right| \left|\left(\frac{\delta b}{b}\right)\right| \quad .$$

*One standard deviation.

Values of μ' and σ' would be expected, to a 67 percent confidence level, to fall in the ranges

$$\mu' \exp[-\delta(\ell n(\mu'))] < \mu' < \mu' \exp[\delta(\ell n(\mu'))]$$

$$\sigma' \exp[-\delta(\ell n(\sigma'))] < \sigma' < \sigma' \exp[\delta(\ell n(\sigma'))] \quad .$$

These ranges are included in the output from the POOL subroutine.

The size distribution of particles emerging from the water pool do not, in general, fit perfectly a lognormal size distribution. A linear correlation coefficient for the least squares analysis is:

$$R^2 = \frac{(N-1)\sum_{i=1}^{N-1} x_i y_i - \sum_{i=1}^{N-1} x_i \sum_{i=1}^{N-1} y_i}{\left\{\left[(N-1)\sum_{i=1}^{N-1} x_i^2 - \left(\sum_{i=1}^{N-1} x_i\right)^2\right]\left[(N-1)\sum_{i=1}^{N-1} y_i^2 - \left(\sum_{i=1}^{N-1} y_i\right)^2\right]\right\}^{1/2}}$$

and is included in the output. Comparison of the printed value to critical values for N-3 degrees of freedom provides an indication of the probability that a set of N-1 randomly selected points would produce such a large or larger value of R^2. Some critical values for N = 20 are:

Critical Value of R^2	Probability
0.176	50 Percent
0.327	20 Percent
0.412	10 Percent
0.482	5 Percent
0.606	1 Percent
0.725	0.1 Percent

11. Subroutine SRG

Subroutine SRG calculates the oxidation of metals by gases evolved from the concrete and the partial pressures of permanent gases. The procedure utilized for these calculations is described in Chapter IV of this report. "Coking" of the melt is not considered. The effect of coking will be reflected in the results if it has been considered in the model of melt/concrete interactions used to compute input for the VANESA code.

12. Subroutine SRPP (A1, A2, p1, p2, A3)

Subroutine SRPP calculates the equilibrium partial pressures of condensible vapors. The information in the calling sequence is

A1 = array of moles of condensed material in the melt

A2 = array of species free energies

p1 = sum of moles in the oxide phase

p2 = sum of moles in the metal phase

A3 = array of species partial pressures.

The older version of the VANESA code required that the total pressure be 1 atmosphere. There is no such constraint in this version.

13. Function SRZ

The function SRZ calculates $\exp(-\Delta G/RT)$ used in subroutine SRPP. It assures against underflow by setting the exponential equal to zero if $\Delta G/RT < -40$. This also serves to eliminate from consideration vapor pressures that are so small that the existence of the vapor species for the conditions in question can be doubted.

14. Subroutine SUBSIZ (μ, σ, y, $d^{(o)}$, d)

The subroutine SUBSIZ solves the equation

$$y = \frac{1}{2}\left(1 + \operatorname{erf}\left[\frac{\ell n(d/\mu)}{\sqrt{2}\ \ell n(\sigma)}\right]\right)$$

for d, given y, μ, and σ. A zero order approximation of d is provided in the calling sequence for the subroutine. If $d^{(k)}$ is the k^{th} order approximation of d, then

$$d^{(k+1)} = d^{(k)} - \frac{\left\{\frac{1}{2}\left(\operatorname{erf}\left[\frac{\ell n(d^{(k)}/\mu)}{2\ \ell n(\sigma)}\right] + 1\right) - y\right\}}{\frac{1}{2}\sqrt{\frac{2}{\pi}}\exp\left[-\left(\frac{\ell n(d^{(k)}/\mu)}{2\ \ell n(\sigma)}\right)^2\right]\left(\frac{1}{d^{(k)}\ \ell n(\sigma)}\right)} .$$

A solution is declared if

$$\left| d^{(k+1)} - d^{(k)} \right| \leq 10^{-6} \quad .$$

The loose convergence criterion is employed in the released version of the code so that it will operate on short word-length machines.

Subroutine SUBSIZ will produce an error message if y > 1.

15. Subroutine VANESA

Subroutine VANESA does most of the computations of the model except those related to the effects of an overlying water pool. In particular, the subroutine formulates and solves the kinetic rate expressions for vaporization from the oxide and metal phases of the melt. The routine also does the "bookkeeping" for the release from the melt.

16. Block Data XNDAR

The block data XNDAR contains an array of molecular weights for the species of interest. It also contains an array of densities for the condensed species. The number sequence for these arrays is described in Table 56.

C. Options

There are few options in the use of the computer code. All of these options are controlled by input. The major optional features are:

1. The frequency with which results obtained for the VANESA routine are printed and the frequency with which boundary conditions for the VANESA routine calculations are updated.

2. Whether source attenuation by an overlying water pool is to be considered.

3. Whether particle diffusion and particle impaction are to be considered as mechanisms of source attenuation by an overlying water pool.

The input information necessary to exercise these options is discussed in greater detail below.

D. General Discussion of the Input Requirements

The input requirements for the computer code may be categorized as:

1. Initial condition information obtained typically from analyses of the in-vessel phases of a severe reactor accident.

2. Boundary condition information obtained typically from models of core debris interactions with concrete.

3. Boundary condition information derived from the descriptions of the particular nuclear plant in question.

4. Operational parameters used in the computer code.

The most important initial condition information required by the computer code is the initial composition of the core debris when it emerges from the reactor vessel into the reactor cavity. This information was derived in the source term reassessment calculations[2] from the results of analyses with the ORIGEN,[257] MARCH,[3] and CORSOR[43] codes. ORIGEN is used to define the composition of the reactor fuel at the time the accident starts. The MARCH and CORSOR codes provide a description of the evolution of the core material composition as the accident progresses. The MARCH code treats reactor fuel as urania although it does not attempt to define the precise stoichiometry. It also recognizes that zirconium will oxidize to form ZrO_2. Otherwise, the ORIGEN, MARCH, and CORSOR codes deal with core debris compositions in elemental terms with no attempt to determine the chemical forms of constituents in the core debris.

The VANESA computer code accepts elemental compositions as provided by the MARCH and CORSOR codes. The speciation of the debris is estimated within the code in subroutine BCLTOV. Acceptance of elemental compositions is done to facilitate input checking.

The code will accept initial composition data for the following elements and oxides:

Composition Accepted as:	Converted to:
Antimony (Sb)	Sb
Barium (Ba)	BaO
Cerium (Ce)	CeO_2
Cesium (Cs)	CsI and Cs_2O
Chromium (Cr)	Cr
Chromium oxide (Cr_2O_3)	Cr_2O_3
Iodine (I)	CsI
Iron (Fe)	Fe
Iron Oxide (FeO)	FeO
Krypton (Kr)	--
Lanthanum (La)	La_2O_3
Manganese (Mn)	Mn
Molybdenum (Mo)	Mo
Neodymium (Nd)	Nd_2O_3

Composition Accepted as:	Converted to:
Nickel (Ni)	Ni and NiO
Niobium (Nb)	NbO
Palladium (Pd)	Pd
Plutonium (Pu)	PuO_2
Praseodymium (Pr)	Pr_2O_3
Rhodium (Rh)	Rh
Rubidium (Rb)	Rb_2O
Ruthenium (Ru)	Ru
Samarium (Sm)	Sm_2O_3
Silver (Ag)	Ag
Strontium (Sr)	SrO
Technetium (Tc)	Tc
Tellurium (Te)	Te
Tin (Sn)	Sn
Uranium dioxide (UO_2)	UO_2
Xenon (Xe)	--
Yttrium (Y)	Y_2O_3
Zirconium (Zr)	Zr
Zirconium dioxide (ZrO_2)	ZrO_2

Also shown in this list are the chemical forms the current implementation of the VANESA model assumes for the elements.

The code accepts input concerning the noble gas (Xe, Kr) content of the core debris. The authors doubt, however, that the core debris which has melted, slumped from the core region, and penetrated the vessel would contain noble gases at greater than trace levels. Nevertheless, for some accidents, the MARCH and CORSOR computer codes yield predictions of nonnegligible amounts of noble gases to be in the debris. It facilitates the checking of input to include these elements in the initial core debris composition. Once input has been completed and regurgitated, the current implementation of the VANESA model assumes, without definition of a mechanism, that any Xe or Kr in the melt is instantly expunged and no further attention is directed toward these elements.

Speciation of Cs, Rb, and I in the condensed phase is presumed to be CsI, Cs_2O, RbI, and Rb_2O. The speciation is done on a mass balance basis. It is assumed, as is typically the case, that the sum of the molar amounts of Cs and Rb exceeds the molar amount of I in the debris.

Not all of the elements accepted as input are treated explicitly in the calculations done by the current implementation of the VANESA model. A much shorter list of elements was devised for the source term reassessment calculations. As the source term reassessment progressed, reviewers and sponsors of the work requested that more elements be treated explicitly. Unfortunately, the pace of the reassessment work was such that assembling needed data and making code

changes to treat additional elements was not possible. Throughout the code suite used for the reassessment work, approximate methods were devised to examine the release and behavior of the additional elements. The approximation made in the CORSOR model of release during core degradation was to assume that release rate coefficients for the additional elements were identical to coefficients for one of the elements that was explicitly treated. The approximation made in the current implementation of the VANESA model is called "release grouping."

Release grouping amounts to associating elements whose release chemistries are sufficiently similar that they can be treated as identical. Then, the release of all members of the group is derived from the explicit treatment of one member of the group. To understand grouping further, consider N(G) elements whose chemistries are similar. Assume that there are M(i) for i = 1 to N(G) moles of the i^{th} member of the group in the melt. Let K be the subscript designating the representative member of the group. A vaporization reaction for the k^{th} member of the group might be

$$[M_k(c)] \rightarrow M_k(g) \quad .$$

The rate of vaporization of the k^{th} member of the group by this process is then

$$\frac{dM(k)}{dt} = -A\ K(k,eff)[P(M_k,eq) - P(M_k,bulk\ gas)]$$

where A = free surface area available for vaporization,

K(k,eff) = effective rate constant,

$P(M_k,eq)$ = equilibrium partial pressure of $M_k(g)$, and

$P(M_k,bulk\ gas)$ = actual partial pressure of $M_k(g)$ in the bulk gas.

There will be no loss of generality in the ensuing discussion if $P(M_k,bulk\ gas)$ is taken to be zero. The equilibrium partial pressure of $M_k(g)$ can be found from:

$$P(M_k,eq) = X(k)\exp[-\Delta G(k)/RT]$$

where $\Delta G(k)$ is the standard-state free-energy change associated with the vaporization reaction and $X(k)$ is the mole fraction of the k^{th} species in the melt.

The molar rate of vaporization of all members of the group by the particular reaction is similarly given by:

$$\frac{dM(G)}{dt} = \frac{d\left[\sum_{i=1}^{N(G)} M(i)\right]}{dt} = -A \sum_{i=1}^{N(G)} K(i,eff)X(i)\exp\left[\frac{-\Delta G(i)}{RT}\right] .$$

Now assume that the chemistries (not the release) of the elements in the group are the same as the chemistry of the k^{th} member of the group. Then

$$\frac{dM(G)}{dt} = -A\, K(k,eff)\exp\left[\frac{-\Delta Gk(k)}{RT}\right] \frac{\sum_{i=1}^{N(G)} M(i)}{M_T}$$

where $M(G)$ = sum of molar amounts of member of the group in the melt = $\sum_{i=1}^{N(G)} M(i)$ and

M_T = total number of moles of all constituents in the melt.

Thus, the molar release of the group is approximated by explicitly calculating the release of the k^{th} member of the group assuming the melt content of the k^{th} member to be $M(G)$ rather than $M(k)$. This approximation is subject to the constraints that the condensed phase be ideal and that the molecularity of the vapor species and the condensed species is the same. When grouping is done, the molar composition of the released material is the same as the molar make up of the group at the onset of vaporization.

The grouping of elements was first introduced to the reactor safety community by the Reactor Safety Study[1] and has been used frequently since then. The chemical basis for groupings and the feasibility of grouping has been discussed by Powers.[259] In some cases, grouping is readily justified. For instance, it is difficult to imagine that grouping the release behavior of cesium and rubidium would introduce significant error. In other cases, the justification must be based on appeals to expediency or cost control.

The groupings of elements considered in the current implementation of the VANESA model are:

1. Cesium group: Cesium and rubidium are the members of this group and the release of cesium is taken as representative of the group behavior.

2. Ruthenium group: The members of the group are Ru, Tc, Rh, and Pd. Ruthenium is taken as the representative element.

3. Cerium group: Cerium, neptunium, and plutonium are the group members. Cerium is the representative element.

4. Lanthanum group: Lanthanum, yttrium, samarium, neodymium, and praseodymium constitute this group. When ad hoc addition of gadolinium, europium, and promethium are done, these elements are also members of the group. Lanthanum is the representative member of the group.

The grouping of technetium with ruthenium has been criticized by Powers.[9] There does not appear to be a satisfactory grouping for technetium. An alternative would be to group it with manganese. Grouping with manganese will result in a higher and perhaps unrealistic release of technetium. As is always the case when grouping is done, it would be preferable to treat the element explicitly.

Grouping of cerium, plutonium, and neptunium is discussed in an appendix to this document.

The errors attendant with grouping the trivalent rare-earths can be estimated by examining the vaporization rates for the pure oxides. The vaporization rates[181] for several of these oxides relative to that of lanthanum are shown in Table 38 for temperatures of 2000 and 2500 K. Clearly, the vaporization rates are not identical as is assumed when grouping is done. The errors caused by grouping are appreciable, however, only for europium and yttrium. Grouping results in overprediction of yttrium release and underprediction of europium release.

The most important boundary condition information for the calculations with the current implementation of the VANESA model are obtained from the models of core debris interactions with concrete. The calculations have been done typically using information derived from results of calculations by the CORCON code.[5,6] Some calculations have been done with results of calculations with the INTER subroutine of MARCH[3,57] and with IDCOR's DECOMP model.[43] Experimental data have also been used as input to the code.

The inputs concerning the nature of core debris interactions with concrete are:

1. Core debris temperatures,

2. Gas generation rates,

3. Concrete ablation rates, and

4. Debris pool diameter.

The need for core debris temperatures is obvious. What is used by the model is the bulk phase (oxide or metal) temperature. When the CORCON code predicts there to be both dense and light oxide phases present, the dense oxide phase temperature is used by the current implementation of the VANESA model.

The gas generation data accepted by the code are the amounts of the gases emerging from the core debris including any gas hypothesized in the model of the core debris/concrete interactions to "by-pass" the melt. These gases--CO, CO_2, H_2, and H_2O--are converted to CO_2 and H_2O liberated from the concrete. That is, CO and H_2 emerging from the core melt are added on a molar basis to CO_2 and H_2O, respectively, emerging from the melt. The code then recomputes the composition of the gases that develops as a result of the reaction with the core debris. If melt "coking" is hypothesized to occur in the model of core debris/concrete interactions, any CO_2 liberated from the concrete and converted to carbon by reactions with the core debris does not appear in the input data to the VANESA code. On the other hand, carbon oxidized to CO during decarburization does appear in the input and is considered in the analysis of release.

Concrete ablated by the action of a high temperature melt is incorporated into the oxide phase of the melt. It is the condensed products of concrete ablation that are added to the melt. An essential input to the code is then the composition of these condensed products of concrete decomposition rather than the composition of the concrete itself. Compositions are specified in terms of the weight fractions of CaO, SiO_2, Al_2O_3, Na_2O, K_2O, and FeO.*

*Concrete also contains reinforcing steel. The current implementation of the model assumes 0.149 grams of iron is added to the metallic melt phase per gram of ablated concrete.

Three concretes have been used typically in severe reactor accident analyses. These concretes have been characterized in terms appropriate for the analysis of melt interactions with concrete.[17] They are the default concretes used in the CORCON code.[5,6] The compositions for these concretes accepted by the current implementation of the VANESA model are shown in Table 57.

All concretes contain at least some silica. If nothing else, there is silica in the cement binder. Consequently, the inventory of silica in the core debris as reported by the melt/concrete interaction model is used to determine the amount of concrete that has been incorporated into the melt. The amounts of incorporated concrete are then converted in the CVRMSI routine into rates of concrete addition to the melt.

The debris pool radius is used together with the melt volume to compute pool depths and, consequently, the times available for vaporization into rising bubbles. The pool is considered to be a cylinder having the radius given by the maxiumum pool radius for the depth calculations. This gives, of course, a lower bound on the true depth of the melt.

E. Format of the Input

The current implementation of the VANESA model is being supplied as an appendage to the CORCON mod2 code.[6] The CORCON code prepares the input data concerning the nature of the core debris interactions with concrete. The balance of the needed input data are described in Table 58.

Card group 1 consists of timing information. The first input variable, ST1, controls the frequency of printed output. This is also the time step between updates to the boundary condition information (debris temperatures, gas generation rates, debris geometry, and concrete ablation rates) used in the VANESA calculations. The next time increment, ST2, is a time step used within the VANESA model to update the chemical conditions that affect release. This time step must always be less than ST1. The code will stop if ST2 is greater than ST1. A recommended value for ST2 is 1/20 of ST1. If ST2 is larger than ST1/20, a warning will be printed, but computations will proceed.

Card group 2 consists of the weight fraction of SiO_2 in the concrete. This variable, FRACS, is used to convert silica concentrations in the debris reported from CORCON into amounts of concrete incorporated in the core debris.

Card group 3 is the specification of the melt composition. The input data are to be in kilograms of mass. The input order is shown in Table 58.

Table 57

Composition of the Condensed
Products of Concrete Ablation

Constituent	Weight Percent in Melted		
	Basaltic Concrete	Limestone/ Common Sand Concrete	Limestone Concrete
CaO	16.40	42.99	87.52
Al_2O_3	9.08	4.87	2.95
SiO_2	59.84	48.43	6.17
Na_2O	1.97	0.11	0.14
K_2O	5.88	1.65	1.17
FeO	6.83	1.95	2.05

Table 58

Input Instructions for the Code

Card Group Number	Field	Format	Variable Name	Description
1	1-10	F10.1	ST1	Time increment in seconds given in CORCON input
	11-20	F10.1	ST2	Computing time increment; recommended value is less than ST1/20
2	1-10	F10.1	FRACS	Weight fraction silicon dioxide in molten concrete
3	1-80	F10.1	CES, IOD, XEN, KRY TE, BA, SN, RU	Mass in (Kg) of melt constituents
	1-80	F10.1	UO2, ZR, ZRO2 FE, FEO, MO, SR SB, Y, TC, RH, PD LA, CE, PR, ND	
	1-80	F10.1	SM, PU, CR, MN, NI AG, SB, NB	
4	1-80	A		Comment card
5	1-10	F10.1	WF(1)	Weight fraction CaO in molten concrete
	11-20	F10.1	WF(2)	Weight fraction Al_2O_3 in molten concrete
	21-30	F10.1	WF(3)	Weight fraction Na_2O in molten concrete
	31-40	F10.1	WF(4)	Weight fraction K_2O in molten concrete
	41-50	F10.1	WF(5)	Weight fraction SiO_2 in molten concrete
	51-60	F10.1	WF(6)	Weight fraction FeO in molten concrete
6	1-80	A	---	Comment card

Table 58 (continued)

Card Group Number	Field	Format	Variable Name	Description
7	1-80	8F10.1	DEPTH(i) for i=1 to N*	Depth of the water pool overlying the molten core debris; N* = no. of result printouts sought
8	1-80	A	---	Comment card
9	1-80	8F10.1	PRESS(i) for i=1 to N*	Ambient pressure over the water pool
10	1-80	A	---	Comment card
11	1-80	8F10.1	TEMP(i) for i=1 to N*	Temperature of the water pool
12	1-80	A	---	Comment card
13	1-10	I10	NOSC	Number of size segments used to describe the aerosol size distribution. Default = 20.
	11-20	F10.1	GSD	Geometric standard deviation of the size distribution of aerosols entering the water pool. Default = 2.3.
	21-30	I10	IDMF	Switch that allows the diffusion mechanism for aerosol entrapment by a water pool to be turned off. Default value is 1 which activates on the diffusion mechanism.
	31-40	I10	IMPF	Switch that allows the impaction mechanism for aerosol entrapment by a water pool to be deactivated. Default value is 1 which activates the impaction mechanism.
	41-50	F10.1	BSIZI	Diameter of gas bubbles at the base of the water pool (cm). Default value = 1 cm.
	51-60	F10.1	VROVR	V(rel)/V(rise), the ratio of the gas velocity within the bubble to the rise velocity of the bubble. Default value = 1.

Card group 4 is a comment card usually used to describe the input being provided in card group 5.

Card group 5 is the specification of the composition of ablated concrete. The information is provided as the weight fractions of the species indicated in Table 58. Note that the silica content of the melted concrete has to be the same as is specified in card group 2.

The remainder of the input information relates to calculating the effects of an overlying water pool. Card group 6 is a comment card. Card group 7 specifies the water pool depth. The depths are specified for each time printed output is obtained from the VANESA routine. If no water pool is present, specify a zero depth. The pool routine will then do no calculations for this time step.

Card group 7 may be omitted if the user chooses to bypass calculations of the aerosol scrubbing by an overlying water pool.

Card 8 is a comment card. Card group 9 specifies the ambient atmospheric pressure over the water pool. The pressure is supplied in atmospheres for each time printed output is to be obtained from the VANESA routine.

Card 10 is a comment card usually used to label data provided in card group 11. Card group 11 specifies the temperature of the water pool. Again, water pool temperatures are specified at each time printed output is obtained from the VANESA routine. There are no constraints on the water pool temperatures that are received by the code. But, the POOL routine is written assuming the pool to be saturated. There is then an interplay between ambient pressure and the water pool temperature that should be recognized by the code user.

Card 12 is a comment card usually used to label the operational parameters for calculations with the POOL routine. These operational parameters are specified on card group 13. Entering -1 (or -1.0) for any one of the parameters on card 13 will result in a default value for that parameter being used in the calculations.

The first operational parameter, NOSC, is the number of size segments to be used to describe the aerosol size distribution. The default value for NOSC is 20 and NOSC must be greater than 3 and less than 51. Calculations have been done with NOSC as large as 50 and as small as 7. Since size segmentation is done in the code so that each size segment contains the same fraction of the aerosol mass, the overall decontamination factor is not especially sensitive to NOSC.

The accuracy with which the extremes of the aerosol size distribution is treated is sensitive to NOSC.

The next operational parameter, GSD, is the geometric standard deviation of the lognormal size distribution for aerosols emerging from the debris mass. The default value is 2.3. This default value was selected based on data obtained in experiments that did not involve an overlying water pool. It is possible that the size distribution of aerosols emerging from core debris in the presence of a water pool could be significantly narrower. It is unlikely, however, that the geometric standard deviation would be less than 1.4. Of course, a value less than 1 is physically meaningless. A value of exactly 1 (monodisperse aerosol) will cause an overflow error in the POOL subroutine.

The next two operational parameters specify the physical mechanisms that result in decontamination of aerosol-laden gases passing through an overlying water pool. The first of these parameters, IDMF, controls the mechanism of particle diffusion to the bubble walls. The default condition for this parameter is to have the diffusion mechanism operational. It is possible that a user may want to see what effects might arise if Stephan forces on aerosol particles prevent the particles from reaching the bubble walls. Entering zero for IDMF will eliminate diffusion as a mechanism for aerosol entrapment by an overlying water pool.

The second physical parameter, IMPF, controls impaction as a mechanism of aerosol entrapment by a water pool. The default status of IMPF is to have impaction included as a mechanism. There is, however, controversy over whether gases within bubbles rising through an overlying water pool circulate. Contamination of the bubble surfaces might inhibit such circulation of gases and eliminate impaction as a decontamination mechanism. To assess the effects of not having impaction as an aerosol trapping mechanism, IMPF should be set to zero. Impaction is such a potent mechanism of aerosol entrapment that additional control of this mechanism is permitted by means of the parameter VROVR discussed below.

The next operational parameter is the size of the gas bubble rising through the overlying water pool. A default value of 1 cm is used for BSIZ1. Any other size can be put in for BSIZ1. Bubbles larger than about 5 cm are probably unstable and will shatter during rise through the pool though the current implementation of the VANESA model does not consider this possibility. Bubbles initially smaller than about 0.5 cm have not been observed in experiments.

The final operational parameter, VROVR, provides additional control over the impaction mechanism of decontamination. VROVR is the ratio of gas velocities within the rising

bubble to the rise velocity of the bubble. The default value for VROVR is 1. For spherical bubbles with uncontaminated surfaces rising sufficiently fast that potential flow theory is applicable, the theoretical value of VROVR is 1.5. Any contamination of the bubble surfaces will reduce VROVR. As bubbles distort from spherical, impaction becomes a more efficient mechanism of aerosol entrapment--if gases circulate within the bubble. Improvements in the efficiency of impaction can be taken into account in an effective manner by putting in values of VROVR greater than 1.5

F. Output

The first outputs of the code are regurgitations of the input. (See sample problem Section H). The input provided by the CORCON code is printed first. This output consists of the problem name, the listing of the time (in seconds) after the start of melt interactions with concrete, the temperatures of the metal phase (TMETAL) and the oxide phase (TOXIDE) in Kelvin, the maximum core debris pool radius in meters, and the amount of silica (in kg) in the oxide phase of the core debris.

The next regurgitation of CORCON-prepared input consists of, again, the problem name and a listing of the cumulative masses (in kg) of CO, CO_2, H_2, and H_2O that have emerged from the debris pool after indicated times (in seconds) following the start of core debris interactions with concrete.

The inputs provided the code as described in Section E above are then printed.

In some of the available versions of the VANESA code, there is then printed a variety of code inputs and the results of the manipulations. These are vestiges of the time the code was used in a stand-alone fashion. These printouts have been eliminated in more recent releases of the code and are discussed no further here.

The next set of outputs begins with a restatement of the problem name. Then, the data used for the calculations are listed. The listing begins with a mean value of the condensed phase diffusion coefficient (cm^2/s) for constituents in the melt. The diameter of bubbles (cm) rising through the melt is listed. The next two lines describe the approximate treatment of mechanical aerosol generation. The first of these lines states the number of aerosol particles thrown off by a bursting bubble. It is assumed that all of these particles are entrained in the gas flow from the core debris. The next line states the assumed diameter of the mechanically generated aerosol particles in micrometers.

Users wanting to change any of the prescribed values cited in the previous paragraph will find the appropriate lines of code labelled in the DRIVER routine.

The composition of melted concrete is listed. Entries in the table are weight fractions of the indicated constituent.

The initial composition of the core debris and the assumed chemical forms of the core debris constituents are listed next. Compositions are specified in terms of the kilograms of the constituent present in the debris.

Finally, under the heading "STEP DATA," the assembled boundary condition information used in the analyses are listed. For each time (seconds after the start of melt attack on concrete), the following information is reproduced:

Label	Meaning
VGASR	Volume of gas (cm^3 at 1 atmosphere pressure and 298 K) passing through the melt per second.
H_2OM	Moles of steam passing into the melt per second.
CO_2M	Moles of carbon dioxide passing into the melt per second.
TEMP	Temperature of the oxide phase of the core debris (K).
ADDRT	Rate of concrete addition to the core debris (kg/s)
AREA	Effective horizontal floor area covered by melt (m^2).

The next section of output consists of results from the VANESA routine. This output is repeated for each time step (ST1). A typical example of this output is shown in Figure 67. The output reproduced in this figure is annotated with line numbers that are used to organize the discussion below:

Line	Description
1	"T" is the time (in seconds) after the start of melt attack on concrete. "T(K)" is the temperature of the oxide phase of the core debris in Kelvin.

```
T=       0.0      T(K)=    2125.0                                          Line 1
      VAPOR= 7.58543E-06                                                   Line 2
      BURST= 1.64388E-08                                                   Line 3
      AEROSOL(G/CC)-AMBIENT CONDITIONS= 7.60187E-06                        Line 4
      AEROSOL(G/CC)-STANDARD STATE CONDITIONS= 5.42080E-05                 Line 5
GAS(G-MOLES/S)= 1.16343E+00                                                Line 6
G/S= 1.54224E+00                                                           Line 7
AEROSOL RHO=    5.3639                                                     Line 8
    AEROSOL C
SIZE= 5.74447E-01
        2       4.21120E+01   %                                            Line 9
        3       7.51105E-13   %                                            Line 10
        4       1.72707E-01   %                                            Line 11
        5       2.19819E-08   %                                            Line 12
        6       1.88530E-07   %                                            Line 13
        7       4.94049E-01   %                                            Line 14
        8       0.00000E+00   %                                            Line 15
        9       9.33255E-01   %                                            Line 16
       10       0.00000E+00   %                                            Line 17
       11       1.51235E+01   %                                            Line 18
       12       0.00000E+00   %                                            Line 19
       13       0.00000E+00   %                                            Line 20
                                                                           Line 21

       14       0.00000E+00   %                                            Line 22
       15       0.00000E+00   %                                            Line 23
       16       0.00000E+00   %                                            Line 24
       17       3.22000E-01   %                                            Line 25
       18       3.81770E-02   %                                            Line 26
       19       1.64799E+01   %                                            Line 27
       20       8.99959E+00   %                                            Line 28
       21       7.47206E+00   %                                            Line 29
       22       1.76497E-01   %                                            Line 30
       23       5.35225E-01   %                                            Line 31
       24       7.00889E+00   %                                            Line 32
       25       1.32195E-01   %                                            Line 33
   GAS C

        1   1.37782E-03   %      G/S= 2.88786E-04                          Line 34
        2   9.83477E+01   %      G/S= 2.30661E+00                          Line 35
        3   3.61057E-01   %      G/S= 4.23425E-03                          Line 36
        4   4.13368E-15   %      G/S= 8.17930E-16                          Line 37
        5   1.18567E-08   %      G/S= 2.20629E-09                          Line 38
        6   9.73390E-15   %      G/S= 3.62378E-15                          Line 39
        7   3.76027E-06   %      G/S= 1.92535E-06                          Line 40
        8   1.28986E+00   %      G/S= 4.20342E-01                          Line 41
```

Figure 67. Annotated Output From the VANESA Subroutine

```
MELT C

  2          7.01631E+04  KG                                  Line 42
  3          1.11000E+04  KG                                  Line 43
  4          6.16400E+03  KG                                  Line 44
  5          2.09100E+02  KG                                  Line 45
  6          3.42198E+02  KG                                  Line 46
  7          5.57000E+02  KG                                  Line 47
  8          0.00000E+00  KG                                  Line 48
  9          2.79891E+01  KG                                  Line 49
 10          0.00000E+00  KG                                  Line 50
 11          1.23332E+03  KG                                  Line 51
 12          1.06953E+01  KG                                  Line 52
 13          3.60502E-01  KG                                  Line 53
 14          1.71086E-02  KG                                  Line 54
 15          1.42979E-01  KG                                  Line 55
 16          7.54000E-01  KG                                  Line 56
 17          1.59391E+05  KG                                  Line 57
 18          3.29943E+04  KG                                  Line 58
 19          3.30079E-01  KG                                  Line 59
 20          9.67918E+01  KG                                  Line 60
 21          6.90569E+01  KG                                  Line 61
 22          9.63384E+02  KG                                  Line 62
 23          8.17575E+02  KG                                  Line 63
 24          6.14479E+00  KG                                  Line 64
 25          4.08236E-02  KG                                  Line 65
202          8.25202E+02  KG                                  Line 66
302          1.97964E-06  KG                                  Line 67
```

Figure 67. Annotated Output From the VANESA Subroutine (Continued)

Line	Description
2	"VAPOR" is the aerosol mass per cubic centimeter of gas at the ambient pressure and the oxide phase temperature that was created by vaporization.
3	"BURST" is the aerosol mass per cubic centimeter of gas at the ambient pressure and the oxide phase temperature that was created by mechanical processes.
4	"AEROSOL (G/CC) AMBIENT CONDITIONS" is the total aerosol mass per cubic centimeter of gas at the ambient pressure and the oxide phase temperature.
5	"AEROSOL (G/CC) STANDARD STATE CONDITIONS" is the total aerosol mass per cubic centimeter of gas at 1 atmosphere pressure and 298 K.
6	"GAS (G-MOLES/S)" is the gas flow through the core debris in gram-moles per second.
7	"G/S" is the total grams of aerosol evolved from the core debris per second.
8	"AEROSOL RHO" is the overall material density of the aerosolized material in grams/cm^3.
9	"SIZE" is the mean aerosol particle size in micrometers.

The aerosol composition is given in lines 10-33. Compositions are given in terms of the weight percents of the assumed constituents. These constituents are chosen to be those conventionally used by assayers to report the bulk chemical composition of a material. In no sense should the indications of the melt constituents be taken as a prediction of the chemical form of constituents of the aerosol. The current implementation of the VANESA model does not attempt to predict the chemical form of the aerosol.

The compositions listed for the aerosol do not necessarily add to 100 percent. This is because the composition is reported in terms of assayer's constituents. If, for instance, manganese is vaporized as MnO(g) and condenses as MnO(s), it is reported as Mn(s). Thus, the contribution of oxygen to the mass is not considered in the assay report.

The labeling of the aerosol assay report is as follows:

Line	Meaning
10	"2" = weight % FeO
11	"3" = weight % Cr_2O_3
12	"4" = weight % Ni
13	"5" = weight % Mo
14	"6" = weight % Ru
15	"7" = weight % Sn
16	"8" = weight % Sb
17	"9" = weight % Te
18	"10" = weight % Ag
19	"11" = weight % Mn
20	"12" = weight % CaO
21	"13" = weight % Al_2O_3
22	"14" = weight % Na_2O
23	"15" = weight % K_2O
24	"16" = weight % SiO_2
25	"17" = weight % UO_2
26	"18" = weight % ZrO_2
27	"19" = weight % Cs_2O
28	"20" = weight % BaO
29	"21" = weight % SrO
30	"22" = weight % La_2O_3
31	"23" = weight % CeO_2
32	"24" = weight % NbO
33	"25" = weight % CsI

The next set of output from the code is the composition of the gases liberated during attack on concrete. (This section is titled "GAS C.") The compositions in mole percent (or equivalently volume percent) and the gas generation rate in grams per second are listed. The labeling of this output is as follows:

Line	Meaning
34	"1" = volume % H_2O
35	"2" = volume % H_2
36	"3" = volume % H
37	"4" = volume % OH
38	"5" = volume % O
39	"6" = volume % O_2
40	"7" = volume % CO_2
41	"8" = volume % CO

The composition of the melt is given under the heading "MELT C." The entries are in kilograms. The labeling is as follows:

Line	Meaning
42	"2" = kilograms Fe
43	"3" = kilograms Cr
44	"4" = kilograms Ni
45	"5" = kilograms Mo
46	"6" = kilograms Ru
47	"7" = kilograms Sn
48	"8" = kilograms Sb
49	"9" = kilograms Te
50	"10" = kilograms Ag
51	"11" = kilograms Mn
52	"12" = kilograms CaO
53	"13" = kilograms Al_2O_3
54	"14" = kilograms Na_2O
55	"15" = kilograms K_2O
56	"16" = kilograms SiO_2
57	"17" = kilograms UO_2
58	"18" = kilograms ZrO_2
59	"19" = kilograms Cs_2O
60	"20" = kilograms BaO
61	"21" = kilograms SrO
62	"22" = kilograms La_2O_3
63	"23" = kilograms CeO_2
64	"24" = kilograms NbO
65	"25" = kilograms CsI
66	"202" = kilograms FeO
67	"302" = kilograms Cr_2O_3

Some versions of the code include an output labeled "LOSS." This is a listing of the moles lost from the melt over the time step. The labeling is the same as for the melt composition.

Once the output from the VANESA routine has been completed, the output from the POOL routine is printed. This output is more thoroughly labeled than that from the VANESA routine. Only some clarifications of the output are provided here.

Input used by the POOL model is reproduced at the beginning of this section of the output. The selections concerning operational parameters are listed first. Then, boundary condition information concerning the water pool depth, the water temperature, and the ambient atmospheric pressure is printed next. Finally, the input data concerning the aerosols prepared by the VANESA subroutine is listed. The labels on this final listing are:

Label	Meaning
"Mean Size (UM)"	Mean aerosol particle size in micrometers.
"MASS/S (G/S)"	Rate of aerosol mass production in grams per second.
"PART. DENSITY (G/CC)"	Aerosol particle material density in grams per cubic centimeter.

This listing is concluded with an indication of the assumed geometric standard deviation of the aerosol particle size distribution.

The results of the calculations with the POOL routine are then listed for each time step. The labels on the listing of results are as follows:

Label	Meaning
"SIZE RANGE"	Interval in micrometers for a segment of the size distribution chosen to have initially a fraction of the mass equal to 1/NOSC.
"CHARACTERISTIC SIZE"	The particle size in micrometers chosen so that half the mass in the indicated size range has smaller sizes. This is the particle size used to represent the size segment.
"MASS IN RANGE"	This amount of mass left in the size range in the aerosol that emerges from the water pool.
"DECONTAMINATION FACTOR"	Mass in the size range that enters the pool divided by the mass within the size range that emerges from the water pool.

At the end of this listing, the overall decontamination factor is listed. This overall decontamination factor is the total mass entering the water pool divided by the total mass emerging from the water pool. The mass emerging is also listed under the label "MASS OUT." The units on the emerging mass are grams per second.

The final printed result is the fit of the emerging particle size distribution to a lognormal distribution. The mean and the geometric standard deviation found by the least-squares fitting procedure are printed. Uncertainty ranges for the mean aerosol particle size and the geometric standard deviation of the particle size distribution are printed. These uncertainty ranges are found by incrementing and reducing the log of the distribution by one standard deviation as derived from a least squares fit of the results from calculations done in the POOL subroutine.

A linear correlation coefficient for the fit is also printed. The probability that a completely random data set would yield such a high value of the linear correlation coefficient can be found from appropriate probability tables using NOSC-2 degrees of freedom.

G. Program Listing and Sample Problem

A listing of the code and a sample problem are provided in the microfiche attachment to this report.

H. Operational Experience

The most important use of the current implementation of the VANESA model has been in connection with the source term reassessment work sponsored by the U.S. Nuclear Regulatory Commission. Results obtained with the model are reported in reference 2.

There have been several sensitivity studies of the model. Results obtained in these sensitivity studies are reported in references 351-353. It is found usually that results obtained with the model are strongly dependent on:

(1) input obtained from the models of the in-vessel phase of the accident,

(2) the boundary conditions specified by the input concerning the nature of the melt interactions with concrete, and

(3) whether or not a water pool overlies the melt while it attacks the concrete.

Of the inputs obtained from models of the in-vessel phase of an accident, perhaps the most important is the amount of zirconium clad that has not oxidized by the time melt comes into contact with concrete. The treatment of this metallic zirconium by models of the melt/concrete interactions will affect significantly the results obtained with the current implementation of the VANESA model.

Users of the model are urged to examine the sensitivity studies of the model. These sensitivity studies will assist the analysis and interpretation of results obtained with the model.

I. Ongoing Development

The current implementation of the VANESA model is an abbreviated, fast-running description of aerosol production and radionuclide release during core debris interactions with concrete. It is most applicable to risk assessment analyses of reactor accidents. Its predictions are being compared to experimental results.[354] It is being incorporated into systems level codes such as CONTAIN and MELCOR.

Further developments of the VANESA model are following two paths. One of these paths is the full integration of the model into the CORCON model of melt interactions with concrete. This integration will assure there is consistancy in the treatment of the melt interactions and the release of radionuclides. In particular the effects of release on decay heat will be considered. The other development pathway is the preparation of a more detailed version of the model that provides an in-depth treatment of the many facets of aerosol production and radionuclide release described in Chapters III - VI in this document. It is anticipated that this refined version of the model will be of most use for the analyses of experimental examinations of radionuclide release and aerosol production.

REFERENCES

1. USNRC, Reactor Safety Study - An Assessment of Accident Risks in U.S. Commercial Nuclear Power Plants, WASH-1400, NUREG-75/04, October 1975.

2. J. A. Gieseke et al., Radionuclide Release Under Specific LWR Accident Conditions, Volumes II-VII, Battelle Columbus Laboratory, Columbus, OH, BMI-2104 (draft), July 1984.

3. MARCH 2 Manual, Draft number 2, unpublished manual, Battelle Columbus Laboratory, Columbus, OH. See also: R. O. Wooton and H. I. Avci, MARCH 1.1 (Meltdown Accident Response Characteristics) Code Description and User's Manual, Battelle Columbus Laboratory, Columbus, OH, NUREG/CR-1711, October 1980.

4. M. R. Kuhlman, D. J. Lehmicke, and R. O. Meyer, CORSOR User's Manual, Battelle Columbus Laboratory, Columbus, OH, NUREG/CR-4173, BMI-2122, March 1985.

5. J. F. Muir et al., CORCON-MOD1: An Improved Model for Molten-Core/Concrete Interactions, Sandia National Laboratories, Albuquerque, NM, NUREG/CR-2142, SAND80-2415, July 1981.

6. R. K. Cole, Jr., D. P. Kelly, and M. A. Ellis, CORCON-Mod2: A Computer Program for Analysis of Molten Core Concrete Interactions, Sandia National Laboratories, Albuquerque, NM, NUREG/CR-3920, SAND84-1246, August 1984.

7. H. Bunz, M. Koyro, and W. Schock, NAUA Mod 4. A Code for Calculating Aerosol Behavior in LWR Core Melt Accidents. Code Description and User's Manual, Kernforschungszentrum Karlsruhe, Karlsruhe, West Germany, KfK-3554.

8. P. C. Owczarski, A. K. Postma, and R. L. Schrek, Technical Bases and User's Manual for SPARC - A Suppression Pool Aerosol Removal Code, NUREG/CR-3317, PNL-4742, 1983.

9. R. J. Lipinski et al., Uncertainty in Radionuclide Release Under Specific LWR Accident Conditions Volumes I-IV, Sandia National Laboratories, Albuquerque, NM, SAND84-0410.

10. K. D. Bergeron et al., User's Manual for CONTAIN 1.0, A Computer Code for Severe Nuclear Reactor Accident Containment Analysis, Sandia National Laboratories, Albuquerque, NM, NUREG/CR-4085, SAND84-1204, May 1985.

11. D. A. Powers, "Aerosol Generation During Core Debris/Concrete Interactions," 7th Int'l LWR Safety Research Information Exchange Meeting, Gaithersburg, MD, 1978.

12. D. A. Powers in Light Water Reactor Safety Research Program Quarterly Report Jan-March, 1978, Sandia National Laboratories, Albuquerque, NM, NUREG/CR-0324, SAND78-1511, October 1978.

13. W. B. Murfin and D. A. Powers, "Interaction of the Melt With Concrete and MgO" Chapter 5 in Report of the Zion/Indian Point Study, Volume I, Sandia National Laboratories, Albuquerque, NM, NUREG/CR-1410, SAND80-0617/1, August 1980.

14. J. E. Brockmann, "Aerosol Source Term for Ex-Vessel Core Debris/Concrete Interaction," May 5, 1982, Memorandum, Sandia National Laboratories, Albuquerque, NM.

15. Staff Reports to the President's Commission on the Accident at Three Mile Island, Vol. IV, 1979.

16. U.S. Nuclear Regulatory Commission, Technical Bases for Estimating Fission Product Behavior During LWR Accidents, NUREG-0772, June 1981.

17. D. A. Powers and F. E. Arellano, Large-Scale Transient Tests of the Interaction of Molten Steel With Concrete, Sandia National Laboratories, Albuquerque, NM, NUREG/CR-2282, SAND81-1753, January 1982.

18. D. A. Powers and F. E. Arellano, Direct Observation of Melt Behavior During High Temperature Melt/Concrete Interactions, Sandia National Laboratories, Albuquerque, NM, NUREG/CR-2283, SAND81-1754, January 1982.

19. BOF Steelmaking, R. D. Pehlke, ed., Process Technology Division Iron and Steel Society of the American Institute of Mining, Metallurgical and Petroleum Engineers, 1975.

20. A. F. Ellis and J. Grover, J. Iron and Steel Institute 209, p. 593 (1971).

21. J. P. Morris, J. P. Riott, E. G. Illig, and R. H. Jefferson, The Cause of Fuming in Oxygen Steelmaking, report of investigations 7047, U.S. Bureau of Mines, 1976.

22. M. G. Krasheninnikov, S. I. Filippov, and A. N. Borodin, Steel in the USSR, p. 22 (1979).

23. V. Berner and A. Berner, Annual Conf. GAeF, p. 191.

24. D. C. Blanchard, Prog. in Oceanography 1, M. Sears, editor (The MacMillian Company, 1963).

25. J. Fischer, J. D. Schilb, and M. G. Chasanov, J. Nucl. Materials 48, p. 233 (1973).

26. H. Alsmeyer, L. Barleon, J. Koster, I. Michael, V. Miller, and M. Reimann, A Model Describing the Interaction of a Core Melt With Concrete, Kernforschungszentrum Karlsruhe, Karlsruhe, West Germany, NUREG/TR-0039, English translation of KfK 2395, September 1978.

27. L. D. Reed, H. Jordan, and J. A. Gieseke, J. Aerosol Science 8, p. 457 (1977).

28. J. Rosinski, D. Werle, and C. T. Nagamoto, J. Colloid Science 17, p. 703 (1962).

29. H. C. Yeh, G. J. Newton, O. G. Raabe, and D. R. Boor, J. Aerosol Science 7, p. 245 (1976).

30. B. R. Fish and R. L. Walker, Aerosol Physics of Radioactive Particles, Oak Ridge National Laboratory, Oak Ridge, TN, ORNL-P-1313, 1965.

31 F. W. Sciacca, K. D. Bergeron, K. K. Murata, and P. E. Rexroth, Testing of the CONTAIN Code, Sandia National Laboratories, Albuquerque, NM, NUREG/CR-3310, SAND83-1149, April 1984.

32. F. Gelbard, MAEROS Users' Manual, Sandia National Laboratories, Albuquerque, NM, NUREG/CR-1391, SAND80-0822, 1982.

33. H. Jordan, P. M. Schumacher, and J. A. Gieseke, QUICK Users' Manual, Battelle Columbus Laboratories, Columbus, OH, NUREG/CR-2105, BMI-2082, May 1981.

34. B. K. Hilliard, J. D. McCormack, and A. K. Postma, Results and Code Predictions for ABCOVE Code Validation, Hanford Engineering Development Laboratory, Richland, WA, HEDL-TME-83-16, November 1983.

35. USNRC, Preliminary Assessment of Core Melt Accidents at the Zion and Indian Point Nuclear Power Plants and Strategies for Mitigating Their Effects, Volume I, Containment Failure Modes, NUREG-0850, November 1981.

36. Commonwealth Edison Co., Zion Probabilistic Safety Study, 1981.

37. Fauske and Associates, Technical Report 14.1A Key Phenomenological Models for Assessing Explosive Steam Generation Rates, Atomic Industrial Forum, 1983.

38. W. W. Tarbell and D. Bradley, "Attack of Fragmented Core Debris on Concrete in the Presence of Water," 10th Water Reactor Safety Research Meeting, Gaithersburg, MD, October 1982.

39. R. E. Blose et al., Advanced Reactor Safety Research Quarterly Report April-June 1982, Vol. 22, Sandia National Laboratories, Albuquerque, NM, SAND82-0904 (2 of 4), October 1983.

40. R. E. Blose et al., SWISS 1 and 2: Sustained Interaction of Molten Stainless Steel and Concrete in the Presence of Water, to be published.

41. N. A. Fuchs, The Mechanics of Aerosols (Pergamon Press, 1964).

42. R. N. Oehlberg, EPRI Journal, pp. 61-62 (June 1984).

43. IDCOR, Technical Report 15.3 Core-Concrete Interactions, Atomic Industrial Forum, Inc., 1983; see also R. E. Henry, "A Model for Core-Concrete Interactions," paper TS 12.10, Proc. Int'l Mtg. on LWR Severe Accident Evaluation, Vol. II, Cambridge, MA, 1983.

44. N. Claussen, G. Petzow, and J. Jahn, "High Melting Metal-Ceramic Eutectics," Plansee Proc. 8th, Vol. II, paper No. 45, ORNL-Translation 2873, 1974.

45. C. Politus, Investigations of the Uranium-Zirconium-Oxygen System, KfK-2167, English translation SAND76-6027, 1976.

46. H. G. Plein et al., Summary of the First Three Incore PAHR Molten Fuel Pool Experiments, Sandia National Laboratories, Albuquerque, NM, SAND79-0081C.

47. J. T. Hitchcock and J. E. Kelley, Post-test Examinations of the In-Pile Molten-Pool Experiments, Sandia National Laboratories, Albuquerque, NM, SAND82-1519C.

48. D. A. McArther, N. K. Hayden, and P. K. Mast, In-Core Fuel Freezing and Plugging Experiments: Preliminary Results of the Sandia TRAN Series 1 Experiments, Sandia National Laboratories, Albuquerque, NM, NUREG/CR-3675, SAND81-1726, August 1984.

49. G. W. Parker, G. E. Creek, and A. L. Sutton, Jr., "Influence of Variable Physical Process Assumptions on Core-Melt Aerosol Release," Proc. Int'l. Mtg. on Thermal Nuclear Reactor Safety, Chicago, IL, 1982.

50. G. A. Greene and T. Ginsberg, "BNL Program in Support of LWR Degraded Core Accident Analysis," Proc. USNRC 9th Water Reactor Safety Research Information Meeting, NUREG/CP-0024, Vol. 3, 1982.

51. G. A. Greene et al., "Heat Transfer Between Immiscible Liquids Enhanced by Gas Bubbling," Proc. of the Int'l. Mtg. on Thermal Reactor Safety, Chicago, IL, 1982.

52. M. Lee and M. S. Kazime, "Interfacial Heat Transfer Between Bubble Agitated Immiscible Liquid Layers," Proc. 6th Information Exchange on Debris Coolability, Los Angeles, CA, November 7-9, 1984.

53. Lamont, Canadian J. Chemical Engineering 36, p. 153 (1958).

54. M. Peehs and K. Hassmann, Paper IAEA-SM-236/26, Thermodynamics of Nuclear Materials 1979, Vol. II International Atomic Energy Agency, 1980.

55. D. A. Powers and F. E. Arellano, Aerosol Production During Transient Corium/Concrete Interactions, Sandia National Laboratories, Albuquerque, NM.

56. D. A. Powers, Stratification of Reactor Core Melts, Sandia National Laboratories, Albuquerque, NM.

57. W. B. Murfin, A Preliminary Model for Core-Concrete Interactions, Sandia National Laboratories, Albuquerque, NM, SAND77-0370, October 1977.

58. J. Gronager et al., TURC1: Large-Scale Metallic Melt/Concrete Experiment and Analysis, Sandia National Laboratories, Albuquerque, NM, SAND85-0707.

59. B. M. Jeffery, J. Nucl. Materials 22, p. 33 (1967).

60. J. I. Bramman et al., J. Nucl. Materials 25, p. 201 (1968).

61. D. A. Powers, Solubility of Gases in Reactor Core Melts, Sandia National Laboratories, Albuquerque, NM, SAND85-XXXX.

62. J. Fischer, J. D. Schilb, and M. G. Chasanov, J. Nucl. Materials 48, p. 233 (1973).

63. F. D. Richardson, Physical Chemistry of Melts in Metallurgy (Academic Press, 1974).

64. M. Veeraburns and W. O. Philbrook, "Observations on Liquid-Liquid Mass Transfer With Bubble Stirring" in Physical Chemistry of Process Metallurgy Part 1, G. R. St. Pierre, ed. (Interscience Publishers, 1959).

65. J. Szekely and N. J. Themelis, Rate Phenomena in Process Metallurgy (Wiley-Interscience, 1971).

66. C. R. Wilke, Chem. Eng. Prog. 45, p. 218 (1949).

67. D. A. Powers and A. W. Frazier, VISRHO: A Computer Subroutine for Estimating the Viscosity and Density of Complex Silicate Melts, Sandia National Laboratories, Albuquerque, NM, SAND76-0649, June 1977.

68. D. A. Powers, D. A. Dahlgren, J. F. Muir, and W. B. Murfin, Exploratory Study of Molten Core Material/Concrete Interactions July 1975-March 1977, Sandia National Laboratories, Albuquerque, NM, SAND77-2042, February 1978.

69. S. E. Ziemniak, "A Study of Interfacial Resistance to Mass Transfer at High Evaporation Rates," Doctoral Thesis, Rensselaer Polytechnic Institute, 1968.

70. S. Zwick, J. Appl. Phys. 31, p. 1735 (1960).

71. R. Kucherov and L. Rikenglaz, Doklady Akad. Nauk SSR 133, p. 1130 (1960).

72. J. P. Hirth and G. M. Pound, Condensation and Evaporization - Nucleation and Growth Kinetics (Pergamon Press, 1963).

73. N. D. Obradovic and G. H. J. Bennett, J. Inst. of Metals 97, p. 186 (1969).

74. W. A. Fischer, D. Janke, and K. Stahlschmidt, Arch. Eisenhüttenwes 45, p. 509 (1974).

75. F. D. Richardson, Physical Chemistry of Melts in Metallurgy, Vol. 2 (Academic Press, 1974).

76. E. M. Mortensen and H. Eyring, J. Phys. Chem. 64, p. 847 (1960).

77. M. Baranaev, J. Phys. Chem. USSR 13, p. 1635 (1939).

78. W. Göring, Z. Electrochem 63, p. 1069 (1959).

79. Smithells Metals Reference Book, E. A. Brandes, ed., 6th edition (Butterworths, 1983).

80. P. Hofmann, D. Kerwin-Peck, and P. Nikolopoulos, Physical and Chemical Phenomena Associated With the Dissolution of Solid UO2 by Molten Zircaloy, Kernforschungszentrum Karlsruhe GmbH, Karlsruhe, West Germany, PNS-No. 675/82, May 1982.

81. H. Lamb, Hydrodynamics 6th Edition, Cambridge University Press, 1932.

82. F. C. Hull, Metals Progress 96, p. 139 (1969).

83. C. S. Kim, Thermophysical Properties of Stainless Steels, Argonne National Laboratory, Argonne, IL, ANL-75-55, September 1975.

84. J. K. Fink, M. G. Chasanov, and L. Leibowitz, Thermodynamic Properties of Uranium Dioxide, Argonne National Laboratory, Argonne, IL, ANL-CEN-RSD-80-3, August 1980.

85. W. Eitel, Silicate Science Vol. 1, Academic Press, 1965.

86. Y. Bottinga and D. F. Weill, Am. J. Sci 269, p. 169 (1970).

87. C. R. Masson, J. Iron and Steel Inst. 192, p. 89 (1972).

88. C. H. P. Lupis, Chemical Thermodynamics of Materials, North-Holland Elsevier, 1983.

89. R. Defay, I. Prigogine, and A. Bellemans, Surface Tension and Adsorption (J. Wiley and Sons, Inc., 1966).

90. J. R. Grace, Trans. Inst. Chem. Eng. 51, p. 116 (1973).

91. J. R. Grace, T. Wairegi, and T. H. Nguyen, Trans. Inst. Chem. Eng. 54, p. 167 (1976).

92. R. Clift, J. R. Grace, and M. E. Weber, Bubbles, Drops, and Particles (Academic Press, 1978).

93. B. Rosenberg, Rept. No. 727, The David Taylor Model Basin, U.S. Navy Dept., 1950.

94. T. Takadi and S. Maeda, Chem. Eng. (Tokyo) 25, p. 254 (1961).

95. P. Savic, Nat'l. Res. Council Canad., Rept. No. MT-22, 1953.

96. A. I. Johnson and L. Braida, Canad. J. Chem. Eng. 35, p. 165 (1957).

97. W. N. Bond and D. A. Newton, Philos. Mag. 5, p. 794 (1928).

98. J. Barin and O. Knacke, Thermochemical Properties of Inorganic Substances (Springer-Verlag, 1973).

99. J. S. Hadamard, Compte. Rend. Acad. Sci. 152, p. 1735 (1911).

100. L. E. Scriven, Chem. Eng. Sci. 12, p. 98 (1960).

101. A. Frumkin and V. G. Levich, Zh. Fiz. Khim 21, p. 1183 (1947).

102. V. G. Levich, Physicochemical Hydrodynamics (Prentice-Hall, 1962).

103. R. Defay and I. Prigogine, Trans. Faraday Soc. 46, p. 199 (1950).

104. J. A. Redfield and G. Houghton, Chem. Eng. Sci. 20, p. 131 (1965).

105. R. D. Pehlke and J. F. Elliot, Trans. AIME 227, p. 844 (1963).

106. C. Bachhuber and C. Sanford, J. Appl. Physics 45, p. 2567 (1974).

107. P. R. Kry and R. List, Phys. Fluids 17, p. 1087 (1974).

108. P. R. Kry and R. List, Phys. Fluids 17, p. 1093 (1974).

109. R. List, U. W. Rentsch, A. C. Byram, and E. P. Lozowski, J. Atmos. Sci. 30, p. 653 (1973).

110. H. D. Mendelson, J. Am. Inst. Chem. Eng. 13, p. 250 (1967).

111. R. Comolet, C. R. Acad. Sci. Ser. A 272, p. 1213 (1971).

112. R. M. Davies and G. I. Taylor, Proc. Roy. Society Series A 200, p. 375 (1950).

113. T. Wairegi and J. R. Grace, Int'l. J. Multiphase Flow 3, p. 67 (1976).

114. P. H. Calderbank, "Mass Transfer," Chapter 6 in Mixing Theory and Practice, Volume II, V. W. Uhl and J. B. Gray, eds. (Academic Press, 1967).

115. A. C. Lochiel and P. H. Calderbank, Chem. Eng. Sci. 19, p. 471 (1964).

116. S. Winnikow, Chem. Eng. Sci 22, p. 477 (1967).

117. A. H. Abdel-Alim and A. E. Hamielec, Ind. Eng. Chem. Fundamentals 14, p. 308 (1975).

118. M. H. I. Baird and J. F. Davidson, Chem. Eng. Sci. 17, pp. 87-93 (1962).

119. E. Ruckenstein, Int. J. Heat and Mass Transfer 10, p. 1785 (1967).

120. B. T. Chao, J. Heat Tansfer 91, p. 273 (1969).

121. N. Konopliv and E. M. Sparrow, J. Heat Transfer 94, p. 266 (1972).

122. P. H. Calderbank and M. B. Moo-Young, Chem. Eng. Sci. 16, p. 39 (1961).

123. R. M. Griffith, Chem. Eng. Sci. 12, p. 198 (1960).

124. F. H. Deindoerfer and A. E. Humphrey, Ind. Eng. Chem. 53, p. 755 (1961).

125. A. B. Newman, Trans. Am. Inst. Chem. Eng. 27, p. 203 (1931).

126. R. Konig and J. C. Brink, Appl. Sci. Res. Sect. A 2, p. 142 (1950).

127. F. H. Garner and J. J. Lane, Trans. Am. Inst. Chem. Eng. 37, p. 162 (1959).

128. F. G. Blottner, Hydrodynamics and Heat Transfer Characteristics of Liquid Pools With Bubble Agitation, Sandia National Laboratories, Albuquerque, NM, NUREG/CR-0944, SAND79-1132, November 1979.

129. F. Yoshida and K. Akita, J. Am. Inst. Chem. Eng. 11, p. 9 (1965).

130. R. B. Bird, W. E. Stewart, and E. N. Lightfoot, Transport Phenomena (John Wiley and Sons, 1960).

131. R. C. Reid and J. M. Prausnitz, The Properties of Gases and Liquids, 3rd edition (McGraw Hill Book Co., 1977).

132. C. R. Wilke and P. Change, AICHE J 1, p. 264 (1955).

133. E. G. Scheibel, Ind. Eng. Chem. 46, p. 2007 (1954).

134. K. A. Reddy and L. K. Doraiswarmy, Ind. Eng. Chem. Fundamentals 10, p. 474 (1971).

135. C. F. Knight and B. A. Phillips, J. Nucl. Mater. 84, p. 196 (1979).

136. R. H. Lamoreaux and D. L. Hildenbrand, J. Phys. Chem. Ref. Data 13, p. 151 (1984).

137. W. Fritz, Physik 36, p. 379 (1965).

138. V. K. Dhir, J. N. Castle, and J. Patton, J. Heat Transfer 99, p. 411 (1977).

139. J. Szekely and G. P. Martins Trans. AIME 245, p. 629 (1969).

140. R. Clift and J. R. Grace, Chem. Eng. Sci. 27, p. 2309 (1972).

141. R. Clift, J. R. Grace, and M. E. Weber, Ind. Eng. Chem. Fundamentals 13, p. 45 (1974).

142. J. R. Grace, T. Wairegi, and J. Brophy, Canadian J. Chem. Eng. 56, p. 3 (1978).

143. J. O. Hirschfelder, C. F. Curtiss, and R. B. Bird, Molecular Theory of Gases and Liquids (J. Wiley, 1954).

144. E. R. Gilliland, Ind. Eng. Chem. 26, p. 681 (1934).

145. L. Andrussow, Z. Elektrochem. 54 p. 567 (1950).

146. K. Schafer, H. Corte, and H. Moesta, Z. Electrochem. Ang. Phys. Chem. 55, p. 662 (1951).

147. P. C. Singh and S. Singh, Int'l. Comm. Heat Mass Transfer 10, p. 123 (1983).

148. BOF Steelmaking Vol. 2 Theory, R. D. Pehlke, ed., AIME, 1975.

149. J. K. Fink, M. G. Chasanov, L. Leibowitz, Transport Properties of Uranium Dioxide, Argonne National Laboratories, Argonne, IL, ANL-CEN-RSD-80-4, September 1980.

150. R. E. Boni and G. Derge, Trans. AIME J. Metals, p. 53 (1956).

151. A. Dietzel, Kolloid Zeitschrift 100, p. 368 (1942).

152. E. C. Lyon, J. Am. Cer. Soc. 27, p. 186 (1944).

153. J. H. Swisher and E. T. Turkdogan, Trans. Metallurgical Society AIME, 239, p. 602 (1967).

154. K. Momma and H. Suto, Trans. Japanese Institute of Metals 1, p. 69 (1950).

155. L. S. Darken and R. W. Gurry, J. Amer. Chem. Soc. 68, p. 798 (1946).

156. P. Kozakevitch, Rev. Mét. 46, p. 505 (1949).

157. W. D. Kingery, J. Am. Ceram. Soc. 42, p. 6 (1959).

158. J. L. Bates, C. E. McNeilly, and J. J. Rasmussen, Battelle Northwest Laboratory, Richland, WA, BNWL-SA 3579, 1970.

159. H. C. Tsai and D. R. Olander, J. Nucl. Mat'ls. 44, p. 83 (1972).

160. D. A. Powers and F. E. Arellano, Large-Scale Transient Tests of the Interaction of Molten Steel With Concrete, Sandia National Laboratories, Albuquerque, NM, NUREG/CR-2282, SAND81-1753, January 1982.

161. D. A. Powers, "Chemical and Physical Processes of Reactor Core Meltdown." Chapter 4 in Core Meltdown Experimental Review, W. B. Murfin, ed., Sandia National Laboratories, Albuquerque, NM, NUREG/CR-0205, SAND74-0382 (revision), March 1977.

162. J. Kendell and K. P. Monroe, J. Am. Chem. Soc. 39, p. 1802 (1917).

163. Y. Bottinga and D. F. Weill, Am. J. Sci. 272, p. 438 (1972).

164. H. R. Shaw, Am. J. Sci. 272, p. 870 (1972).

165. S. M. Walas, Phase Equilibria in Chemical Engineering (Butterworths, 1985).

166. B. I. Lee and M. G. Kesler, AIChE Journal 21, p. 510 (1975).

167. J. M. Prausnitz, Molecular Thermodynamics of Fluid Phase Equilibria (Prentice Hall, 1969).

168. R. Hultgren, P. D. Desai, D. T. Hawkins, M. Gleiser, and K. K. Kelley, Selected Values of the Thermodynamic Properties of Binary Alloys (Amer. Society for Metals, 1973).

169. Old Testament; "Genesis," Chapter 29.

170. P. P. Budnikov, S. G. Tresvyatskii, and V. I. Kushakovskii, Proc. 2nd World Conference on the Peaceful Uses of Atomic Energy, Geneva, 1958.

171. S. M. Lange, F. P. Knudsen, C. L. Filmore, and R. S. Roth, Nat'l. Bureau of Standards Circular 568:17 (1956).

172. C. H. Lungu, Rev. de Phys. 7, p. 419 (1962).

173. W. A. Lambertson and M. H. Mueller, J. Am. Ceramic Soc. 36, p. 365 (1953).

174. P. K. Mast et al. Uncertainty in Radionuclide Release Under Specific LWR Accident Conditions Volume IV TC Analyses, SAND84-0410 Vol. IV Sandia National Laboratories, Albuquerque, NM, December 1985.

175. J. Williamson and F. P. Glasser, Science 148, p. 1589 (1965).

176. I. Ellezer, N. Ellezer, R. A. Howald, M. C. Verwolf, and P. Viswanadham, CALPHAD 3, p. 1 (1979).

177. D. M. Sanders and W. K. Haller, "A High-Temperature Apparatus for the Study of the Atmosphere Above Viscous, Incongruently Vaporizing Melts," Proc. 10th Materials Research Symposium on Characterization of High Temperature Vapors and Gases, Gaithersburg, MD, p. 111 (1978).

178. E. R. Plante, "Vapor Pressure Measurements of Potassium Over K_2O-SiO_2 Solutions by a Knudsen Effusion, Mass Spectroscopic Method," Proc. of the 10th Materials Research Symposium on Characterization of High Temperature Vapors and Gases, Gaithersburg, MD, p. 265 (1978).

179. C. Wagner, Thermodynamics of Alloys (Addison Wesley, 1952).

180. D. A. Powers, Behavior of Control During Core Degradation I: Pressurization of Silver-Indium Cadmium Control Rods, Sandia National Laboratories, Albuquerque, NM, SAND85-0469, October 1985.

181. G. V. Samsanov, The Oxide Handbook (Plenum Press, 1982).

182. J. C. Evans, E. L. Lepel, R. W. Sanders, C. L. Wilkerson, W. Silker, C. W. Thomas, K. H. Abel, and D. R. Robertson, Long-Lived Activation Products in Reactor Materials, Pacific Northwest Laboratory, Richland, WA, NUREG/CR-3474, August 1984.

183. M. Hansen, Constitution of Binary Alloys, 2nd edition (McGraw-Hill Book Co., 1958).

184. W. A. Fischer and A. Hoffman, Archive Eisenhüttenw 28, p. 738 (1957).

185. T. S. Jones, S. H. Kimura and A. Muan, J. Amer. Ceram. Soc. 50, p. 137 (1967).

186. P. V. Riboud and A. Muan, Trans. Metal. Soc. AIME 230, p. 88 (1964).

187. J. C. Cassdanne, Anais Acad. Bras. Ciene. 36, p. 13 (1964).

188. O. Levenspiel, Chemical Reaction Engineering (J. Wiley and Sons, 1962).

189. D. A. Powers, T. McNeil, R. S. Subramanian, R. Cole, and R. B. Sucha, J. Am. Ceram. Soc. 65, p. 289 (1982).

190. C. F. Cooper and J. A. Kitchner, J. Iron and Steel Instit. London, 193, p. 48 (1959).

191. J. H. Swisher and C. L. McCabe, Trans. Metall. Soc. AIME 230, p. 1669 (1964).

192. G. A. Hughmark, Ind. Eng. Chem. Design & Develop. 6, p. 218 (1967).

193. J. F. Muir and A. S. Benjamin, "Modelling of Molten Fuel/Concrete Interactions," Proc. ANS/ENS Topical Meeting on Thermal Reactor Safety, Knoxville, TN, CONF-800403/V-1, 1980.

194. H. Alsmeyer et al., A Model Describing the Interaction of a Core Melt with Concrete, Kernforschungszentrum Karlsruhe, West Germany, NUREG/TR-0039, translation of KfK-2395, October 1977.

195. J. F. Davidson and B. O. G. Schuler, Trans Inst. Chem. Eng. 38, p. 144 (1960).

196. J. F. Davidson and B. O. G. Schuler, Trans Inst. Chem. Eng. 38, p. 335 (1960).

197. R. Clift and J. R. Grace, Chem. Eng. Sci. 27, p. 705 (1972).

198. T. F. Abraham, Physics of Fluids 13, p. 2194 (1970).

199. J. R. Grace, T. Wairegi, and J. Brophy, Canad. J. Chem. Eng. 56, p. 3 (1978).

200. M. S. Plesset and C. G. Whipple, Physics of Fluids 17, p. 1 (1974).

201. A. C. Lochiel and P. H. Calderbank, Chem. Eng. Sci. 19, p. 471 (1964).

202. I. Kataoka and M. Ishii, Mechanistic Modeling and Correlations for Pool-Entrainment Phenomenon, Argonne National Laboratories, Argonne, IL, NUREG/CR-3304, ANL-83-37, April 1983.

203. I. Kataoka and M. Ishii, Int. J. Heat Mass Transfer 27, p. 1999 (1984).

204. T. Ginsberg, Nucl. Sci. and Eng. 89, p. 36 (1985).

205. T. Ginsberg, "Aerosol Generation From Sparging of Molten Pools of Corium by Gases Released During Core-Concrete Interactions," paper TS11.4, Proc. Int'l. Mtg. on LWR Severe Accident Evaluation, Cambridge, MA, August 28 to September 1, 1983.

206. A. M. Rozen, S. I. Golub, and T. I. Votintseva, Teploenergetika 23, p. 59 (1976).

207. A. M. Rozen, S. I. Golub, and I. F. Davydov, Soviet Physics - Doklady 19, p. 338 (1974).

208. Y. S. Touloukian, S. C. Saxena, and P. Hestermans, Thermophysical Properties of Matter Volume II Viscosity, IFI/Plenum.

209. L. von Bogdandy and H. D. Pantke, Stahl und Eisen 85, p. 721 (1965).

210. F. MacIntyre, Scientific American 230, p. 62 (1965).

211. Y. Toba, J. Oceanography Society of Japan 15, p. 3 (1959).

212. D. S. Azbel et al., "Acoustic Resonance Theory for the Rupture of Film Cap of a Gas Bubble at a Horizontal Gas-Liquid Interface," in Two Phase Momentum, Heat and Mass Transfer in Chemical Process and Energy Engineering Systems, Vol. 1 (Hemisphere Publ. Co., 1978), pp. 159-170.

213. M. Tomaides and K. T. Whitby, "Generation of Aerosols by Bursting of Single Bubbles", in Fine Particles, B. H. Y. Liu, Ed. (Academic Press, 1976).

214. F. H. Garner, S. R. M. Ellis, and J. A. Lacey, Trans. Instit. Chem. Engrs. 32, p. 222 (1954).

215. R. J. Cipriano and D. C. Blanchard, J. Geophys. Res. 86, Cq, p. 8085 (1981).

216. J. A. Day, Quarterly J. of the Royal Meteorological Society 90, p. 72 (1964).

217. Nucleation, A. C. Zetlemoyer, ed. (Marcel Dekker, Inc., 1969).

218. J. P. Hirth and G. M. Pound, Condensation and Evaporation--Nucleation and Growth Kinetics (Pergamon Press, 1963).

219. K. Nishioka and G. M. Pound, "Homogeneous Nucleation in Vapor," Chapter 4, Surface and Colloid Science, E. Matijevic, editor (J. Wiley and Sons, 1976).

220. F. F. Abraham, Homogeneous Nucleation Theory (Academic Press, 1974).

221. R. Becker and W. Doering, Ann. Phys. (Leipzig) 24, p. 719 (1935).

222. J. Loethe and G. M. Pound, J. Chem. Phys. 36, p. 2080 (1962).

223. J. Feder, K. C. Russel, J. Loethe, and G. M. Pound, Adv. Phys. 15, p. 111 (1966).

224. H. Reiss, J. I. Katz, E. R. Cohen, J. Chem. Phys. 48, p. 5553 (1968).

225. H. Reiss, J. Statistical Physics 2, p. 83 (1970).

226. M. Volmer and A. Weber, Z. Physik. Chem. (Leipzig) 119, p. 277 (1926).

227. K. C. Russell, J. Chem. Phys. 50, p. 1809 (1969).

228. J. R. Brock, J. Colloid and Interfacial Science 39, p. 32 (1972).

229. P. Middleton and J. Brock, J. Colloid Interfacial Science 54, p. 249 (1976).

230. J. R. Brock, "On Growth Processes of Condensation Aerosols," Transactions of the 28th Conference of Army Mathematicians, Bethesda, MD, June 1982.

231. T. E. Ramabhadran, T. W. Peterson, and J. H. Seinfeld, AIChE J. 22, p. 840 (1976).

232. M. Smoluchowski, Z. Phys. 16, p. 320 (1915).

233. M. Smoluchowski, Z. Phys. 17, p. 588 (1916).

234. J. T. Lindt and R. G. DeGroot, Chem. Eng. Sci. 29, p. 957 (1974).

235. A. Chatterjee, M. Kerker, and D. D. Cooke, J. Colloid and Interfacial Science 53, p. 71 (1975).

236. G. A. Nicolson and M. Kerker, "Brownian Coagulation of Aerosols at Low Knudsen Number," Faraday Symposia of The Chemical Society No. 7 Fogs and Smokes, pp. 133-142 (1974).

237. M. B. Ranade, D. T. Wasan, and R. Davies, AIChE J. 20, p. 273 (1974).

238. R. J. Ollerenshaw, Fundamental Processes Involved in the Formation of Metallurgical Fume, Warren Spring Laboratory, Stevenage, Hertfordshire SG12BX, United Kingdom, 1978.

239. G. Zebel, "Coagulation of Aerosols" in Aerosol Science, C. N. Davies, editor (Academic Press, 1966).

240. C. G. Granquist and R. A. Buhrman, Solid State Communications 18, p. 123 (1976).

241. N. A. Fuchs and A. G. Sutugrin, "Generation and Use of Monodisperse Aerosols," Aerosol Science, C. N. Davies, editor (Academic Press, 1966).

242. R. W. Hermsen and R. Dunlap, Combustion and Flame 13, p. 253 (1969).

243. G. D. Ulrich, Combustion Science Technology 4, p. 47 (1971).

244. C. L. Senior and R. C. Flagan, Aerosol Science and Technology 1, p. 371 (1982).

245. S. C. Graham and J. B. Homer, Faraday Symposia of the Chemical Society No. 7 Fogs and Smokes, pp. 85-86 (1974).

246. J. Corner, Proc. Royal Society (London) A211, p. 417 (1952).

247. J. Holmgren, J. D. Gibson, C. Sheer, J. Electrochem. Society 111, p. 362 (1964).

248. J. Amick and J. Turkevich, "Electron Microscopic Examination of Aerosols Formed in the Direct Arc," in Ultrafine Particles, W. E. Kuhn, editor (J. Wiley, 1963).

249. E. J. Davis, P. Ravindran, and A. K. Ray, Chem.Eng. Communications 5, p. 251 (1980).

250. R. L. Steinbergen and R. E. Treybal, AIChE J. 6, p. 227 (1960).

251. F. J. Moody, "Derivation of an Elliptical Suppression Pool Scrubbing Model," General Electric Co., 1983.

252. L. J. Flanigan et al., "Radionuclide Scrubbing in Water Pools: Bubble Hydrodynamics," Thermal-Hydraulics of Nuclear Reactors, Volume I, Proc. Second International Topical Meeting on Nuclear Thermal Hydraulics, American Nuclear Society, Santa Barbara, CA, January 11-14, 1983..

253. A. E. Handlos and T. Baron AIChE J. 3, p. 127 (1957).

254. J. E. Brockmann, "Uncertainties in Aerosol Removal by Suppression Pool Scrubbing," Appendix E in P. K. Mast et al., Uncertainty in Radionuclide Release Under Specific LWR Accident Conditions Volume IV: TC Analysis, Sandia National Laboratories, Albuquerque, NM, SAND84-0410/4.

255. F. Moody and S. G. Nagy, "Estimated Effects of Interfacial Vaporization on Fission Product Scrubbing," General Electric Co., 1983.

256. L. M. Milne-Thomson, Theoretical Hydrodynamics, Fifth edition (The MacMillan Co., 1968), p. 499.

257. A. G. Groff, A User's Manual for the ORIGEN2 Computer Code, Oak Ridge National Laboratory, Oak Ridge, TN, ORNL/TM-7175, 1980.

258. P. R. Bevington, Data Reduction and Error Analysis for the Physical Sciences (McGraw Hill Book Co., 1969).

259. D. A. Powers, "Elements, Isotopes, and Chemical Classes," Chapter 2 in Fission Product Behavior During Severe LWR Accidents - Modeling Recommendations for the MELCOR Code System, SAND85-2743, NUREG/CR-4481 Sandia National Laboratories, Albuquerque, NM.

260. J. Campserveux and P. Gerdanian, J. Solid State Chem. 23, p. 73 (1978).

261. R. J. Panlener and R. N. Blumenthal, AEC Report COO-1441-18 (1972).

262. Bulletin 542, U.S. Bureau of Mines (1954).

263. R. A. Robie, B. S. Hemingway, and J. R. Fisher, Thermodynamic Properties of Minerals and Related Substances at 298.15 K and 1 Bar Pressure and at Higher Temperatures, Geological Survey Bulletin 1452, 1978.

264. L. B. Pankratz, Thermodynamic Properties of Elements and Oxides, PB83-174052, U.S. Bureau of Mines, Albany, OR, 1983.

265. C. E. Holley, Jr., E. J. Huber, Jr., and F. B. Baker, "The Enthalpies, Entropies, and Gibbs Energies of Formation of the Rare Earth Oxides," Progress in the Science and Technology of the Rare Earths, L. Eyring, ed., Vol. 3 (Pergamon Press, 1968).

266. C. E. Wieks and F. E. Block, U.S. Bureau of Mines Bulletin 605 (1963).

267. A. Vahed and D. A. R. Kay, Metall. Trans. B 7B, p. 375 (1976).

268. E. G. King and A. U. Christensen, Jr., "High Temperature Heat Contents and Entropies of Cerium Dioxide and Columbium Dioxide," RI Bulletin 5789 (1961).

269. O. A. Mordovin, N. I. Timofeeva, and L. N. Drozdov, Izv. Nauk SSR, Neorgan. Mater. 3, p. 187 (1965).

270. M. Sherman et al., The Behavior of Hydrogen During Accidents in Light Water Reactors, Sandia National Laboratories, Albuquerque, NM, NUREG/CR-1561, SAND80-1495, August 1980.

271. S. R. Brinkley, J. Chem. Phys. 14, p. 563 (1946).

272. W. R. Smith and R. W. Missen, Chemical Reaction Equilibrium Analysis: Theory and Algorithms (J. Wiley and Sons, 1982).

273. H. J. Hancock and T. S. Motzkin, "Analysis of the Mathematical Model for Chemical Equilibrium," Proc. 1st Conf. High Temp. Systems 82-9 (1960).

274. D. A. Powers, Generation of Combustible Gases During Core Debris Interactions with Concrete, in preparation.

275. R. M. Erick and R. A. Sallach, "Fission Product Chemistry in the Primary System," Paper TS4.6-1, Proc. Int'l. Mtg. on LWR Severe Accident Evaluation, Cambridge, MA, 1983.

276. R. K. Woodley, CARBON 7, p. 609 (1969).

277. O. T. Sorensen, "Thermodynamics and Defect Structure of Nonstoichiometric Oxides," in Nonstoichiometric Oxides, O. T. Sorensen, ed. (Academic Press, 1981), Chapter 1.

278. P. E. Blackburn, J. Nucl. Materials 46, p. 244 (1973).

279. a. D. R. Stull and H. Prophet, JANAF Thermochemical Tables, 2nd Edition, NSRDS-NBS-37, Nat'l Bureau of Standards, June 1971.

b. M. W. Chase, Jr., J. L. Curnutt, A. T. Hu, H. Prophet, A. N. Syverud, and L. C. Walker, J. Phys. Chem. Ref. Data 3, p. 311 (1974).

c. M. W. Chase, Jr., J. L. Curnutt, H. Prophet, R. A. McDonald, and A. N. Syverud, J. Phys. Chem. Ref. Data 4, p. 1 (1975).

d. M. W. Chase, Jr., J. L. Curnutt, R. A. McDonald, and A. N. Syverud, J. Phys. Chem. Ref. Data 7, p. 793 (1978).

e. M. W. Chase, Jr., J. L. Curnutt, J. R. Downey, Jr., R. A. McDonald, A. N. Syverud, and E. A. Valenzuela, J. Phys. Chem. Ref. Data 11, p. 695 (1982).

280. F. MacIntyre, J. Geophys. Res. 77, p. 5211 (1972).

281. K. H. Sargent, Recent Advances with Oxygen in Iron and Steelmaking (Butterworths, 1964).

282. H. Jordan, J. A. Gieseke, and P. Baybutt, TRAP-MELT User's Manual, Battelle Columbus Laboratory, Columbus, OH, NUREG/CR-0632, BMI-2017, February 1979.

283. A. S. Damle, D. S. Ensor, and M. B. Ranade, Aerosol Science and Technology 1, p. 119 (1982).

284. B. P. LeClair and A. E. Hamielec, Canadian J. Chem. Eng. 49, p. 713 (1971).

285. J. F. Wilson, R. J. Grenda, and J. F. Patterson, Trans. ANS 5 (Series 25), p. 151 (1962).

286. L. S. Sterman, Soviet Physics, p. 1479 (1957).

287. D. D. Jackson, Thermodynamics of Gaseous Hydroxides, Lawrence Livermore Laboratory, Livermore, CA, UCRL-51137, December 1971.

288. K. C. Mills, Thermodynamic Data for Inorganic Sulphides, Selenides, and Tellurides (Butterworths, 1974).

289. J. B. Pedley and E. M. Marshall, J. Phys. Chem. Ref. Data 12, p. 967 (1983).

290. I. Barin, O. Knacke, and O. Kubachewski, Thermochemical Properties of Inorganic Substances, Supplement (Springer-Verlag, 1977).

291. D. D. Wagman et al., J. Phys. Chem. Reference Data 11 (1982) Supplement No. 2, "The NBS Tables of Chemical Thermodynamic Properties."

292. L. Haar, A. S. Friedman, and C. W. Beckett, Ideal Gas Thermodynamic Functions and Isotope Exchange Functions for the Diatomic Hydrides, Deuterides, and Tritides, NBS Monograph 20, National Bureau of Standards, May 1961.

293. R. Hultgren, P. D. Desai, D. T. Hawkins, M. Gleiser, K. K. Kelley, and D. D. Wagman, Selected Values of the Thermodynamic Properties of Elements, American Society for Metals, 1973.

294. F. Garisto, Thermodynamics of Iodine, Cesium, and Tellurium in the Primary Heat Transport System Under Accident Conditions, Atomic Energy of Canada Limited, Pinawa, Manitoba, AECL-7782, November 1982.

295. O. Glemser and A. Müller, Z. Anorg. Allg. Chem. 334, p. 150 (1964).

296. N. Ellezer, R. Howard, M. Marinkovic, and I. Ellezer, J. Phys. Chem. 82, p. 1021 (1978).

297. I. Ellezer, N. Ellezer, R. A. Howard, and M. Verwolf, J. Phys. Chem. 82, p. 2080 (1978).

298. O. Glemser, R. Haeseler, and A. Müller, Z. Anorg. Allg. Chem. 329, p. 51 (1964).

299. C. Alexander, unpublished result.

300. D. W. Green, Tables of Thermodynamic Functions for Gaseous Thorium, Uranium, and Plutonium Oxides, Argonne National Laboratory, Argonne, IL, ANL-CEN-RSD-80-1, March 1980.

301. D. W. Green and L. Leibowitz, Vapor Pressures and Vapor Compositions in Equilibrium With Hypostoichiometric Uranium Dioxide at High Temperatures, Argonne National Laboratory, Argonne, IL, ANL-CEN-RSD-81-1, June 1981.

302. A. Rouanet, Hebd. Seances Acad. Sci. Series C 266, p. 908 (1968).

303. D. T. Vier, Thermal and Other Properties of Refractories, Los Alamos Scientific Laboratory, Los Alamos, CA, LA-5937-MS, 1975.

304. V. Piacente, G. Bardi, L. Malaspina, and A. Desider, J. Chem. Phys. 59, p. 31 (1973).

305. R. J. Ackermann and E. G. Rauh, J. Chem. Therm. 3, p. 609 (1971).

306. J. P. Couteres, R. Verges, and M. Foex, Rev. Haut. Temp. et des Refractaries 12, p. 181, (1975).

307. F. Sibieude and M. Foex, J. Nucl. Mater. 56, p. 229 (1975).

308. R. J. Ackermann and E. G. Rauh, J. Chem. Thermo. 3, p. 445 (1971).

309. Y. Ikeda, H. Ito, T. Mizuno, K. Amioka, and G. Matsumoto, High Temperature Science 16, p. 1 (1983).

310. R. P. Burns, G. DeMaria, J. Draowart, and R. T. Grimley, J. Chem. Phys. 32, p. 1363 (1960).

311. B. K. Kassnos and Yu. V. Trusthov, Russ. J. Inorg. Chem. 14, p. 5 (1969).

312. A. P. Malinauskus, J. W. Gooch, Jr., and J. D. Redman, Nuclear Applications and Technology 8, p. 52, (1970).

313. B. Rosen, Donnes Spectroscopiques relatives aux Molecules Diatomiques (Pergamon, 1970).

314. K. P. Huber and G. Hertzberg, Molecular Spectra and Molecular Structure IV. Constants of Diatomic Molecules (Van Nostrand Reinhold Co., 1979).

315. C. L. Sullivan, M. J. Zehe, and K. D. Carlson, High Temperature Science 6, p. 80 (1974).

316. S. R. Dharwadkar, S. N. Tripathi, M. D. Karkhanavala, and M. S. Chandrasekharaiah, "Thermodynamic Properties of Gaseous Uranium Hydroxide," IAEA-SM-190/132, Thermodynamics of Nuclear Materials, International Atomic Energy Agency, Vienna, Austria.

317. R. J. Ackermann, E. G. Rauh, and C. A. Alexander, High Temperature Science 7, p. 304 (1975).

318. E. Murad, J. Chem. Phys. 73, p. 1383 (1980).

319. I. Barin and O. Knacke, Thermochemical Properties of Inorganic Substances (Springer-Verlag, 1973).

320. J. L. Bates, C. A. Hinman and T. Kavada, J. Amer. Ceramic Soc. 50, p. 652 (1967).

321. R. S. McDowell, A. B. Asprey, and L. C. Hoskins, J. Chem. Phys. 56, p. 5712 (1972).

322. V. A. Muller, B. Krebs, S. J. Cyvin, and E. Diemann, Z. Anorg. Allgem. Chemi. 359, p. 194 (1968).

323. P. Thirugnanasambandam and S. Mohan, Indian J. Physics 49, p. 808 (1975).

324. S. R. Gunn, W. L. Jolly, and L. G. Green, J. Phys. Chem. 64, p. 1334 (1960).

325. J. H. Norman, H. G. Staley, and W. E. Bell, "Mass Spectroscopic Study of Noble Metal Oxides," Mass Spectrometry in Inorganic Chemistry, 1966.

326. H. Scheafer, A. Tebben, and W. Gerardt, Z. Anorg. Allgem. Chem. 321, p. 41 (1963).

327. T. D. Autokratov, Analytic Chemistry of Ruthenium, Israel Program of Scientific Translations, 1963.

328. W. E. Bell and M. Tagami, J. Phy. Chem. 67, p. 2432 (1963).

329. C. E. Moore, Atomic Energy Levels, U.S. Bureau of Standards Circular 467, Volumes I, II, and III.

330. L. Kaufman and H. Bernstein, Computer Calculation of Phase Diagrams (Academic Press, 1970).

331. L. Brewer and G. M. Rosenblatt, Chem. Rev. 61, p. 257, (1961).

332. A. D. Walsh, J. Chem. Soc., p. 2266 (1953).

333. E. B. Wilson, J. C. Decius, and P. C. Cross, Molecular Vibrations (McGraw-Hill, 1955).

334. W. C. Martin, Phys. Rev. A 3, p. 1810 (1971).

335. J. Hilsenrath, C. G. Messina, and W. H. Evans, Ideal Gas Thermodynamic Properties for 73 Atoms and Their First and Second Ions to 10,000°K, Kirtland AFB, Albuquerque, NM, TDR-64-44, 1964.

336. J. Kordis and K. A. Gingerich, J. Chem. Phys. 66, p. 483 (1977).

337. C. Cordiss and J. Sugar, J. Phys. Chem. Ref. Data 6, p. 1253 (1977).

338. J. H. Perry, C. H. Chilton, and S. D. Kirkpatrick, Chemical Engineers' Handbook, 4th Edition (McGraw-Hill Book Co., 1963).

339. F. E. Arellano and J. E. Brockmann, Sandia National Laboratories, Albuquerque, NM, ongoing work.

340. K. O. Reid, DF-1 Results and Analysis, Sandia National Laboratories, Albuquerque, NM.

341. R. A. Lorenz, E. C. Beahm, and R. P. Wichner, "Review of Tellurium Release Rates from LWR Fuel Elements Under Accident Conditions" Paper TS 4.4, Proceedings Int'l. Mtg. on LWR Severe Accident Evaluation, August 28 - September 1, 1983, Cambridge, Mass.

342. O. Kubaschewski, E. Ll. Evans, and C. B. Alcock, Metallurgical Thermochemistry, 4th Edition Pergamon Press, 1967.

343. C. R. Masson, I. B. Smith, and S. G. Whiteway, Canadian J. Chem. 48, p. 1456 (1970).

344. D. R. Gaskell, Metall. Trans. 4, p. 185 (1973).

345. M. L. Kapoor, G. M. Mehrotra, and M. G. Frohberg, Proc. Australasia Inst. Min. Metall. 254, p. 11 (1975).

346. C. F. Baes, Jr., J. Solid State Chem. 1, p. 159 (1979).

347. P. C. Hess, Geochimica et Cosmochimica Acta 35, p. 285 (1971).

348. Y. Bottinga, D. F. Weill, and P. Richet, in Thermodynamics of Minerals and Melts, R. C. Newton A. Navrotsky and B. J. Wood, editors (Springer-Verlag, 1981).

349. R. J. Charles, J. American Ceramic Soc. 50, p. 631 (1967).

350. D. W. Marguardt, J. Soc. Ind. Appl. Math. 11, p. 431 (1963).

351. D. A. Powers, "VANESA Sensitivity Study" in R. J. Lipinski et al., Uncertainty in Radionuclide Release Under Specific LWR Accident Conditions Volume II TMLB Analyses, SAND84-0410, Vol. 2. Sandia National Laboratories, Albuquerque, NM, May 1985.

352. D. A. Powers, "Sensitivity of the VANESA Model" Appendix D in Uncertainty in Radionuclide Release Under Specific LWR Accident Conditions Volume 4 TC Analyses, SAND84-0410 Vol. 4, Sandia National Laboratories, Albuquerque, NM.

353. D. A. Powers and D. R. Bradley, Some Causes of Uncertainty in Estimates of Ex-Vessel Radionuclide Release During Severe Accidents, NUREG/CR-4296 SAND85-1780, Sandia National Laboratories, Albuquerque, NM.

354. D. A. Powers and J. E. Brockmann, "A Mechanistic Model of Release of Radionuclides and Generation of Aerosols During Reactor Core Melt Interactions with Concrete" Presentation at the 16th Annual Meeting of the Fine Particle Society, Miami Beach, Florida, April 1985.

355. D. A. Powers, Thermochemical Data for the Analysis of Radionuclide Revaporization During Reactor Accidents - Systems Involving Cesium and Iodine, NUREG/CR-4578, SAND86-0750 Sandia National Laboratories, Albuquerque, NM.

356. The activity coefficients of both Na_2O and K_2O have been set to 10^{-8} irrespective of temperature or composition in most previous calculations with the VANESA code. This activity coefficient has been erroneously cited as 10^{-2} by the authors in some documents. More recent versions of the code use: $\ln(\gamma(K_2O)) = -0.570 - 37284/T + 53.6502x^2 - \ln(x)$ where x is the mole fraction of K_2O (see E. R. Plante, Proc. 10th Mat'ls Research Symp. on Characterization of High Temperature Vapors and Gases, Gaithersburg, MD, p 265 (1978)) and

$\ell n(\gamma(Na_2O)) = -0.08574 - 30700/T + 34.7562x^2 - \ell n(x)$ where x is the mole fraction of Na_2O (see D. M. Sanders and W. K. Haller, ibid., p 111). These expressions are appropriate for Na_2O and K_2O in silica melts. The compositional dependence must be considered quite uncertain for VANESA applications. The functional form of these activity coefficients are indicative of the types of activity coefficients that should be incorporated in the VANESA model for all species.

357. Older versions of the code used Nb_2O_5 as the condensed form of niobium.

APPENDIX

SIMILARITIES IN THE VAPORIZATION THERMODYNAMICS OF CERIUM, PLUTONIUM AND NEPTUNIUM OXIDES

The concept of "grouping" releases of radionuclides into classes represented by the behavior of particular members of each class is discussed in Chapter 4 of the main text. Grouping is an artifice used by most radionuclide release models, including the VANESA model, to avoid the expense of explicitly treating the release of all radionuclides. In the Reactor Safety Study (1) only seven classes of radionuclides were considered. Since the time of the Reactor Safety Study, larger numbers of radionuclide classes have been employed. In some cases, grouping the releases and behavior of a set of radionuclides is a transparent exercise that entails little error. Grouping the behavior of xenon and krypton is such an acceptable case. The grouping of other elements is not so obvious as grouping the noble gases. The adequacy of the approximate treatment of such groups can be evaluated only after explicit analyses have been made for each radionuclide.

A particularly large class of radionuclides considered in the Reactor Safety Study was one composed of the lanthanides, the actinides and other miscellaneous elements. Such broadly based grouping which encompasses an extensive range of chemical behavior has been avoided in the VANESA model. Nevertheless, yttrium and the lanthanides with the exception of cerium are grouped. The merits of the lanthanide group have been discussed in the main text of this document. In this appendix, detailed examinations of the behaviors of cerium, plutonium and neptunium are presented and the merits of grouping the release behavior of these radionuclides are discussed.

The attention devoted to this group really arises for two reasons. The first reason is the high radioactivity of neptunium. Because of the rapid decay of Np, this radionuclide could make inordinately large contributions to the consequences of radionuclide release(2). Estimates of its release behavior that are more accurate than can be achieved by grouping might be required. The second reason arises because of plutonium. The inventory of this element in irradiated fuel is not especially large in current reactors. There is interest, however, in using fuel to much higher burnups than is currently done. Increasing fuel burnup can cause substantially higher inventories of plutonium to be present. It might be necessary, then, to explicitly calculate the release behavior of plutonium rather than relying on an approximate treatment.

A) Simplistic Analysis of the Vaporization of Pure, Stoichiometric Oxides

Typical inventories of cerium, plutonium and neptunium in a light-water reactor core for the purposes of reactor accident analyses are (2):

Cerium	238 gram-atoms
Plutonium	1527 gram-atoms
Neptunium	33 gram-atoms

Within the approximations of the VANESA model, these elements partition preferentially into the oxide melt. They are treated as though they were CeO_2 (ℓ), $PuO_2(\ell)$ and $NpO_2(\ell)$ dissolved in an ideal solution. The release behavior for the group is based on the behavior of $CeO_2(\ell)$.

Inspection of the models of radionuclide release kinetics shows that little error should arise from grouping the behaviors of cerium, plutonium, and neptunium because of kinetic consideration. Significant errors associated with grouping are more likely to be the result of differences in the thermodynamics of vaporization of CeO_2, PuO_2 and NpO_2. As a first approximation in the search for substantial errors, the vaporization of the pure, liquid dioxides (which may be supercooled liquids) are examined in this appendix.

The thermodynamic data necessary to calculate the vapor pressure over $CeO_2(\ell)$ have been discussed in Chapter 4 of the main text of this report. For the analyses presented here, the only cerium-bearing vapor species to be considered are Ce(g), CeO(g), and CeO_2(g). This restriction is made because of limitations on the available data base for plutonium-bearing and neptunium-bearing vapor species.

Data necessary to calculate the vaporization behavior of $PuO_2(\ell)$ are assembled in Table A-1. The sources of these data are discussed below:

(1) Condensed Plutonium Dioxide

Green et al.(3) have recently surveyed the literature concerning plutonium dioxide. These authors have prepared a tabulation of single state data for PuO_2. The data for the solid, stoichiometric dioxide have been accepted here. Green et al. have estimated the heat of fusion of the stoichiometric dioxide to be 22540 cal/mole. This estimate was obtained by surveying the entropies of fusion per gram-atom for those materials listed in the JANAF Tables(4). The average value, 1.4

times the gas constant, was then taken as the entropy of fusion per gram-atom for PuO_2. This cannot be considered a highly reliable procedure. The melting point of stoichiometric PuO_2 was taken to be 2701K. The heat capacity of liquid PuO_2 was taken to be 22.94 cal/mole-K.

The estimates of the heat of fusion of PuO_2 obtained by Green et al. were accepted here, and the free-energy of liquid PuO_2 was found from:

$$G(PuO_2;\ell) = H_{Tm}(PuO_2;s) - T_m S_{Tm}(PuO_2;s) + \Delta H_m - T\Delta S_m$$
$$+ Cp(T - T_m) - TCp\ell n(T/T_m)$$

where T_m = 2701K, ΔH_m is the enthalpy of fusion and ΔS_m is the entropy of fusion

Free-energies of formation were found using thermochemical data for Pu in its reference state tabulated by Oetting et al.(5). Data for O_2 were from the JANAF Tables(4).

(2) Pu(g)

Thermochemical data for Pu(g) were taken from the tabulation by Oetting et al(5). These data were computed using 1075 energy levels up to 42823 cm^{-1}.

(3) PuO(g)

Green et al.(6) have published tabulated thermodynamic data for PuO(g) as have Pedley and Marshall(7). These tabulations are not in good agreement. There are some differences in molecular geometry and the Pu-O vibration frequency used by the two sets of authors. The bigger sources of differences arise, however, from the choices of the enthalpy of PuO(g) formation and the treatment of the electronic contributions to the thermodynamic properties of PuO(g). Pedley and Marshall took the enthalpy of formation of PuO(g) to be -29000 cal/mole. They calculated the thermodynamic functions considering the ground electronic state to be a singlet and neglecting any excited electronic states. Green, on the other hand, took the enthalpy of PuO(g) formation to be -21800 cal/mole and considered the possible presence of rather numerous electronic states. Green assumed energy levels to be present at

$$\epsilon_n = 260\ n \quad cm^{-1}$$

Table A-1. Free Energies of Formation of Neptunium and Plutonium Compounds

	ΔG_f (cal/mole)									
Temp	PuO_2(s)	PuO_2(ℓ)	Pu(g)	PuO(g)	PuO_2(g)	NpO_2(s)	NpO_2(ℓ)	Np(g)	NpO(g)	NpO_2(g)
500	-229374	-209568	68462	-32000	-111600	-234187	-214719	93667	-11437	-109273
600	-224618	-205645	66011	-33700	-111300	-229792	-211158	90465	-13205	-109275
700	-219909	-2018805	63632	-35400	-110800	-225329	-207530	87462	-14761	-109091
800	-215249	-198028	61319	-37000	-110400	-220888	-203923	84512	-16247	-108860
900	-210612	-194302	59055	-38600	-109900	-216411	-200281	81681	-17599	-108516
1000	-205975	-190577	56873	-40100	-109300	-211785	-196489	79078	-18702	-107942
1100	-201338	-186886	54724	-41500	-108800	-207150	-192689	76534	-19727	-107303
1200	-196773	-183236	52590	-42900	-108100	-202548	-188921	74026	-20694	-106623
1300	-192208	-179622	50468	-44300	-107500	-197962	-185170	71547	-21608	-105902
1400	-187620	-176041	48352	-45700	-106900	-193386	-181428	69095	-22473	-105143
1500	-183198	-172488	46239	-47000	-106200	-188849	-177726	66664	-23294	-104350
1600	-178752	-168965	44126	-48300	-105500	-184293	-174004	64252	-24072	-103526
1700	-174331	-165468	42010	-49500	-104900	-179782	-170328	61856	-24808	-102671
1800	-169933	-161995	39890	-50800	-104200	-175319	-166699	59474	-25509	-101787
1900	-165583	-158539	37764	-52000	-013400	-170832	-163047	57104	-26173	-100874
2000	-161233	-155108	35630	-53200	-102700	-166358	-159407	54743	-26802	-99935
2100	-156931	-151694	33488	-54400	-102000	-161941	-155825	52392	-27399	-98971
2200	-152629	-148299	31337	-55600	-101200	-157503	-152221	50047	-27967	-98981
2300	-148375	-144920	29178	-56800	-100500	-153147	-148700	47709	-28505	-96971
2400	-144144	-141558	27006	-57900	-99700	-148785	-145172	45378	-29014	-95936
2500	-139938	-138208	24825	-59100	-98900	-144469	-141691	43047	-29493	-94877
2600	-135755	-134873	22634	-60200	-98100	-140172	-138228	40722	-29948	-93798
2700	-131597	-131555	20432	-61300	-97300	-135890	-134781	38399	-30378	-92700
2800	-127402	-128247	18220	-62400	-96500	-131569	-131294	36080	-30831	-91581
2900	-123220	-124952	15997	-63400	-95700	-127239	-127799	33762	-31164	-90443
3000		-121672	13763	-64500	-94900	-122953	-124347	31446	-31522	-89288

where n is an integer. The degeneracies of the energy levels were found from

$$g_n = \frac{1}{1-0.9\epsilon_n/IP}$$

where IP is the ionization potential which is 47000 cm^{-1}.

Green's motivation for the involved treatment of electronic contributions to the thermodynamic functions of PuO(g) was prompted by experimentally determined properties of PuO(g) obtained by Ackermann et al.(8):

$$\Delta G_f(PuO;g) = -28500 - 9.7T \quad \text{for } 1600 < T < 2150K$$

Green preferred(9) this result based on second and third law analyses of the data(4) to results obtained by Battles et al.(10):

$$\Delta G_f(PuO;g) = -16840 - 10.25T$$

Some other experimental determinations of the free-energy of formation of PuO(g) reported in the literature are:

$$\Delta G_f(PuO;g) = -17500 + 19.275T \qquad \text{ref. 11}$$

$$\Delta G_f(PuO;g) = -20600 - 18.4T \qquad \text{ref. 12}$$

For the work here thermodynamic properties tabulated by Green have been used.

(3) $PuO_2(g)$

Again, the data tabulated by Green(6) have been adopted for $PuO_2(g)$. As with the data for PuO(g), these tabulated data involve rather complex contributions from electronic excitations. Energy levels were assumed to be at:

$$\epsilon_n = 670\ n\ cm^{-1}$$

and the degeneracies of the energy levels are found from:

$$g_n = \frac{1}{1 - \frac{0.9\epsilon_n}{75000}}$$

The experimental results of Ackermann et al.(8):

$$\Delta G_f(PuO_2;g) = -112600 + 6.6T$$

have been accepted in preference to those obtained by Battles et al.(10):

$$\Delta G_f(PuO_2;g) = -111590 + 14.23T$$

or results cited by Oetting(11):

$$\Delta G_f(PuO_2;g) = -114400 + 7.7T$$

Substantially less data are available concerning the neptunium oxides. The data that were used are summarized in Table A-1. The sources of these data are described below:

(1) Condensed Neptunium Dioxide

Ackermann et al.(13) suggest the free-energy of formation of $NpO_2(s)$ can be estimated as the numerical average of the free-energies of formation of $PuO_2(s)$ and $UO_2(s)$. They estimated the free-energy of formation of $NpO_2(s)$ in the temperature range of 1850 to 2475K to be:

$$\Delta G_f(NpO_2;s) = -254100 + 40.5T \quad cal/mole$$

Based on the suggestion of Ackermann et al., but using data for $PuO_2(s)$ from reference 3 and data for $UO_2(s)$ from reference 15, somewhat different values for the free-energy of formation of $NpO_2(s)$ were found here. The values in the temperature interval of 1800 to 2500K could be correlated by

$$\Delta G_f(NpO_2;s) = -254562 + 44.078T \text{ cal/mole}$$

The melting point of NpO_2 is 2833 ± 50K(16). Using procedures similar to those employed for estimating thermodynamic properties of melting PuO_2, the entropy of fusion of NpO_2 was estimated to be 8.345 cal/mole-K and the enthalpy of fusion was estimated to be 23640 cal/mole. The properties of $NpO_2(\ell)$ were then estimated using

$$G(NpO_2;\ell) = G(NpO_2;s) + \Delta H_m - T\Delta S_m$$

2) Np(g)

Data from the compilation assembled by Oetting et al.(5) were used here for Np(g).

3) $NpO(g)$

Data tabulated by Pedley and Marshall(7) were used.

4) $NpO_2(g)$

Thermodynamic functions of $NpO_2(g)$ were calculated assuming this molecule had the same geometry and vibrational characteristics as $PuO_2(g)$. The ground electronic state was assumed to be a triplet and excited electronic states were neglected. The enthalpy of formation was estimated to be -108000 cal/mole using the free-energy of NpO_2 sublimation in the temperature range 1850-2475K found by Ackermann et al.(13) and the data for $NpO_2(s)$ estimated as described above.

The free-energy data for all of the plutonium and neptunium compounds were correlated as described in Chapter 4 of the main text. Results of the correlations are shown in Table A-2.

No data were available to the authors concerning hydrides of plutonium and neptunium or for such species as $Pu_2(g)$, $Np_2(g)$, $(PuO)_2(g)$ or $(NpO_2)_2(g)$. Jackson(17) has estimated data for the monohydroxides and dihydroxides of plutonium and neptunium. There is little evidence these hydroxides are important species. As a consequence, the vapor pressure calculations described here are based on considering only the metal-bearing species M(g), MO(g) and $MO_2(g)$ where M = Ce, Pu, and Np.

Vapor pressures of the pure stoichiometric liquids $CeO_2(\ell)$, $NpO_2(\ell)$ and $PuO_2(\ell)$ are functions of both temperature and the ambient oxygen potentials. The calculated pressures of metal bearing vapors (P(M(g)) + P(MO(g)) + $P(MO_2(g))$ for temperatures between 1500 and 3000K are shown in figures A-1 and A-2 for $P(H_2)/P(H_2O)$ = 1 and 10^4, respectively.

When $P(H_2)/P(H_2O)$ = 1, cerium dioxide produces the highest pressure of metal-bearing species. The sum of the partial pressures of Ce(g), CeO(g), and $CeO_2(g)$ is greater by about a factor of thirty than the corresponding sum of partial pressures of plutonium-bearing species. The sum of the partial pressures of the plutonium species is, in turn, about a factor of 5 greater than the sum of the partial pressures of neptunium-bearing species.

When the ratio $P(H_2)/P(H_2O)$ is increased to 10^4, the sum of the partial pressures of Ce(g), CeO(g), and $CeO_2(g)$ is only about a factor of 3 greater than the sum for plutonium-bearing species. The sum for cerium is, however, much greater than the sum for neptunium-bearing species.

Table A-2. Correlation of the Thermodynamic Properties of Plutonium and Neptunium Species

Species	χ	Parameters* α_1	α_2	α_3	α_4	α_5	α_6	α_7	α_8
PuO_2(s)	2.6×10^{-4}	-189.547	-1068.71	2636.65	-1842.71	-41.6498	-0.103641	-879.206	-252796
PuO_2(ℓ)	7×10^{-8}	79.0825	1.00675	-2.40398	1.50936	23.0110	0.684890	0.888491	-230013
Pu(g)	1.1×10^{-7}	67.2102	91.4508	-149.698	64.6775	7.55133	0.161910	61.0424	82500
PuO(g)	8×10^{-6}	76.2459	1.21844	5.60209	6.68252	7.86304	0.268413	-13.8564	-21800
PuO_2(g)	8×10^{-6}	57.7605	-74.0127	193.233	-89.4502	4.11802	0.298147	-103.141	-112100
NpO_2(s)	9.0×10^{-5}	-58.8124	-422.842	+1046.86	-656.425	-11.5158	25.8014	-387.249	0
NpO_2(ℓ)	9.1×10^{-5}	-60.0787	-421.390	1043.47	-654.406	-11.4212	23.4384	-385.966	0
Np(g)	2.1×10^{-7}	70.2202	62.5433	-107.299	48.0975	7.26330	0.164678	45.5513	111100
NpO(g)	1.3×10^{-7}	65.1694	-21.4974	57.3425	-25.4511	4.76224	0.197511	-31.9986	-1000
NpO_2(g)	2.3×10^{-7}	69.0208	-47.3709	125.054	-55.5514	6.02024	0.299473	-69.2915	-108000

*$G(T) = \alpha_8 - T[\alpha_1 + \alpha_2 x + \alpha_3 x^2 + \alpha_4 x^3 + \alpha_5 \ln(x) + \alpha_6/x + \alpha_7 x \ln(x)]$

where

$x = T/10000$

Fit only over the range 298-3000 K.

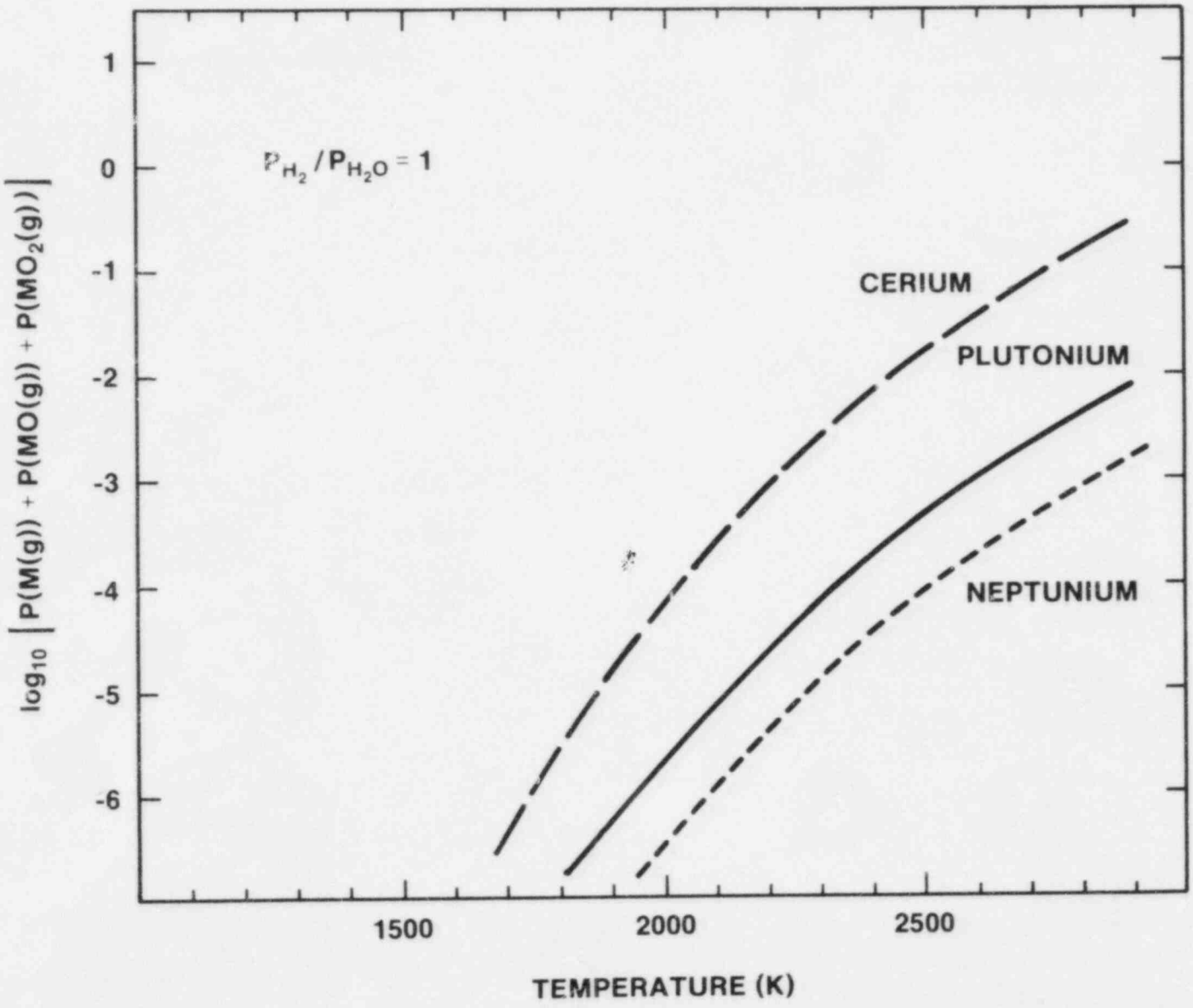

Figure A-1. Pressure of Metal-Bearing Species over $CeO_2(\ell)$ (long dashes) $PuO_2(\ell)$ (solid line) and $NpO_2(\ell)$ (short dashes) as Functions of Temperature for $P(H_2)/P(H_2O) = 1$

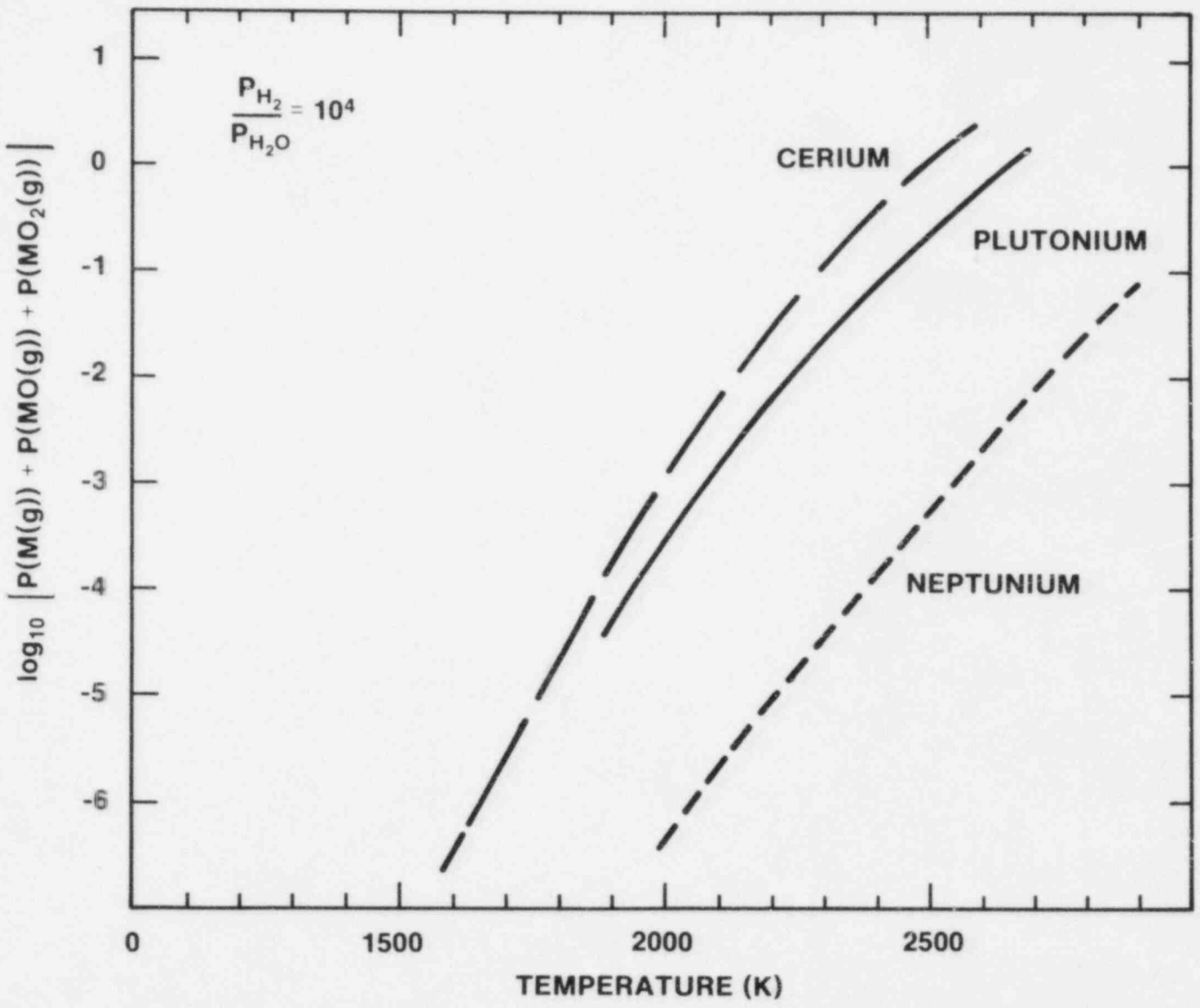

Figure A-2. Pressure of Metal-Bearing Species over $CeO_2(\ell)$ (long dash line), $PuO_2(\ell)$ (solid line), and $NpO_2O(\ell)$ (short dash line) as Functions of Temperature for $P(H_2)/P(H_2O) = 10^4$

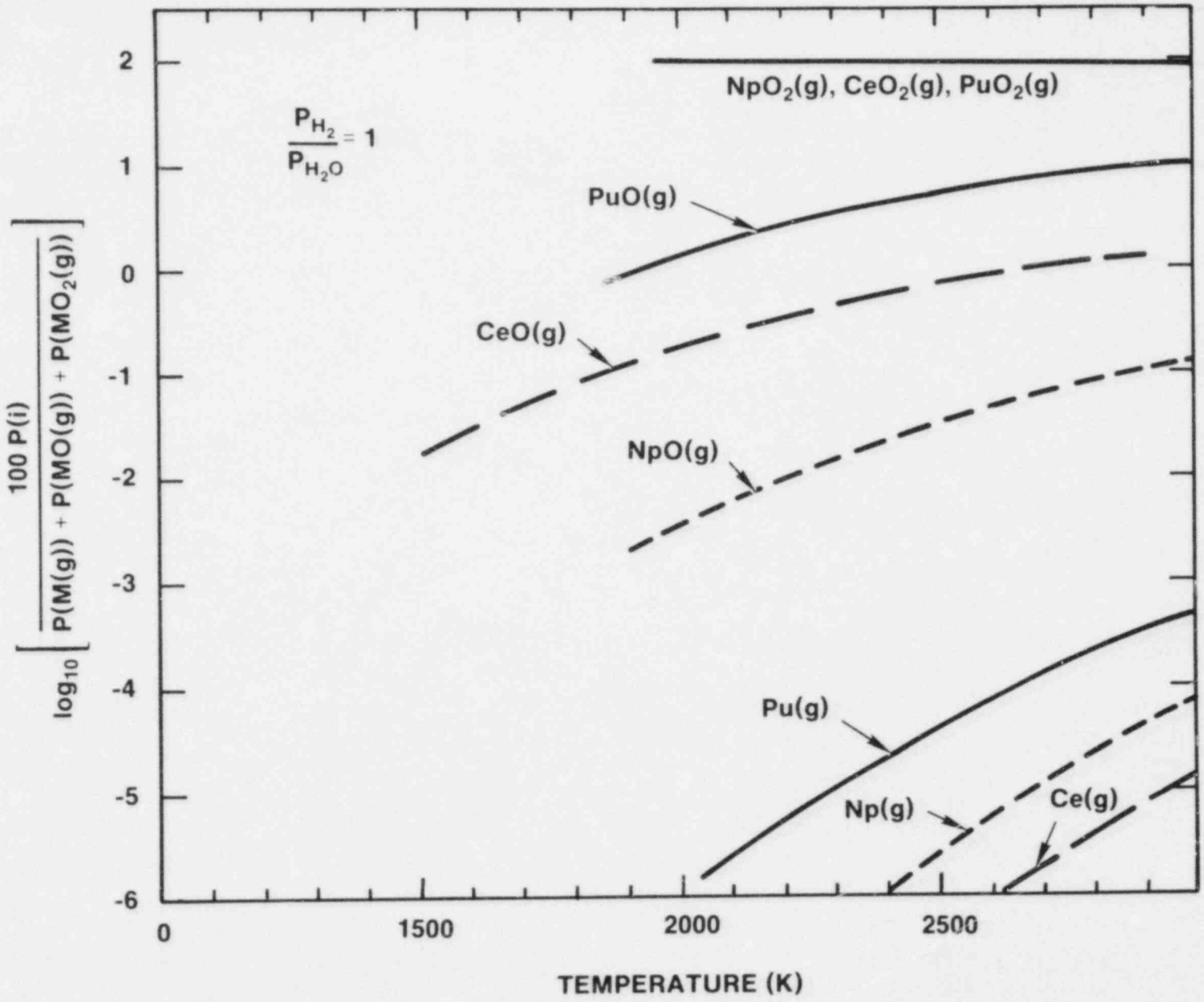

Figure A-3. Composition of Metal-Bearing Vapors Over Pure, Stoichiometric $CeO_2(\ell)$, $NpO_2(\ell)$ and $PuO_2(\ell)$ when $P(H_2)/P(H_2O) = 1$

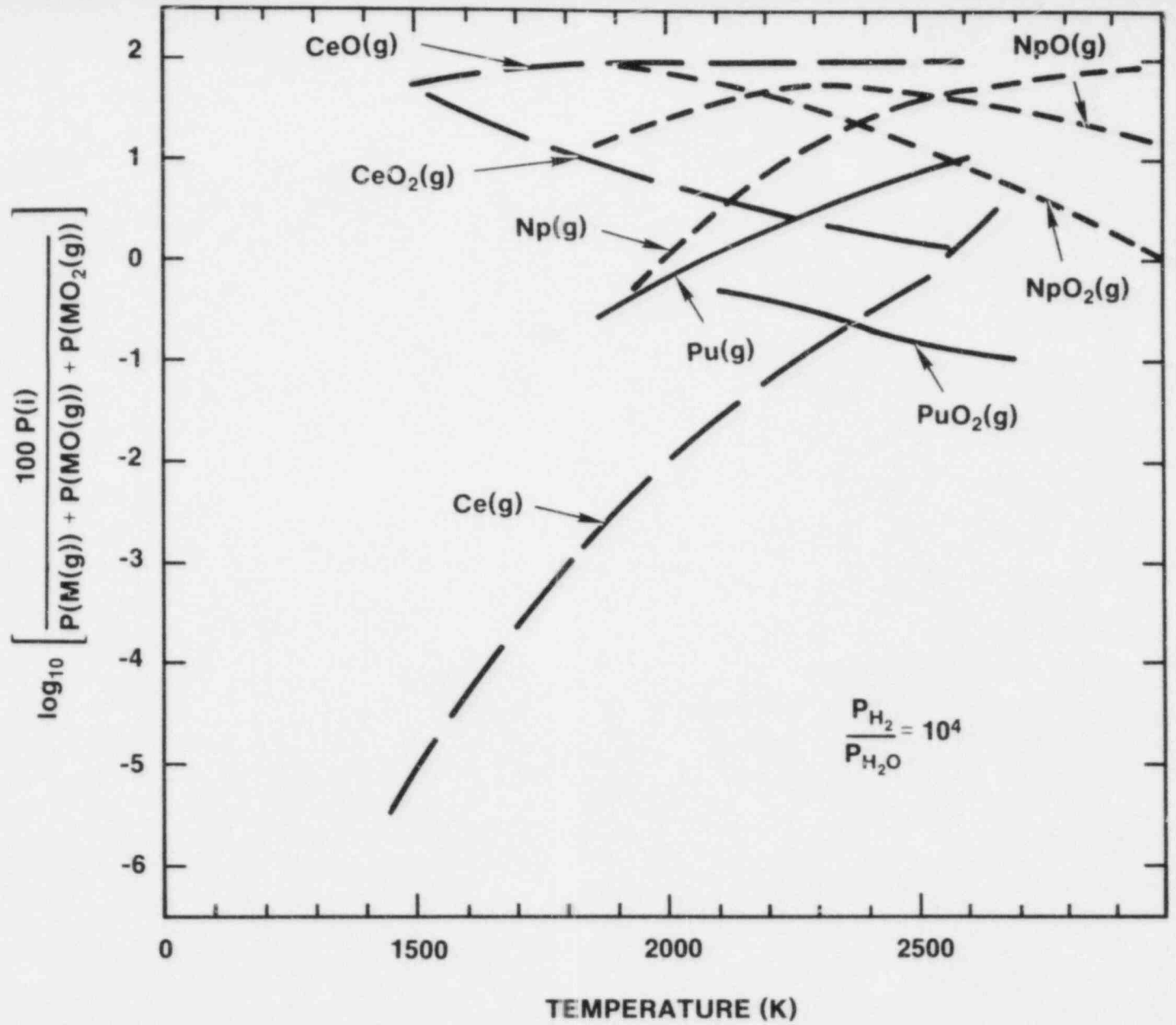

Figure A-4. Composition of Metal-Bearing Vapors Over Pure Stoichiometric $CeO_2(\ell)$ $NpO_2(\ell)$ and $PuO_2(\ell)$ when $P(H_2)/P(H_2O) = 10^4$

When $P(H_2)/P(H_2O) = 1$, the dominant vapor species over all the pure, liquid dioxides is the vapor phase dioxide (see Figure A-3). Relative to the corresponding monoxides and atomic vapors, $NpO_2(g)$ is more stable than either $CeO_2(g)$ or $PuO_2(g)$. Vapor compositions over the pure liquids are, however, similar in qualitative sense when $P(H_2)/P(H_2O) = 1$.

When $P(H_2)/P(H_2O) = 10^4$, the qualitative similarity in the vapor compositions is no longer seen (see Figure A-4). Though the relative contributions of dioxides, monoxides and atomic species are similar for cerium and plutonium, these relative contributions are quite different for neptunium over much of the temperature range because of the apparently higher stability of $NpO_2(g)$.

These results suggest that $CeO_2(\ell)$ may not be a good representative of the vaporization of $NpO_2(\ell)$. The results may, however, be more indicative of the poor quality of the thermodynamic data for NpO_2 and the neptunium-bearing vapor species than the errors attendant to "grouping" the vaporization behavior of CeO_2 and NpO_2. In any case, it is apparent that using cerium as the representative of the group composed of cerium, plutonium and neptunium will not lead to underprediction of plutonium and neptunium vapor pressures.

B) Effects of Non-Stoichiometry

In the section above, it was assumed that the dioxides of cerium, neptunium and plutonium were stoichiometric at all temperatures and oxygen potentials. In fact, it is well-established that cerium dioxide (18,19) and plutonium dioxide (3,9,20) exhibit broad ranges of stoichiometry at elevated temperatures. Above about 1000K there are two compounds in the Ce-O system - CeO_{2-x} where x can be as large as about 0.34 and $CeO_{1.5-y}$ where y is a function of temperature(19). Similarly, there are two compounds in the Pu-O system - PuO_{2-x} where x can be as large as 0.39 and $PuO_{1.5}$.

The authors are not aware of phase studies of the Np-O system that demonstrate the non-stoichiometry of NpO_2. The complexities of fragmentary studies of the Np-O system may well be evidence of non-stoichiometry.

The stoichimetry of CeO_{2-x} or PuO_{2-x} is a function of both temperature and the ambient oxygen potential. The stoichiometry can affect the vaporization as can be seen from the following general reaction:

$$MO_{2-x}(s) \leftrightharpoons (1-x)MO_2(g) + xMO(g)$$

and

$$MO(g) + 1/2\ O_2 \leftrightharpoons MO_2(g)$$

The thermodynamics of non-stoichiometric plutonium dioxide have been extensively studied. (For a review see reference number 20.) To illustrate the effects of non-stoichiometry, calculations including and neglecting this behavior were done and the results are shown in Figure A-5. Data published by Tetenbaum(9) on the free-energy of formation of PuO_{2-x} and the partial molar free energy of atomic oxygen were used to calculate the sum of the partial pressures of Pu(g), PuO(g) and PuO_2(g) as a function of the oxygen-to-metal ratio for the condensed phase. Results are shown as a solid line in Figure A-5. Then, the sum of the partial pressures were calculated for stoichiometric plutonium dioxide taking as the ambient oxygen potential that which would be in equilibrium with PuO_{2-x}. Tetenbaum's data for stoichiometric PuO_2 were used in these calculations. The results are shown in Figure A-5 as a dashed line. Comparison of the results shows that neglecting non-stoichiometry of plutonium dioxide leads to over-prediction of the vapor pressure. For modest non-stoichiometry the over-prediction is about a factor of 2. The over-prediction increases with the oxygen-to-metal ratio so that for $PuO_{1.69}$ the over-prediction amounts to about a factor of ten.

The error in the vapor pressure caused by neglecting non-stoichiometry may be compared to errors from other sources. For instance, uncertainty in the free-energy of formation of PuO_2 leads to uncertainty in the vapor pressure. The magnitude of this uncertainty can be seen by considering the calculation of vapor pressure over PuO_2 using data provided by Tetenbaum(9) and data provided by Greene et al.(3). These data from Greene et al. are recommended here. Results of calculations using the Tetenbaum data are shown in Figure A-5 as the dashed line. Results of calculations using the data from Greene et al. are shown in this figure as the dash-dot line. The discrepancies in the results are not large (less than a factor of two) and are nearly constant over the range of non-stoichiometries shown in Figure A-5.

Another source of error in the vapor pressure calculation is the uncertainty in thermodynamic properties of gaseous, plutonium-bearing, species. Typically, the limiting uncertainty in the thermodynamic properties of gaseous species is the enthalpy of formation. From Hultgren et al.(21) the uncertainty in the enthalpy of formation of Pu(g) is ± 500 cal/mole could be

ascribed to these data. Pedley and Marshall(7), on the other hand, considered the enthalpy of formation of PuO(g) to be uncertain by ± 8000 cal/mole. Here the uncertainty is taken to be ± 4000 cal/mole. Greene et al. were not confident in the thermodynamic properties of $PuO_2(g)$. An uncertainty of ± 5000 cal/mole can be derived from second and third law analyses of available data.

The effects of uncertainties in the thermodynamic properties of gaseous species are shown by repeating the calculations of the vapor pressure over PuO_{2-x} using data for the gases at the limits of the above uncertainty range. Again, Tetenbaum's data for non-stoichiometric plutonium dioxide were used for the calculations. Results are shown as dotted lines in Figure A-5. As can be seen, the span in vapor pressures is about a factor of 10 over the entire range of non-stoichiometries shown in the figure. The uncertainty in the vapor pressure caused by uncertainties in the vapor properties are consistent with uncertainties caused by neglecting non-stoichiometry of the condensed phase.

Several analytic models of the non-stoichiometry of PuO_2 have been developed. Bessman and Lindamer have prepared a correlational model(20). In this model the equilibrium partial pressure of oxygen over solid PuO_{2-x} is given by:

$$RT\ell nP_{O_2} = \left\{-196224 + 40.2653 - 3RT\ell n \left[\frac{1.5x(1-x/2)^{1/3}}{(1-2x)^{4/3}}\right] - \left[\frac{3x^2 - 12x + 3}{(1 - \frac{x}{2})^2}\right](15170 - 11.80T)\right\}$$

The free-energy of PuO_{2-x} can be found from

$$G(PuO_{2-x}) = G(PuO_2) - \frac{x}{2} G(O_2) - \frac{RT}{2}\int_o^x \ell nP_{O_2} dx$$

This result, the equilibrium oxygen partial pressure, and thermodynamic data for the vapor species are sufficient for the calculation of vapor pressures over the non-stoichiometric solid.

Green et al.(3) have described a somewhat more physical model based on the equilibrium:

$$2Pu^{4+} + O^{2-} \rightleftharpoons 2Pu^{3+} + 1/2\ O_2$$

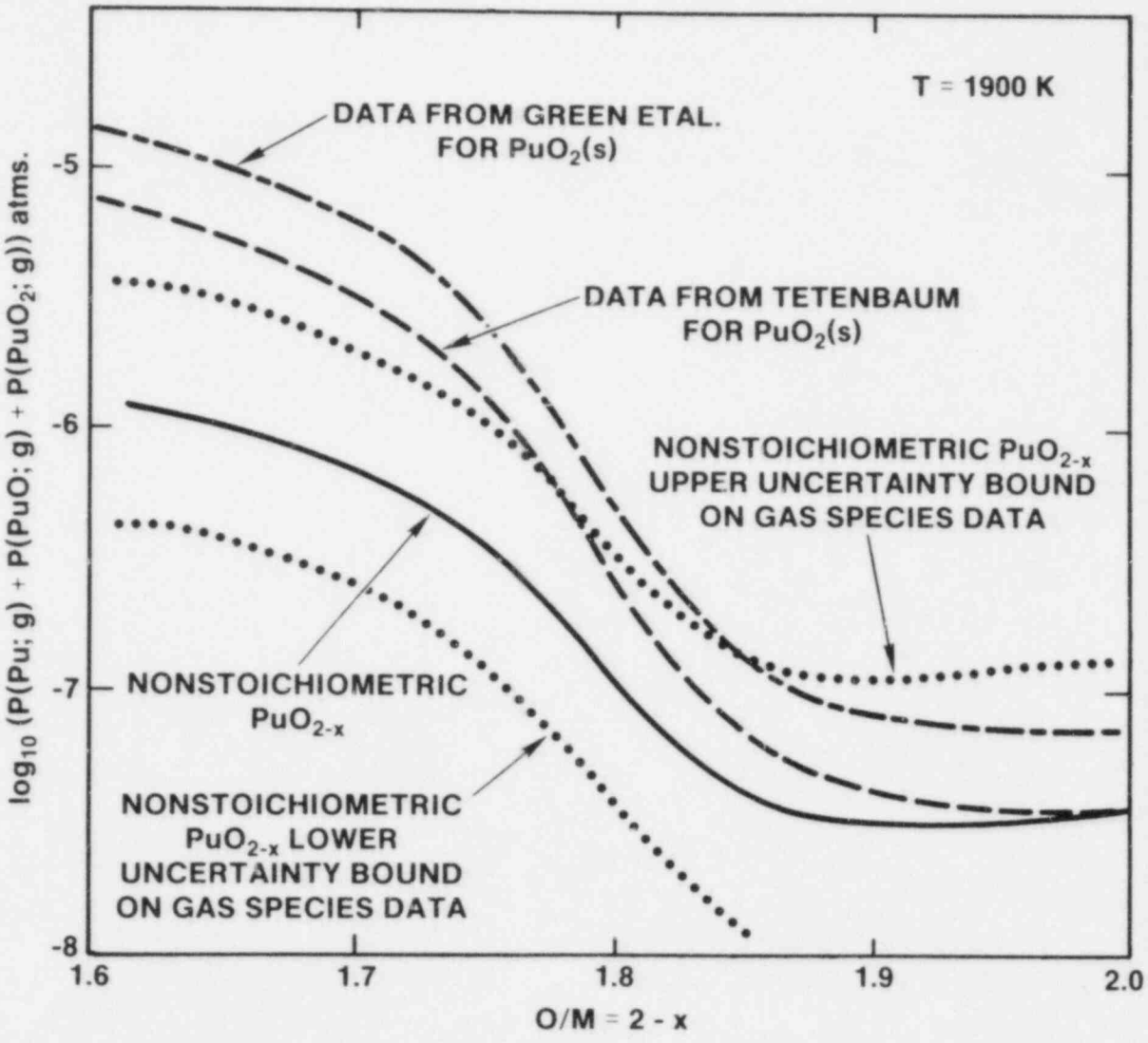

Figure A-5. Comparison of Vapor Pressures Calculated for PuO_{2-x} (solid line) and Vapor Pressures Calculated for PuO_2 (dashed line) at the Equilibrium Oxygen Partial Pressure for PuO_{2-x}. Comparisons are also shown for Vapor Pressure Recognizing Uncertainties in Vapor Species Thermodynamics.

TABLE A-3

Standard Free Energies of Formation of PuO_{2-x} and the Partial Molar Free Energy of Atomic Oxygen for $1600 < T < 2150K$

x	$\Delta G_f(PuO_{2-x}) = A + BT$ (cal/mole)		$\Delta G(O) = A' + B'T$ (cal/mole)	
	A	B	A'	B'
[A0	-249000	42.6	-204750	87.7
0.02	-246200	41.3	-181750	63.4
0.05	-242600	39.9	-178000	59
0.08	-239200	38.7	-173750	54.1
0.10	-237000	38	-171150	50.8
0.15	-231600	36.4	-164250	43.4
0.20	-226600	35.2	-157500	36.1
0.25	-222000	34.4	-151500	29.5
0.30	-217500	33.8	-149250	26.5
0.35	-213100	33.3	-150250	26.1
0.39	-209500	32.9	-153000	26.9

The model is restricted to regions for which $0.005 < x < 0.1$. The equilibrium partial pressure of oxygen is given by

$$nP_O = 4\ell n \left[\frac{(1 - 2x)}{2x}\right] + 2\ell n(2-x) + \ell n\ K_s$$

where for solid PuO_{2-x}

$$\ell n\ K_s = 20.8 - 101600/T$$

The free-energy of PuO_{2-x} is given by

$$G\left[PuO_{2-x}\right] = G\left[PuO_2\right] - \frac{x}{2} G\left[O_2\right] - \frac{RT}{2} \left\{-2(1-2x)\ell n(1-2x)\right.$$

$$+ 4(1-x)\ell n(2) - 4x\ell n(x) - 2x - 2(2-x)\ell n(2-x)$$

$$\left. + x\ \ell n\ K_s\right\}$$

This model is of interest because Green et al. also provide estimates of the effects of melting on the oxygen partial pressure over PuO_{2-x}. They indicate that the range of applicability of the model can be extended by also considering the equilibrium:

$$2Pu^{3+} + O^{2-} \leftrightharpoons 2Pu^{2+} + 1/2\ O_2$$

There are data in the literature(18) that could be used to formulate models of the non-stoichiometry of CeO_{2-x} similar to the models developed for PuO_{2-x}.

C) Conclusions

It is apparent from the analyses presented in this Appendix that releases of plutonium and neptunium are not underpredicted by the grouping procedure and the use of CeO_2 as the representative of the group. To the contrary, it is apparent that this approximation may lead to overprediction of these releases. In the case of plutonium, the overprediction is of the same order of magnitude as errors suggested by experimental data for the treatment of the lanthanides as a group represented by La_2O_3. The error in the predicted releases of neptunium can be much larger if the thermodynamic data cited here for $NpO_2(\ell)$ and neptunium-bearing vapor species are to be believed. Quite frankly, the authors do not have confidence in these data.

The analyses presented in this appendix also show the need to avoid any temptation to group releases if significance is to be attached to releases of elements not treated explicitly.

Explicit treatment of the releases of refractory radionuclides raises questions of whether non-stoichiometry should be included in the analyses. Results shown here for plutonium dioxide vaporization indicate that non-stoichiometry could affect vaporization. But, the effects are not especially dramatic. The complexities of reactor core melts may preclude detailed, a priori treatment of non-stoichiometry. Effects of non-stoichiometry may be treated adequately with empirically-determined activity coefficients.

REFERENCES

1. USNRC, The Reactor Safety Study - An Assessment of Accident Risks in U.S. Commercial Nuclear Power Plants, WASH 1400, NUREG-075/14, October, 1975.

2. D.J. Alpert, D.I. Chanin and L.T. Ritchie, Relative Importance of Individual Elements to Reactor Accident Consequences Assuming Equal Release Fractions, NUREG/CR-4467, SAND85-2575, Sandia National Laboratories, Albuquerque, NM, March, 1986.

3. D.W. Green, J.K. Fink, and L. Leibowitz, Vapor Pressures and Vapor Compositions in Equilibrium with Hypostoichiometric Plutonium Dioxide at High Temperatures. ANL-CEN-RSD-82-1, Argonne National Laboratories, Argonne, Illinois, June, 1982.

4. D.R. Stull and H. Prophet, JANAF Thermochemical Tables, Second Edition, NSRDS-NBS37, National Bureau of Standards, June, 1971.

5. F.L. Oetting, M.H. Rand, and R.J. Ackermann The Chemical Thermodynamics of Actinide Elements and Compounds Part 1 Actinide Elements, International Atomic Energy Agency, 1976.

6. D.W. Green, Calculation of the Thermodynamic Properties of Fuel-Vapor Species From Spectroscopic Data, ANL-CEN-RSD-80-2, Argonne National Laboratory, Argonne, Illinois, September, 1980. See also D.W. Green, Tables of Thermodynamic Functions for Gaseous Thorium, Uranium, and Plutonium Oxides, ANL-CEN-RSD-80-1, Argonne National Laboratory, Argonne, Illinois, March, 1980.

7. J.B. Pedley and E.M. Marshall, "Thermochemical Data for Gaseous Monoxides", J. Phys. Chem. Ref. Data 12 (1983) 967.

8. R. Ackermann, L.J. Faircloth, and M.H. Rand, J. Phys. Chem. 70 (1966) 3698. See also R.J. Ackermann and M.S. Chandrasekhariah, Thermodynamics of Nuclear Materials, 1974, International Atomic Energy Agency, 1975.

9. M. Tetenbaum, "Thermodynamic Aspects of the Plutonium-Oxygen System", Plutonium Chemistry, W.T. Carnall and G.R. Choppin, editors, American Chemical Society Symposium Series 216, 1983.

10. J.E. Battles, W.A. Shinn, and J.W. Reishus, ANL-7575 p.77, Argonne National Laboratories, Argonne, Illinois.

11. F.L. Oetting, Chemical Review 67 (1967) 261.

12. R.J. Ackermann and R.J. Thorn, Thermodynamics of Nuclear Materials 1962, International Atomic Energy Agency, Vienna, Austria.

13. R.J. Ackermann, R.L. Faircloth, E.G. Rauh and R.J. Thorn, J. Inorg. Nucl. Chem. 28 (1566) 111.

14. I. Barin, O. Knacke, and O. Kubaschewski, Thermochemical Properties of Inorganic Substances - Supplement, Springer Verlag, 1977.

15. D.W. Green and L. Leibowitz, Vapor Pressures and Vapor Compositions in Equilibrium with Hypostoichiometric Uranium Dioxide At High Temperatures, ANL-CEN-RSE-81-1, Argonne National Laboratory, Argonne, Illinois.

16. T.D. Chikalla, C. McNeilly, J.L. Bates, and J.J. Rasmussen, Colloq. Int. Cent. Nat. Rech. Sci. 205 (1972) 351. See also BNWL-SA-3818.

17. D.D. Jackson, Thermodynamics of Gaseous Hydroxides, UCRL-51137, Lawrence Livermore Laboratory, Livermore, California, December, 1971.

18. R.J. Panlener and R.N. Blumenthal, A Thermodynamic Study of Nonstoichiometric Cerium Dioxide, COO-1441-18, AEC Report, 1972.

19. R.J. Ackermann and E.G. Rauh, J. Chem. Thermodynamics 3 (1971) 609.

20. T. Bessman and T. Lindamer, J. Nucl. Materials,130 (1985) 489.

21. R. Hultgren, P.D. Desai, D.T. Hawkins, M. Gleiser, K.K. Kelley, and D.D. Wagman, Selected Values of the Thermodynamic Properties of Elements, American Society for Metals, 1973.

DISTRIBUTION:

U.S. Government Printing Office
Receiving Branch (Attn: NRC Stock)
8610 Cherry Lane
Laurel, MD 20707
365 copies for R3, R4, R7

U.S. Nuclear Regulatory
Commission (19)
Office of Nuclear Regulatory Research
Washington, DC 20555
Attn: M. Ernst
C. N. Kelber
R. T. Curtis
M. Silberberg
G. Marino
L. Chan
C. Ryder
R. W. Wright
T. Walker
R. O. Meyer
J. Mitchell
S. B. Burson (5)
T. Lee
M. Cunningham
P. Wood

U.S. Nuclear Regulatory Commission
Office of Nuclear Reactor Research
Washington, DC 20555
Attn: L. G. Hulman
P. Easky
J. Rosenthal
B. Hardin
Z. Rosztoczy
R. Barrett

U.S. Department of Energy (2)
Albuquerque Operations Office
P. O. Box 5400
Albuquerque, NM 87185
Attn: J. R. Roeder, Director
J. A. Morley, Director
For: C. B. Quinn
R. N. Holton

U.S. Department of Energy
Office of Nuclear Safety Coordination
Washington, DC 20545
Attn: R. W. Barber

Electric Power Research Institute (3)
3412 Hillview Avenue
Palo Alto, CA 94303
Attn: R. Vogel
R. Ritzman
W. Lowonstein

Brookhaven National Laboratory
Upton, NY 11973
Attn: R. A. Bari
T. Pratt
G. Greene
T. Ginsberg

Professor R. Seale
Department of Nuclear Engineering
University of Arizona
Tucson, Az 85721

Oak Ridge National Laboratory
P. O. Box Y
Oak Ridge, TN 37830
Attn: T. Kress

K. Holtzclaw
General Electric--San Jose
Mail Code 682
175 Kurtner Avenue
San Jose, CA 95125

Argonne National Laboratory (4)
9700 S. Cass Avenue
Argonne, IL 60439
Attn: J. Rest
C. Johnson
L. Baker, Jr.
D. Cho

Cathy Anderson
Nuclear Safety Oversight Commission
1133 15th St., NW
Room 307
Washington, DC 20005

Battelle Columbus Laboratory (3)
505 King Avenue
Columbus, OH 43201
Attn: P. Cybulskis
R. Denning
J. Gieseke

J. E. Antill
Berkeley Nuclear Laboratory
Berkeley GL 139 PB
Gloucestershire
United Kingdom

W. G. Cunliffe
Bldg. 396
British Nuclear Fuels, Ltd.
Springfield Works
Salwick, Preston
Lancashire
United Kingdom

R. Deem
Power Authority State of NY
10 Columbus Circle
New York, NY 10019

Professor Agustine Alonso
E.T.S. Ingenieros Industriales
Jose Gutierrez Abascal, 2
28006 Madrid, Spain

Dr. Alfonso Perez
Departmento de Seguridad Nuclear
Junta de Energia Nuclear
Avenida Complutense, 22
Madrid - 3
Spain

R. Sherry
JAYCOR
P. O. Box 85154
San Diego, CA 92138

Los Alamos National Laboratories
P. O. Box 1663
Los Alamos, NM 87545
Attn: M. Stevenson

UCLA (2)
Nuclear Energy Laboratory
405 Hilgaard Avenue
Los Angeles, CA 90024
Attn: I. Catton
D. Okrent

University of Wisconsin
Nuclear Engineering Department
1500 Johnson Drive
Madison, WI 53706
Attn: M. L. Corradini

EG&G Idaho
Willow Creek Bldg, W-3
P. O. Box 1625
Idaho Falls, ID 83415
Attn: R. Hobbins

Battelle Pacific Northwest Laboratory
P. O. Box 999
Richland, WA 99352
Attn: M. Freshley

Wiktor Frid
Swedish State Power Board
S-162 FACH 87 VALLINGBY
Sweden

W. Stratton
2 Acoma Lane
Los Alamos, NM 87544

Gesellschaft fur Reaktorsicherheit
(GRS)
Postfach 101650
Glockengrasse 2
5000 Koeln 1
Federal Republic of Germany

Kraftwerk Union
Hammerbacher Strasse 1214
Postfach 3220
D-8520 Erlangen 2
Federal Republic of Germany
Attn: Dr. M. Peehs

UKAEA
Reactor Development Division (5)
Winfrith, Dorchester
Dorset DT2 8DH
United Kingdom
Attn: R. Potter
A. Nichols
B. Bowsher
P. Smith
T. Butland

Nucleare e della Protenzione
Sanitaria (DISP) (2)
Ente Nazionale Energie Alternative
(ENEA)
Viale Regina Margherita, 125
Casella Postale M. 2358
I-00100 Roma A.D., Italy
Attn: Mr. Manilia
Mr. G. Petrangeli

Dr. K. J. Brinkman
Reactor Centrum Nederland
1755 ZG Petten
The Netherlands

Dr. S. J. Niemczyk
1545 18th Street, NW
#112
Washington, DC 20036

Kernforschungszentrum Karlsruhe
Postfach 3640
75 Karlsruhe
Federal Republic of Germany
Attn: H. Rininsland

M. H. Bairiot, Chief
Department LWR Fuel
Belgonucleaire
Rue de Champde Mars. 25
B-1050 Brussels, Belgium

Japan Atomic Energy Research
Institute
Tokai-Mura, Naka-Gun
Ibaraki-Ken 319-11
Japan
Attn: S. Saito

Wang Lu
TVA
400 Commerce, W9C157-CK
Knoxville, TN 37902

M. Fontana
Director, IDCOR Program
ENERGEX
575 Oak Ridge Turnpike
Oak Ridge, TN 37830

Fauske and Associates, Inc. (2)
16W070 West 83rd Street
Burr Ridge, IL 60521
Attn: R. Henry
M. Plys

Peter Bieniarz
Risk Management Associates
2309 Dietz Farm Road, NW
Albuquerque, NM 87107

Dr. K. Soda, Manager
Chemical Engineering Safety
Laboratory
Department of Nuclear Fuel Safety
Japan Atomic Energy Research
Institute
Tokai-Muri, Naku-Gun, Ibaraki-Ken
319-11
Japan

K. Sato, Director
Department of Reactor Safety Research
Japan Atomic Energy Research
Institute
Tokai-Mura, Naka-Gun, Ibaraki-Ken
319-11
Japan

P. Fehrenbach
Atomic Energy Canada, Ltd.
Chalk River, Ontario
Canada K0J 1J0

M. Hayns
UKAEA
Safety and Reliability Directorate
Wigshaw Lane
Culcheth
Warrington WA3 4NE
Cheshire
United Kingdom

J. R. Matthews
Aere Harwell
Didcot
Oxfordshire OX11 0RA
United Kingdom

F. Briscoe
UKAEE Culham Laboratory
Abingdon
Oxfordshire OX14 3DB
United Kingdom

H. J. Teague (3)
UKAEA
Safety and Reliability Directorate
Wigshaw Lane
Culcheth
Warrington, WA3 4NE
United Kingdom

M. Jankowski
IAEA
Division of Nuclear Reactor Safety
Wagranerstrasse 5
P. O. Box 100
A/1400 Vienna, Austria

Statens Karnkraftinspektion
L. Hammer
P. O. Box 27106
S-10252 Stockholm, Sweden

Studsvik Energiteknik AB
K. Johansson
S-611 82 Nykoping, Sweden

Atomic Energy Canada, Ltd.
M. Notley
Chalk River, Ontario
Canada K0J 1J0

Atomic Energy Canada, Ltd. (2)
Pinawa, Manitoba
Canada R0E 1L0
Attn: H. Rosinger
D. Wren

Korea Adv. Energy Research Inst.
H. R. Jun
P. O. Box 7
Daeduk-Danji
Choong-Nam, Korea

Institute of Nuclear Energy Research
Sen-I Chang
P. O. Box 3
Lungtan
Taiwan 325, Republic of China

1512 D. Rader
3141 S. A. Landenberger (5)
3151 W. L. Garner
6400 A. W. Snyder
6410 J. W. Hickman
6411 A. S. Benjamin
6412 A. L. Camp
6414 D. M. Ericson, Jr.
6414 A. W. Shiver (3)
6415 F. E. Haskin
6415 J. L. Sprung
6420 J. V. Walker
6421 P. S. Pickard
6422 D. A. Powers (5)
6422 M. D. Allen
6422 R. Blose
6422 J. E. Brockman (5)
6422 R. M. Elrick
6422 E. R. Copus
6422 W. W. Tarbell
6423 T. R. Schmidt
6425 D. R. Bradley
6425 W. J. Camp
6425 M. Pilch
6425 A. Suo-Anttila
6427 M. Berman
6440 D. A. Dahlgren
6442 W. A. von Riesemann
6444 R. K. Cole
6444 S. W. Webb
6449 K. D. Bergeron
6449 D. C. Williams
6454 G. L. Cano
7530 T. B. Lane
7537 N. R. Keltner
8024 P. W. Dean

NRC FORM 335 (2-84) NRCM 1102, 3201, 3202

U.S. NUCLEAR REGULATORY COMMISSION

BIBLIOGRAPHIC DATA SHEET

SEE INSTRUCTIONS ON THE REVERSE

1 REPORT NUMBER (Assigned by TIDC, add Vol. No., if any)
NUREG/CR-4308
SAND85-1370

2 TITLE AND SUBTITLE
VANESA: A Mechanistic Model of Radionuclide Release and Aerosol Generation During Core Debris Interactions With Concrete

3 LEAVE BLANK

4 DATE REPORT COMPLETED
MONTH: September YEAR: 1985

5 AUTHOR(S)
D.A. Powers, J.E. Brockmann, A.W. Shiver

6 DATE REPORT ISSUED
MONTH: July YEAR: 1986

7 PERFORMING ORGANIZATION NAME AND MAILING ADDRESS (Include Zip Code)
Sandia National Laboratories
P.O. Box 5800
Albuquerque, NM 87185

8 PROJECT/TASK/WORK UNIT NUMBER

9 FIN OR GRANT NUMBER
FIN #A1019

10 SPONSORING ORGANIZATION NAME AND MAILING ADDRESS (Include Zip Code)
Division of Accident Evaluation
U.S. Nuclear Regulatory Commission
Washington, DC 20555

11a TYPE OF REPORT

b PERIOD COVERED (Inclusive dates)

12 SUPPLEMENTARY NOTES

13 ABSTRACT (200 words or less)

This document describes a model, called VANESA, of the release of radionuclides and generation of aerosol accompanying reactor core melt interactions with structural concrete. The document also serves as a user's manual for an implementation of the VANESA model as a computer code. The technical bases for the VANESA model are reviewed. This review includes a description of the thermodynamics and kinetics of vaporization from melts sparged by gases evolving from concrete. The thermochemistries of 25 elements of interest in reactor accident analyses are described. Limitations to the rate of vaporization caused by condensed phase mass transport, surface processes, and gas phase mass transport are discussed. Limitations on the extent of vaporization caused by the behavior of bubbles rising in a melt are treated. Mechanical generation of aerosols as bubbles burst at melt surfaces or as a result of liquid entrainment is considered. A description of these processes based on data for gas-sparged water systems is included in the VANESA model. The document concludes with a description of a computer code implementation of the VANESA model. This implementation of the model was used in recent assessments of the behavior of radionuclides during severe reactor accidents. Comparisons of the predictions of radionuclide release during core debris/concrete interactions obtained with the VANESA model and with older models are presented.

14 DOCUMENT ANALYSIS - a KEYWORDS/DESCRIPTORS
Melt/concrete interactions, vaporization, kinetics, vaporization thermodynamics, thermochemistry, nucleation, condensation, aerosols, radionuclides, fission products, gas sparging, suppression pool, bubble behavior, mass transport, VANESA, CORCON, severe reactor accident

b IDENTIFIERS/OPEN ENDED TERMS

15 AVAILABILITY STATEMENT
GPO Sales
NTIS

16 SECURITY CLASSIFICATION
(This page) Unclassified
(This report) Unclassified

17 NUMBER OF PAGES
472

18 PRICE

☆ U.S. GOVERNMENT PRINTING OFFICE: 1986—676-049/41006